Transactions of the ASME

PUBLISHING STAFF
Mng. Dir., Publ., J. J. FREY
Director, Technical Publishing, JOS. SANSONE
Managing Editor, CORNELIA MONAHAN
Production Editor, JACK RUMMEL
Editorial Prod. Asst., BETH DARCHI

HEAT TRANSFER DIVISION
Chairman, A. S. RATHBUN, JR.
Secretary, F. A. KULACKI
Senior Technical Editor, K. T. YANG
Technical Editor, M. EPSTEIN
Technical Editor, G. M. FAETH
Technical Editor, R. H. PLETCHER
Technical Editor, V. E. SCHROCK
Technical Editor, R. K. SHAH
Technical Editor, R. SIEGEL
Technical Editor, R. VISKANTA

BOARD ON COMMUNICATIONS
Chairman and Vice President
MICHAEL J. RABINS

Members-at-Large
W. BEGELL,
J. CALLAHAN,
M. HELMICH,
D. KOENIG,
M. KUTZ,
F. LANDIS,
J. LOCKE,
J. ORTLOFF,
C. PHILLIPS,
K. REID

President, SERGE GRATCH
Executive Director & Secretary, BURKE E. NELSON
Treasurer, ROBERT A. BENNETT

Journal of Heat Transfer (ISSN 0022-1481) is edited and published quarterly at the offices of The American Society of Mechanical Engineers, United Engineering Center, 345 E. 47th St., New York, N. Y. 10017. ASME-TWX No. 710-581-5267, New York. Second-class postage paid at New York, N.Y., and at additional mailing offices.
CHANGES OF ADDRESS must be received at Society headquarters seven weeks before they are to be effective. Please send old label and new address.
PRICES: To members, $30.00, annually; to nonmembers, $60.00. Single copies, $20.00 each. Add $5.00 for postage to countries outside the United States and Canada.
STATEMENT from By-Laws. The Society shall not be responsible for statements or opinions advanced in papers or . . . printed in its publications (B7.1, para. 3).

INDEXED by the Engineering Index, Inc.

Journal of Heat Transfer

Published Quarterly by The American Society of Mechanical Engineers
VOLUME 104 • NUMBER 3 • August 1982

ANNOUNCEMENTS

409 Change of address form for subscribers

437 Mandatory excess-page charges

571 Call for papers: Second Symposium on Numerical and Physical Aspects of Aerodynamic Flows

572 Call for papers: International Conference on Numerical Methods in Thermal Problems

Inside back cover Information for authors

TECHNICAL PAPERS

397 Thermal Turbulent Boundary Layer Under Strong Adverse Pressure Gradient Near Separation
N. Afzal

403 Heat Convection in Annular Type Crevices
Shi-chune Yao and Ying Huei Hung

410 Corrugated-Duct Heat Transfer, Pressure Drop, and Flow Visualization
J. E. O'Brien and E. M. Sparrow

417 Multidimensional Numerical Modeling of Heat Exchangers
W. T. Sha, C.I. Yang, T. T. Kao, and S. M. Cho

426 Radiation Configuration Factors Between Disks and a Class of Axisymmetric Bodies (81-HT-56)
M. H. N. Naraghi and B. T. F. Chung

432 Optimal Finite Analytic Methods
R. Manohar and J. W. Stephenson

438 The Motion of Particles Inside a Droplet (81-WA/HT-45)
J. N. Chung

446 Heat Transfer From a Buoyant Plume to an Unconfined Ceiling (81-HT-7)
L. Y. Cooper

452 Laminar Wavy-Film Flow: Part I, Hydrodynamic Analysis (81-HT-13)
R. I. Hirshburg and L. W. Florschuetz

459 Laminar Wavy-Film Flow: Part II, Condensation and Evaporation (81-HT-14)
R. I. Hirshburg and L. W. Florschuetz

465 Heat Transfer From Vertical/Inclined Boundaries of Heat-Generating Boiling Pools
T. C. Chawla and S. H. Chan

474 Latent and Sensible Heat-Transfer Rates in the Boiling of Binary Mixtures (81-HT-28)
J. R. Thome

479 Lower Plenum Voiding
D. Bharathan, G. B. Wallis, and H. J. Richter

487 The Effect of Noncondensible Gases on Bubble Condensation in an Immiscible Liquid (79-WA/HT-26)
H. R. Jacobs and B. H. Major

493 Free Convection Heat Transfer From Upward-Facing Isothermal Horizontal Surfaces
W. W. Yousef, J. D. Tarasuk, and W. J. McKeen

501 Experiments on Free Convection Between Vertical Plates With Symmetric Heating
R. A. Wirtz and R. J. Stutzman

508 Two-Dimensional Study of Heat Transfer and Fluid Flow in a Natural Convection Loop
A. Mertol, R. Greif, and Y. Zvirin

515 Effect of Thermal Boundary Conditions on Natural Convection in Vertical and Inclined Air Layers
S. M. ElSheriby, K. G. T. Hollands, and G. D. Raithby

521 Measurements of Natural Convection Across Tilted Rectangular Enclosures of Aspect Ratio 0.1 and 0.2
R. A. Wirtz, J. Righi, and F. Zirilli

527 Experimental Investigation of Natural Convection in Partitioned Enclosures
S. M. Bajorek and J. R. Lloyd

533 Transient Natural Convection Experiments in Shallow Enclosures
R. Yewell, D. Poulikakos, and A. Bejan

(Contents Continued on Page 425)

(Contents Continued)

539 Heat Transfer Through a Double Pane Window
S. A. Korpela, Yee Lee, and J. E. Drummond

545 High Rayleigh Number Solutions to Problems of Latent Heat Thermal Energy Storage in a Horizontal Cylinder Capsule
T. Saitoh and K. Hirose

TECHNICAL NOTES

554 Laminar Mixed Convection From a Vertical Heated Surface in a Crossflow
G. H. Evans and O. A. Plumb

558 Mixed Convection Flow Over a Semi-Infinite Horizontal Plate With Vectored Mass Transfer
J. Dey

560 Buoyancy Effects on the Temperature Field in Downward Spreading Flames
R. A. Altenkirch, D. C. Winchester, and R. Eichhorn

563 Heat Transfer Between a Horizontal Cylinder and a Mixed Particle Size Fluidized Bed
D. R. Pitts, R. S. Figliola, and K. M. Hamlyn

565 An Approximate Model of Bubble Phase Convective Heat Transfer to a Horizontal Tube in a Large Particle Fluid Bed
R. L. Adams

567 Incipient Vapor Nucleation of Methanol From an Artificial Site-Uniform Superheat
T. R. Jemison, R. J. Rivers, and R. Cole

569 Film Breakdown and Bundle-Depth Effects in Horizontal-Tube, Falling-Film Evaporators
J. J. Lorenz and D. Yung

Thermal Turbulent Boundary Layer Under Strong Adverse Pressure Gradient Near Separation

N. Afzal[1]
International Centre for Theoretical Physics,
34100 Trieste, Italy

The problem of the thermal turbulent boundary layer under the influence of strong adverse pressure gradients near separation is analysed by the method of matched asymptotic expansions. The limit corresponding to the neighborhood of separation, as formulated by Afzal [3], is employed. The thermal boundary layer problem is analysed using the appropriate inner and outer expansions (both above the thermal wall layer). It is found by matching that there exists an inertial sublayer where temperature distribution obeys the inverse half power laws. The comparison of the theory with the measurement shows that the slope and intercept of the wall (inner) law may be regarded as universal numbers, whereas the intercept of outer law shows a linear dependence on $\tau_w/\delta p_x$.

1 Introduction

The problem of thermal turbulent boundary layer approaching separation under the influence of a strong adverse pressure gradient has received little attention in the literature. Perry, Bell, and Joubert [1] have analysed the temperature distribution in the wall region, but the agreement of their theory with the measurements is not satisfactory. Further, no attention is paid to describing the flow in the outer region, away from the wall. Tetervin [2] has studied the effects of pressure gradient on the heat transfer by estimating the Reynolds analogy factor. However, for large pressure gradients its utility is limited as the Reynolds analogy between momentum and heat transfer is not valid. Also, near separation the skin friction approaches zero and the Reynolds analogy factor become unbounded.

In this paper, the problem of the thermal turbulent boundary layer approaching separation is analysed using the method of matched asymptotic expansions. The corresponding momentum boundary layer problem has been studied by Afzal [3]. The momentum boundary layer, following the earlier work of Stratford and Townsend (see Townsend [4]) has been extensively studied. None of these proposals made so far is in satisfactory agreement with the experiments (Samuel and Joubert [5]). Recently Kader and Yaglom [6] have considered the problem using similarity and dimensional arguments. A detailed comparison of Kader and Yaglom [6] shows that while there are some similarities, the results [3] are different on a variety of points. It is shown that Afzal [3] has achieved a more rational solution to the problem, and the comparisons with experiments are also in better agreement.

2 Equations

The thermal boundary layer equations for the two-dimensional mean turbulent motion of an incompressible fluid are

$$\frac{\partial u}{\partial x}+\frac{\partial v}{\partial y}=0 \tag{1}$$

$$u\frac{\partial u}{\partial x}+v\frac{\partial u}{\partial y}=-p_x/\rho+\nu\frac{\partial^2 u}{\partial y^2}+\frac{\partial \tau}{\partial y}-\frac{\partial \Gamma}{\partial x} \tag{2}$$

$$p_x=-\rho U U_x \tag{3}$$

$$u\frac{\partial T}{\partial x}+v\frac{\partial T}{\partial y}=\frac{\nu}{\sigma}\frac{\partial^2 T}{\partial y^2}+\frac{\partial Q}{\partial y} \tag{4}$$

The boundary conditions are

$$y=0,\ u=v=\tau=\Gamma=Q=0,\ T=T_w(x) \tag{5}$$

$$y\to\infty\ u\to U(x);\ \tau,\Gamma,Q\to 0,\ T\to T_\infty \tag{6}$$

Here x and y are the coordinates measured along and normal to the surface, u and v are the mean velocity components in x and y directions, respectively, and T is the temperature. τ and Γ are Reynolds shear and normal stresses, and Q is the appropriate Reynolds heat flux. $U(x)$ is the freestream velocity, $U_x(x)$ is the streamwise velocity gradient, p_x is the pressure gradient, T_w and T_∞ are the wall and free stream temperatures. Further, ν is the kinematic molecular viscosity, ρ the density and σ is the molecular Prandtl number.

3 Velocity Profile

We here briefly describe the arguments of Afzal [3] for the momentum boundary layer approaching separation under the influence of an adverse pressure gradient. The chief non-dimensional parameters are

$$\begin{aligned} R_p&=U_p\delta/\nu, & \Lambda&=\tau_w/\delta p_x\\ U_p&=(\nu p_x/\rho)^{1/3}, & U_\delta&=(\delta p_x/\rho)^{1/2}\end{aligned} \tag{7}$$

where δ is the boundary layer thickness, and τ_w is the wall shear stress. The limit that is appropriate to the strong adverse pressure gradient boundary layer near separation (Afzal [3]) is

$$R_p\to\infty,\ \Lambda\to 0,\ \Lambda R_p=O(1) \tag{8}$$

The momentum boundary layer equations are analysed using the appropriate outer and inner expansions, both above a wall layer possibly scaling with τ_w and ν.

The outer variables are

$$x=-\int_0^x U_x/U\,dx,\ Y=y/\delta \tag{9}$$

$$u=U\partial F/\partial Y,\ \tau=U_\delta^2 G(X,Y),\ \Gamma=U_\delta^2\bar{\Gamma}(X,Y).$$

The outer limit is defined as X, Y fixed for $R_p\to\infty$, and the outer expansions are

$$\begin{aligned} F&=F_0(X,Y)+(U_\delta/U)F_1(X,Y)+0(U_\delta/U)\\ G&=G_0(X,Y)+(U_\delta/U)G_1(X,Y)+0(U_\delta/U)\\ \bar{\Gamma}&=\Gamma_0(X,Y)+0(1)\end{aligned} \tag{10}$$

[1] Permanent address: Department of Mechanical Engineering, Aligarh Muslim University, Aligarh 202001, India

Contributed by the Heat Transfer Division for publication in the JOURNAL OF HEAT TRANSFER. Manuscript received by the Heat Transfer Division February 3, 1981.

The lowest order terms lead to the equations that correspond to the development of a nonlinear wake. Under a constant eddy viscosity ($\nu_\tau = U\,\delta^*/R_s$, where δ^* is the displacement thickness and R_s is the universal eddy Reynolds number [4]) closure model and self-similar transformation

$$F_0(X,Y) = e\,h(\eta)$$
$$Y = e\,\eta$$
$$e^2 = -\beta\,U\,\delta^*/(\delta^2 U_x R_s)$$
$$\beta = a/(1+a) \tag{11}$$
$$a = U_x\delta/(U\,\delta_x)$$

the lowest order velocity profile is governed by

$$h''' + hh'' + \beta(1-h'^2) = 0 \tag{12}$$
$$h(0) = 0,\ h''(0) \simeq 0,\ h'(\infty) = 1$$

a Falkner-Skan equation for wakes. At the point of separation $h'(0) = 0$, the solution leads to $\beta = \beta_0 = -0.1988$, and the normalized profile is in very good agreement with the Coles wake function. An approximate solution of the above problem gives the velocity at the axis [7]

$$F_0'(X,0) = 1 - 1.363(1+2\beta)/(1+\beta) \tag{13}$$

needed for matching the outer expansions with the inner expansions. It may be pointed out that first of the relations (10) is different from the usual defect law as the reference velocity is not independent of Y.

The inner variables are

$$\xi = \int_0^x \frac{1}{\mathfrak{L}}\,dx,\ \zeta = yU_p/\nu \tag{14a}$$

$$u = U_p\frac{\partial f}{\partial \zeta}(\xi,\zeta),\ \tau = U_p^2 g(\xi,\zeta),\ \Gamma = U_p^2\gamma(\xi,\zeta) \tag{14b}$$

where $\mathfrak{L}(x)$ is the order of streamwise flow variations in the inner layer. The inner expansions are

$$f = f_1(\xi,\zeta) + 0(1) \tag{15}$$
$$g = g_1(\xi,\zeta) + 0(1)$$
$$\gamma = \gamma_1(\xi,\zeta) + 0(1)$$

The matching of the outer and inner expansions by Millikan's [8] argument shows that there exists an inertial sublayer where the velocity distribution obeys the half power laws

$$u/U_p = A(\wedge)\,\zeta^{1/2} + C(\wedge R_p),\ \zeta \to \infty \tag{16a}$$

$$u/U = F_0'(X,0) + (U_\delta/U)[A(\wedge)\,Y^{1/2} + D(X,\wedge,\beta,\ldots)],\ Y \to 0 \tag{16b}$$

along with the relation

$$F_0'(X,0) = C(\wedge R_p)\,U_p/U - D(X,\wedge,\beta,\ldots)U_\delta/U \tag{17}$$

Here $F_0^1(X, 0)$ is the velocity at the surface, given by the solution of Falkner - Skan equation (12) for wakes. The matching of Reynolds stress leads to

$$g_1 = \hat{\alpha}\zeta + \wedge R_p \quad \zeta \to \infty \tag{18a}$$

$$G_1 = \hat{\alpha}\,Y + \wedge \quad Y \to 0 \tag{18b}$$

where $\hat{\alpha}$ is a constant of order unity.

The comparison of present theory with all the two-dimensional measurements (Coles and Hirst [9]) for $\wedge \lesssim 0.2$ leads to the results [3, 7] given below

$$A = 3.5 + 19\wedge \tag{19}$$
$$C = 2.5\wedge R_p - 0.012(\wedge R_p)^2, 0 \le \wedge R_p \le 100$$
$$D = 0.65(\beta - \beta_0) + 0(\wedge)$$

4 Analysis for Thermal Boundary Layer

The thermal boundary layer equation (4) along with the boundary conditions (5) and (6) are analysed here in terms of inner and outer layers, both above the thermal wall layer, possibly scaling with surface heat flux q_w in addition to τ_w and ν.

Nomenclature

a = nondimensional velocity gradient
A_t = slope of inverse half power law
C_t = intercept of inverse half power wall law
C_p = specific heat
D_t = intercept of inverse half power outer law
$h(\eta)$ = self-similar lowest order outer velocity profile
H = shape factor
K = slope of law (64a)
L = outer scale of flow variation in x direction
$\mathfrak{L}$ = inner scale of flow variations in x direction
p = pressure
p_x = pressure gradient
q = nondimensional Reynolds heat flux in inner layer
q_w = heat flux at the wall
Q = Reynolds heat flux
$\tilde{Q}$ = nondimensional Reynolds heat flux in outer layer
R_L = local Reynolds number (UL/ν)
R_p = characteristic Reynolds number ($U_p\delta/\nu$)
R_s = eddy Reynolds number
R_x = local Reynolds number (Ux/ν)
St = Stanton number
T = temperature
T_p = inner scale for temperature
T_w = wall temperature
T_∞ = free stream temperature
T_δ = outer scale for temperature
u = streamwise flow velocity
$U(x)$ = free stream velocity
U_x = velocity gradient
U_p = inner scale for velocity
U_δ = outer scale for velocity
U_τ = friction velocity
x = coordinate along the wall
y = coordinate normal to the wall
X = nondimensional x-coordinate in outer layer
Y = outer variable
α = kinematic pressure gradient
β = pressure gradient parameter [a/(1 + a)]
β_0 = value of $\beta = -0.1988$ at separation
δ = boundary layer thickness
δ^* = displacement thickness
Γ = normal Reynolds stress
ϵ_p = inner scale for Reynolds heat flux
ϵ_δ = outer scale for Reynolds heat flux
ξ = nondimensional x-coordinate in inner layer
ζ = inner variable
η = similarity variable for outer layer
θ = nondimensional temperature in inner layer
ϑ = nondimensional temperature in outer layer
θ_τ = friction temperature
$\wedge$ = characteristic parameter ($\tau_w/\delta p_x$)
ν = molecular kinematic viscosity
ν_τ = eddy viscosity
ρ = density of fluid
σ = molecular Prandtl number
σ_t = turbulent Prandtl number
τ = Reynolds shear stress
τ_w = skin friction
Ω = kinematic heat flux at the wall

Subscript

x = total differentiation with respect to x

The inner limit is defined as ξ, ζ and σ fixed for $R_p \to \infty$. Let us consider the following inner variables

$$\theta = (T - T_w)/T_p \tag{20}$$

$$q = Q/\epsilon_p \tag{21}$$

where T_p and ϵ_p are the scales of temperature and Reynolds heat flux in the inner layer. Introducing these variables in the thermal boundary layer equation (4) and integrating once with respect to ζ we get

$$\sigma^{-1}\frac{\partial\theta}{\partial\zeta} + \frac{\epsilon_p}{T_p U_p} q = \frac{\Omega}{U_p T_p} + \frac{\nu}{U_p \mathfrak{L}} \int_0^\zeta \left[\frac{\partial f}{\partial\zeta}\frac{\partial\theta}{\partial\xi} - \frac{\partial f}{\partial\xi}\frac{\partial\theta}{\partial\zeta} + \left(\frac{dT_w}{T_p d\xi} + \frac{dT_p}{T_p d\xi}\theta \right) \frac{\partial f}{\partial\zeta} \right] d\zeta \tag{22}$$

and

$$\Omega = q_w/\rho C_p \tag{23}$$

In the inner region the molecular conduction and Reynolds heat flux are expected to be of equal order, implying

$$\epsilon_p = U_p T_p \tag{24}$$

If the surface heat flux q_w is nonzero, then the first term on the right hand side of (22) is also of order unity and this provides us the magnitude of the temperature fluctuation

$$T_p = \Omega/U_p \tag{25}$$

It therefore follows that the order of the Reynolds heat flux is the product of the orders of velocity fluctuation U_p and temperature fluctuation T_p.

The inner asymptotic expansions may be written as

$$T = T_w + T_p\theta_1(\xi,\zeta) + 0(T_p) \tag{26a}$$

$$Q = U_p T_p q_1(\xi,\zeta) + 0(U_p T_p) \tag{26b}$$

The leading terms satisfy the following equation

$$\sigma^{-1}\frac{\partial\theta_1}{\partial\zeta} + q_1 = 1 \tag{26c}$$

which shows that in the inner region the total heat flux is constant.

The outer limit is defined as X, Y fixed for $R_p \to \infty$. The outer variables are

$$\vartheta = T/T_\infty,\ \hat{Q} = Q/\epsilon_\delta \tag{27}$$

where ϵ_δ is the scale of Reynolds heat flux. The order of velocity fluctuation in the outer layer is U_δ [3]. If the order of temperature fluctuations in the outer layer is T_δ then it follows that ϵ_δ should be of order $U_\delta\ T_\delta$. Without loss of generality let

$$\epsilon_\delta = U_\delta\ T_\delta \tag{28}$$

In terms of outer variables (9), (27), and (28), the thermal boundary layer equation (4) becomes

$$b\frac{\partial\hat{Q}}{\partial Y} + CF\frac{\partial\vartheta}{\partial Y} + \frac{\partial F}{\partial X}\frac{\partial\vartheta}{\partial Y} - \frac{\partial F}{\partial Y}\frac{\partial\vartheta}{\partial X} = \frac{\nu}{\sigma\delta^2 U_x}\frac{\partial^2\vartheta}{\partial Y^2} \tag{29}$$

where

$$b = \frac{T_\delta/T_\infty}{U_\delta/U} \tag{30a}$$

$$C = -\left(1 + \frac{\delta_x U}{U_x \delta}\right) \tag{30b}$$

As the outer scale for temperature is T_δ, the outer expansions for temperature and Reynolds heat flux may be written as

$$\vartheta = \vartheta_0(X,Y) + (T_\delta/T_\infty)\vartheta_1(X,Y) + \ldots \tag{31a}$$

$$\hat{Q} = Q_0(X,Y) + (T_\delta/T_\infty)Q_1(X,Y) + \ldots \tag{31b}$$

The equation governing the lowest order terms in (31) using (10) is given by

$$b\frac{\partial Q_0}{\partial Y} + CF_0\frac{\partial\vartheta_0}{\partial Y} + \frac{\partial F_0}{\partial X}\frac{\partial\vartheta_0}{\partial Y} - \frac{\partial F_0}{\partial Y}\frac{\partial\vartheta_0}{\partial X} = 0 \tag{32}$$

The first order terms in (31) are governed by

$$b\frac{\partial Q_1}{\partial Y} + CF_0\frac{\partial\vartheta_1}{\partial Y} + C_1\frac{\partial F_0}{\partial Y}\vartheta_1 + \frac{\partial F_0}{\partial X}\frac{\partial\vartheta_1}{\partial Y} - \frac{\partial F_0}{\partial Y}\frac{\partial\vartheta_1}{\partial X} + \left[(C + C_2)F_1\frac{\partial\vartheta_0}{\partial Y} + \frac{\partial F_1}{\partial X}\frac{\partial\vartheta_0}{\partial Y} - \frac{\partial F_1}{\partial Y}\frac{\partial\vartheta_0}{\partial X} \right]/b = 0 \tag{33}$$

where

$$C_1 = -\frac{U}{U_x}\frac{T_{\delta x}}{T_\delta} \tag{34a}$$

$$C_2 = -1 + \frac{U}{U_x}\frac{U_{\delta x}}{U_\delta} \tag{34b}$$

Here subscript x is used to denote the total differentiation with respect to x. The equations (32) and (33) represents the temperature distribution associated with the outer wake like flow.

The matching of inner and outer expansions is now carried out in the overlap domain. Using the conventional matching principle (Van Dyke [10]), the temperature distribution in inner and outer layer requires

$$\lim_{\substack{Y\ \text{fixed} \\ R_p \to \infty}} [T_w + T_p\theta_1(\xi,\zeta)] \sim \lim_{\substack{\zeta\ \text{fixed} \\ R_p \to \infty}} [T_\infty\vartheta_0(X,Y) + T_\delta\vartheta_1(X,Y)] \tag{35}$$

By applying the limit process, the above relation may be written, for fixed R_p, as

$$T_w + T_p\theta_1(\xi,\zeta\to\infty) \sim T_\infty\vartheta_0(X,Y\to 0) + T_\delta\vartheta_1(X,Y\to 0) \tag{36}$$

This is a functional equation, the solution of which is obtained by following the Milliken's [8] argument. Differentiating (36) with respect to y we get

$$\frac{U_p T_p}{\nu}\frac{\partial\theta_1}{\partial\zeta} \sim \frac{T_\infty}{\delta}\frac{\partial\vartheta_0}{\partial Y} + \frac{T_\delta}{\delta}\frac{\delta\vartheta_1}{\partial Y} \tag{37}$$

To proceed further we need to determine T_p/T_δ. The matching of the Reynolds heat flux expansions (26b) and (31b) demands

$$T_p U_p = T_\delta U_\delta \tag{38}$$

Eliminating T_p/T_δ between the relations (37) and (38), we get

$$\zeta^{3/2}\frac{\partial\theta_1}{\partial\zeta} = \frac{T_\infty}{T_\delta}Y^{3/2}\frac{\partial\vartheta_0}{\partial Y} + Y^{3/2}\frac{\partial\vartheta_1}{\partial Y} \tag{39}$$

To the lowest order we have

$$Y^{3/2}\frac{\partial\vartheta_0}{\partial Y} \to 0 \text{ as } Y\to 0 \tag{40}$$

and now the relation (39) reduces to

$$\zeta^{3/2}\frac{\partial\theta_1}{\partial\zeta} \sim Y^{3/2}\frac{\partial\vartheta_1}{\partial Y} \tag{41}$$

The relation (41) implies that each side should approach a function, say A_t, independent of ζ and Y. The solution to the equation (41) is

$$\theta_1 = A_t\zeta^{-1/2} - C_t,\ \zeta\to\infty \tag{42a}$$

$$\vartheta_1 = A_t Y^{-1/2} + D_t,\ Y\to 0 \tag{42b}$$

where C_t and D_t are functions of integration. Substituting (42) into (36) we get the relation for the heat transfer law as

$$T_w - T_\infty\vartheta_0(X,0) = T_p C_t + T_\delta D_t \tag{43}$$

The matching of Reynolds heat flux, similarly leads to

$$q_1(\xi,\zeta)\to 1 \quad , \quad \zeta\to\infty \tag{44a}$$

$$Q_0(X,Y)\to 1 \quad , \quad Y\to 0 \tag{44b}$$

It may be noted that in the matching procedure, the dependence of A_t, C_t, and D_t on the parameters of the problem remain hidden (Afzal [11]). As there is no common parameter in the inner (26) and outer equation (32), it is suggested that A_t may be a universal number. However, if the interaction of the thermal layer with the momentum layer is significant, then A_t could depend on the parameter $\wedge$ of the momentum boundary layer. Therefore, we write

$$A_t = A_t(\wedge) \tag{45}$$

Likewise, the intercept C_t in the wall law (42) could possibly depend on $\wedge R_p$ (a parameter of inner momentum layer). Further, if the inner thermal equation (26) contains σ as a parameter, the intercept C_t may be written as

$$C_t = C_t(\sigma,\wedge R_p) \tag{46}$$

Similarly, the dependence of outer law (42*b*) intercept D_t may be expressed as

$$D_t = D_t(X,\wedge,\beta,\chi_m,\ldots) \tag{47a}$$

where χ_m is defined by

$$\chi_m = \frac{U}{m}\frac{\partial m}{\partial U}, \; m=\delta, T_\delta \tag{47b}$$

It is instructive to analyse the outer temperature distribution by using a constant eddy conductivity closure model

$$Q = \frac{\nu_\tau}{\sigma_t}\frac{\partial T}{\partial y} \tag{48}$$

where σ_t is the turbulent Prandtl number. To the lowest-order relation (48), using (27) and (31) yields

$$\sigma_t b Q_0 = \frac{\nu_\tau}{\delta^2 U_x}\frac{\partial \vartheta_0}{\partial Y} \tag{49}$$

Substituting (49) in the order outer equation (32) and using the relations (11), we get

$$\sigma_t^{-1}\frac{\partial \vartheta_0}{\partial \eta^2} + h\frac{\partial \vartheta_0}{\partial \eta} - \frac{dh}{d\eta}\frac{\partial \vartheta_0}{\partial X} = 0 \tag{50}$$

The boundary condition at the outer edge is

$$\vartheta_0(X,\infty) = 1 \tag{51}$$

The matching condition (44*b*), along with the relations (11) and (49), gives a condition at the wall

$$\frac{\partial \vartheta_0}{\partial \eta}(X,0) = \sigma_t\beta(T_w/T_\infty - 1)\mathrm{St}(\delta R_s/\delta^*)^{1/2} \tag{52}$$

where St is a Stanton number defined by

$$\mathrm{St} = \frac{F}{U(T_w - T_\infty)} \tag{53}$$

It may be noted that at large Reynolds number the Stanton number is small and the right hand side of (52), as shown by data [1, 12], can be approximated to

$$\frac{\partial \vartheta_0}{\partial \eta}(X,0) \simeq 0 \tag{54}$$

Now the solution to equation (50), under boundary conditions (51) and (54), is

$$\vartheta_0(X,Y) = 1 \tag{55}$$

In view of relation (55), the outer expansion for temperature (31*a*) reduces to

$$T = T_\infty + T_\delta\vartheta_1(X,Y) + \ldots \tag{56}$$

a defect law of usual kind as reference temperature is independent of Y. Also in view of (55), the matching relations (43) for heat transfer law simplifies to

$$T_w - T_\infty = T_p C_t + T_\delta D_t \tag{57}$$

5 Results and Discussion

The main results of the present analysis for the temperature distribution in the overlap region of inner and outer layer are

$$(T - T_w)/T_p \sim A_t(\wedge)\zeta^{-1/2} - C_t(\sigma,\wedge R_p), \zeta\to\infty \tag{58}$$

$$(T - T_\infty)/T_\delta \sim A_t(\wedge)Y^{-1/2} + D_t(X,\wedge,\beta,\chi_m,\ldots), Y\to 0 \tag{59}$$

The relation (58) may be termed as the inner law and (59) as the outer law. The heat-transfer relation (57) may be expressed in terms of Stanton number (53) as

$$\mathrm{St}^{-1} = R_L^{1/2}C_t + (\delta/L)^{-1/2}D_t \tag{60}$$

Here R_L is a Reynolds number defined by

$$R_L = UL/\nu, \; L = -U/U_x \tag{61}$$

The inner and outer scales of temperature are related by

$$T_p U_p = T_\delta U_\delta = q_w/(\rho C_p) \tag{62}$$

A comparison of present theory with the measurements [1, 12] in air ($\sigma = 0.71$) is made. The data [12] in terms of inner and outer layer coordinates are displayed in Figs. 1 and 2, respectively. The figures show that the substantial inverse square root regions do, in fact, exist as proposed by relations (58) and (59). In view of the fact that the data covers a small range of $\wedge$, it is not possible to ascertain that slope A_t depends on $\wedge$. To a good engineering approximation the slope may be regarded as a constant, i.e., $A_t = -2.8$.

Figure 1 also shows that the inverse half-power law for temperature exists in the range $0.15 < (\nu/yU_p)^{1/2} < 0.35$. For the same data [12] the half-power law (16*a*) for velocity profile exists for the range $3 < (yU_p/\nu)^{1/2} < 10$ [7]. Therefore, the domains of validity of the half-power law for velocity distribution and inverse half-power law for temperature distribution are roughly the same. Further, the departure of the data in Fig. 1 from inverse half-power law for $(\nu/yU_p)^{1/2} < 0.15$ corresponds to the outer layer. This departure is due to the temperature distribution associated with the outer wake-like flow and may be analysed with the help of (32) and (33).

The expression (58) for inner (wall) law shows that intercept C_t is possibly not a universal function, and for a given σ could depend on $\wedge R_p$. The values of intercept C_t, from Fig. 1, are displayed in Fig. 3 against $\wedge R_p$. In the same figure, we have also displayed the value of C_t obtained from Fig. 13 of [1]. From the scatter in Fig. 3, it is not easy to ascertain that C_t depends on $\wedge R_p$, but $C_t = 3.6$ would not be inconsistent with the data. The inner law (58) may now be written as

$$(T_w - T)/T_p \sim 2.8(\nu/yU_p)^{1/2} + 3.6 \tag{63}$$

The relation (63) may be compared with the wall law of Perry et al. [1],

$$(T_w - T)/\theta_\tau = K(\sigma)(\alpha y/U^2)^{-1/2} + \Delta\theta_1/\theta_\tau \tag{64a}$$

$$\frac{\Delta\theta_1}{\theta_\tau} = \frac{\Delta\theta_1}{\theta_\tau}\left(\frac{U_\tau^3}{\alpha\nu}\right) \tag{64b}$$

where θ_τ ($= q_w/\rho C_p U_\tau$) is the friction temperature, U_τ is the friction velocity and α ($= P_x/\rho$) is the kinematic pressure gradient. The correlation (64*b*) for the intercept describes the data for $U_\tau^3/\alpha\nu \le 100$ (see their Fig. 13), and for $U_\tau^3/\alpha\nu > 100$ their correlation fails even though the pressure gradient is quite large. On the other hand, the present relation (63) not only describes all the data but also reveals the universality of the intercept. Further, the slope $K(\sigma)$ in their law (64*a*) depends on Prandtl number, σ, whereas the present relation (58) shows that the slope is independent of σ. If this were not

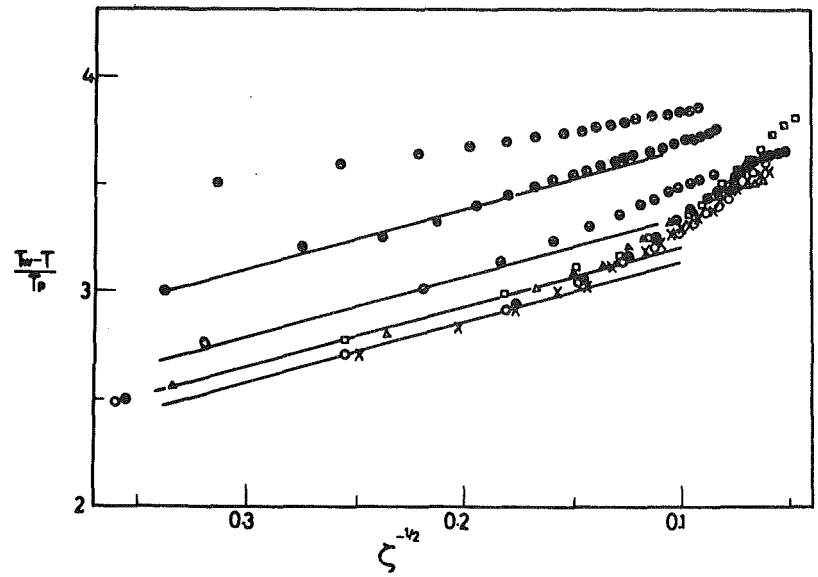

Fig. 1 Temperature distribution in law-of-the-wall (58) coordinates (for legend, see Fig. 2)

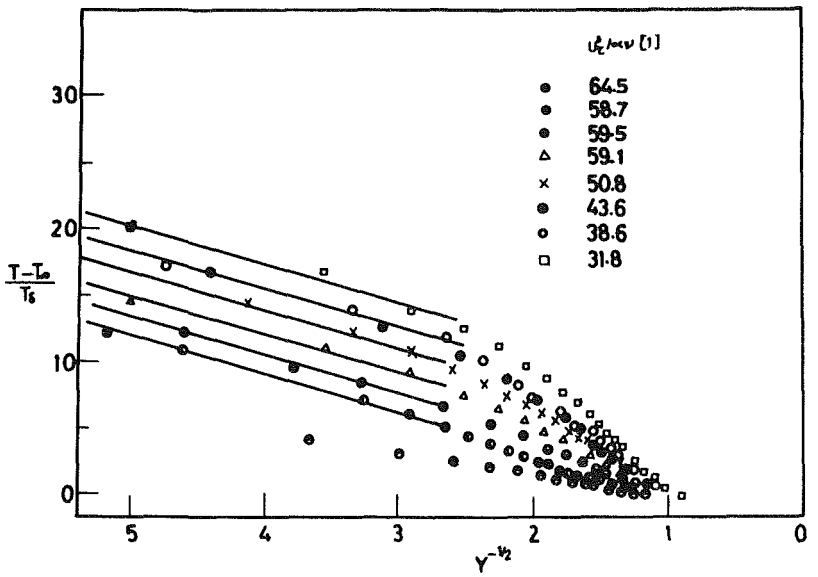

Fig. 2 Temperature distribution outer law (59) coordinates

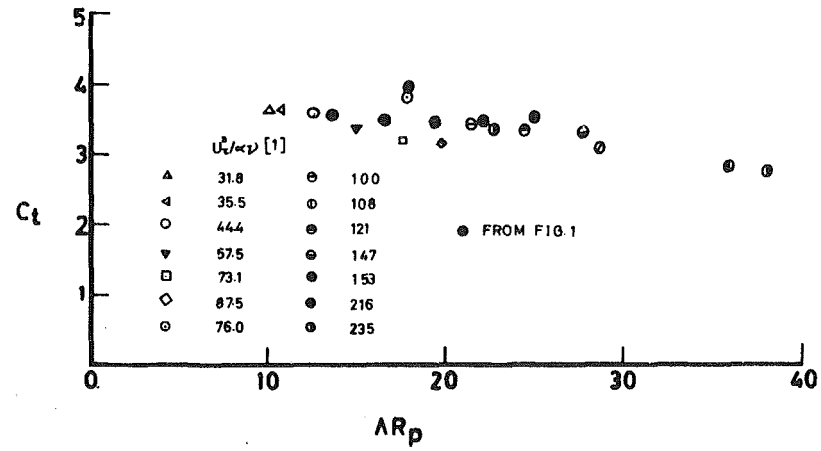

Fig. 3 Intercept C_t of the law-of-the-wall (58)

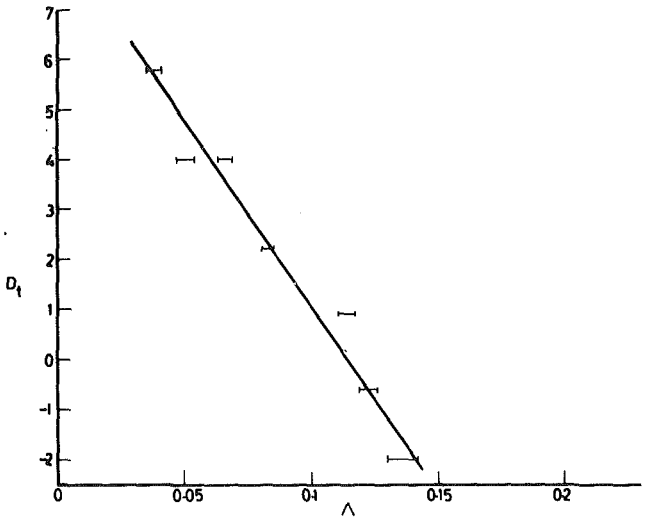

Fig. 4 Intercept D_t of the outer law (59)

so, then the inertial sublayer (overlap region) would depend on the molecular transport processes and the flow cannot be regarded as fully developed turbulence.

Figure 2 shows that the intercept of the outer law (59) is not a universal number. The present theory shows that the intercept D_t could depend on a variety of parameters, X, Λ, β, χ_m, and the history of motion. If the outer layer is assumed to be in equilibrium and the interaction with the momentum layer is significant, then to a first approximation D_t may be expected to depend on β and Λ. The data [12] cover a small range for values of β, and it is not easy to analyse the behaviour of D_t in terms of β. The data [12] for intercept D_t are therefore displayed again Λ in Fig. 4. In the figure, the small horizontal lines show the uncertainty in the value of Λ associated with the different values of skin friction given in [12]. Figure 4 shows that a linear relation

$$D_t = 8.5 - 74\Lambda \tag{65}$$

offers a very good approximation to the data. The outer law (59) may now be written as

$$(T_\infty - T)/T_\delta \sim 2.8\, Y^{-1/2} - D_t,\ Y \to 0 \tag{66}$$

The heat-transfer data is displayed as St^{-1} versus $(\sigma R_x)^{1/3}$ in Fig. 5, where $R_x = Ux/\nu$ is the local Reynolds number based on streamwise coordinate, x. The figure shows that the heat-transfer data is described quite well by the relation

$$\mathrm{St}^{-1} = 2(\sigma R_x)^{1/3} + 365$$

Finally, let us consider the results of Tetervin [2] for the Reynolds analogy factor. His expression (32) for very small Λ, in present notations, may be written as

$$2C_h/C_f = \Lambda^{-a}(\sin \pi a/\pi a),\ a = (H-1)/2 \tag{67}$$

where C_f and C_h are the coefficients of skin friction and heat transfer and H is the shape factor (the ratio of displacement to momentum thickness). Equation (67) may also be written as

$$2C_h = C_f^{1-a}(-2\,\delta\, U_x/U)^a \sin \pi a/\pi a \tag{68}$$

It may be noted that, in general, $1 < H < 2.6$ [2], and, therefore, $0 < a < 1$. Now for $a < 1$ as separation is approached $C_f \to 0$ and the relation (51) implies that $C_h \to 0$.

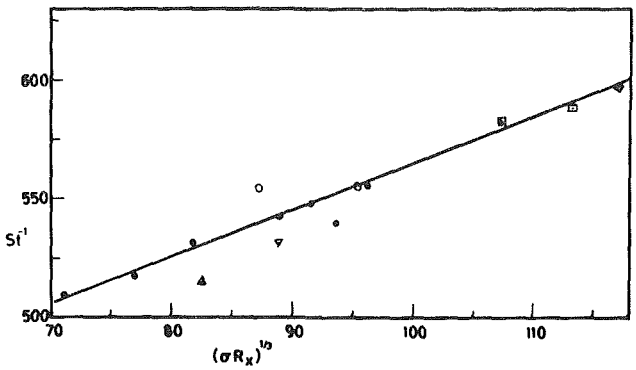

Fig. 5 Correlation of heat-transfer rate in a turbulent boundary layer with strong adverse pressure gradient

However, in general, near separation, C_h may be finite. Therefore, in the domain of strong adverse pressure gradients, the predictions based on the Reynolds analogy are bound to fail.

Acknowledgment

I am thankful to Professor Abdus Salam, Nobel Laureate, for the warm hospitality. Thanks are also due to International Atomic Energy Agency and UNESCO for providing the financial assistance at International Centre for Theoretical Physics, Trieste.

References

1 Perry, A. E., Bell, J. B., and Joubert, P. N., "Velocity and Temperature Profiles in Adverse Pressure Gradient Turbulent Boundary Layers," *Journal of Fluid Mech.*, Vol. 25, 1966, pp. 299-320.

2 Tetervin, N., "Approximate Calculation of Reynolds Analogy for Turbulent Boundary Layer with Pressure Gradient," *AIAA Journal*, Vol. 7, 1969, pp. 1079-1083.

3 Afzal, N., "Asymptotic Analysis of Turbulent Boundary Layer Near Separation," *Proceedings of the First Asian Congress on Fluid Mechanics*, Bangalore, 1980, Paper No. A.16, pp. 1-7.

4 Townsend, A. A., *The Structure of Turbulent Shear Flows*, Cambridge University Press, 2nd ed., 1976.

5 Samuel, A. E., and Joubert, P. N., "A Boundary Layer Developing in an Increasing Adverse Pressure Gradient," *Journal of Fluid Mech.*, Vol. 66, 1974, pp. 481-505.

6 Kader, B. A., and Yaglom, A. M., "Similarity Treatment of Moving Equilibrium Turbulent Boundary Layer in Adverse Pressure Gradient," *Journal of Fluid Mech.*, Vol. 89, 1978, pp. 305-342.

7 Afzal, N., "Analysis of a Turbulent Boundary Layer Subjected to a Strong Adverse Pressure Gradient," Submitted to *International Journal of Engineering Sciences.*

8 Millikan, C. B., "A Critical Discussion of Turbulent Flow in Channels and Circular Tubes," In Proceedings of the 5th International Congress of Applied Mechanics, John Wiley and Sons, 1939, pp. 386-392.

9 Coles, D. and Hirst, E. A., "The Computations of Turbulent Boundary Layer," *Proc. 1968 AFOSR-IFP-Stanford Conference, Vol. 2: Data Compilation*, 1969.

10 Van Dyke, M., *Perturbation Methods in Fluid Mechanics*, Parabolic Press, New York, 1975.

11 Afzal, N., "Effects of Longitudinal Curvature, Vorticity and Displacement for Two Dimensional Turbulent Boundary Layer with Heat and Mass Transfer," *J. de Mecanique*, Vol. 14, 1975, pp. 823-841.

12 Bell, J. B., "Boundary Layer on Heated Plate in Moderate Positive Pressure Gradient," in *Proceedings of Computation of Turbulent Boundary Layers—1968 AFOSR-IFP—Stanford Conference, Vol. II: Data Compilation*, 1969, pp. 310-321.

Heat Convection in Annular Type Crevices

Shi-chune Yao
Associate Professor.
Mem. ASME

Ying-Huei Hung
Graduate Student.

Department of Mechanical Engineering,
Carnegie-Mellon University,
Pittsburgh, Pa. 15213

The laminar flow and heat convection in annular type crevices of various eccentricities and inclinations are analyzed. The annulus is heated by hot flowing fluid at the inside of the inner tube. The flow field is calculated using creeping flow approximation of boundary layer theory. The thermal field is studied two-dimensionally in terms of the local bulk mean temperature of the fluid. Calculation is performed numerically but in nondimensional form. It is observed that the angle of inclination influences the flow and heat transfer significantly, especially when the eccentricity is severe. When the angle of inclination increases, the flow rate is reduced, the bulk mean temperature at the exit of crevice increases, and the averaged heat-transfer coefficient in crevice decreases. Comparisons are made with respect to the results of concentric annulus.

Introduction

The fluid flow and heat-transfer behavior in concentric annulus are well known [1]. However, in many practical thermal systems the axis of the inner tube may be inclined with respect to the outer shroud. Since the annular gap could be very narrow, if the inner tube is slightly off-centered the periferal variation of the flow channel gap-thickness could be very severe. The fluid flow and heat transfer in this kind of annular-type-crevices will be relatively complex. In conventional shell-and-tube heat exchangers and steam generators, the hot tube runs through the hole in baffle-plate or support-plate with a narrow mechanical clearance in between of the tube and wall of the hole. Due to the misalignment of the plates and the displacement of tube in the flow field, it is likely that the tube may be inclined in the hole to form an inclined annular-type crevice.

The flow is forced through the crevice by the pressure difference across the plate. The fluid is also heated by the hot tube in the crevice. The knowledge of the flow rate and temperature of the leakage stream is of great importance to the understanding of the thermal performance of these heat exchange equipments. This type of heat-transfer problems also occur in many other industrial applications.

The analysis of the fluid flow in concentric annular orifices has been reported in references [2, 3]. The fluid mechanic study of annuli of small clearances has also been performed in references [4, 5] for concentric and eccentric configurations. However, no analysis has been conducted for the general case of annular-type crevices with the inner tube inclined and placed eccentrically. The analysis of the flow in this generalized condition is one of the objectives of the present study.

The other objective of the present study is to analyze generally the convective heat transfer in annular-type crevices. In most applications the tube is heated from inside by another flowing hot fluid such that the outside surface condition of the tube is neither at a constant heat flux nor at a constant temperature. The heat transfer of eccentric annulus at constant heat flux has been studied in [6] for slug flow. However, no analysis has been performed for laminar flow in annular-type crevices with inclined inner tube. In fact, this information is of great importance to the heat exchanger designs [7].

In the following sections the fluid flow and heat convection of annular-type-crevices will be analyzed. To limit the complexity of the problem the following assumptions were made:

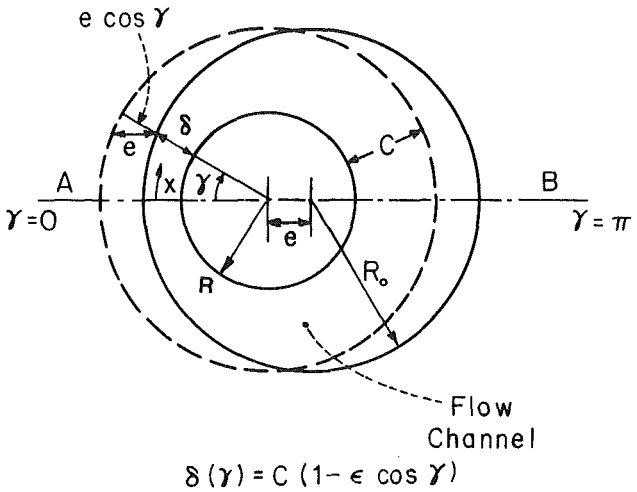

Fig. 1 The bottom view of eccentric annulus

1 The problem is steady state with constant properties for the fluid.

2 The flow is laminar in the crevice with negligible inertial effect and negligible energy dissipation. The entrance effects are neglected.

3 Heating is provided by the hot fluid in the tube. The tube is generally not in contact with the shroud. Should contact occur, the contact will be limited to a point.

Formulation

Geometry. To describe the geometry of the annular-type crevices accurately the local gap thickness of the flow channel has to be quantified. At any cross-sectional cut view of the crevice the configuration of the flow channel can be described as an eccentric annulus. For two eccentric circles with eccentricity e and with their radii having a small difference c, the gap thickness δ can be evaluated approximately from Fig. 1 as

$$\delta(\gamma) = c(1 - \epsilon \cos \gamma) \tag{1}$$

where

$$\epsilon = e/c \tag{2}$$

is the eccentricity ratio which varies between 0 and 1.

If the inner tube is inclined with respect to the outer shroud, the eccentricity ratio ϵ would be a function of the axial location. The displacement of the inner tube can be decomposed as two steps. First, the tube moves from the concentric position to an eccentric position. Then the tube is inclined with an angle. In the present study, a simple but typical condition is considered that the plane of inclination of

Contributed by the Heat Transfer Division for publication in the JOURNAL OF HEAT TRANSFER. Manuscript received by the Heat Transfer Division September 17, 1981.

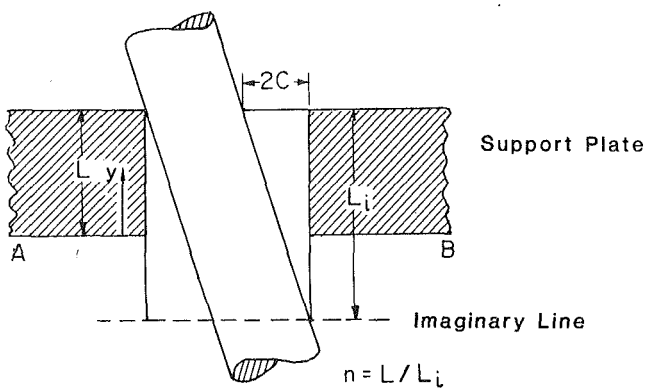

$$\delta(x,y) = C\left\{1-\epsilon\left[1-2n\left(1-\frac{y}{L}\right)\right]\cos\gamma\right\}$$

Fig. 2 The side view of an inclined annular crevice

the inner tube passes through the center line of the outer shroud. This is shown in Fig. 2. The general formulation for the gap of crevice is

$$\delta = c\{1-\epsilon[1-2n(1-(y/L))]\cos\gamma\} \tag{3}$$

where the eccentricity ratio ϵ is the value at the cross section where $y=L$. The n, called the index of inclination, controls the angle of inclination of the inner tube. When n equals zero the inner tube is in parallel with the outer shroud. At this moment equation (3) is the same as equation (1). When the n increases but with the ϵ fixed, the angle of inclination of the tube increases while its relative position at $y=L$ is not changed. When n equals unity, the inner tube inclines symmetrically in the crevice from a side view. For the extreme condition of $\epsilon=1$ and $n=1$, the inner tube contacts the outer shroud at two points $y=0$ and $y=L$ respectively.

The cross-sectional view of the crevice, as shown in Fig. 1, is symmetric with respect to the line A-B. Therefore, only half of the total crevice has to be calculated. In the present study, the gap thickness δ is generally much smaller than the tube radius R, such that the curvature of the crevice can be neglected. Therefore, the crevice can be analyzed as a flattened channel with the varying height δ as shown schematically in Fig. 3. The dimension of the flat channel is L in the y direction and πR in the x direction with a local height $\delta(x,y)$. The symmetry conditions will be applied to the lines of $x=0$, and $x=\pi R$.

Flow Field. The creeping flow approximation to the

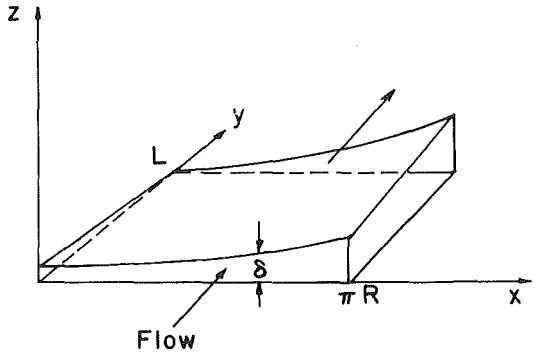

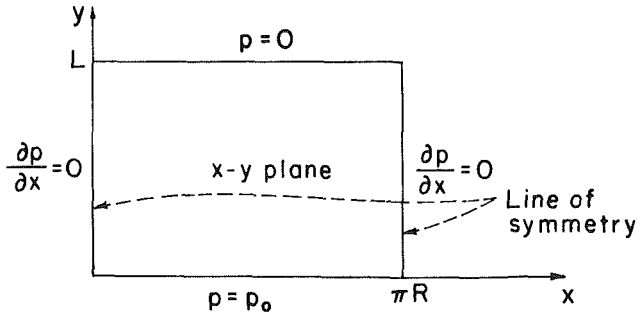

Fig. 3 Typical geometry of the crevice considered in analysis

boundary layer theory will be applied to the annular-type crevices. For the laminar flow in narrow flow passage, the flow field will be dominated by the viscous force and the pressure driving force. The fluid inertia force may be neglected [8] if

$$\frac{v^* L}{\nu}\left(\frac{c}{L}\right)^2 << 1 \tag{4}$$

where the v^* is the characteristic velocity of fluid in the crevice and will be defined later. At this condition the velocity profiles become parabolic. The parabolic velocity profiles can be substituted into the equation of continuity and integrated across the gap from 0 to δ. The result is

$$\frac{\partial}{\partial x}\left(\delta^3\frac{\partial p}{\partial x}\right)+\frac{\partial}{\partial y}\left(\delta^3\frac{\partial p}{\partial y}\right)=0 \tag{5}$$

which is the Reynold's equation of lubrication [8] when the

Nomenclature

A = cross-section area of axial flow in crevice
c = averaged gap thickness in the crevice
C_p = specific heat of the fluid in crevice
e = eccentricity, defined in Fig. 1
f = apparent friction factor for crevice, defined in equation (31)
h_i = heat-transfer coefficient inside the tube
h_0 = local heat-transfer coefficient at outside of tube in crevice
$\bar{h}$ = averaged heat-transfer coefficient on the tube in the whole crevice
H = local overall heat-transfer coefficient from the inside of the tube to crevice defined in equation (17).
k_1 = thermal conductivity of the fluid in crevice
k_s = thermal conductivity of the tube material
L = the axial length of tube in crevice
$\dot{m}$ = the total mass flow rate through the crevice
n = index of inclination of the tube
Nu* = characteristic Nusselt number of crevice, defined in equation (28)
$\bar{\text{Nu}}$ = averaged Nusselt number in crevice, defined in equation (34)
p = local pressure of fluid
p_0 = pressure difference across the crevice
P = nondimensional pressure, p/p_0
Pe* = characteristic Peclet number of crevice, defined in equation (29)
$\bar{q}_w$ = averaged heat flux of the tube
R_0 = radius of the shroud
R = radius of the tube
s = the thickness of the tube
S = ratio of the dimensions of the flattened crevice, $L/\pi R$
T = local temperature of fluid
$\bar{T}$ = local bulk mean temperature of the fluid in crevice

walls are not in motion. In this equation, the δ is given from the known geometry of crevice and the pressure field is unknown. The boundary conditions are

$$p(x, 0) = p_0 \tag{6}$$

$$p(x, L) = 0 \tag{7}$$

where the p_0 is the driving pressure over the crevice, and

$$\frac{\partial p}{\partial x}(0, y) = 0 \tag{8}$$

$$\frac{\partial p}{\partial x}(\pi R, y) = 0 \tag{9}$$

for the symmetry condition as described previously.

Once the pressure field has been solved, the "averaged" fluid velocity of the parabolic profile can be evaluated from

$$\bar{u} = -\frac{1}{12\mu}\frac{\partial p}{\partial x}\delta^2 \tag{10}$$

$$\bar{v} = -\frac{1}{12\mu}\frac{\partial p}{\partial y}\delta^2 \tag{11}$$

Heat Transfer. Considering the constant properties and neglecting the viscous dissipation, the energy equation of the laminar flow in the crevice becomes

$$u\frac{\partial T}{\partial x} + v\frac{\partial T}{\partial y} = \alpha\left(\frac{\partial^2 T}{\partial x^2} + \frac{\partial^2 T}{\partial y^2} + \frac{\partial^2 T}{\partial z^2}\right) \tag{12}$$

The order of magnitude analysis can be performed to justify the importance of each term. Normalize the velocity by v^*, x and y by L, and z by δ. The convective terms are of the order 1; the conduction in x and y directions are of the order $(v^*L/\alpha)^{-1}$, and the conduction in z direction becomes on the order of $[(v^*L/\alpha)(\delta/L)^2]^{-1}$. Considering the criterion in equation (4) and assuming the Prandtl number of the order 1, the conduction in z direction would be dominant. The conduction in the x or y directions would be negligible because the characteristic Peclet number (v^*L/α) is generally much larger than one. The omitting of the conduction in the x and y directions is further supported by the particular type of heating condition in the present study. The temperature of the hottest point in the crevice is limited by the hot fluid temperature in the tube; therefore, a severe hot spot is not likely to occur and the conduction in x or y direction will be limited too.

The remaining energy equation can be integrated with respect to z from 0 to δ and gives

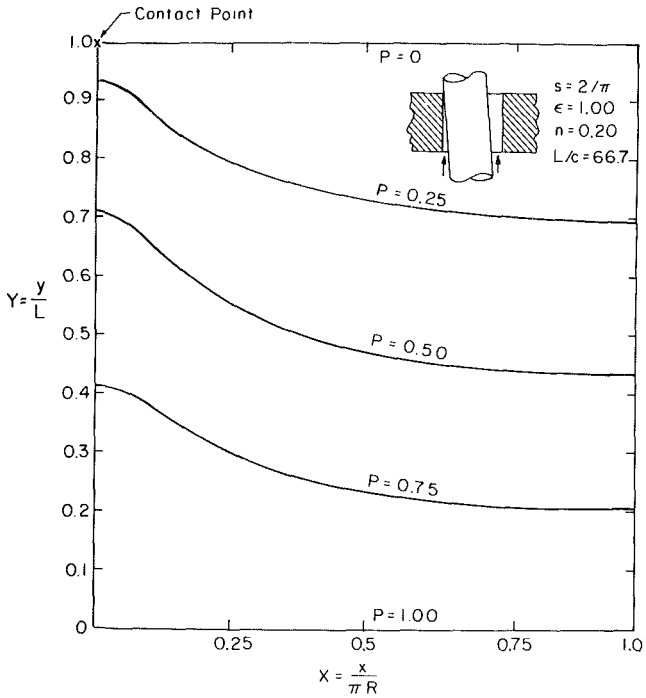

Fig. 4 The nondimensional pressure distribution for one-point-contact crevice

$$\int_0^\delta u\frac{\partial T}{\partial x}dz + \int_0^\delta v\frac{\partial T}{\partial y}dz = \alpha\frac{\partial T}{\partial z}\Big]_0^\delta \tag{13}$$

Following the derivation in the Appendix, the first term of the equation (13) can be written as

$$\int_0^\delta u\frac{\partial T}{\partial x}dz = \delta\bar{u}\frac{\partial \bar{T}}{\partial x} - \int_0^\delta \frac{\partial u}{\partial x}(T - \bar{T})dz \tag{14}$$

where the $\bar{T}$ is the local bulk mean temperature of the fluid. Since the gap of the crevice is narrow, the local temperature of fluid is very close to the local bulk mean temperature. When the gap thickness δ does not vary strongly in the crevice, the value of $\partial u/\partial x$ will also be small. Therefore, the last term in the equation (14) can be neglected in general. Approximate the second term in equation (13) in the same manner, the energy equation becomes

$$\bar{u}\delta\frac{\partial \bar{T}}{\partial x} + \bar{v}\delta\frac{\partial \bar{T}}{\partial y} = \alpha\frac{\partial T}{\partial z}\Big]_0^\delta \tag{15}$$

If the crevice is heated from the inner tube and insulated at

Nomenclature (cont.)

T_i = bulk mean temperature of hot fluid inside tube
T_0 = temperature of fluid at inlet of crevice
$\bar{T}_e$ = bulk mean temperature of fluid at the exit of crevice
u = local velocity of fluid in θ direction, a function of z
$\bar{u}$ = local velocity of fluid in θ direction, averaged over the gap
U = nondimensional velocity of fluid in θ direction, $\frac{\mu\bar{u}\pi R}{p_0 c^2}$
v = local axial velocity of fluid, a function of z
$\bar{v}$ = local axial velocity of fluid, averaged over the gap
v^* = characteristic axial velocity of fluid, defined in equation (30)
V = nondimensional axial velocity of fluid, $\frac{\mu\bar{v}L}{p_0 c^2}$
x = coordinate measured in θ direction
X = nondimensional x coordinate, $x/\pi R$
y = coordinate measured in axial direction
Y = nondimensional y coordinate, y/L
z = coordinate measured normal to tube surface across the gap
α = thermal diffusivity of fluid in crevice
δ = local thickness of gap in crevice
Δ = nondimensional gap thickness of crevice, δ/c
ϵ = eccentricity ratio defined in equation (2)
γ = angle, defined in Fig. 1
θ = nondimensional local bulk mean temperature of fluid, $\frac{\bar{T} - T_0}{T_i - T_0}$
μ = viscosity of fluid in crevice
ν = kinematic viscosity of fluid in crevice
ρ = density of fluid in crevice

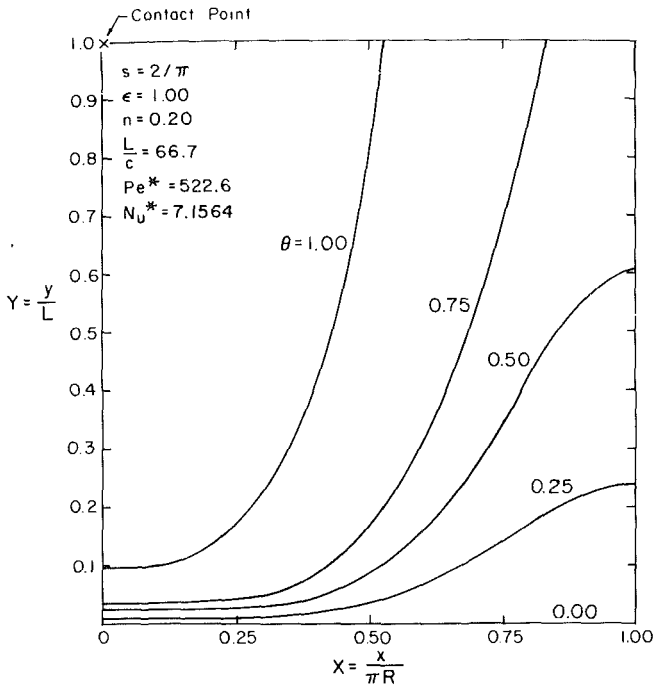

Fig. 5 The isotherm map for one-point-contact crevice with constant bulk mean temperature of fluid inside tube

the outer tube, the last term in the equation (15) can be written as $q_w/\rho C_p$. The wall heat flux q_w can be described as $H(T_i - \bar{T})$. Therefore, the energy equation is

$$\bar{u}\frac{\partial \bar{T}}{\partial x} + \bar{v}\frac{\partial \bar{T}}{\partial y} = \frac{H}{\delta(x,y)\rho C_p}(T_i - \bar{T}) \tag{16}$$

where the H is the overall heat-transfer coefficient defined as

$$\frac{1}{H} = \frac{1}{h_i} + \frac{s}{k_s} + \frac{1}{h_0} \tag{17}$$

The energy equation (16) is a first-order, linear partial differential equation of the hyperbolic form. The initial conditions are

$$\bar{T}\Big|_{y=0} = T_0 \text{ at inlet, and} \tag{18}$$

$$\frac{\partial \bar{T}}{\partial x}\Big|_{x=0} = 0 \text{ for the symmetry.} \tag{19}$$

Nondimensionalization. The parameters can be nondimensionalized using X, Y, S, Δ, P, U, V, and θ as defined in the section of nomenclature. Then the Reynold's equation and the boundary conditions become

$$S^2\frac{\partial}{\partial X}\left(\Delta^3\frac{\partial P}{\partial X}\right) + \frac{\partial}{\partial Y}\left(\Delta^3\frac{\partial P}{\partial Y}\right) = 0 \tag{20}$$

with

$$P(X,0) = 1, P(X,1) = 0 \tag{21}$$

$$\frac{\partial P}{\partial X}(0,Y) = 0, \frac{\partial P}{\partial X}(1,Y) = 0 \tag{22}$$

The nondimensional velocity field is described by

$$U = -\frac{1}{12}\Delta^2\frac{\partial P}{\partial X} \tag{23}$$

$$V = -\frac{1}{12}\Delta^2\frac{\partial P}{\partial Y} \tag{24}$$

The energy equation and its initial conditions are

$$S^2 U\frac{\partial \theta}{\partial X} + V\frac{\partial \theta}{\partial Y} = \frac{1}{\Delta}\left(\frac{L}{c}\right)\left(\frac{\text{Nu}^*}{\text{Pe}^*}\right)(1-\theta) \tag{25}$$

with

$$\theta = 0 \text{ at } Y = 0 \tag{26}$$

$$\frac{\partial \theta}{\partial X} = 0 \text{ at } X = 0 \tag{27}$$

where

$$\text{Nu}^* = \frac{H2c}{k_1} \tag{28}$$

$$\text{Pe}^* = \frac{v^*2c}{\alpha} \tag{29}$$

$$v^* = \frac{P_0 c^2}{\mu L} \tag{30}$$

the v^* is the characteristic axial velocity in the crevice at laminar flow.

Numerical Method

The pressure field is calculated from the Reynold's equation of lubrication as shown in equations (20) to (22). To solve this Poisson equation, the method of Alternative Directional Implicit numerical scheme [9] is used. The implicit calculations are performed along horizontal lines for the whole region of the flow field; then the calculations are performed along all the vertical lines alternatively. In the implicit scheme of the solution along a line, the method of Gauss Elimination is used to solve the system of equations.

The thermal field is then calculated using the known velocity field which is derived from the pressure field. In solving the energy equation the upwind-difference scheme [10] has been used to maintain a stable numerical computation.

The whole field is typically discretized into 20×18 meshes. Approximately 20 iterations are required in the Alternative Directional Implicit calculations to reach a converged solution. The result is validated with hand calculations. The overall computer time for the calculation is about 12 cpu s using a DEC-20 computer.

Results and Discussion

To illustrate the result of fluid flow and heat-transfer calculations, a specific example is studied in detail. The inner tube contacts with the outer shroud at the top but with a small angle of inclination. Fluid flows upward in the crevice. The calculated pressure field is shown in Fig. 4 in nondimensional form. The geometric configuration of the crevice is also specified in this figure. The pressure field is distorted and the flow stream diverts from the point of contact where the gap thickness is the minimum.

For the same crevice, the thermal field is shown in Fig. 5 in nondimensional form. Since the gap is wide at the location where the X is large, the flow is faster over there and the local bulk mean temperature rises relatively slow along the stream. In the region where X is small, the flow is retarded due to the narrow gap thickness. The fluid temperature rises fast and reaches the temperature of hot fluid inside the tube in a short distance. This high temperature region is relatively large in this example. If the inner tube is not in contact with the outer shroud, the hot region would be small or inexist.

Many other cases are studied for various eccentricity ratio ϵ and inclination index n for this crevice. The parameters of this crevice have been listed in Table 1. For the same crevice, the ratio of the mass flow rates at various conditions and the mass flow rate at concentric configuration are shown in Fig. 6 with the eccentricity ratio ϵ as horizontal coordinate and the inclination index n as parameter. When n equals zero, the tube is in parallel to the shroud. As shown in Fig. 6, the result of

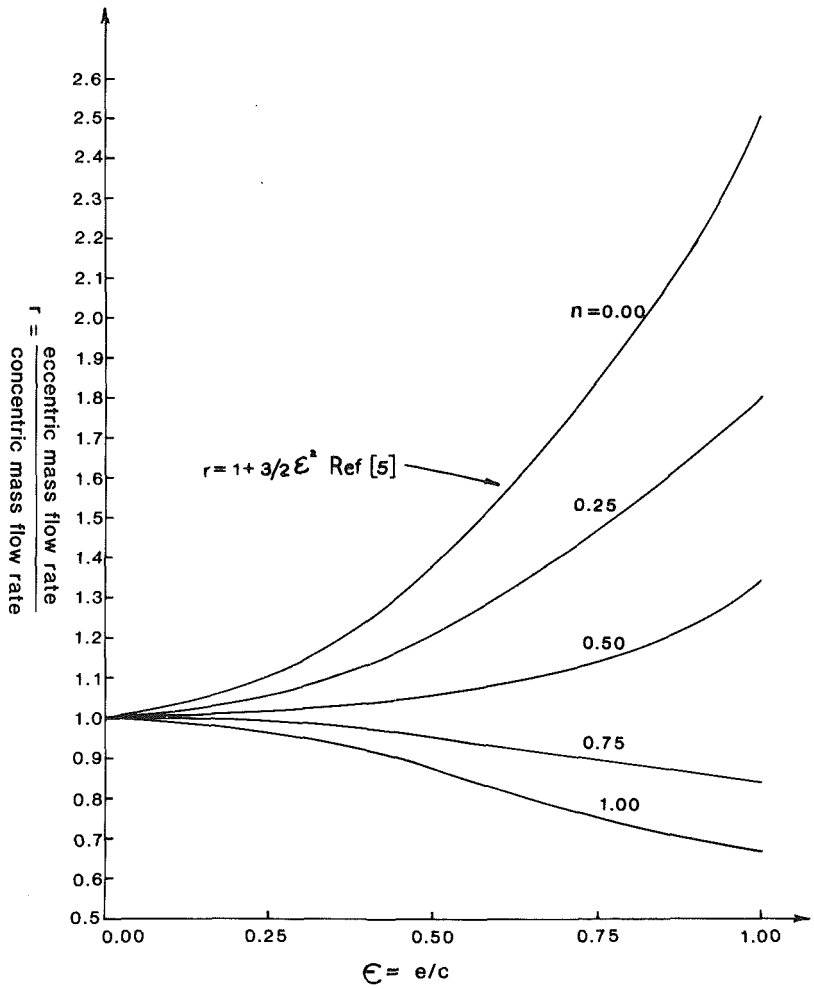

Fig. 6 Flow ratio of various crevices at laminar flow

present study is exactly the same as the result reported in the reference [5]. As indicated in Fig. 6, at a fixed ϵ the more the inclination (i.e., higher value of n) the lower the mass flow rate. This is because the flow streams are distorted when the tube is inclined in the crevice. The extreme conditions occur when ϵ equals unity, where the inner tube contacts the outer shroud at the top edge. When n equals zero, the tubes have a line of contact with shroud in crevice. Large amounts of fluid pass through the wide opening at the other side of the crevice and give the highest possible mass flow rate in all the configurations (2.5 times that of concentric annulus). If n equals unity, the tube has two contact points at the top and bottom of crevice, respectively. The mass flow rate at this condition is the lowest of all the cases studied (about 70 percent of the concentric annulus).

The overall flow resistance of the crevice can be characterized by an "apparent" friction factor which is defined in a conventional manner as

$$\Delta p = f\left(\frac{L}{2c}\right)\frac{1}{2}\frac{\dot{m}^2}{\rho A^2} \tag{31}$$

It is interesting to point out that for a crevice with fixed dimensions the total cross-sectional area A of the flow is a constant value irrespective to the eccentricity of the tube in the crevice. The apparent friction factor of the crevice is shown in Fig. 7 for various ϵ and n. The Reynolds number here is based upon the area averaged axial velocity of the fluid in crevice. The nature of this figure is similar to that of Fig. 6 due to their interrelationship in equation (31). The calculated friction factors of reference [5] for eccentric annulus with various gaps are also shown in Fig. 7. The present study of narrow

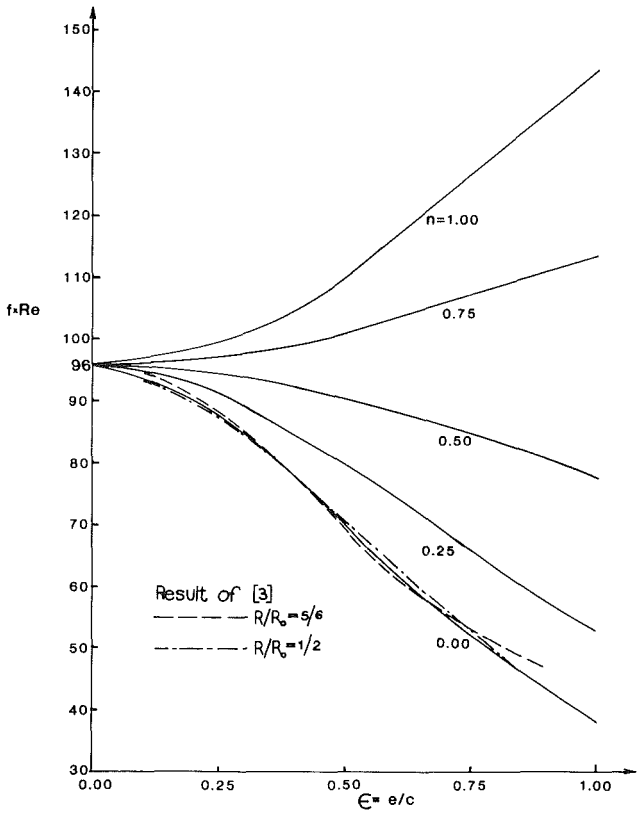

Fig. 7 Apparent friction factor of various crevices

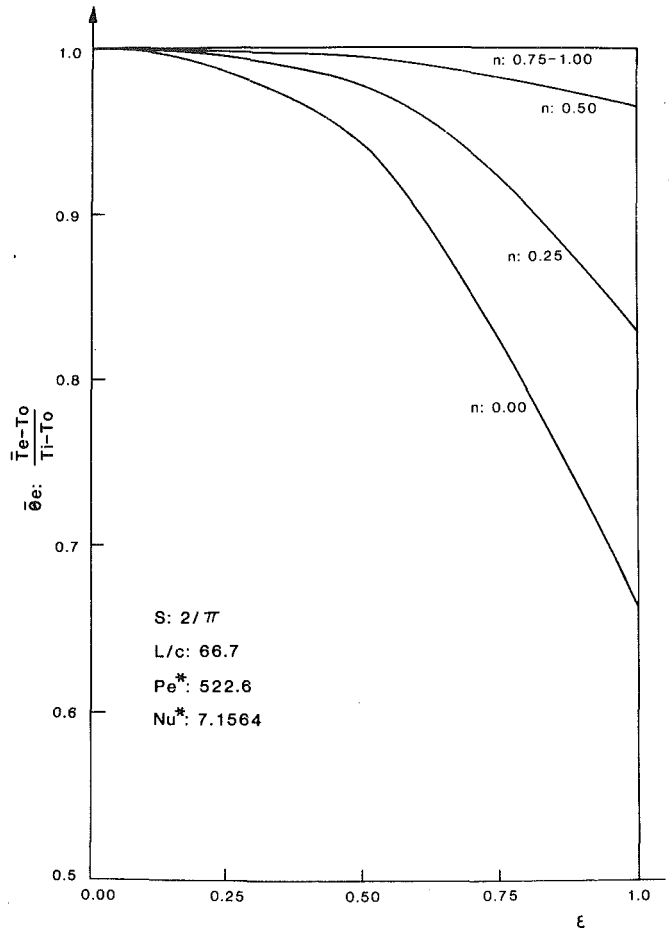

Fig. 8 Bulk mean temperature of exit stream of various crevices

Table 1 Parameters of the crevice studied here

S	L/c	Pe*	Nu*
$\frac{2}{\pi}$	66.7	522.6	7.156

annulus gives almost the same result as those gaps when the tube and shroud are in parallel.

The nondimensional bulk mean temperature of the leakage stream leaving the crevice is shown in Fig. 8 for various values of ϵ and n. The condition of heating is described in Table 1. When the tubes are concentric ($\epsilon=0$), the leakage is as hot as the temperature of fluid in the tube. If the leakage stream is more (for example, $\epsilon>0.5$ but $n<0.5$), the temperature of the leakage stream becomes lower. However, when the inner tube is further inclined, with the n value equals or larger than 0.75, the leakage stream could be equal or less than that of concentric annulus (see Fig. 6), and the temperature of leakage stream will be as hot as the fluid temperature inside the tube.

Based upon the foregoing information on the flow rate as well as temperature of the leakage stream, the averaged heat transfer from the hot tube in the crevice can be evaluated. We may define the averaged heat-transfer coefficient as

$$\bar{q}_w=\bar{h}(T_i-T_0) \tag{32}$$

By energy conservation for the whole crevice, the averaged heat flux is

$$\bar{q}_w=\frac{\dot{m}C_p(\bar{T}_e-T_i)}{2\pi RL} \tag{33}$$

Therefore the averaged Nusselt number in the crevice can be calculated.

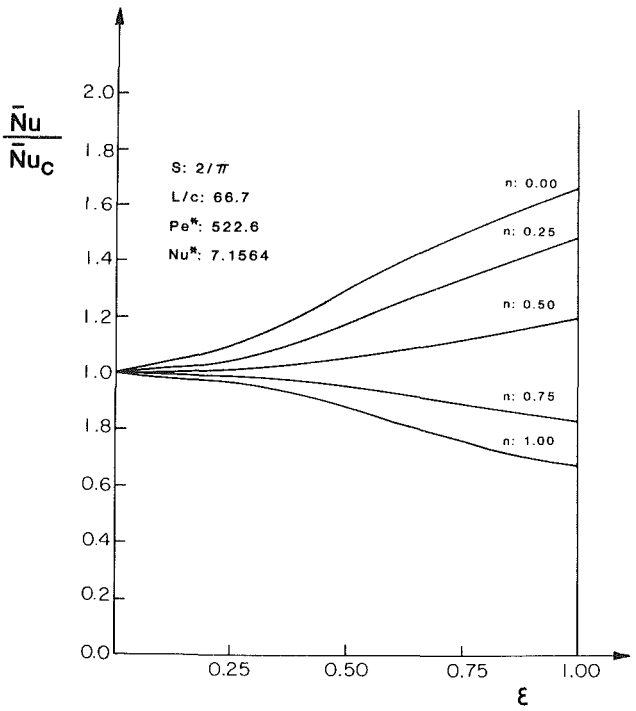

Fig. 9 Averaged Nusselt number of various crevices

$$\bar{\mathrm{Nu}}=\frac{C_p c\dot{m}\bar{\theta}_e}{\pi RLk_1} \tag{34}$$

The averaged Nusselt numbers of crevice with various geometric configurations are shown in Fig. 9 as a ratio to the Nusselt number of concentric annulus. It is interesting to notice that for the condition of present study, the configurations with $n<0.5$ give higher heat-transfer coefficient, although the bulk mean temperature of the exit stream, as shown in Fig. 8, is not as hot as the temperature of fluid inside the tube. This is mainly due to the high flow rate at these conditions as indicated in Fig. 6. The $\bar{\mathrm{Nu}}$ is essentially related with the product of mass flow rate and exit bulk mean temperature as stated in the equation (34).

Conclusion

The laminar flow and heat transfer in annular-type crevices of various geometric configurations are studied in detail. The flow field can be calculated using creeping flow approximation. The thermal field can be formulated in two dimensions based upon the local bulk mean temperature in crevice. Compared with the behavior of the concentric annulus, the eccentric annulus with a small inclination of the inner tube gives a higher mass flow rate, lower bulk mean temperature at exit, but a higher averaged heat-transfer coefficient in crevice. If the angle of inclination is large, the behavior is reversed. It is suggested that the fluid flow and heat-transfer behavior of confined geometry with other types of configurations can also be analyzed in a similar manner.

Acknowledgment

The authors are grateful for the support of the Office of Naval Research (under Contract No. N00014-79-C-0623) in performing this research.

References

1 Kays, W. M., *Convective Heat and Mass Transfer*, McGraw-Hill, 1966.

2 Bell, K. J. and Bergelin, O. P., "Flow Through Annulus Orifices," Trans. ASME, Vol. 79, 1957, pp. 593-601.

3 Snyder, W. T. and Goldstein, G. A., "Analysis of Fully Developed Laminar Flow in an Eccentric Annulus," *AIChE Journal*, Vol. 11, No. 3, 1965, pp. 462-467.

4 Nootbaar, R. F., and Kintner, R. C., "Fluid Friction in Annuli of Small Clearance," *Proceedings of Second Midwestern Conference of Fluid Mechanics*, Ohio State University, Eng. Exp. Station, Bulletin No. 149, 1952, pp. 185–199.

5 Tao, L. N., and Donovan, W. F., "Through-Flow in Concentric and Eccentric Annuli of Fine Clearance With and Without Relative Motion of the Boundaries," Trans. ASME, Vol. 77, 1955, pp. 1291–1301.

6 Snyder, W. T., "An Analysis of Slug Flow Heat Transfer in an Eccentric Annulus," *AIChE Journal*, Vol. 9, No. 4, 1963, pp. 503–506.

7 Palen, J. W., and Taborek, J., "Solution of Shell Side Flow Pressure Drop and Heat Transfer by Stream Analysis Method," *CEP Symp. Series*, Vol. 65, No. 92, 1969, pp. 53–63.

8 Schlichting, H., *Boundary-Layer Theory*, McGraw-Hill, 1968, p. 109.

9 Carnahan, B., Luther, M. A., and Wilkes, J. O., *Applied Numerical Methods*, John Wiley and Sons, Inc., 1969.

10 Patankar, S. V., *Numerical Heat Transfer and Fluid Flow*, McGraw-Hill, 1980.

APPENDIX A

The Derivation of Equation (14)

Following the definition of average velocity and bulk mean temperature, we get

$$\bar{u}\frac{\partial \bar{T}}{\partial x} = \left(\frac{\int_0^\delta u dz}{\delta}\right)\frac{\partial}{\partial x}\left[\frac{\int_0^\delta uTdz}{\int_0^\delta udz}\right] \tag{A1}$$

$$= \frac{1}{\delta}\left[\frac{\partial}{\partial x}\int_0^\delta uTdz - \frac{\int_0^\delta uTdz}{\int_0^\delta udz}\frac{\partial}{\partial x}\int_0^\delta udz\right] \tag{A2}$$

$$= \frac{1}{\delta}\left[\frac{\partial}{\partial x}\int_0^\delta uTdz - \bar{T}\frac{\partial}{\partial x}\int_0^\delta udz\right] \tag{A3}$$

use Lebnitz's rule for both of the integrals

$$\bar{u}\frac{\partial \bar{T}}{\partial x} = \frac{1}{\delta}\left\{\left[\int_0^\delta u\frac{\partial T}{\partial x}dz + \int_0^\delta T\frac{\partial u}{\partial x}dz + \cancel{u(0)}\,T(\delta)\frac{\partial \delta}{\partial x} - 0\right]\right.$$

$$\left. - \bar{T}\left[\int_0^\delta \frac{\partial u}{\partial x}dz + \cancel{u(0)}\frac{\partial \delta}{\partial x} - 0\right]\right\} \tag{A4}$$

when the non-slip condition for velocity at δ is used, this equation becomes

$$\delta\bar{u}\frac{\partial \bar{T}}{\partial x} = \int_0^\delta u\frac{\partial T}{\partial x}dz + \int_0^\delta \frac{\partial u}{\partial x}(T-\bar{T})dz$$

Corrugated-Duct Heat Transfer, Pressure Drop, and Flow Visualization

J. E. O'Brien

E. M. Sparrow
Fellow ASME

Department of Mechanical Engineering,
University of Minnesota,
Minneapolis, Minn. 55455

Experiments were performed to determine forced convection heat-transfer coefficients and friction factors for flow in a corrugated duct. The corrugation angle was 30 deg and the interwall spacing was equal to the corrugation height. The Reynolds number, based on the duct hydraulic diameter, ranged from 1500 to 25,000, and the Prandtl number ranged from 4 to 8 (water). Flow visualization, using the oil-lampblack technique, revealed a highly complex flow pattern, including large zones of recirculation adjacent to the rearward-facing corrugation facets. Nusselt numbers in the periodic fully developed regime, when correlated, resulted in a Reynolds-number dependence of $Re^{0.614}$ and a Prandtl-number dependence of $Pr^{0.34}$. The enhancement of heat transfer as compared to a conventional parallel-plate channel was about a factor of 2.5. Friction factors obtained from measured axial pressure distributions were virtually independent of the Reynolds number and equal to 0.57, a value appreciably greater than that for unidirectional duct flows.

Introduction

The need for more efficient heat exchange devices has led to the development of a variety of unconventional internal flow passages to enhance the heat-transfer coefficient. One such passage is the corrugated-wall channel, or corrugated duct, in which fluid flows perpendicular to the corrugations and moves along an undulating path as it encounters the successive peaks and valleys. For example, heat sinks of certain high-speed digital computers have recently incorporated water-cooled corrugated-wall passages into their cooling systems. The potential benefits that can be realized from the use of corrugated passages in heat exchangers, together with the scarcity of relevant design information presently available, serve to motivate this research.

The corrugated duct of the present experiments had a corrugation angle of 30 deg and an interwall spacing equal to the corrugation height such that all corrugation peaks lie in the same plane. Heating of the duct wall was accomplished by resistance wire imbedded in grooves on the back side of each corrugated wall. The duct walls were machined from solid copper and have sharp-edged corrugation peaks. Axial wall temperature distributions were determined by means of fifty fine-gage thermocouples. Water was the working fluid for the heat-transfer experiments.

A separate corrugated duct with the same internal geometry as the aforementioned duct, but with air as the working fluid, was constructed out of plexiglass and used in fluid flow experiments. In one set of experiments, pressure distributions were measured as a function of position along the length of the duct. The plexiglass test section was also used for a flow visualization study utilizing the oil-lampblack technique.

The Reynolds-number range of the experiments was from 1500 to 25,000, and the Prandtl number for the heat-transfer study extended from 4 to 8.

Some related work has been performed in the past regarding heat transfer in corrugated ducts. Beloborodov and Volgin [1] employed a corrugated duct having an interwall spacing and corrugation angle different from that of the present investigation. Unfortunately, the experimental apparatus of [1] is not well defined, but it appears to have been a two-fluid heat exchanger, with no direct measurement of wall temperature, such that the obtained heat-transfer coefficients are averages for the device as a whole. The corrugations were formed from sheet metal and thus could not have had the sharp-edged corrugation peaks of the present work. In light of these uncertainties, it is difficult to accord a great deal of generality to the correlations presented in [1].

The research performed by Goldstein [2] represents another contribution to the literature on heat transfer in corrugated flow passages. This work was largely concerned with the low Reynolds-number range from $Re = 150$ to $Re = 2000$, within which secondary flows were identified by high-resolution local mass-transfer measurements. The corrugated channel of [2] had only two corrugation cycles, and thus the Sherwood-number results are applicable only to the region of flow development near the inlet of the corrugated duct.

A situation which has certain similarities to corrugated-duct flow is flow through tube banks, commonly encountered in heat exchangers. The similarities include periodic regions of both recirculating and forward flows. Tube-bank information [3–5] will be called upon to provide perspective for the present Nusselt-Reynolds-Prandtl correlations.

For the purposes of evaluating the level of heat-transfer enhancement associated with the corrugated-duct flow, the Nusselt numbers of the present experiments will be compared to those of a conventional unidirectional parallel-plate channel flow, as represented by the correlations of Dittus-Boelter and Petukhov-Popov [6].

The Experiments

As was already noted in the Introduction, two different but complementary apparatuses were employed for the present experiments. Each apparatus will be discussed separately. A detailed presentation of the design and fabrication of the experimental apparatuses is available in [7].

Water Flow System. The experiments for determining heat-transfer coefficients for water flowing in a corrugated duct utilized the open-loop system shown in the upper diagram of Fig. 1. City water first enters the system at an elevated constant-head tank (not shown) and is ducted to a large upstream plenum chamber. The corrugated test section spans between the upstream plenum chamber and a smaller downstream

Contributed by the Heat Transfer Division for publication in the JOURNAL OF HEAT TRANSFER. Manuscript received by the Heat Transfer Division November 23, 1981.

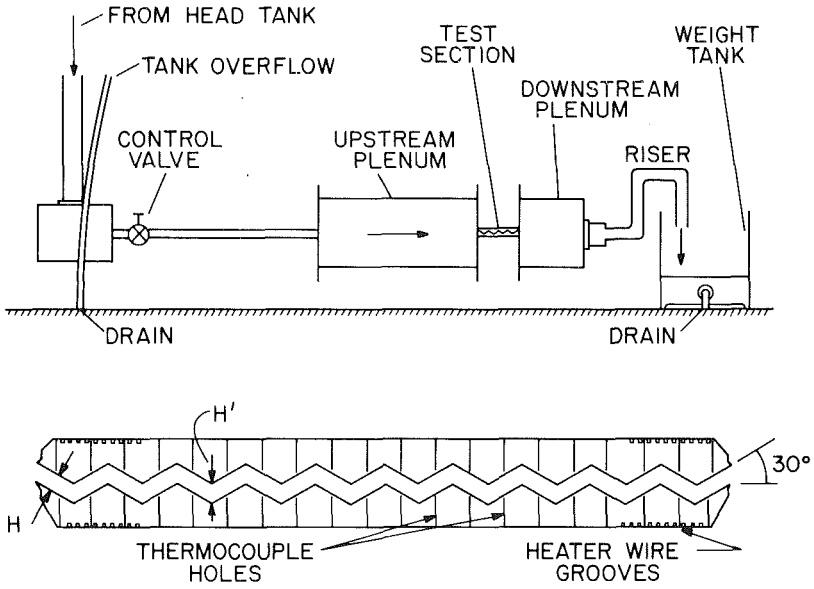

Fig. 1 Water flow system (upper diagram) and side view of the principal walls of the duct (lower diagram)

plenum. The purpose of the plenum chambers was to provide a well-defined abrupt inlet and exit for the test section. The water exits the downstream plenum chamber and empties into a weight tank, which enables direct determination of mass flow rate.

Each system component will now be discussed in greater detail, starting with the heart of the system, the corrugated-duct test section.

Test Section. The duct is formed by two corrugated copper plates, which are the principal walls, and two side walls (also of copper) that fix the spacing between the principal walls. Each of the corrugated walls was fabricated from 1.27-cm-thick copper plate, 5.08-cm wide and 20.32-cm long. The machining of the transverse grooves which form the corrugations was accomplished by means of a special cutting tool which had a 120 deg included angle, resulting in a corrugation angle of 30 deg, measured from the horizontal as shown in the lower diagram of Fig. 1. In the machining, care was taken to achieve a hydrodynamically smooth surface finish on the corrugations.

The side view of the test section shows the assembled relative positions of the top and bottom walls which form the corrugated duct. As seen there, the walls are positioned in such a way that the peaks of both the top and bottom walls lie in the same plane. The perpendicular spacing, H, (Fig. 1) between the walls is 0.508 cm, yielding a 10:1 cross-sectional aspect ratio. All told, there are twenty sloping facets in each of the corrugated walls.

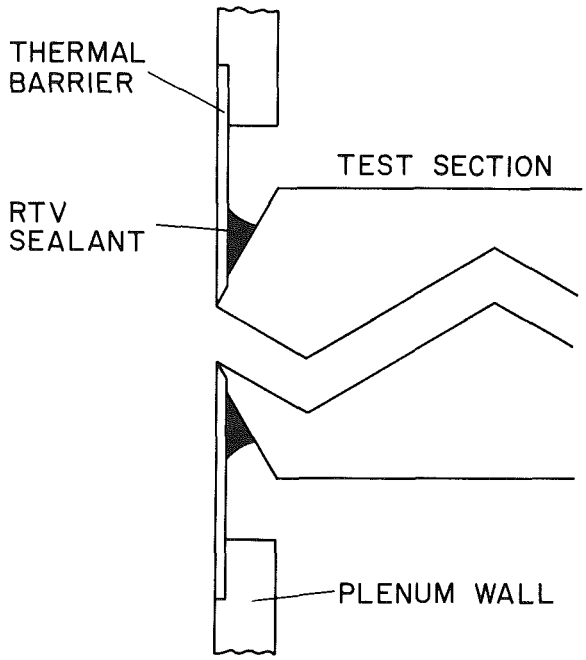

Fig. 2 Thermal barrier – test section junction

Special cuts were made on the inlet and exit ends of the top and bottom walls (see Fig. 1, lower diagram) in order to facilitate the joining of the respective ends to a low-

Nomenclature

A = cross-sectional area of corrugated duct
D_h = hydraulic diameter
f = fully developed friction factor
H = perpendicular spacing between corrugated walls, Fig. 1
H' = vertical spacing between corrugated walls, Fig. 1
h = fully developed heat transfer coefficient
k = thermal conductivity of fluid
$\dot{m}$ = mass flow rate
Nu = fully developed Nusselt number
P = perimeter of corrugated duct
Pr = Prandtl number
Pr_w = Prandtl number corresponding to wall temperature
p = pressure
p_{atm} = ambient pressure
p_x = pressure at axial station x
Q' = heat transfer rate per unit length along the x coordinate and per side
Re = Reynolds number
Sc = Schmidt number
Sh = Sherwood number
T = temperature
T_b = bulk temperature
T_{bi} = inlet bulk temperature
V = mean velocity
x = axial coordinate measured along a straight-line (non-undulating) path
ρ = density
μ = viscosity

conductivity thermal barrier which connects the heated test section to the walls of the plenum chamber. Figure 2 shows an assembled view of the thermal barrier–test section junction. Each thermal barrier is inlaid into its host plenum chamber wall such that its inside surface is flush with that of the wall. Water leakage was prevented along the perimeter of the thermal barrier–test section junction by a fillet of RTV silicone rubber sealant.

The side walls of the duct were fabricated from 0.508-cm-thick copper plate. Each side wall has two grooves sized to accommodate O-ring material which prevents water leakage along the length of the duct. The ends of the side walls also have special cuts designed to mate with the thermal barrier.

The arrangement pictured in Fig. 2 was adopted in order to avoid direct contact between the upstream and downstream faces of the heated walls and the water entering and leaving the test section. Such contact, had it occurred, would have resulted in large extraneous heat losses.

Heating of the test section was accomplished by means of rear-side, groove-imbedded resistance wire, as shown in the lower diagram of Fig. 1. The grooves were spaced 0.254 cm apart and had an axial width of 0.114 cm and were 0.127-cm deep. Based on a two-dimensional conduction model of this discrete groove-heating arrangement, the maximum estimated temperature nonuniformity on the convectively active surface, expressed as the ratio, $(T_w - T_b)_{\max}/(T_w - T_b)_{\min}$, was only a few tenths of one percent.

The wire chosen as a heating element was 21-gage cupron (a nickel-chrome alloy), 0.072 cm in dia, wrapped with a 0.01-cm thickness of double-glass, silicon-impregnated electrical insulation. This wire was chosen for its thin, abrasion-resistant, high-temperature insulation as well as for its convenient resistance per unit length.

The locations of the thermocouples used to measure the duct wall temperature distributions are also shown in the lower diagram of Fig. 1. Fine gage (0.00762 cm) specially calibrated copper-constantan thermocouples were employed with the intent of minimizing the disturbance of the temperature field in the vicinity of the thermocouple junctions. The thermocouples were installed in holes drilled into the back side of the duct walls to within 0.0254 cm of the corrugation surface. The holes were centered on each facet and filled with copper oxide cement during thermocouple installation. Four thermocouples, positioned just upstream of the duct inlet, were used to measure the entering bulk temperature.

The test section was supported and positioned during the experiments by eight sharp-tipped nylon adjustment screws which were threaded, four in a set, into two U-shaped plexiglass frames. Fifteen cm of fiberglass insulation surrounded the test section during operation.

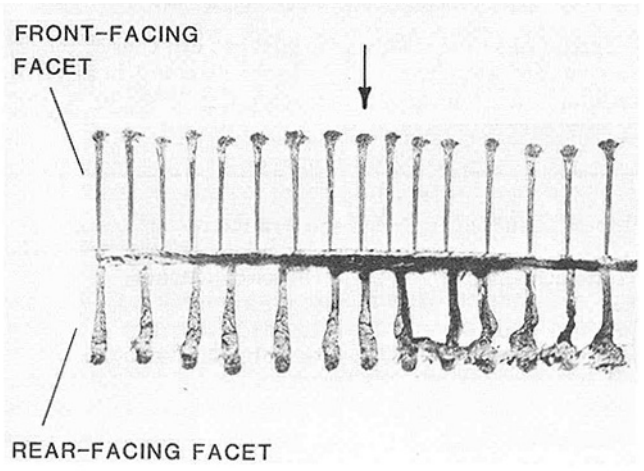

Fig. 3 Visualizations of the fluid-flow patterns adjacent to the front-facing and rear-facing facets

System Components. Flow through the test section was maintained by a constant head tank supported from the laboratory ceiling which received hot, cold, or a mixture of hot and cold water (depending on the desired Prandtl number), from a building water supply line. A ball valve located upstream of the plenum chambers was used to control the flow rate through the system.

Upon entering the upstream plenum chamber, which is 91.4 cm in length and has a 30.5-cm square cross section, the water encounters a 10-cm dia baffle plate installed in line with the plenum entrance. This baffle plate, together with three fine-mesh screens located further downstream, minimize inlet flow disturbances and provide a uniform low-velocity inlet flow to the test section. The upstream plenum was fitted with three small globe valves located on its upper surface to allow air to escape during the filling process which preceded each data run. It also had two plexiglass windows. The windows allowed access to the inlet side of the test section and thermal barrier and also enabled visual inspection of the filling process. Examination of the flow passing these windows indicated the absence of air bubbles.

After exiting the test section, the water enters the downstream plenum chamber, which is a 30.5-cm cube. This chamber has one air-escape valve. Access to the exit end of the test section and the thermal barrier was possible through a 7.62-cm dia aperture in the downstream face of this plenum chamber. This aperture also accommodates a flange for the downstream piping which leads to the weight tank. A riser pipe, located downstream of the plenum chamber, ensures that the test section and both plenums are completely full of water during operation.

Electrical power was supplied to the test section heating wire by two independent circuits, one for the top duct wall and one for the bottom. The source of power for each circuit was an autotransformer, supplied from a standard 120-V, 60-cycle a.c. wall outlet. These autotransformers were designed for a load voltage output of 0–140 V, with a maximum current of 20 amps.

The voltage drops across each resistance wire and across two shunt resistors (to measure the heater currents) were conveyed to a multimeter. These readings permitted calculation of the power dissipation in the resistance wires.

The thermocouple voltage outputs were fed into a Fluke model 2240C scanning data logger which had the capability to time-average the outputs. This feature was useful since the inlet water temperature was not generally constant with time.

Air Flow System. In order to obtain information on pressure drops and friction factors and also to perform flow visualization utilizing the oil-lampblack technique, a separate apparatus for use with air was constructed out of plexiglass.

The test section of this apparatus, which was designed for quick disassembly during the flow visualization tests, had the same internal geometry as the heat-transfer test section. Pressure taps, centered on each facet, were located in the lower duct wall. The test section was mounted between an upstream baffle plate and a downstream plenum, which provided the same inlet and exit conditions as in the heat-transfer experiment. All machined surfaces of the test section were polished with successively finer grades of lapping compound up to grit size 1200 since a transparent duct was desired for flow visualization.

Air from the laboratory room was drawn through the system by a downstream blower. The flow rate was controlled by a valve and measured by a rotameter. Pressure information from the wall taps was channeled through a pressure selector switch and presented to an MKS Baratron capacitance-type,

solid-state pressure meter, which has a resolution of 10^{-4} Torr.

Experimental Procedure. After the establishment of an overflow from the constant head tank and filling the plenum chambers, the flow control valve was opened to the maximum flow rate in order to wash any air bubbles or pockets out of the corrugated duct which may have formed while the system was at rest. The flow control valve was then adjusted to the desired flow rate for the run, as measured by the weight tank.

The inlet bulk temperature was then tailored to attain a desired Prandtl number by adjusting the relative amounts of hot and cold water which entered the constant head tank. The Prandtl numbers studied, from the coldest inlet water temperature (13.9°C) to the hottest (46.7°C), ranged from 8.2 to 3.8.

Next, heating was initiated by the adjustment of the autotransformers to predetermined voltage outputs. The power settings were based on a rise in bulk temperature of 0.8°C to 1.1°C. Equal power input per unit heated length was established in the top-wall and bottom-wall heating circuits.

Data acquisition began after steady-state operation was achieved. The data logger was first programmed to scan and time average the outputs from the top duct wall and the inlet bulk thermocouples. This averaging occupied thirty data logger input channels, the maximum number of channels available for time-averaging. The averaging process consisted of a scan of all thirty of these channels every 15 s for a total of ninety-nine scans, after which the time-averaged values were printed on paper tape. A similar 25-m averaging process was then carried out for the bottom duct wall and the inlet bulk. Two cycles of such scans were typically performed. The inlet bulk temperatures were included in the time-averaging process for both the top and bottom duct wall temperatures, because the inlet bulk temperature tended to fluctuate with time, thus making it necessary to relate the wall temperatures to the prevailing bulk temperature. After the temperature data had been acquired, the system was shut down.

Measurements of axial pressure drop were made using the plexiglass corrugated duct which was fitted with eighteen pressure taps, each centered on a facet. The pressure difference between the laboratory room from which the air was drawn and the axial station of interest was sensed by the Baratron pressure meter. At a given flow rate as measured by the rotameter, the data were taken by selecting the station of interest from the pressure-selector switch and reading the output from the Baratron with a Hewlett-Packard multimeter. The laboratory pressure p_{atm} was read prior to and after each pressure data run.

The oil-lampblack technique for flow visualization was also performed in the plexiglass corrugated duct. White contact paper, cut to the width of the duct, was carefully applied to the corrugations of the lower duct wall. A mixture of oil and lampblack, whose fluidity could be varied by using various oils and also by adding different proportions of lampblack to the oils, was applied to the surface of the contact paper. Application of dots of the tracer fluid resulted in a streak pattern, revealing the surface-adjacent flow direction. Global application in which the entire surface of the contact paper was coated with tracer fluid displayed the overall flow pattern and the zones of relatively strong and weak surface-adjacent flows.

After application of the oil-lampblack mixture to the surface of the contact paper, the duct was reassembled and the blower activated. Since the duct walls were transparent, the motion of the tracer fluid could be observed. Photographs of the flow patterns were obtained after the contact paper was removed from the duct and laid flat on a white sheet of paper.

Data Reduction. The primary goal of this experiment was the determination of fully developed Nusselt numbers for water flowing in a corrugated duct. The independent parameters were the Reynolds number and the Prandtl number. The Reynolds number based on the duct hydraulic diameter is given by

$$\mathrm{Re} = \rho V D_h / \mu = 4\dot{m}/\mu P \tag{1}$$

where $\dot{m}$ is the mass flow rate. The hydraulic diameter, D_h, was evaluated from its conventional definition

$$D_h = 4A/P \tag{2}$$

in which A is the cross-sectional area of the duct, perpendicular to the facets, and P is the perimeter which bounds A. The viscosity and the Prandtl number of the water, which are strongly temperature dependent, were evaluated at the average bulk temperature, halfway through the duct.

The determination of fully developed Nusselt numbers from the experimental data began with the calculation of the overall bulk temperature rise based on an energy balance on the flowing water. The slope of this temperature rise was then obtained by dividing by the heated length of the duct (i.e., the length of duct backed by heater wire). A plot of the measured duct wall temperatures was then prepared in order to determine the range over which the slope of the wall temperatures was equal to the calculated bulk temperature slope, indicating the region of fully developed heat transfer, free of end effects.[1]

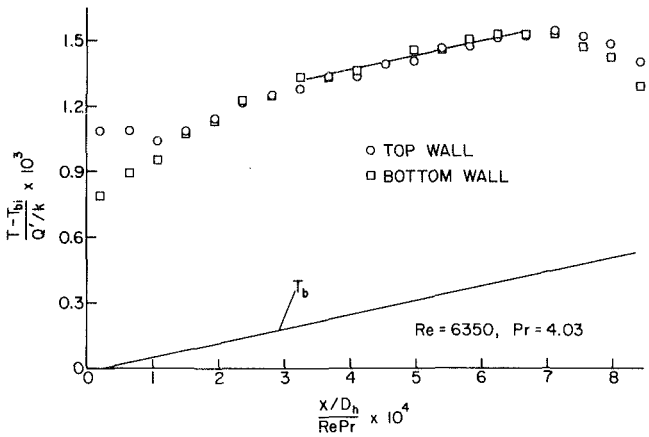

Fig. 4 Representative nondimensional temperature distribution

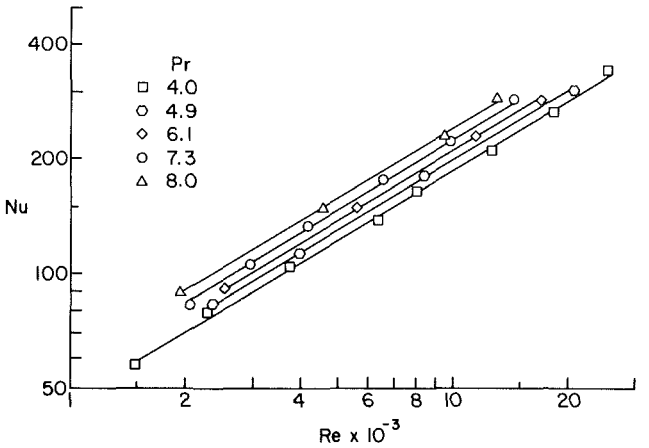

Fig. 5 Fully developed Nusselt numbers for several distinct Prandtl numbers

[1] In the fully developed regime, the heat input per module is the same from module to module. The wall and bulk temperatures experience an identical per-module increase which is also the same from module to module.

A line parallel to the bulk temperature line was then fitted by least squares through the wall temperature data and used for determination of the wall-to-bulk temperature difference. The data acquisition scheme discussed earlier necessitated separate handling of the data from the two duct walls. The heat flux for each duct wall (heat input per unit transfer surface area) was then calculated and divided by the wall-to-bulk temperature difference, yielding a heat-transfer coefficient.

The corresponding fully developed Nusselt number is given by

$$\mathrm{Nu} = hD_h/k \tag{3}$$

where h is the heat-transfer coefficient, and the thermal conductivity, k, was evaluated at the mean bulk temperature. Nusselt numbers for the top and bottom walls, which typically differed by about 6 percent, were averaged, yielding the desired Nusselt-number result for the data run.

Five sets of data were acquired, each set consisting of four to eight data runs at varying Reynolds numbers but at nearly equal Prandtl numbers. A power-law curve fit was performed to establish a Nusselt-Reynolds relation for each data set. For an intermediate Reynolds number in the investigated range, a Nusselt number was evaluated for each of the five sets using the fitted equations. These Nusselt numbers were plotted as a function of the average Prandtl number for each set, and a power-law curve fit yielded a Prandtl-number dependence of $\mathrm{Pr}^{0.34}$. Then, by bringing together all of the data in the form of $\mathrm{Nu}/\mathrm{Pr}^{0.34}$, an overall Reynolds-number dependence of $\mathrm{Re}^{0.614}$ was determined.

The friction factor was evaluated using the pressure gradient obtained from least-squares lines fitted through the pressure-distribution data in conjunction with the defining equation

$$f = \frac{(-dp/dx)D_h}{\frac{1}{2}\rho V^2} \tag{4}$$

Results and Discussion

The presentation will begin with the flow visualization patterns, to be followed by the heat-transfer results and then the friction factors.

Flow Visualization. A representative photograph showing the visualized patterns of fluid flow adjacent to the front-facing and rear-facing facets of the corrugated wall is presented in Fig. 3. In the photograph, the dark centrally positioned horizontal band represents an accumulation of the oil-lampblack tracer fluid just downstream of the peak of a corrugation. The array of parallel streaks above the band depicts the direction of fluid flow along the forward-facing facet. Visual observation of the development of the streaks from the dots of tracer fluid placed at the base of the facet indicated a forward flow direction. The parallelism of these streaks demonstrates that the flow was two-dimensional and not significantly affected by the side walls.

In contrast, the streaks on the rearward facet (i.e., below the dark horizontal band) revealed the presence of a backflow (opposite to the mainflow direction) adjacent to the facet. This backflow is one leg of a recirculation zone which blankets the rearward face. The recirculation results from the separation of the mainflow at the peak of the corrugation.

The visual observations showed the forward flow on the front-facing facet to be more vigorous than the backflow adjacent to the rearward facet. In general, the presence of a large recirculation zone in each cycle of the corrugations means that the flow under investigation is markedly different from that encountered in conventional duct flows. No evidence of secondary flow (i.e., Görtler vortices) was observed.

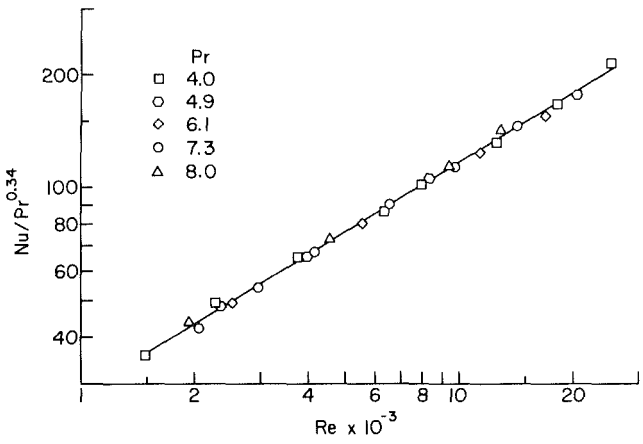

Fig. 6 Correlation of the fully developed Nusselt numbers

Temperature Distributions. A representative non-dimensional temperature distribution plot is shown in Fig. 4. In this figure, the ordinate variable is the dimensionless temperature difference $(T-T_{bi})/(Q'/k)$, where Q' is the rate of heat transfer to the flowing water per unit length per side. The abscissa variable in Fig. 4 is often called the Graetz number and is a dimensionless representation of the linear axial coordinate.

The most important portion of the wall-temperature distribution is the central segment through which a straight line has been fitted parallel to the line representing the fluid bulk temperature. The vertical distance between this line segment and the bulk-temperature line indicates the wall-to-bulk temperature difference used in calculating the fully developed heat-transfer coefficient.

The departure of the wall temperature data from straight-line behavior at the upstream and downstream ends of the duct was due mainly to the absence of rear-side heating at these ends (see Fig. 1, lower diagram). Other factors possibly influencing these end wall temperatures include flow development (at the upstream end) and small extraneous conduction losses.

The periodic nature of the fully developed heat-transfer regime can be observed in the temperature distribution. Each relatively high wall temperature is followed in sequence by a relatively low wall temperature.

Nusselt Numbers. The fully developed Nusselt numbers are displayed on log-log coordinates in Figs. 5 and 6. Figure 5 shows Nusselt numbers plotted as a function of Reynolds number for five separate Prandtl numbers. The Prandtl number of each data set is tabulated in the figure along with its corresponding data symbol. Each Nusselt number shown has been corrected to its set-reference Prandtl number by a $\mathrm{Pr}^{0.34}$ dependence.

Table 1 Comparison of present Nu values with those of Dittus-Boelter (D-B) and Petukhov-Popov (P-P)

	Pr = 4			Pr = 8		
Re	Present	D-B	P-P	Present	D-B	P-P
10,000	187	63.5	68.9	237	83.7	90.9
17,500	264	99.3	108.	334	131.	144.
25,000	329	132.	144.	416	174.	194.

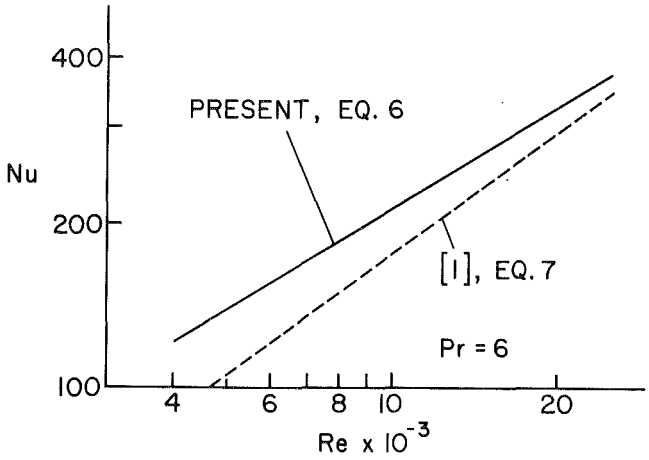

Fig. 7 Comparison of present Nusselt number results with those of Beloborodov and Volgin [1]

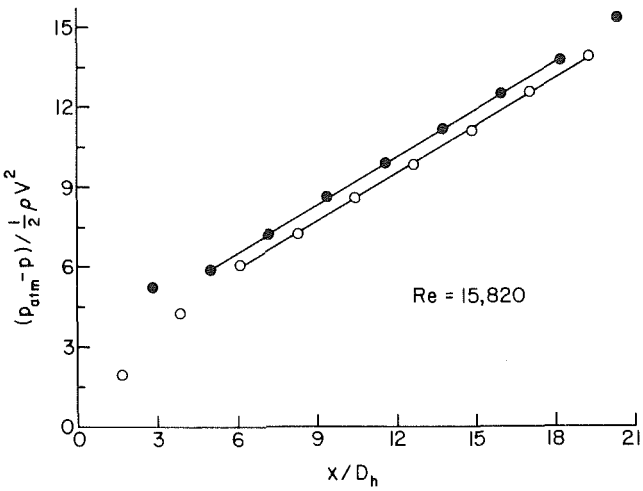

Fig. 8 Representative nondimensional axial pressure distribution. Open symbols denote pressures on successive forward-facing facets and black symbols denote pressures on successive rearward-facing facets.

The straight lines fitted through each set of data in Fig. 5 are parallel and have a Reynolds-number dependence of $Re^{0.614}$, determined from a power-law curve fitted through all of the data points.

Figure 6 displays the same data as Fig. 5, with the Prandtl-number dependence imbedded in the ordinate variable. The straight line fitted through the data points represents the power-law relationship given by

$$Nu/Pr^{0.34} = 0.409\ Re^{0.614} \tag{5}$$

which can be rewritten as

$$Nu = 0.409\ Re^{0.614} Pr^{0.34} \tag{6}$$

for the purposes of comparison to other correlations.

Literature Comparisons. The 0.614 value of the Reynolds-number exponent appears low when compared to the 0.8 exponent for a standard turbulent duct-flow situation. This finding is not unexpected, however, since the corrugated-duct flow contains large zones of recirculation not present in conventional duct flows.

The correlations of Zhukauskas [3] for predicting average fully developed Nusselt numbers in rows of tube banks, a flow situation which also includes large, periodic recirculation zones, involve a dependence of $Re^{0.60}$ for staggered banks and $Re^{0.63}$ for in-line banks. Grimison [4] gives another correlation for both staggered and in-line tube banks in which the Reynolds-number exponent is very close to 0.57 for in-line arrays and 0.60 for staggered arrays.

The Prandtl-number exponent of 0.34 in equation (6) is intermediate with respect to other values found in the literature for turbulent flows, which range from 0.3 to 0.4. An exponent of 1/3 is quite common in the older literature. Zhukauskas [3] has found a Prandtl-number exponent of 0.36 to be useful for tube banks, while the tube-bank correlations of Grimison [4] and Whitaker [5] use 1/3.

To examine the enhancement provided by the corrugated duct, comparisons of the present Nusselt numbers with those for parallel-plate channels will now be made. The channel results will be represented by the correlations of Dittus-Boelter and of Petukhov-Popov (cited in [6]) which, although originally based on circular tube data, are purported to yield good approximations of fully developed Nusselt numbers for parallel-plate channels when the hydraulic diameter is used as the characteristic dimension. These correlations are based on data for Reynolds numbers exceeding 10,000.

The comparison, shown in Table 1, demonstrates the level of heat-transfer enhancement associated with the corrugated duct. The enhancement factor ranges from a minimum of 2.14 at Re = 25,000 and Pr = 8 to a maximum of 2.71 at Re = 10,000 and Pr = 4, when compared to Petukhov-Popov. These impressive levels of enhancement project the corrugated duct as a strong candidate for use in applications where high heat-transfer coefficients are needed.

The Nusselt number correlation of equation (6) will now be compared to previous experiments on corrugated ducts found in the literature.

In Fig. 7, a comparison is made to a correlation obtained by Beloborodov and Volgin [1]

$$Nu = 0.097\ Re^{0.73} Pr^{0.43} (Pr/Pr_w)^{0.25} \tag{7}$$

Since the Prandtl number dependence identified in this equation is different from that of the present work, the correlations were evaluated at the intermediate Prandtl number of 6.0. The average value of the quantity $(Pr/Pr_w)^{0.25}$ for the present experiments was about 1.02. Therefore, equation (7) was evaluated with this numerical factor included.

The level of agreement of the two correlations, ranging from 30 percent at Re = 5000 to 9 percent at Re = 25,000, is fairly good, considering the many differences between the two experiments that were cited in the Introduction. The importance of recirculating flow is believed to be greater for the present experiments due to the tighter spacing and sharper corrugation peaks, resulting in the lower Reynolds-number exponent.

The final comparison to be made is with the data of Goldstein [2], and Table 2 has been prepared for this purpose. The experiments of [2] were performed using the naphthalene sublimation technique, which corresponds to a uniform wall temperature boundary condition. There are two other major differences between the present work and that of Goldstein. First, the duct of [2] had only two corrugation facets, owing to the difficulty of fabricating a long corrugated duct using naphthalene; as a consequence of the short duct, fully developed conditions were not attained. Second, the corrugation angle of [2] was only 21 deg. Also, it is likely that sublimation rounded the corrugation peaks during the data runs performed by Goldstein.

To match the dimensionless parameters of [2], the characteristic dimension now to be used in the tabulated Nusselt, Sherwood, and Reynolds numbers is $2H'$, where H' is the vertical inter-wall spacing (see Fig. 1). Furthermore, to attain a form comparable to $Nu'/Pr^{0.34}$, the Sherwood numbers of [2] were divided by $Sc^{0.34}$ where Sc, the Schmidt number, is equal to 2.5 for the napthalene-air system.

The table shows that the values of $Sh'/Sc^{0.34}$ obtained by

Table 2 Comparison of present Nu values with those of Goldstein [2]

Re′	$Nu'/Pr^{0.34}$	$Sh'/Sc^{0.34}$
2040	46.6	31.9
2210	49.0	33.9
2370	51.2	37.9
3070	59.9	50.0
3080	60.0	43.4
3930	69.6	53.8
6270	92.5	75.0
8560	111.9	87.8

Primed quantities are based on characteristic dimension $2H'$

Table 3 Corrugated duct friction factors

Re	f
2160	0.586
3760	0.572
5880	0.557
10,790	0.565
16,230	0.566
20,870	0.576
25,060	0.577

Goldstein range from 50 percent lower than the $Nu'/Pr^{0.34}$ of the present study at the lowest Reynolds numbers to 27 percent lower at the highest Reynolds numbers shown. This level of disagreement must be due to the differences in geometry, degree of flow development, and boundary conditions mentioned previously.

Pressure Distributions and Friction Factors. Before considering the pressure distribution data, it should be noted that, downstream of an initial development region, the flow pattern repeats itself periodically from one corrugation cycle to another. This behavior may be characterized as periodically fully developed. Furthermore, in such a regime, the pressures at cyclically corresponding locations on successive forward-facing facets should decrease linearly in the downstream direction, and a similar behavior is expected at corresponding locations on successive rearward-facing facets. However, on a given facet, the pressure variation along the facet will, in general, not be linear.

A representative nondimensional axial pressure distribution is shown in Fig. 8. The open data symbols represent data at cyclically corresponding locations on the forward-facing facets, while the black symbols denote similar data for the rearward-facing facets. Least-squares straight lines have been passed through the data points which fall in the periodically fully developed regime. As follows from the theory of the periodic fully developed regime, the two straight lines are of identical slope.

The onset of the linear pressure drop occurs at an axial coordinate five hydraulic diameters downstream of the duct inlet, on the fifth facet.

Friction factors were calculated from equation (4) using the slopes (dp/dx) of the measured pressure distributions as input, and the results are listed in Table 3. The Reynolds number range in this table is the same as that covered in the heat transfer experiments.

Over the entire Reynolds number range, very little, if any, dependence on the Reynolds number can be detected from the values shown, indicating that the pressure drop is solely due to inertial losses.

The magnitude of the friction factors is very high compared to typical values for pipe flows. This result is not surprising in light of the cyclically separating, recirculating, and redeveloping flow pattern of the corrugated duct.

Concluding Remarks

The experiments described herein represent the first definitive study of fully developed heat transfer for water flowing in a corrugated duct. The duct had a corrugation angle of 30 deg and an interwall spacing equal to the corrugation height. The Reynolds number based on hydraulic diameter was varied from 1500 to 25,000, and the Prandtl number was varied from 4 to 8.

Flow visualization studies revealed a highly complex flow pattern including a strong forward flow adjacent to the surface of the front-facing facets and an oppositely-directed recirculating flow adjacent to the rearward facets.

A periodic, fully developed, heat-transfer regime was identified by axial wall temperature measurements. From these temperature distributions, which provided a wall-to-bulk temperature difference, and from the measured heat flux, Nusselt numbers were determined. These Nusselt numbers, when correlated with a power-law representation, resulted in a Reynolds-number exponent of 0.614 and a Prandtl-number exponent of 0.34. The 0.614 Reynolds-number exponent agrees quite well with exponents used for forced convection in tube banks [3, 4], which have similarly periodic separation and high turbulence levels. The 0.34 Prandtl-number exponent is intermediate with respect to values found in the literature for turbulent flows.

A high level of heat-transfer enhancement, when compared to the conventional parallel-plate channel, was associated with the corrugated duct flow. This enhancement, at about a factor of 2.5, projects the corrugated duct as a strong candidate for high heat-flux applications.

Axial pressure distributions were used to determine friction factors, which exhibited virtually no dependence on Reynolds number, indicating the dominance of inertial-type losses. The magnitude of the friction factors, averaging 0.57, is very high when compared to conventional pipe flows.

The results obtained here correspond to a specific geometry and, until other information becomes available, they should only be applied to configurations which do not differ appreciably from that investigated here.

References

1 Beloborodov, V. G., and Volgin, B. P., "Heat Transfer and Pressure Drop in Heat Transfer Equipment with Slot Channels of Varying Cross Section," *International Chemical Engineering*, Vol. 11, 1971, pp. 229–233.

2 Goldstein, Leonardo, Jr., and Sparrow, E. M., "Heat/Mass Transfer Characteristics for Flow in a Corrugated Wall Channel," ASME JOURNAL OF HEAT TRANSFER, Vol. 91, 1977, pp. 187–195.

3 Zhukauskas, A., "Heat Transfer from Tubes in Crossflow," *Advances in Heat Transfer*, Vol. 8, 1972, pp. 93–160.

4 Grimison, E. D., "Correlation and Utilization of New Data on Flow of Gases over Tube Banks," Trans. ASME, Vol. 59, 1937, pp. 583–594.

5 Whitaker, S., "Forced Convection Heat Transfer Correlations for Flow in Pipes, Past Flat Plates, Single Cylinders, Single Spheres and for Flow in Packed Beds and Tube Bundles," *AIChE Journal*, Vol. 18, 1972, pp. 361–365.

6 Karlekar, B. V., and Desmond, R. M., *Engineering Heat Transfer*, West Publishing Company, St. Paul, Minn., 1977.

7 O'Brien, J. E., "Corrugated-Duct Heat Transfer, Pressure Drop, and Flow Visualization," Ph.D. thesis, Department of Mechanical Engineering, University of Minnesota, Minneapolis, Minnesota, 1981.

Multidimensional Numerical Modeling of Heat Exchangers

W. T. Sha

C. I. Yang
Argonne National Laboratory,
Argonne, Ill. 60439

T. T. Kao

S. M. Cho
Mem. ASME

FW Energy Applications, Inc.,
Livingston, N.J. 07039

A comprehensive, multidimensional, thermal-hydraulic model is developed for the analysis of shell-and-tube heat exchangers for liquid metal services. For the shellside fluid, the conservation equations of mass, momentum and energy for continuum fluids are modified using the concept of porosity, surface permeability and distributed resistance to account for the blockage effects due to the presence of heat transfer tubes, flow baffles/shrouds, the support plates, etc. On the tubeside, the heat transfer tubes are connected in parallel between the inlet and outlet plenums, and tubeside flow distribution is calculated based on the plenum-to-plenum pressure difference being equal for all tubes. It is assumed that the fluid remains single-phased on the shell side and may undergo phase-change on the tube side, thereby simulating the conditions of Liquid Metal Fast Breeder Reactor (LMFBR) intermediate heat exchangers (IHX) and steam generators (SG). The analytical model predictions are compared with three sets of test data (one for IHX and two for SG) and favorable results are obtained, thus providing a limited validation of the model.

Introduction

Accurate and detailed knowledge of the fluid flow field and thermal distribution inside a heat exchanger becomes invaluable as a larger, more efficient and reliable unit is sought. This information is needed to provide proper evaluation of thermal and structural performance characteristics of a heat exchanger. Thermal-hydraulically unbalanced design or operation of a heat exchanger often causes unequal thermal loadings among the heat-transfer tubes, which may result in excessive thermal stresses in the tube bundle, thus impacting upon the integrity and reliability of the unit. The structural integrity of the pressure-bearing boundaries has direct safety implications for nuclear heat exchangers.

The flow pattern and the thermal map of a shell-and-tube heat exchanger may be obtained either through actual testing of a scale model or using an analytical prediction method. Scale model testing using a liquid metal is, in general, prohibitively expensive, often costing millions of dollars. Instrumentation used in liquid metal experiments must be able to withstand high temperature (often up to 550 °C) and corrosive environment. Other supporting equipments, such as pumps, valves, piping, are, in general, of special order. Substituting liquid metals with other heating transferring media, such as water, is not fully satisfactory because of the inherently special heat-transfer characteristics of liquid metals. Pressurized water can be used, however, in the case of isothermal flow field testing [1]. Another problem associated with scale model test is that suitable similarity parameters must be obtained and matched between the scale model and the actual unit. Otherwise all the conclusions and information drawn from the experimental data will be of limited value.

On the other hand, an analytical prediction method, when properly validated, will greatly reduce the need of scale model testing and aid in the optimization of heat-exchanger design, thus tremendous savings on cost and schedule are being realized. With the advent of large digital computers and advances in the development of computational fluid mechanics [2], it has become possible to provide analytical prediction through numerical solution of the complex conservation equations of mass, momentum and energy for both the shellside and tubeside fluids. This numerical modeling technique will be a valuable, cost-effective design tool for development of advanced nuclear heat exchangers.

This paper presents the detailed development of a transient, three-dimensional, thermal-hydraulic computer code known as COMMIX-IHX/SG. The shellside fluid is single-phased while the tubeside fluid is either single- or two-phased. This code is suitable for the analysis of liquid metal heat exchangers such as sodium-to-sodium intermediate heat exchangers and sodium-to-water steam generators, and of other types such as water-to-water and water-to-steam exchangers. The code was run for the three sets of experimental data and the resulting comparisons are reported herein.

It may be noted that detailed heat-exchanger tube bundle thermal hydraulics of the type presented in this paper are considered to be in their infancy of development. It is hoped that the present paper will spur further interest in this area.

Previous Analytical Methods

In the past, several investigations have been made to obtain the flow distribution inside a heat exchanger through solutions of the continuum Navier-Stokes equations. The idea of using distribution resistances to simulate the presence of heat-transfer tubes and baffle plates on the shell side of a heat exchanger was first introduced by Patankar and Spalding [3]. These authors assumed that the space inside a heat exchanger is uniformly filled with fluid, throughout which, however, a resistance to fluid motion is distributed on a fine scale. But they did not calculate tubeside flow distribution. More recently, AbuRomia et al. [4] applied the distributed resistance concept to obtain the flow field between the typical tube support spans of the Clinch River Breeder Reactor Plant (CRBRP) Intermediate Heat Exchangers. This analysis was limited to an isothermal flow field and included a turbulence model which is perhaps more suitable for a plenum than for a tube bundle.

Present Analysis Method

In all the previous analyses, the distributed resistance concept was utilized for the shellside fluid to simulate the presence of the tube bundle, and the fluid porosity was assumed to be a volumetric one only. Consequently, the actual velocity vector, and thus the directional fluid

Contributed by the Heat Transfer Division and presented at the 1982 ASME-ANS Nuclear Engineering Conference. Manuscript received by the Heat Transfer Division October 19, 1981.

momentum, could not be adequately simulated because the tube bundle porosity or permeability is, in general, anisotropic. In the present analysis, a combination of volume porosity, surface permeability and distributed resistance concept [5, 6] is used to modify the continuum Navier-Stokes equations in order to properly account for the presence of the tube bundle, tube support baffles, flow baffles, etc., on the shellside of the heat exchanger (more details to follow). It may be noted that, without the volumetric porosity/surface permeability factors, the calculated fluid momentum would be lower than the actual momentum; and without the distributed resistance, the calculated pressure drop would be less than the actual pressure drop.

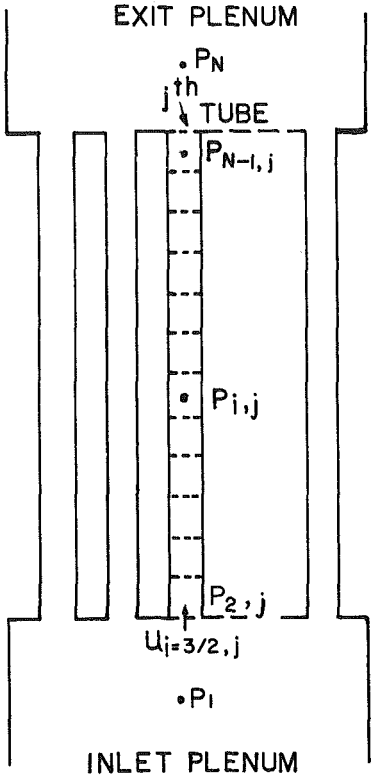

Fig. 1 Tubeside model

Since most liquid metal heat exchangers are of cylindrical geometry, the polar-cylindrical coordinate system is adopted in the development of conservation equations for the shellside fluid. These equations are:

Continuity Equation:

$$\frac{\partial}{\partial t}(\gamma_v \rho) + \frac{1}{r}\frac{\partial}{\partial r}(\gamma_r \rho r u) + \frac{1}{r}\frac{\partial}{\partial \theta}(\gamma_\theta \rho v) + \frac{\partial}{\partial z}(\gamma_z \rho w) = 0 \quad (1)$$

Momentum Equations:

$$\frac{\partial}{\partial t}(\gamma_v \rho u) + \frac{1}{r}\frac{\partial}{\partial r}(\gamma_r \rho r u^2) + \frac{1}{r}\frac{\partial}{\partial \theta}(\gamma_\theta \rho u v) + \frac{\partial}{\partial z}(\gamma_z \rho u w) - \gamma_\theta \rho \frac{v^2}{r} =$$

$$-\gamma_v \frac{\partial p}{\partial r} + \frac{\partial}{\partial r}\left[\mu_{\text{eff}} \gamma_r \frac{1}{r}\frac{\partial}{\partial r}(ru)\right] + \frac{1}{r^2}\frac{\partial}{\partial \theta}\left[\mu_{\text{eff}} \gamma_\theta \frac{\partial u}{\partial \theta}\right] + \frac{\partial}{\partial z}\left[\mu_{\text{eff}} \gamma_z \frac{\partial u}{\partial z}\right]$$

$$-2\mu_{\text{eff}} \gamma_r \frac{1}{r^2}\frac{\partial v}{\partial \theta} + \gamma_v R_r + \frac{\partial}{\partial r}\left\{\mu_{\text{eff}}\left[\frac{1}{r}\frac{\partial}{\partial r}(\gamma_r r u) + \frac{1}{r}\frac{\partial}{\partial \theta}(\gamma_\theta v) + \frac{\partial}{\partial z}(\gamma_z w)\right]\right\} + \gamma_v \rho g_r \quad (2)$$

$$\frac{\partial}{\partial t}(\gamma_v \rho v) + \frac{1}{r}\frac{\partial}{\partial r}(\gamma_r \rho u v) + \frac{1}{r^2}\frac{\partial}{\partial \theta}(\gamma_\theta \rho v^2)$$

Nomenclature

A = flow area (m^2)
c = specific heat (kJ/kg, °C)
d = tube inner diameter (m)
e_{ij} = twice strain rate
F = frictional pressure drop term defined in equation (21)
f = friction factor
g = gravitational acceleration (m/sec^2)
h = fluid enthalpy (kJ/kg)
K = turbulent kinetic energy (m^2/sec^2)
k_{eff} = effective thermal conductivity (W/m, °C)
k_m = molecular thermal conductivity (W/m, °C)
k_t = turbulent thermal conductivity (W/m, °C)
l = Prandtl's mixing length (m)
p = fluid pressure (Pa)
Pr = Prandtl number
Q = volumetric heat source or sink (J/m^3, sec)
R_i = distributed flow resistance in the i^{th} direction (N/m^3)
r = radial coordinate (m)
r_t = thermal resistance between heat transfer tube and tubeside fluid (m^3, °C/W)
r_0 = thermal resistance between heat transfer tube and shellside fluid (m^3, °C/W)
T = temperature (primarily shellside fluid) (°C)
t = time (s)
u = velocity in the r-direction or on tubeside (m/s)
V = flow velocity (m/s)
v = velocity in the θ-direction (m/s)
w = velocity in the z-direction (m/s)
y = distance measured from wall (m)
z = axial coordinate (m)
α = void fraction
β = coefficient of volumetric expansion
γ_i = surface permeability component
γ_v = volumetric porosity
ΔP = pressure difference (Pa)
ϵ_M = eddy diffusivity for momentum transport (m^2/s)
μ = dynamic viscosity (Pa, s)
ν = kinematic viscosity (m^2/s)
ρ = density (kg/m^3)
ϕ^2 = Martinelli-Nelson's two phase flow friction multiplier
Ω = modification factor to Martinelli-Nelson multiplier

Subscripts

eff = effective
f = fluid condition
l = liquid phase
g = gas phase
r = radial direction
s = velocity slip
t = turbulent quantity, or tubeside fluid
w = tube wall condition
z = axial direction
θ = circumferential or azimuthal direction

$$+\frac{2}{r}\gamma_\theta\rho uv)+\frac{\partial}{\partial z}(\gamma_z\rho uw)=$$

$$-\frac{\gamma v}{r}\frac{\partial p}{\partial\theta}+\frac{\partial}{\partial r}\left[\mu_{\text{eff}}\gamma_r\frac{1}{r}\frac{\partial}{\partial r}(rv)\right]$$

$$+\frac{1}{r^2}\frac{\partial}{\partial\theta}\left[\mu_{\text{eff}}\gamma_\theta\frac{\partial v}{\partial\theta}\right]+\frac{\partial}{\partial z}\left[\mu_{\text{eff}}\gamma_z\frac{\partial v}{\partial z}\right]$$

$$+2\mu_{\text{eff}}\gamma_\theta\frac{1}{r^2}\frac{\partial u}{\partial\theta}$$

$$+\gamma_v R_\theta+\frac{1}{r}\frac{\partial}{\partial\theta}\left\{\mu_{\text{eff}}\left[\frac{1}{r}\frac{\partial}{\partial r}(\gamma_r ru)+\frac{1}{r}\frac{\partial}{\partial\theta}(\gamma_\theta v)\right.\right.$$

$$\left.\left.+\frac{\partial}{\partial z}(\gamma_z w)\right]\right\}+\gamma_v\rho g_\theta \tag{3}$$

$$\frac{\partial}{\partial t}(\gamma_v\rho w)+\frac{1}{r}\frac{\partial}{\partial r}(\gamma_r\rho uw)+\frac{1}{r}\frac{\partial}{\partial\theta}(\gamma_\theta\rho vw)$$

$$+\frac{\partial}{\partial z}(\gamma_z\rho w^2)=-\gamma_v\frac{\partial p}{\partial z}+\frac{1}{r}\frac{\partial}{\partial r}\left[\mu_{\text{eff}}\gamma_r r\frac{\partial w}{\partial r}\right]$$

$$+\frac{1}{r^2}\frac{\partial}{\partial\theta}\left[\mu_{\text{eff}}\gamma_\theta\frac{\partial w}{\partial\theta}\right]+\frac{\partial}{\partial z}\left[\mu_{\text{eff}}\gamma_z\frac{\partial w}{\partial z}\right]$$

$$+\gamma_v R_z+\frac{\partial}{\partial z}\left\{\mu_{\text{eff}}\left[\frac{1}{r}\frac{\partial}{\partial r}(\gamma_r ru)\right.\right.$$

$$\left.\left.+\frac{1}{r}\frac{\partial}{\partial\theta}(\gamma_\theta v)+\frac{\partial}{\partial z}(\gamma_z w)\right]\right\}+\gamma_v\rho g_z \tag{4}$$

Energy Equation:

$$\frac{\partial}{\partial t}(\gamma_v\rho h)+\frac{1}{r}\frac{\partial}{\partial r}(\gamma_r\rho ruh)+\frac{1}{r}\frac{\partial}{\partial\theta}(\gamma_\theta\rho vh)$$

$$+\frac{\partial}{\partial z}(\gamma_z\rho wh)=\frac{1}{r}\frac{\partial}{\partial r}\left(\gamma_r k_{\text{eff}} r\frac{\partial T}{\partial r}\right)$$

$$+\frac{1}{r^2}\frac{\partial}{\partial\theta}\left(\gamma_\theta k_{\text{eff}}\frac{\partial T}{\partial\theta}\right)+\frac{\partial}{\partial z}\left(\gamma_z k_{\text{eff}}\frac{\partial T}{\partial z}\right)+Q \tag{5}$$

Here γ_v is the volumetric porosity, γ_i the surface permeability component, R_i the distributed resistance component, Q the amount of heat transferred into the shellside fluid from the heat-transfer tube per unit volume of the shellside fluid; the other symbols are defined in the nomenclature. The energy equation has neglected viscous dissipation and compression work terms since they are of secondary importance in heat exchange equipment.

Note that the only difference between the continuum Navier-Stokes equations and the above conservation equations for the shellside fluid is the presence of the volume porosity and surface permeability factors and the distributed resistance terms. In the absence of detailed information on these quantities in the tube bundle fluid flow, one may use the following approximations: (*a*) volume porosity = fraction of volume occupied by fluid in the control volume, (*b*) surface permeability factor = fraction of open projected flow area in the direction of flow component in the control volume (descrete values were used at the nodal points), and (*c*) distributed resistance = pressure loss term in the direction of flow component through submerged obstacles such as flow baffles and tube support plates.

It may also be noted that $\partial p/\partial x_i$ are normal static presure gradients. Distributed flow resistance terms are added to account for pressure losses due to the presence of discontinuous flow obstacles (such as tubes). Without these terms, the momentum equations cannot be treated as continuum fluid mechanics. Distributed flow resistance terms are input and thus cannot be readily combined with the regular pressure difference ($\partial p/\partial x_i$) terms.

These equations will become identical to the continuum fluid equations if both the volumetric porosity and surface permeability factors are set equal to unity and the distributed resistance terms are dropped out.

For the terms that include the turbulence effects, a one-equation turbulence model for a tube bundle based on the tranport equation for the turbulent kinetic energy is developed as shown:

$$\frac{\partial}{\partial t}(\alpha\rho K)+\frac{1}{r}\frac{\partial}{\partial r}(\gamma_r\rho ruK)+\frac{1}{r}\frac{\partial}{\partial\theta}(\gamma_\theta\rho vK)$$

$$+\frac{\partial}{\partial z}(\gamma_z\rho wK)=\mu_t\left[e_{rr}\frac{\partial}{\partial r}(\gamma_r u)\right.$$

$$+e_{r\theta}\frac{\partial}{\partial r}(\gamma_r v)+e_{rz}\frac{\partial}{\partial r}(\gamma_r w)+\gamma_r\frac{u}{r}e_{\theta\theta}$$

$$+e_{r\theta}\frac{1}{r}\frac{\partial}{\partial\theta}(\gamma_\theta u)+e_{\theta\theta}\frac{1}{r}\frac{\partial}{\partial\theta}(\gamma_\theta v)$$

$$+e_{\theta z}\frac{1}{r}\frac{\partial}{\partial\theta}(\gamma_\theta w)-\gamma_\theta\frac{v}{r}e_{r\theta}+e_{rz}\frac{\partial}{\partial z}(\gamma_z u)$$

$$\left.+e_{\theta z}\frac{\partial}{\partial z}(\gamma_z v)+e_{zz}\frac{\partial}{\partial z}(\gamma_z w)\right]$$

$$-C_t\beta\mu_t\rho\frac{K\alpha}{\epsilon}\left[(g_r e_{rr}+g_\theta e_{r\theta}+g_z e_{rz})\frac{\partial T}{\partial r}\right.$$

$$+(g_r e_{r\theta}+g_\theta e_{\theta\theta}+g_z e_{z\theta})\frac{1}{r}\frac{\partial T}{\partial\theta}$$

$$\left.+(g_r e_{rz}+g_\theta e_{z\theta}+g_z e_{zz})\frac{\partial T}{\partial z}\right]$$

$$+C_s\left[\frac{1}{r}\frac{\partial}{\partial r}\left(\mu_t\gamma_r r\frac{\partial K}{\partial r}\right)+\frac{1}{r^2}\frac{\partial}{\partial\theta}\left(\mu_t\gamma_\theta\frac{\partial K}{\partial\theta}\right)\right.$$

$$\left.+\frac{\partial}{\partial z}\left(\mu_t\gamma_z\frac{\partial K}{\partial z}\right)\right]-R_t-\rho\epsilon \tag{6}$$

where

$$\epsilon=C_D\frac{K^{3/2}}{l} \tag{7}$$

$$\mu_t=C_\mu\rho K^{1/2}l \tag{8}$$

$$R_t=C_r\alpha R_r|u|+R_\theta|v|+R_z|w| \tag{9}$$

Note that l is the mixing length, e_{ij} two times the strain rate, R_t turbulent kinetic energy due to distributed resistance, and C_D, C_r, C_s, C_t, C_μ are empirical constants. The mixing length as experimentally obtained for a rod bundle by Carajilescov and Todreas [7] is used in the present analysis:

$$\frac{l}{\bar{y}}=0.44+0.66\sin\left[\frac{\pi}{0.38}\left(\frac{y}{\bar{y}}-0.44\right)\right]\quad\text{for } 0.44\le\frac{y}{\bar{y}}\le 1.0 \tag{10a}$$

$$\frac{l}{\bar{y}}=\frac{y}{\bar{y}}\quad\text{for } 0\le\frac{y}{\bar{y}}\le 0.44 \tag{10b}$$

where $\bar{y}$ is the radial distance from the tube all to the maximum velocity line.

The above expressions (equations 10(*a*) and 10(*b*)) were used in the absence of tube bundle data. However, the dominant mixing mechanism in the heat-exchanger tube bundles under consideration is that due to the physical fluid

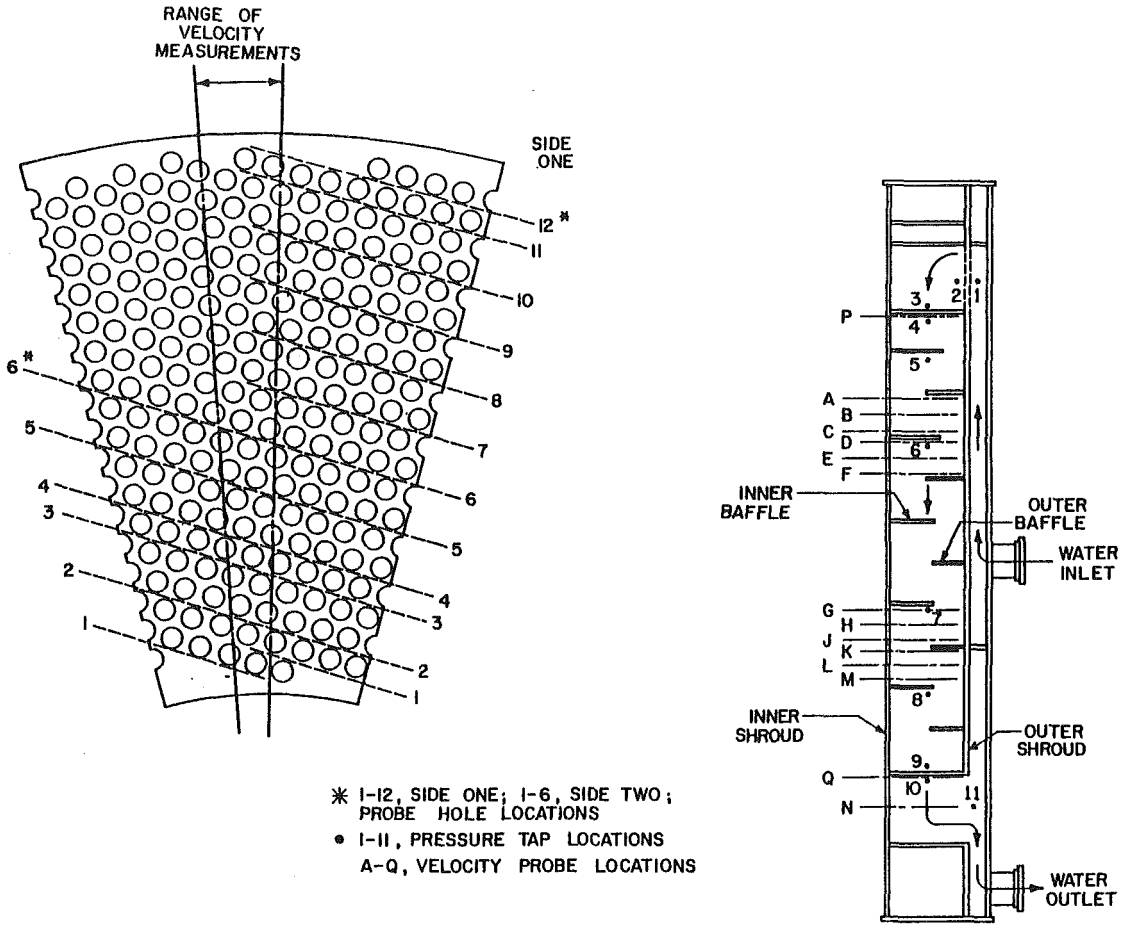

Fig. 2 CRBRP-IHX tube bundle flow model

Table 1 Tubeside thermal/hydraulic correlations for water

Heat-transfer correlations	
Subcooled water	Dittus-Boelter
Subcooled boiling	Thom
Nucleate boiling	Chen and Jens-Lottes
Critical heat flux	Westinghouse and Atomics International (AI) correlations
Film boiling	Bishop-Sandberg-Tong and AI correlations
Superheated steam	Heineman
Pressure drop correlations	
Single phase	Colebrook
Two-phase flow	Modified Martinelli-Nelson

Table 2 AI-MSG physical dimensions

Tubes	
Outside diameter (mm)	15.875
Tube wall thickness (mm)	2.921
Tube length (tubesheet to tubesheet) (m)	
Shortest tube	20.88
Longest tube	21.47
Active heat-transfer length (m)	17.68
Active heat-transfer area (m^2)	139.0
Number of tubes	158.0
Average pitch to diameter ratio	1.885
Material	2¼ Cr-1Mo steel
Tubesheets	
Thickness (mm	152.4
Outside diameter (mm)	482.6
Shell	
Main shell outside diameter (mm)	457.2
Main shell thickness (mm)	19.05
Header shell outside diameter (mm)	609.6
Header shell thickness (mm)	50.8
Tube Spacers	
Thickness (mm)	19.05
Number of tube spacers	24.0
Support	8 tierods
Hole diameter (mm)	16.18

mixing, rather than turbulence-induced mixing whose effect is therefore considered to be rather small.

The effective fluid viscosity μ_{eff} and thermal conductivity k_{eff} are defined by:

$$\mu_{\text{eff}} = \mu + \mu_t \tag{11}$$

$$k_{\text{eff}} = k_m + k_t \tag{12}$$

Here the turbulent viscosity μ_t and the turbulent thermal conductivity k_t are interrelated through the turbulent Prandtl number. In the present analysis, Dwyer's expression for the turbulent Prandtl number for liquid metal flow through a tube bundle is adopted [8]:

$$(\text{Pr})_t = \frac{c\mu_t}{k_t} = 1 - \frac{1.82}{\text{Pr}(\epsilon_M/\nu)^{1.4}} \tag{13}$$

As for the tubeside fluid, flow is considered as a multichannel, one-dimensional flow between two common plenums, as shown in Fig. 1. The state of fluid can be either single phase as in an intermediate heat exchanger or two phase as in a steam generator. In the following, the two-phase conservation equations are developed. However, these

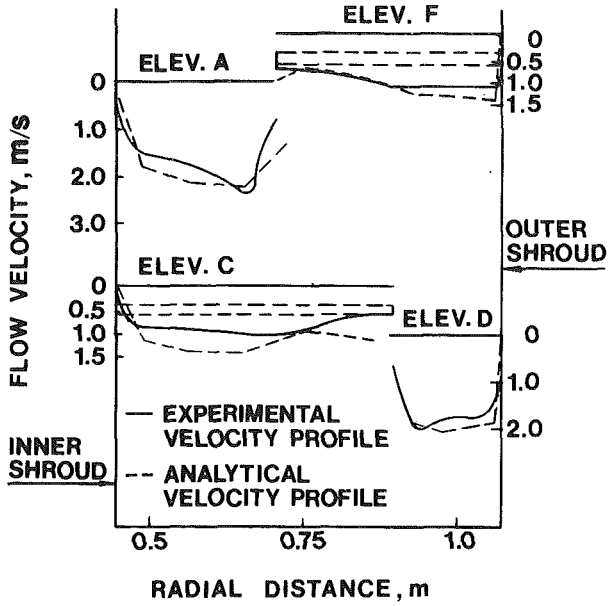

Fig. 3 Axial velocity profile at 100 percent flow

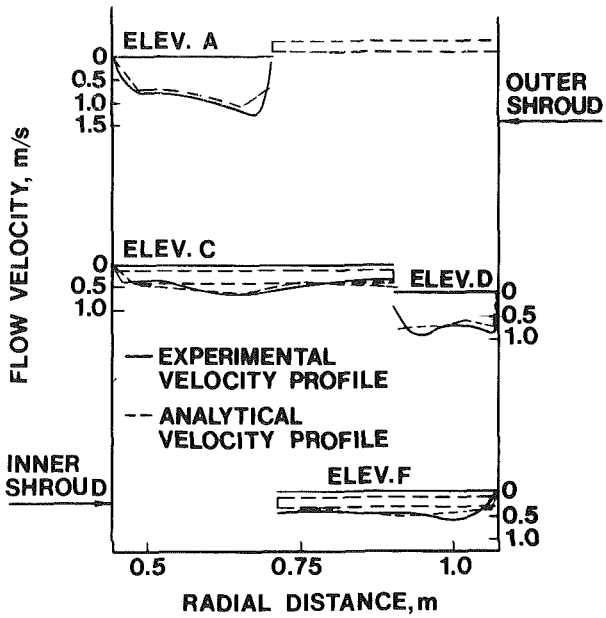

Fig. 4 Axial velocity profile at 40 percent flow

equations can be reduced to the single-phase equations with proper adjustment of parameters (e.g., $\alpha = 0$).

Adopting a homogeneous, equilibrium, two-phase flow model with the velocity slip between the liquid and vapor phases, one may write the conservation equations in the form:

Continuity Equation:

$$\frac{\partial \rho}{\partial t} + \frac{\partial}{\partial z}(\rho u) = 0 \tag{14}$$

Momentum Equation:

$$\frac{\partial}{\partial t}(\rho u) + \frac{\partial}{\partial z}(\rho u^2) = -\frac{\partial p}{\partial z} + \rho g - \frac{\partial F}{\partial z} - \frac{\partial}{\partial z}\left[\frac{\alpha(1-\alpha)\rho_g \rho_l}{\rho} V_s V_s\right] \tag{15}$$

Energy Equation:

$$\frac{\partial}{\partial t}(\rho h) + \frac{\partial}{\partial z}(\rho u h) = \frac{T_w - T_l}{r_t} + \frac{Dp}{Dt} \tag{16}$$

Here, r_t is the thermal resistance between the tube wall and the tubeside fluid. The thermal-hydraulic correlations used for the tubeside heat transfer and pressure drop for water are summarized in Table 1. The two-phase fluid density, mass flux, and phase velocities are given by:

$$\rho = \alpha\rho_g + (1-\alpha)\rho_l \tag{17}$$

$$\rho u = \alpha\rho_g V_g + (1-\alpha)\rho_l V_s \tag{18}$$

$$v_g = \frac{\rho u + (1-\alpha)\rho_l V_s}{\rho} \tag{19}$$

$$V_l = \frac{\rho u - \alpha\rho_g V_s}{\rho} \tag{20}$$

A water/steam slip and void fraction correlation based on experimental data for upward water/steam flow obtained by Thom [9] is used in the model. The water/steam property subroutine based on the 1967 ASME Steam Tables [15] has been incorporated into the code.

The friction pressure drop term $\partial F/\partial z$ in equation (15) is related to the friction factor by an equation:

$$\frac{\partial F}{\partial z} = \Omega\phi^2 \frac{f}{d} \cdot \frac{1}{2}\rho |u| u \tag{21}$$

The tubeside flow distribution is governed by two boundary conditions. First, all fluid channels have common inlet and exit plenum pressures and thus the pressure difference remains the same for all channels:

$$(\Delta p)_i = (\Delta p)_j \tag{22}$$

Second, the sum of all the mass-flow rates at the channel inlets must be equal to the total mass-flow rate supplied to the tubeside at any time.

$$\sum_{i=1}^{N} (\rho u A)_i, \text{ Inlet} = \text{Total tubeside flow} \tag{23}$$

Conservation equations have been developed above for both the shellside and tubeside fluids. The linkage between these two fluids is the energy conservation equation for the heat-transfer tube wall, which may be written in the form:

$$\rho_w c_w \frac{\partial T_w}{\partial t} = \frac{T - T_w}{r_0} + \frac{T_l - T_w}{r_t} \tag{24}$$

where r_0 is the thermal resistance between the tube wall and the shellside fluid.

The above set of conservation equations for the shellside and tubeside fluids, and the tube wall, are put into finite-difference form using Harlow's Implicit Continuum-fluid Eulerian (ICE) method [10] and solved on a digital computer. The ICE method has been widely used in fluid flow computation, and will not be repeated here.

The computer code developed above is named the COMMIX-IHX/SG code or simply COMMIX code.

Validation of Analytical Model

In order for an analytical modeling technique to be useful as a design tool, proper validation must be done. A limited quantitative validation effort has been made. Comparisons with three different sets of experimental data are presented in the following. It is noted that both two- and three- dimensional computations were made for validation runs, but only two-dimensional cases are presented in this paper. The results are presented in dimensional form, primarily because generalization using dimensionless parameters is very difficult and also time-consuming from a computational standpoint.

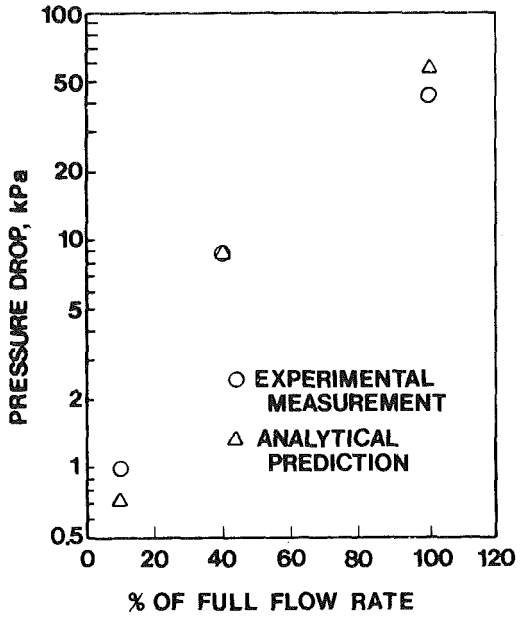

Fig. 5 30 deg sector model pressure drop

Comparison with 30° Sector Full-size CRBRP Intermediate Heat Exchanger Flow Model Test. This is an isothermal flow model test conducted by Foster Wheeler Energy Corporation [1]. The 30-deg sector, full-scale test model duplicates the Clinch River Breeder Reactor Plant (CRBRP) Intermediate Sodium Heat Exchanger tube bundle configuration, including the tubes, baffles, and inner and outer shrouds. The model length, however, is shorter by three baffle spans than the corresponding IHX bundle. Figure 2 shows the tube bundle configuration and a vertical cross-sectional view of the experimental setup. The tube bundle has been assembled with 219 stainless steel tubes of 22-mm (7/8 in.) o.d. in an equilateral pitch of 33.3 mm (1.312 in.). The upper half of the bundle has 2/3 area overlapping baffles and the lower half contains 1/2 area overlapping baffles. Water at temperature of 77°C (170°F) was used as a working fluid, in order to simulate sodium viscosity and Reynolds number. The full flow rate for the model was 10.56 m^3/min (2790 GPM) which corresponds to the full flow rate of the CRBRP-IHX.

The COMMIX computer model of the above 30-deg sector IHX test module is a two-dimensional, axisymmetric one, consisting of 9 radial nodes and 76 axial nodes. Several computer runs were made with different inlet flow rates ranging from 100 to 10 percent of full flow. The results for the axial velocity components at various elevations near the flow baffles are shown in the broken lines in Figs. 3 and 4 for 100 and 40 percent of full flow conditions, respectively. Superimposed on these analytical velocity profiles are the corresponding measured velocity profiles. The agreement between analytical predictions and experimental indications appears satisfactory, considering experimental uncertainties and analytical complexities. At 100 percent flow rate, the analytical solution overestimates the axial velocity components implying that the crossflow resistance correlation used in the analysis may be conservative. A comparison for the pressure drop across the test unit is shown in Fig. 5. The agreement is quite good, even though the analytical predictions tend to be higher at 100 percent flow, and lower at 10 percent, flow than the measurements.

Comparison with AI-Modular Steam Generator Test. The Atomics International Modular Steam Generator (AI-MSG) is a counterflow, once-through, sodium-to-water heat exchanger of an inverted hockey stick configuration. Sodium flows downward on the shell side and water/steam flows upward inside 158 tubes. Sodium nozzles are located at some distance away from water and steam nozzles, and semistagnant sodium regions exist in the tube bundle between the sodium outlet and the water inlet, and between the sodium inlet and the steam outlet. The physical dimensions of the MSG are summarized in Table 2. The further details of the MSG and its operation may be found in [11].

Table 3 AI-MSG steady-state operation test conditions (102.8 percent power)

Water flow (kg/hr)	57,800
Sodium flow (kg/hr)	735,000
Water inlet temperature (°C)	246
Sodium inlet temperature (°C)	464
Steam outlet pressure (MPa)	17.9
Steam outlet temperature (°C)	439
Sodium outlet temperature (°C)	341
Thermal duty (MW)	32.1

Table 4 50-MWT SNR-steam generator physical dimensions

Tubes	
Outside diameter (mm)	17.2
Tubewall thickness (mm)	2.9
Heating surface based on o.d. (m^2)	104.2
Active heat transfer tube length (m)	13.87
Number of tubes	139
Tube arrangement	Triangular
Tube pitch (mm)	27.5
Material	2¼ Cr-1Mo steel
Tube spacer/support	
Number of tube supports	20
Perforation	75%
Shell	
i.d. (mm)	468
Thickness (mm)	20

The COMMIX computer model for the AI-MSG unit, shown in Fig. 6, is an axisymmetric model with 8 radial and 82 axial nodes, totaling 656 nodes. (See Fig. 7 for unit configuration.) The active heat-transfer region consists of axial nodes 11 through 73. The upper hockey-stick bend area is simulated by a vertical cylindrical sections (nodes 1 through 10) because the present version of the code does not have provisions to model a bend or elbow configuration. The lower stagnation region is modeled by nodes 74 through 82. In the radial direction, the tube bundle is modeled by nodes 1 through 6. Radial node 7 simulated the tubeless space between the bundle and the shell.

The thermal hydraulic operating conditions used for the COMMIX simulation model is summarized in Table 3. This steady-state condition corresponds to 102.8 percent power condition.

In the MSG test, thermocouples were mounted on the shell wall and inside of the tube bundle. The thermocouple data points for the Table 3 test conditions are shown in Fig. 7 as a function of the active heat-transfer length of the bundle. The solid line indicates the average temperature profile based on these thermocouple data. Superimposed on this, in broken lines, are the analytical results from the COMMIX Code. Fairly good agreement between the test data and the predicted values is seen.

Also plotted in Fig. 7 are the average water/steam temperature profiles. Note that, on the water/steam side, only the inlet water and outlet steam temperatures were measured by test facility thermocouples. The solid line water/steam temperature profile is computed based on the measured

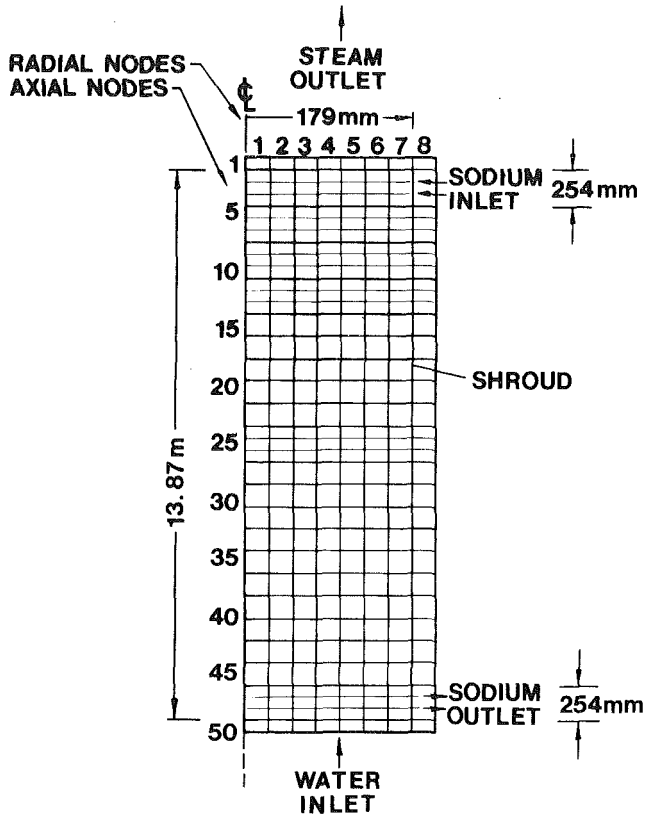

Fig. 6 COMMIX model for modular steam generator

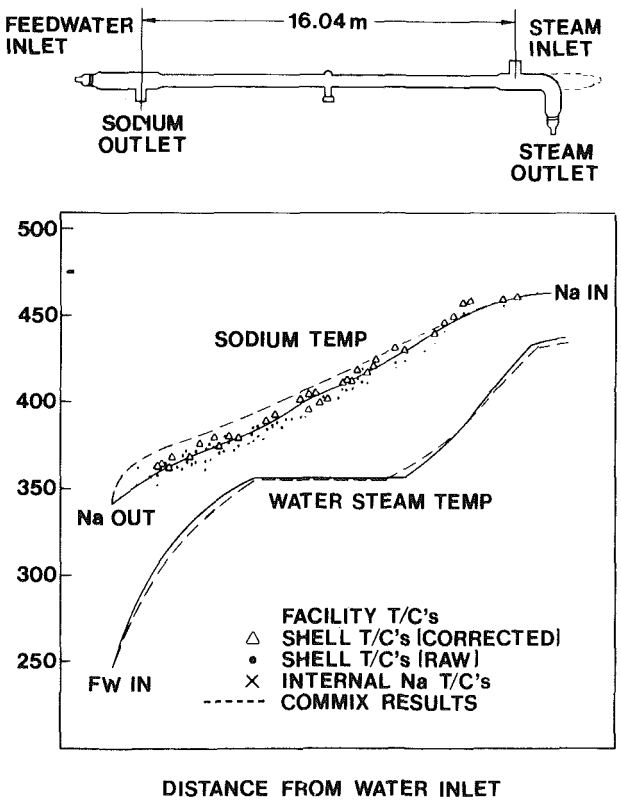

Fig. 7 MSG performance data and COMMIX prediction

averaged sodium temperature along the steam generator. The discrepancy between the predicted exit steam temperature (435°C) and the measured value (439°C) is nearly within the experimental measurement error band of ±3°C which was

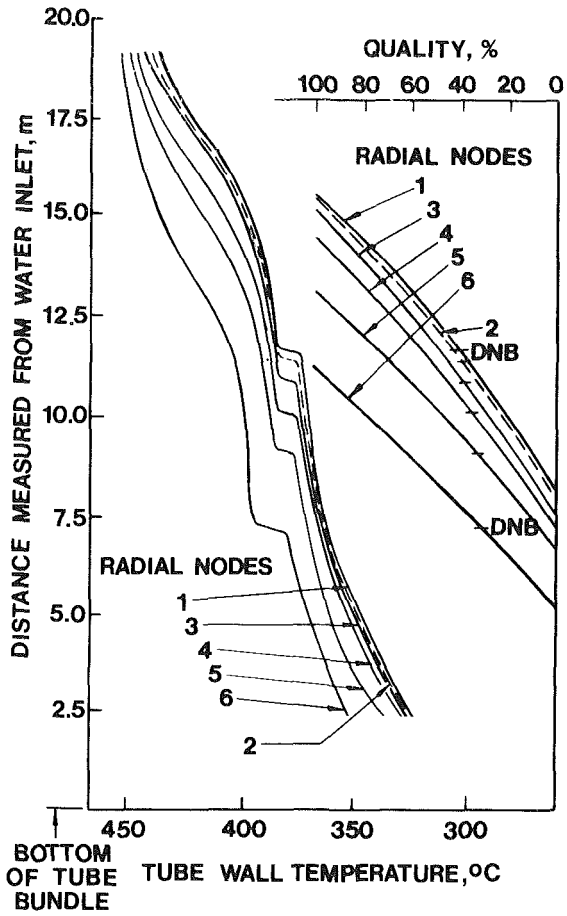

Fig. 8 MSG steam quality and tube temperature profiles

estimated for the exit steam temperature. From a standpoint of enthalpy pickup by water/steam, the above discrepancy of 4°C for the exit steam temperature amounts to less than 0.3 percent difference.

Figure 8 shows the steam quality and the tube-wall temperature profiles for all radial tube rows that were simulated in the COMMIX model. Due to generally higher sodium temperatures around the outer tubes, the heat input is greater for the outer tubes and, therefore, the departure from nucleate boiling (DNB) point occurs earlier (7.16 m from tube entrance) and at a lower quality (32 percent) for the outermost tubes. The average DNB quality for all tubes is 38 percent, which is close to the experimentally-determined DNB quality of 40 percent. Due to the lack of local measurement data, a detailed comparison cannot be made.

The tubeside flow maldistribution, induced by thermal unbalance on the shellside, is predicted to be approximately ±2 percent. This relatively small variation is probably because the tube bundle diameter is relatively small (0.46 m). The shellside entrance/exit crossflow effect is thus minimized. The overall tubeside pressure drop is computed to be 661 kPa, which compares favorably with the 669 kPa drop measured in the experiment.

Comparison with 50 MWt SNR-Steam Generator Test. The 50-MWt, SNR-steam generator is a shell-and-tube, liquid sodium heated steam generator which was designed, constructed and tested by NERATOOM for Dutch LMFBR program [12]. Since actual design drawings for the steam generator were not available, a COMMIX computer model was constructed based on limited information available [12–14].

The 50-MWt, SNR-steam generator under consideration is

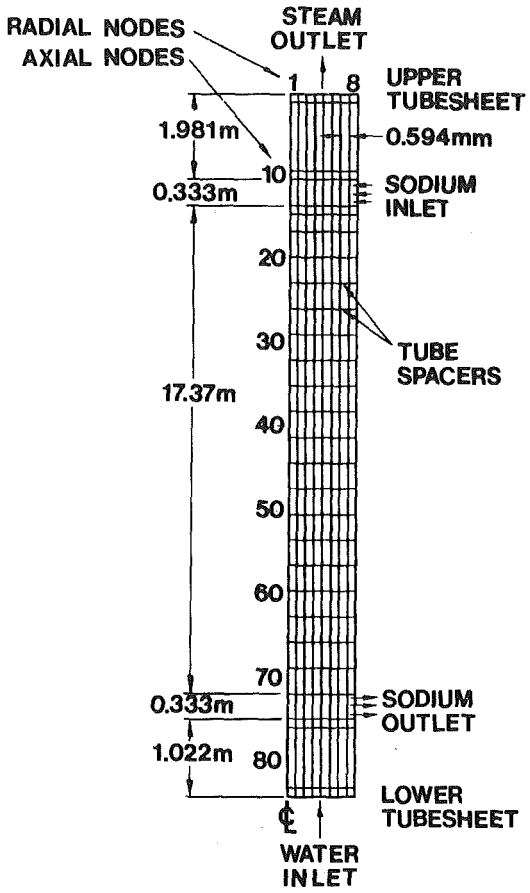

Fig. 9 COMMIX model for SNR prototype steam generator

a straight-tube, verticaly mounted, shell-and-tube heat exchanger, employing longitudinal flow on the shell side. The analytical computer model for the steam generator is an axisymmetric one with 8 radial nodes and 50 axial nodes as shown in Fig. 9. In the radial direction the tube bundle is modeled by nodes 1 to 7. Since detail drawings were not available, both the inlet and exit windows were assumed to be 254-mm high. This assumption is not expected to result in any significant errors. All support plates are assumed to have 75 percent open flow area. The physical dimensions of the unit are summarized in Table 4.

In the SNR-steam generator test, seven thermocouples were placed at the steam exit ends of seven radially-positioned heat transfer tubes (but only five thermocouple readings were reported), and therefore, the computer model has 7 radial nodes to reflect this T/C arrangement and, thus, to provide proper comparisons between test data and predicted values. A comparison has been made in Fig. 10 for the radial temperature distribution of the existing steam. In both experiment and prediction, the steam exit temperature is higher at the shroud location, probably due to the combined effects of the hotter shellside fluid temperature at the entrance and of possible flow bypassing on the shellside along the shroud. An agreement is excellent for the tubes located at both edges of the tube bundle, and deviations up to 11°C are realized in the middle of the bundle. On the average, the simulation underpredicts the exit steam temperature by approximately 6°C. However, in terms of an overall enthalpy (or thermal energy) pickup, this difference amounts to less than 0.5 percent difference. A few factors can cause this discrepancy. As indicated earlier, the physical dimensions used are only approximate at best because detail drawings of the steam generator are not available at the time of this study. The heat-transfer and DNB correlations used in analytical simulation may also contribute to the differences.

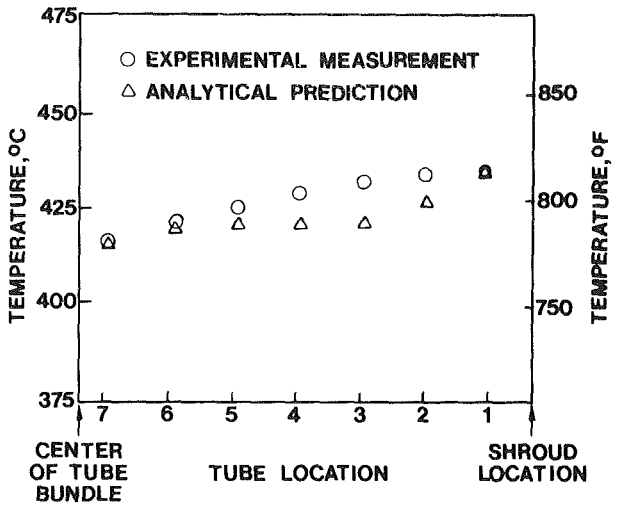

Fig. 10 SNR radial steam exit temperature profile

It may be noted that a typical computing time was 5 CPU min and a storage requirement was 300K on a CDC-176 computer. Also grid independence of solutions was not closely examined (not the subject of the paper).

Conclusions

The detailed development of a comprehensive, multidimensional, thermal hydraulic, heat-exchanger analysis computer code is presented. The concept of porosity, permeability and distributed flow resistance has been employed on the shellside fluid, to modify the continuum Navier-Stokes equations to properly accent for the blockage effects of the heat exchanger tube bundle. The tubeside flow is considered as a multichannel, parallel flow between two common inlet and exit plenums. The conservation equations were put into finite-difference form using the implicit continuum-fluid Eulerian method and solved on a digital computer.

The above analytical model was tested using three sets of experimental data. The first set of data were taken from isothermal water test results in a tube bundle, and the other two sets of data from the nonisothermal, sodium-heated steam generator tests. The comparisons between analytical predictions and experimental indications appear satisfactory considering analytical complexities and experimental uncertainties, thus rendering a credence to the analytical model. However, there definitely exists a room for further improvements in the analytical approaches.

Acknowledgment

The authors wish to thank all members of the program team at Argonne National Laboratory and FW Energy Applications, Inc. This paper is based on work which was supported by the U.S. Department of Energy under ANL Contract No. 31-109-38-381 and Foster Wheeler Contract No. 8-33-3088 and 8-51-3864.

References

1 AbuRomia, M. M., Bosch, R. J., Jr., Cho, S. M., Dietz, D., and Jaisingh, G., "Flow Model Test Development of CRBRP Intermediate Heat Exchanger," ASME/IEEE Joint Power Generation Conference, Los Angeles, Calif., Sept. 18–21, 1977, ASME Paper No. 77-JPGC-NE-10.

2 Harlow, F. H., ed., *Computer Fluid Dynamics-Recent Advances,* AIAA Selected Reprint Series, Vol. XV, Feb. 1973.

3 Patankar, S. V., and Spalding, D. B., "A Calculation Procedure for the Transient and Steady-State Behavior of Shell-and-Tube Heat Exchangers," *Heat Exchangers: Design and Theory Sourcebook,* edited by N. H. Afgan and E. V. Schlünder, McGraw-Hill, 1974, pp. 155–176.

4 AbuRomia, M. M., Chan, B. C., and Cho, S. M., "Flow Distribution

Analysis in Nuclear Heat Exchangers with Applications to CRBRP-IHX," *Proceedings of the 1976 Heat Transfer and Fluid Mechanics Institute,* Stanford University Press, 1976, pp. 468–482.

5 Sha, W. T., "An Overview of Rod Bundle Thermal-Hydraulic Analysis," Argonne National Laboratory, Report No. NUREG/CR-1825, ANL-79-10, Nov. 1980.

6 Sha, W. T., Domanus, H. M., Schmitt, R. C., Oras, J. J., and Li, E. I. H., "COMMIX-1: A Three-Dimensional Transient Single Phase Component Computer Program for Thermal Hydraulic Analysis," Argonne National Laboratory Report, NUREQ/CR-0785, ANL-77-96, Sept. 1978.

7 Caragilescov, P., and Todreas, N. E., "Experimental and Analytical Study of Axial Turbulent Flows in an Interior Subchannel of a Base Rob Bundle," ASME JOURNAL OF HEAT TRANSFER, Vol. 98, 1976, pp. 262–268.

8 Dwyer, O. E., *Liquid Metal Heat Transfer,* Brookhaven National Laboratory Report No. BNL-11936R, 1969.

9 Thom, J. R. S., "Prediction of Pressure Drop Forced Circulation Boiling of Water," *International Journal of Heat and Mass Transfer,* Vol. 7, 1964, pp. 709–724.

10 Harlow, F. H., and Amsden, A. A., "A Numerical Fluid Dynamics Calculation Method for All Flow Speeds," *Journal of Computational Physics,* Vol. 8, 1976, pp. 197–213.

11 McDonald, J. S., Harty, R. B., and DeBear, W. S., "Sodium Heated Steam Generator Test Performance," ASME-IEEE Joint Power Generation Conference New Orleans, Lousiana, Sept. 16–19, 1973, ASME Paper No. 73-PWR-9.

12 Ludwig, P. W. P. H., and Hus, B. M., "Some Results of the 50 MW Straight Tube Steam Generator Test in the TNO 50 MW SCTF at Hengelo," Study Group Meeting on Steam Generators for LMFBR's, held in Bensberg, FRG, Oct. 14–17, 1974.

13 Van Westenbrugge, J. K., Tromp, Th. J., and DeMaeijer, J. R. A., "Results of the Test and Inspection Program of the Prototype SNR-300 Steam Generator," Ferritic Steel for Fast Reactor Steam Generators, BNES, London, 1978, pp. 16–21.

14 Knapp, M. H., Ratzel, W., and Van Westenbrugge, J. K., "Steam Generator Design and Experience in the SNR-Project," ASME Century 2 Nuclear Engineering Conference, San Francisco, Calif., Aug. 19–21, 1980, ASME Paper No. 80-C2/NE-31.

15 *ASME Steam Tables*, ASME, New York, 1967.

Radiation Configuration Factors Between Disks and a Class of Axisymmetric Bodies

M. H. N. Naraghi
Graduate Research Assistant.

B. T. F. Chung
Professor.

Department of Mechanical Engineering,
The University of Akron,
Akron, Ohio 44325

A general formulation is developed for the radiation shape factors between a disk and a class of coaxial axisymmetric bodies such as cylinder, cone, ellipsoid, and paraboloid. In certain cases, the view factors can be derived analytically directly from the present technique, while in others, they can be generated from a single numerical integration. The analytical solutions for view factors from a disk to a coaxial cylinder based on the present approach are found to agree with those published earlier. The analytical formulae of view factors from disks or annular rings to circular cones, truncated cones, ellipsoid, paraboloids, and truncated praboloid are herein presented.

Introduction

The determination of radiative view factors between disks and axisymmetric bodies is of practical importance in the design of annular fin-tube radiators for thermal control systems of satellites and in the computation of radiative exchange between a spacecraft and its engine exhaust plume. Mathematically, the view factors from a disk to axisymmetric bodies are in terms of complicated quadruple integrals. The evaluation of such expressions are extremely tedious even with the aid of digital computers. Closed-form solutions to these integrals are available for only a few simple cases [1-4].

With the aid of digital computers, configuration factors of more complicated geometries were obtained [5-8]. More recently Chung and Naraghi [9, 10] introduced a general formulation for the angle factors from a sphere to a class of axisymmetric bodies. In this study a similar approach as presented in reference [9] is employed to develop a general formulation for radiative configuration factors between a disk and certain axisymmetric bodies such as paraboloid, ellipsoid, cone, and cylinder. This method requires the use of a single numerical integration at the worst condition. For many cases, exact solutions are obtainable.

Mathematical Analysis and General Formulation

The following procedures are used to formulate the configuration view factor from a disk to an arbitrary coaxial axisymmetric body: (*i*) The contour integral method [11] is first applied to derive the shape factor between a disk and a differential element with an arbitrary orientation; (*ii*) an analytical expression for the configuration view factor between a disk and a coaxial differential ring is obtained by rotating the above differential element around the perpendicular axis passing through the center of the disk; (*iii*) the resulting expression mentioned above is then integrated over the surface of the axisymmetric body to give the view factor from a disk to a coaxial axisymmetric body. Mathematical detail of the above procedure is described below.

View Factor from a Differential Planar Source to a Disk. This problem can be divided into two parts; namely, the disk is fully visible by the differential element, and the disk is partially visible from the differential element (see Fig. 1). The first case holds when the plane of the differential element does not intersect the disk, while the second case corresponds to the situation when dA_2 and the disk intersect.

Case I. The disk is fully visible by the element. This case holds when $-\pi/2 \le \theta \le \pi/2$ and $\tan^{-1}[h/(p-r)] \le \theta \le \tan^{-1}[h/(p+r)]$. The shape factor F_{dA_2-d} can be obtained from the contour integrals given below:

$$F_{dA_2-d} = l_2 \oint_C \frac{(z-z_2)\,dy-(y-y_2)\,dz}{2\pi L^2} + m_2 \oint_C \frac{(x-x_2)\,dz-(z-z_2)\,dx}{2\pi L^2} + n_2 \oint_C \frac{(y-y_2)\,dx-(x-x_2)\,dy}{2\pi L^2} \quad (1)$$

where C is the contour around the disk and l_2, m_2, and n_2 are the direction cosines of the outward normal vector, $\vec{n}_2$. It can be seen from Fig. 1 that $x_2 = 0$, $y_2 = p$, $z_2 = 0$, $x = r\sin\omega$, $y = r\cos\omega$, $z = h$, l_2, $= 0$, $m_2 = \sin\theta$, $n_2 = \cos\theta$ and $L^2 = r^2 \sin^2\omega + (p - r\cos\omega)^2 + h^2 = r^2 + p^2 + h^2 - 2pr\cos\omega$. Substituting the above expressions into equation (1) and carrying out the integration yields:

$$F_{dA_2-d} = \tfrac{1}{2}\left\{\left(1+\frac{r^2-p^2-h^2}{[(r^2+p^2+h^2)^2-4p^2r^2]^{1/2}}\right)\cos\theta + \frac{h}{p}\left(1-\frac{r^2+p^2+h^2}{[(r^2+p^2+h^2)^2-4p^2r^2]^{1/2}}\right)\sin\theta\right\} \quad (2a)$$

where $\tan^{-1}[h/(p-r)] \le \theta \le \tan^{-1}[h/(p+r)]$

Case II. The disk is partially visible by the element. This

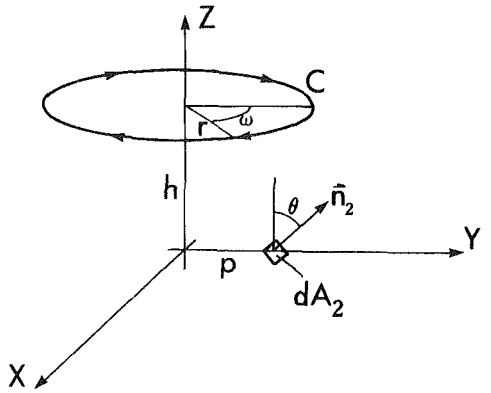

Fig. 1 Differential element-disk view factor geometry

Contributed by the Heat Transfer Division and presented at the 20th ASME/AIChE National Heat Transfer Conference, Milwaukee, Wisconsin, August 2-5, 1981. Manuscript received by the Heat Transfer Divison August 14, 1981. Paper No. 81-HT-56.

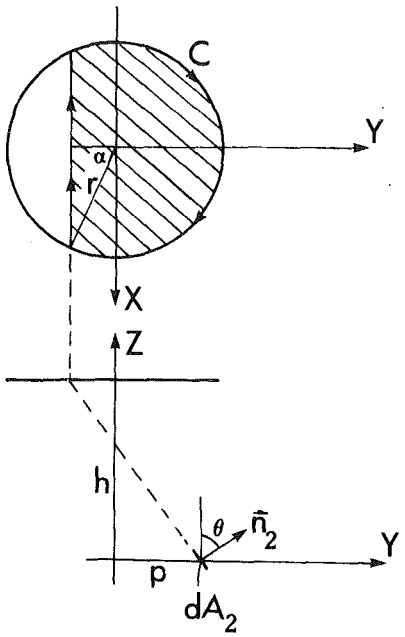

Fig. 2 Detail of contour C

case holds when $0 \le \theta \le \pi$ and $\tan^{-1}[h/(p+r)] \le \theta \le \tan^{-1}[h/(p-r)]$. As shown in Fig. 1, the differential element can only "see" a part of the disk (the shaded part in the top view of Fig. 2).

The corresponding contour, C, consists of a partial circle and a straight line. For the part of circle, $x = r\sin\omega$, $y = r\cos\omega$, $z = h$ and $L^2 = r^2 + p^2 + h^2 - 2pr\cos\omega$, for the part of straight line, $y = p - h\cot\theta$, $z = h$ and $L^2 = x^2 + h^2\cot^2\theta + h^2$. Substituting the foregoing expressions into equation (1) and integrating yields

$$F_{dA_2-d} = \frac{(r^2-p^2-h^2)\cos\theta - (r^2+p^2+h^2)(h\sin\theta)/p}{\pi[(r^2+p^2+h^2)^2 - 4p^2r^2]^{1/2}} \tan^{-1}\left\{\left[\frac{(r^2+p^2+h^2+2pr)(r-p+h\cot\theta)}{(r^2+p^2+h^2-2pr)(r+p-h\cot\theta)}\right]^{1/2}\right\}$$

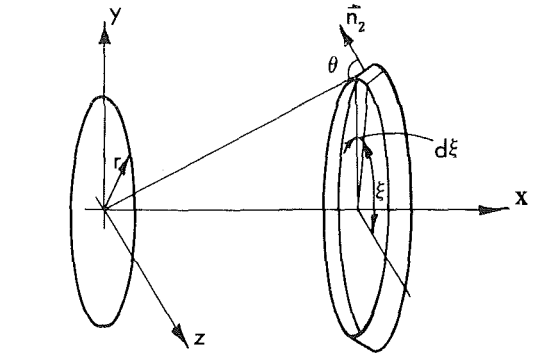

Fig. 3 Disk-differential conical ring view factor geometry

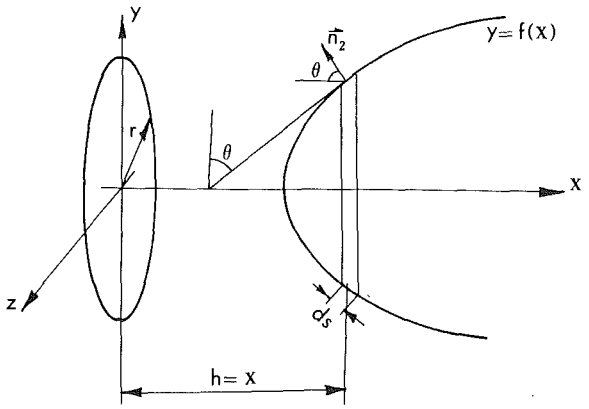

Fig. 4 Disk-axisymmetric body view factor geometry

$$+\frac{1}{2\pi}\left(\cos\theta + \frac{h}{p}\sin\theta\right)\cos^{-1}\left(\frac{p-h\cot\theta}{r}\right) + \frac{1}{\pi}\tan^{-1}\left(\frac{[r^2-(p-h\cot\theta)^2]^{1/2}\sin\theta}{h}\right) \qquad (2b)$$

In the limiting case of $p = 0$, equations (2a) and (2b) are respectively reduced to the following expressions

Nomenclature

a,b = dimensional half-length of the axes of the ellipsoid
C = contour of the disk
e = distance between the focus and vertex of the paraboloid (focal length of the paraboloid)
E = e/r
$f(x)$ = function generator of the axisymmetric body
F = radiation view factor
h = distance between center of the disk and the origin of coordinates in Fig. 1
H = h/r
l = length of the cylinder or paraboloid
L = l/r or distance between the differential element and the contour, C
l_2,m_2,n_2 = direction cosines of vector $\vec{n}_2$
$\vec{n}_2$ = unit vector outward normal from a differential element dA_2
p = distance between the differential element and the origin of coordinates
P = p/r
r = radius of the disk
r_2 = radius of the cylinder or cone
R = r_2/r
s = distance between disk and axisymmetric body
S = s/r

Greek Symbols

α = half angle of the nose of the cone
θ = angle between $\vec{n}_2$ and z-axis

Subscripts

ax = axisymmetric body
d = disk
d' = annular ring
dA_2 = differential element
c = cone
cy = cylinder
i = internal common tangent point
e = external common tangent point, or ellipsoid
p = paraboloid
I = the region in the axisymmetric body of which the tangent planes never intersect the disk but is visible from the disk
II = the region in the axisymmetric body of which the tangent planes always intersect the disk
δr = differential ring

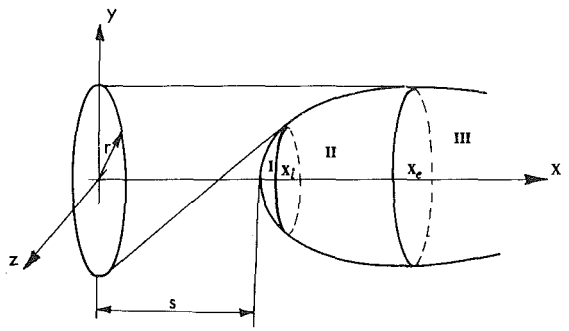

Fig. 5 Illustration of three regions in disk-axisymmetric body view of factor geometry

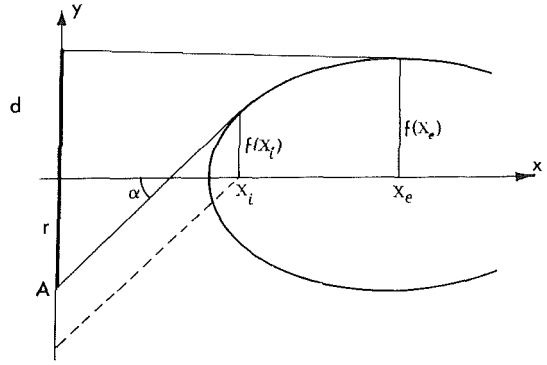

Fig. 6 Positions of points x_i and x_e

$$F_{dA_2-d}=\frac{r^2}{r^2+h^2}\cos\theta \tag{2c}$$

and

$$F_{dA_2-d}=\frac{rh\sin\theta}{\pi(r^2+h^2)}\left[1-\left(\frac{h\cot\theta}{r}\right)^2\right]^{1/2}+\frac{r^2\cos\theta}{\pi(h^2+r^2)}\cos^{-1}\left(\frac{-h\cot\theta}{r}\right)+\frac{1}{\pi}\tan^{-1}\left[(r^2-h^2\cot^2\theta)^{1/2}\frac{\sin\theta}{h}\right] \tag{2d}$$

When $\theta=\pi/2$, equations (2c) and (2d) become identical to those presented earlier by Chung and Sumitra [15] and Juul [16].

View Factor from a Disk to a Coaxial Differential Ring. We now consider the radiation between the disk and any differential element on the conical ring, as shown in Fig 3. The application of the reciprocal rule leads to

$$dF_{d-dA_2}=\frac{dA_2}{\pi r^2}F_{dA_2-d}=\frac{yd\xi\,ds}{\pi r^2}F_{dA_2-d} \tag{3}$$

Integrating dF_{d-dA_2} with respect to ξ and noting that the F_{dA_2-d} is independent of ξ due to the symmetrical configuration, we obtain a closed form solution for the view factor from the disk to the coaxial differential ring:

$$dF_{d-\delta r}=\int_0^{2\pi}\frac{yds}{\pi r^2}F_{dA_2-d}\,d\xi=\frac{2y}{r^2}F_{dA_2-d}\,ds \tag{4}$$

where F_{dA_2-d} is given by equations (2a) and (2b).

View Factor From a Disk to a Coaxial Axisymmetric Body. Let the differential ring obtained from equation (4) be a differential section of an axisymmetric body and let $y=f(x)$ be the function generator of this axisymmetric body (i.e., the axisymmetric body is generated from the rotation of $f(x)$ around the x-axis). Referring to Fig 4, we have

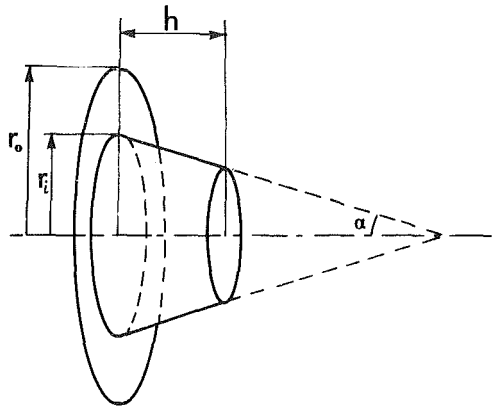

Fig. 7 Annular ring-covergent cone view factor geometry

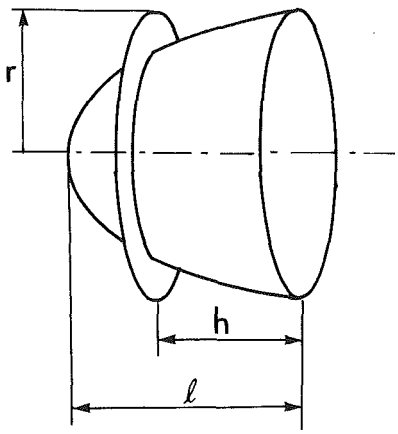

Fig. 8 Annular ring-intersecting paraboloid view factor geometry

$$ds=(1+[f'(x)]^2)^{1/2}dx,\ \theta=\cot^{-1}[f'(x)] \tag{5}$$

Substituting equations (2a) and (2b) into equation (4) and making use of equations (5) we obtain the following results for $dF_{d-\delta r}$ in terms of x, r, and $f(x)$.

$$dF_{(d-\delta r)_I}=\frac{1}{r^2}\left\{f(x)f'(x)\left[1+\frac{r^2-[f(x)]^2-x^2}{[(r^2+[f(x)]^2+x^2)^2-4[f(x)]^2r^2]^{1/2}}\right]+x\left[1-\frac{r^2+[f(x)]^2+x^2}{[(r^2+[f(x)]^2+x^2)-4[f(x)]^2r^2]^{1/2}}\right]\right\}dx \tag{6a}$$

where

$$s\le x\le x_i$$

and

$$dF_{(d-\delta r)_{II}}=\frac{2}{\pi r^2}\left\{\frac{-r^2[x-f'(x)f(x)]-[x+f'(x)f(x)](x^2+[f(x)]^2)}{[r^4+2r^2(x^2-[f(x)]^2)+([f(x)]^2+x^2)^2]^{1/2}}\tan^{-1}\left[\frac{[(r+f(x))^2+x^2][r+xf'(x)-f(x)]}{[(r-f(x))^2+x^2][r-xf'(x)+f(x)]}\right]^{1/2}+\tfrac{1}{2}[x+f'(x)f(x)]\cos^{-1}\left[\frac{f(x)-xf'(x)}{r}\right]+f(x)(1+[f'(x)]^2)^{1/2}\right.$$

Table 1 View factors from disks or annual disks to axisymmetric bodies

Configurations	View Factor Formulae
1. Annular Ring to Cylinder 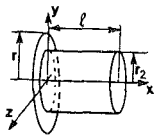	$F_{d'-cy} = \frac{1}{\pi(1-R^2)}\left\{(1-R^2)\tan^{-1}\left(\frac{1+R}{1-R}\right)^{1/2} - \left[(1+R^2+L^2)^2 - 4R^2\right]^{1/2}\cdot \tan^{-1}\left[\frac{(1+R^2+L^2+2R)(1-R)}{(1+R^2+L^2-2R)(1+R)}\right]^{1/2} + \frac{1}{2}L^2\cos^{-1}R + 2RL\tan^{-1}\left[(1-R^2)^{1/2}/L\right]\right\}$ where $R = r_2/r$ and $L = \ell/r$
2. Disk to Cone 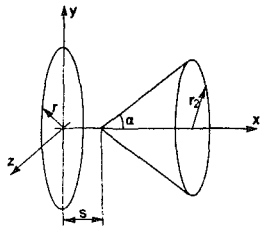	$F_{d-c} = F_{d-ax} = F_{d-I} = \frac{1}{2}\left[R^2 + (S + R\cot\alpha)^2 + 1 - \left(\left[1 + R^2 + (S + R\cot\alpha)^2\right]^2 - 4R^2\right)^{1/2}\right]$ If $\alpha \geq \tan^{-1}(r/s)$ $F_{d-c} = \frac{1}{\pi}\left\{-AB\tan^{-1}\left(\frac{AC}{AD}\right) + (1+S^2)\tan^{-1}\frac{C}{D} + \frac{\sin\alpha}{\cos^2\alpha}\left[EF\tan^{-1}\frac{CD}{E} + S^2\tan^{-1}\frac{CD}{E} + (CD)^2\left(\tan^{-1}\frac{E}{CD} - \tan^{-1}\frac{S}{CD}\right)\right] + \left[\frac{R(E+S)}{\sin 2\alpha} - SR\tan\alpha\right]\cos^{-1}(-S\tan\alpha)\right\}$ If $\alpha \leq \tan^{-1}(r/s)$ where $A = \left[(S + R\cot\alpha)^2 + (1+R)^2\right]^{1/2}$, $B = \left[(S + R\cot\alpha)^2 + (1-R)^2\right]^{1/2}$, $C = (\cos\alpha + S\sin\alpha)^{1/2}$, $D = (\cos\alpha - S\sin\alpha)^{1/2}$, $E = R\cot\alpha + S$, $F = R\cot\alpha - S$, $S = s/r$
3. Annular Ring to Truncated Cone 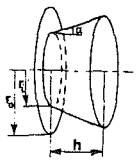	$F_{d'-c} = \frac{1}{\pi(1-R_i^2)}\left\{-A'B'\tan^{-1}\left(\frac{A'C'}{B'D'}\right) + (C'D')^2\tan^{-1}\frac{D'}{C'} + \frac{\sin\alpha}{\cos^2\alpha}\left[\left(H^2 + \frac{2HR_i}{\tan\alpha}\right)\cdot \tan^{-1}\frac{(E')^{1/2}}{H} + E'\tan^{-1}\frac{H}{(E')^{1/2}}\right] + \left(\frac{H^2}{2\cos^2\alpha} + HR_i\tan\alpha\right)\cos^{-1}(R_i)\right\}$ where $A' = \left[H^2 + (1 + H\tan\alpha + R_i)^2\right]^{1/2}$, $B' = \left[H^2 + (1 - H\tan\alpha - R_i)^2\right]^{1/2}$, $C' = (1-R_i)^{1/2}$, $D' = (1+R_i)^{1/2}$, $E' = (1 - R_i^2)\cos^2\alpha$, $R_i = r_i/r_o$
4. Disk or Annular Ring to Ellipsoid 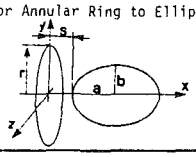	$F_{d-e} = F_{d-I} + F_{d-II}$ (see eqs. (8a) and (8b) for F_{d-I} and F_{d-II}) x_i & $x_e = \frac{d(r^2a^2 + d^2b^2 - b^2a^2) \pm ra^2(r^2a^2 + d^2b^2 - b^2a^2)^{1/2}}{d^2b^2 + r^2a^2}$ $F_{d'-e} = F_{c-II}\frac{r^2}{\left[r^2 - b^2(1 - d^2/a^2)\right]}$, $x_i = 0$
5. Disk or Annular Ring to Paraboloid 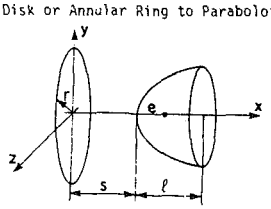	x_i & $x_e = \frac{r^2 + 4es \pm r(r^2 + 4es)^{1/2}}{2e}$ 1) $x_i > s+\ell$, $F_{d-p} = \frac{1}{2}\left\{4EL + (S+L)^2 + 1 - \left([1 + 4EL + (S+L)^2]^2 - 16EL\right)^{1/2}\right\}$ 2) $x_i \leq s+\ell \leq x_e$, $F_{d-p} = F_{d-I} + F_{d-II}$, $x_e = s + \ell$, $E = e/r$ 3) $x_e > s+\ell$, same as case 2 except that x_e does not change $F_{d'-e} = F_{d-e}\frac{r^2}{(r^2 - 4es)}$, $x_i = 0$, x_e is replaced by h if $x_e > h$

$$\cdot \tan^{-1}\left[\frac{(r^2 - [xf'(x) - f(x)]^2)^{1/2}}{x(1 + [f'(x)]^2)^{1/2}}\right]\Bigg\} dx \qquad (6b)$$

when

$$x_i \leq x \leq x_e$$

To determine the configuration factor between the disk and a coaxial axisymmetric body, expressions given by equations (6*a*) and (6*b*) have to be integrated over the entire axisymmetric body. To do so, we divide the axisymmetric body into the following three regions as illustrated in Fig. 5.

Region I: The region which can be seen from the disk and with none of the tangent planes intersect, i.e., $s \leq x \leq x_i$.

Region II: The portion of the axisymmetric body whose tangent planes always intersect the disk, i.e., $x_i < x \leq x_e$.

Region III: The part of the axisymmetric body which cannot be seen by the disk, i.e., $x > x_e$.

Integrating $dF_{d-\delta r}$ over Regions I and II just mentioned yields the radiation shape factor from the disk to the entire axisymmetric body, F_{d-ax}

$$F_{d-ax} = \int_s^{x_i} dF_{(d-\delta r)_I} + \int_{x_i}^{x_e} dF_{(d-\delta r)_{II}} = F_{d-I} + F_{d-II} \qquad (7)$$

The firts term on the right hand side of the above equation can be integrated analytically. Knowing $f(s) = 0$, this integral is expressed by

$$F_{d-I} = \frac{1}{2r^2}\left\{[f(x_i)]^2 + x_i^2 + r^2 - [(r^2 + [f(x_i)]^2 + x_i^2)^2 - 4[f(x_i)]^2 r^2]^{1/2}\right\} \qquad (8a)$$

The second part of the integrals in equation (7), F_{d-II} is most unlikely to be integrated exactly, except for certain particular cases. It can be rewritten in the following compact form:

$$F_{d-II} = \frac{2}{\pi r^2}\int_{x_i}^{x_e}\left[-\tfrac{1}{2}\frac{d(\phi\psi)}{dx}\tan^{-1}\left(\frac{\psi\eta}{\phi\lambda}\right) + \tfrac{1}{2}\xi\cos^{-1}\left(\frac{\lambda^2 - r}{r}\right) + f(x)\mu\tan^{-1}\left(\frac{\lambda\eta}{x\mu}\right)\right] dx \qquad (8b)$$

where

$$\phi = [r^2 + x^2 + [f(x)]^2 - 2rf(x)]^{1/2}$$
$$\psi = [r^2 + x^2 + [f(x)]^2 + 2rf(x)]^{1/2}$$
$$\eta = [r + xf'(x) - f(x)]^{1/2}$$

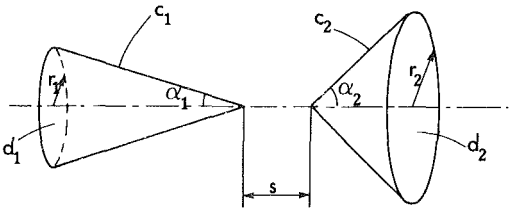

Fig.9 Cone-cone view factor geometry

$$\lambda = [r - xf'(x) + f(x)]^{1/2}$$
$$\xi = x + f'(x) f(x)$$
$$\mu = [1 + [f'(x)]^2]^{1/2}$$

It should be pointed out that not necessarily all axisymmetric bodies consist of all three regions previously mentioned. For certain geometries, such as cylinder, region I does not exit, i.e., F_{d-1} vanishes. On the other hand, for certain circular cones and caps, region II does not exist, and consequently F_{d-II} becomes zero.

Referring to Fig. 6, the integration limits in equation (8*b*) can be obtained as

$$x_i f'(x_i) - f(x_i) = r \tag{9}$$

and

$$-x_e f'(x_e) + f(x_e) = r \tag{10}$$

Once $f(x)$ and r are specified, x_i and x_e can be determined from equations (9) and (10). Note that equations (9) and (10) are not valid for those configurations for which either region I or II does not exist. For the cases of radiation from disk to cylinder or circular cones, the corresponding limits of integrations are the two end points of the axisymmetric body.

Applications and Results

Based on the aforementioned general formulations, equations (8) through (10), the view factors from a disk to a class of axisymmetric bodies, are investigated. These axisymmetric bodies include cylinders, right circular cone, truncated cone, ellipsoid, ellipsoidal cap, and paraboloid. The resulting formulae for view factors are summarized in Table 1. Details of derivation may be found in reference [12] and some graphical representations of view factors have also been presented in reference [13].

The view factors from an annular ring to an attached coaxial cylinder is given by the first row of Table 1. To determine the view factor from the right hand side of the whole disk to the external surface of the cylinder, we simply multiply $F_{d'-cy}$ by $(1-R^2)$. The formula agrees with those presented previously by sparrow et al. [3] and Rea [14] in which different approaches are employed.

Exact solutions for the shape factor from a disk to coaxial cone are obtainable from equation (8*a*) or integration of equation (8*b*), depending whether the angle α is greater or less than $\tan^{-1}(r/s)$. The result is given in the second row of Table 1.

Another interesting case encountered frequently in engineering applications is the radiation between an annular ring and an attached coaxial truncated cone (see No. 3 of Table 1). The shape factor for this configuration can be obtained using equation (8*b*) with $x_i = 0$ and $x_e = h$. The geometry factor from a disk or annular ring to a detached coaxial truncated cone can be obtained easly via flux algebra. Replacing α in $F_{d'-c}$ by $-\alpha$, we obtain the angle factor from an annular ring to a convergent truncated cone (see the configuration in Fig. 7).

The determination of view factor from a disk to a coaxial ellipsoid requires a single numerical integration of F_{d-II} given by equation (8*b*). The upper and lower bounds of this integral can be solved directly from equations (9) and (10), repsectively. Note that the first part of F_{d-e} is analytically obtained from equation (8*a*). For a special case with $a/b = 1$, the view factor from disk to ellipsoid reduces to that from disk to sphere.

When the disk under consideration intersects the ellipsoid, the lower limit of the integral mentioned above becomes identical to zero, and the upper limit, x_e, remains the same. In this case, F_{d-I} vanishes, and the view factor from the disk to the ellipsoid is identical to F_{d-II}.

In the derivation of equation (8*b*), we assumed that the whole surface of the right hand side of the disk is radiating. When the disk intersects the ellipsoid, part of the disk is covered by the ellipsoid. To determine the view factor from the annular ring to the truncated ellipsoid, the results obtained by equation (8*b*) has to be multiplied by $r^2/[r^2 - b^2(1 - d^2/a^2)]$.

In the derivation of view factor from a disk to a coaxial paraboloid, consideration must be given to three different situations: (*i*) The disk does not intersect the paraboloid, and $x_i > s + l$. In this case none of the tangent planes of the paraboloid intersect the disk. Consequently, F_{d-II} of equation (7) vanishes and a closed-from solution is obtained. (*ii*) When $x_i \le x + l \le x_e$, both equations (8*a*) and (8*b*) are required with the upper limit x_e being replaced by $s + l$. (*iii*) When $x_e > s + l$, the same relations as case 2 are applied except that x_e does not change. For both cases 2 and 3, Gauss Quadrature technique was employed to integrate equation (8*b*).

When the disk intersects the paraboloid ($s < 0$), then F_{d-I} in equation (7) vanishes. Consequently, the lower limit of integration in equation (8*b*), x_i, is zero; the upper limit of the integration is determined from equation (10), if $x_e \le h$; otherwise $x_e = h$ (see Fig. 8).

In order to determine the view factor from the annular ring to the intersected paraboloid, the above results are necessarily multiplied by the area ratio $r^2/(r^2 - 4es)$.

With the aid of the present results, the view factors for many other configurations can be easily derived. To mention a few examples, the view factor from an axisymmetric body to a differential ring can be obtained from the reciprocal rule and differentiation of F_{ax-d}. The view factor from an axisymmetric body to the internal surfce of a coaxial cylinder can be calculated from the difference of view factors from the axisymmetric body to the two disks, $F_{ax-d_2} - F_{ax-d_1}$, where d_2 and d_1 correspond to the circular openings at the two ends of the cylinder. The view factor from the base of the cylinder (or other axisymmetric bodies) between two adjacent circular fins to the outside environment, F_{b-0}, can be computed from the simple expressions: $F_{b=0} = 1 - (2A_d'/A_b) F_{d'-cy}$, where A_d' and A_b are the two areas of the circular ring and the base, respectively, and $F_{d'-cy}$ is the view factor from the annular ring to the external surface of the cylinder. The shape factor between the separated coaxial cones shown in Fig. 9 can be expressed in terms of the view factor between disk and cone. For example, $F_{c_1-c_2} = A_{d_2}/A_{c_1} \cdot F_{d_2-c_1}$ if $\alpha_2 \ge \alpha_1$; otherwise, $F_{c_1-c_2} = A_{d_1}/A_{c_1} \cdot F_{d_1-c_2}$.

Conclusion

A general formulation of radiative configuration factors from a disk to a class of coaxial axisymmetric bodies is developed. This formulation is semianalytical in nature and requires a single numerical integration at most.

The application of the present technique is not restricted only to the geometries mentioned above. This method is applicable as long as the function generator of the axisymmetric body, $f(x)$, is continuous, $f'(x)$ exists, and $f''(x)$ is

less than or equal to zero everywhere in the region between x_i and x_e.

Acknowledgement

The work was partially supported by the Research Center of Firestone Tire and Rubber Company.

References

1 Hamilton, D. C., and Morgan, W. R., *Radiant Interchange Configuration Factors*, NASA TN 2836, 1952.

2 Leunberger, H., and Person, R. A., "Compilation of Radiation Shape Factors for Cylindrical Assemblies," ASME Paper No. 56-A-144, presented at ASME Annual Meeting, New York, 1956.

3 Sparrow, E. M., Miller, G. B., and Jonsson, V. K., "Radiation Effectiveness of Annular-finned Space Radiators, Including Mutual Irradiation between Radiator Elements," *Journal of Aerospace Science*, Vol. 29, No. 11, 1962, pp. 1291–1299.

4 Feingold, A., and Gupta, K. G., "New Analytical Approach to the Evaluation of Configuration Factors in Radiation form Spheres and Infinitely Long Cylinders," ASME JOURNAL OF HEAT TRANSFER, Vol. 92, No. 1, 1970, pp. 69–76.

5 Ballance, J. O., and Donovan, J., "Radiation Configuration Factors for Annular Rings and Hemispherical Sectors," ASME JOURNAL OF HEAT TRANSFER, Vol. 95, No. 2, 1973, pp. 275–276.

6 Mining, C. P., "Shape Factors between Coaxial Annular Disks Separated by a Solid Cylinder," *AIAA J.*, Vol. 17, No. 3, 1979, pp. 318–320.

7 Mining, C. P., "Calculation of Shape Factors Between Parallel Ring Sectors Sharing a Common Centerline," *AIAA J.*, Vol. 14, No. 6, 1976, pp. 813–815.

8 Buschman, A. J., and Pittman, C. M., "Configuration Factors for Exchange of a Radiant Energy Between Axisymmetrical Sections of Cylinders, Cones and Hemispheres and Their Bases," NASA TN D-944, 1961.

9 Chung, B. T. F., and Naraghi, M. H. N., "A Simpler Formulation for View Factors From a Sphere to a Class if Axisymmetic Bodies," ASME JOURNAL OF HEAT TRANSFER, Vol. 104, No. 1, 1982, pp. 201–204.

10 Chung, B. T. F., and Naraghi, M. H. N., "Some Exact Solutions for Radiation View Factors from Spheres," *AIAA J.*, Vol. 19, No. 8, 1981, pp. 1077–1081.

11 Sparrrow, E. M., "A New and Simpler Formulation for Radiative Angle Factors," ASME JOURNAL OF HEAT TRANSFER, Vol. 85, No. 2, 1963, pp. 81–88.

12 Naraghi, M. H. N., "Radiation Configuration Factors Between Disks and Axisymmetric Bodies," M.S. thesis, University of Akron, Akron, Ohio, 1981.

13 Naraghi, M. H. N., and Chung, B. T. F., "Radiation Configuration Factors Between Disk and a Class of Axisymmetric Bodies," ASME Paper 81-HT-56, presented at ASME/AICHE Heat Transfer Conference, Milwaukee, Wi., 1981.

14 Rea, S. N., "Rapid Method for Determining Concentric Cylinder Radiation View Factors," *AIAA J.*, Vol. 13, No. 8, 1975, pp. 1122–1123.

15 Chung, B. T. F., and Sumitra, P. S., "Radiation Shape Factors from Plane Point Sources," JOURNAL OF HEAT TRANSFER, Vol. 94, No. 3, 1972, pp. 328–330.

16 Juul, N. H., "Diffuse Radiation View Factors from Differential Plane Source to Spheres," ASME JOURNAL OF HEAT TRANSFER, Vol. 101, No. 3, 1979, pp. 558–560.

R. Manohar

J. W. Stephenson

Department of Mathematics,
University of Saskatchewan,
Saskatoon, Saskatchewan
S7N OWO Canada

Optimal Finite Analytic Methods

A new method is proposed for obtaining finite difference equations for the solution of linear partial differential equations. The method is based on representing the approximate solution locally on a mesh element by polynomials which satisfy the differential equation. Then, by collocation, the value of the approximate solution, and its derivatives at the center of the mesh element may be expressed as a linear combination of neighbouring values of the solution.

Introduction

In a series of papers, Chen and Li [1-3], and also Chen, Naseri-Neshat, and Li [4, 5] have proposed a numerical method called the Finite Analytic Method (F.A.M.) for solving partial differential equations. The basic idea of the method is to use the analytic solution of the differential equation locally on a mesh element to generate a finite difference scheme. Clearly, the solution of the finite difference scheme preserves the characteristics of the solution of the partial differential equation, at least locally. Similar proposals have been made earlier by others [6-8], however, Chen and Li pursued the idea in great detail and applied their method to a variety of problems including a nonlinear fluid flow problem [4, 5].

In this paper we examine the Finite Analytic Method of Chen et al. We restrict our attention to two classical problems, viz., the Laplace and heat equations. These problems have been chosen because Chen and Li have given a detailed derivation of the F.A.M. for these two problems in [2, 4]. For the Laplace equation, Chen and Li arrived at a nine-point difference formula. However, this nine-point formula does not produce results which are as accurate as those produced by another nine-point formula which was reported by Bickley [13], Kantorovich and Krylov [11] and later by Greenspan [9, 10]. Chen and Li noted that their formula, which was derived in a completely different way, produced a difference scheme which was very close to the nine-point formula given by Greenspan. However, they did not carry out a comparative study of the numerical solutions obtained by the two slightly different nine-point formulas. They did observe that their scheme produced results which were more accurate than those computed by using the conventional five-point formula. However, in this report we will show that when the mesh size is reduced, the error in the F.A.M., as given by Chen and Li, reduces at a rate which is no faster than the rate for the five-point formula. Furthermore, we feel that a comparison of a nine-point formula with a five-point formula is not germain, because the bandwidth of the matrix for the nine-point scheme is greater and consequently the computational effort is also greater. Similar remarks apply to the difference scheme obtained by Chen and Li for the heat equation. Their scheme uses the same mesh points as the Crank-Nicolson scheme and it is not as accurate.

In order to arrive at their difference scheme, Chen and Li need to use some approximation of the solution over the boundary of the mesh element. The approximation they use is an interpolating polynomial on each side of the element, which interpolates nodal values of the solution on the boundary of the element. For each side of a mesh element a different polynomial is used and the only way in which these polynomials are connected is by the common nodal value shared by two adjacent sides of an element. The accuracy of their method is thus limited by the accuracy of the polynomial approximations on the boundaries of the element. Chen and Li have recognized this as the weakness of their method and have proposed the use of higher degree polynomials. This would increase the number of nodal points on the boundary of the mesh element and consequently the bandwidth of the matrix.

In this paper we propose additional conditions that can be imposed on the boundary approximations in order to arrive at a more accurate approximation without increasing the number of nodes in the element. With our choice of the boundary approximations we arrive at a difference scheme which has the highest order of truncation error for a given set of nodal points, therefore, we call such formulas "optimal." In the case of the Laplace equation with Dirichlet boundary conditions, the optimal F.A.M. produces the nine-point formula of Kantorovich, Krylov, Greenspan, Bickley and others. Similarly, for the heat equation, the optimal F.A.M. produces the formula of Lebedev and Douglas [12] which is known to have the highest order of accuracy.

The derivation of these optimal formulas by Chen and Li's procedure is lengthy and unnecessarily complicated. We propose a new derivation which leads to these formulas more easily than Chen and Li's procedure or the conventional difference procedures used earlier in the literature. The key idea in our derivation is the same as that of Chen and Li, viz., the use of local analytic solutions of the differential equation. Chen and Li use spectral methods to get the analytic solutions which are expressed in terms of infinite series, and then impose boundary approximations which are polynomials. We use polynomial solutions of the differential equations for both the interior of the element and the boundaries, and derive the optimal formulas with ease and elegance.

Laplace Equation

Dirichlet Boundary Conditions. Chen and Li [2] have developed a nine-point formula for a subregion in the case of the two-dimensional Laplace equation,

$$\Delta u = u_{xx} + u_{yy} = 0 \tag{1}$$

with

$$u = f_S(x) \text{ on } y = -h,\ u = f_N(x) \text{ on } y = h$$

$$u = f_W(y) \text{ on } x = -k,\ u = f_E(y) \text{ on } x = k$$

The nine-point formula obtained by Chen and Li for $h = k$ is,

$$u_0 = c_1(u_{EC} + u_{NC} + u_{WC} + u_{SC}) + c_2(u_{SE} + u_{SW} + u_{NE} + u_{NW}) \tag{2}$$

with $c_1 = 0.20531458674$ and $c_2 = 0.044685413126$.

Formula (2) was obtained by assuming that the boundary functions $f_S(x), f_E(y), f_N(x), f_W(y)$ are quadratic polynomials and that each polynomial interpolates three nodal values on the boundary. Observe that the four quadratic polynomials

Contributed by the Heat Transfer Division for publication in the JOURNAL OF HEAT TRANSFER. Manuscript received by the Heat Transfer Division March 4, 1981.

are independent and are connected only through the nodal values at the corners. In all, there are eight free parameters in the boundary functions and these are expressed in terms of the eight nodal values on the boundaries. In order to derive a formula of optimal order using the same nodes as in (2), we need to use polynomials of as high a degree as possible without increasing the number of free parameters. This can be done by imposing certain available constraints. As a first step we may require that all the four polynomials be derived from a single polynomial in x and y. Naturally, such polynomials of degree two have six parameters and those of degree three have ten parameters. Therefore, we could not possibly include all the third-degree terms and get cubics on the boundaries. Additionally, we could impose the condition that this common boundary function should also satisfy the differential equation (1). No further conditions are available within the framework of our problem. It will now be shown that these conditions allow us to choose a polynomial of degree four in x and y and consequently the boundary functions can be chosen as polynomials of degree four.

Consider the polynomial

$$f(x,y)=A_0+A_1x+A_2y+A_3x^2+A_4xy+A_5y^2 + \ldots + A_{14}y^4 \tag{3}$$

If $\Delta f \equiv 0$, then we must have

$$A_3+A_5=0,\ 3A_6+A_8=0,\ A_7+3A_9=0,\ A_{11}+A_{13}=0$$

$$A_{12}=-6A_{10}=-6A_{14}$$

Therefore (3) can be written as:

$$f(x,y)=a_0+a_1x+a_2y+a_3(x^2-y^2)+a_4xy+a_5(x^3-3xy^2)+a_6(3x^2y-y^3)+a_7(x^4-6x^2y^2+y^4)+a_8(x^3y-xy^3) \tag{4}$$

Note that the function $f(x, y)$ consists of the real and imaginary parts of powers of $x + iy$, which are the solutions of equation (1). With the boundary functions $f_S(x)$, $f_E(y)$, $f_N(x)$ and $f_W(y)$ defined as restrictions of the function $f(x, y)$ in (4), the F.A.M. [2] gives the following nine-point formula in the place of formula (2),

$$u_0=1/5(u_{EC}+u_{NC}+u_{WC}+u_{SC})+1/20(u_{SE}+u_{NE}+u_{NW}+u_{SW}) \tag{5}$$

It is interesting to note that the formula (5) is well-known in the literature and has been derived by Bickley [13], Collatz [14], Kantorovich and Krylov [11], Greenspan [9], and others by using the Taylor series expansion or other standard finite differencing techniques which are quite different from the finite analytic method of Chen and Li.

The use of the boundary function (4) in the derivation of (5) has led us to yet another procedure for the derivation of the formula (5). This derivation is much simpler than either the finite analytic procedure of Chen and Li or the Taylor series expansion methods.

An Alternate Finite Analytic Procedure

Let us define the solution $u(x, y)$ over a subregion as a linear combination of the solutions of the differential equation (1) so that

$$u(x,y)=a_0+a_1x+a_2y+a_3(x^2-y^2)+a_4xy+a_5(x^3-3xy^2)+\ldots$$

Here we have chosen the real and imaginary parts of powers of $x + iy$ which form a complete basis for the harmonic functions which are analytic. Next, we approximate the local solution $u(x, y)$ by retaining only a finite number of terms in the expansion. This also limits the number of free parameters appearing in the expression for $u(x, y)$. These free parameters are expressed in terms of nodal values of u at a preselected number of mesh points of the element by collocation. Since $u(0, 0) = a_0$ and a_0 is expressed as a linear combination of the nodal values at other mesh points of the element, we get a difference formula.

As an example, let us assume that $u(x, y) = f(x, y)$, where $f(x, y)$ is given in (4). In the case $h = k$, the parameters $a_0, a_1, \ldots, a_8$ are obtained in terms of the eight nodal values on the boundary of the element. Observe that the parameter a_8 does not appear because of the symmetry. In any case, the value of a_0 expressed in terms of the other nodal values gives the formula (5).

The procedure described here can be used to derive the well-known five-point formula or the higher order thirteen-point formula for the Laplace equation. The whole procedure can be written down in a matrix form and the derivation of a formula simply involves the inversion of a small matrix. The same procedure can be applied to derive difference formulas for other linear equations and also for the Neumann problem of the Laplace equation as will be shown later.

It can be shown by the Taylor series expansion that the formula (2) has a truncation error of $0(h^2)$ and the formula (5) has a truncation error of $0(h^6)$. From the numerical results, it is seen that the overall discretization errors are also of order h^2 and h^6, respectively, when these formulas are used for solving the Laplace equation with Dirichlet boundary conditions.

If a nonuniform rectangular mesh is needed, for example $\Delta x = 3\,\Delta y = h$, we get the following formulas instead of the usual five-point and the nine-point formulas.

$$u_0=9/20(u_{NC}+u_{SC})+1/20(u_{WC}+u_{EC}) \tag{6}$$

$$u_0=1/20(u_{NE}+u_{NW}+u_{SW}+u_{SE})+11/25(u_{NC}+u_{SC})-1/25(u_{WC}+u_{EC}) \tag{7}$$

These formulas are order h^2 and h^4, respectively, and numerical results obtained using these formulas are given later. Although the weight for $(u_{WC} + u_{EC})$ in (7) is negative, this affects neither the order of the formula nor its numerical performance. By considering $\Delta x = k\ \Delta y$, we were able to show that the weight 1/20 for $(u_{NE} + u_{NW} + s_{SW} + u_{SE})$ in (7) is independent of the parameter, k, whilst the coefficient of $(u_{WC} + u_{EC})$ in (7) is positive if $k < \sqrt{5}$, zero for $k = \sqrt{5}$, and negative for $k > \sqrt{5}$.

Nomenclature

u = exact solution
$\bar{u}$ = computed solution
e_u = maximum $|\bar{u}-u|$
e_{u_x} = maximum $|\bar{u}_x-u_x|$
f_s = function defined on south boundary
f_N, f_E, f_W = similar to f_S
u_{SE} = value of u at south-east corner of subregion
u_{NE}, u_{SW}, u_{NW} = similar to u_{SE}
u_{SC} = value of u at the center of the southern edge of subregion
u_{EC}, u_{NC}, u_{WC} = similar to u_{SC}
u_0 = value of u at the center of the subregion
$z=x+iy$ = is a complex number
$0(h^n)$ = of the order h^n

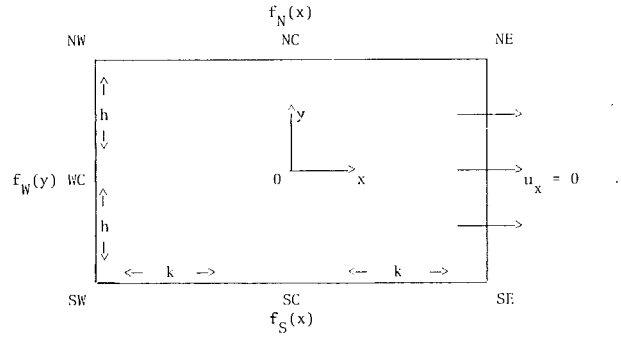

Fig. 1 Subregion with Neumann condition

For the method described here, it is not necessary to have a rectangular mesh. Any distribution of collocation points for which the system of equations can be solved, will give a difference formula. In general, the truncation error of such a formula depends upon the number of terms retained in the expansion of u and hence upon the number of points chosen for collocation. For example, the truncation error when four points are chosen for collocation is at least of order h^2 and when eight points are chosen it is at least of order h^4. By a judicious choice of collocation points, particularly, by taking advantage of symmetry, one can achieve a higher order of accuracy. This was possible in the case of the Laplace equation due to the symmetry of the operator, and we did get a difference formula of $0(h^6)$ with only eight mesh points for collocation. Formulas with nonuniform mesh may be needed when the region is not rectangular. Also, the procedure given here can be used to derive formulas for the mesh points in the neighborhood of curved or irregular boundaries. In this paper, we have restricted ourselves to simple equations and regions which can be divided into square subregions.

Formulas For Derivatives

Chen and Li have obtained formulas for the derivatives u_x and u_y by differentiating the series solution for u and evaluating this series at the center point 0 and at a mid-point on one boundary of the subregion.

These formulas can be made optimal by substituting the higher degree boundary function (4) in the integrals for the Fourier coefficients. In the case of $(u_x)_0$ this results in the formula

$$(u_x)_0 = a_1 = 1/h[1/12(u_{NE} - u_{NW}) + 1/3(u_{EC} - u_{WC}) + 1/12(u_{SE} - u_{SW})] \quad (8)$$

The method we have developed for deriving the optimal formula provides an easier method of deriving the formulas for the derivatives. For this purpose, let us write (4) as:

$$u(x, y) = \sum_{i=0}^{7} a_i B_i(x, y) \quad (9)$$

and

$$u_x(x, y) = \sum_{i=0}^{7} a_i \frac{\partial B_i}{\partial x}(x, y) \quad (10)$$

Hence

$$u_x(0, 0) = (u_x)_0 = a_1$$

$$u_x(h, 0) = (u_x)_{EC} = a_1 + 2a_3 h + 3a_5 h^2 + 4a_7 h^3$$

When we write the parameters $a_1, \ldots a_7$ in terms of the nodal values we get the formula (8) for $(u_x)_0$ and the formula

$$(u_x)_{EC} = 1/h[23/15u_{EC} - 2/15u_{WC} - 11/30(u_{NE} + u_{SE}) - 3/10(u_{NC} + u_{SC}) - 1/30(u_{NW} + u_{SW})] \quad (11)$$

The Heat Equation

For the heat equation, we consider a rectangular subregion of length, $2h$, and width, k. The equation and the boundary conditions are,

$$u_t = a^2 u_{xx} \quad -h \le x \le h, \ 0 \le t \le k$$

$$u(x, 0) = f_S(x), \ u(-h, t) = f_W(t), \ u(h, t) = f_E(t) \quad (12)$$

In Chen and Li's derivation of a computational formula for the heat equation [3], $f_S(x)$ is assumed to be a quadratic polynomial interpolating the nodal values u_{SW}, u_{SC}, and u_{SE}. Similarly, the boundary functions $f_W(t)$ and $f_E(t)$ are approximated by linear polynomials in t. The computational formula in general can be written down as

$$u_p = u(0, k) = \frac{r\theta}{1+2r\theta}(u_{NE} + u_{NW}) + \frac{r(1-\theta)}{1+2r\theta}(u_{SE} + u_{SW}) + \left(1 - \frac{2r}{1+2r\theta}\right)u_{SC} \quad (13)$$

where $r = a^2k/h^2$ and different values of θ determine different schemes; e.g., $\theta = 1$ gives the implicit scheme and $\theta = 1/2$ the Crank-Nicolson scheme. For Chen and Li's computational formula, θ is given by:

$$\theta = \frac{1}{1 - 4S(r)} - 1/2r,$$

where

$$S = S(r) = \sum_{m=1}^{\infty} \frac{(-1)^{m-1} e^{-r\alpha_m^2}}{\alpha_m^3}, \quad (14)$$

$$\alpha_m = \frac{2m-1}{2}\pi \text{ and S depends upon } r$$

Unfortunately, one is required to compute S every time r is changed. Even then the scheme given in (13) and (14) is not as accurate as the Crank-Nicolson scheme. Naturally, the computational formula can be made more accurate to get an optimal formula by increasing the degree of the approximating polynomials as was done for the Laplace equation.

In order to show how this formula is derived following Chen's procedure we shall assume $a = 1$, without loss of generality, and write the boundary function (x, t) as

$$f(x, t) = a_0 + a_1 x + a_2(x^2 + 2t) + a_3(x^3 + 6xt) + a_4(x^4 + 12x^2 t + 2t^2) \quad (15)$$

The values of the parameters $a_0, \ldots, a_4$ can be determined in terms of the five nodal values. The boundary function $f_S(x)$ can be written down from $f(x, t)$ as a polynomial of degree four and both $f_E(t)$ and $f_W(t)$ as polynomials of degree two each. Carrying out the analysis we found that

$$\theta = 1/2 - 1/(12r) \quad (16)$$

in place of (14). Alternatively, one can derive (13) by using $u(x, t) = f(x, t)$ and collocating $u(x, t)$ at the nodal points. The value of $u_p = a_0 + 2a_2 k + 12a_4 k^2$ leads to the same value of θ as in (16). The formula (13) with θ given in (16) was derived by Lebedev and also by Douglas [12] and is known to have the truncation error $0(h^4 + k^2)$. Note that for r large, θ approaches 1/2, and the results of computation with large values of r do not differ significantly from those given by Crank-Nicolson, however, when r is not too large ($r \approx 1$), the results obtained by using the optimal formula are in general more accurate.

Table 1 Comparison for $u = R(e^z)$, $(\Delta x = 1/4)$

Method	$\lvert e_u/u\rvert$	$\lvert e_{u_x}/u_x\rvert$
M_5	0.73236E-3	0.95991E-2
M_c	0.69002E-4	0.97480E-3
M_9	0.13224E-7	0.21502E-4
R_5	0.4141E-3	
R_9	0.1174E-5	

Homogeneous Neumann Problem

Assume for the sake of simplicity that we wish to solve the two-dimensional Laplace equation on a square. The values of the solution are given on three sides and the normal derivative on the remaining side is zero. In order to solve this problem it is necessary to have two different computational schemes. For the interior subregions, the nine-point formula (5) for the Dirichlet problem is used. Along a boundary where the Neumann condition is imposed, we need to develop another formula for the subregion shown in Fig. 1.

Following [2] and using quadratic interpolating polynomials for the boundary functions, we get (for $h = k$) the difference formula

$$u_0 = 0.3705092831(u_{NC} + u_{SC}) + 0.2230556987u_{WC} + 0.0179628676(u_{NW} + u_{SW}) \quad (17)$$

In order to get an optimal formula in place of (17), we again define $f(x, y)$ as in (4) but impose an additional constraint that $\partial f/\partial x = 0$ on $x = h$. This means that

$$a_5 = -4a_7h,\ a_4 = -6a_6h \text{ and } a_1 = -2a_3h + 8a_7h^3 \quad (18)$$

The boundary functions $f_S(x)$, $f_N(x)$, and $f_W(y)$ are now polynomials of degree four obtained from $f(x, y)$ in (4) and give the following "optimal" formula,

$$u_0 = 3/8(u_{NC} + u_{SC}) + 1/4u_{WC} \quad (19)$$

This formula could also have been derived by simply defining $u(x, y) = f(x, y)$ with the additional constraints given in (18), and collocating $u(x, y)$ at the element nodes. Numerical results clearly show that the formula (19) gives much more accurate results in general than the formula (17).

We can also generate other useful optimal formulas using our procedure, for example

$$(u_x)_0 = 1/h[7/24(u_{NC} + u_{SC}) - 1/6(u_{NW} + u_{SW}) - 1/4u_{WC}] \quad (20)$$

and

$$(u_y)_0 = 1/h[4/9(u_{NC} - u_{SC}) + 1/18(u_{NW} - u_{SW})] \quad (21)$$

The value of u at $(h, 0)$ is often needed and is given by

$$(u)_{EC} = 19/36(u_{NC} + u_{SC}) - 1/9(u_{NW} + u_{SW}) + 1/6u_{WC} \quad (22)$$

We believe that the formulas (20–22) are new. Also the method of handling the Neumann boundary condition by using (19) differs from what is conventionally done. Normally, a fictitious point is taken outside the boundary and the normal derivative on the boundary is replaced by some suitable finite difference, thereby modifying the computational scheme near the boundary. In our procedure it is not necessary to include the points on the boundary, and the solution on the boundary can be calculated, if desired, using (22). Our formula (19) is in fact a five-point formula as the weights at the nodes NW and SW turn out to be 0. This formula could be used in conjunction with the usual five-point formula for the interior elements. In this paper we give numerical results demonstrating how Neumann problems can be solved using the formulas presented here. A more complete analysis of these formulas together with error analysis and numerical comparisons with conventional methods will be reported later [15, 16, 17].

Numerical Examples

In this section we give numerical comparisons of results obtained by the formulas discussed in this paper.

We first consider the two-dimensional Laplace equation with Dirichlet boundary conditions on a unit square and compare the results obtained by using the five-point formula

$$M_5: u_0 = 1/4(u_{EC} + u_{NC} + u_{WC} + u_{SC}),$$

the nine-point optimal formula, M_9, given in (7); and the nine-point formula M_c given in (2), and the formulas R_5 and R_9 given in (6) and (7), respectively, for a rectangular mesh with $\Delta x = 3\ \Delta\ y$. For problems whose exact solution is a polynomial $R(Z^n)$, $I(Z^n)$, $n = 2, 3, \ldots, 7$ we find that only M_9 gives exact answers for $n \leq 7$, while R_9 gives exact answers for $n \leq 5$, and both R_5 and M_5 give exact answers for $n \leq 3$. We solved many other problems with exact solutions such as $R(e^z)$, $R(ln\ z)$, $R(z \sin z)$, $R(\cos 3z)$, $R(\sin 5z)$, $I(\cosh z)$ etc., with consistent results. A typical result for the case when $u = R(e^z)$ is given in Table 1. The notation used is u = exact solution, $\bar{u}$ = computed approximation,

$$e_u = \max_{\text{mesh points}} |\bar{u} - u|,\ e_{u_x} = \max_{\text{mesh points}} |\bar{u}_x - u_x|$$

where the derivatives are computed by central differences in the case of M_5, by the formula given by Chen and Li in [2] for M_c, by the formula (8) for M_9. In Table 1, we give the relative error at the point where the maximum absolute error occurs.

As the mesh size is reduced, the rate of improvement in the results obtained by M_c is no better than the rate of improvement given by M_5. We illustrate this important fact in Tables 2 and 3, where the ratio of the absolute errors at a particular point is calculated as the mesh is refined. The results for the case when $u = R(ln\ z)$ are given in Table 2, the region considered is $0.1 \leq x, y \leq 1.1$ and the errors are compared at the point $x = y = 0.1 + 1/3$. The results for the case when $u = R(\sin 5z)$ are given in Table 3, the region is $0 \leq x, y \leq 1$, and the errors are compared at the point $x = y = 2/3$.

The results in Tables 2 and 3 show that Chen and Li's formula M_c is only of second order, and although the results are more accurate than those obtained by the five-point formula M_c, it is questionable whether the increased bandwidth and consequent computational effort justifies the use of their formula. However, the optimal nine-point formula, M_9, is of sixth order and seems to perform well even near a singularity. The formula R_5 based on rectangular subregions is as good as M_5, while the formula R_9 is of fourth order and is better than M_c but not as good as M_9.

For the heat equation (12) with $a = 1$ and $0 \leq x \leq 1$, we have carried out numerical experiments using the finite difference formula (13) with $\theta = 1$ (implicit-scheme), $\theta = 1/2$ (Crank-Nicolson scheme), $\theta = 1/2 - 1/(12r)$ (the optimal scheme of (16)), and θ given in (14) for Chen and Li's scheme. A variety of problems were considered, in particular, problems whose solutions were of the type appearing in (15). We also considered the problem whose exact solution is given by $e^{-\pi^2 t}\sin x$ and the problem treated by Chen and Li, whose exact solution is given by;

$$1 - 4\sum_{n=1}^{\infty} 1/(n\pi)e^{-n^2\pi^2 t}\sin \pi x$$

The mesh, Δx, was taken to be 1/4, 1/8, and 1/16, and Δt was chosen such that the ratio $\Delta t/\Delta x^2 = r$ varied between 1/2 to 16. The following conclusion can be drawn on the basis of the numerical results.

Table 2 Error reduction for $u = R(lnz)$

Method	Δx	e_u	Ratio	e_{u_x}	Ratio
M_5	1/3	0.26465E-1		0.11256E0	
			3.2		3.0
	1/6	0.81378E-2		0.37519E-1	
			3.7		3.5
	1/12	0.21508E-2		0.10437E-1	
M_c	1/3	0.20373E-2		0.21160E-1	
			3.5		8.6
	1/6	0.58018E-3		0.24473E-2	
			3.0		2.4
	1/12	0.19209E-2		0.10176E-2	
M_9	1/3	0.52575E-2		0.37271E-1	
			25.7		21.3
	1/6	0.20496E-3		0.17538E-2	
			44.6		24.6
	1/12	0.45896E-5		0.71391E-4	
R_5	1/3	0.1568E-1			
			3.4		
	1/6	0.4622E-2			
R_9	1/3	0.2117E-2			
			21.6		
	1/6	0.9796E-4			

Table 3 Error reduction for $u = R(\sin 5z)$

Method	Δx	e_u	Ratio	e_{u_x}	Ratio
M_5	1/3	0.58685E0		0.19880E2	
			4.3		5.7
	1/6	0.13736E0		0.34808E-1	
			4.2		4.7
	1/12	0.32920E-1		0.74137E0	
M_c	1/3	0.45922E-1		0.56343E1	
			3.9		9.5
	1/6	0.11712E-1		0.59045E0	
			4.0		5.6
	1/12	0.29167E-2		0.10504E0	
M_9	1/3	0.63899E-2		0.37580E1	
			52.4		19.2
	1/6	0.12189E-3		0.19545E0	
			77.2		16.7
	1/12	0.15795E-5		0.11697E-1	
R_5	1/3	0.3663E0			
			4.8		
	1/6	0.7715E-1			
R_9	1/3	0.3966E-1			
			17.4		
	1/6	0.2277E-2			

Table 4 Comparison of maximum absolute errors

Method	e_u	e_{u_x}	e_{u_y}
M_5	0.16193E-1	0.44795E1	0.56504E0
M_c	0.95280E-2	0.47488E1	0.50837E-1
M_9	0.11061E-2	0.47872E1	0.27303E-2

Table 5 Error reduction for $u = R(ln\,(z-1+2i))$

Method	Δx	No. of Nodes	e_u	e_{u_x}	e_{u_y}
M_5	1/3	6	0.16753E-3	0.18261E-2	0.24161E-2
	1/6	30	0.65543E-4	0.59791E-3	0.70629E-3
M_c	1/3	4	0.12274E-3	0.36799E-3	0.22163E-3
	1/6	25	0.18321E-4	0.75040E-4	0.99663E-4
	1/12	121	0.23171E-5	0.22801E-4	0.223189E--4
M_9	1/3	4	0.30249E-4	0.56278E-4	0.19941E-4
	1/6	25	0.15050E-5	0.38869E-5	0.24736E-5
	1/12	121	0.44703E-7	0.23283E-6	0.23469E-6

Chen and Li's method does give more accurate results than the implicit method. The implicit method is the least accurate one among the four methods tested. It was unfortunate that Chen and Li chose to compare their method with the implicit method. Both the optimal method and the Crank-Nicolson method perform significantly better in all cases than Chen and Li's method. For large values of r, there is no significant difference between the results obtained by the Crank-Nicolson method and the optimal method, as expected. However, as r is made small (<2), the optimal method gives better accuracy and the improvement is significant for $r = 1$ or $1/2$.

Finally, we consider the two-dimensional Laplace equation with homogeneous Neumann boundary condition on the east edge of a unit square and Dirichlet boundary conditions on the remaining boundaries. We compute results obtained by the standard five-point formula which uses nodes on the east

boundary and fictitious nodes outside the region. We compare these results with those obtained using Chen and Li's formulas (4) and (17) and our optimal formulas (7) and (19). These formulas do not use nodes on the east boundary, and the dimension of the resulting matrix is reduced by one column of mesh points.

For problems whose exact solution is a polynomial, for example, $R(z-1)^2$, $I(z-1)^3$, $R(z-1)^4$, $I(z-1)^5$ etc., it was found that only M_9 gives exact answers for degree 4 and 5. We give here in Table 4 results for the problem whose exact solution is $u = \sin(\pi x/2)\,[3\sinh(\pi y/2) + 7\sinh(\pi(y-1)/2)]$ in the case when $\Delta x = \Delta y = 1/4$, and $0 \le x, y \le 1$.

Again, it is more revealing to observe the reduction in these absolute errors as the mesh size is reduced. In Table 5 we give such a comparison for the problem whose exact solution is $u = R(ln\ (z-1+2i))$ so that the singularity is outside of the unit square $0 \le x, y \le 1$. The errors in this table are the maximum absolute errors which do not necessarily occur at the same point in each mesh.

Conclusions

Using Chen and Li's Finite Analytic Method we have derived difference formulas of higher order than those given by Chen and Li without increasing the number of nodes involved. These formulas which we call "optimal" formulas are not only more accurate but are simpler than those given by Chen and Li and contain no infinite series. Some of these formulas are well known in the literature and have been derived by using the Taylor series expansion method. Here we have given an alternative procedure to derive these formulas by using local analytic polynomial solutions. This process of derivation is simpler than any other procedure given in the literature. Its simplicity allows us to generate other difference schemes as has been done here for the Neumann problem of the Laplace equation.

Our numerical results clearly show that the difference formulas obtained by Chen and Li perform poorly at least for the cases considered here. Besides proposing a new derivation technique to get optimal finite analytic difference formulas, we also suggest a novel way in which derivative boundary conditions (Neumann) can be handled and how derivatives of the solutions, which are often required, can be evaluated more accurately. Extension of our procedure to other problems is under investigation [18, 190].

References

1 Chen, C. J., and Li, P., "Finite-Differential Method in Heat Conduction — Application of Analytic Solution Technique," ASME Paper No. 79-WA/HT-50, ASME Winter Annual Meeting, New York, 1979.

2 Li, P., and Chen, C. J., "The Finite Differential Method—A Numerical Solution to Differential Equations," *Proceedings of the 7th Canadian Congress of Applied Mechanics,* Sherbrook, May 1979, p. 909.

3 Chen, C. J., and Li, P., "The Finite Analytic Method for Steady and Unsteady Heat Transfer Problems," presented at the 1980 U.S. National Heat Transfer Conference, Orlando, Fla.,

4 Chen, C. J., Naseri-Neshat, H., and Li, P., "The Finite analytic Method, Applications of Analytic Solution Technique to Numerical Solutions of Ordinary and Partial Differential Equations," Report ECJC-1-80, Jan. 1980, Energy Division, The University of Iowa, Iowa City.

5 Chen, C. J., Naseri-Neshat, H., and Ho, K. S., "Finite Analytic Numerical Solution of Heat Transfer in Two-Dimensional Cavity Flow," presented in the 1980 ASME Winter Annual Meeting at Chicago, Ill.

6 Allen, D. N., De, G., and Southwell, R. V., "Relaxation Methods Applied to Determine the Motion in Two Dimensions of a Viscous Fluid Past a Fixed Cylinder," *Quart, J. Mech, Appl. Math.,* Vol. 6, 1955, pp. 129–145.

7 Roscoe, D. F., "New Methods for the Derivation of Stable Difference Representations for Differential Equations," *J. Inst. Maths. Applic.,* Vol. 16, 1975, pp. 291–301.

8 Kellogg, R. B., and Tsan, A., "Analysis of Some Difference Approximations for a Singular Perturbation Problem Without Turning Points," *Math of Computation,* Vol. 32, 1978, pp. 1025–1039, (other references given).

9 Greenspan, D., "On a 'Best' Nine-Point Difference Equation Analogue of Laplace Equations," *Journal of the Franklin Institute,* Vol. 263, 1957, pp. 425–430.

10 Greenspan, D., "Note on Nine-Point Analogues of Laplace's Equation," *Journal of the Franklin Institute,* Vol. 263, 1957, pp. 253–255.

11 Kantorovich, L. V., and Krylov, V. I., *Approximate Methods of Higher Analysis,* P. Noordhoff Ltd., Groningen, 1958, p. 211.

12 Saul-yev, V. K., *Integration of Equations of Parabolic Type by Methods of Nets,* Pergamon Press, 1964, p. 94.

13 Bickley, W. G., "Finite Difference Formulae for the Square Lattice," *Quart. J. Mech.* Vol. 1, pp. 35–42, 1948.

14 Collatz, L., *Numeriche behandlung von differential gleichunger,* Springer-Verlag, 1951.

15 Manohar, R., and Stephenson, J. W., "High Order Difference Schemes for Linear Partial Differential Equations," submitted for publication.

16 Manohar, R., and Stephenson, J. W., "High Order Methods for the Laplace Equation with Neumann Conditions," submitted for publication.

17 Manohar, R., and Stephenson, J. W., "New High Order Difference Methods for Solving the Poisson Equation," *Proceedings of the Eleventh Annual Conference on Numerical Mathematics and Computing,* University of Manitoba, 1981.

18 Kwon, Y., Manohar, R., and Stephenson, J. W., "Single Cell Fourth Order Methods for the Biharmonic Equation," *Proceedings of the Eleventh Annual Conference on Numerical Mathematics and Computing,* University of Manitoba, 1981.

19 Gupta, M. M., Manohar, R., and Stephenson, J. W., "A Fourth-Order, Cost-Effective, and Stable-Finite Difference Scheme for the Convection-Diffusion Equation," *Proceedings of the Second National Symposium on Numerical Methods in Heat Transfer,* College Park, Maryland, 1981.

The Motion of Particles Inside a Droplet

J. N. Chung
Assistant Professor,
Department of Mechanical Engineering,
Washington State University,
Pullman, Wash. 99164

Equations of motion for particles translating inside a droplet with internal circulation were developed. The forces experienced by these particles and their relative importance are also summarized. Sample calculations for coal particles in oil droplets show that for high-droplet Reynolds numbers, particles will accumulate near the droplet surface before substantial evaporation of the droplet, based on the results that the characteristic time of transport is two orders of magnitude smaller than the droplet lifetime. These accumulations of particles near the droplet surface will probably result in particle agglomeration. Fow low-droplet Reynolds numbers, the particles are making slow looping motions and the characteristic time of transport is comparable to the droplet lifetime. This results in a more even distribution of particles in the droplet with slightly higher particle density near the surface. This indicates a higher particle burning rate and the possibility of internal boiling and microexplosion due to heterogeneous nucleation initiated from those coal particles.

Introduction

As engineering technology advances, more emphasis will be placed on the transport processes involving bubbles, droplets, small particles or combinations of these, simply because they offer larger interfacial areas which could significantly enhance the transport rates. The use of both droplets and small particles in the same process could be found in many engineering applications. A special application is to place the particles inside those droplets to achieve uniform dispersion of both phases. One example of this special application is in the area of spray combustion where finely-crushed coal particles are mixed with oil and then the mixture is sprayed into a furnace in the form of oil droplets containing coal particles. This is a promising technology for the efficient utilization of coal.

Since the transport rates associated with these particle-containing droplets are closely related to the resistances due to the interior of the droplet, the knowledge of the motion and the distribution pattern of the particles in a droplet is of fundamental importance to the general understanding of the transport phenomena of droplet-particle systems.

The problem of fluid motion inside a droplet has been analyzed extensively [1-2]. Only recently Prakash and Sirignano [3] included the viscous effects on the internal motion of a liquid droplet moving in a gas environment. But none of the investigations involved particles in droplets. Experimental works have been reported on the combustion characteristics of coal/oil droplets. Law et al. [4] suggested, based on experiments, that the characteristics of combustion of coal/oil droplets depend on the intensity of internal circulation. Rapid internal motion favors batch-distillation types of varporization which cause the coal particle to agglomerate. On the other hand, slow internal motion traps the volatile components in the inner core of the rapidly-heated droplet and may eventually lead to boiling and subsequent fragmentation of the droplet. Experiments [5] have been performed upon free-falling coal particle/oil droplets in electric furnances at atmospheric pressure. They concluded that coal burns in the form of agglomerates instead of individual particles. Upon incresing the volatility of the oil component of the droplet, the required time for the combustion of the entire droplet was incresed. Also, the addition of water did little to enhance the fragmentation.

Contributed by the Heat Transfer Division and presented at the ASME Winter Annual Meeting, Washington D.C., November 15-20, 1981. Manuscript received by the Heat Transfer Division September 29, 1981. Paper No. 81-WA/HT-45.

The problem of predicting particle motion in a fluid has been analyzed extensively only in the area of rectilinear acceleration of particles in a stagnant fluid column due to gravity and the creeping flow was assumed. Odar and Hamilton [6] investigated the higher Reynolds number conditions and the correction factors for inertia effect were suggested. Odar [7, 8] also did experiments concerning the effects of curvature and unsteady acceleration. Cliff et al. [9] gave a thorough review on the accelerated particle motion.

Mathematical Model

A spherical solid particle-containing droplet translating in a hot gas environment is considered. The main concern in this analysis is to predict the particle trajectory inside a droplet with internal circulation. Since we have a two-phase (solid-liquid) system, it is convenient to discuss the fluid mechanics of the continuous phase (liquid content of the droplet) and mechanics of the dispersed phase (particles) separately.

The schematic of the model is shown in Fig. 1. The basic assumptions on which the mathematical model is developed are listed below:

(*a*) The particle loading is light such that the presence of coal particles does not affect the flow field of the continuous phase, but the particle trajectories are completely dominated by the motion of the continuous phase.

(*b*) The interactions among particles are included through a "mixture viscosity model" proposed by Ishii and Zuber [10]. This mixture viscosity reflects the nonuniformity of the surrounding fluid and extra forces experienced by the particle due to the existence of other particles.

(*c*) The heat and mass transfer through the droplet surface are not included, mainly because we are interested in the maximum particle transport time from the vortex center to the surface.

(*d*) Both the droplet and particles are spherical.

(*e*) The fluid properties are assumed constant.

The Flow Field of Continuous Phase (Droplet Fluid). In most of the spray system, liquid droplets formed through spray nozzles move with a velocity relative to the gas. Both the droplet formation and liquid-gas relative velocity will contribute to the droplet internal circulating motion. For this analysis, the internal motion is assumed fully developed and steady because the characteristic time for the droplet to establish a steady motion is at least one order of magnitude smaller than the droplet lifetime [3]. In creeping flow,

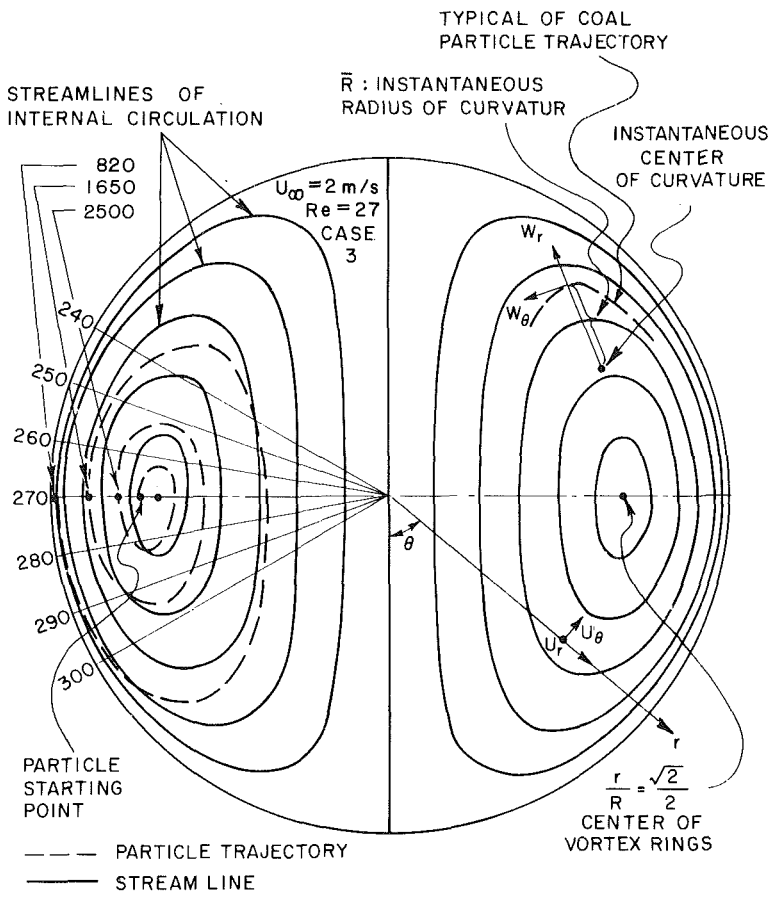

Fig. 1 Schematic of mathematical model and the effects of u_∞

Hadamard [11] and Rybcznski's [12] viscous solution is valid for the whole droplet, while for high Reynolds number flow, three separate regions of flow can, in general, be discerned: an interior core flow, a boundary layer type flow near the surface of the droplet, and an internal wake flow [2]. Interior core flow is basically an inviscid vortex streamline corresponding to Hill's vortex [13]. The boundary layer flow is thin and the thickness is 0 ($\mathrm{Re}^{-1/2}$). Therefore, the Hill's vortex solution will be used to represent the flow field inside the droplet for high-droplet Reynolds number. The error of the order of $\mathrm{Re}^{-1/2}$ will be introduced due to the neglect of the boundary layer [14].

Both Hadamard streamlines and Hill's vortex streamlines can be expressed by a general vortex stream function,

$$\psi = \frac{A}{2}(R^2 r^2 - r^4)\sin^2\theta \tag{1}$$

where A, the strength of the vortex, is given by

$$A = U_\infty / 2(k+1)R^2 \text{ for low Re}$$

or

$$A = 3U_\infty / 2R^2 \tag{2}$$

for full strength Hill's vortex. The Re is defined as $U_\infty R/\nu_\infty$, where U_∞ is the velocity of the droplet relative to the hot gas, R is the radius of the droplet, ν_∞ is the kinematic viscosity of the hot ambient gas, and k is the dynamic viscosity ratio of droplet fluid to outside gas. It is noted that the full strength

Nomenclature

A = strength of vortex inside the droplet
b = typical oil droplet evaporation constant
C_d = drag coefficient
Fr = $(2/9)g_0 R_p / U_\infty^2$, Froude number
g = gravitational acceleration vector
g_0 = gravitational constant
k = dynamic viscosity ratio of droplet fluid to outside gas
P = Pressure
r = radial coordinate
R = radius of the droplet
$\bar{R}$ = radius of curvature of particle trajectory
Re = $R_\infty R/\nu_\infty$, droplet Reynolds number
Re_f = $U_\infty R_p/\nu_f$, reference Reynolds number
Re_r = radial particle Reynolds number
Re_θ = tangential particle Reynolds number
Δt = time step size of numerical integration
$U(t)$ = instantaneous particle velocity
U_∞ = droplet velocity with respect to ambient gas
V = volume
α_d = particle void fraction
α_{dm} = maximum particle packing
θ = tangential coordinate
μ = dynamic viscosity
μ_M = mixture viscosity
ν = kinematic viscosity
ψ = stream function of droplet inside flow

Subscripts

f = droplet fluid
p = particle
r = radial direction
θ = tangential direction
∞ = ambient gas

given above for Hill's vortex is only appropriate for a bubble translating in another liquid. For the case of a liquid droplet moving in a hot gas environment, the viscous effect is important. Prakash and Sirignano [3] suggested that $U_\infty/AR^2 = 10$ for oil droplets in a combustor. The velocities are found through the definition of stream function,

$$U_r = \frac{1}{r^2 \sin\theta}\frac{\partial \psi}{\partial \theta};\ U_\theta = \frac{-1}{r\sin\theta}\frac{\partial \psi}{\partial r} \tag{3}$$

The Equation of Motion of Particles inside a Droplet. The characteristic time of transport is defined as the typical time for a particle to move from near the vortex center to the close vicinity of the droplet surface through a looping motion induced by the continuous phase. The equation of motion is written for a single particle based on the "mixture viscosity model" [10], which treats the presence of multiparticle and their interacting effects with an effective viscosity. Therefore, even though we have a single particle model, the characteristic time of transport obtained will reflect a multiparticle system. The problem of solid particles moving in a liquid is much more complicated than that of particles in a gas where the drag is insensitive to acceleration and calculation of the motion is greatly simplified [9].

Basset [15] was the first to investigate the unsteady creeping motion of a rigid spherical particle in a stagnant fluid. It is interesting that the Stokes drag on a particle which is in an accelerated motion still carries the same formula as the steady drag, $6\pi\mu R_p U(t)$, where $u(t)$ is the instantaneous particle velocity. There are two new force terms resulting from the unsteady motion. First, the "added mass" term arises because the acceleration of the particle requires acceleration of the surrounding fluid. The volume of the added mass of the surrounding fluid is equal to one-half of the particle volume. The Basset force term, which is the time integral of the acceleration weighted by $(t - s)^{1/2}$, where $(t - s)$ is the time elapsed since the past acceleration, is due to the transient formation of a boundary layer near the particle surface. For high Reynolds number motion, Odar and Hamilton [6] have studied the force experienced by an accelerating solid sphere on a straight line. They maintained the basic formula of creeping flow and introduced correction factors to account for the inertia effect. They found the drag force, like the low Reynolds number case, still can be expressed by the steady drag formula

$$C_D \frac{\pi R_p^2 \rho}{2} U^2(t)$$

C_D is the traditional steady drag coefficient. The added mass and Basset historical force were calculated using the creeping flow formula multiplied by an empirical correction coefficient. These coefficients are

$$\Delta_A = 2.1 - 0.132 M_A^2/(1 + 0.12 M_A^2)$$

and

$$\Delta_H = 0.48 + 0.52 M_A^3/(1 + M_A)^3 \tag{4}$$

$$M_A = 2R_p \left|\frac{dU}{dt}\right| / U^2 \tag{5}$$

The above discussion is only appropriate for the particle translating in a stagnant continuous phase. Particles moving in a continuous fluid, which is also in motion itself, experience pressure gradient force, curvature force if not a straight line motion, and lift force in addition to those forces mentioned above.

A new Reynolds number characterizing the relative motion between particle and droplet fluid is defined:

$$\mathrm{Re}_r = \frac{|U_r - U_{rp}| R_p}{\nu_f},\quad \mathrm{Re}_\theta = \frac{|U_\theta - U_{\theta p}| R_p}{\nu_f} \tag{6}$$

where U_{rp} and $U_{\theta p}$ are particle radial and tangential velocities, respectively, and U_r and U_θ are continuous phase radial and tangential velocities, respectively, R_p is the particle radius, and ν_f is the droplet fluid kinematic viscosity. The particle Reynolds numbers, Re_r and Re_θ, are different from the droplet Reynolds number, Re, previously defined.

Case 1. Low Re_r and Re_θ (Re_r or $Re_\theta < 1$). The forces experienced by a particle during unsteady accelerated motion are listed as follows:

(*i*) Gravitational force

$$F_g = \vec{g}(\rho_p - \rho) V_p \tag{7}$$

where ρ_p and ρ are the densities of the particle and the droplet fluid, respectively, $\vec{U}_P$, $\vec{U}$ are the velocities of the particle and the droplet fluid, respectively, and V_p is the volume of the particle.

(*ii*) Drag force

$$F_d = 6\pi\mu_M R_p(\vec{U} - \vec{U}_p) \tag{8}$$

where μ_M, the mixture viscosity, is based on the concept of "mixture viscosity model" suggested by Ishii and Zuber [10] to include the multiparticle effect, and it is given by,

$$\mu_M = \mu_f\left(1 - \frac{\alpha_d}{\alpha_{dm}}\right) - 2.5\alpha_{dm} \tag{9}$$

μ_f is the actual droplet viscosity, α_d is the particle void fraction and α_{dm} is the maximum packing, and $\alpha_{dm} = 0.62$ was suggested [10].

(*iii*) Added mass force

$$F_a = (\rho/2) V_p d(\vec{U} - \vec{U}_p)/dt \tag{10}$$

(*iv*) Pressure gradient force

$$F_p = -V_p \partial P/\partial X_i \tag{11}$$

(*v*) Basset force

$$F_B = 6R_p^2\sqrt{\pi\rho\mu_M}\int_0^t \frac{d(\vec{U} - \vec{U}_p)/(dt)|_s}{\sqrt{t-s}} ds \tag{12}$$

(*vi*) Curvature forces

$$F_c(\text{centrifugal}) = \frac{W_\theta^2}{\bar{R}} \tag{13}$$

$$F_c(\text{coriolis force}) = \frac{W_\theta x W_r}{\bar{R}} \tag{14}$$

where W_r and W_θ are the particle radial and tangential velocities, respectively, with respect to the instantaneous center of the radius of curvature, and $\bar{R}$ is the instantaneous radius of curvature.

Because of the unsteady motion of the particle, the center of the radius of curvature, the magnitude of the radius of curvature, and the vector radius of curvature are all changing with time. They should be evaluated at each time step. The methods of calculating the above were taken from Randolph [16].

The equation of motion for the particle now be written as follows:

$$\rho_p V_p \frac{d\vec{U}_p}{dt} = \vec{g}(\rho_p - \rho) V_p + 6\pi\mu_M R_p(\vec{U} - \vec{U}_p)$$

$$+ \frac{\rho}{2} V_p \frac{d(\vec{U} - \vec{U}_p)}{dt} - V_p \frac{\partial P}{\partial x_i} + 6R_p^2\sqrt{\pi\rho\mu_M}\int_0^t \frac{\frac{d}{dt}(\vec{U} - \vec{U}_p)|_S}{\sqrt{t-s}} ds$$

$$+ \rho_p V_p f\left(\frac{W_\theta^2}{\bar{R}}, \frac{W_\theta X W_R}{\bar{R}}\right) \tag{15}$$

Table 1 Effects of U_∞

(Methanol droplet, $R = 0.1\times10^{-2}$m, $R_p = 0.1\times10^{-4}$m)

Case	U_∞	Re	Re_f	t_1	t_1'	t_2	t_3
1	10 m/s	135	144	146	195	375	6.9×10^4
2	5	67	72	292	360	730	8.9×10^4
3	2	27	29	730	820	2500	1.2×10^5
4	0.5	6.7	7.2	9.2×10^3	9.5×10^3	7.5×10^4	1.7×10^5
5	0.1	1.3	1.4	4.6×10^4	4.6×10^4	$>2.2\times10^5$	2.2×10^5

t_1 = estimated dimensionless time for one loop of motion from (30) or (31)
t_1' = actual calculated dimensionless time for one loop of motion
t_2 = dimensionless time of transport of particle from vortex center to droplet surface
t_3 = dimensionless droplet lifetime
For $R_p = 0.1\times10^{-4}$m. 1 dimensionless time = 3.527×10^{-5}s.

Table 2 Effects of particle size, R_p

(Methanol droplet, $R = 0.1\times10^{-2}$m, $U_\infty = 5$ m/s)

Case	R_p	t_1'	t_2	t_3	
6	0.5×10^{-5}m	1260	3750	3.58×10^5	1 dim'less time = 8.78×10^{-6}s
7	0.1×10^{-4}m	360	730	8.9×10^4	1 dim'less time = 3.53×10^{-5}s
8	0.15×10^{-4}m	175	330	3.99×10^4	1 dim'less time = 7.89×10^{-5}s
9	0.25×10^{-4}m	75	130	3.21×10^4	1 dim'less time = 9.78×10^{-5}s

For all cases examined here, particles have enough time to move to the surface, even the particle which is as small as 5 microns.

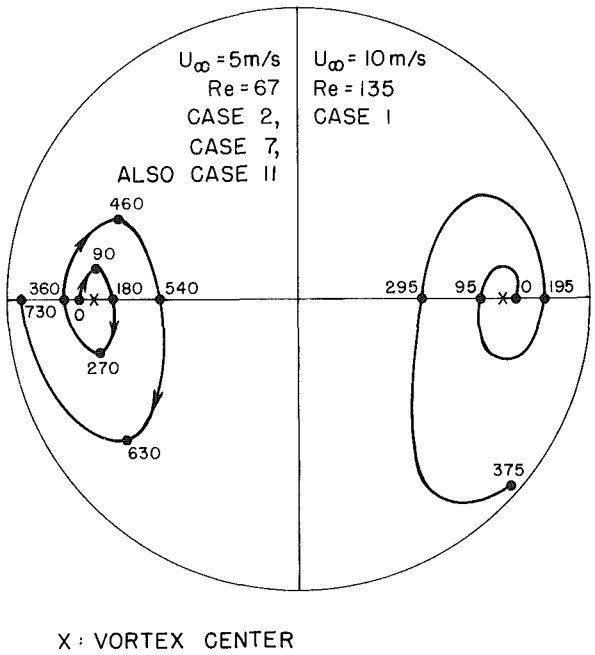

Fig. 2 The effects of U_∞ for high Reynolds number

Introducing the following nondimensionalization parameters,

$$r' = \frac{r}{R}, t' = \frac{9}{2}\frac{t_f^v}{R_p^2}, \vec{g}' = \frac{\vec{g}}{g_0}, \vec{U}_p' = \frac{\vec{U}_p}{U_\infty}, \vec{U}' = \frac{\vec{U}}{U_\infty},$$

$$p' = \frac{P}{\mu_f U_\infty/R}, W_\theta' = \frac{W\theta}{U_\infty}, W_R' = \frac{W_r}{U_\infty}, \bar{R}' = \frac{\bar{R}}{R} \tag{16}$$

we obtain

$$\gamma\frac{d\vec{U}_p'}{dt'} = \mathrm{FrRe}_f\vec{g}'(\gamma-1) + \gamma_M(\vec{U}' - U_p') + \frac{1}{2}\frac{d(\vec{U}' - "\mathrm{U}'_p)}{dt'}$$

$$- \frac{2}{9}\gamma_R 2\frac{\partial P'}{\partial x_i'} + \left(\sqrt{\frac{9}{2\pi}}\right)\sqrt{\gamma_M}\int_0^{t'}\frac{\frac{d}{dt'}(\vec{U}' - \vec{U}_p')|_{s'}}{\sqrt{t'-s'}}\,ds'$$

$$+ \frac{2}{9}\gamma_R\gamma\mathrm{Re}_f f\left(\frac{W_\theta'^2}{\bar{R}'}, \frac{W_\theta' \times W_r'}{\bar{R}'}\right) \tag{17}$$

where

$$\gamma = \rho_p/\rho, \gamma_M = \mu_M/\mu_f, \gamma_R = R_p/R, \ \mathrm{Fr} = \frac{2}{9}\frac{g_0 R_p}{U_\infty^2},$$

$$\mathrm{Re}_f = \frac{U_\infty R_p}{\nu_f}.$$

Drop the prime for all dimensionless quantities and also note that $d\bar{U}/dt = 0$ because the continuous phase motion is assumed steady. The dimensionless equations of motion for a particle in tangential and radial directions may be written as:

$$\left(\gamma+\frac{1}{2}\right)\frac{dU_{\theta p}}{dt} = \mathrm{FrRe}_f(\gamma-1)\sin\theta + \gamma_M(U_\theta - U_{\theta P})$$

$$- \frac{2}{9}\gamma_R^2\left(\frac{1}{r}\frac{\partial P}{\partial\theta}\right) - \left(\sqrt{\frac{9}{2\pi}}\right)\sqrt{\gamma_M}\int_0^t\frac{\frac{d}{dt}(U_{\theta p})|_s}{\sqrt{t-s}}\,ds$$

$$+ \frac{2}{9}\gamma_R\gamma\mathrm{Re}_f f_1\left(\frac{W_\theta^2}{\bar{R}}, \frac{W_\theta x W_r}{\bar{R}}\right) \tag{18}$$

$$\left(\gamma+\frac{1}{2}\right)\frac{dU_{rp}}{dt} = \mathrm{FrRe}_f(\gamma-1)\cos\theta + \gamma_M(U_r - U_{rp})$$

$$- \frac{2}{9}\gamma_R^2\left(\frac{\partial P}{\partial r}\right) - \left(\sqrt{\frac{9}{2\pi}}\sqrt{\gamma_M}\int_0^t\frac{\frac{d}{dt}(U_{rp})|_s}{\sqrt{t-s}}\,ds\right.$$

$$+ \frac{2}{9}\gamma_R\gamma\mathrm{Re}_f f_2\left(\frac{W_\theta^2}{\bar{R}}, \frac{W_\theta x W_r}{\bar{R}}\right) \tag{19}$$

where

$$\left.\begin{aligned} U_r &= \frac{\sin\theta}{2(1+k)}(1-r^2) \\ U_\theta &= \frac{-\sin\theta}{2(1+k)}(1-2r^2) \end{aligned}\right\}\text{low Re} \qquad \left.\begin{aligned} U_r &= \frac{1}{10}(1-r^2)\cos\theta \\ U_\theta &= \frac{-1}{10}(1-2r^2)\sin\theta \end{aligned}\right\}\text{high Re} \tag{20}$$

$$\left.\begin{aligned} \frac{\partial P}{\partial r} &= \frac{-5\cos\theta}{(1+k)} \\ \frac{1\partial P}{r\partial\theta} &= \frac{5\sin\theta}{(1+k)} \end{aligned}\right\}\text{low Re}$$

$$\left.\begin{aligned} \frac{\partial P}{\partial r} &= \left(\frac{\mathrm{Re}_f}{100\gamma_R}\right)\left[(1-r^2)2r - \frac{1}{r}\sin\theta(3r^2-4r^4)\right] \\ \frac{1\partial P}{r\partial\theta} &= \left(\frac{\mathrm{Re}_f}{100\gamma_R}\right)\left[\frac{-1}{r}\sin\theta\cos\theta(3r^2-2r^4)\right] \end{aligned}\right\}\text{high Re} \tag{21}$$

f_1 and f_2 are forces due to the curvature of motion. Because particle motion is unsteady and the transient nature of the radius of curvature, therefore, both centrifugal and coriolis forces contribute to radial and tangential forces, respectively.

Case 2 Intermediate and high Re_θ and Re_r ($1 < Re_\theta$ or $Re_r < 100$).

$$\text{drag force} = \frac{C_d}{2}\pi R_p^2\rho(\vec{U}-\vec{U}_p)\,|\vec{U}-\vec{U}_p| \tag{22}$$

$$\text{added mass} = \lambda\frac{\Delta_A}{2}\rho V_p\frac{d(\vec{U}-\vec{U}_p)}{dt} \tag{23}$$

$$\text{Basset force} = \chi\Delta_H 6R_p^2\sqrt{\pi\rho\mu_M}\int_0^t \frac{\frac{d}{dt}(\vec{U}-\vec{U}_p)\,|_s}{\sqrt{t-s}}\,ds \tag{24}$$

Δ_A and Δ_H are defined before for including the effect of inertia, and λ and χ are suggested by Odar [15] for including the effect of curved motion. The rest of the terms stay the same as before; using the same nondimensionalization set, the dimensionless equations of motion are given below:

$$\left(\gamma+\frac{\lambda\Delta_A}{2}\right)\frac{dU_{\theta p}}{dt} = \mathrm{Fr}\mathrm{Re}_f(\gamma-1)\sin\theta + \gamma_M\frac{\mathrm{Re}_f}{12}C_{d\theta}(U_\theta - U_{\theta P})\,|U_\theta - U_{\theta p}| - \frac{2}{9}\gamma_p^2\left(\frac{1\partial P}{r\partial\theta}\right) - \chi\Delta_H\left(\sqrt{\frac{9}{2\pi}}\right)\sqrt{\gamma_M}\int_0^t \frac{\frac{d}{dt}(U_{\theta p})\,|_s}{\sqrt{t-s}}\,ds + \frac{2}{9}\gamma_R\gamma\mathrm{Re}_f f_1\left(\frac{W_\theta^2}{\bar{R}'}\frac{W_r x W_\theta}{\bar{R}}\right) \tag{25}$$

$$\left(\gamma+\frac{\lambda\Delta_A}{2}\right)\frac{dU_{rp}}{dt} = \mathrm{Fr}\mathrm{Re}_f(\gamma-1)\cos\theta + \gamma_M\frac{\mathrm{Re}_f}{12}C_{dr}(U_r - U_{rp})\,|U_r - U_{rp}| - \frac{2}{9}\gamma_p^2\left(\frac{\partial P}{\partial r}\right) - \chi\Delta_H\left(\sqrt{\frac{9}{2\pi}}\sqrt{\gamma_M}\int_0^t \frac{\frac{d}{dt}(U_{rp})\,|_s}{\sqrt{t-s}}\,ds + \frac{2}{9}\gamma_R\gamma\mathrm{Re}_f f_2\left(\frac{W_\theta^2}{\bar{R}}\frac{W_r x W_\theta}{\bar{R}}\right)\right. \tag{26}$$

$$C_{d\theta} = (3\mathrm{Re}_\theta^{0.72} + 24)/\mathrm{Re}_\theta$$

$$C_{dr} = (3\mathrm{Re}_r^{0.72} + 24)/\mathrm{Re}_r \tag{27}$$

The velocity profiles of the continuous phase, U_θ and U_r' and the pressure gradient terms are given by (20) and (21) also.

Solution Procedure

Equations (18–19) for low Re_r and Re_θ and equations (25–26) for intermediate and high Re_r and Re_θ must be solved with a proper initial condition to determine the particle trajectory. Due to the unsteady and irregular nature of the terms on the right hand side of the governing equations, an analytical solution is impossible according to the author's knowledge. Equations (18–19) or (25–26) were integrated through the fourth-order Runge-Kutta Method. A supplementary subroutine was developed and was incorporated with the main program to optimize the size of the time steps and also to keep track of the single step and accumulated errors in order to maintain a desired accuracy. Particle Reynolds numbers, Re_r and Re_θ, were calculated at the beginning of each time step to determine which equations among (18–19) and (25–26) should be used.

The Basset integral needs special attention because of the singular point at the upper integration limit. It is evaluated through the following formula [25].

$$\int_0^t \frac{\dot{U}\,|s}{\sqrt{t-s}}ds = \int_0^{n\Delta t}\frac{\dot{U}\,|s}{\sqrt{t-s}}ds = \frac{\Delta t}{6}\sum_{i=1}^{n-1}\left(\frac{\dot{U}_{i-1}}{\sqrt{n\Delta t-(i-1)\Delta t}} + \frac{2(\dot{U}_{i-1}+\dot{U}_i)}{\sqrt{n\Delta t-\left(i-\frac{1}{2}\right)\Delta t}} + \frac{\dot{U}_i}{\sqrt{n\Delta t-i\Delta t}}\right) + \frac{0.9\Delta t}{6}\left(\frac{\dot{U}_{n-1}}{\sqrt{\Delta t}} + \frac{2(\dot{U}_{n-1}+\dot{U}_n)}{\sqrt{0.55\Delta t}} + \frac{\dot{U}_n}{\sqrt{0.1\Delta t}}\right) + \frac{0.1\Delta t}{2}\left(\frac{8\sqrt{2}}{3}\frac{\dot{U}_n}{\sqrt{0.05\Delta t}} + \frac{4}{3}\frac{\dot{U}_n}{\sqrt{0.1\Delta t}}\right)$$

Model Application and Sample Calculations

The mathematical model developed in the previous section could be applied to predict the particle trajectories and the general trends of particle distribution inside a liquid droplet with internal circulatory motion. This information is considered as prerequisite for investigating other transport mechanisms associated with translating liquid droplets containing solid particles. Therefore, applications of this model could be found in chemical engineering processes, two-phase droplet flow, and spray droplet combustion. For example, in spray combustion, a promising technology is to mix finely-crushed coal with oil and use these coal-oil droplets in furnaces or boilers. Before we could study the heat-and mass-(evaporation) transfer and combustion characteristics of these coal-oil mixture droplets, the coal particle trajectories and general distribution patterns have to be understood. Sample calculations are provided here to illustrate the capability of the model and to extend a first attempt to investigate, theoretically, the motion of coal particles inside a light hydrocarbon droplet. It is noted that this model is limited to the condition that the coal particles do not severely affect the circulatory motion of the liquid fuel. Therefore, the model is not expected to work for heavy coal loading where droplets would actually consist of wet films surrounding coal particles and therefore the liquid circulation does not exist.

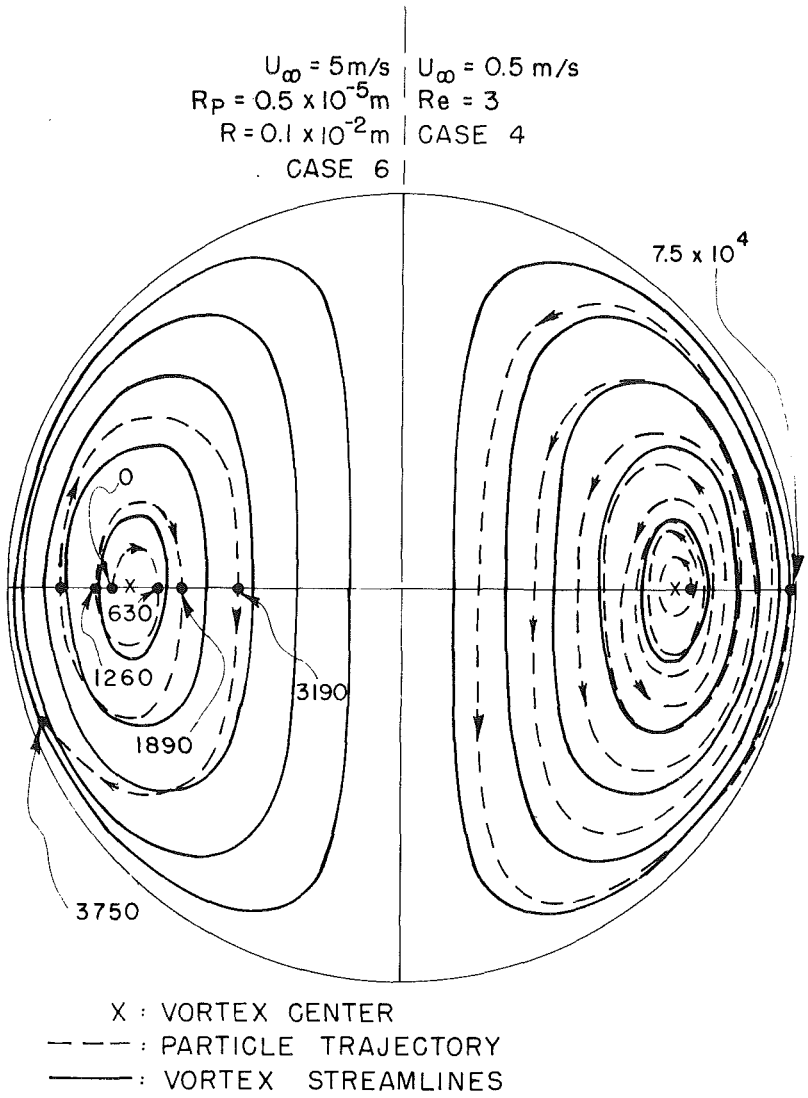

Fig. 3 The effects of U_∞ for low Reynolds number (right) and the effects of particle radius (left).

Table 3 Effects of droplet size, R

(Methanol droplet, $R_p = 0.5 \times 10^{-4}$m, $U_\infty = 5$ m/s)

Case	R	t_1'	t_2	t_3	
10	0.5×10^{-3}m	195	360	2.79×10^4	1 dim'less time = 3.53×10^{-5}s
11	0.1×10^{-2}m	360	730	8.9×10^4	1 dim'less time = 3.53×10^{-5}s
12	0.5×10^{-2}m	1425	7175	1.2×10^6	1 dim'less time = 3.53×10^{-5}s

For different sizes of droplets, the characteristic times of transport are at least two orders of magnitude smaller than the droplet life time.

A methanol droplet is adopted for the numerical calculations because its fluid mechanics properties, density and dynamic viscosity are very close to most oils like n-Hexane and n-Decane. A comparison between methanol and n-Hexane is also made for a typical case. The properties of the droplet are evaluated, based on the average value of droplet initial temperature (25°C) and droplet boiling point. The ambient is assumed to be air at 750°K. The range of the parameters are given below:

droplet relative velocity to hot gas, U_∞	$0.1 - 10$m/s
droplet radius, R	$5 \times 10^{-3} - 5 \times 10^{-4}$m
particle radius, R_p	$5 \times 10^{-6} - 2.5 \times 10^{-5}$m

Coal particle density is assumed 1386 kg/m^3. For most of the calculation, the particle void fraction is assumed 5 percent, the mixture viscosity, μ_M, is $1.139\mu_f$ (μ_f being actual droplet fluid dynamic viscosity) according to equation (9). A comparison is also made for particle void fraction of 10 percent.

Results and Discussion

Numerical solutions for coal particle trajectories inside a circulating light hydrocarbon droplet are presented in terms of droplet radius, particle radius, droplet relative velocity to hot gas, particle loading, and droplet material.

Before the presentation and the discussion of the results, it is helpful to clarify the relative importance of each term on the right hand side of the equations of motion. Generally, the drag force term is always the important term, because γ_M is

always greater than unity. Pressure gradient force is at least one order of magnitude smaller than drag force or Basset force if the droplet internal flow is Hill's vortex function (high Re and Re_f, if is noted that for the cases analyzed, Re is almost equal to Re_f) where $\partial p'/\partial x_i'$ is multiplied by Re_f $\gamma_R/100$, and the pressure gradient term is of second-order effect by Hadamard where $\partial p'/\partial x_i'$ is multiplied by γ_R^2 only, because Re_f is 0(100) and γ_R is $0(10^{-2})$. Basset force is also always an important term; as indicated above, γ_M is 0(1). The curvature force term is effective only for high Re_f conditions where the continuous phase is moving quite fast (U_∞ Large) and, therefore, induces larger curvature forces. The gravity force is usually small, but it could be important when the product Fr and Re_f is large (in other words, larger particle sizes and slower continuous phase flow). The influence of each force on the particle trajectory is explained next. The gravity force is trying to pull the particle downward because, in the current study, gravity is assumed to be parallel to the axis of symmetry and is pointing downward. The drag force is responsible for keeping the particle on the streamlines and is the main driving force for particle motion. As can be seen later, particles will stay almost right on the streamline if drag force is the sole dominant term. The pressure gradient force is always pointing to the concave side of the curved streamlines, or inward to the center of vortex. Basset force is generally opposite to pressure gradient force, it moves the particle toward the droplet surface. The centrifugal force is pointing outward if the particles are doing looping motion, while the coriolis force is tangent to the trajectory.

The Effects of U_∞. The effect of U_∞ is characterized by Re_f for cases with constant R_p and ν_f. In this section, R_p is kept at 0.1×10^{-4}m, R is 0.1×10^{-2}M, and ν_f is 0.63×10^{-6}m^2/s. The results are summarized in Table 1. For high-Re flow (cases 1, 2 and 3), the Basset force plus the curvature force are stronger than the pressure force, therefore, the particle is moving outward, toward the surface. Case 3 is plotted in the left semicircle of Fig. 1. Cases 2 and 1 are plotted in Fig. 2. It is apparent that as Re_f becomes larger, the Basset force and curvature forces become more effective and particles all follow the general looping motion due to drag force, but lesser loops are required for the particle to be transported from near the vortex center to the surface as Re_f increases. It takes the particle less than two loops for case 1, two loops for case 2, and three loops for case 3, to reach the surface. For all cases, the particles start at $r = 0.75$, $\theta = 90$ deg, which is very close to the vortex center ($r = 0.707$, $\theta = 90$ deg). Therefore, the time of transport, t_2, is almost the maximum time of transport. In other words, most of the particles in the same droplet will reach the surface sooner than that. The particle starting velocity is assumed to be zero. It was found that this starting velocity does not affect the time of transport and particle trajectories because the particles will be adjusted to the droplet internal flow almost immediately due to the drag force. The particle initial velocity will make a slight difference only when $\gamma_R = R_p/R$ is greater than 0.1, which is not of practical importance. The lifetime of a vaporizing droplet, a characteristic time relevant for comparison with other characteristic times, can be estimated by using empirical correlation [18] for a vaporizing droplet in a convective field, as follows:

$$t_3 = R^2/b(1+0.3\mathrm{Re}^{1/2}\mathrm{Pr}^{1/3})t_0, t_0 = (2/9)R_p^2/\nu_f \qquad (29)$$

where b is the evaporation constant and is 10^{-7}m^2/s, typically, Based on Table 1, the characteristic time of transport of particles, t_2, is at least two orders of magnitude smaller than characteristic droplet life time, t_3. Therefore, for high Re, most of the particles will settle near the surface before substantial vaporization of the droplet.

For cases 4 and 5, the low-Re flow, both the curvature forces and pressure gradient force are of secondary effect. Therefore, the Basset force and drag force are dominant. Case 4 is plotted in Fig. 3. The particle stays very close on the Hadamard streamline and moves toward the surface very slowly due to Basset force. In low-Re flow, particles generally move slowly and stay on the stramlines. Their characteristic time of transport is comparable to droplet life time. More uniform distribution of coal particles is expected for low-Re flow with concentration increasiong slightly toward the droplet surface. It is also clearly indicated by the results of Table 1 that each loop will take the particle approximately the same time of traveling, t_1', even though the total arc length for each loop is different. In all figures, the dimensionless time of travelling to the dot on the trajectory is indicated near the dot. This characteristic time of one loop motion can be stimated by the time for the Hill's streamline or Hadamard streamline to travel a loop. They are:

$$t_1 = \frac{(2+\pi)R}{(U_\infty/10)(2/9)(R_p^2/\nu_f)} \quad \text{for Hill's streamline} \qquad (30)$$

$$t_1 = \frac{(2+\pi)R}{[U_\infty/2(1+k)](2/9)(R_p^2/\nu_f)} \quad \text{for Hadamard's streamline} \qquad (31)$$

The Effects of Particle Size, R_p. The size of the coal particles appears in three dimensionless numbers, Fr, Re_f, and γ_R. Based on equation (17), gravitational force, pressure gradient force, and curvature force will be affected. The particle trajectories are plotted in Fig. 2 (left side) and Fig. 3 (left side). As the particle size increases, the particle will move down farther than its upward motion due to gravitational force. As mentioned previously, the Basset force and the curvature forces are responsible for the outward motion with respect to the vortex center. Particles of larger size, starting at the same location and with the same initial velocity, will move to the surface with less loops of motion due to higher Basset and curvature forces. Table 2 summarizes the effects of particle size.

The Effects of Droplet Size, R. The size of droplet is involved with γ_R only, therefore, pressure gradient force and curvature force will be affected if the droplet radius is the only variable. With decreasing droplet size, the pressure gradient and curvature forces are increasingly important, therefore, the particles in smaller droplets are making larger looping motions and moving toward the surface faster. Table 3 summarizes the droplet size effects.

The Effects of Coal Particle Loading. The effects of the coal particle loading is included through the mixture viscosity, μ_M. As suggested by Ishii and Zuber [10], the mixture viscosity model would work when the coal void fraction, α_d, is as high as 62 percent, but the current model is expected to be qualitatively valid for the coal particle loading of as high as 25 percent by volume, such that the particles do not severely alter the droplet fluid motion and the general circulatory pattern is maintained. It is noted that coal loading of higher than 30 percent might result in difficulties with atomization process and also complete burning of coal particles is hard to achieve. Three different loadings were investigated and Table 4 shows

Table 4 The effect of α_d

(Methanol droplet $R_p = 0.1 \times 10^{-4}$m, $R = 0.1 \times 10^{-2}$m, $U_\infty = 5$ m/s)

α_d	t_1'	t_2	t_3
5%	360	730	8.9×10^4
10%	405	1175	8.9×10^4
15%	460	1700	8.9×10^4

Table 5 The effects of droplet material

($R = 0.1 \times 10^{-2}$m, $R_p = 0.1 \times 10^{-4}$m, $U_\infty = 5$ m/s)

droplet material	ρ (kg/m^3)	ν_f (m^2/s)	t_1'	t_2	t_3
Methanol	762	6.31×10^{-7}	360	730	8.9×10^4,1 dim'less time = 3.53×10^{-5}s
n-Hexane	596	7.75×10^{-7}	445	920	8.9×10^4,1 dim'less time = 2.87×10^{-5}s

the comparison. More time is needed for the particles to move to the surface as the loading is increased because particles would experience higher resistence from other particles.

The Effects of Different Droplet Material. A run was made using a mixture of n-Hexane and coal particles. Table 5 provides the comparison. No significant differences were found between methanol and n-Hexane. Therefore, all results shown above can be applied to most oil droplets which have hydrodynamic properties similar to n-Hexane.

More plots particle trajectories for different droplet sizes, different particle loadings, and n-Hexane droplets are shown in [19].

The important results obtained may be summarized as follows:

For high droplet Reynolds numbers, particles most likely will accumulate near the droplet surface and form agglomerates before substantial evaporation of the droplet could take place, because the transport time is two orders of magnitude smaller than the droplet life time. For low droplet Reynolds numbers, particles will be evenly distributed with slightly higher particle density near the surface. These findings may offer an alternate explanation for the recent experimental results of Law et al., [4] and Miyasaka and Law [5]. They concluded that rapid internal circulation (high-droplet Reynolds numbers) would enhance coal particle agglomeration and slow internal motion enhances burning of coal particles and internal boiling due to heterogeneous nucleation. Miyasaka and Law [5] found that the agglomerates are hollow inside, which fits the pattern predicted in the sample calculations that particles will settle near the surface and form agglomerates for high droplet Reynolds numbers. They have used droplets of 700 μm in diameter in a free fall condition; these droplets carried Reynolds numbers of 200 or larger, which are definitely in the high-droplet Reynolds number regime.

Conclusions

Equations of motion for particles translating inside a circulating droplet were developed. Numerical solutions to these complicated differential-integral equations for the motion of coal particles inside a light hydrocarbon droplet were obtained using fourth-order Runge-Kutta methods with step size control according to desired accuracy. Coal particles generally make looping motions due to existing vortex streamlines. Particles generally move outward with respect to the vortex center. For high-droplet Reynolds numbers, particles most likely will accumulate near the droplet surface before substantial evaporation of the droplet, because the transport time is two orders of magnitude smaller than droplet lifetime. For low droplet Reynolds numbers, particles will be evenly distributed with slightly higher particle density near the surface.

Acknowledgment

The research work was supported by a Department of Energy Grant DE EG22-80PC30216.

References

1 Tavlarides, L. L., Coulaloglou, C. A., Zeitlin, M. A., Klinging, G. E. and Gal-Or, B., "Bubbles and Drops Phenomena," *Ind. and Eng. Chemistry*, Vol. 62, No. 11, 1970, pp. 6-27.

2 Harper, J. F., and Moore, D. W., "The Motion of a Spherical Liquid Drop at High Reynolds Number," *Journal of Fluid Mechanics*, Vol. 32, 1968, pp. 367-391.

3 Prakash, S., and Sirignano, W. A., "Liquid Fuel Droplet Heating With Internal Circulation," *Internal Journal of Heat and Mass Transfer*, Vol. 21, 1978, pp. 885-895.

4 Law, C. K., Law, H. K., and Lee, C. H., "Combustion Characteristics of Droplets of Coal/Oil and Coal/Oil/Water Mixtures," *Energy*, Vol. 4, 1979, pp. 329-339.

5 Miyasaka, K., and Law, C. K., "Combustion and Agglomeration of Coal-Oil Mixtures in Furnace Environment," ASME/AIChE Heat Transfer Conference, 1980, Paper No. 80-HT-124.

6 Odar, F., and Hamilton, W. S., "Forces on a Sphere Accelerating in a Viscous Fluid," *Journal of Fluid Mechanics*, Vol. 18, 1964, pp. 302-314.

7 Odar, F., "Forces on a Sphere Moving Steadily Along a Circular Path in a Viscous Fluid," ASME *Journal of Applied Mechanics*, Vol. 35, 1968, pp. 235-241.

8 Odar, F., "Unsteady Motion of a Sphere Along a Circular Path in a Viscous Fluid," ASME *Journal of Applied Mechanics*, Vol. 35, 1968, pp. 652-654.

9 Cliff, R., Grace, J. R., and Weber, M. E., *Bubbles, Drops, and Particles*, Academic Press, 1978.

10 Ishii, M., and Zuber, N., "Drag Coefficient and Relative Velocity in Bubbly, Droplet or Particulate Flows," *AIChE Journal*, Vol. 25, 1979, pp. 843-855.

11 Hadamard, J., "Movement Permanent Lent d'une sphers liquide et visqueuse dans une liquide visqueux," *C.R.Acad.Sci.*, Vol. 152, 1911, pp. 1735-1738.

12 Rybczynski, W., "On The Translating Motion of a Fluid Sphere in a Viscous Medium," *Bull. Int. Acad. Pol. Sci. Math. Natur.*, Ser.A, 1911, pp. 40-46.

13 Milne-Thomson, L. M., *Theoretical Hydrodynamics*, The MacMillan Company, New York, 5th ed., 1968, pp. 578-579.

14 Brignell, A. S., "Solute Extraction From an Internally Circulating Spherical Liquid Drop," *Internal Journal of Heat and Mass Transfer*, Vol. 18, 1975, pp. 61-68.

15 Basset, A. B., *A Treatise on Hydrodynamics*, Vol. 2, ch. 22, Deighton Bell, Cambridge, England, 1888.

16 Randolph, J. F., *Calculus and Analytical Geometry*, Wadsworth Publishing Company, 1961.

17 Berezin, I. S., and Zhidkov, N. P., *Computing Methods*, Addison-Wesley Publishing Company, 1965.

18 Ranz, W., and Marshall, W., "Evaporation from Drops," *Chem. Engr. Prog.*, Vol. 48, 1952, pp. 141-146 and pp. 173-180.

19 Chung, J. N., "The Motion of Coal Particles Inside an Oil Droplet," ASME Paper No. 81-WA/HT-45, 1981.

Heat Transfer From a Buoyant Plume to an Unconfined Ceiling

L. Y. Cooper
Center for Fire Research,
National Bureau of Standards,
Washington, D.C. 20234
Assoc. Mem. ASME

The heat transfer to ceilings during enclosure fires is related to the heat transfer to unconfined ceiling surfaces from buoyant plume driven ceiling jets. This paper briefly discusses this relationship, and then focuses attention on the unconfined ceiling problem. Previously published theoretical and experimental studies dealing with interactions of unheated free jets and solid surfaces, as well as literature which focuses directly on fire plume-unconfined ceiling interactions are brought to bear on the problem. A critical review of this literature results in easily applicable formulae for estimating the heat transfer in question.

Introduction

For a fire in an enclosure an estimate of the time and position-dependent convective heat transfer to the ceiling surface is key to the modeling of gas temperatures and ceiling surface temperatures. Several analytic and experimental studies have attacked aspects of the problem of obtaining such estimates. However, except for some experimental results of Zukoski and Kubota [1] and You and Faeth [2], all of these studies have addressed the unconfined ceiling problem. In terms of actual enclosure fires where ceiling surfaces are inherently confined, one anticipates that the results of such unconfined ceiling studies would be relevant at relatively early times subsequent to the ignition of the fire. At such times, an upper hot gas layer, which will eventually start to fill the enclosure, has not yet developed to such an extent as to significantly modify the initial fire plume-ceiling jet gas dynamics and heat transfer. Figure 1 depicts the phenomena in question near the fire plume during this early time interval. For a given fire energy release rate, Q, and fire-to-ceiling distance, H, it is evident that the more expansive the ceiling surface (enclosure floor area) the longer is this early time interval.

In due course the upper layer starts to grow in depth, and the phenomena governing the heat transfer become more complex. These phenomena are depicted in Fig. 2. Note that a description of the scenario of Fig. 2 must include two parameters which do not appear in Fig. 1. These are: the thickness of the upper layer, Δ (or the distance of the interface above the fire, $Z = H - \Delta$), and the average absolute temperature of the upper layer, T_{up}. In addition to Q, H, absolute surface temperatures, T_s, and absolute ambient temperatures, T_{amb}, which may be adequate in formulating the unconfined ceiling problem, the parameters, Δ and T_{up}, must also be accounted for in any general theory for estimating the ceiling heat transfer during enclosure fires. Cooper [3] has outlined such a theory for estimating convective heat transfer in the general confined ceiling scenario. Application of this theory requires formulae for estimating heat transfer to an unconfined ceiling.

The above discussion points to the need of working formulae for estimating the convective heat trasnfer, q, from buoyant plume driven ceiling jets to unconfined ceiling surfaces. It is the purpose of this paper to critically review relevant literature and to develop such formulae.

The development of working formulae for q will be in two parts. One of these parts will deal with the stagnation zone immediately surrounding the plume axis-ceiling surface point of impingement, while the other part, the first in the order of discussion, will deal with the region outside the stagnation zone. Following [2], the stagnation zone will be defined in this paper by the range of radius, r_{stag}, which satisfies

$$0 \le r_{stag}/H \le 0.2 \tag{1}$$

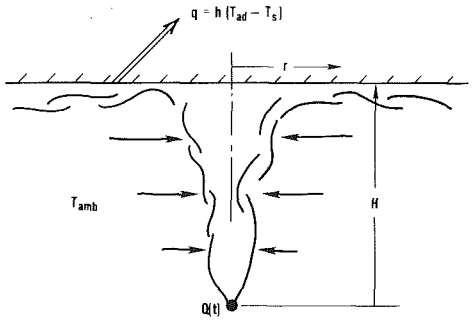

Fig. 1 Heat transfer to an unconfined ceiling

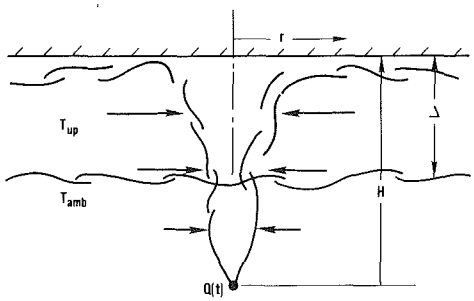

Fig. 2 Heat transfer to a confined ceiling with an upper layer

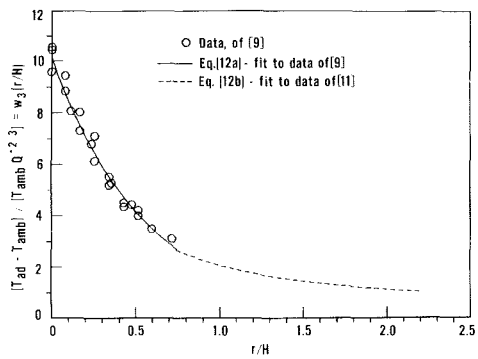

Fig. 3 Correlation for $(T_{ad} - T_{amb})/(T_{amb}Q^{*2/3}) = w_3(r/H)$ per equations (12) and plot of data from [9]

Contributed by the Heat Transfer Division and presented at the 20th ASME/AIChE National Heat Transfer Conference, Milwaukee, Wisconsin, August 2–5, 1981. Manuscript received by the Heat Transfer Division October 7, 1981. Paper No. 81-HT-7.

Outside of the Stagnation Zone

A Heat-Transfer Coefficient Based on T_{max}. Referring to Fig. 1, the heat transfer to the ceiling can be represented by

$$q = h_1 (T_{max} - T_s) \tag{2}$$

where T_{max} is the local (i.e., at a given radial position) maximum absolute temperature of the ceiling jet, and h_1 is the heat-transfer coefficient based on the $T_{max} - T_s$ temperature difference.

Outside of the stagnation zone and for cases where the friction factor[1], f, is uniform in radius and of a generally realistic magnitude of the order of 0.01, Alpert [4, 5] invoked Reynold's analogy for turbulent boundary flows essentially in the form

$$h_1 = \rho_{amb} C_p \mathrm{Pr}^{-2/3} V_{max} f \tag{3}$$

Here ρ_{amb} is the ambient density, C_p is the specific heat at constant pressure, Pr is the Prandtl number and V_{max} is the local maximum velocity in the ceiling jet. A technique for computing h_1 by means of an integral method is developed in [4, 5]. (In these constant f calculations the actual computation was for V_{max} which, by virtue of the constant f assumption and Reynold's analogy, is proportional to h_1.) The implications of the results of the computations presented in [4] are that for $r/H < 2$, and outside of the stagnation zone, h_1 (i.e., V_{max}) is relatively insensitive to likely variations in normalized ceiling jet temperature profile and velocity profile and to variations in T_s within the entire range $T_{amb} \leq T_s \leq T_{max}$. Note that under the usual condition of a ceiling surface material initially at ambient temperature (or at least relatively cool compared to the maximum temperatures in the impinging buoyant plume) and relatively well-insulated from above, and in the absence of significant radial conduction, the condition $T_s \to T_{max}$, which would develop with increasing time, corresponds to that of an adiabatic ceiling (i.e., when $T_s \to t_{max}$, then $T_{max} \to T_{ad}$). After an initial transient time interval such an adiabatic ceiling condition would be closely approximated in the plume driven ceiling jet experiments of [1] to be referred to below.

The studies of [4, 5] were for heated turbulent ceiling jet flows. As will be seen, the work of Poreh, Tsuei, and Cermak [6] on flows in unheated turbulent wall jets[2] as well as the results of other wall jet studies can bring significant insight to the heated ceiling jet problem presently under discussion. In particular, one is led to anticipate an equivalence between these two types of boundary layer flows and the heat transfer from them. This is on account of the fact that buoyancy effects in the case of turbulent plume generated ceiling jet flows have been shown in [4, 5] to play a relatively minor role in the most interesting r/H range of small to moderate values; i.e., independent of the size of Q and H, Richardson numbers of the actual ceiling jet are small.

The experimental unheated wall jet results of [6] indicate that for smooth surfaces the friction factor varies only slightly with radius and is proportional to $(\sqrt{K}/\nu)^{-0.3} = \mathrm{Re}_P^{-0.3}$ where K is the kinematic momentum flux of the unheated impinging free jet (invariant along the jet axis) and Re_P is a characteristic Reynolds number of this jet. In a direct analogy to the present problem, the results of [6] specifically indicate that when an unheated turbulent free air jet impinges from below on a smooth, ambient temperature ceiling surface the friction factor of the resulting unheated ceiling jet outside of the stagnation zone would be given by

$$f = 0.172\ \mathrm{Re}_P^{-0.3} (r/b)^{0.1} \tag{4}$$

where b is the distance of the effective point source of the jet below the ceiling, and r is the radial distance along the ceiling from the point of impingement. (The experiments of [6] actually involved downward directed jets.) Reference [6] also provides the result

$$V_{max}/(\sqrt{K}/b) = 1.32(r/b)^{-1.1} \tag{5}$$

If an equivalence is now drawn between the momentum and mass fluxes of the free jet and of a buoyant plume at the position of their respective impingement with the ceiling surface, then from a calculation procedure presented in the Appendix, equations (4) and (5) become

[1] The friction factor for the ceiling jet is defined as

$$f = \tau_w / (\rho_{amb} V_{max}^2)$$

where τ_w is the local shear stress at the surface-jet boundary and where V_{max} is the local maximum of the ceiling jet velocity profile.

[2] The wall jet is analagous to the present heated ceiling jet and is formed when an unheated free jet impinges on a solid surface.

Nomenclature

b = distance of jet source from wall
C = a factor in equation (19)
C_p = specific heat
f = friction factor
g = acceleration of gravity
H = distance between fire and ceiling
h = a heat-transfer coefficient equation, (10)
h_1 = a heat-transfer coefficient equation, (2)
$\tilde{h}$ = a characteristic heat-transfer coefficient, $\rho_{amb} C_p g^{1/2} H^{1/2} Q^{*1/3}$
K = kinematic momentum flux of jet
k = thermal conductivity
Nu_5 = Nusselt number as per [8], equation (16)
Pr = Prandtl number
Q = energy release rate of fire
Q^* = dimensionless energy release rate, equation (6b)
q = rate of heat transfer equations (2) and (10)
Re_H = Reynolds number, equation (6a)
Re_P = Reynolds number as per [6]
Ri = Richardson number
r = radial distance from impingement point
r_{stag} = r at edge of stagnation zone
r_5 = r where velocity in plume/jet is $w_c/2$
T_{ad} = ceiling surface temperature for an adiabatic ceiling
T_{amb} = ambient temperature
T_{max} = local maximum ceiling jet temperature
T_{up} = upper layer temperature
T_s = ceiling surface temperature
V_{max} = local maximum ceiling jet velocity
$\tilde{V}$ = characteristic velocity of ceiling jet, $g^{1/2} H^{1/2} Q^{*1/2}$
w_1, w_2, w_3, w_4 = dimensionless functions of r/H
w_c = centerline velocity of plume/jet in plane of impingement
Z = distance between fire and interface
Δ = thickness of layer
λ_r = fraction of Q radiated from combustion zone
ν = kinematic viscosity
τ_w = shear stress at ceiling surface

Subscripts

BP = buoyant plume
FJ = force jet

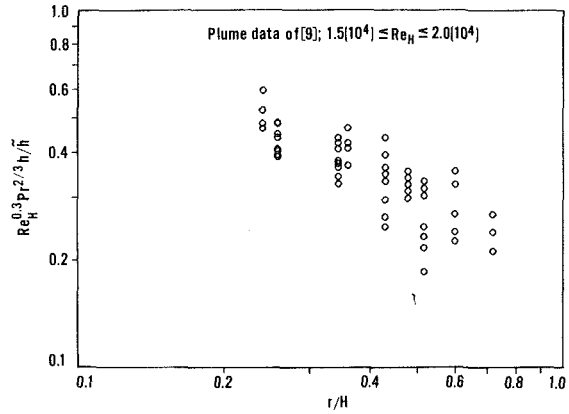

Fig. 4 *h* data of [9] outside of stagnation zone plotted per correlation of equation (14)

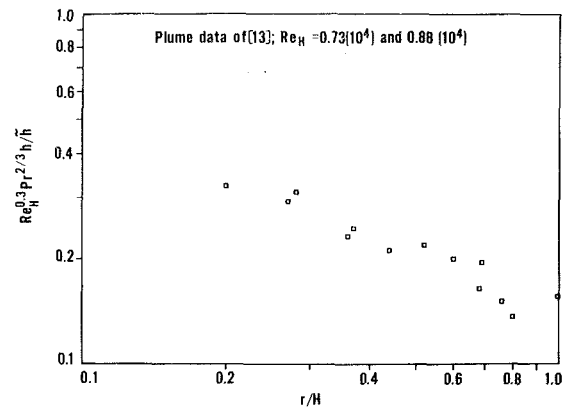

Fig. 5 *h* data of [2, 12, 13] (flame heights .08*H* and .10*H*) outside of stagnation zone plotted per correlation of equation (14)

$$f = 0.200 \mathrm{Re}_H^{0.3} (r/H)^{-0.1} \tag{4'}$$

$$V_{\max}/\tilde{V} = V_{\max}/(g^{1/2}H^{1/2}Q^{*1/3}) = 0.853(r/H)^{-1.1} \tag{5'}$$

where

$$\mathrm{Re}_H = \tilde{V}H/\nu = g^{1/2}H^{3/2}Q^{*1/3}/\nu \tag{6a}$$

$$Q^* = (1-\lambda_r)Q/(\rho_{\mathrm{amb}} C_p T_{\mathrm{amb}} g^{1/2} H^{5/2}) \tag{6b}$$

and where these correlations were obtained in [6] for equivalent values of r/H and Re_H in the range $0.2 \le r/H \le 4.0$ and $0.8(10^5) < \mathrm{Re}_H < 6.0(10^5)$. In equations (6*a*) and (6*b*), ν is a characteristic kinematic viscosity of the ceiling jet, and g is the acceleration of gravity. In equation (6*b*), λ_r is the fraction of Q which is lost by radiation from the fire's combustion zone and from the plume itself. Thus, $(1 - \lambda_r)Q$ is the effective portion of Q which actually drives the plume's upward convection.

Having obtained the above results for f and $V_{\max}$, it is not immediately obvious to what extent they are applicable to the present heated ceiling jet problem. For example, for a given mass and momentum flux at impingement the buoyancy of the heated gases in the buoyant plume driven ceiling jet would likely lead to a thinner ceiling jet with a larger V_{max} and possibly a higher friction factor than would be estimated in equations (4′) and (5′).

In [5] the constant f-analysis for the heated ceiling jet is extended in a manner as to take account of a friction factor which varies with radius. Limited results of this analysis are presented which verify a weak dependence of f on r/H consistent with the above $(r/H)^{-0.1}$ proportionality of [6]. With regard to the dependence of f on Re_H, a -0.24 rather than a -0.3 exponent in equation (4′) can be extracted from the results of some of the limited number of variable-f computer calculations presented in [5]. Also, Rosenbaum and Donaldson [7] perform an integral analysis of the heat transfer from a heated wall to an unheated wall jet and obtain -0.2 for the value of this exponent. It is noteworthy that the variable f- analyses of [4], [5], and [7] assume zero turbulent shear stress at local positions of maximum ceiling jet velocity. This is in contrast to the data acquired during detailed probings of the wall jet profiles, carried out in the experiments of [6], which indicate that this assumption is invalid. Finally, Donaldson, Snedeker, and Margolis [8] acquire data for the heat transfer between an unheated wall jet and an elevated temperature wall. Consistent with the results of [7], they plot their data for the heat-transfer coefficient in a manner consistent with f being proportional to $\mathrm{Re}_H^{-0.2}$, although, as will be discussed below, a plot based on a $\mathrm{Re}_H^{-0.3}$ proportionality would have correlated their data in a no less satisfactory manner. All of the above suggests that the equation (4′) result $f \sim \mathrm{Re}_H^{-0.3}$, for unheated wall jets should be applied to heated, buoyancy driven ceiling jets until substantial evidence suggesting likely deficiencies in this result can be brought to bear.

In the case of heated ceiling jets, there are no apparent data to substantiate the 0.200 constant of equation (4′). Yet, with the above suggestions that the Re_H and r/H dependence of f is unchanged from the unheated jet case, any anticipated increase of f in the present buoyancy driven ceiling jet problem would have to be accounted for in this remaining factor. In this vein, it is consistent with the ideas presented in [5] that the factor 0.200 is the unheated wall jet limit of a factor which is dependent on the characteristic Richardson number, Ri, (gravitational stability) of the heated ceiling jet. (For the case of a purely buoyant plume driven ceiling jet, reference [5] estimates a universal Ri, based on a characteristic ceiling jet thickness, density defect and velocity, to be approximately 0.024 at the position where the flow exists the stagnation zone.) This dependence is assumed here to be rather weak, and the 0.200 constant is assumed to hold.

Consistent with the above three paragraphs, equation (4′) for f will be assumed to maintain its validity for buoyant plume driven ceiling jets in the range $0.2 \le r/H \le 4.0$.

With regard to the applicability of the equation (5′) result for $V_{\max}$ to the heated ceiling jet problem, there is a question as to a preferable value for the r/H exponent. Results of calculations of [4] suggest (for a Gaussian velocity profile) the approximation

$$V_{\max}/\tilde{V} = 1.06\sqrt{2}(r/H)^{-.691} \tag{7}$$

Experimental data catalogued in [4] on direct velocity measurements in both large and small scale experiments do not support a preference for -0.691 over the -1.1 exponent value of equation (5′). Indeed, the estimate of equation (7) does not appear to provide any better of a correlation of the data plotted in Fig. 12 of [4] and Fig. 4 of [5] than does that of equation (5′). Nevertheless, at least up to $r/H = 2$ there is strong experimental support for the main contention of [4] regarding the variation of $V_{\max}$, viz.,

$$V_{\max}/\tilde{V} = w_1(r/H) \tag{8}$$

where w_1 is simply some function of r/H.
Using equations (4′) and (8) in equation (3) results in

$$h_1/\tilde{h} = h_1/(\rho_{\mathrm{amb}} C_P g^{1/2} H^{1/2} Q^{*1/3}) = \mathrm{Pr}^{-2/3} \mathrm{Re}_H^{-0.3} w_2(r/H) \tag{9}$$

In the work of [4], the value of $\sqrt{2}h_1$ was measured in two small scale experiments in air whose values of $\mathrm{Re}_H^{-0.3}$ differ by 6 percent. The results are consistent with equation (9) in that the measured values of w_2 do seem to correlate on a w_2, r/H plot.

A Heat-Transfer Coefficient Based on T_{ad}. In a series of small scale, buoyant plume driven ceiling jet experiments,

where radiation effects were reported to be negligible and where λ_r will be approximated by $\lambda_r = 0$, Veldman, Kubota, and Zukoski [9] acquire data for a heat-transfer coefficient, h, based on the temperature difference $T_{ad} - T_s$. Thus

$$q = h(T_{ad} - T_s) \tag{10}$$

Referring to equation (2), note that h appears to theoretically correspond to h_1 when $T_{max} \to T_{ad}$, i.e., late in time when the adiabatic condition corresponding to $T_s \to T_{max}$ is achieved. Also, where the ceiling jet temperature profile has a basic Gaussian shape, except for a sublayer of negligible thickness with $T_s = T_{amb}$, it is again possible for h to correspond to h_1. In general, however, h is different from h_1.

If a simple representation for h could be obtained, then the formulation of equation (10) has a distinct advantage over that of equation (2). This is on account of the fact that T_{ad} is a property only of Q, H, and the ambient conditions (i.e., T_{ad} is property of the characteristics of the plume immediately prior to impingement). In particular, T_{ad} is independent of the ceiling surface material properties or temperature and is independent of time. Such is not the case for T_{max}, which would have a relatively strong dependence on the time-varying, surface-material-dependent surface temperature (e.g., see Fig. 7 of [9]).

Regarding an estimate for the T_{ad} of equation (10), Heskestad [10] has shown that the dependence of $T_{ad} - T_{amb}$ on r/H is of the general form

$$(T_{ad} - T_{amb})/(T_{amb} Q^{*2/3}) = w_3(r/H) \tag{11}$$

The following estimate for w_3 was constructed by approximating the $T_{ad} - T_{amb}$ data presented (in curve form) by Thomas [11] in the range $0.75 < r/H < 2.2$, and by obtaining a least-squares curve fit of $T_{ad} - T_{amb}$ data points presented in [9] in the range $0 \le r/h \le 0.75$

$$w_3(r/H) = \begin{cases} 10.22\exp(-1.77\ r/H), & 0 \le r/H \le 0.75 \quad (12a) \\ 2.10(r/H)^{-0.88}, & 0.75 \le r/H \quad (12b) \end{cases}$$

w_3 of equations (12a) and (12b) is plotted in Fig. 3 together with the data points of [9]. In the experiments of [11], the published data does not lend itself to an estimate for $(1 - \lambda_r)Q$. The r/H dependence of $T_{ad} - T_{amb}$ presented in [11] in the range $r/H \ge 0.75$ was therefore scaled according to equation (11) in a manner as to match equation (12a) at $r/H = 0.75$. This resulted in equation (12b).

The h data acquired in [9] are plotted there in the form

$$h/\tilde{h} = w_4(r/H) \tag{13}$$

In the interest of generalizing these small scale results, it is reasonable to expect that, as in the case of h_1, Reynold's analogy can be applied to yield a result, analogous to equation (9), that h is proportional to $\mathrm{Re}_H^{-0.3}\mathrm{Pr}^{-2/3}$. Accordingly, outside of the stagnation zone the data of [9] are replotted here in Fig. 4 in the form

$$h/\tilde{h} = \mathrm{Re}_H^{-0.3}\mathrm{Pr}^{-2/3} w(r/H) \tag{14}$$

where Pr was taken to be 0.7 and Re_H was computed from the definition of equation (6a). The equation (14) correlation is a key result of this work.

The h data of [9] were acquired while time varying values of T_s deviated significantly from both T_∞ and T_{max}. Yet, even under experimental conditions which include large T_s variations, the Fig. 4 plot of this data is consistent to within bounds of engineering accuracy with the simple formulation of equation (10) and the h correlation of equation (14).

The experimental conditions of [9] included the relatively small Re_H variation $1.5\ (10^4) < \mathrm{Re}_H < 2.0\ (10^4)$. The values of $\mathrm{Re}_H^{-0.3}$ for these tests deviated less than 6 percent from an average value of 18.8. Accordingly, the Fig. 4 plot of the h data of [9] does not "test" the $\mathrm{Re}_H^{-0.3}$ part of the equation (14) correlation. Fortunately, there are other data that can be used to confirm the general utility of equation (14) in this regard.

You and Faeth [2, 12, 13] acquired data on heat transfer to unconfined ceilings from impinging fire generated buoyant plumes. Test conditions included the constraint $T_s = T_{amb}$. The tests involved both premixed and diffusion flames with unconfined flame heights varying from 0.08 H to 6.7 H, where H was of the order of 1 m. Except for those tests were flame heights are small fraction of H, radiation is expected to play a significant role both in the heat transfer to the ceiling surface and in the heat transfer from the combustion zone itself [i.e., λ_r of equation (6b) is both unknown and non-negligible]. For the purpose of the present work only data from the "point source-like" tests involving flame heights $\le$ 0.10 H will be considered for correlation. As was the case for the tests of [9], radiation effects under such conditions can be neglected, and λ_r will be taken to be zero.

Since $T_s = T_{amb}$, it can be shown that $H^2 q/Q$ and $\mathrm{Ra}^{1/3}$ of [2, 12, 13] are identical to $w_3(r/H)h/\tilde{h}$ and Re_H, respectively when $(1 - \lambda_r) \approx 1$. using these identities the data of [13] for two tests with flame heights of .08 H and .10 H are plotted in Fig. 5 according to the correlation of equation (14) and the w_3 estimate of equations (12a) and (12b). These two tests had equivalent Re_H values of 0.88 (10^4) and 0.73 (10^4), respectively.

Data on the heat transfer from heated constant temperature walls to unheated free jet driven wall jets are presented in [8]. Just as the previously discussed wall jet flow measurements of [6] brought insight to the flow characteristics of plume generated ceiling jets, so the wall jet heat transfer measurements of [8] can be correlated with the plume driven heat-transfer data of [9] and [13]. In order to do so a relationship must be drawn between the measured properties of a free jet of [8] and the properties of its equivalent buoyant plume at their respective points of impingement. Such an equivalence is developed in the Appendix and it leads to the following relationships

$$r_5 = 0.109H; \mathrm{Re}_5 \equiv w_c r_5/\nu = 0.422\mathrm{Re}_H \tag{15}$$

where, in the notation of [8] and in the plane of impingement, w_c is the measured centerline axial velocity of the free jet (in the absence of the wall), and r_5 is the radial distance where the measured axial velocity drops to $w_c/2$.

Continuing to follow the formulation of equation (10) the Appendix also develops the following relationship between the heat-transfer measurements of [8] and the $h/\tilde{h}$ of this work

$$\mathrm{Nu}_5 = 0.109\mathrm{Pr}\mathrm{Re}_H h/\tilde{h} \tag{16}$$

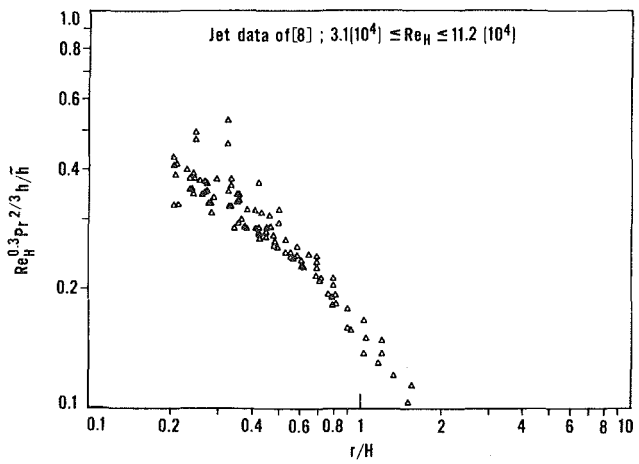

Fig. 6 h data of [8] outside of stagnation zone plotted per correlation of equation 14

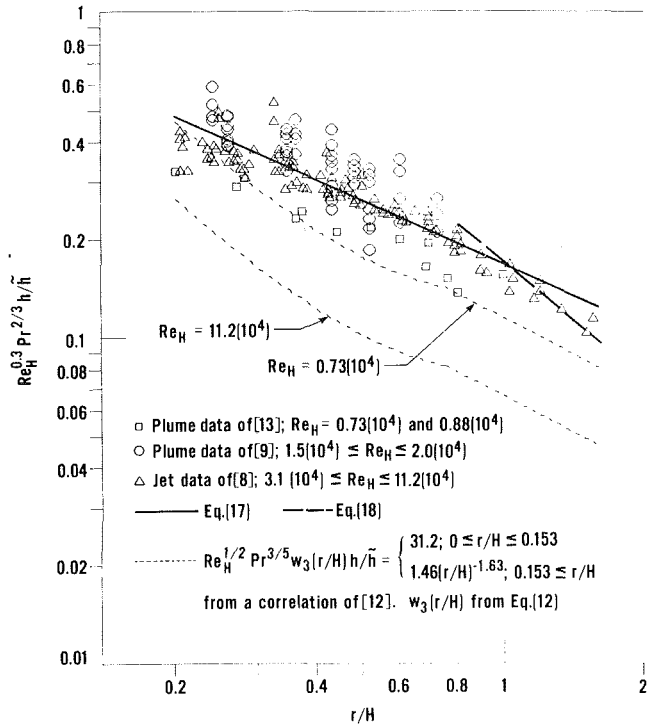

Fig. 7 Replot of all Fig. 4-6 data, recommended *h* estimates of equations (17) and (18), and *h* estimates from [12]

where, in the notation of [8], Nu_5 is a dimensionless heat-transfer coefficient (a Nusselt number).

All of the heat-transfer data of [8], plotted there in the form $Nu_5/Re_5^{0.8} = f(r/r_5)$, are replotted here in Figure 6 according to the correlation of equation (14) and the relationships of equations (15) and (16). These data are the result of thirteen separate tests whose equivalent Re_H values varied in the range $3.08\,(10^4) \le Re_H \le 11.2\,(10^4)$.

All of the data plotted in Figs. 4-6 are combined in the plot of Fig. 7. A least squares curve fit of this data results in the following estimate for *h* outside of the stagnation zone

$$h/\tilde{h} = 0.168 Re_H^{-0.3} Pr^{-2/3} (r/H)^{-0.65} \qquad (17)$$

The largest r/H value of the data is 1.6. Beyond this r/H value, no data for *h* are available. However, for large r/H it may be reasonable to use the results of equations (4′) and (5′) together with the equation (3) version of Reynold's analogy where *h* replaces h_1. Taken together these three equations yield the result

$$h/\tilde{h} = 0.171 Re_H^{-0.3} Pr^{-2/3} (r/H)^{-1.2} \qquad (18)$$

which matches the *h* of equation (17) at $r/H = 1.03$. The *h* estimates of equations (17) and (18) are plotted in Fig. 7. Estimates for *h* which were generated from a H^2q/Q correlation in [12] are also included in Fig. 7.

As mentioned earlier, it has been estimated in [5] that the ceiling jet leaves the stagnation zone in a "weakly stratified" state with a Richardson number, Ri, approximately equal to 0.024. However, analytic results of [4, 5] also indicate that Ri grows to the order of r/H as r/H grows to the order of 1. Thus, although the effects of stable stratification (e.g., buoyant plume driven ceiling jets versus unheated free jet driven ceiling jets) appear to play an insignificant role on the flow and, ultimately, on *h* from the stagnation zone to, say, $r/H = 2.$, these effects may become more pronounced for larger values of r/H. If such is the case, then at such r/H values, equation (18), which does not account for buoyancy effects in the ceiling jet, may be inadequate. This potential shortcoming of equation (18) is not likely to have any significant practical effect for two reasons. First, in the case

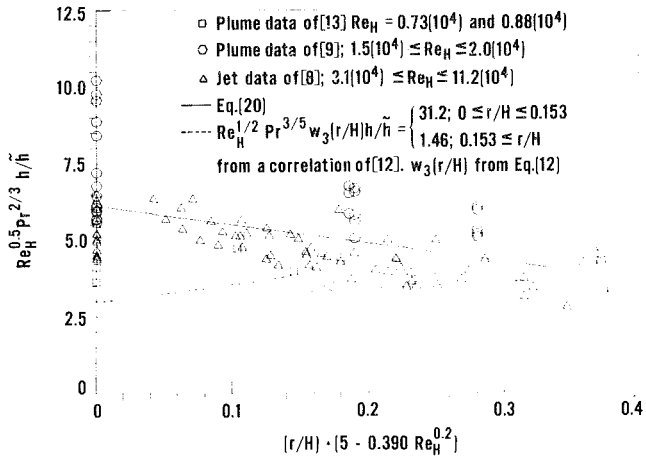

Fig. 8 Plot of *h* data of [2, 8, 9, 12, 13] within stagnation zone, recommended *h* estimates of equation (20), and *h* estimates from [12]

where room ceiling surfaces are expansive (i.e., larger r/H), the total rate of heat transfer to the ceiling in the far field [where the use of equation (18) becomes questionable] will likely be small compared to the total rate of heat transfer in the near field. Second, in the case of rooms where maximum values of r/H are moderate the question of the validity of equation (18) for large r/H is academic.

Equations (17) and (18) will form the basis for a recommended estimate for *h* outside of the stagnation zone.

Within the Stagnation Zone

Based on reviews of the literature, the following form for *h* at the stagnation point is recommended in [2] and [8]

$$h(r/H=0)/\tilde{h} = CPr^{-2/3} Re_H^{1/2} \qquad (19)$$

where *C* is a factor which accounts for the effect of the turbulence level in the impinging jet. This factor can vary by a factor of about 2 but tends toward an asymptotic (high) value in the case of impingement points well within the fully developed turbulent jet/plume region [8]. As is the case in [2], *C* will be taken here to be a constant. The exponent of Pr in equation (19) has been taken to be $-2/3$ instead of the $-3/5$ value in [2] or the -1 value in [8].

In the stagnation zone, *h* will be approximated as a linear function of r/H in the stagnation zone. Further, *h* is required to have the form of equation (19) at $r/H = 0$ and to match the *h* of equation (17) at the outer edge of the stagnation zone, $r/H = 0.2$. With these constraints and within the stagnation zone, a least squares fit of all the data of [8] and [9] as well as the low flame height data of [13] results in the following estimate for *h*

$$h/\tilde{h} = 6.11 Pr^{-2/3} Re_H^{1/2} [1 - (5.0 - 0.390 Re_H^{0.2}) r/H] \qquad (20)$$

A plot of all of this data together with the above correlation is presented in Fig. 8. Estimates for *h* obtained from a correlation in [12] are also included in this figure. Note that when $5.0 - 0.390 Re_H^{0.2} < 0$, i.e., $Re_H > 3.5(10^5)$, the correlation of equation (20) predicts a heat-transfer coefficient increasing with *r* within the stagnation zone. This effect, which is consistent with [8], can be explained by the fact that *h* tends to be proportional to $Re_H^{1/2}$ and $Re_H^{0.3}$ at the stagnation point and outside of the stagnation zone, respectively. Thus, at some large enough value of Re_H and beyond, the stagnation point heat transfer is expected to be relatively small compared to the heat transfer at the edge of the stagnation zone.

Recommended Procedure for Estimating the Heat Transfer to Unconfined Ceilings

In view of the results of the last two sections the following

procedure is recommended for estimating the heat transfer to unconfined ceilings:

(*a*) Estimate T_{ad} by using equations (11) and (12)
(*b*) Estimate h according to:
  (*i*) stagnation zone: $0 \le r/H \le 0.2$, use equation (20)
  (*ii*) outside stagnation zone: $0.2 < r/H \le 1.03$, use equation (17); $1.03 < r/H$, use equation (18)
(*c*) Compute q from equation (10) by using the known surface temperature distribution

References

1 Zukoski, E. E., and Kubota, T., "An Experimental Investigation of the Heat Transfer From a Buoyant Gas Plume to a Horizontal Ceiling—Part 2: Effects of Ceiling Layer," Cal. Institute of Technology, report prepared for NBS/CFR, NBS-GRC-77-98, 1975.

2 You, H-Z., and Faeth, G. M., "Ceiling Heat Transfer During Fire Plume and Fire Impingement," *Fire and Materials*, Vol. 3, No. 3, 1979, pp. 140-147.

3 Cooper, L. Y., "Convective Heat Transfer to Ceilings Above Enclosure Fires," 19th International Symposium on Combustion, Haifa, 1982.

4 Alpert, R. L., "Fire Induced Turbulent Ceiling-Jet," Factory Mutual Research Report FMRC Serial No. 19722-2, May 1971.

5 Alpert, R. L., "Turbulent Ceiling—Jet Induced by Large-Scale Fires," *Combustion Science and Technology*, Vol. 11, 1975, pp. 197-213.

6 Poreh, M., Tsuei, Y. G., and Cermak, J. E., "Investigation of a Turbulent Radial Wall Jet," ASME *Journal of Applied Mechanics*, June 1967, pp. 457-463.

7 Rosenbaum, H., and Donaldson, C. DuP., "An Analysis of Jet Impingement Heat Transfer," Aero. Res. Associates of Princeton, Inc., Rep. 101, 1967.

8 Donaldson, C. DuP., Snedeker, R. S., and Margolis, D. P., "A Study of Free Jet Impingement—Part 2: Free Jet Turbulent Structure and Impingement Heat Transfer," *Journal of Fluid Mechanics*, Vol. 45, Part 3, 1971, pp. 477-512.

9 Veldman, C. C., Kubota, T., and Zukoski, E. E., "An Experimental Investigation of the Heat Transfer From a Buoyant Gas Plume to a Horizontal Ceiling—Part 1: Unobstructed Ceiling," Cal. Institute of Technology, report prepared for NBS/CFR, NBS-GCR-77-97, 1975.

10 Heskestad, G., "Similarity Relations for the Initial Convective Flow Generated by Fire," ASME Winter Annual Meeting, Paper No. 72-WA/HT-17, Nov., 1972.

11 Thomas, P. H., "The Distribution of Temperature and Velocity Due to Fires Beneath Ceilings," F. R. Note 141, Fire Research Station, Boreham Wood, Herts, England, 1955.

12 You, H-Z., and Faeth, G. M., "An Investigation of Fire Impingement on a Horizontal Ceiling," Pennsylvania State University, report prepared for NBS/CFR Grant 7-9020, Oct. 1979.

13 You, H-Z., and Faeth, G. M., private communication.

14 Ricou, F. P., and Spalding, D. B., "Measurements of Entrainment by Axisymmetrical Turbulent Jets," *Journal of Fluid Mechanics*, Vol. 11, 1961, pp. 21-32.

15 Zukoski, E. E., Kubota, T., and Cetegen, B., "Entrainment in Fire Plumes," *Fire Safety Journal*, Vol. 3, 1980/81, pp. 107-121.

APPENDIX

Some Equivalences Between Free Jet Driven Wall Jets and Buoyant Plume Driven Ceiling Jets

From the Work of Poreh et al. [6]. In experiments on free jet driven wall jets, the work of [6] measures the momentum flux, $\rho_\infty K_{FJ}(x=0)$, at the orifice source of unheated free jets. This momentum flux is conserved at every position, x, along the jet axis. Thus

$$\rho_{amb} K_{FJ}(x) = 2\pi \int_0^\infty \rho(r,x) u^2(r,x) r dr = \rho_{amb} K = \text{constant} = \rho_{amb} K_{FJ}(x=0) \quad \text{(A1)}$$

where $\rho(r,x) = \rho_{amb}$ and $u(r,x)$ are the density and axial velocity in the jet. Results of Ricou and Spalding [14] provide the following estimate for the mass flux in the jet

$$m_{FJ}(x) = 2\pi \int_0^\infty \rho(r,x) u(r,x) r dr = 0.282 x K^{1/2} \rho_{amb} \quad \text{(A2)}$$

Turning attention to the buoyant plume driven by a point source of energy release, the plume description of Zukoski et al. [15] leads to the following estimate for the momentum flux and mass flux

$$\rho_{amb} K_{BP}(x) = 0.404 \rho_{amb} g x^3 Q^{*2/3}(x) \quad \text{(A3)}$$

$$m_{BP}(x) = 0.209 \rho_{amb} g^{1/2} x^{5/2} Q^{*1/3}(x) \quad \text{(A4)}$$

where $Q^*(x)$ is defined by equation (6*b*) with x replacing H.

At their respective impingement points ($x=b$ for the free jet and $x=H$ for the buoyant plume) an equivalence is now drawn between the free jet and the buoyant plume. Reasonable criteria for such an equivalence are identical values for the mass and momentum flux. Applying such criteria leads to the following

$$\mathrm{Re}_P \equiv K^{1/2}/\nu = 0.636 \mathrm{Re}_H \quad \text{(A5)}$$

$$b = 1.17 H \quad \text{(A6)}$$

where

$$\mathrm{Re}_H = H\tilde{V}/\nu; \tilde{V} = g^{1/2} H^{1/2} Q^{*1/3}(H) \quad \text{(A7)}$$

and where Re_P is the Reynolds number of [6].

Using the equivalent relationships of equations (A5) and (A6) in equations (4) and (5) leads to equations (4′) and (5′).

From the Work of Donaldson et al [8]. The heat transfer from constant temperature heated surfaces to wall jets generated by unheated free jets is measured in [8]. In that work, heat-transfer data is correlated with measured properties of the free jet in the plane of impingement (but in the absence of the heated surface). In the nomenclature of [8] these measurements include the velocity on the jet axis, w_c, and the radial position, r_5, where the axial velocity drops to $w_c/2$. The heat-transfer data is actually correlated with the Reynolds number, $\mathrm{Re}_5 = w_c r_5/\nu$, and r_5.

In order to interpret the heat-transfer data of [8] in the context of the present work, a correspondence is drawn between the measured impingement point properties of a given free jet and the impingement point properties of an equivalent buoyant plume. Turning again to the Gaussian plume description of [15], and by definition of r_5, w_c, and Re_5, the following criteria for equivalence result

$$w_c = 3.87 g^{1/2} H^{1/2} Q^{*1/3}(H) \quad \text{(A8)}$$

$$1/2 = \exp[-58.3(r_5/H)^2] \rightarrow r_5 = 0.109\, H \quad \text{(A9)}$$

$$\mathrm{Re}_5 = 0.422\, \mathrm{Re}_H \quad \text{(A10)}$$

where equation (A7) was used to obtain equation (A10) from equations (A8) and (A9).

To complete the analogy between the experiments of [8] and the heat-transfer formulation of equation (10), it is noted that for the experiments of [8] T_{ad} must be interpreted as T_∞, since the free jets which generated the wall jets were unheated. Using this interpretation, the Nusselt number data, Nu_5, of [8] is seen to be defined as $\mathrm{Nu}_5 = hr_5/k$, where k is the thermal conductivity. Using equations (A7), (A9), (A10) and (9) the following equivalence can now be drawn between the wall jet heat-transfer data of [8] and the buoyant plume driven ceiling jet heat transfer of present concern

$$\mathrm{Nu}_5 = 0.109\, \mathrm{Pr}\mathrm{Re}_H h/\tilde{h}$$

R. I. Hirshburg[1]
Research Engineer,
E. I. duPont de Nemours,
Photo Products Department,
Brevard, N. C.
Assoc. Mem. ASME

L. W. Florschuetz
Professor,
Department of Mechanical Engineering,
Arizona State University,
Tempe, Ariz. 85287
Mem. ASME

Laminar Wavy-Film Flow: Part I, Hydrodynamic Analysis

The hydrodynamic characteristics of thin, laminar, gravity-driven, wavy-film flow are considered. A theoretical model is developed to predict the hydrodynamic features of asymptotic, wavy-flow states. The mathematical closure question arising in asymptotic-state analyses is resolved by incorporating the results of a prior stability analysis of smooth-film flow. Calculated values for mean film thickness, trough-to-crest dimension, wave celerity, and wavelength are found to be consistent with published experimental data for these quantities.

Introduction

Thin films flowing down vertical surfaces have been extensively studied because of their common occurrence in a variety of engineering applications. The transport properties typical of thin-film flows are especially suited to applications in industrial process equipment. The efficient heat- and mass-transfer characteristerics of the film are primarily the result of the thinness of the film and are further enhanced by the presence of waves on the liquid-vapor interface.

Casual observation of a thin film on a vertical surface reveals certain important characteristics of the flow. The most obvious feature is the essential unsteadiness of the motion. With disturbances normally present in laboratory situations waves will develop on the liquid-vapor interface. For disturbances with a dominant perturbing frequency and a limited side-band width, a finite-amplitude, wavy-flow state can be observed. In this situation, a constant wave amplitude is approached asymptotically with flow length as nonlinear interaction of wave modes results in an equilibrium condition. In other, more common situations, the presence of a wide spectrum of perturbing disturbances precludes the possibility of an observable stable equilibrium state. However, it does appear that developing flow characteristics can be satisfactorily described for much of the flow length by these asymptotic states.

The objective of Part I of this work is to investigate periodic asymptotic-flow states of a thin, vertical laminar film. An equation of free-surface deflection is developed from the equations of fluid motion via a permanent-wave transformation and appropriate assumptions. This equation is solved for film Reynolds numbers up to 1000 using a Fourier series representation truncated after six harmonics. The mathematical closure problem for the most appropriate solution is resolved with an assumption relating the wavy state at the line of wave inception with the results of a prior linear stability analysis [1]. Calculated results for mean film thickness, trough-to-crest dimension, wavelength, and wave celerity as a function of Reynolds number are compared with experimental data from the literature. In Part II, the results are utilized in a heat-transfer model describing laminar-film condensation and evaporation in the presence of a wavy liquid-vapor interface.

Thin-Film Evolution

Before developing a predictive model, it is instructive to qualitatively describe the evolution of a thin film flowing down the surface. Such a description is constructed by assimilating a multitude of published experimental observations and theoretical hydrodynamic-stability results. The following discussion of film evolution is a condensed version of that found in [2].

Immediately following initiation of the film there exists a waveless region. However, throughout the flow length the film is subjected to a wide frequency spectrum of normally small-amplitude disturbances. The response of the film to these disturbances is to amplify those of certain frequencies and dampen others. Of the amplified frequencies, a wave of a particular frequency is subjected to the maximum rate of amplification. There is considerable conjecture that this most highly-amplified wave usually evolves into the initial finite-amplitude wave. The observable portion of this wave growth is so rapid that the nominal location of the initial sighting of waves is referred to as the line of wave inception [1]. For small flow rates, say $\mathrm{Re}(=4B_0/\nu) < 20$, the amplification rate is extremely small; hence, the film appears to be smooth throughout flow lengths of practical importance [3]. For higher Reynolds number flows the amplification rate increases considerably and finite-amplitude waves are imminent.

The finite-amplitude waves appearing at the line of wave inception have a two-dimensional character with roughly sinusoidal wave fronts moving down the surface. These sinusoidal-like waves (hereafter referred to simply as sinusoidal waves) persist for a short distance but soon begin to distort since they are not stable to the sideband disturbances usually present [4, 5]. In the region of flow immediately following the sinusoidal waves, there is significant spatial variation in wavelength and dispersion characteristics [6]. Wave features become increasingly random and three-dimensional. However, Salazar and Marschall [7] concluded that the wavy motion is primarily of a two-dimensional nature for all $\mathrm{Re} < 1500$. This important conclusion was based on detailed optical studies using laser techniques. Statistically meaningful trends of this region include an increase in mean wavelength and wave celerity and a decrease in mean wave frequency [6]. Eventually, a preferred wave-separation distance and celerity are approached. The wave profiles in this region have a teardrop shape with a long sloping back portion and a relatively steep wave front [8, 9, 10]. These waves appear to be moving independently of one another on a substrate of constant thickness and are consequently referred to as single waves [11].

This wave structure is interrupted by the appearance of yet another type of wave, the roll wave. Roll waves are large, roughly two-dimensional waves having amplitudes typically much larger than the mean thickness, and wave separation distances two orders of magnitude larger than the wave structures previously described [12]. These waves increase in

[1]Formerly Research Assistant, Department of Mechanical Engineering, Arizona State University

Contributed by the Heat Transfer Division for publication in the JOURNAL OF HEAT TRANSFER. Manuscript received by the Heat Transfer Division May 15, 1981. Paper No. 81-HT-13.

mean frequency as the Reynolds number is increased substantially above 400 and as the location of observation is moved downstream [6]. This wave structure is obviously not periodic and hence cannot be predicted via a periodic asymptotic state analysis. Consequently, the present analysis is restricted to short and moderate flow lengths where the effect of roll waves is small due to their infrequency.

Formulation

The laminar flow of a film down a vertical surface may be accurately described by the constant-property, unsteady Navier-Stokes system,

$$\frac{\partial \tilde{u}_i}{\partial t} + \tilde{u}_j \tilde{u}_{i,j} = -\frac{1}{\rho} p_{,i} + \nu \tilde{u}_{i,jj} + g_i \tag{1}$$

$$\tilde{u}_{i,i} = 0 \tag{2}$$

The velocity and coordinate conventions are as designated in Fig. 1.

The appropriate boundary conditions at the solid wall are the no slip/no penetration conditions. The surface of the liquid at $x_2 = \delta$ is assumed to be a free surface. Thus,

$$e_{ij} n_j t_i = 0 \tag{3}$$

and

$$-(\tilde{p} - \tilde{p}_v) + 2\mu e_{ij} n_j n_i = \sigma\left(\frac{1}{R_1} + \frac{1}{R_2}\right) \tag{4}$$

at $x_2 = \delta$.

The relationship (3) expresses the absence of an applied shearing stress at the surface and (4) is a balance of normal forces across the interface.

A solution to the transient problem requires an initial condition consisting of a specified velocity field at arbitrary initial time $t = 0$. This field may be taken as any distribution consistent with the governing equations and boundary conditions. However, the following specifications include the cases of most interest: (*i*) the velocity field is a smooth-film parabolic distribution with superposed small-amplitude disturbance waves; (*ii*) the velocity field corresponds with a given wavy-flow state with or without small disturbances. The first case includes both the linear and nonlinear stability analyses of laminar film flow. The second case includes the stability of finite-amplitude wavy states of infinitesimal as well as finite disturbances. This and the nonlinear stability problem are areas of considerable recent interest [4, 5]. Because of the mathematical complexities of the unsteady nonlinear equations of motion, perturbation techniques are usually employed in these analyses. Unfortunately, a consideration of higher-order terms results in severe

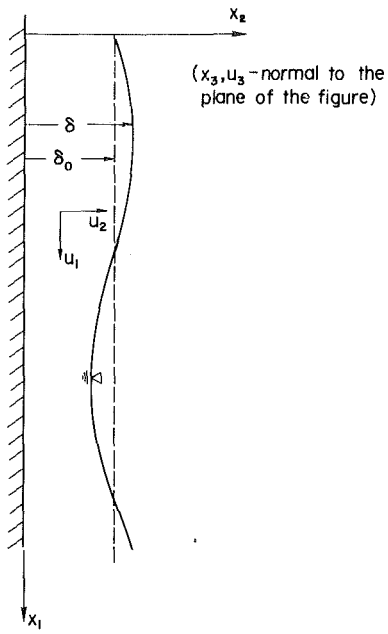

Fig. 1 Velocity and space coordinate conventions

Nomenclature

a = dimensionless film thickness (δ/δ_0)
A_n = amplitude of nth harmonic (sine component)
B_n = amplitude of nth harmonic (cosine component)
B = local volumetric flow rate per unit film width
B_0 = mean volumetric flow rate per unit film width over a wavelength
b = dimensionless local volumetric flow rate (B/B_0)
c = wave celerity
e_{ij} = rate of strain tensor
f = wave frequency (c/λ)
f_u = frequency of most unstable wave
f^+ = wave frequency normalized by that of most unstable wave (f/f_u)
Fr = Froude number ($g\delta_0/U_0^2$)
g = gravitational acceleration
n_j = unit normal vector at free surface
$\tilde{p}$ = pressure in liquid
p = dimensionless pressure in liquid ($\tilde{p}/\rho U_0^2$)
$\tilde{p}_v$ = vapor pressure at free surface
p_v = dimensionless vapor pressure at free surface ($\tilde{p}_v/\rho U_0^2$)
Re = film Reynolds number ($4B_0/\nu$)
R_1, R_2 = orthogonal radii of curvature at free surface
t = time
t_i = unit tangential vector at free surface
$\tilde{u}_i$ = local velocity in liquid film
u_1, u_2 = dimensionless local velocity components in liquid film ($\tilde{u}_1/U_0, \tilde{u}_2/\alpha U_0$)
U = liquid velocity component parallel to surface averaged across film thickness
U_0 = characteristic velocity (B_0/δ_0)
We = Weber number ($\rho U_0^2 \delta_0/\sigma$)
x_i = Cartesian coordinates (see Fig. 1)
z = dimensionless wave celerity (c/U_0)

Greek

α = wave number (δ_0/λ)
β = amplitude of first harmonic
Γ = dimensionless surface tension parameter $[\sigma(\nu^4 g)^{-1/3}/\rho]$
δ = local film thickness
δ_0 = mean film thickness over a wavelength
λ = wavelength
ν = kinematic viscosity
ξ_1 = normalized coordinate $[(\alpha/\delta_0)(x_1 - ct)]$
ξ_2 = normalized coordinate (x_2/δ_0)
ρ = liquid density
σ = surface tension
τ = dimensionless time ($\alpha U_0 t/\delta_0$)
ϕ = dimensionless free surface deflection ($a - 1$)

mathematical difficulties which presently prevent extensive quantitative application of this research.

As indicated previously, the intent of this work is to describe asymptotic, wavy-flow states without solving for the transient solution. Consequently, an explicit statement of the initial conditions is not required. As already noted, the wavy motion for the laminar regime is primarily of a two-dimensional nature [7]. For the flow states of interest, the following characteristic dimensions are apparent: for x_1, the wavelength of the wavy surface, λ; for x_2, the mean thickness of the film over a wavelength, δ_0; and for $\tilde{u}_1$, the characteristic velocity, $U_0(=B_0/\delta_0)$. With these characteristic quantities, the governing differential equations (1) and (2) can be normalized. In addition, it is convenient to employ a "permanent-wave" transformation of the form

$$\tau = \frac{\alpha U_0}{\delta_0} t$$

$$\xi_1 = \frac{\alpha}{\delta_0}(x_1 - ct)$$

$$\xi_2 = \frac{x_2}{\delta_0}$$

where $\alpha(=\delta_0/\lambda)$ is the wave number, and c is the wave celerity. The governing differential equations for the asymptotic flow states are then obtained by setting $\partial(\ )/\partial\tau = 0$. The resultant equations are

$$(u_1 - z)u_{1,1} + u_2 u_{1,2} = -p_{,1} + \frac{4}{\alpha \mathrm{Re}}(u_{1,22} + \alpha^2 u_{1,11}) + \frac{\mathrm{Fr}}{\alpha} \quad (5)$$

$$\alpha^2[(u_1 - z)u_{2,1} + u_2 u_{2,2}] = -p_{,2} + \frac{4\alpha}{\mathrm{Re}}(u_{2,22} + \alpha^2 u_{2,11}) \quad (6)$$

and

$$u_{1,1} + u_{2,2} = 0$$

where $z(=c/U_0)$ is the dimensionless wave celerity. Time is no longer an explicit independent variable in (5) and (6), but the undetermined parameter z has been introduced resulting in a mathematical closure problem. This problem arises because of neglecting information in the form of initial conditions when considering only asymptotic wave states. Consequently, closure must be achieved by introducing an additional independent relationship via some physical or mathematical constraint. The resolution of this problem will be discussed in detail in a later section.

Turning attention to the boundary conditions, (3) is specialized to two dimensions and the continuity equation is applied. This yields, in normalized form

$$u_{1,2} + \alpha^2 u_{2,1} = \frac{4a^2 a_{,1}}{1 - \alpha^2 a_{,1}^2} u_{1,1} \quad \text{at } \xi_2 = a(\xi_1) \quad (7a)$$

The same procedure applied to (4), with the aid of (7*a*), results in

$$p - p_v = -\frac{\alpha^2}{\mathrm{We}} \frac{a_{,11}}{(1 + \alpha^2 a_{,1}^2)^{3/2}} - \frac{8\alpha}{\mathrm{Re}} \frac{1 + \alpha^2 a_{,1}^2}{1 - \alpha^2 a_{,1}^2} u_{1,1}$$
$$\text{at } \xi_2 = a(\xi_1) \quad (7b)$$

The boundary conditions (7*a*) and (7*b*) can also be obtained directly from equations (3.8′) of [13] specialized to a free surface and normalized as above.[2]

Waves on the surface of a thin film are observed to be long waves; consequently, $\lambda >> \delta_0$ (or $\alpha << 1$). Thus, equations (5) and (6) can be approximated by

$$(u_1 - z)u_{1,1} + u_2 u_{1,2} = -\frac{dp}{d\xi_1} + \frac{4}{\alpha \mathrm{Re}} u_{1,22} + \frac{\mathrm{Fr}}{\alpha} \quad (8)$$

where it has also been assumed that $\alpha\mathrm{Re} \sim 1$ and $\mathrm{Fr}/\alpha \sim 1$.

The boundary equations are similarly scaled. Substituting the pressure distribution from (7*b*) into (8), with p_v constant, yields

$$(u_1 - z)u_{1,1} + u_2 u_{1,2} = \frac{\alpha^2}{\mathrm{We}} a_{,111} + \frac{4}{\alpha \mathrm{Re}} u_{1,22} + \frac{\mathrm{Fr}}{\alpha} \quad (9)$$

Note that for some liquids and flows of interest $\alpha^2/\mathrm{We} \sim 1$.

Equation (9) can be simplified further via an appropriate assumption for the x_2-dependence of the velocity field. The most frequently assumed distribution is the parabolic profile

$$u_1 = 3\frac{U}{U_0}\left[\frac{x_2}{\delta} - \frac{1}{2}\left(\frac{x_2}{\delta}\right)^2\right] \quad (10)$$

where $U(x_1, t)$ is the average film velocity at x_1 and t. From the experimental velocity distribution studies of Ueda and Tanaka [14] it is apparent that this parabolic profile is quite accurate.

Substituting u_1 from (10) and u_2 determined from the conservation of mass into (9), then integrating from $\xi_2 = 0$ to a yields

$$\frac{\alpha^2}{\mathrm{We}} a^3 a''' + \left(za^2 - \frac{9}{10}ab\right)b' + \left(\frac{6}{5}b^2 - \frac{3}{2}zab\right)a' - \frac{12}{\alpha \mathrm{Re}} b + \frac{\mathrm{Fr}}{\alpha} a^3 = 0 \quad (11)$$

where $(\ )' = d(\ )/d\xi_1$.

The film flow rate may be related to the local film thickness by integration of the continuity equation over the film thickness. For an asymptotic, wavy-flow state this results in a surface kinematic relation which may be written in dimensionless form as

$$\frac{d}{d\xi_1}(b - za) = 0 \quad (12)$$

Integrating and then averaging over a wavelength to fix the constant of integration yields

$$b = z\phi + 1 \quad (13)$$

where a has been replaced in favor of the dimensionless deflection of the free surface from its mean location, i.e.,

$$\phi = a - 1 \quad (14)$$

Now using (13) and (14) in (11) yields an equation of free-surface deflection

$$\frac{\alpha^3}{\mathrm{We}}(1 + \phi)^3 \phi''' + \frac{\alpha}{5}[(5z^2 - 12z + 6) - z^2\phi(2 + \phi)]\phi' + \mathrm{Fr}\phi^2(3 + \phi) + \left(3\mathrm{Fr} - \frac{12z}{\mathrm{Re}}\right)\phi + \left(\mathrm{Fr} - \frac{12}{\mathrm{Re}}\right) = 0 \quad (15)$$

The boundary conditions are cyclic since a periodic solution is required. In addition

$$\int_0^1 \phi(\xi_1) d\xi_1 = 0$$

Kapitza [11] first formulated an equation of free-surface deflection similar to (15). Several subsequent investigators have extended Kapitza's work by including certain terms in the equations of motion neglected in Kapitza's analysis. Bushmanov [15] added the cross-film convection term ($u_2 u_{1,2}$) excluded by Kapitza. In addition, Massot et al. [16] included the downstream diffusion term ($\nu u_{1,11}$). The viscosity effect in the normal-stress free-surface boundary condition was considered in an analysis by Gollan and Sideman [17]. Shkadov [18] developed an equation essentially equivalent to (15). However, because of limited solution techniques and

[2] It should be noted, however, that there is an error in equations (3.8′) of [13]. The exponent of the denominator in the viscous terms should be unity rather than one-half.

inappropriate closure schemes these extensions did not significantly alter Kapitza's [11] basic results.

Solution Method

The periodicity and zero mean value requirements on $\phi(\xi_1)$ render the solution of (15) particularly amenable to Fourier series analysis. Consequently, ϕ is assumed to be represented by a series of the form

$$\phi(\xi_1) = \beta \sin 2\pi\xi_1 + \sum_{n=2}^{N} \beta^n (A_n \sin 2\pi n\xi_1 + B_n \cos 2\pi n\xi_1) \quad (16)$$

Note that the term $\beta\cos 2\pi\xi_1$ does not appear since the relative phase of the surface wave is of no consequence. Substituting (16) in (15), then equating the subsequent coefficient of each orthogonal component with zero yields a set of $2N + 1$ nonlinear algebraic equations in $2N + 2$ unknowns $-\alpha$, z, Fr, β, A_2, B_2, ..., A_N, B_N. The mathematical closure problem is thus apparent since there is an insufficient number of independent relationships to determine the unknowns.

Previous Fourier series solution attempts have employed only the first two harmonics. As a consequence only the sinusoidal wave state has been predicted. In this work, the Fourier series is truncated after six harmonics. Substitution of this series into (15) results in a system of thirteen nonlinear equations. These equations are quite lengthy and are reported in [2]. The system of equations was solved via a multivariable search scheme comprised of a simplex method to improve initial guesses and a discrete Newton-Raphson method to rapidly converge to the appropriate solution.

Closure Problem

A major criticism of previous asymptotic film flow analyses is that the various closure methods employed lack theoretical justification [19]. A frequently used closure method is the assumption of an extremum principle. Examples of extremum principles are Kapitza's [11] minimization of energy dissipation and Shkadov's [18] minimization of the average film thickness. With these assumptions it is inferred that there exists a unique, stable periodic-flow state to which the film will tend regardless of the initial condition. Such assumptions cannot be appropriate since analyses by Krishna and Lin [5] and Lin [4] indicate a continuous manifold of stable states depending on the characteristics of the initial conditions.

An alternate approach is to simply present solutions to (15) parameterized by some variable of the analysis. Mei [20] reported wave amplitude as a function of wave celerity, an "amplitude-dispersion curve". Another interesting approach was employed by Lee [21] who related wave characteristics to wave amplitude by requiring periodicity of solutions to successive linear perturbation equations derived from a free-surface deflection equation.

As described previously, a wide frequency spectrum of destabilizing disturbances is present in most cases. Nevertheless, the mean characteristics of the ensuing wavy flow appear to be fairly reproducible. Consequently, the closure question should be stated as: What particular flow state is most commonly observed in experiments without intentional excitation of the system? Recall that for a smooth film subject to room disturbances, a particular frequency wave is subject to a maximum rate of amplification. If it is assumed that the nonlinear amplification process does not distort the developing wave excessively, then the finite-amplitude wave most frequently appearing at the line of wave inception will be of this same frequency. Consequently, it is assumed that the sinusoidal wave regime displays a frequency equal to the frequency of the most unstable wave of the linear stability analysis.

The accuracy of this assumption can be judged by comparing the frequency of the most unstable wave from a linear stability analysis by Pierson and Whitaker [1] with published experimental results taken just after the line of wave inception. This comparison is displayed in Fig. 2 for water at 20°C. There is excellent agreement up to $\mathrm{Re} \sim 100$. Though experimental data are sparse above this value, the data show a trend to frequencies lower than those predicted. Two reasons are suggested for this apparent disagreement. As the Reynolds number is increased above 100, the sinusoidal waves distort at an increasing rate as they travel down the surface from the line of wave inception. Consequently, true indications of sinusoidal regime wave frequencies are difficult to accurately measure. Furthermore, the frequency-selection process becomes rather uncritical above $\mathrm{Re} \sim 100$. As pointed out by Pierson, the amplification-rate curves for $\mathrm{Re} > 100$ do not display a sharp peak at the maximum amplification. Consequently, the prevalent frequency at wave inception is strongly dependent on the features of the room disturbances.

A theoretical specification for asymptotic-state frequencies downstream of the line of wave inception is a more difficult undertaking. Because of considerable variation in wavelength and wave celerity, adjacent waves frequently coalesce. As a result of wave coalescence and the distortion of the sinusoidal waves, the wave frequency decreases down the flow surface and only asymptotically approaches a constant value. A coalescence model would entail a statistical evaluation of the wave characteristics during this transient. Such a model is

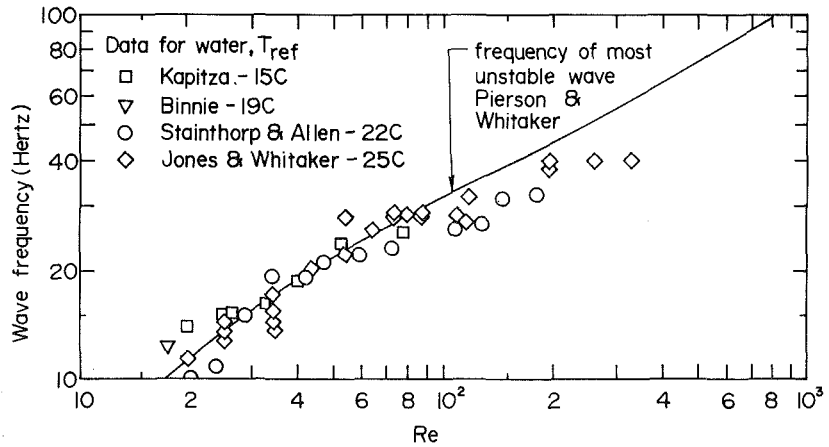

Fig. 2 Frequency of most unstable wave from linear stability analysis compared with measured values just downstream from line of wave inception

clearly beyond the scope of this analysis. In view of these difficulties the asymptotic state frequencies in this region will simply be reported according to their relative frequency, f^+ ($=f/f_u$), where f_u is the frequency of the most unstable wave. Unfortunately, quantitative information for frequencies as a function of flow length is limited for $Re < 1000$. However, Stainthorp and Batt [9] reported a decrease of wave frequency for Re = 100 on the order of 50 percent over a flow length of approximately 60 cm. Therefore, theoretical results were determined for the range of relative frequencies 0.35 to 0.80.

Results

The search program was executed for Re up to 1000 and $800 \leq \Gamma \leq 5550$. Two solution branches were found. An example of the first branch is illustrated in Fig. 3(*a*) for Re = 100 and $\Gamma = 3450$. This wave profile is roughly sinusoidal and is characteristic of experimentally observed profiles occurring immediately following the line of wave inception, which were originally termed periodic waves by Kapitza [11]. This profile is illustrated for $f^+ = 1$ (i.e., the frequency of the most unstable wave). Examples of wave profiles belonging to the second solution branch are illustrated in Fig. 3(*b*) for the same Re and Γ. They display long teardrop shapes with relatively steep wavefronts similar to single waves. However, they do not exhibit the long, flat substrate commonly observed in the single wave region. These solutions do, in fact, describe an asymptotic state first observed experimentally by Kapitza. He named these waves intermediate waves since they displayed features of both the sinusoidal and the single wave regimes. These intermediate waves do appear to be representative of at least the mean wave characteristics in the transient region between the sinusoidal waves at wave inception and the onset of single waves. The solution profiles selected for illustration in Fig. 3(*b*) are for several values of f^+ less than unity for reasons outlined in the preceding section.

Figure 4 displays a comparison of the calculated mean film thickness with published experimental data for water at approximately 20°C ($\Gamma = 3450$). The spread in experimental data is primarily because of difficulty in accurately measuring this quantity. The spread is most apparent for the higher Reynolds numbers. The bulk of the data in this range, however, fall below the Nusselt line, including the recent measurements of Salazar and Marschall [22] utilizing a laser technique. The hydrodynamic model predictions are consistent with the bulk of the data. Of the intermediate-wave solutions, only the prediction for $f^+ = 0.50$ is presented since there is little variation between results for $f^+ = 0.35$ and 0.80. The mean film thickness for the intermediate-wave solution is slightly below that for the sinusoidal-wave solution. Since the intermediate-wave solution represents film characteristics in the region downstream from the sinusoidal-wave region, it can be implied from these results that for a given Re the time-mean thickness decreases down the surface. This trend has been observed by Salazar and Marschall [22] and Takahama and Kato [6] for the Reynolds number range considered here.

The calculated trough-to-crest dimensions for water at 20°C ($\Gamma = 3450$) are compared with experimental values for water at 15, 20, and 25°C in Fig. 5. The results agree quite favorably with the experimental data and appear to yield the appropriate trends at higher Reynolds number indicated by the data. Note that the curves for the sinusoidal wave and intermediate wave are virtually the same for $Re < 100$, yet they imply an increase in amplitude with distance downstream for $Re > 100$. The same trend is displayed in the experimental data.

Results for wavelength vs. Reynolds number are displayed in Fig. 6, again for water at 20°C. The experimental data are

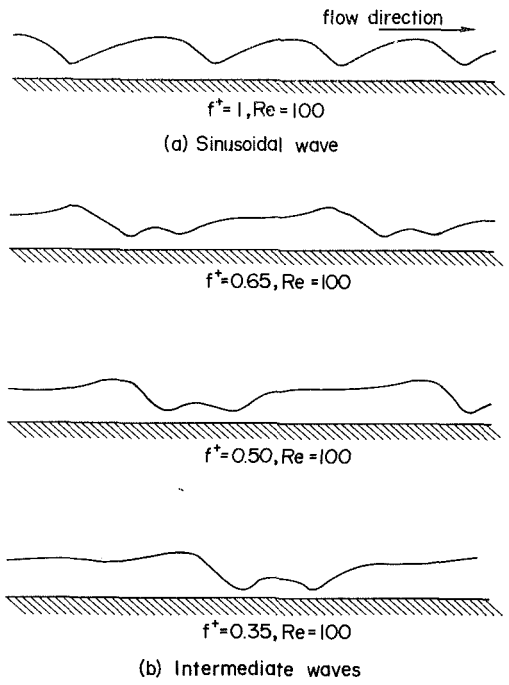

Fig. 3 Sample predicted wave profiles ($\Gamma = 3450$)

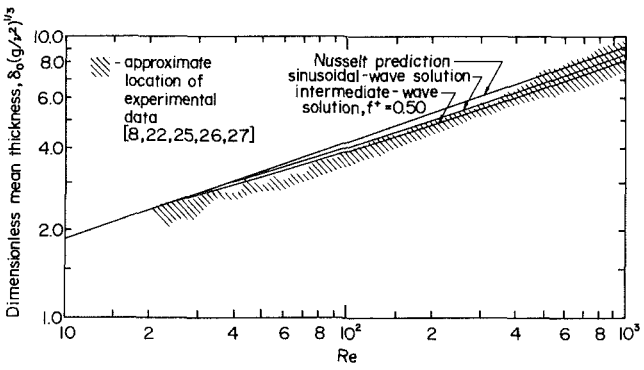

Fig. 4 Mean film thickness predictions of present model compared with experimental data for water ($\Gamma = 3450$)

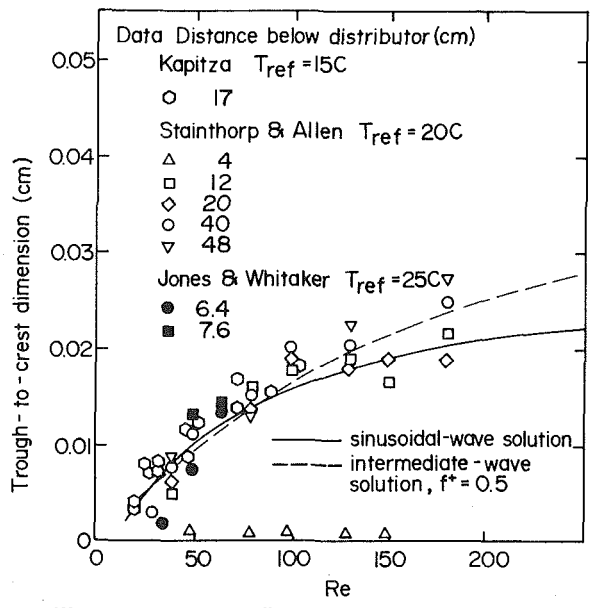

Fig. 5 Wave trough-to-crest dimension predicted by present model compared with experimental data for water ($\Gamma = 3450$)

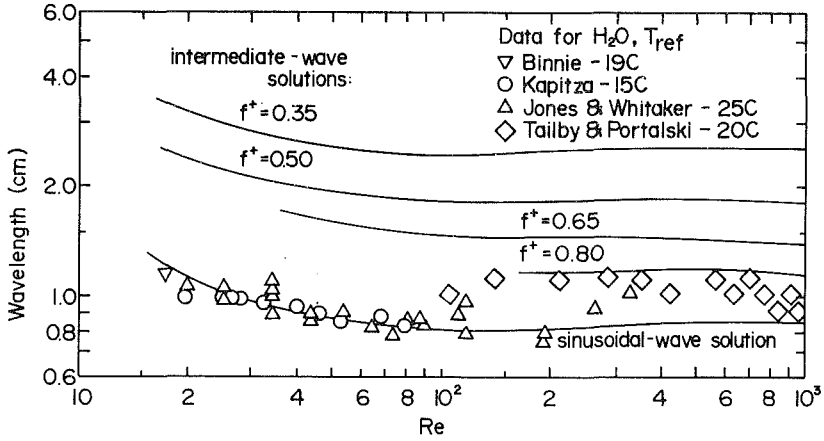

Fig. 6 Wavelength predicted by present model compared with experimental data for water ($\Gamma = 3450$)

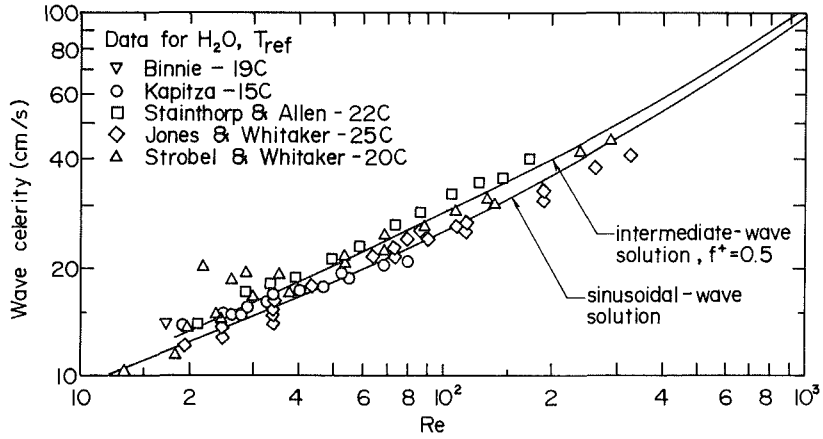

Fig. 7 Wave celerity predicted by present model compared with experimental data for water ($\Gamma = 3450$)

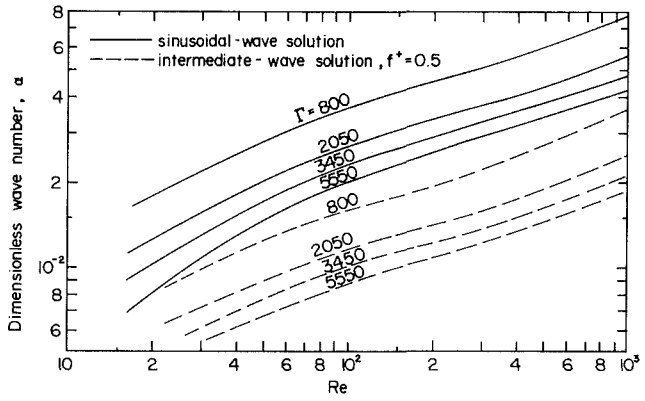

Fig. 8 Dimensionless wave number – the effect of Γ

more appropriate for the sinusoidal regime. Correspondingly, these results are accurately predicted by the sinusoidal solution. This is especially evident for $Re < 100$. Above this Reynolds number the experimental values are subject to transient effects, as mentioned previously. Observe that the wavelengths for the intermediate-wave solutions increase as f^+ decreases (implying that λ increases down the flow surface). This trend is in agreement with experimental observations [8, 9].

Finally, Fig. 7 displays calculated wave celerity compared with published experimental results (water, 15–25°C). The agreement is quite good throughout the range of available experimental data.

The effect of variation in fluid properties on the asymptotic solution is demonstrated in Figs. 8 and 9. In Fig. 8, the

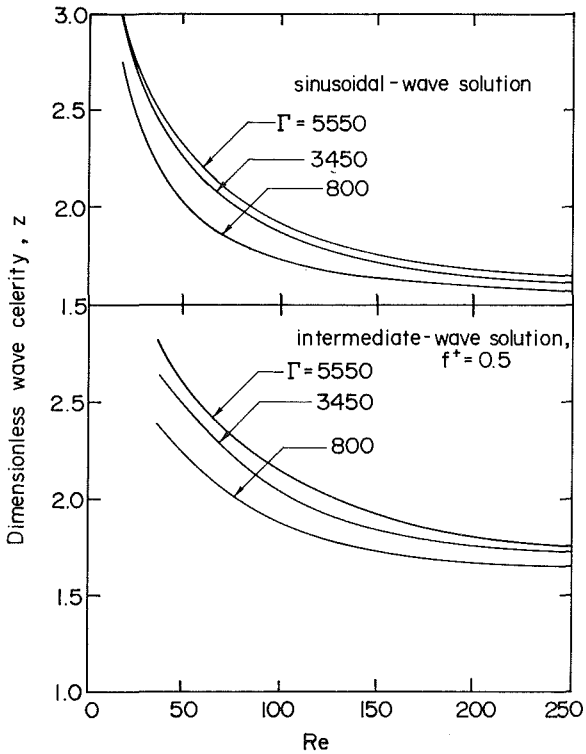

Fig. 9 Dimensionless wave celerity – the effect of Γ

dimensionless wave number is displayed for several values of the surface tension parameter, Γ. In both the sinusoidal-wave and intermediate-wave solutions, an increase in Γ results in a decrease in α. In Fig. 9, the dimensionless celerity is shown for various Γ. The variation due to changes in Γ is not so pronounced as for α, but, for either solution regime, an increase in Γ corresponds with increase in z.

Concluding Remarks

The thin-film theoretical model presented describes a number of important wavy-film characteristics. For the sinusoidal regime, this model yields solution parameters in excellent agreement with experimentally-observed values. Although experimental results for the transient region are scarce, the trends indicated by existing data and various qualitative experimental observations are consistent with the intermediate-wave solutions.

The predicted wave profiles exhibit the same characteristic shapes as those experimentally observed by Kapitza [11] and others for the sinusoidal and intermediate-wave regimes. A solution describing the single-wave regime was not predicted with the hydrodynamic model. Possibly, the single-wave state observed in experimental investigations is not an asymptotic periodic-flow state in the usual sense but, rather, a succession of independently acting disturbances traveling down the surface. The resultant individual wave systems are then appropriately described by $\lambda \to \infty$ and $\alpha \to 0$. Such infinite-domain systems are not amenable to Fourier series analysis, and other solution techniques must be utilized.

Acknowledgment

The work reported herein was supported in part by the National Science Foundation.

References

1 Pierson, F. W., and Whitaker, S., "Some Theoretical and Experimental Observations of the Wave Structure of Falling Liquid Films," *Industrial and Engineering Chemistry, Fundamentals*, Vol. 16, 1977, pp. 401–408.

2 Hirshburg, R. I., "Laminar Film Flow Phenomena—Theory and Application to the Two-Phase Closed Thermosyphon," Ph.D. dissertation, Department of Mechanical Engineering, Arizona State University, 1980.

3 Benjamin, T. B., "Wave Formation in Laminar Flow Down an Inclined Plane," *Journal of Fluid Mechanics*, Vol. 2, 1957, pp. 554–574.

4 Lin, S. P., "Finite Amplitude Side-Band Stability of a Viscous Film," *Journal of Fluid Mechanics*, Vol. 63, 1974, pp. 417–429.

5 Krishna, M. V. G., and Lin, S. P., "Nonlinear Stability of a Viscous Film with Respect to Three-Dimensional Side-Band Disturbances," *Physics of Fluids*, Vol. 20, 1977, pp. 1039–1044.

6 Takahama, H., and Kato, S., "Longitudinal Flow Characteristics of Vertically Falling Liquid Films without Concurrent Gas Flow," *International Journal of Multiphase Flow*, Vol. 6, 1980, pp. 203–215.

7 Salazar, R. P., and Marschall, E., "Three-Dimensional Surface Characteristics of a Falling Liquid Film," *International Journal of Multiphase Flow*, Vol. 4, 1978, pp. 487–496.

8 Stainthorp, F. P., and Allen, J. M., "The Development of Ripples on the Surface of a Liquid Film Flowing Inside a Vertical Tube," *Transactions of the Institute of Chemical Engineers*, Vol. 43, 1965, pp. T85–T91.

9 Stainthorp, F. P., and Batt, R. S. W., "The Effect of Co-Current and Counter-Current Air Flow on the Wave Properties of Falling Liquid Film," *Transactions of the Institute of Chemical Engineers*, Vol. 45, 1967, pp. T372–T382.

10 Tailby, S. R., and Portalski, S., "Hydrodynamics of Liquid Films Flowing on a Vertical Surface," *Transactions of the Institute of Chemical Engineers*, Vol. 38, 1960, pp. 324–330.

11 Kapitza, P. L., and Kapitza, S. P., "Wavy Flow of Thin Layers of Viscous Fluid," *Collected Papers of P. L. Kapitza*, Vol. 2, Pergamon, New York, 1965, pp. 662–709.

12 Chu, K. J., and Dukler, A. E., "Statistical Characteristics of Thin, Wavy Films: Part II. Studies of the Substrate and Its Wave Structure," *American Institute of Chemical Engineers Journal*, Vol. 20, 1974, pp. 695–706. "Part III. Structure of the Large Waves and Their Resistance to Gas Flow," *American Institute of Chemical Engineers Journal*, Vol. 21, 1975, pp. 583–593.

13 Wehausen, J. V., and Laitone, E. V., "Surface Waves," *Handbuch der Physik*, Springer-Verlag, Berlin, 1960, pp. 446–778.

14 Ueda, T., and Tanaka, H., "Measurements of Velocity, Temperature and Velocity Fluctuation Distribution in Falling Liquid Films," *International Journal of Multiphase Flow*, Vol. 2, 1975, pp. 261–272.

15 Bushmanov, V. K., "Gidrodinamicheskaya Ustoichivost Zhidkogo Sloyna Na Vertikal'noi Stenke," *Zhurnal Eksperimental'noi I Teoreticheskoi Fiziki*, Vol. 39, 1960, pp. 1251–1257.

16 Massot, C., Irani, F., and Lightfoot, E. N., "Modified Description of Wave Motion in a Falling Film," *American Institute of Chemical Engineers Journal*, Vol. 12, 1966, pp. 445–455.

17 Gollan, A., and Sideman, S., "On the Wave Characteristics of Falling Films," *American Institute of Chemical Engineers Journal*, Vol. 15, 1969, pp. 301–303.

18 Shkadov, V. Y., "Wave Flow Regimes of a Thin Layer of Viscous Fluid Subject to Gravity," *Fluid Dynamics*, Vol. 2, No. 1, 1967, pp. 29–34.

19 Dukler, A. E., "Characterization Effects and Modeling of the Wavy Gas-Liquid Interface," *Progress in Heat and Mass Transfer*, Vol. 6, 1972, pp. 207–234.

20 Mei, C. C., "Nonlinear Gravity Waves in a Thin Sheet of Viscous Fluid," *Journal of Mathematical Physics*, Vol. 45, 1966, pp. 266–288.

21 Lee, J., "Kapitza's Method of Film Flow Description," *Chemical Engineering Science*, Vol. 24, 1969, pp. 1309–1319.

22 Salazar, R. P., and Marschall, E., "Time-Average Local Thickness Measurement in Falling Liquid Film Flow," *International Journal of Multiphase Flow*, Vol. 4, 1978, pp. 405–412.

23 Binnie, A. M., "Experiments on the Onset of Wave Formation on a Film of Water Flowing Down a Vertical Plane," *Journal of Fluid Mechanics*, Vol. 2, 1957, pp. 551–553.

24 Jones, L. O., and Whitaker, S., "An Experimental Study of Falling Liquid Films," *American Institute of Chemical Engineers Journal*, Vol. 12, 1966, pp. 525–529.

25 Portalski, S., "Studies of Falling Liquid Film Flow," *Chemical Engineering Science*, Vol. 18, 1963, pp. 787–804.

26 Fulford, G. D., *Gas-Liquid Flow in an Inclined Channel*, Ph.D. dissertation, University of Birmingham, England, 1962.

27 Charvonia, D. A., "An Experimental Investigation of the Mean Liquid Film Thickness and the Characteristics of the Interfacial Surface in Annular Two-Phase Flow," ASME Paper No. 61-WA-243, 1961.

28 Strobel, W. J., and Whitaker, S., "The Effect of Surfactants on the Flow Characteristics of Falling Liquid Films," *American Institute of Chemical Engineers Journal*, Vol. 15, 1969, pp. 527–532.

R. I. Hirshburg[1]
Research Engineer,
E. I. duPont de Nemours,
Photo Products Department,
Brevard, N. C.
Assoc. Mem. ASME

L. W. Florschuetz
Professor,
Department of Mechanical Engineering,
Arizona State University,
Tempe, Ariz. 85287
Mem. ASME

Laminar Wavy-Film Flow: Part II, Condensation and Evaporation

The Nusselt theory for laminar film condensation or evaporation is shown to significantly underpredict existing experimental data because of the presence of waves on the liquid-vapor interface. A heat transfer model is presented which incorporates the results of a previously developed hydrodynamic wavy-film model (Part I). Results based on the model for both local and mean Nusselt numbers are shown to be consistent with available experimental data, and to satisfactorily account for the deviation of the data from the classical Nusselt theory.

Introduction

The phenomena of laminar film condensation and laminar film evaporation occur in numerous industrial processes. Correspondingly, a large number of studies have been reported concerning the prediction of heat-transfer rates accompanying these phenomena. Very few works have considered the influence of the usually present interfacial waves. However, these waves can significantly enhance the heat-transfer coefficient associated with a thin, falling film.

The intent of the present investigation is to theoretically investigate the effect of waves on laminar film condensation and evaporation. Prior investigations, in which one or more of the assumptions leading to Nusselt's [1] smooth-film analysis were relaxed, are first reviewed. With the exception of the influence of waves, none of the effects involved can satisfactorily account for the frequently observed underprediction of measured heat-transfer rates by the Nusselt theory.

In this paper, a wavy-film heat-transfer model is developed by assuming the dominance of cross-film conduction. The influence of waves is included by assuming that the asymptotic wavy states predicted in Part I represent local-film characteristics in the presence of condensation or evaporation. Both time-average local and surface-average heat-transfer coefficients are computed and compared with experimental data available from the literature. The model results are consistent with the data and successfully describe data trends with Reynolds number and flow length.

Background

The majority of previous studies have considered laminar film condensation as opposed to evaporation. However, the two processes are very similar. The primary difference is the direction of heat transfer and, subsequently, the direction of the net flux of molecules at the liquid-vapor interface.

The local rate of heat transfer can be determined with knowledge of the temperature difference between the bulk vapor and the wall and the thermal resistances between these points. As shown in Fig. 1, for the case of condensation, these thermal resistances include those of the liquid-vapor and liquid-wall interfaces, the resistance in the vapor, and the liquid film resistance.

For condensation to occur on a liquid film the vapor pressure at the liquid-vapor interface must exceed that of the liquid [2]. The corresponding "temperature jump" across the interface is then viewed as the result of an interfacial thermal resistance. This resistance is found to be significant for liquid metals whereas for the most common working fluids it appears to be negligible [3]. Van der Walt and Kroger [4] suggested the existence of a liquid-wall interfacial resistance arising due to imperfect contact between the liquid and wall. However, it seems reasonable to assume that this effect is negligible except possibly at extremely low-film Reynolds numbers. The presence of noncondensable gases in stagnant gas-vapor mixtures can have a significant effect [5]. However, no such effect is present in evaporating systems or in pure condensing systems. Under many conditions the thermal resistance of the liquid film is by far the most significant. For the case of evaporation or pure-vapor condensation on a liquid of moderate or high Prandtl number, the prediction of heat fluxes usually depends on the accurate determination of this liquid film resistance.

Nusselt [1] was the first to analyze laminar film condensation on an isothermal inclined surface by predicting the liquid film resistance. Nusselt's analysis included the following simplifying assumptions: (*a*) no interfacial shear stress, (*b*) no inertia effect of condensing vapor, (*c*) linear temperature distribution across the film, (*d*) negligible subcooling of condensing vapors, (*e*) constant liquid properties, (*f*) laminar flow, and (*g*) smooth liquid-vapor interface (the absence of waves).

Theoretical analyses subsequent to that of Nusselt have attempted to relax one or more of these assumptions. Rohsenow [6] considered the effects of subcooling in the condensate film and nonlinear temperature distributions. However, the effect is quite small for most working fluids.

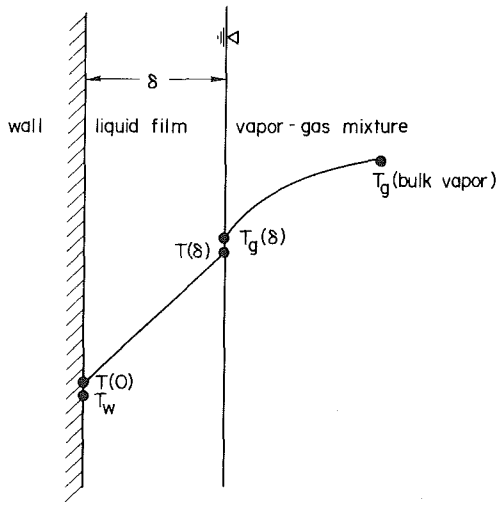

Fig. 1 Temperature distribution in film condensation system with interfacial resistances and noncondensable gas

[1] Formerly Research Assistant, Department of Mechanical Engineering, Arizona State University.

Contributed by the Heat Transfer Division for publication in the JOURNAL OF HEAT TRANSFER. Manuscript received by the Heat Transfer Division May 15, 1981. Paper No. 81-HT-14.

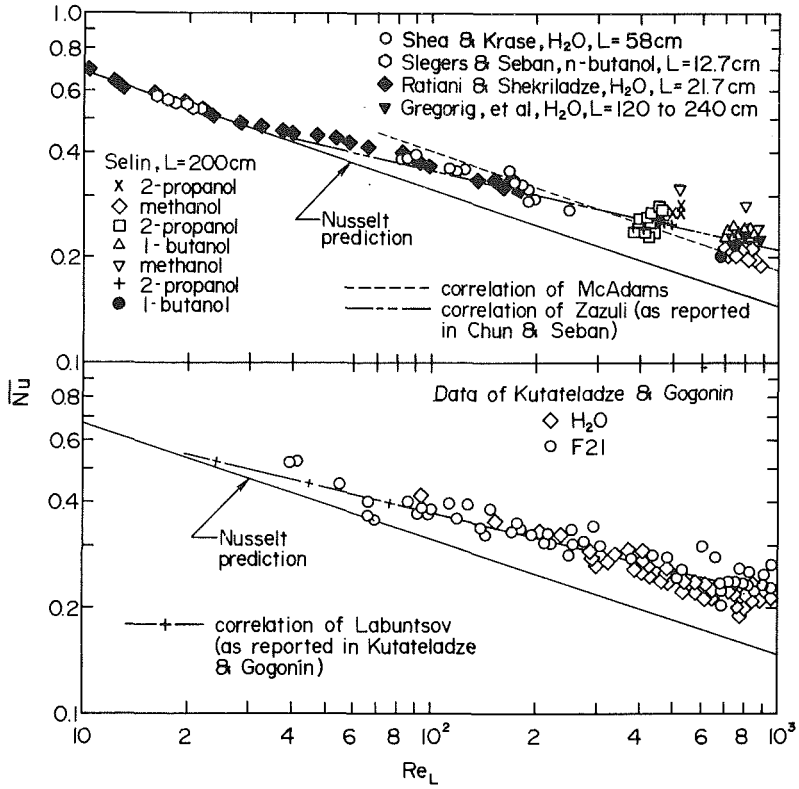

Fig. 2 Experimental laminar film condensation data

The effect of variable properties is also quite small for temperature differences normally encountered and can be adequately accounted for by evaluating liquid properties at a mean film temperature. The inertia effect of the quiescent vapor condensing on the moving liquid film was shown to be negligible for all fluids except those with extremely low liquid Prandtl numbers [7]. Finally, the vapor drag due to the contact of stagnant vapor with the moving interface was similarly shown to be negligible for all but extremely low Prandtl number fluids [5].

Numerous experimental investigations of laminar film condensation on vertical surfaces have been reported. The majority of investigators report surface-average heat-transfer coefficients rather than local values due to the relative ease in obtaining accurate overall measurements (the heat rate is simply related to the total condensate flow rate.) A number of the significant published results are shown plotted in Fig. 2, along with the empirical correlations of Zazuli [8], McAdams [9] and Labuntsov [10] and the theoretical prediction of Nusselt.

For low Reynolds number cases the condensate film is essentially smooth and the Nusselt theory might be expected to accurately predict experimental results. This is indeed the case for the results of Slegers and Seban [12] and Ratiani and Shekriladze [13]. The low Reynolds number results of other investigations indicate heat transfer coefficients both above and below that of the Nusselt theory. However, accurate low Reynolds number data are difficult to obtain due to the small temperature differences to be measured and the frequent presence of noncondensable gases.

At higher Reynolds numbers the experimental heat-transfer coefficients are consistently above the Nusselt prediction. The difference between the predicted and experimental results also tends to increase with Reynolds number. From the previous discussion it appears that, aside from the consideration of a wavy liquid-vapor interface, the theoretical solution of this condensation problem has been thoroughly examined. In the case of laminar film condensation of a quiescent pure vapor, the effects considered are quite small and not significant relative to the differences between the Nusselt prediction and

Nomenclature

f^+ = wave frequency normalized by that of most unstable wave
g = gravitational acceleration
h = convective heat transfer coefficient $(q/\Delta T)$
h_{fg} = enthalpy of vaporization
k = thermal conductivity of liquid
L = length of heat-transfer surface in flow direction
$\dot{m}$ = mass flow rate of film per unit film width
Nu = film Nusselt number $[h(\nu^2/g)^{1/3}/k]$
Pr = Prandtl number of liquid
q = surface heat flux
Re = film Reynolds number $(4\dot{m}/\mu)$
Sc = Schmidt number
T = temperature in liquid film
T_g = saturation temperature
T_w = wall temperature
x_1 = space coordinate parallel to surface

Greek

δ = local film thickness
ΔT = temperature difference $(T_g - T_w)$
Γ = dimensionless surface tension parameter $[\sigma(\nu^4 g)^{-1/3}/\rho]$
μ = dynamic viscosity of liquid
ν = kinematic viscosity of liquid
ρ = density of liquid
σ = surface tension

Subscripts and Superscripts

L = refers to value at $x_1 = L$
$(\bar{\ })$ = overbar refers to mean value over length L

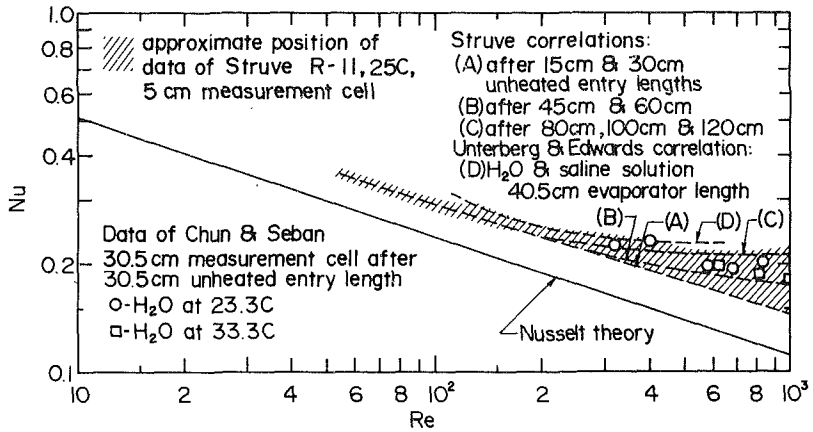

Fig. 3 Experimental laminar film evaporation data

the data. Consequently, it may be hypothesized that these differences are due to the effects of waves at the liquid-vapor interface.

The experimental condensation data discussed above are average values over the entire length of the condensate film. Accordingly, these results include the influence of the initial length of smooth condensate film. The more significant local effect of waves is then somewhat concealed. A more revealing result is for the local Nusselt number at a position sufficiently downstream of this smooth length to allow visually-observable waves to be present. Such investigations of local condensation rates are scarce; however, evaporation data of a local nature are available. In these evaporation studies, a smooth film is initiated and allowed to become wavy before reaching the heated surface. By adjusting the heat rate such that the evaporation rate is a small fraction of the total flow rate, the Reynolds number remains essentially constant over a relatively short test section.

The results of the local film evaporation studies are shown in Fig. 3, along with the Nusselt prediction. Due to the large number of data points, some of the results are displayed in terms of the correlations suggested by each investigator. A comparison of these results and the Nusselt prediction again demonstrates the heat transfer enhancing effect of waves. Overall, the difference in the experimental results and the Nusselt prediction is slightly larger for these local values than for the surface-average condensation data. Furthermore, from the data of Struve displayed in Fig. 3, it appears that the heat-transfer coefficient increases with distance at the same Re. This flow-length effect is at least partly the cause of the wide range of local and surface-average heat-transfer coefficients observed for Reynolds numbers above 300.

In contrast with the large number of theoretical analyses of secondary effects on condensation, very few analyses have been published concerning the effect of waves. Kapitza [18] first analyzed the flow of a wavy thin film on a vertical surface, then utilized these results in a one-dimensional heat-conduction model [18,19]. Kapitza's estimate resulted in about a 20 percent increase in heat-transfer rate over the smooth film case, independent of Reynolds number. This prediction appears to be reasonably good for Reynolds numbers in the limited range between about 80 and 200. However, it does not reflect the trend of the data with Reynolds number, nor the overall level of the data outside this range. Since this analysis does not satisfactorily predict important trends observed in the data, an improved model based on more detailed theoretical results for the wavy nature of the film is desirable.

Heat Transfer Model

Following the original lead of Nusselt it is assumed that the dominant mechanism controlling the heat rates for laminar film condensation or evaporation is conduction across the film thickness. Even in the presence of the wavy interface the effect of temperature gradients along the film should be negligible compared with the effect of cross-film gradients. However, it is appropriate to reconsider the importance of convective transport relative to conduction. Insight to this comparison is obtained by contrasting the heat-transfer problem with an analogous problem in thin-film mass transport where convective transport is important. The hydrodynamic characteristics of the two problems should be quite similar. Furthermore, the scalar transport equations for the two problems are identical except convective terms are multiplied by the Schmidt number, Sc, in the mass-transport problem and by the Prandtl number, Pr, in the heat-transfer problem. However, for the most common situations, Sc is large, whereas moderate Prandtl number fluids are of interest here (e.g., for the absorption of CO_2 gas in liquid water, Sc = 580 and for water at 20°C, Pr = 6.8). The convective and molecular diffusion transport mechanisms turn out to be of the same order of importance in the gaseous absorption data of Chung and Mills [20] and Kamei and Oishi [21]. Since $Pr << Sc$, it is indicated that molecular diffusion will dominate the transport of thermal energy across the film. Accordingly, convective transport can be omitted from the analysis with negligible error.

Additional support for this conclusion is implied from the experimental results of Ueda and Tanaka [22]. The temperature distribution across the film of a high Prandtl number liquid ($Pr \sim 100$) was measured using a thin thermocouple wire. The film Reynolds number ranged from 180 to 5030. Temperature measurements revealed the existence of a thick conduction layer adjacent to the wall. Near the liquid-vapor interface the temperature was approximately uniform, indicating the presence of mixing motions. However, according to Ueda and Tanaka, "the Prandtl number in this experiment is very high, even a slight eddy motion may flatten the temperature profile." They concluded further that "eddy diffusivity at a distance from the wall is of insignificant extent."

With the exception of the smooth-surface assumption, all of the Nusselt assumptions remain appropriate for all but extremely low Prandtl number fluids. Consequently these assumptions are again invoked. In addition, it is assumed that the wavy characteristics of the film at a given location may be described by asymptotic wavy-flow states predicted by the hydrodynamic model developed in Part I. This assumption implies that the presence of condensation or evaporation does not appreciably affect the hydrodynamic characteristics of the film. It also implies that the wavy film is adequately described by its asymptotic state at every flow location or, equivalently, for every local Reynolds number. For the moderate heat rates

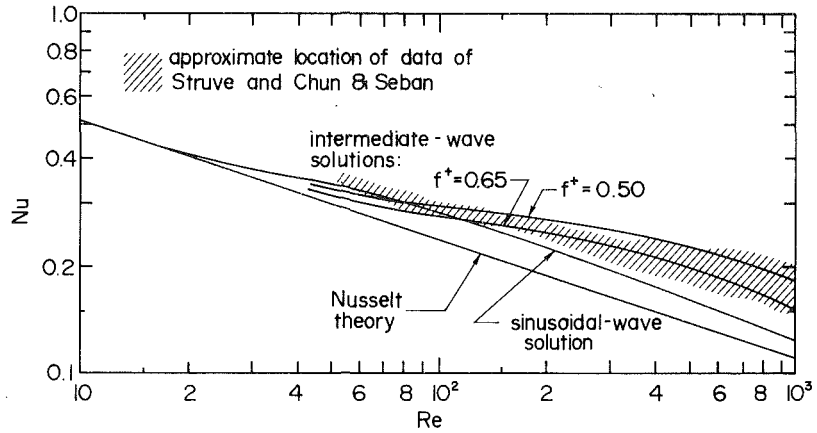

Fig. 4 Local Nusselt number predicted by present model ($\Gamma = 3450$) compared with laminar film evaporation data

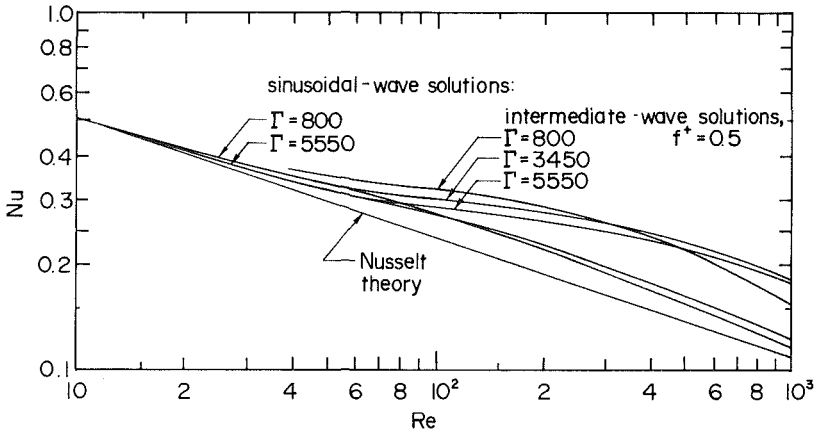

Fig. 5 The effect of surface tension parameter Γ on predicted local Nusselt number

considered here, these assumptions appear to be quite reasonable. It may be noted that condensation and evaporation have, in fact, been shown to have stabilizing and destabilizing influences on the film, respectively [23, 24]. However, the effect is limited to low Re where the calculated wave amplitude and the corresponding wave effect on heat transfer rates turns out to be small.

Two asymptotic wavy-flow states were found with the hydrodynamic model in Part I. The first, characterized by roughly sinusoidal waves (here referred to simply as sinusoidal-waves) describes film characteristics in a region starting at the line of wave inception. The second, described by the intermediate-wave solution branch, represents the characteristics of the transient-region immediately following the sinusoidal waves. The intermediate-wave solutions are parameterized by relative wave frequency, f^+ (wave frequency normalized by that of most unstable wave as defined in Part I). Since wave frequency decreases in the flow direction, a decreasing f^+ implies locations further down the surface.

Consider the characteristics of this idealized condensing/evaporating film at a particular location on the flow surface. The time-average value of the heat flux at this location is equal to the average heat flux over a wavelength of the film at the same local Reynolds number.
Thus,

$$\mathrm{Nu} = \left(\frac{\nu^2}{g}\right)^{1/3} \frac{1}{\lambda} \int_0^{\lambda} \frac{dx_1}{\delta(x_1)} \tag{1}$$

The local film thickness $\delta(x_1)$ is available as the result of the hydrodynamic model from Part I. This thickness was represented as a Fourier series truncated after six harmonics with parameters Re and Γ. Consequently, the integration in (1) was performed numerically.

The results for local Nusselt number are displayed as a function of Re in Fig. 4 for $\Gamma = 3450$ (e.g., water at 20°C). The shaded areas of the figure show the approximate position of the experimental data which was displayed in more detail in Fig. 3. The solid-line curves are the calculated results based on the heat-transfer model. The sinusoidal and intermediate-wave results shown essentially cover the range in observed Nusselt number values. The various curves tend to converge as the Reynolds number is decreased. The sinusoidal solution essentially yields the smooth-film result just below a Reynolds number of 20. Above Re = 100, the curves slowly diverge, showing the influence of wave profile and mean film thickness. The sinusoidal solution predicts the smallest increase in heat-transfer rate. Above a Reynold's number of approximately 300, the sinusoidal solution underpredicts the data. This is evidently due to the decrease in length of the sinusoidal-wave region at these higher flow rates. The intermediate-wave solutions predict increasing heat transfer coefficients with decreasing wave frequency. As discussed in Part I, this decrease in wave frequency is associated with an increase in distance down the flow surface. For a given Reynolds number, the intermediate-wave solutions thus indicate an increase in heat transfer coefficient with increased distance down the surface. This trend is in complete agreement with the experimental data of Struve.

The effect of variation in the dimensionless surface-tension

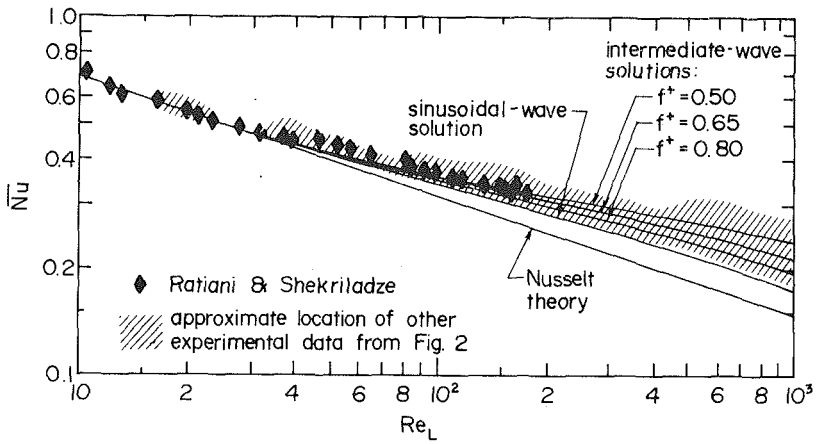

Fig. 6 Mean Nusselt number predicted by present model ($\Gamma = 3450$) compared with laminar film condensation data

parameter, Γ, is displayed in Fig. 5. Except at extremely high Reynolds number, a variation in Γ of 800 to 5550 results in a variation in Nusselt number on the order of 5–10 percent. At low and moderate film Reynolds numbers, smaller Γ values yield larger Nusselt numbers. This trend corresponds with the hydrodynamic model result that a larger amplitude is predicted for smaller Γ. This tendency does not persist at higher Reynolds numbers where the curve for $\Gamma = 800$ drops below the curves for the two larger values of Γ.

With the local heat-transfer results available, the average value for a condensing system may be determined. The average heat-transfer coefficient over length, L, may be defined as

$$\bar{h} = \frac{1}{L}\int_0^L h(x_1)dx_1 \tag{2}$$

However, the predicted local heat-transfer coefficient is available as a function of Re (or, equivalently, flow rate, $\dot{m}$), not x_1. Therefore, consider an energy balance on an element of the film which yields

$$h\Delta T dx_1 = h_{fg} d\dot{m}$$

Considering h as a function of x_1, assuming a constant ΔT, and integrating over L with $\dot{m} = 0$ at $x_1 = 0$ results in

$$\int_0^L h dx_1 = \frac{h_{fg}\dot{m}_L}{\Delta T} \tag{3}$$

Integration considering h as a function of $\dot{m}$ leads to

$$L = \frac{h_{fg}}{\Delta T}\int_0^{\dot{m}_L} \frac{d\dot{m}}{h} \tag{4}$$

Substituting (3) and (4) into (2) yields in dimensionless form

$$\overline{\mathrm{Nu}} = \frac{\mathrm{Re}_L}{\displaystyle\int_0^{\mathrm{Re}_L} \frac{d\mathrm{Re}}{\mathrm{Nu}(\mathrm{Re})}} \tag{5}$$

The average Nusselt number for laminar film condensation on an isothermal wall over a length, L, was determined based on (5).

Ideally, the local Nusselt number appearing in the integrand of (5) should be characteristic of the local flow regime. That is, Nu(Re) should be representative of the smooth, sinusoidal or transition (intermediate-wave) regimes as they occur in turn along the flow length. Such a specification of regime type is beyond the scope of the hydrodynamic model. Consequently, the integration in (5) was performed utilizing results for a particular asymptotic solution throughout the Re range of integration. This is not a serious deficiency since both the sinusoidal and intermediate-wave results converge to the smooth film result for decreasing Re. The results for $\Gamma = 3450$ are shown in Fig. 6, along with shaded areas indicating the range of the experimental data of Fig. 2. The individual data points of Ratiani and Shekriladze [13] are also reproduced since this data set spans the entire range of Re from 10 to 200. The sinusoidal solution again appears to provide a lower limit to the data. The intermediate-wave results fall within the data band throughout the Reynolds number range.

Concluding Remarks

The results of the heat-transfer model incorporating wave effects are consistent with published experimental condensation and evaporation data. Heat-transfer coefficients of these systems are demonstrated to be significantly enhanced over the smooth-film Nusselt prediction due to the presence of waves on the film surface. The trend of the degree of enhancement as a function of Reynolds number also agrees with that of the experimental data. Finally, results of the analysis are consistent with the observed trend in Struve's [16] data for local evaporation with various flow lengths; i.e., an increase in heat-transfer coefficient for longer flow lengths at a given Reynolds number.

Acknowledgment

The work reported herein was supported in part by the National Science Foundation.

References

1 Nusselt, W., "Die Oberflachenkondensation des Wasserdampfes," *Zeitschrift Verein Deutscher Ingenieure*, Vol. 60, 1916, pp. 541–546 and 569–575.

2 Schrage, R. W., *A Theoretical Study of Interphase Mass Transfer*, Columbia University Press, New York, 1953.

3 Merte, H., "Condensation Heat Transfer," in *Advances in Heat Transfer*, edited by I. Irvine and J. Hartnet, Vol. 9, Academic Press, New York, 1973.

4 Van der Walt, J., and Kroger, D., "Heat Transfer Resistances during Film Condensation," *Proceedings of the Fifth International Heat Transfer Conference*, Vol. 3, 1974, pp. 284–288.

5 Minkowycz, W. J., and Sparrow, E. M., "Condensation Heat Transfer in the Presence of Noncondensables, Interfacial Resistance, Superheating, Variable Properties, and Diffusion," *International Journal of Heat and Mass Transfer*, Vol. 9, 1966, pp. 1125–1144.

6 Rohsenow, W. M., "Heat Transfer and Temperature Distribution in Laminar Film Condensation," *Transactions of the American Society of Mechanical Engineers*, Vol. 78, 1956, pp. 1645–1648.

7 Sparrow, E. M., and Gregg, J. L., "A Boundary-Layer Treatment of Laminar Film Condensation," ASME JOURNAL OF HEAT TRANSFER, Vol. 81, 1959, pp. 13–18.

8 Chun, K. R. and Seban, R. A., "Heat Transfer to Evaporating Liquid Films," ASME JOURNAL OF HEAT TRANSFER, Vol. 93, 1971, pp. 391–396.

9 McAdams, W. H., *Heat Transmission*, McGraw-Hill, New York, 1954.

10 Kutateladze, S. S., and Gogonin, I. I., "Heat Transfer in Film Condensation of Slowly Moving Vapour," *International Journal of Heat and Mass Transfer*, Vol. 22, 1979, pp. 1593–1599.

11 Shea, F. L., and Krase, N. W., "Drop-Wise and Film Condensation of Steam," *Transactions of the American Institute of Chemical Engineers*, Vol. 36, 1940, pp. 463–487.

12 Slegers, L., and Seban, R. A., "Nusselt Condensation of n-Butyl Alcohol," *International Journal of Heat and Mass Transfer*, Vol. 12, 1969, pp. 237–239.

13 Ratiani, G. V., and Shekriladze, I. G., "An Experimental Study of the Heat Exchange Process on Transition from Laminar to Turbulent Flow of the Film," *Thermal Engineering*, Vol. 11, No. 3, 1964, pp. 101–103.

14 Gregorig, R., Kern, J., and Turek, K., "Improved Correlation of Film Condensation Data Based on a More Rigorous Application of Similarity Parameters," *Warme-und Stoffubertragung*, Vol. 7, 1974, pp. 1–13.

15 Selin, G., "Heat Transfer by Condensing Pure Vapours Outside Inclined Tubes," *International Developments in Heat Transfer, Proceedings of the Heat Transfer Conference* (Part II), University of Colorado, Boulder, 1961, pp. 279–289.

16 Struve, H., "Heat Transfer to an Evaporating Falling Refrigerant Film," paper presented at the 12th Congress of the International Institute of Refrigeration, Madrid, 1967.

17 Unterberg, W., and Edwards, D. K., "Evaporation from Falling Saline Water Films in Laminar Transitional Flow," *American Institute of Chemical Engineers Journal*, Vol. 11, 1965, pp. 1073–1081.

18 Kapitza, P. L., and Kapitza, S. P., "Wavy Flow of Thin Layers of a Viscous Fluid," *Collected Papers of P. L. Kapitza*, Vol. 2, Pergamon, New York, 1965, pp. 662–709.

19 Kapitza, P. L., "Heat Conductivity and Diffusion in a Liquid Medium under Periodic Flow Conditions," *Collected Papers of P. L. Kapitza*, Vol. 2, Pergamon, New York, 1965, pp. 743–757.

20 Chung, D. K., and Mills, A. F., "Experimental Study of Gas Absorption into Turbulent Falling Films of Water and Ethylene Glycol-Water Mixtures," *International Journal of Heat and Mass Transfer*, Vol. 19, 1976, pp. 51–59.

21 Kamei, S., and Oishi, J., *Memorandum of the Faculty of Engineering*, Vol. 17, Kyoto University, 1956, pp. 277–289.

22 Ueda, T., and Tanaka, H., "Measurements of Velocity, Temperature and Velocity Fluctuation Distribution in Falling Liquid Films," *International Journal of Multiphase Flow*, Vol. 2., 1975, pp. 261–272.

23 Unsal, M., and Thomas, W. C., "Nonlinear Stability of Film Condensation," ASME JOURNAL OF HEAT TRANSFER, Vol. 93, 1980, pp. 483–488.

24 Kocamustafaogullari, G., and Zuber, N., "The Effects of Heat and Mass Transfer on the Dynamics of Film Flow," AIChE Paper, 20th National Heat Transfer Conference, Milwaukee, Wis., Aug. 1981.

Heat Transfer From Vertical/Inclined Boundaries of Heat-Generating Boiling Pools[1]

T. C. Chawla
Reactor Analysis and Safety Division,
Argonne National Laboratory,
Argonne, Ill 60439
Mem. ASME

S. H. Chan
Professor and Chairman,
Department of Mechanical Engineering,
University of Wisconsin-Milwaukee,
Milwaukee, Wis. 53201

A model for heat transfer from the sides of a volume heated boiling pool is proposed. Because of the density difference caused by volume boiling and by thermal expansion due to the temperature difference between the bulk fluid and the fluid near the wall, the lighter liquid and vapor bubbles cause movement of the bulk fluid in the upward direction. The rising liquid between the bubbles finds a return path along the walls or sides of the pool and forms a boundary layer which may be laminar in its initial length followed by transition to turbulent depending, of course, on the conditions prevailing at the entry to the sides and in the bulk of the pool. The analysis for the laminar case provides the definition of equivalent Grashof number for the combined two-phase and thermal expansion driven natural convection along the sides of pool. The turbulent boundary layer is analyzed by assuming a two-layer model in which the inner layer is characterized by viscous and conduction terms and the outer by mean convection terms. The similarity analysis of the governing equations yields universal profiles for temperature and velocity and the scaling laws for the inner and outer layers. An asymptotic matching of the temperature profile in the overlap region leads to a heat transfer law which correlates the available experimental data on volume heated boiling pools exceedingly well.

1 Introduction

The phenomenon of heat transfer from volumetrically heated boiling pools is of considerable interest in the analysis of a number of hypothetical accident scenarios for liquid metal cooled fast breeder reactors (LMFBRs) such as transition phase and post-accident heat removal (PAHR) [1]. The heat transfer from internally heated boiling pools is also of potential interest in chemical reactor engineering.

The initial experimental study of heat transfer from boiling pools with internal heat generation was carried out by Stein et al. [2]. Subsequently their work was extended with various refinements in an experiment by Gabor et al. [3]. Following this work was an experimental study by Gustavson et al. [4]. However, as pointed out by Green et al. [5], their measurements of the heat-transfer coefficient and the local void fraction suffered from large inaccuracies and differed substantially from the data reported by Gabor et al. [3]. With various refinements in Gustavson's experiment, Green et al. [5] obtained substantially more accurate data, both for heat transfer to vertical and inclined walls. In each of these studies, semiempirical correlations for the heat-transfer coefficient from side walls were presented. However, the mechanistic models proposed are very diverse and do not agree with each other. In addition, each of these models contains a number of free parameters.

The present analytical study proposes a mechanism for heat transfer from side walls and successfully attempts to correlate the heat-transfer data of both Gabor et al. [3] and Greene et al. [5].

2 Formulation of Model

Consider the schematic diagram of a volume-heated boiling pool as shown in Fig. 1 with vertical or inclined walls maintained at a uniform temperature, T_w, which is less than the temperature of the bulk fluid. Heat generation in the bulk of the fluid causes boiling and creates a density difference by both boiling and thermal expansion between the bulk fluid and the fluid near the wall. Buoyancy forces, acting both on the lighter liquid and vapor bubbles, cause an upward movement of the fluid in the bulk of the pool. Upon reaching the free surface, part of vapor escapes into the space above the pool and part condenses in the upper part of the pool, the rising liquid between the bubbles and that condensed in the upper part of the pool find a return path along the walls of the vessel and form a boundary layer which might be laminar or turbulent depending upon the conditions prevailing. The flow

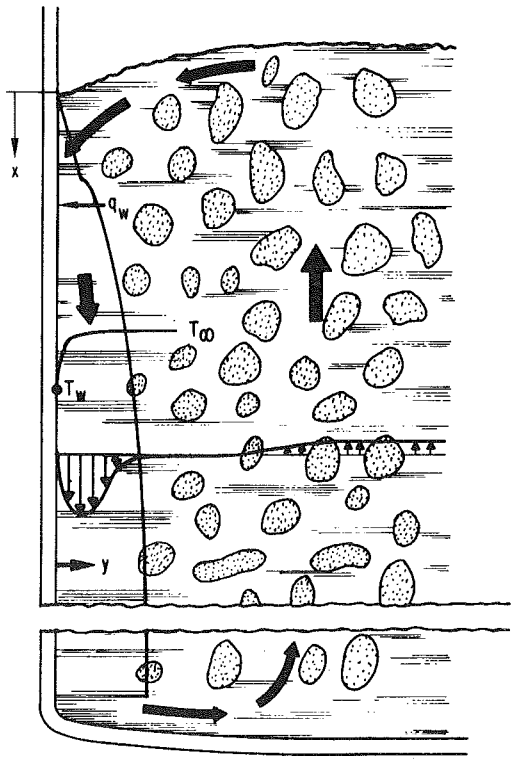

Fig. 1 Mechanistic model for heat transfer to the side walls from volume heated boiling pools

[1] Work supported by the U.S. Department of Energy.
Contributed by the Heat Transfer Division for publication in the JOURNAL OF HEAT TRANSFER. Manuscript received by the Heat Transfer Division June 1, 1981.

of the returning liquid outside of the boundary layer is assumed to have negligible velocity due to opposing motion of the two-phase flow in the bulk of the pool. It is thus proposed that the heat transfer to the side walls takes place entirely in the natural convection boundary layer driven by the density difference caused by boiling and thermal expansion.

In view of these assumptions, the equations governing the heat transfer and fluid flow in a turbulent boundary along a vertical or inclined wall in the spirit of the Boussinesq approximation can be written as [6]

$$\frac{\partial u}{\partial x} + \frac{\partial v}{\partial y} = 0, \tag{1}$$

$$\rho\left(u\frac{\partial u}{\partial x} + v\frac{\partial u}{\partial y}\right) = -\frac{\partial P}{\partial x} + \mu\frac{\partial^2 u}{\partial y^2} + \rho\frac{\partial}{\partial y}(-\overline{u'v'}) + \rho\bar{g} \tag{2}$$

$$u\frac{\partial T}{\partial x} + v\frac{\partial T}{\partial y} = \lambda\frac{\partial^2 T}{\partial y^2} + \frac{\partial(-\overline{v'T'})}{\partial y} + \frac{\dot{q}}{\rho C_p} \tag{3}$$

We may note that Boussinesq approximation for free-convection flows consists of a two-part approximation: (*a*) it neglects all variable property effects in the three equations except for density variation in the momentum equation, and (*b*) it approximates this density through a simplified equation of state:

$$\rho = \rho_{l\infty} - \rho\beta(T - T_\infty) \tag{4}$$

Boundary layer simplifications of the full Reynolds equations for turbulent flow imply that the pressure is a function of x only. Further, we may assume that the two-phase flow in the bulk of fluid is moving upward at very low mixture velocities and that the void fraction and velocity field are approximately independent of the coordinate parallel to the sides of the pool (that is, approximately fully developed conditions prevail over most of the height of the boiling pool). In actuality, as seen in the measurements by Gustavson et al. [4], the void fraction is dependent on height x near the bottom of the pool, but it very rapidly achieves a near asymptotic value with the increasing height. Under these assumptions, the momentum equation (2) for the bulk fluid simplifies to

$$0 = -\frac{dP}{dx} + \rho_\infty\bar{g} \tag{5}$$

with

$$\rho_\infty = \alpha\rho_g + (1-\alpha)\rho_{l\infty} \tag{6}$$

In view of equations (4) through (6), the combined pressure gradient and gravity term in equation (2) become:

$$-\frac{dP}{dx} + \rho\bar{g} = (\rho - \rho_\infty)\bar{g} = [\rho\beta(T_\infty - T) + \alpha(\rho_{l\infty} - \rho_g)]\bar{g} \simeq (\rho\beta\Delta T + \alpha\rho_{l\infty})\bar{g} \tag{7}$$

where we have assumed that $\rho_{l\infty} >> \rho_g$. Substituting equation (7) in equation (2) and dividing through by the density ρ, we obtain

$$u\frac{\partial u}{\partial x} + v\frac{\partial u}{\partial y} = \nu\frac{\partial^2 u}{\partial y^2} + \frac{\partial(-\overline{u'v'})}{\partial y} + (\beta\Delta T + \alpha)\bar{g} \tag{8}$$

where we assumed in the spirit of Boussinesq's approximation that $\rho_{l\infty}/\rho \simeq 1$. The boundary conditions on equations (1), (3), and (8) are

$$u, v = 0,\ T = T_w \text{ at } y = 0 \tag{9a}$$

$$u, v = 0\ T = T_\infty \text{ at } y = \delta \tag{9b}$$

In writing down equations (9*b*), we have assumed that the momentum and thermal boundary layers are of equal thickness. This assumption is valid for moderate Prandtl number fluids of interest to the present study.

3 Integral Method of Analysis for Laminar Flow

For a Grashof number, $Gr \leq 10^9$, the flow in the boundary layer generally is laminar. For moderate Prandtl number fluids the transition to turbulent flow occurs between $Gr = 10^9$ to 10^{10} [7]. Almost all the data available for boiling pools are in the turbulent regime. However, in some LMFBR safety applications, both prior to boiling and at very low void fractions during boiling, a laminar flow regime may prevail. Furthermore, at low Grashof numbers, the volumetric heat source, particularly in the single phase molten pools, may significantly affect the rate of heat transfer to the side walls,

Nomenclature

A_k = coefficients of expansion for characteristic velocity in the laminar boundary layer
A_T = integration constant in equation (56*a*)
A_u = integration constant in equation (55*a*)
B_k = coefficients of expansion for boundary layer thickness for laminar flows
B_T = integration constant in equation (56*b*)
B_u = integration constant in equation (55*b*)
C_p = specific heat at constant pressure
F' = $(u - U_m)/u_0$, velocity profile for outer layer
f' = u/U_I, velocity profile for inner layer
G = nondimensional turbulent shear stress
Gr_L = $(\beta\Delta T_w + 3\alpha)\bar{g}L^3/\nu^2$, Grashof number based on characteristic length, L
Gr_x = Grashof number based on characteristic length, x
$\bar{g}$ = $g\cos\gamma$, effective gravitational acceleration
g = acceleration due to gravity
H = nondimensional total buoyancy function
h = heat-transfer coefficient
K = thermal conductivity of liquid
L = characteristic length scale in x direction
m = exponent in expansion (25*a*) for characteristic velocity
n = exponent in expansion (25*b*) for boundary layer thickness
Nu_x = hx/K, Nusselt number based on length, x
Nu = $\overline{\mathrm{Nu}}_x$, Nusselt number based on average heat-transfer coefficient
Nu_{ox} = Nusselt number in the absence of internal heat generation
Pr = $\mu C_p/K$, Prandtl number
P = pressure
q_w = wall heat flux
$\dot{q}$ = volumetric heat generation rate
Ra = PrGr, Rayleigh number
Ra_p = $\mathrm{Ra}/[1 + (0.492/\mathrm{Pr})^{9/16}]^{16/9}$
T = temperature
T' = turbulent fluctuations in temperature, T
ΔT = $T_\infty - T$
ΔT_w = $T_\infty - T_w$
U = characteristic velocity in x direction in laminar boundary layer
U_0, U_1, U_2 = first, second and third order nondimensional velocities in the expansion of U^*
U_m = the velocity maximum

as was found by Randall and Sesonski [8]. To proceed with the analysis for the laminar case of boiling pools, we adopt the combination of integral and perturbation methods utilized by Randall and Sesonski [8].

For laminar flow in the boundary layer we drop the turbulent diffusion terms in equations (8) and (3) and integrate these equations together with equations (1) and (9), over the boundary layer thickness to obtain

$$\frac{\partial}{\partial x}\int_0^\delta u^2 dy = \tilde{g}\beta\int_0^\delta (T_\infty - T)\,dy + \tilde{g}\alpha\delta - \nu\left(\frac{\partial u}{\partial y}\right)_{y=0} \tag{10}$$

$$\frac{\partial}{\partial x}\int_0^\delta u(T_\infty - T)\,dy = -\lambda\left[\frac{\partial (T_\infty - T)}{\partial y}\right]_{y=0} - \frac{\dot{q}\delta}{\rho C_p} \tag{11}$$

Assuming the following profiles for velocity and temperature:

$$\frac{u}{U} = \eta(1-\eta)^2,\ \theta = \frac{T_\infty - T}{T_\infty - T_w} = (1-\eta)^2 \tag{12}$$

reduces equations (10) and (11) to

$$\frac{1}{105}\frac{d(\delta U^2)}{dx} = \frac{\delta}{3}(\beta\Delta T_w + 3\alpha)]g - \frac{\nu U}{\delta} \tag{13}$$

and

$$\frac{1}{30}\frac{d(\delta U)}{dx} = \frac{2\lambda}{\delta} - \frac{\dot{q}\delta}{\rho C_p \Delta T_w} \tag{14}$$

Nondimensionalizing the above equations by introducing the following nondimensional variables: $\delta^* = \delta/\delta_s$, $x^* = x/L$, $U^* = U/U_s$, we obtain

$$\frac{1}{105}\frac{dU^{*2}\delta^*}{dx^*} = \frac{\delta^*}{3U_s^2}(\beta\Delta T + 3\alpha)\tilde{g}L - \frac{\nu L}{U_s\delta_s^2}\left(\frac{U^*}{\delta^*}\right) \tag{15}$$

$$\frac{1}{30}\frac{dU^*\delta^*}{dx^*} = \frac{2\lambda L}{U_s\delta_s^2\delta^*} - \frac{\dot{q}L}{\rho C_p \Delta T_w U_s}\delta^* \tag{16}$$

If we choose the following scales

$$U_s = \sqrt{(\beta\Delta T_w + 3\alpha)\tilde{g}L},\ \delta_s = \left(\frac{\nu L}{U_s}\right)^{1/2} = \frac{L}{\mathrm{Gr}_L^{1/4}} \tag{17a}$$

and the perturbation parameter ϵ as

$$\epsilon = \frac{\dot{q}L}{\rho C_p \Delta T_w[(\beta\Delta T_w + 3\alpha)\tilde{g}L]^{1/2}} \tag{17b}$$

then in the limit as $\epsilon \to 0$ we have

$$\frac{1}{105}\frac{dU^{*2}\delta^*}{dx^*} = 0(1),\ \frac{\delta^*}{3} = 0(1),\ \frac{U^*}{\delta^*} = 0(1) \tag{18}$$

With the choice of scales given by equation (17), equation (15) and (16) become

$$\frac{1}{105}\frac{dU^{*2}\delta^*}{dx^*} = \frac{\delta^*}{3} - \frac{U^*}{\delta^*} \tag{19}$$

$$\frac{1}{30}\frac{dU^*\delta^*}{dx^*} = \frac{2}{\mathrm{Pr}}\frac{1}{\delta^*} - \epsilon\delta^* \tag{20}$$

The effect of internal heat generation in the boundary layer will be included through the perturbation parameter, ϵ. It will be demonstrated subsequently that $\epsilon << 1$ both for reactor applications and for the experiments performed to obtain boiling pool heat-transfer data. However, in reactor applications, ϵ has a much bigger value than that for the experiments.

Seeking solution of equations (19) and (20) in the form

$$U^* = \sum_{k=0}^{\infty}\epsilon^k U_k,\ \delta^* = \sum_{k=0}^{\infty}\epsilon^k \delta_k \tag{21}$$

Substituting the above expansions into equations (19) and (20) and equating terms of like coefficients up to ϵ^2 we obtain

$$\epsilon^0: \quad \frac{1}{105}\frac{dU_0^2\delta_0}{dx^*} = \frac{\delta_0}{3} - \frac{U_0}{\delta_0} \tag{22a}$$

$$\frac{1}{30}\frac{dU_0\delta_0}{dx^*} = \frac{2}{\mathrm{Pr}}\frac{1}{\delta_0} \tag{22b}$$

$$\epsilon^1: \quad \frac{1}{105}\frac{d}{dx^*}(U_0^2\delta_1 + 2U_0U_1\delta_0) = \frac{\delta_1}{3} - \left(\frac{U_1}{\delta_0} - \frac{U_0\delta_1}{\delta_0^2}\right) \tag{23a}$$

Nomenclature (cont.)

u = x component of mean velocity in the boundary layer
u' = turbulent fluctuations in u component
u_T = velocity sale for turbulent fluctuations in the outer layer
v = y component of mean velocity in the boundary layer
v' = turbulent fluctuations in v component
x = coordinate in direction parallel to the wall from the top of pool
y = coordinate in direction normal to the wall
y^* = y/Λ, dimensionless inner variable
α = void fraction in the boiling pool
β = thermal expansion coefficient
γ = angle of inclination of the walls or sides of the pool from vertical direction
δ = boundary layer thickness
$\delta_0, \delta_1, \delta_2$ = first-, second-, and third-order nondimensional boundary layer thickness in the expansion for δ^*
ϵ = perturbation parameter defined by equations (17b) and (32)
ϵ_m = perturbation parameter defined by equation (32)
η = y/δ, dimensionless outer variable
θ = $(T - T_w)/T_l$
κ_1 = universal constant in velocity profile (55)
κ_2 = universal constant in temperature profile (56)
λ = $K/\rho C_p$, thermal diffusivity
μ = dynamic viscosity
ν = kinematic viscosity
ρ = fluid density
Φ_w = $q_w/\rho C_p$, scale for turbulent heat flux
ϕ = nondimensional turbulent flux in the boundary layer
Ψ = $(T - T_\infty)/T_0$

Subscripts

0 = pertaining to outer layer
∞ = pertaining to bulk fluid properties
I = pertaining to inner layer
g, v = pertaining to vapor phase
l = pertaining to liquid phase
s = pertaining to characteristic scale
w = pertaining to a wall

Superscripts

* = pertaining to nondimensional variables

$$\frac{1}{30}\frac{d}{dx^*}(U_0\delta_1+U_1\delta_0)=-\frac{2}{\mathrm{Pr}}\frac{\delta_1}{\delta_0^2}-\delta_0 \tag{23b}$$

$$\epsilon^2:\quad \frac{1}{105}\frac{d}{dx^*}(\delta_0U_1^2+2\delta_0U_0U_2+2U_0\delta_1U_1+U_0^2\delta_2)$$

$$=\frac{\delta_2}{3}-\left(\frac{U_2}{\delta_0}-\frac{U_1\delta_1}{\delta_0^2}+\frac{U_0\delta_1^2}{\delta_0^3}-\frac{U_0\delta_2}{\delta_0^2}\right) \tag{24a}$$

$$\frac{1}{30}\frac{d}{dx^*}(\delta_0U_2+\delta_1U_1+U_0\delta_2)=-\frac{2}{\mathrm{Pr}}$$

$$\left(\frac{\delta_2}{\delta_0^2}-\frac{\delta_1^2}{\delta_0^3}\right)-\delta_1 \tag{24b}$$

We assume a solution of the form

$$U_k=A_kx^{*k/2}x^{*m} \tag{25a}$$

$$\delta_k=B_kx^{*k/2}x^{*n} \tag{25b}$$

The substitution of equations (25) in equations (22) yields,

$$m=\tfrac{1}{2},\ n=\tfrac{1}{4},\ A_0=\sqrt{(80/3)}\left(\frac{20}{21}+\mathrm{Pr}\right)^{-\frac{1}{2}} \tag{26a}$$

$$B_0=\mathrm{Pr}^{-\frac{1}{2}}\left[240\left(\frac{20}{21}+\mathrm{Pr}\right)\right]^{\frac{1}{4}} \tag{26b}$$

The substitution of equations (25) in equations (23) yields,

$$A_1=\frac{24(60\,A_0+20\,B_0^2-A_0^2B_0^2)}{(2\,A_0B_0^2+60)B_0b_0},\quad B_1=24/b_0 \tag{27a}$$

$$b_0=\frac{A_0^2B_0^2-20\,B_0^2-60\,A_0}{(2\,A_0B_0^2+60)B_0}-\frac{A_0}{B_0}-\frac{48}{B_0^3\mathrm{Pr}} \tag{27b}$$

The use of equations (25) in equations (24) gives,

$$A_2=-\left(\frac{A_0}{B_0}+\frac{240}{7\mathrm{Pr}}\frac{1}{B_0^3}\right)\frac{b_R}{b_L}$$

$$+\left(\frac{240}{7\mathrm{Pr}}\frac{B_1^2}{B_0^4}-\frac{120\,B_1}{7\,B_0}-\frac{B_1A_1}{B_0}\right) \tag{28a}$$

$$B_2=\frac{b_R}{b_L},b_L=\left(\frac{3}{140}A_0^2-\frac{A_0}{B_0^2}-\frac{1}{3}\right)$$

$$-\left(\frac{3}{70}B_0A_0+\frac{1}{B_0}\right)\left(\frac{A_0}{B_0}+\frac{240}{7\mathrm{Pr}}\frac{1}{B_0^3}\right) \tag{28b}$$

$$b_R=\frac{A_1B_1}{B_0^2}-\frac{A_0B_1^2}{B_0^3}-\frac{3}{140}(B_0A_1^2+2A_0B_1A_1)-$$

$$-\left(\frac{3}{70}B_0A_0+\frac{1}{B_0}\right)\left(\frac{240}{7\mathrm{Pr}}\frac{B_1^2}{B_0^4}-\frac{120B_1}{7B_0}-\frac{B_1A_1}{B_0}\right) \tag{28c}$$

Reference 1 tabulates the values of coefficients A_k and B_k as a function of Prandtl number, Pr. The selection of the range of Pr variation was made to cover values of interest to nuclear reactor safety analysis and the experiments performed on boiling pools. Using equations (25) and (26*a*) in equation (21), we obtain the following three term expansions:

$$U^*=A_0x^{*\frac{1}{2}}+\epsilon A_1x^*+\epsilon^2A_2x^{*3/2} \tag{29a}$$

$$\delta^*=B_0x^{*\frac{1}{4}}+\epsilon B_1x^{*\frac{3}{4}}+\epsilon^2B_2x^{*5/4} \tag{29b}$$

It was found [1] that numerical values of coefficients A_1, A_2 (only for $\mathrm{Pr}\le 3.0$), and B_1 are negative, and it is then clear that the volumetric heat source both tends to decrease the characteristic (e.g., maximum) velocity as well as the boundary layer thickness. The effect of this behavior on the heat transfer coefficient is evaluated below.

Heat-Transfer Coefficient. From the definition of the Nusselt number and equations (12), (17*a*), (26), and (29), we get

$$\mathrm{Nu}_x=\frac{q_wx}{K(T_w-T_\infty)}=\frac{2x}{\delta}=\frac{2B_0'\mathrm{Ra}_x^{\frac{1}{4}}}{1+\epsilon_mB_1'\mathrm{Ra}_x^{1/6}+\epsilon_m^2B_2'\mathrm{Ra}_x^{\frac{1}{3}}} \tag{30a}$$

where

$$B_0'=\mathrm{Pr}^{\frac{1}{4}}\left[240\left(\frac{20}{21}+\mathrm{Pr}\right)\right]^{-\frac{1}{4}},\ B_1'=B_1\mathrm{Pr}^{\frac{1}{3}}$$

$$\left[240\left(\frac{20}{21}+\mathrm{Pr}\right)\right]^{-\frac{1}{4}} \tag{30b}$$

$$B_2'=B_2\mathrm{Pr}^{1/6}\left[240\left(\frac{20}{21}+\mathrm{Pr}\right)\right]^{-\frac{1}{4}} \tag{30c}$$

$$\epsilon_m=\frac{\nu^{\frac{1}{3}}}{[(\beta\Delta T_w+3\alpha)\,\bar{g}]^{\frac{1}{3}}}\frac{\dot{q}}{\rho C_p\Delta T_w} \tag{30d}$$

$$\mathrm{Ra}_x=\mathrm{PrGr}_x,\ \mathrm{Gr}_x=(\beta\Delta T_w+3\alpha)\,\bar{g}x^3/\nu^2 \tag{30e}$$

From the definition of ϵ_m and equation (17*b*), it is clear that $\epsilon_m=\epsilon$ if the length scale L is chosen as

$$L=\frac{\nu^{\frac{2}{3}}}{[(\beta\Delta T_w+3\alpha)\,\bar{g}]^{\frac{1}{3}}} \tag{31a}$$

With the above choice of the length scale, L, U_s, and δ_s as given by equations (17*a*) become

$$U_s=[\nu(\beta\Delta T_w+3\alpha)\,\bar{g}]^{\frac{1}{3}},\ \delta_s=\frac{\nu^{\frac{2}{3}}}{[(\beta\Delta T_w+3\alpha)\,\bar{g}]^{\frac{1}{3}}} \tag{31b}$$

It is clear that with the choice of scales as given by equations (31) the requirement imposed by equation (18) on the order of various terms is still satisfied. With these scales it is evident that for the perturbation scheme to work, we must have

$$\epsilon=\epsilon_m=\frac{\nu^{\frac{1}{3}}}{[(\beta\Delta T_w+3\alpha)\,\bar{g}]^{\frac{1}{3}}}\frac{\dot{q}}{\rho C_p\Delta T_w}<<1 \tag{32}$$

Assuming that the above condition is satisfied, then in the limit as $\epsilon\to 0$, i.e., with negligible effect of internal heat generation, equation (30*a*) becomes

$$\mathrm{Nu}_x=2B_0'\mathrm{Ra}_x^{\frac{1}{4}}=0.508\,\mathrm{Pr}^{\frac{1}{4}}\left(\frac{20}{21}+\mathrm{Pr}\right)^{-\frac{1}{4}}\mathrm{Ra}_x^{\frac{1}{4}} \tag{33}$$

This is identical to the expression obtained by Squire [9] for temperature driven natural convection boundary layers provided, of course, an equivalent Grashof number (which hereafter will simply be referred to as a two-phase Grashof number) for the combined two-phase and temperature driven boundary layer is defined such as by equation (30*e*). These findings, however, cannot be verified directly by experimental data, as all experiments performed to date for two-phase driven boundary layers are for the case of turbulent flow, i.e., for $\mathrm{Gr}>10^9$. If, however, we can verify within the accuracy of the data available that a similar correspondence exists between the correlation for temperature driven turbulent boundary layers and for combined two-phase and temperature driven turbulent boundary layers, then one expects the above findings to be valid for laminar flow as well.

Since B_1 has a negative value [1], it is clear from equations (30*a*) and (30*b*) that internal heat generation tends to increase the heat-transfer coefficient by decreasing the thickness of the boundary layer. These findings, of course, are identical to those by Randall and Sesonski [8] for a temperature driven laminar boundary layer.

To illustrate the effect of internal heat generation on heat transfer in boiling pools, we choose two examples: one is that of boiling stainless steel in a molten reactor fuel, and the other

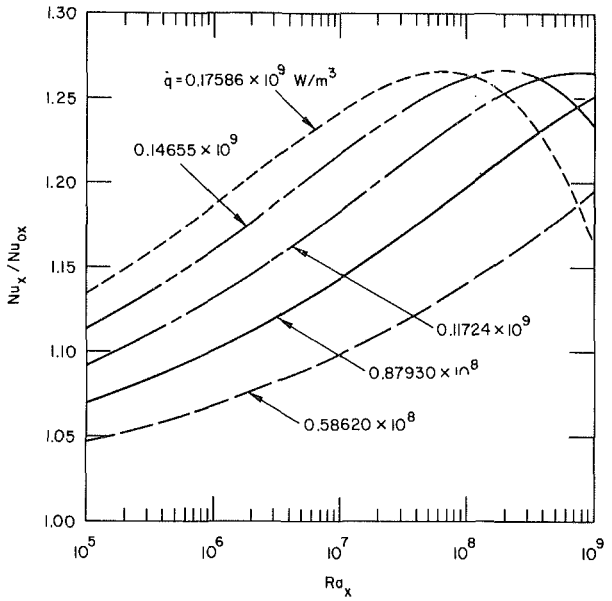

Fig. 2 Effect of internal heat generation on Nusselt number for laminar flow with $\alpha = 0.1$ and $\Delta T_w = 24$ K

is that of heat transfer in boiling of fuel alone in a molten pool of mixed oxide fuel. Both of these examples are of interest to transition phase analysis and PAHR in the LMFBR safety area. Figure 2 shows the plot of Nu_x/Nu_{ox} against the Rayleigh number, Ra_x, with $\alpha = 0.1$, $\Delta T_w = 24$ K, and internal heat generation $\dot{q}$ varying from 58.62×10^6 W/m³ (14 cal/cm³) to 175.86×10^6 W/m³ (42 cal/cm³). The ratio of the Nusselt numbers increases both as Ra_x and internal heat generation increase. However, this trend is interrupted when internal heat generation is high. For example, at $\dot{q} = 175.86 \times 10^6$ W/m³, the ratio first increases with Ra_x until about $Ra_x = 10^8$ and then begins to decrease with increasing Ra_x. This behavior can be understood by considering the competing terms in equation (30*a*). Over the range of $\dot{q}$ considered, $\epsilon (= \epsilon_m)$ varies from 2.11×10^{-3} to 6.33×10^{-3}. At low values of ϵ (i.e., low values of $\dot{q}$) the second term in the denominator having a negative value of B_1' (see equation (30*c*) and reference [1]) dominates the third term in the denominator having a positive value of B_2' even at high values of Ra_x. However, at high values of ϵ (i.e., high values of $\dot{q}$) the third term begins to compete with the second term at very high values of Ra_x (since it only contains one-third the power of Ra_x as against one-sixth the power in the second term). This behavior could also be achieved even at lower values of $\dot{q}$ if it were possible to assume the applicability of equation (30*a*) beyond 10^9. For example, at $\epsilon = 3.1659 \times 10^{-3}$ (i.e., $\dot{q} = 87.93 \times 10^6$ W/m³) and $Ra_x = 10^{11}$, equation (30*a*) gives the value of the Nusselt number ratio as 1.122 which is significantly less than the value of 1.25 at $R_{ax} = 10^9$ (see Fig. 2). This discussion, in turn, implies that at very high Rayleigh numbers characteristic of turbulent flow, the effect of internal heat generation both at low and high values of $\dot{q}$ would be significantly less than that for laminar flow. Furthermore, the boundary layer for turbulent flow is considerably thicker than that for laminar flow and temperature profile is significantly steeper near the wall than for laminar flow. It is therefore expected that the perturbation caused by internal heat generation on the boundary layer thickness and the temperature profile for turbulent flow will be relatively less significant than for laminar flow. In view of these comments, we will not consider the effect of internal heat generation for the case of turbulent flow to be treated later.

In the second example we consider the boiling of fuel with $\Delta T_w = 544$ K keeping all other parameters the same as in the first example. For these parameters, ϵ ranged from 8.83×10^{-5} to 2.65×10^{-4}. For these values of ϵ, a calculation with equation (30*a*) shows that the changes in h caused by internal heat generation are less than 3 percent. Therefore it is not necessary to include the effect of internal heat generation for the case of fuel boiling. (The properties utilized in these two examples were evaluated at $(T_w + T_\infty)/2$.) Corresponding to $\Delta T_w = 544$ K in this example, freezing of the fuel on the wall will take place. However, this process is extremely slow due to very poor conductivity of the frozen fuel crust and therefore there is negligible effect on the heat transfer due to this phase change. On the other hand, because of this freezing phenomenon, the boundary condition of constant temperature along the wall becomes very valid.

An assessment of the effect of internal heat generaton in the experiments of Gabor et al. [3] and Greene et al. [5] was also made. Both of these data sets, which we will be using in the subsequent analysis, are in the turbulent flow regime. The values of ϵ given by equation (32) are of $0(10^{-4})$, clearly indicating that the effect of internal heat generation was negligible in these experiments. It is interesting to note that the distance x during which the flow remains laminar in the illustrations considered above was less than 5 cm in both cases. This is very small compared to the depths of pools of interest. This in turn implies that the flow is turbulent over most of the depth of the pool.

4 Two-Layer Model of Turbulent Boundary Layers

The integral method utilized for laminar flow proved to be very successful (the error in the expression for Nusselt number is less than 6 percent from the exact analysis, see for example, reference [10]). However, this is not the case for turbulent flow next to a vertical surface. For example, the integral approach by Eckert and Jackson [11] predicts a two-fifths power law for the Rayleigh number in the expression for the Nusselt number, whereas the majority of the experimental data predicts a one-third power (see for example reference [12]). This discrepancy in their analysis arose because of the poor choice for the temperature profile [13].

An alternative approach is based on a two-layer model as in the case of forced flows [14]. George and Capp [15] have shown that the fully developed turbulent boundary layer in temperature driven natural convection consists of two regions: an outer region constituting most of the boundary layer in which viscous and conduction terms are negligible. They further identify that the inner region is a constant heat flux layer made up of two major subdivisions: an inner subregion consisting of a conductive and viscous sublayer existing right next to the wall in which velocity and temperature profiles are cubic and linear, respectively, and an outer subregion existing at the outer part of the constant heat flux layer is referred to as the buoyant sublayer. An asymptotic matching in the buoyant sublayer between the inner and outer layers yields velocity and temperature profiles which show the cube root and the inverse cube root dependence of distance from the wall, respectively. These universal similarity laws, in turn, yield asymptotic heat-transfer and friction laws. These predictions are seen to be in excellent agreement with the existing experimental data.

In the present analysis we will extend the two-layer model of George and Capp [15] to combined temperature and two-phase buoyancy driven turbulent boundary layers existing next to the sides of boiling pools. Because of the presence of two-phase buoyancy forces originating outside the boundary layer, the majority of the scaling laws are distinctly different from those arrived at by George and Capp on dimensional grounds. We will obtain the scaling laws formally from the required governing equations by assuming separate similarity solutions for the inner and the outer layers.

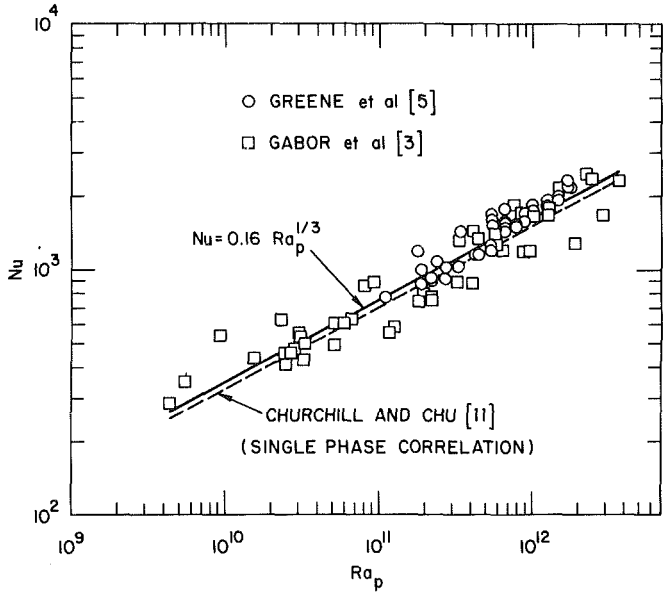

Fig. 3 Correlation of average heat-transfer coefficient data of Gabor et al. [3] and Greene et al. [5]

Scaling of Buoyancy Term. The choice of a scale for the buoyancy term $(\beta\Delta T + \alpha)\bar{g}$ in equation (8) requires very special consideration. In the turbulent boundary layer driven by temperature difference alone, the inner and outer scales for the buoyancy term are clearly determined by the choices for temperature scales for the two layers. However, for the case of two-phase driven flows the buoyancy contribution $\alpha\bar{g}$ being generated outside the boundary layer remains invariant both in the inner and the outer layers. Hence, for this contribution to survive in the momentum equations governing the inner and the outer layers, we must use the same scale for the two layers. In the inner layer, however, where most of the temperature drop occurs (this follows from the analogy with the forced convection), it is clear that $\Delta T = 0(\Delta T_w)$, and hence $(\beta\Delta T + \alpha) = 0(\beta\Delta T_w + 3\alpha)$, where a factor of 3 for α is preserved by analogy with the laminar case with an aim to show an equivalence between the two-phase driven flows and those driven by thermal expansion alone. In the analysis to follow, we will show that $\Delta T << \Delta T_w$ for the outer layer. Thus, so long as $\alpha > \beta\Delta T_w/3$, we can continue to use the *same scale as used for the inner layer, namely,* $\beta\Delta T_w + 3\alpha$, since $(\beta\Delta T + \alpha) = 0(\beta\Delta T_w + 3\alpha)$.

The Inner Layer. Let us assume a similarity solution of the form:

$$u = U_I f'(y/\Lambda,\mathrm{Pr}),\ T - T_w = T_I\theta(y/\Lambda,\mathrm{Pr}) \tag{34a}$$

$$-\overline{u'v'} = u_s^2 G_I(y/\Lambda,\mathrm{Pr}),\ -\overline{v'T'} = \Phi_I\phi_I(y/\Lambda,\mathrm{Pr}) \tag{34b}$$

$$\beta\Delta T + \alpha = (\beta\Delta T_w + 3\alpha)H_I(y/\Lambda,\mathrm{Pr}) \tag{34c}$$

where $H_I = B_v + \epsilon_I(1-\theta)$, $B_v = \alpha/(\beta\Delta T_w + 3\alpha)$, $\epsilon_I = \beta\Delta T_w/(\beta\Delta T_w + 3\alpha)$. Here we have used the fact that $T_I = \Delta T_w$. In the case of temperature driven boundary layers, George and Capp [15] have amply verified the existence of the above similarity solutions for temperature and velocity by comparing with the existing experimental data. Substituting equations (34) in equations (1), (8), and (3), we obtain

$$\frac{\Lambda}{U_I}\frac{dU_I}{dx}(f'^2 - ff'') - \frac{d\Lambda}{dx}ff'' = \frac{\nu}{U_I\Lambda}f''' + \frac{u_s^2}{U_I^2}G_I' + \frac{(\beta\Delta T_w + 3\alpha)\bar{g}\Lambda}{U_I^2}H_I \tag{35a}$$

$$\frac{\Lambda}{T_I}\frac{dT_I}{dx}f'\theta - \left(\frac{d\Lambda}{dx} + \frac{\Lambda}{U_I}\frac{dU_I}{dx}\right)f\theta' = \frac{\lambda}{\Lambda U_I}\theta'' + \frac{\Phi_I}{U_I T_I}\phi_I' \tag{35b}$$

In the light of earlier discussions, we have dropped the internal heat generation term from the energy equation. Since molecular and turbulent diffusion (of both momentum and heat) terms must be retained in the inner layer, we choose

$$\Lambda = \lambda/U_I,\ \Phi_I = T_I U_I,\ u_s = U_I \tag{36}$$

For the buoyancy terms to be of the same order as the diffusion terms, it is clear that

$$U_I = [(\beta\Delta T_w + 3\alpha)\bar{g}\Lambda]^{1/2} = [(\beta\Delta T_w + 3\alpha)\bar{g}\lambda]^{1/3} \tag{37a}$$

with

$$\Lambda = \lambda/U_I = \lambda^{2/3}/[(\beta\Delta T_w + 3\alpha)\bar{g}]^{1/3} \tag{37b}$$

$$T_I = \Lambda\Phi_I/\lambda = \Delta T_w \tag{37c}$$

In the above choice for the length scale Λ, it is implicit that $\mathrm{Pr} = 0(1)$. In the above selection for various scales, it is clear that U_I, Λ, T_I, and Φ_I are not a function of x, hence equations (35) simplify to

$$0 = \mathrm{Pr}f''' + G_I' + H_I \tag{38a}$$

$$0 = \theta'' + \phi' \tag{38b}$$

The integration of equation (38*b*) together with the use of equation (37) yields

$$\theta' + \phi_I = -\frac{q_w}{\rho C_p \Phi_I} \tag{39}$$

From the above equation it is clear that Φ_I must be chosen as

$$\Phi_I = \frac{q_w}{\rho C_p} \tag{40}$$

Equations (37) imply that Φ_I is a constant; therefore, the above choice for Φ_I will be valid only if q_w is constant. This assumption is borne out by data for boundary layers driven by temperature difference alone. They show that $\mathrm{Nu}_x \sim \mathrm{Ra}_x^{1/3}$ (see for example reference [12]) which implies that $h = q_w/(T_w - T_\infty)$ is independent of position x; hence, for constant wall temperature q_w is also constant. It is thus clear from equation (39) that the inner layer is a constant heat flux layer. In the outer layer the heat flux varies from its maximum value q_w at its inner edge to a value of zero at the outer edge. It then follows that the scale Φ_0 for the heat flux in the outer layer is also given by equation (40), that is,

$$\Phi_0 = \frac{q_w}{\rho C_p} \tag{41}$$

Outer Layer. For the outer layer, by analogy to the force convection case, we assume the similarity to be of the form:

$$(u - U_m)/u_0 = F'(y/\delta),\ T - T_\infty = T_0\Psi(y/\delta) \tag{42a}$$

$$-\overline{u'v'} = u_T^2 G_0(y/\delta),\ -\overline{v'T'} = \Phi_0\phi_0(y/\delta) \tag{42b}$$

$$\beta\Delta T + \alpha = (\beta\Delta T_w + 3\alpha)H_0(y/\delta) \tag{42c}$$

where $H_0 = B_v - \epsilon_0\Psi$, $\epsilon_0 = \beta T_0/(\beta\Delta T_w + 3\alpha)$. The existence of the above similarity solutions for velocity and temperature have been well-demonstrated by George and Capp [15] for the case of thermal expansion driven boundary layer. The use of equations (42) in equations (1), (8), and (3) yields

$$\frac{\delta}{U_m}\frac{du_0}{dx}(F'^2 - FF'') + \frac{\delta}{U_m}\frac{dU_m}{dx}(F' - \eta F'') + \frac{\delta}{u_0}\frac{du_0}{dx}F' - \frac{d\delta}{dx}\eta F'' - \frac{u_0}{U_m}\frac{d\delta}{\partial x}FF'' + \frac{\delta}{u_0}\frac{dU_m}{dx}$$

$$= \frac{\nu}{U_m \delta} F''' + \frac{u_T^2}{u_0 U_m} G_0' + \frac{(\beta \Delta T_w + 3\alpha)\, \bar{g}\delta}{u_0 U_m} H_0 \tag{43a}$$

$$\frac{d\delta}{dx}\left[\frac{\delta}{T_0}\frac{dT_0}{d\delta}(F'+1)\Psi - \eta\Psi' - \frac{\delta}{u_0}\frac{du_0}{d\delta}F\Psi' - F\Psi' - \frac{\delta}{u_0}\frac{du_0}{d\delta}\eta\Psi'\right]$$

$$= \frac{1}{\mathrm{Pr}}\frac{\nu}{\delta u_0}\Psi'' + \frac{\Phi_0}{u_0 T_0}\phi_0 \tag{43b}$$

Since by assumption the outer layer is dominated by mean convection, turbulent diffusion and buoyancy terms, equations (43) will have similarity solution (42) provided the coefficients on the left-hand side of each equation are constants. That is

$$\frac{d\delta}{dx} = C_1 \tag{44a}$$

$$\frac{\delta}{U_m}\frac{du_0}{dx} = C_2 \tag{44b}$$

$$\frac{\delta}{U_m}\frac{dU_m}{dx} = C_3 \tag{44c}$$

$$\frac{\delta}{u_0}\frac{du_0}{dx} = C_4 \tag{45a}$$

$$\frac{u_0}{U_m}\frac{d\delta}{dx} = C_5 \tag{45b}$$

$$\frac{\delta}{u_0}\frac{dU_m}{dx} = C_6 \tag{45c}$$

$$\frac{\delta}{T_0}\frac{dT_0}{dx} = C_7 \tag{46}$$

Condition (44*a*) implies that $\delta \sim x$. We may recall that in the forced convection $\delta \sim x^{0.8}$, implying that this condition is satisfied approximately. Asymptotically for large values of the Grashof number, one can also expect this behavior for natural convection flows as well. It then follows from equation (45*b*) that $u_0/U_m = C_5/C_1$. Without any loss of generality, we can choose

$$u_0 = U_m \tag{47}$$

In view of equation (44) and (47), it is clear that

$$\frac{\delta}{u_0}\frac{du_0}{d\delta} = b, \quad \frac{\delta}{T_0}\frac{dT_0}{d\delta} = d \tag{48}$$

where b and d are constants. Equations (48) yield

$$u_0 = a\delta^b, \; T_0 = c\delta^d \tag{49}$$

where a and c are integration constants.

Since the turbulent diffusion and buoyancy terms must also be retained in the outer layer,

$$u_T = u_0 \tag{50a}$$

$$u_0 = [(\beta \Delta T_w + 3\alpha)\, \bar{g}\delta]^{1/2} \tag{50b}$$

$$u_0 T_0 = \Phi_0 = q_w/\rho C_p \tag{50c}$$

where we have substituted for Φ_0 from equation (41). From these equations we get

$$T_0 = \Phi_0/[(\beta \Delta T_w + 3\alpha)\, \bar{g}\delta]^{1/2} = q_w/\{\rho C_p [(\beta \Delta T_w + 3\alpha)\, \bar{g}\delta]^{1/2}\} \tag{50d}$$

Comparison of equations (49) with equation (50*b*) and (50*d*) shows that $b = 1/2$, $d = -1/2$, $a = [(\beta \Delta T_w + 3\alpha)\, \bar{g}]^{1/2}$, $c = \Phi_0/[(\beta \Delta T_w + 3\alpha)\, \bar{g}]^{1/2}$. Thus the choice of scales given by equations (47) and (50) ensures the existence of similarity solution (42) provided the condition (44*a*) is satisfied at least approximately. In the limit as $\delta u_0/\nu \to \infty$, equations (43) become

$$\frac{1}{2}\frac{d\delta}{dx}(F'^2 + 2F' - 3FF'' - 3\eta F'' + 1) = G_0' + H_0 \tag{51a}$$

$$-\frac{1}{2}\frac{d\delta}{dx}[(1+F')\Psi + 3\eta\Psi' + 3F\Psi'] = \phi_0 \tag{51b}$$

It is also of interest to obtain the ratios of the inner to outer scales for velocity and temperature. From equations (37) and (50), we get

$$U_I/u_0 = (\Lambda/\delta)^{1/2} \tag{52a}$$

$$T_I/T_0 = (\delta/\Lambda)^{1/2} \tag{52b}$$

5 Asymptotic Matching

The adoption of a two-layer model has greatly simplified the governing equations. However, in spite of these simplifications, equations (38) for the inner layer and equations (51) for the outer layer still cannot be solved due to lack of closure laws for turbulent diffusion terms. Because of strong coupling between the momentum and energy equations, traditional formulations for eddy diffusivities for momentum and heat transfer based on force convection flows cannot be extended to the case of natural convection flows. An alternative approach is feasible. Since turbulent boundary layers have all the characteristics of singular-perturbation problems [6, 16, 17], some specific results can be obtained by carrying out asymptotic matching between the inner and the outer layers. The asymptotic constraints imposed on the velocity and temperature profiles make ad-hoc assumptions on the relation between the Reynolds stress and the velocity gradient and between the turbulent heat diffusion and the temperature gradient unnecessary.

In the proposed two-layer model, we sought the solution for the inner layer in the form given by equations (34*a*) and for the outer layer in the form given by equations (42*a*). However, as shown by Tennekes and Lumley [6], the existence of a matched layer or a region of overlap between the inner and the outer layers is possible only if the limits $y^* = y/\Lambda \to \infty$ and $\eta = y/\delta \to 0$ can be taken simultaneously. This, however, is possible since

$$\frac{\delta}{\Lambda} = (\nu/\lambda)^{2/3}[(\beta \Delta T_w + 3\alpha) g\delta^3/\nu^2]^{1/3}$$

$$= (\mathrm{PrRa}_\delta)^{1/3} \to \infty \text{ as } \mathrm{Ra}_\delta \text{ or } \mathrm{Gr}_\delta \to \infty \tag{53}$$

Consequently, the principle of asymptotic matching when applied to velocity and temperature gradients yields,

$$\lim_{y^* \to \infty}\left[y^{*1/2} f''\right] = \lim_{\eta \to 0}\left[\eta^{1/2} F''\right] = \frac{\kappa_1}{2} \tag{54a}$$

$$\lim_{y^* \to \infty}\left[y^{*3/2}\theta'\right] = \lim_{\eta \to 0}\left[\eta^{2/3}\Psi'\right] = -\frac{\kappa_2}{2} \tag{54b}$$

The integration of these equations gives the velocity profile as

$$\frac{u}{U_I} = \frac{u}{[(\beta \Delta T_w + 3\alpha)\bar{g}\lambda]^{1/3}} = \kappa_1 y^{*1/2} + A_u(\mathrm{Pr}) \tag{55a}$$

$$\frac{u - U_m}{u_0} = \kappa_1 \eta^{1/2} + B_u \tag{55b}$$

and the temperature profile as

$$\frac{T - T_w}{T_I} = \kappa_2 (y^*)^{-1/2} + A_T(\mathrm{Pr}) \tag{56a}$$

$$\frac{T-T_\infty}{T_0} = \kappa_2 \eta^{-1/2} + B_T \tag{56b}$$

These profiles show square root and inverse square root variation with respect to distance from the wall as against cube root and inverse cube root behavior for the case of thermal expansion driven profiles as obtained by George and Capp [15]. This difference arises because of difference in the choice of inner and outer scales which have been dictated by the buoyancy effect of the volume boiling outside the boundary layer rather than the thermal expansion.

Requiring now that the profiles (55) and (56) themselves match at a given point in the overlap region, we obtain

$$\frac{U_m}{u_0} = A_u(\mathrm{Pr})\left(\frac{\Lambda}{\delta}\right)^{1/2} - B_u \tag{57a}$$

$$C_H'^{-1} = \frac{T_w - T_\infty}{T_I} = B_T\left(\frac{\Lambda}{\delta}\right)^{1/2} - A_T(\mathrm{Pr}) \tag{57b}$$

In obtaining the above relations, we have made use of equations (52). From equations (57) it is clear that

$$U_m/u_0 \to -B_u,\ C_H'^{-1} \to -A_T(\mathrm{Pr}) \text{ as } \Lambda/\delta \to 0 \text{ or as } \mathrm{Ra}_\delta \to \infty \tag{58a}\ (58b)$$

Condition (47), required as one of the conditions for the existence of similarity solution in the outer layer, is a special case of the asymptotic relation (58*a*). From equations (57*b*), (37*b*), (37*c*), and (40), we obtain

$$C_H' = \frac{T_I}{T_w - T_\infty} = \frac{q_w x}{(T_w - T_\infty)K}\left\{\frac{(\lambda/\nu)^{2/3}}{[(\beta\Delta T_w + 3\alpha)\tilde{g}\tilde{x}^3/\nu^2]^{1/3}}\right\} \tag{59}$$

which yields

$$\mathrm{Nu}_x = C_H(\mathrm{Pr})\mathrm{Ra}_x^{1/3} \tag{60}$$

where $C_H' = \mathrm{Pr}^{1/3}\, C_H$. From the asymptotic relation (58*b*) it is clear that C_H is a function of the Prandtl number only.

Since heat-transfer coefficient h given by equation (60) is independent of x, $\overline{\mathrm{Nu}}_x = \mathrm{Nu}_x$, where $\overline{\mathrm{Nu}}_x$ denotes the average of the Nusselt number over length x. For simplicity in notation, we will denote $\overline{\mathrm{Nu}}_x$ by Nu and $\overline{\mathrm{Ra}}_x$ by Ra. Equation (60) can thus also be written as

$$\mathrm{Nu} = C_H(\mathrm{Pr})\mathrm{Ra}^{1/3} \tag{61}$$

To show an equivalence between the above heat-transfer law and that obtained for boundary layers driven by temperature difference alone, we give below a very reliable empirical correlation obtained by Churchill and Chu [12] after a study of numerous sets of experimental data:

$$\mathrm{Nu} = \frac{0.15\ \mathrm{Ra}_T^{1/3}}{[1+(0.492/\mathrm{Pr})^{9/16}]^{16/27}} \tag{62}$$

where $\mathrm{Ra}_T = \mathrm{Ra}\,|_{\alpha=0}$. The equivalence between these laws will be demonstrated by the experimental data on the average heat-transfer coefficient for boiling pools. Figure 3 shows the data of Gabor et al. [3] and of Greene et al. [5] plotted as Nu versus $\mathrm{Ra}_p = \mathrm{Ra}/[1+(0.492/\mathrm{Pr})^{9/16}]^{16/9}$. These two data sets constitute about 94 data points which also include data points for inclined sides with three values, namely, 0, 15 and 30 deg, for the angle of inclination, γ, from the vertical direction. These latter data were obtained by Greene et al. Also shown in this figure is the plot of the expression (62) with Ra_T replaced by the "equivalent" Rayleigh number, Ra. Maintaining a slope of one-third on the log-log scale as predicted by expression (61), we also show in this figure the following least squares fit through this data.

$$\mathrm{Nu} = \frac{0.16\ \mathrm{Ra}^{1/3}}{[1+(0.492/\mathrm{Pr})^{9/16}]^{16/27}} = 0.16\ \mathrm{Ra}_p^{1/3} \tag{63}$$

Figure 3 clearly shows that the data are correlated very satisfactorily by the above expression. A comparison of two expressions (62) and (63) shows that these two expressions differ by less than 7 percent. This deviation is well within the accuracy of the available data [5]. In arriving at equation (63), we have assumed the same Prandtl number dependence of C_H as implied in the original expression (62) by Churchill and Chu. Such a close agreement between the two expressions clearly verifies the validity of the model proposed for heat transfer from the sides of the volume heated boiling pools.

6 Comparison with Previous Correlations

In order to contrast equation (63) with the previous correlations, we briefly review these models. However, it will not be possible to present a quantitative comparison by showing all these correlations in the same plot because the dependent variables used in forming these correlations is different in each case. Stein et al. [2] has assumed natural and forced convection as two distinct cooling regimes in the boundary layer. Natural convection is driven by temperature difference alone and the heat-transfer coefficient is given by conventional laminar single-phase correlation. The forced convection regime is driven by upward free stream flow having velocity V_B correlated empirically as $V_B = 40\ Q_B^{0.72}$ (where Q_B in the vaporized energy flux in cal/sec cm^2). The heat-transfer coefficient is then given by standard laminar forced convection single-phase correlation with Reynolds number based on free stream velocity V_B. The natural convection regime prevails when $V_B/V_{TC} < 0.2$ (where $V_{TC} = (g\beta\Delta T_w L)^{1/2}$) and the forced convection regime is dominant when $V_B/V_{TC} > 3$. Gabor et al. [3] assumed a correlation of the form $\mathrm{Nu} = C\mathrm{Re}^{1/2}$, with $\mathrm{Re} = V_B L/V$. These authors arrived at two values for constant C to correlate their data. In the model presented by Gustavson et al. [4], it was proposed that heat transfer in the boundary was a mixed convection type with natural convection being driven by density difference between the pool and the boundary layer and the forced convection driven by superficial vapor velocity at the pool surface. These two regimes were then combined by a correlation of the form $Y = (1+Z^n)^{1/n}$ (where $Y = \mathrm{Nu}/\mathrm{Nu}_N$ and $Z \doteq \mathrm{Nu}_c/\mathrm{Nu}_N$, subscript c denoting forced convection and N natural convection). Index n was determined by a best fit of their data. Green et al. [5] have proposed a correlation of the form: $\mathrm{Nu} = C\mathrm{Ra}^{*m}$ with $\mathrm{Ra}^* = \tilde{g}\alpha L^3\ \mathrm{Pr}/\nu^2$. They assigned $m = 0.25$, 0.40, 0.0314 and $C = 1.54$ to obtain best fit to their data. The values of these constants for the data of Gabor et al. [3] were slightly different. It is thus clear that each author has introduced several free parameters to obtain the best fit to their data. The present correlations on the other hand are entirely based on equivalence between combined two-phase and temperature-driven boundary layer and that drive by temperature difference alone. Therefore, the present correlations introduce no new parameters other than those that already exist in the standard single-phase correlations.

7 Conclusions

A comparison of the turbulent analysis with experimental data for the heat-transfer coefficient from the sides of the volume heated boiling pools and with the existing well known empirical correlation by Churchill and Chu [12] obtained for turbulent boundary layers driven by temperature difference alone confirms the validity of the proposed heat-transfer model (that is, heat-transfer to the sides of the boiling pool takes place through a single phase liquid turbulent boundary layer driven along these sides by the combined buoyancy forces of the two-phase void distribution and thermal expansion). The experimental data for boiling pools were taken for bubbly and churn-turbulent flow regimes with α ranging

from 0.03 to 0.6 and γ from 0 to 30 deg. Any extrapolation beyond these data ranges is speculative and should be done with caution. The analysis for the laminar case shows that the combined two-phase and thermal expansion driven natural convection along the sides of the pool is characterized by Grashof number, $Gr = (\beta\Delta T_w + 3\alpha)\bar{g}x^3/\nu^2$. With this definition of Gr, both for laminar and turbulent flows, the analysis shows that heat-transfer law for the combined two-phase and thermal expansion driven natural convection and that driven by thermal expansion alone are equivalent.

Acknowledgments

We wish to express our sincere thanks to Jean Allison for her invaluable help in data preparation and computer plots. The work was performed under the auspices of the U.S. Department of Energy.

References

1 Chawla, T. C., et al., "Heat Transfer from Vertical/Inclined Boundaries of Heat-Generating Boiling Pools Pertaining to Transition Phase and PAHR," Argonne National Laboratory Report (to be published).

2 Stein, R. P., Hesson, J. C., and Gunther, W. H., "Studies of Heat Removal from Heat Generating Boiling Pools," in *Proceedings of the Fast Reactor Safety Meeting held in Beverly Hills, California*, CONF-740401-P2, 1974, pp. 865–880.

3 Gabor, J. D., Baker, L., Jr., Cassulo, J. C., and Mansoori, G. A., "Heat Transfer from Heat Generating Boiling Pools," *AIChE Symposium Series*, Vol. 73, 1976, pp. 78–85.

4 Gustavson, W. R., Chen, J. C., and Kazimi, M. S., "Heat Transfer and Fluid Dynamic Characteristics of Internally Heated Boiling Pools," Brookhaven National Laboratory Report, BNL-NUREG-50722, 1977.

5 Greene, G. A., Jones, O. C., Jr., Schwarz, C. E., and Abuaf, N., "Heat Removal Characteristics of Volume Heated Boiling Pools with Inclined Boundaries," Brookhaven National Laboratory Report, BNL-NUREG-51157, 1980.

6 Tennekes, H., and Lumley, J. L., *A First Course in Turbulence*, The MIT Press, Cambridge, Mass., 1972.

7 Kays, W. M., and Crawford, M. E., *Convective Heat and Mass Transfer*, 2nd ed., McGraw-Hill, 1980.

8 Randall, I. E., and Sesonske, A., "Effect of a Volume Heat Source on Free-Convection Heat Transfer," *AIChE Journal*, Vol. 5, 1959, pp. 150–154.

9 Squire, H. B., and Goldstein, S., *Modern Developments in Fluid Dynamics*, Oxford University Press, New York, 1938.

10 Jaluria, Y., *Natural Convection Heat and Mass Transfer*, Pergamon Press, Oxford, 1980.

11 Eckert, E. R. G., and Jackson, T. W., "Analysis of Turbulent Free-Convection Boundary Layer on a Flat Plate," NACA TN 1015, 1950.

12 Churchill, S. W., and Chu, H. H. S., "Correlating Equations for Laminar and Turbulent Free Convection from a Vertical Plate," *International Journal of Heat and Mass Transfer*, Vol. 18, 1975, pp. 1323–1329.

13 Cheesewright, R., "Turbulent Natural Convection from a Vertical Plane Surface," ASME JOURNAL OF HEAT TRANSFER, Vol. 90, 1968, pp. 1–8.

14 George, W. K., Jr., "Outline of a Unified Similarity Theory for Turbulent Convection Next to Vertical Surfaces," *Proceedings of the 6th International Heat Transfer Conference*, Toronto, 1978, pp. 1–6.

15 George, W. K., Jr., and Capp, S. P., "A Theory for Natural Convection Turbulent Boundary Layers Next to Heated Vertical Surfaces," *International Journal of Heat and Mass Transfer*, Vol. 22, 1979, pp. 813–826.

16 Tennekes, H., "Outline of a Second-Order Theory of Turbulent Pipe Flow," *AIAA Journal*, Vol. 6, 1968, pp. 1735–1740.

17 Chawla, T. C., and Tennekes, H., "Turbulent Boundary Layers with Negligible Wall Stress: A Singular-Perturbation Theory," *International Journal of Engineering Science*, Vol. 11, 1973, pp. 45–64.

Latent and Sensible Heat-Transfer Rates in the Boiling of Binary Mixtures

J. R. Thome
Assistant Professor,
Department of Mechanical Engineering,
Michigan State University,
East Lansing, Mich. 48824
Mem. ASME

Nucleate pool boiling bubble departure data were obtained for the liquid nitrogen-argon cryogenic binary mixture system at 1.3 atmospheres absolute pressure. The latent and sensible heat transport rates at individual boiling sites were calculated from the data to deduce their effect on the degradation in the boiling heat-transfer coefficient in binary mixtures. The latent heat-transfer rate is a result of the bubble evaporation mechanism and the sensible heat-transport rate is due to cyclic thermal boundary layer stripping by departing bubbles. The latent and sensible heat-transport rates at individual boiling sites were found to decrease to a minimum at the maximum vapor-liquid mole fraction difference for both constant heat flux and wall superheating conditions. The large decrease in binary boiling heat-transfer coefficients was thus partially explained by the retardation of these two mechanisms and should be included in any model for predicting boiling heat-transfer coefficients in binary and multicomponent mixtures.

Introduction

Nucleate pool boiling of binary mixtures has been a subject of research for a number of years. Research has been directed both at the overall mixture boiling heat-transfer coefficients and, in some cases, also the fundamental aspects of mixture boiling. The present study was done at the fundamental level to ascertain the variation in the latent and sensible heat-transport rates with composition at individual boiling sites in a binary liquid mixture. The binary system of liquid nitrogen and liquid argon was used because of safety considerations and also for their simple molecular shapes. Boiling of cryogenic binary mixtures is of importance to both the air separation and LNG industries.

Hsu and Graham [1] discussed three possible mechanisms which could cause the large heat-transfer coefficients in nucleate pool boiling. These were: (*a*) the bubble agitation mechanism, (*b*) the vapor-liquid exchange mechanism, and (*c*) the evaporation mechanism. The vapor-liquid exchange mechanism and the evaporation mechanism will be considered here to determine the effect a second component has on the sensible heat-transfer rate and the latent heat-transfer rate, respectively.

Several previous studies have investigated the variation in bubble departure size and frequency in binary mixtures: Tolubinskiy and Ostrovskiy [2–4], and Valent and Afgan [5]. The general conclusion of these studies was that the bubble departure diameters decreased to a minimum in the mixtures at about the same composition as the absolute maximum in the mole fraction difference between the vapor and liquid, $|y-x|$. Van Stralen's results, summarized in [6], for boiling from a very thin wire supports this conclusion.

Experimental Equipment and Techniques

Details of the experimental pool boiling cryostat have been previously described elsewhere [7, 8], so only a brief summary is given here.

Boiling took place on a horizontal oxygen-free, high-conductivity (OFHC) copper disk facing upward. The diameter of the disk was 18 mm. Five micro-drilled cavities spaced 2 mm apart were made at the center ranging from 21 to 52 microns in dia with essentially cylindrical shapes. The solder joint adjoining the test surface to its support was carefully polished to retard spurious bubbles from forming and obscurring bubbles growing from the specially prepared sites. The growth cycles of the bubbles from the microdrilled cavities were recorded using a high speed cine camera operating from 500 to 4000 frames per s as the various bubble departure frequencies required.

Measurements of the bubble departure diameters and frequencies from the cine films were obtained manually using an optical comparator at 100× magnification and also with a computerized image analysis system. A description of the latter method has been presented elsewhere [8, 9]. The computerized system was ideal for measuring and storing in computer file large amounts of accurate bubble growth and departure data with relative ease and a minimum of effort. The estimated error in measuring the equivalent bubble departure diameter and frequency were 5 and 2 percent, respectively.

The phase equilibrium data of Thorpe [10] for the nitrogen-argon system were used for the investigation. A summary of the correlating methods for determining the thermodynamic and transport properties of the mixtures can be found in Thome [8]. Table 1 gives the relevant physical properties.

Ultra-high-purity argon gas (99.996 percent) and high-purity nitrogen gas (99.992 percent) were condensed into the test chamber to prepare the test liquids. The gases passed through a liquid nitrogen cold trap prior to entering the cryostat in order to freeze out the remaining water vapor and CO_2 impurities. Using the phase equilibria data of Thorpe [10], the measured saturation pressure and temperature were utilized to determine the test liquid compositions to within ±0.015 mole fraction.

Experimental Bubble Departure Results

Two types of experimental procedures were performed for studying bubble departure: (*a*) constant composition with varying wall superheat and (*b*) constant wall heat flux with varying composition. These were all performed during a single cooldown to cryogenic temperatures. The boiling curves can be found in Thome [8].

The vapor generation rate at an individual boiling site is the product of the bubble departure volume, V_d, and the bubble

Contributed by the Heat Transfer Division and presented at the 20th ASME/AIChE National Heat Transfer Conference, Milwaukee, Wisconsin, August 2-5, 1981. Manuscript received by the Heat Transfer Division September 18, 1981. Paper No. 81-HT-28.

Table 1 Physical properties of Nitrogen-Argon at 1.3 Atm

x (N_2)	y (N_2)	T_{sat} (K)	ρ_L (kg/m^3)	ρ_v (kg/m^3)	h_{fg} (kJ/kg)	c_p (kJ/kgK)	k_L (W/mK)	σ (dyn/cm)
0.0	0.000	89.90	1375	7.35	161	1.14	0.121	11.88
0.1	0.265	87.94	1311	7.46	165	1.18	0.123	11.59
0.2	0.438	86.35	1248	7.32	168	1.23	0.124	11.30
0.3	0.570	85.05	1187	7.15	171	1.29	0.125	11.02
0.4	0.668	83.96	1126	6.95	175	1.36	0.126	10.72
0.5	0.748	83.03	1067	6.76	178	1.44	0.127	10.42
0.6	0.813	82.23	1009	6.58	181	1.53	0.128	10.09
0.7	0.865	81.53	953	6.39	184	1.64	0.128	9.72
0.8	0.912	80.87	899	6.22	188	1.77	0.129	9.32
0.9	0.958	80.23	846	6.05	192	1.91	0.130	8.87
1.0	1.000	79.63	796	5.88	196	2.08	0.131	8.36

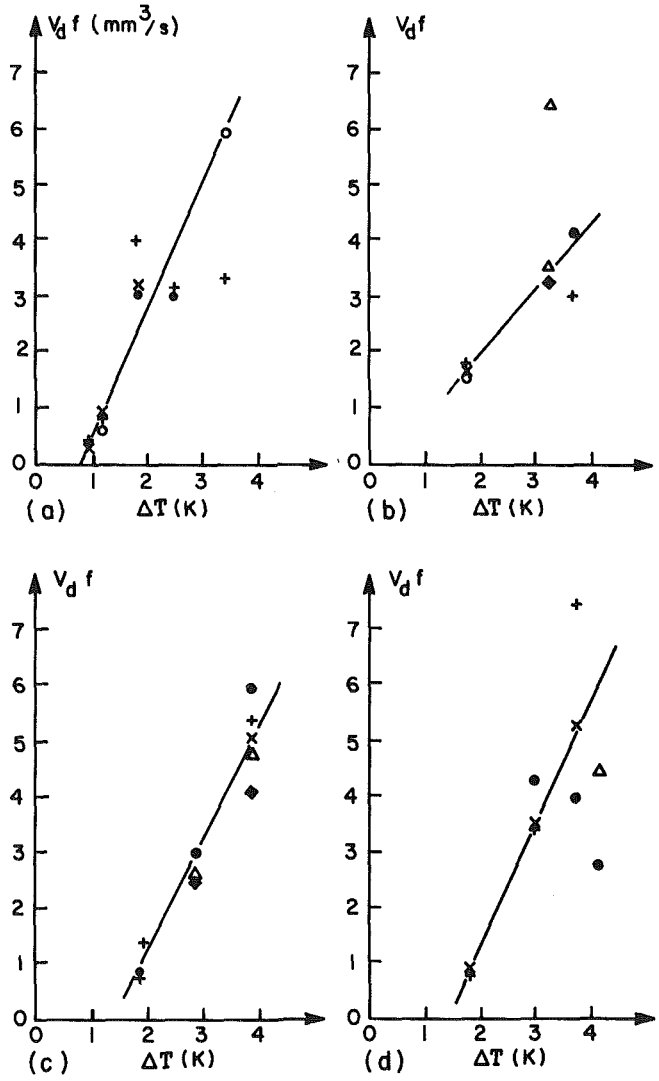

Fig. 1 Variation in vapor generation rate at a boiling site with wall superheat at 1.3 atmospheres pressure: (*a*) nitrogen, (*b*) argon, (*c*) 84 percent mole fraction nitrogen, (*d*) 68 percent mole fraction nitrogen. Legend: x site 1, 52 μm dia; ◆ site 2, 49 μm; • site 3, 40 μm; + site 4, 46 μm; o site 5, 21 μm; ▵ natural sites.

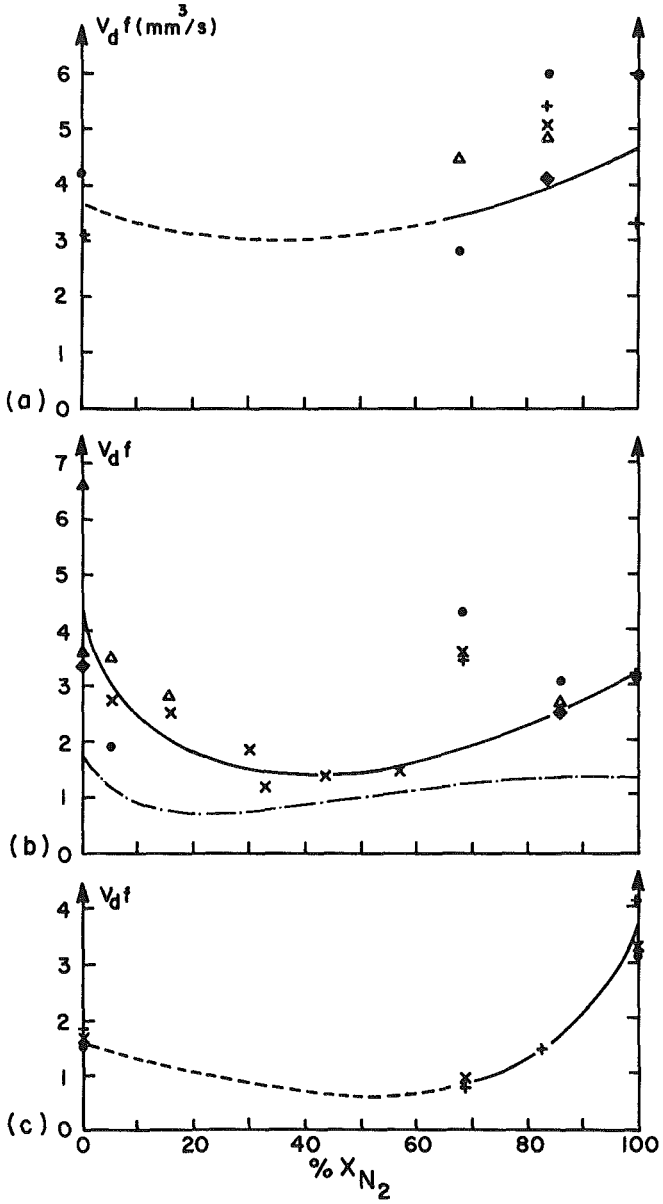

Fig. 2 Variation in vapor generation rate at a boiling site with composition at 1.3 atmospheres pressure and at three heat flux levels: (*a*) 4.3 kW/m^2, (*b*) 2.1 kW/m^2, (*c*) 1.2 kW/m^2. Legend: same as in Fig. 1. The dash/dot/dash line in (*b*) is the theoretical prediction of Thome (*14*).

Nomenclature

c_p = liquid specific heat
D_d = bubble departure diameter
f = bubble departure frequency
h = heat-transfer coefficient
h_{fg} = heat of vaporization
k_L = liquid thermal conductivity
q_{c_p} = sensible heat-transport rate at a boiling site
$q_{h_{fg}}$ = latent heat-transport rate at a boiling site
T_{sat} = saturation temperature
T_w = wall temperature
ΔT = $T_w - T_{sat}$, wall superheat
V_d = bubble departure volume
x = liquid mole fraction
y = vapor mole fraction
ρ_L = liquid density
ρ_v = vapor density

Subscripts

i = ideal
1 = volatile component
2 = nonvolatile component

departure frequency, f. Since the bubble departure volume and frequency tend to vary from one bubble to the next, a sequence of bubble departures was measured at each site and then an average bubble for that site was determined.

The results for the variation of the vapor generation rate, $V_d f$, at individual boiling sites with wall superheat, ΔT, are shown in Fig. 1. The rate of vapor production is seen to increase substantially with a fair amount of scatter among the various boiling sites. The two mixtures with 68 percent and 84 percent nitrogen mole fractions demonstrated this increase in $V_d f$ with superheat with about the same slope as the single components nitrogen and argon. No general trend with respect to cavity diameter was noted. Several natural sites, which happened to be in focus and measurable, have values similar to the values for the artificially made sites. This justifies the usage of artificial sites.

The experimental bubble departure data in Fig. 1(a) compare very favorably with the bubble departure diameters reported by Grigoryev [11] and with the departure diameters and frequencies given by Verkin [12] and Bland [13] for pure liquid nitrogen. No other data appears to be available for liquid argon.

The change in the vaporization rate at a boiling site with composition is shown in Fig. 2 for three different heat flux levels. The intermediate heat flux of 2.1 kW/m^2 was the one where filming was most successful and hence has the widest range of compositions represented. A definite minimum in the vaporization rate is demonstrated at the heat flux of 2.1 kW/m^2. This minimum corresponds fairly closely to the maximum in $|y-x|$ at 33 percent N_2 shown in Fig. 3 for the nitrogen-argon system at 1.3 atmospheres pressure. These same minima in $V_d f$ are found by combining the bubble departure data of Tolubinskiy and Ostrovskiy [3] for the systems: ethanol-water, ethanol-butanol, ethanol-benzene, and methanol-water.

The vaporization rate, $V_d f$, can be estimated theoretically using the bubble departure diameter and frequency equations for binary liquids of Thome [14]. Using a bubble base dia of 50 μm and assuming that the contact angle is 5 deg and that the bubble waiting time is equal to the bubble growth time, the predicted evaporation rate is compared to the 2.1 kW/m^2 heat-flux data in Figure 2(b). Quantitatively, the predicted values are about 50 percent low. But, if the contact angle (which is only known to be small for cryogens) was instead guessed to be 10 deg, the resulting prediction would be quite satisfactory. Also, from a limited number of values deduced from the raw data in the Appendix in Thome [8], the bubble waiting time in the mixtures tends to be about twice the bubble growth time while for pure nitrogen and pure argon they are of roughly the same duration. Including this phenomena, the theory would predict a more profound minimum than shown in Fig. 2(b) and hence yield better qualitative agreement with the data. In summary, the Thome theory is qualitatively correct but better values for the variation in waiting time and contact angle with composition are needed to do a more rigorous test (the theories presented in [1] for predicting the waiting times were not at all successful).

Latent Heat-Transport Rate at a Boiling Site. The latent heat transport rate at an individual boiling site is determined approximately as

$$q_{h_{fg}} = \rho_V h_{fg} V_d f \tag{1}$$

For a bubble growing in a saturated single component liquid this gives a fairly accurate indication of the latent heat-transport rate. For a bubble growing at a heated wall in a saturated binary mixture, however, there will probably be a slight amount of the nonvolatile component condensing at the top of the bubble. As is well known, the binary liquid at the base of the growing bubble is partially stripped of the volatile

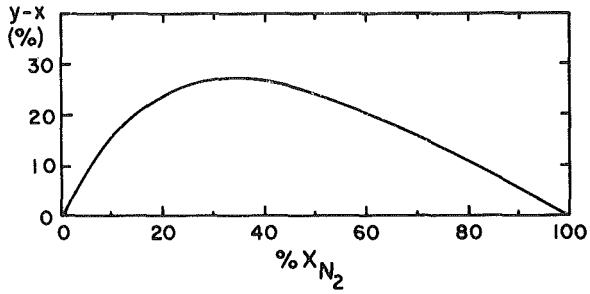

Fig. 3 Vapor-liquid mole fraction difference versus liquid mole fraction of nitrogen for nitrogen-argon system at 1.3 atmospheres

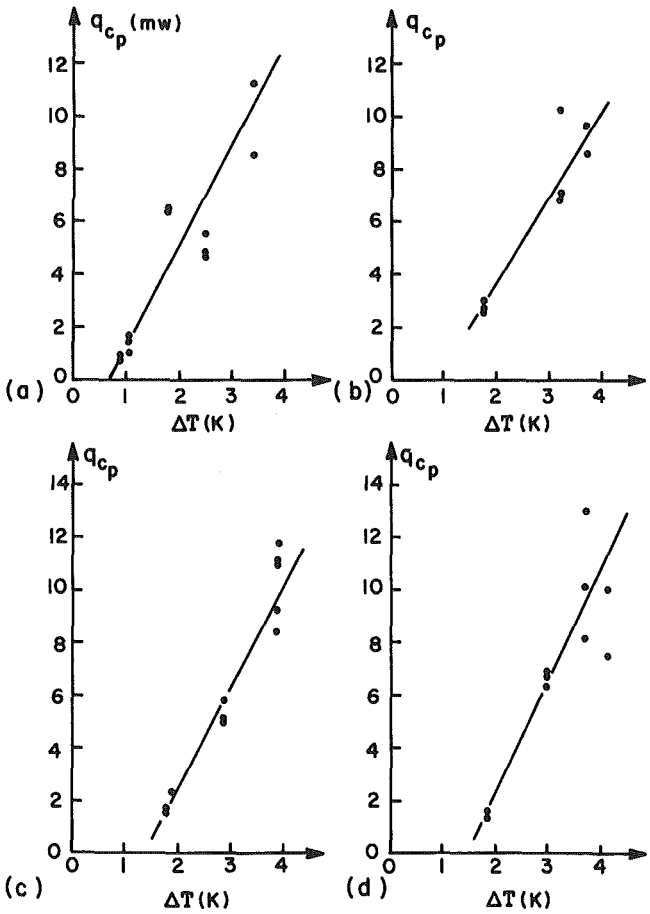

Fig. 4 Change in sensible heat-transport rate at a boiling site with wall superheat: (a) nitrogen, (b) argon, (c) 84 percent nitrogen, (d) 68 percent nitrogen

component (nitrogen) since the vapor mole fraction, y, is greater than the liquid mole fraction, x. Consequently, the local liquid mole fraction at the base of the bubble becomes richer in the nonvolatile component (argon) and more argon is vaporized. However, the top of the bubble is still in contact with the bulk liquid, so the top of the bubble is supersaturated with respect to the nonvolatile component, of which the excess then will tend to condense out. For example, a change in the local saturation temperature of the order of 0.3°C corresponds to a super-saturation of about 3 percent argon in the bubble. If all of this were to condense out, the error in the departure volume would also be on the order of 3 percent, which is within the estimated experimental error in determining V_d. The latent heat-transport rate can still be estimated from equation (1) keeping the above qualification in mind.

Sensible Heat-Transport Rate at a Boiling Site. A number of years ago Forester and Greif [15] proposed a nucleate pool

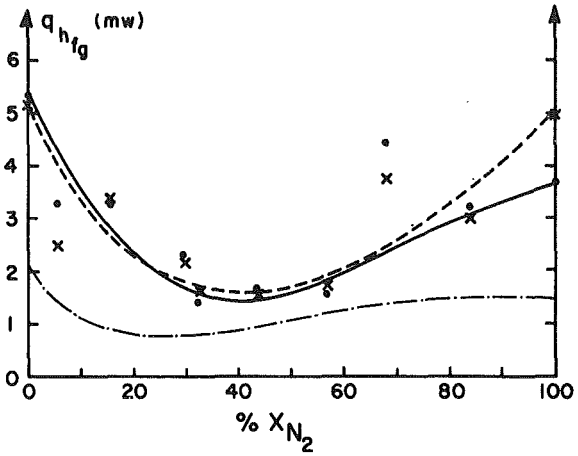

Fig. 5 Variation in the latent heat-transport rate at an average boiling site in the mixtures. Legend: (•) constant heat flux of 2.1 kW/m^2, (x) constant wall superheat of 3.1 K. The dash/dot/dash line is the theoretical prediction of Thome (14).

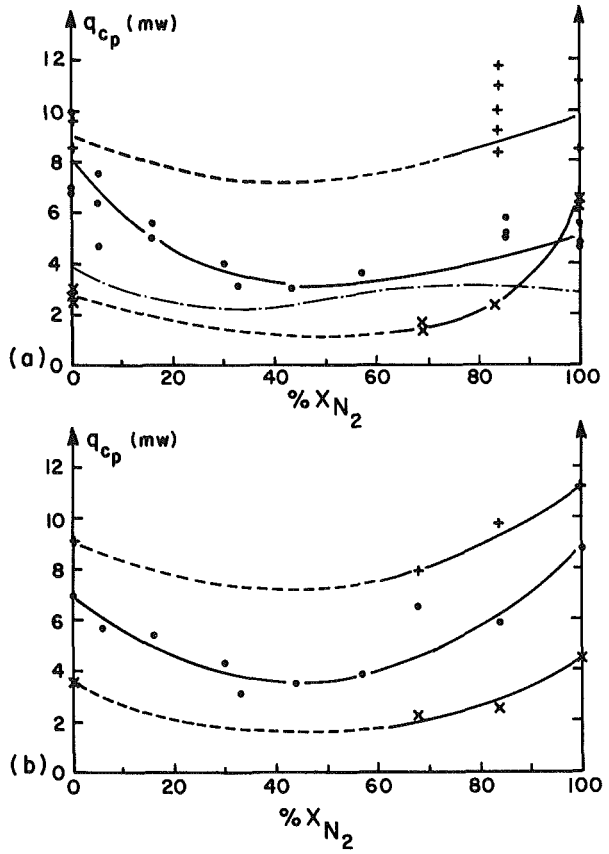

Fig. 6 Variation in the sensible heat-transport rate at a boiling site in the mixtures: (a) constant heat fluxes of 1.2 kW/m^2(x), 2.1 kW/m^2(•), and 4.3 kW/m^2(+), (b) constant wall superheats of 2.0 K(x), 3.1 K(•), and 3.75 K(+). The dash/dot/dash line is the theoretical prediction of Thome.

boiling model for single component liquids based on the vapor-liquid exchange mechanism. They surmized that the thermal boundary layer is cyclically stripped from the heated surface by departing bubbles. They argued that the enthalpy stored in the thermal boundary layer and carried away by a departing bubble is the principal heat-transfer mechanism in boiling. Later, Mikic and Rohsenow [16] developed a similar model and a correlating equation based on this mechanism. Thome [14] has recently extended their model to the nucleate pool boiling of binary mixtures with good agreement to four sets of published boiling data. Basically, the simple model assumes that the volume of hot liquid removed is twice the

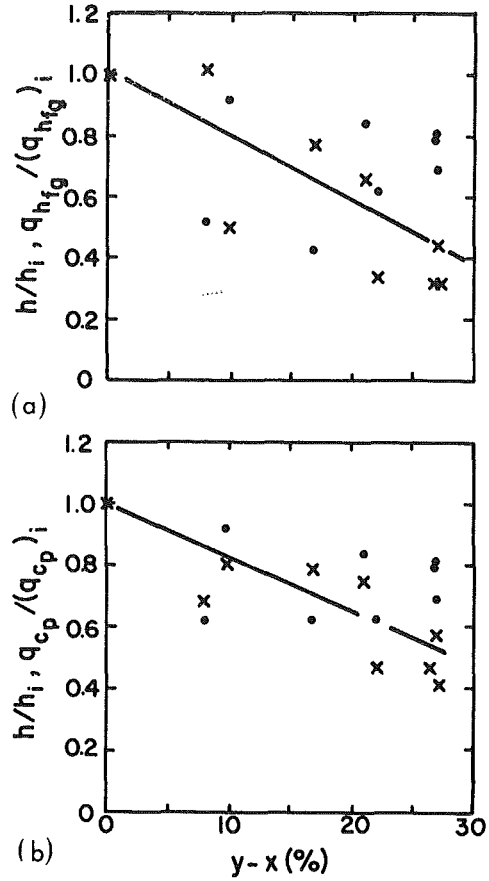

Fig. 7 Comparison of the ratios of the heat-transport rates (x) at an average individual boiling site to the ratio of the overall heat-transfer coefficients (•) for the nitrogen-argon system with a constant wall superheat of 3.1 K: (a) latent heat-transport ratio, (b) sensible heat-transport ratio.

bubble departure diameter in diameter and as thick as the thermal boundary layer. The bubble departure time is used as the characteristic time in calculating the boundary layer thickness from one-dimensional heat conduction to a semiinfinite body. If the average temperature in the boundary layer is also assumed to be ($\Delta T/2$), then the resulting expression for the sensible heat transport rate at a boiling site is:

$$q_{c_p} = \frac{1}{2}\pi^{3/2}(\rho_L c_p k_L f)^{1/2} D_d^2 \Delta T \qquad (2)$$

Variation in Latent and Sensible Heat-Transport Rates with Wall Superheat. Using the nitrogen-argon bubble departure diameters and frequencies, equations (1) and (2) have been evaluated to determine the effect of wall superheat on the latent and sensible heat-transport rates. For the latent heat-transport rates, it is quite evident that these increase exactly the same as $V_d f$ versus ΔT in Fig. 1, but with a multiplying factor of $\rho_v h_{fg}$. The multiplying factors $\rho_v h_{fg}$ for the four cases are: (a) 1.15 mJ/mm^3, Nitrogen; (b) 1.18, Argon; (c) 1.17, 84 percent N_2; and (d) 1.19, 68 percent N_2. The overall wall heat fluxes increased about three and a half times from the superheat of about 1.8°C to the highest value on each graph in Fig. 1, and the increases in the latent heat-transport rates are of the same order.

For the sensible heat-transport rates, their variations with wall superheat are shown in Fig. 4. The sensible heat transport rates increased with roughly the same slope for all four compositions.

Variation in Latent and Sensible Heat-Transport Rates with Composition. A large decrease in the latent heat-transport rates in the mixtures compared to the two single component

liquids is demonstrated in Fig. 5. The solid curve is the best fit to the data for a constant wall heat flux of 2.1 kW/m^2. Since the latent heat-transport rate was shown earlier to be a strong function of wall superheat, the data have been interpolated to a wall superheat of 3.1K to illustrate the effect of composition alone. This is depicted by the dashed line. A large decrease with a minimum in the neighborhood of the maximum in $|y-x|$ is again found.

The Thome theory [14] is shown to qualitatively describe the data in Fig. 5 with the previous comments also applying here.

The variation in the sensible heat-transport rate at three constant heat flux levels is depicted in Fig. 6(*a*). As the sensible heat-transport rates in Fig. 6(*a*) are also dependent on wall superheat, the data have again been interpolated to constant wall superheats of 2.0, 3.1, and 3.75 K as shown in Fig. 6(*b*). Thus, a significant decrease in the rate of sensible heat-transport rate in binary mixtures compared to the two single component liquids is evident.

The qualitative agreement between theory and experiment is again evident in Fig. 6(*a*). Quantitative agreement could be enhanced by using a larger contact angle. The slight maximum in q_{c_p} at 70 percent N_2 predicted theoretically is the result of the rise in ΔT here compared to 100 percent N_2, using the boiling curves in [8] for evaluating equation (2) as was done with the other computations.

Comparison to the Variation in the Overall Heat-Transfer Coefficient with Composition. A simple way to compare the change in the boiling heat-transfer coefficient for the whole heated surface to the variation in the latent and sensible heat-transport rates at an individual boiling site is to define the ideal values as

$$\frac{1}{h_i} = \frac{x_1}{h_1} + \frac{x_2}{h_2} \tag{3}$$

$$(q_{h_{fg}})_i = x_1(q_{h_{fg}})_1 + x_2(q_{h_{fg}})_2 \tag{4}$$

$$(q_{c_p})_i = x_1(q_{c_p})_1 + x_2(q_{c_p})_2 \tag{5}$$

where x_1 and x_2 are the mole fractions of the single components one and two in the mixture. Then the ratios of h/h_i, $q_{h_{fg}}/(q_{h_{fg}})_i$, and $q_{c_p}/(q_{c_p})_i$ can be compared by plotting them versus the vapor-liquid composition difference, $(y-x)$.

Figure 7(*a*) shows the comparison between the heat-transfer coefficient ratio and the latent heat-transport ratio. Figure 7(*b*) depicts the comparison of the heat-transfer coefficient ratio to the sensible heat-transport ratio. These comparisons were made at a constant wall superheat of 3.1K to isolate the effect of composition. The general trend is a decrease in the sensible and latent heat-transport rates compared to the ideal mixture values, which is matched by a similar decrease in the heat-transfer coefficient. Thus the effect of mass diffusion controlled bubble growth in a binary mixture is to retard the basic heat-transport mechanisms which in turn reduces the heat-transfer coefficient. A factor not explicitly included here, of course, is the effect of the variation in the boiling site density with composition.

Summary

The following conclusions were reached:

1 The vapor generation rate at an individual boiling site (*a*) increases with superheat in single and two-component liquids and (*b*) decreases to a minimum in the mixtures at the absolute maximum in the vapor-liquid mole fraction difference.

2 The latent and sensible heat-transport rates at an individual boiling site (*a*) increase with superheat in single and two-component liquids and (*b*) decrease to a minimum in the mixtures at the maximum in $|y-x|$.

3 The decrease in the boiling heat-transfer coefficient in binary mixtures can be partially explained by the decrease in the latent and sensible heat transport rates in binary mixtures.

Acknowledgment

The author performed the experimental studies while at the Cryogenics Laboratory, Department of Engineering Science, University of Oxford with the support of the British Science Research Council and the Heat Transfer-Fluid Flow Service of AERE, Harwell, England. The author also wishes to acknowledge the support of the National Science Foundation during the analysis of the experimental work.

References

1 Hsu, Y. Y., and Graham, R. W., *Transport Processes in Boiling and Two-Phase Systems*, McGraw-Hill, Washington, 1976.

2 Tolubinskiy, V., Ostrovskiy, Y. N., and Kriveshko, A. A., "Heat Transfer to Boiling Water-Glycerine Mixtures," *Heat Transfer—Soviet Research*, Vol. 2, No. 1, 1970, pp. 22-24.

3 Tolubinskiy, V. I., and Ostrovskiy, Y. N., "Mechanism for Heat Transfer in Boiling of Binary Mixtures," *Heat Transfer—Soviet Research*, Vol. 1, No. 6, 1969, pp. 6-11.

4 Tolubinskiy, V. I., and Ostrovskiy, Y. N., "On the Mechanisms of Boiling Heat Transfer," *International Journal of Heat and Mass Transfer*, Vol. 9, 1966, pp. 1463-1470.

5 Valent, V., and Afgan, N., "Bubble Growth Rate and Boiling Heat Transfer in Pool Boiling of Ethylalcohol-Water Mixtures," *Warme-und Stoffubertragung*, Vol. 6, 1973, pp. 235-240.

6 Van Stralen, S. J. D. and Cole, R., *Boiling Phenomena*, Vol. 1, McGraw-Hill, New York, 1979.

7 Thome, J. R., and Bald, W. B., "Nucleate Pool Boiling in Cryogenic Binary Mixtures," *Proceedings of the Seventh International Cryogenic Engineering Conference*, IPC Science and Technology Press, London, July 1978, pp. 523-530.

8 Thome, J. R., "Bubble Growth and Nucleate Pool Boiling in Liquid Nitrogen, Argon, and Their Mixtures," D. Phil thesis, University of Oxford, 1978.

9 Preston, G., Thome, J. R., Bald, W. B., and Davey, G., "The Measurement of Growing Bubbles on a Heated Surface Using a Computerized Image Analysis System," *International Journal of Heat and Mass Transfer*, Vol. 22, 1978, pp. 1457-1459.

10 Thorpe, P. L., "Liquid-Vapour Equilibrium of the System Nitrogen-Argon at Pressures up to Ten Atmospheres," *Trans. Faraday Soc.*, Vol. 64, 1968, pp. 2273-2280.

11 Grigoryev, V. A., Pavlov, Yu. M., Ametistov, E. V., and Klimenko, A. V., "Investigation of the Growth Rate of Vapor Bubbles in the Boiling of Cryogenic Fluids," *Heat Transfer—Soviet Research*, Vol. 7, No. 5, 1975, pp. 135-138.

12 Verkin, B. I., and Kirichenko, Yu. A., "Soviet Investigations on Pool Boiling of Cryogenic Liquids," *Proceedings of the Seventh International Cryogenic Engineering Conference*, IPC Science and Technology Press, London, July 1978, pp. 505-522.

13 Bland, M. E., "Bubble Nucleation in Cryogenic Fluids," D. Phil. thesis, University of Oxford, 1970.

14 Thome, J. R., "Nucleate Pool Boiling of Binary Liquids—An Analytical Equation," *AIChE Symposium Series*, No. 208, Vol. 77, 1981, pp. 238-250.

15 Forster, D. E., and Greif, R., "Heat Transfer to a Boiling Liquid: Mechanism and Correlations," ASME JOURNAL OF HEAT TRANSFER, Vol. 81C, No. 1, 1959, pp. 43-46.

16 Mikic, B. B., and Rohsenow, W. M., "A New Correlation of Pool-Boiling Data Including the Effect of Heating Surface Characteristics," ASME JOURNAL OF HEAT TRANSFER, Vol. 81, 1969, pp. 245-250.

D. Bharathan[1]
Assoc. Mem. ASME

G. B. Wallis
Mem. ASME

H. J. Richter
Mem. ASME

Thayer School of Engineering,
Darmouth College,
Hanover, N.H. 03755

Lower Plenum Voiding

One of the phenomena involved in a loss-of-coolant accident in a pressurized water reactor may be lower plenum voiding. This might occur during the blowdown phase after a cold-leg break in the primary coolant circuit. Steam generated in the reactor core may flow out of the bottom of the reactor core, turn in the lower plenum of the vessel, in a direction countercurrent to the emergency core coolant flow, and escape via the break. If its velocity is high enough, this steam may sweep water from the bottom (lower plenum) of the reactor vessel. Emergency coolant added to the vessel may also be carried out by the escaping steam and thus the reflooding of the core would be delayed. This paper describes a study of two-phase hydrodynamics associated with lower plenum voiding. Several geometrical configurations were tested at three different scales, using air to simulate the steam. Comparisons were made with data obtained by other researchers.

Introduction

A hypothetical double-ended break on one of the coolant supply lines in a nuclear pressurized water reactor (PWR) has been regarded as one of the most serious accidents that could occur. Therefore, this loss-of-coolant accident (LOCA) has received considerable attention from reactor vendors and government regulatory agencies. For a detailed description of water delivery during a LOCA, see Block and Schrock [1].

One of the phenomena involved in the LOCA is lower plenum voiding (LPV) when excess steam generated in a reactor core flows through the bottom of the reactor vessel in a direction countercurrent to normal coolant flow and escapes via the broken coolant line and, in this process, empties, partially or wholly, the coolant from the bottom of the reactor vessel. When LPV is in progress, any coolant added to the reactor core by an emergency coolant injection system may be carried out by the escaping steam and thus made ineffective towards recovering the core.

During coolant injection, many processes such as limitation of water flow countercurrent to steam in the annulus or complete bypass of water, and quenching of superheated walls might occur concurrently with lower plenum voiding. The voiding behavior might limit the water inventory in the vessel at certain times. While the voiding phenomenon has been identified as important following a postulated LOCA, the physical mechanism underlying the process has yet to be systematically explored to obtain an adequate quantitative description.

The objective of the present effort was to examine the hydrodynamics associated with lower plenum voiding. Therefore, only experiments with air and water as the working media in simple cylindrical geometries were conducted. Transparent vessels were used to permit visual observation of the voiding process. Three different vessel sizes were tested to study the effect of vessel scale on the voiding behavior. Within a small range, other parameters such as the annulus gap, the core-exit diameter, and the lower plenum length were varied to illustrate their influences on LPV. Voiding in simulated PWRs with hemispherical lower plena was also studied. The influence of varied gas liquid surface tension on voiding was illustrated by testing with air and methanol.

Besides reporting new data, this paper presents comprehensive comparisons of steam-water and air-water voiding data obtained at various facilities. A simple theory based on a criterion for instability of the horizontal gas-liquid interface is developed and shown to capture the data trend reasonably well.

Modification of the theory by a single coefficient provides a correlation of the behavior of PWR-like geometries; suitable values of this coefficient can be chosen to provide upper and lower bounds to the data.

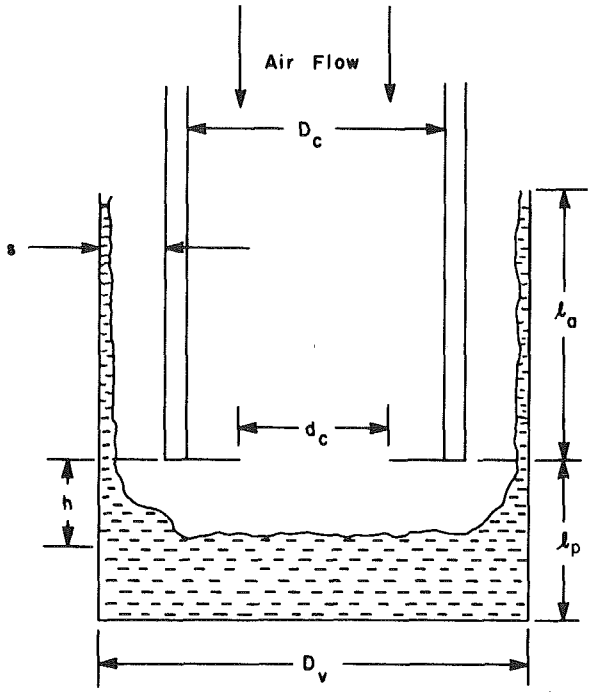

Fig. 1 Schematic diagram of the experimental apparatus

Background. Early LPV data have come from various researchers as byproducts of tests exploring other phenomena. Brief discussions of the early works and first tests may be found in the paper by Crowley and Rothe [3]. Graham [4] tested LPV in a 1/30 scale vessel with different core inlet areas. Detailed studies of LPV were carried out by Crowley and Block [2]. These studies include parametric variations of core inlet open area, vessel diameter, annulus gap size, downcomer length, and lower plenum water injection rate. The voided height is measured as a function of these parameters and the gas flow from the core.

Apparatus. Two different geometries for the apparatus were used in the experiments. One of them consists of a vertical outer cylindrical vessel and a concentric core as shown in Fig. 1. Air flowing downward through the central core impinges on the water surface in the lower plenum and, in this process, carries some water upward through the annulus, which is open at the top.

To simulate restrictions due to tie-plates in the core, an orifice plate at the lower end of the core was introduced in some of the tests.

[1] Now with the Solar Energy Research Institute, Golden, Colorado

Contributed by the Heat Transfer Division and presented at the ASME Winter Annual Meeting, Chicago, Illinois, November 16-21, 1980. Manuscript received by the Heat Transfer Division July 30, 1981.

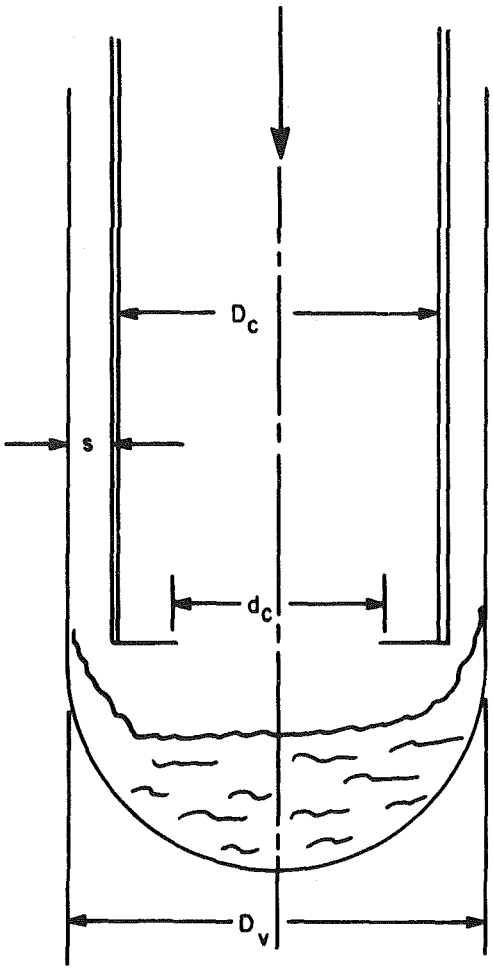

Fig. 2 Sketch of simulated reactor vessel geometry

The important geometric parameters of the apparatus include outer vessel diameter, D_v, inner core diameter, D_c, core exit diameter, d_c, annulus gap, s, length of the annulus l_a, and the length of the lower plenum l_p.

The second series of experiments was conducted with a second apparatus incorporating a hemispherical lower plenum with simulated lower plenum hardware of existing PWRs. A sketch of this apparatus for these experiments is shown in Fig. 2. In addition, tests were conducted with two different orifices fitted at the bottom of the core.

Description of the Voiding Process. During the tests, the plenum is first filled with water to the core level. The blower is turned on and the air flow through the core is set at a desired value. Water is carried out from the plenum and expelled in spurts by the air flow. After a sufficiently long waiting period when only insignificant amounts of water are thrown out, the air flow is turned off and the voided height is recorded. The waiting period may be as long as 20 min in certain ranges of air flow.

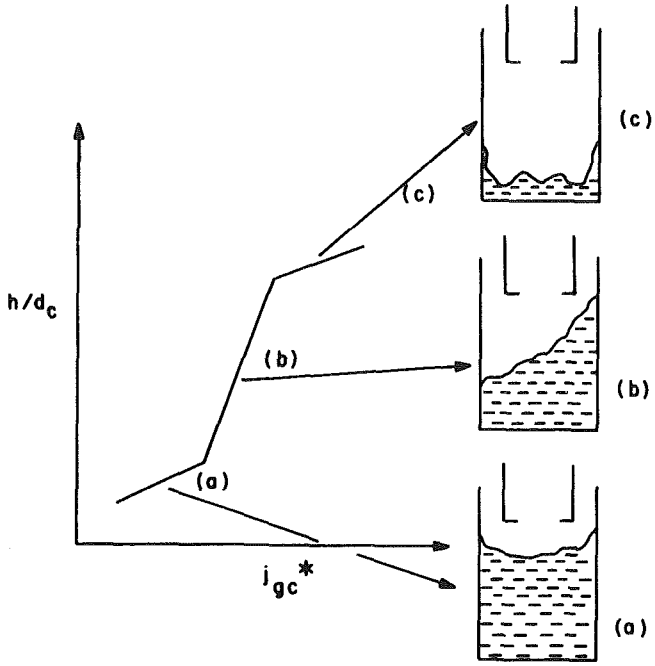

Fig. 3 Typical voided height variation with j_{gc}^* indicating three regions of operation

A typical variation of voiding data is shown in Fig. 3. The water level depression h/d_c is plotted as a function of non-dimensional core air flux defined as:

$$j_{gc}^* = \left[\frac{\rho_g}{(\rho_f - \rho_g) g d_c}\right]^{1/2} j_{gc}$$

$$j_{gc} = \frac{Q_g}{A_c}\,;\; A_c = \frac{\pi d_c^2}{4}$$

For certain geometries (e.g., multiple holes), d_c is replaced by the core inner diameter D_c as the reference dimension.

Three regions of lower plenum voiding may be identified (see Fig. 3). For low air flows in region (a), water is rapidly expelled from the plenum as the air flow is turned on. The equilibrium water level is almost horizontal with a possible standing protrusion near the annulus as shown in inset (a). For somewhat higher air flows, water begins sloshing in bulk in the plenum. Air entrains the water at the crests of the sloshing waves near the vessel wall and expels it in spurts. The sloshing oscillations are gradually built up over 2 or 3 min, intermittently. Long periods (of the order of 20 min) are required before the water level reaches equilibrium at which time an insignificant amount of water is carried out in spurts. The voided height increases three- or four-fold in this range of air flow referred to as the transition range in later discussions. During transition, typical water surface oscillations are indicated in inset (b). For even higher air flows, the transition occurs somewhat quicker; but the rate of change in the voided height with respect to air flows are, once again, comparable to those in the lower range of air flows before transition. The

Nomenclature

D_c = core inner diameter
D_v = vessel diameter
d_c = equivalent core exit diameter
g = gravitational acceleration
h = voided height below core bottom
h_s = height of the separation bubble
h_1 = $h - h_s$
j_{gc} = core gas flux
j_{gc}^* = nondimensional core gas flux
l_a = annulus length
l_p = lower plenum length
p_g = static pressure in the gas
p_f = static pressure in the liquid
p_0 = stagnation pressure
R_v = vessel radius
r = radial distance of static pressure tap
s = annulus gap width
v_c = average velocity at core exit orifice
v_s = core gas velocity
x = fractional height of the separation bubble
β = fractional height of the standing wave
ρ_f = liquid density
ρ_g = gas density

water surface at equilibrium is observed to be nearly horizontal as shown in inset (c).

At low air flow rates in region (a) and again at high air flow rates in region (c), the variation of voided height with air flow appears to follow similar trends, suggesting that the mechanism of water entrainment may be the same in either region. However, at high air flow rates the jet issuing from the core must form a large toroidal separation region. The presence of such a separation region increases the effective air velocity at the air-water interface, resulting in increased entrainment. For air flows in the intermediate region, the transition and the bulk liquid sloshing may be the result of this separation.

Analytical Considerations. The effects of only a few important geometric parameters over ranges relevant to real reactors are considered in this study (see Fig. 1). For cores without and with a single hole orifice, the core exit diameter d_c is used as the reference length, since it is the appropriate dimension to represent the impinging air momentum flux. For cores with orifices containing multiple holes, the core inner diameter D_c has been used as the reference dimension in presenting the voiding data.

Over the range of D_v/D_c and s/d_c tested, both the vessel size and the gap width appear to have minor influence on the present results. In steam-water flows, Crowley and Rothe [3] found that the length of the annulus l_a/d_c influences the voiding insignificantly. The lower plenum length l_p/d_c appears to affect the voiding behavior, however, only in the transition regime. Another parameter of importance is the ratio of core exit diameter to the core diameter d_c/D_c. Hence, the voiding level can be approximated simply as:

$$h/d_c = f\left(\frac{d_c}{D_c}; \frac{l_p}{d_c}; j_{gc}{}^*\right) \tag{1}$$

The influences of d_c/D_c and l_p/d_c are illustrated in later sections.

In the case of simulated reactor hardware, the variation in lower plenum length l_p/d_c is small and thus the influence of l_p on LPV may be considered insignificant, resulting in further simplified representation of the voided height as:

$$h/d_c = f\left(\frac{d_c}{D_c}; j_{gc}{}^*\right) \tag{2}$$

In addition to the geometric parameters included in equations (1) and (2), other fluid properties such as the viscosity of each phase and interfacial surface tension may play important roles in determining the equilibrium voiding level.

Theory. Consider a uniform steady-state flow of air impinging on an initially level liquid surface as shown in Fig. 4. For low air flows, such as in region (a) of Fig. 3, axisymmetric standing waves appear on the interface due to static pressure variations in the jet. Air offers maximum suction at the outer edge of the core where the water is assumed to be picked up. Let h be the separation distance between the bottom of the core and the water surface level at the center line. Also let βh $(0<\beta<1)$ be the maximum water surface protrusion of the standing wave height.

Assuming an incompressible, frictionless flow on the surface with no separation, using Bernoulli's equation, the static pressure in the gas p_g may be related to the axial stream velocity v_c and the stagnation pressure p_0 as:

$$p_0 - p_g = \tfrac{1}{2}\rho_g v_c{}^2\left[\frac{d_c}{4h(1-\beta)}\right]^2 + \beta h \rho_g g \tag{3}$$

The static pressure in the liquid p_f is:

$$p_0 - p_f = \rho_f g \beta h \tag{4}$$

The equilibrium wave protrusion β is obtained by solving (3) and (4) simultaneously. At a given voided height h/d_c,

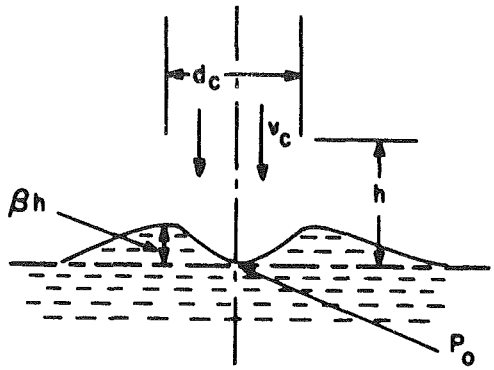

Fig. 4 Idealized jet impingement on a horizontal liquid surface

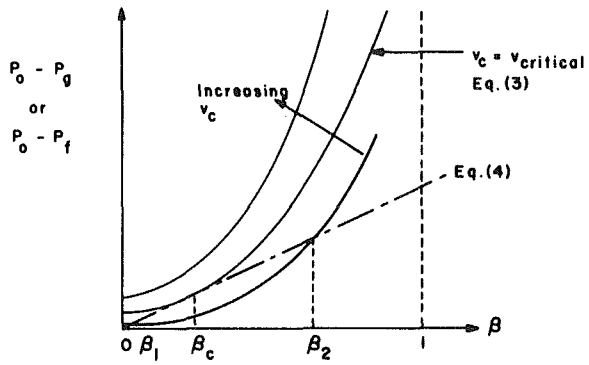

Fig. 5 Simultaneous solution of equations (3) and (4)

equations (3) and (4) can be plotted as functions of v_c and β, as shown in Fig. 5.

At sufficiently low v_c, equations (3) and (4) intersect at two points yielding two different solutions for β denoted by β_1 and β_2. However, simple stability considerations based on small perturbations on the wave height indicate that the wave is stable at $\beta=\beta_1$ and unstable at $\beta=\beta_2$. As v_c is increased further, at a critical value $v_c = v_{\text{critical}}$, the two solutions merge to yield one solution $\beta=\beta_{\text{critical}}$. Any disturbance on the wave height at this point will tend to restore the wave height back to the critical value.

For $v_c > v_{\text{critical}}$, equations (3) and (4) do not intersect within the range $0<\beta<1$, and thus do not yield a solution for the wave protrusion at the given h/d_c. However, since the suction due to air flow is greater than the hydrostatic pressure due to the wave height, water will be continually entrained until h/d_c reaches a large enough value to achieve the critical conditions. At the critical condition, it can be readily shown that $\beta_{\text{critical}} = 1/3$.

Now, equations (3) and (4) can be combined as:

$$\beta = 1/32\frac{\rho_g v_c{}^2}{(\rho_f-\rho_g)gd_c}\left[\frac{d_c}{h}\right]^3\frac{1}{(1-\beta)^2} \tag{5}$$

or

$$\beta = 1/32 j_{gc}{}^{*2}\left[\frac{d_c}{h}\right]^3\frac{1}{(1-\beta)^2} \tag{6}$$

Introducing the critical value for β, one obtains:

$$1/32 j_{gc}{}^{*2}\left[\frac{d_c}{h}\right]^3 = 4/27 \tag{7}$$

Therefore, when equilibrium is reached, the voided height h is related to the gas flux as:

$$\left(\frac{h}{d_c}\right) = 0.595 j_{gc}{}^{*2/3} \tag{8}$$

Though equation (8) results from simplified assumptions, it is found to capture the trend of data in the region (a) in most circumstances as will be shown in later sections.

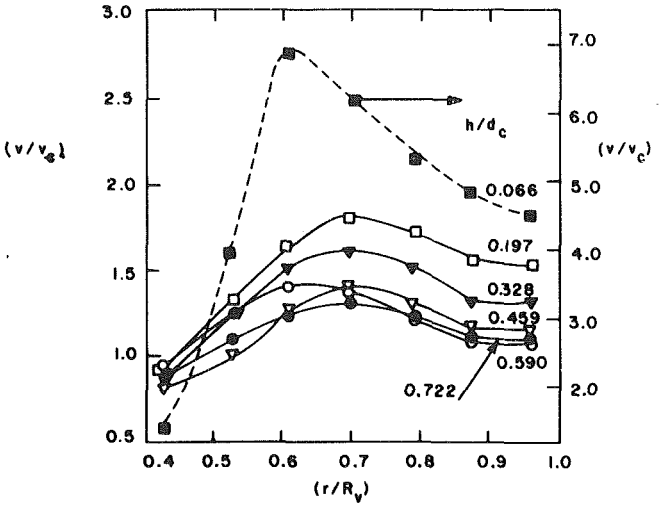

Fig. 6 Ratio of tangential water velocity at vessel bottom to axial core velocity versus radial distance for various distances of separation h/d_c

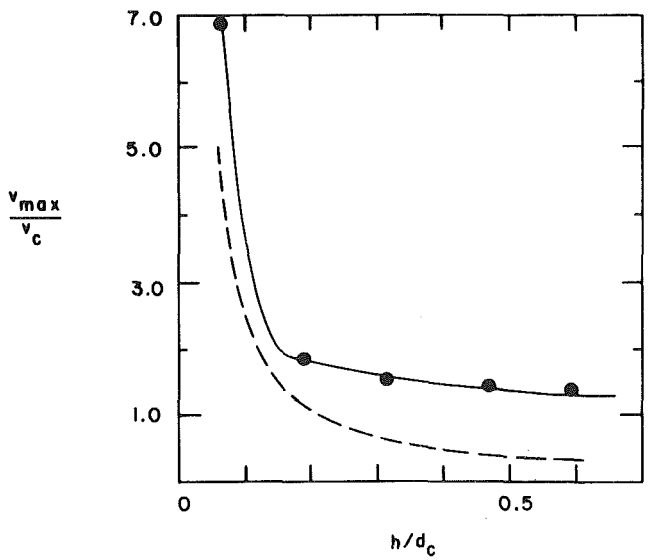

Fig. 7 Variation of maximum tangential velocity with separation distance: • measured; – – – theory for flow with no separated region

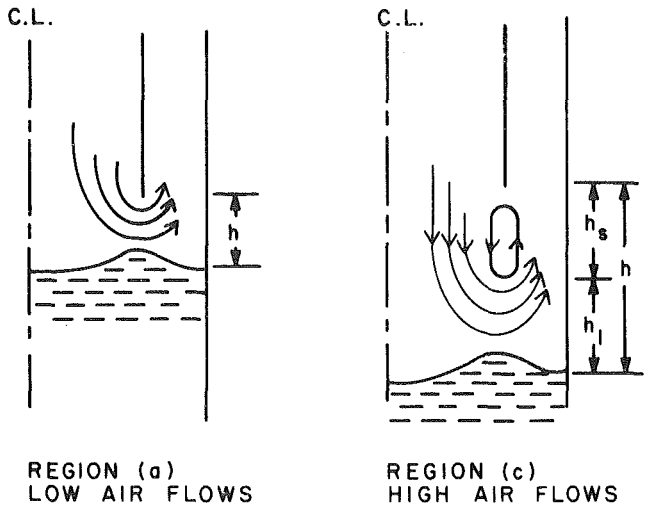

Fig. 8 Flow patterns at low and high air flows

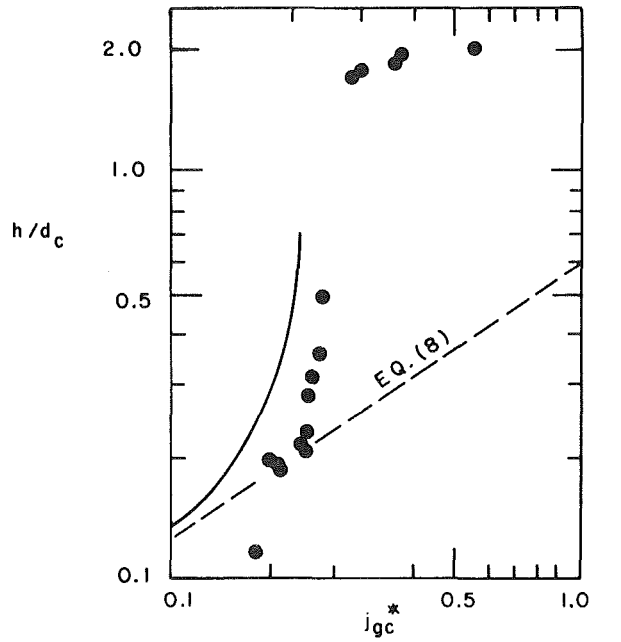

Fig. 9 Comparison of transition region data with prediction to include effects of separated region: — equation (8) modified by using V_{max} from Fig. 7

For somewhat higher air flows in the region (b), the voided height h/d_c increases more rapidly with j_{gc}^*. This transition appears to result from an emerging separation region at the core exit and the accompanying bulk sloshing of the liquid in the lower plenum. A separate set of single phase flow experiments to test this hypothesis was conducted.

Water was introduced through the core and allowed to flow into the lower plenum and exit upward through the annulus. A series of static pressure taps was provided on the flat bottom surface of the lower plenum at various radial locations. Static pressure variations were measured at various water flow rates as a function of separation distance h between the core-exit orifice and the vessel bottom.

At low h/d_c, stable pressure readings were obtained. As h/d_c increased, the fluctuations in the pressure reading increased. For large h/d_c (>0.8), the emerging jet from the core was very unstable. Water was observed to exit from the annulus in spurts randomly at different radial locations. This instability could be caused by an incipient separation region around the core exit. For even larger h/d_c, pressure measurements could not be obtained due to large fluctuations exceeding the magnitude of the desired average reading.

Based on the pressure measurements, the tangential water velocities at the botom surface were deduced at various radial locations r/R_v and are plotted as the ratio v/v_c, where v_c is the average velocity at the core-exit orifice for various separation distances h/d_c in Fig. 6. At any h/d_c, the tangential velocity attains a maximum at $r/R_v \simeq 0.6$ to 0.7.

A cross plot of the maximum v/v_c as a function of h/d_c is shown in Fig. 7. The maximum velocity decreases monotonically with increasing h/d_c. Calculated maximum values of v/v_c, assuming a uniform radial flow below the core, are also shown in this Figure. For $h/d_c > 0.1$, the measured velocities are greater than the calculated values, indicating a separated flow emerging from the core, as sketched in Fig. 8.

A similar variation of the maximum tangential velocity may be assumed to occur in the case of air flow through the core. If the water entrainment occurs at a certain air velocity over the interface, then at a given core gas flux, the equilibrium voided height h/d_c would be greater than predicted by equation (8).

The increase in tangential surface velocity can be related to an increase in voided height by a corresponding ratio. Thus the voided height variation, which includes the effect of the separation region, is shown in Fig. 9. For comparison, the measured voided height in the same apparatus is also shown.

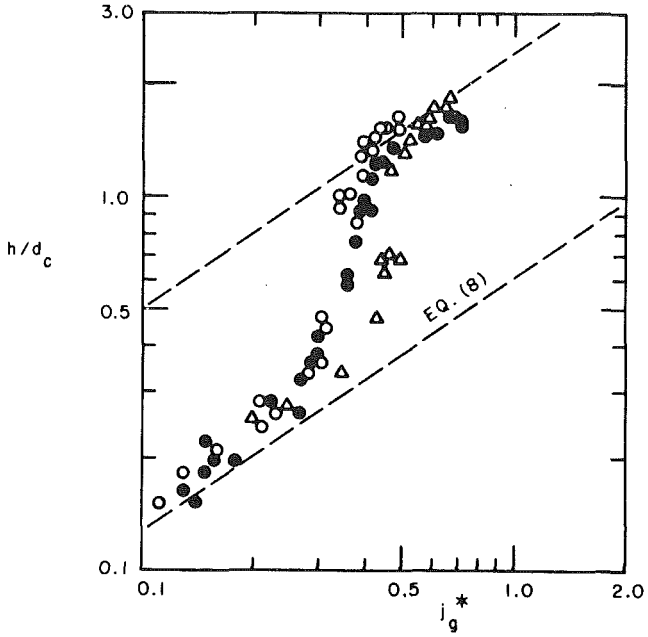

Fig. 10 Voided height versus gas flux in a 29-cm vessel for three annulus gaps: ○ 1.2 cm-gap; • 1.9-cm gap; △ 2.5-cm gap

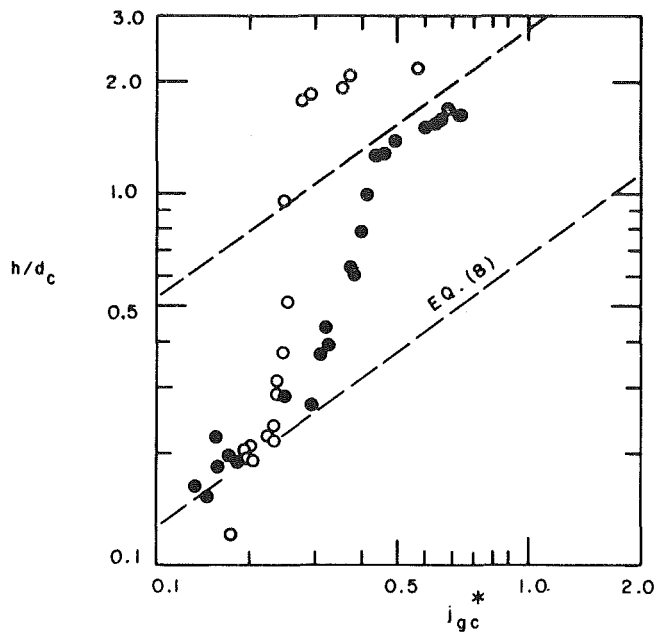

Fig. 11 Effect of core-bottom orifice in 29-cm vessel: • open core; ○ 15.3-cm core bottom orifice

During the transition the measurements generally follow the trend predicted by equation (8), taking into account the increased velocity at the interface resulting from separation of the air jet issuing from the core.

For even higher air flows, i.e., past the transition in region (c), the voided height h/d_c once again varies more gradually with j_{gc}^*, similar to region (a). It is surmised that the entrainment mechanism may be the same in regions (c) and (a), except for the presence of a separation bubble at high air flows as shown in Fig. 8.

Assuming that the separation bubble in region (c) extends axially over a fraction x of the total voided height h, i.e., $h_s = xh$, and that the flow in the axial length h_1 is similar to the flow in region (a), the total voided height h/d_c in region (c) can be related to j_{gc}^* as:

$$h/d_c = \frac{0.595}{(1-x)} j_{gc}^{*2/3} \tag{9}$$

In most tests, the data in the region (c) turn out to be four to five times greater than in region (a) indicating that x lies in the range $0.75 < x < 0.8$.

Results and Discussion

Flat Bottom Vessels. The experimental results of this study and the comparison with other data is condensed in Figs. 10 and 11. The symbols are illustrated in Tables 2 and 3. The voided height variation with core air flow for the 29-cm vessel is shown. Data for three different annulus gaps $s/d_c = 0.045$, 0.076, and 0.104 are included. Each data set exhibits a transition at $j_{gc}^* \simeq 0.4$. The effect of annulus gap is obscured by the scatter in the data, except in the transition regime. For the range of s/d_c tested, lower plenum voiding is generally not influenced by the gap width. The data in the region (a) compare well with equation (8). The trend of h/d_c in the region (c) is approximately four times equation (8).

For the 29-cm vessel with an annulus gap width of $s = 1.9$ cm, the effect of a 15.3-cm dia orifice introduced at the core exit is shown in Fig. 11. At low j_{gc}^* values, the h/d_c data with and without the orifice merge together and fall along equation (8). However, with the orifice, the transition occurs at a lower j_{gc}^*. Above the transition, the h/d_c data with the orifice lie along a line approximately six times the prediction from equation (8).

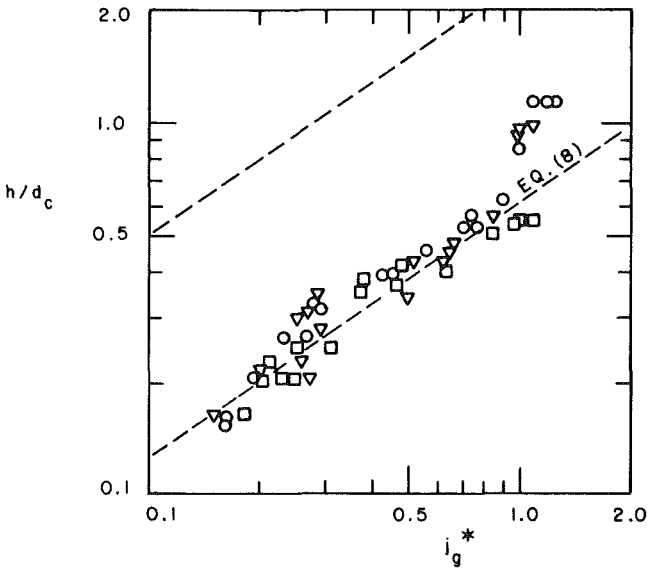

Fig. 12 Effect of lower plenum length on voided height in a 19-cm vessel: ○ l_p = 43 cm; ▽ l_p = 32 cm; □ l_p = 19 cm

Similar voided height data for the 19-cm vessel are shown in Fig. 12. Data for three different lower plenum lengths $l_p/d_c = 0.99$, 1.68, and 2.25 are included. At low l_p/d_c, no transition occurred in the tests. At higher plenum lengths, transitions were observed, and a corresponding jump in the voided height is seen at $j_{gc}^* \simeq 0.9$. However, the data below the transitions for the three plenum lengths cluster together. Excellent agreement between the data and equation (8) is seen.

Two sets of LPV data for steam-water flows obtained by Crowley and Rothe [3] in 15.2-cm and 44.4-cm diameter vessels with deep lower plena are shown in Fig. 13. The data for both vessels exhibit similar trends. At low j_g^* values the h/d_c values are twice as large as given by equation (8) in either case. At high j_g^* values, the h/d_c values are approximately five times those given by equation (8).

The effect of altered surface tension was explored by examining the voiding of methanol from the 29-cm vessel. The relevant properties of water and methanol are listed in Table 1. The voiding data with methanol are compared to

Table 1 Properties of water and methanol

Fluid	Temp. (°C)	Density (kg/m^3)	Viscosity ($N\,s/m^2$)	Surface Tension (N/m)
Water	20	997	89×10^{-5}	73×10^{-3}
Methanol	20	786	56×10^{-5}	23×10^{-3}

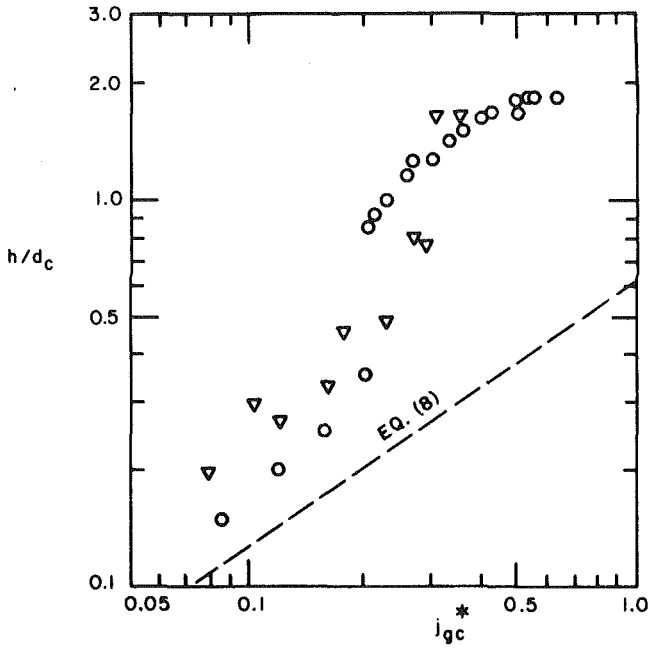

Fig. 13 Steam-water LPV data from Crowley-Rothe (1978): ○ 15.2-cm vessel; ▽ 44.4-cm vessel

those with water in Fig. 14. Below transition, the voiding data for both fluids merge together indicating that the voiding mechanism may be independent of surface tension in this range for sufficiently large vessels. Again, the data in both cases compare well with equation (8).

Hemispherical Bottom Vessels. Plenum voiding data for the simulated reactor hardware and geometries in a 29-cm vessel with hemispherical bottom are shown in Fig. 15. Since the hardware at the core exit contains multiple holes, the reference diameter d_c used is the core diameter of 26.6 cm. The data for the Westinghouse hardware compare reasonably well with equation (8). For the Babcock & Wilcox hardware, at a given j^*_{gc}, the values of h/d_c are approximately twice that given by equation (8). For either hardware, the data lie parallel to equation (8). Both hardwares are described in detail in the report by Crowley and Rothe [3]. For the range of air flows tested, no transition was observed before the plenum was completely emptied.

For similar reactor geometries, LPV data obtained with steam and water by Crowley and Rothe [3] are shown in Fig. 16. For these tests, a "thermally thick" core barrel with 14.6-cm i.d. and 6-cm wall thickness was used. These data therefore correspond to j^*_{gc}, based on the core inner diameter.

For the Babcock & Wilcox geometry, the air-water and steam-water data merge together and compare reasonably well. In the case of Westinghouse geometry, at a given j^*_{gc}, the steam-water data are approximately twice the air-water data.

For the 29-cm vessel with hemispherical plenum, similar sets of data for cores equipped with 23-cm and 18-cm circular orifices are shown in Fig. 17. For these single-holed orifice plates, the orifice diameter is used as the reference length. With either orifice, due to the shallow lower plenum, no transition due to sloshing was observed. The data for the larger orifice compare well with equation (8). Those with the smaller orifice are somewhat above equation (8).

The transition usually was found to occur in deep lower

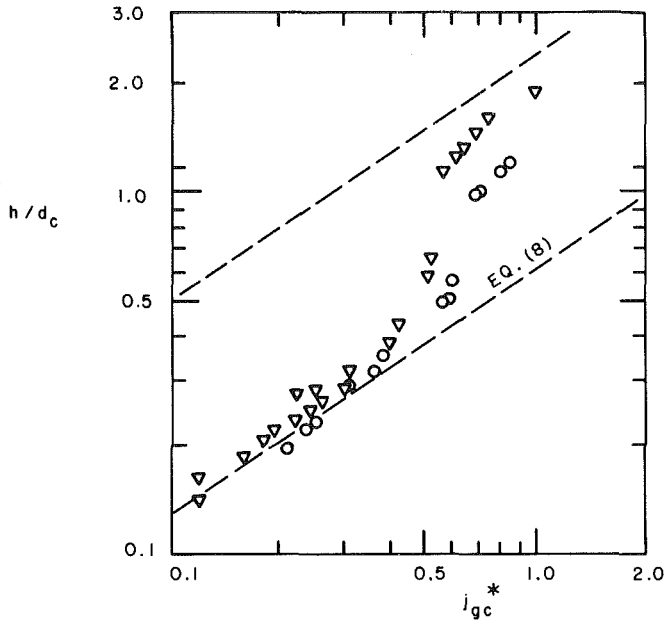

Fig. 14 Comparison of voiding data for different liquids: ▽ methanol; ○ water; 29.1-cm vessel; 1.9-cm annulus gap; 49.2-cm lower plenum length

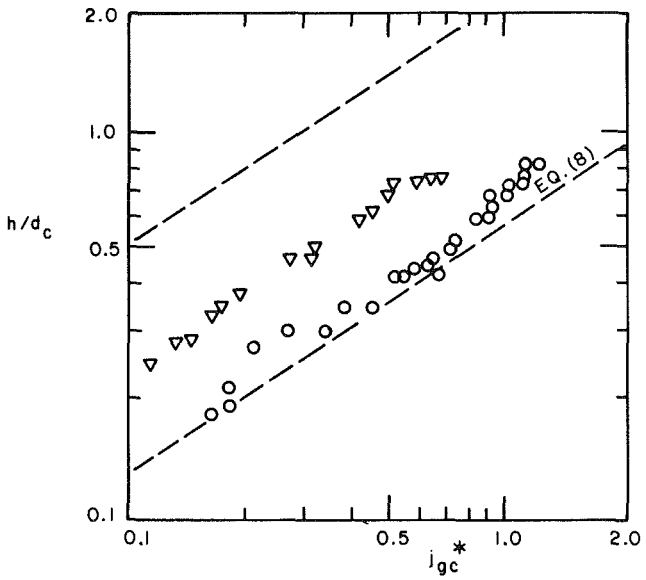

Fig. 15 Voided height versus air flux: simulated reactor geometry; ○ Westinghouse; ▽ Babcock & Wilcox geometry

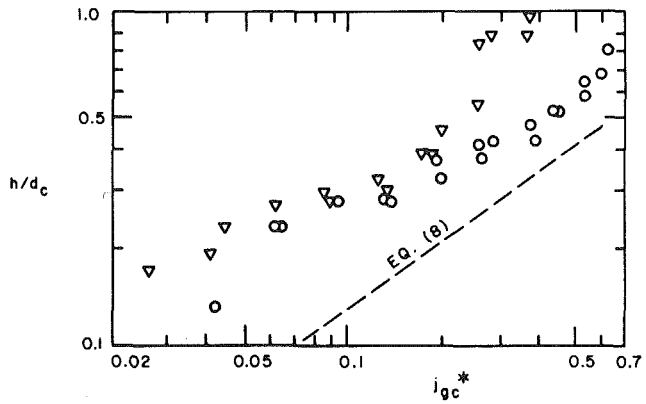

Fig. 16 Steam-water LPV data for simulated reactor geometries: Crowley and Block (2), ○ Babcock & Wilcox, ▽ Westinghouse

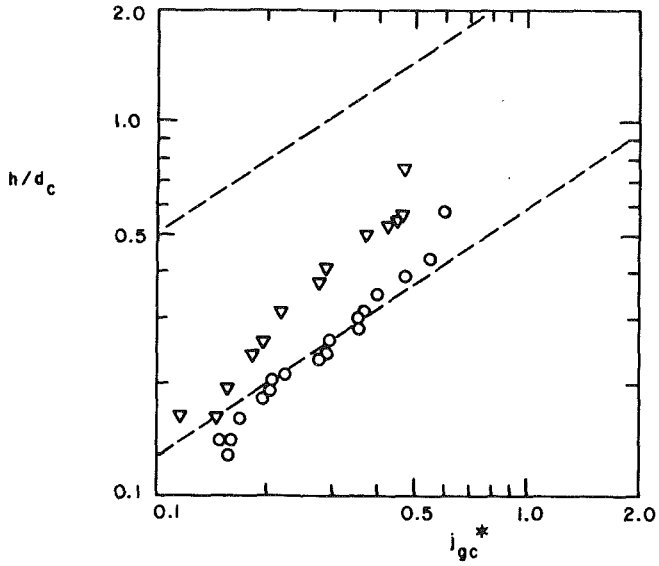

Fig. 17 Voided height versus air flux in hemispherical bottom vessel with core-bottom orifice: ○ 23-cm orifice; ▽ 18-cm orifice

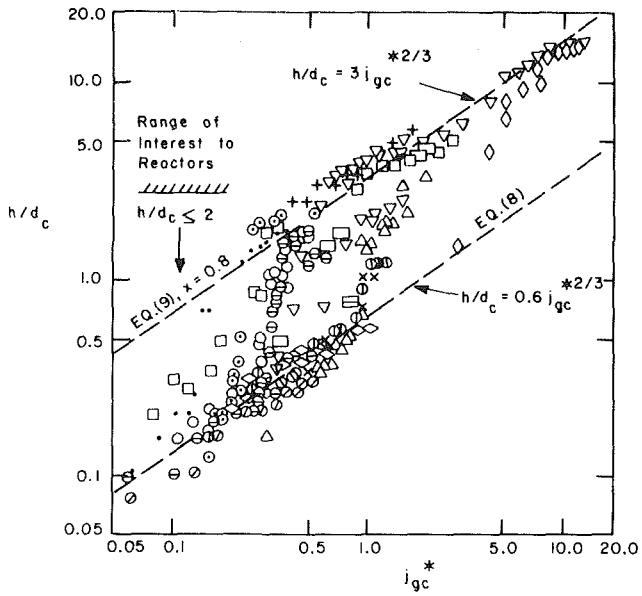

Fig. 18 Lower plenum voiding data comparison, (symbols – see Table 2)

Table 2 Symbol key for LPV data comparison (Fig. 13)

Symbol	Vessel diameter D_v(cm)	Core reference diameter d_c(cm)	Gap width s(cm)	Water injection rate Q_g(gpm)	Remarks
◯	29.1	26.6	1.2	0	
⊙	29.1	24.1	1.9	0	
◯	19.1	15.3	1.3	0	Air-
×	19.1	15.3	1.3	0	water
	19.1	15.3	1.3	0	data
△	10.0	7.6	0.9	0	present
□	44.5	38.7	1.9	0	
•	15.2	12.7	0.6	0	
⊖	15.2	12.7	0.6	0.64	
◯	15.2	12.7	0.6	2.0	
◯	15.2	12.7	0.6	10.0	Steam-
▽	15.2	7.6	3.2	0	water
▽	15.2	7.6	3.2	25.0	Crowley
+	15.2	6.0	0.6	0	and
	15.2	6.0	0.6	1.2	Rothe
▽	15.2	2.5	0.6	0	[3]
	15.2	2.5	0.6	5	
		semiscale	1.2		Naff
△		semiscale	2.5		et al.
					[6]

plena with large l_p/d_c and over long time intervals. In the reactor-like geometries, due to the shallowness of the plenum, no transition was observed. In real reactors lower plenum lengths l_p/d_c are limited to less than one. In addition, sufficient time may not be available to build up sloshing oscillations. Therefore, the voiding data obtained with cylindrical vessels in the transition region may not be directly applicable during transient steam flows expected to occur in a LOCA.

Additional Comparisons. A comprehensive comparison of a wide range of data obtained from various facilities is shown in Fig. 18. All the data, except for those from Semiscale, were obtained in cylindrical plena with flat bottoms. Data obtained with circular orifices at the core bottom and with direct water injection in the lower plenum are included. Various experimental conditions are tabulated in Table 2. For comparison, two lines representing equation (8) and equation (9) with $x=0.8$ are shown. Below transition, the data from various sets compare well with equation (8). The transition appears to occur at different j^*_{gc} for different test conditions. The data above transition appear to fall along lines parallel to equation (8). In this region, the factor x in equation (9) arises due to the separated air flow out of the core and may be a complex function of both d_c/D_c and l_c/d_c. The parameters h/d_c and j^*_{gc} vary over a wide range from 0.05 to 20 in this figure. In typical reactors geometries, the maximum value of h/d_c may not exceed 2, and this limit is shown on the left side of the figure.

Additional comparisons of the present theory with steam-water LPV data obtained by Wallis et al. [5] in an 8.9-cm vessel is shown in Fig. 19. The data below transition follow equation (8) reasonably well. Above transition, the data lie along equation (9) with $x=0.8$.

For reactor-like geometries with hemispherical plena, a comparison of the various LPV data is shown in Fig. 20. For each set of data, there occurs no abrupt change in the general trend of the data indicating the absence of a transition regime. The data from each set lie generally parallel to equation (8). However, since the gas flows through structures with complex geometries at the core exit, the data from the various tests are somewhat scattered. However, equation (8) together with equation (9) with $x=0.8$ offer lower and upper bounds to the voided height variation, respectively.

Concluding Remarks

Lower Plenum voiding in three simple cylindrical geometries and simulated reactor vessels has been investigated. The principal findings may be summarized as follows:

(*a*) In cylindrical vessels, the voiding process occurs in three stages. At low gas flow rates, a level liquid surface with standing waves is observed. At higher gas flows, the liquid undergoes bulk sloshing possibly due to establishment of a separated region around the emerging gas jet from the core. At even higher gas flows, a considerably rougher interface is seen.

(*b*) The transition due to sloshing appears to be a function of the lower plenum length. With a deep lower plenum, the transition is observed to occur. In the hemispherical bottom vessels, no transition is observed due to the shallowness of the lower plenum.

(*c*) The voiding process is strongly influenced by the core-

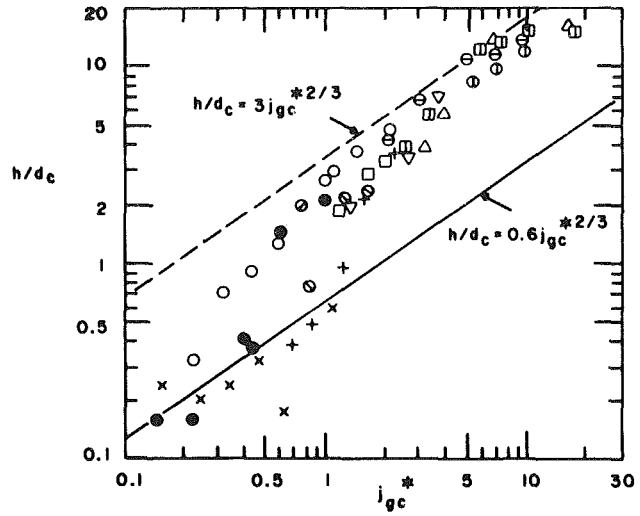

Fig. 19 Comparison of theory and steam-water LPV data in 8.9-cm vessel, Wallis et al. (5), (symbols – see Table 3)

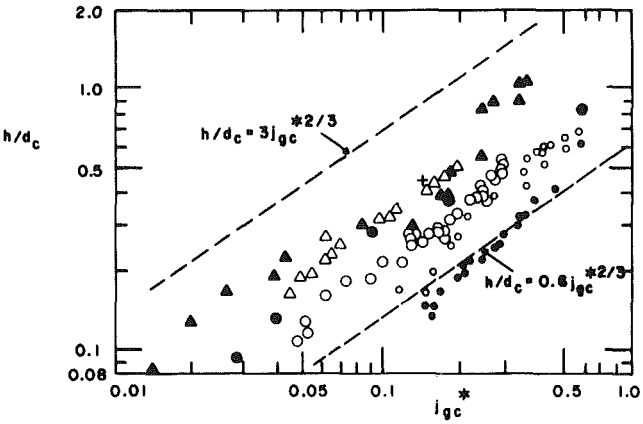

Fig. 20 Lower plenum voiding data for simulated reactor vessels with 29.1-cm diameter with hemispherical lower plenum, (symbols – see Table 4)

exit diameter d_c. At low gas flow rates, in most cases, the voiding data can be correlated as h/d_c versus dimensionless core momentum flux, j^*_{gc}, as

$$h/d_c = \frac{0.6}{(1-x)} j_{gc}^{*2/3}$$

with $x=0$. At higher air flows after the transition, the fraction x representing the fractional length occupied by a separation bubble takes on a value in the range of $0.67 \le x \le 0.8$, which was evaluated from the experiments.

(*d*) Over the range of parameters tested, h/d_c appears to be a weak function of the vessel diameter and the lower plenum length.

(*e*) Nonuniformities in the core gas jet tend to increase the voided height (i.e., enhance the entrainment from the interface).

(*f*) Voiding data with saturated steam and water, with air and water, and with air and methanol, appear to follow similar variations within the scatter of the data.

(*g*) Data obtained in models duplicating some of the features of lower plenum hardware found in PWRs follow the same trends as the data obtained in simple cylindrical vessels and appear to lie between the upper and lower bounds established for those vessels.

Table 3 Symbol key for LPV data from reference [5] (Fig. 19)

Symbol	Core reference diameter d_c(cm)	Gap width s(cm)	Annulus length l_a(cm)
⊖	2.1	0.64	0.0
□	2.1	0.64	7.9
▽	2.1	0.64	39.4
◯	3.8	0.64	0.0
◯	6.4	0.64	0.0
●	6.4	0.64	7.9
×	6.4	0.64	39.4
△	2.1	1.9	7.9
◯	2.1	1.9	39.4
	3.8	1.9	39.4
◯	semiscale data, Naff et al. [6]	1.2	----
	semiscale data, Naff et al. [6]	2.5	----

Table 4 Symbol key for LPV data for simulated reactor vessels with hemispherical lower plenum (Fig. 20)

Symbol	Lower plenum hardware	Media	Reference
◯	Westinghouse	air	present
▲	Westinghouse	steam	Crowley and Block [2]
△	Babcock & Wilcox	air	present
●	Babcock & Wilcox	steam	Crowley and Block [2]
•	22.9-cm orifice	air	present
○	18.3-cm orifice	air	present

Acknowledgment

This work was sponsored by the Nuclear Regulatory Commission under contract number RS-NRR-03-79-102.

References

1 Block, J. A., and Schrock, V. E., "Emergency Cooling Water Delivery to the Core Inlet of PWRs During LOCA," *Thermal and Hydraulic Aspects of Nuclear Reactory Safety*, Vol. 1: *Light Water Reactors*, ASME, 1977.

2 Crowley, C. J., and Block, J. A., 1977, "Lower Plenum Voiding with Scaled PWR Plenum Geometries," CREARE TN-258, CREARE Inc., Hanover, N. H.

3 Crowley, C. J., and Rothe, P. H., "Progress on Lower Plenum Voiding," Nuclear Regulatory Commission Report, NUREG/CR-0121, TN-278, 1978.

4 Graham, G. J., Ludwig, D. L., Wallis, G. B., and Richter, H. J., "Two-Phase Flow in a Model Pressurized Water Reactor Equipped with Vent Valves," Nuclear Regulatory Commission Report, NRC-0193-1, Dartmouth College, 1977.

5 Wallis, G. B., Block, J. A., Crowley, C. J., Thrall, D. W., and Rundstadler, P. W., Jr., "Some Two-Phase Flow Aspects of Light Water Reactor LOCAs," CREARE TN-209, CREARE Inc., Hanover, N.H., 1975.

6 Naff, S. A., Alder, R. S., and Pinson, P. A., "Experimental Data Report for Semiscale System Countercurrent Flow Tests," ANCR-1151, June 1974.

H. R. Jacobs
Professor,
Department of Mechanical and Industrial Engineering,
University of Utah,
Salt Lake City, Utah 84117
Mem. ASME

B. H. Major
Research Engineer,
Sandia Corporation,
Albuquerque, N.M.

The Effect of Noncondensible Gases on Bubble Condensation in an Immiscible Liquid

A numerical study of the collapse of a bubble in a three-component, three-phase system is presented. The heat transfer is modeled using a quasi-steady integral boundary layer approach while the concentration profiles of noncondensibles are determined by solving the transient diffusion equation. It is shown that the experimentally determined collapse of small bubbles (between 1-mm and 3-mm initial radius) agrees with the model, while larger bubbles, which deform during their early history, are better described by a uniformly distributed noncondensible model.

Introduction

Florschuetz and Chao [1] and Wittke and Chao [2] studied the collapse of spherically symmetrical bubbles within their own liquid. Stimulated by interest in desalination processes, Isenberg and Sideman [3] presented a numerical solution for the case of a two-component (pentane-water) system where a bubble of the volatile component was collapsing. The latter system differs from the former, one-component system, in that the condensate remains within the confines of the bubble walls. Later Isenberg et al. [4] presented an approximate quasi-steady state analytical solution for bubble collapse in three-component, three-phase systems. The solution assumed the noncondensibles remained uniformly distributed throughout the vapor. In references [1–3] the bubble's velocity is assumed constant, and either the flow of the liquid moving past the bubble is potential flow or is as if the bubble were a rigid sphere (boundary layer type flow). Isenberg et al. [4] utilized a velocity correction factor and potential flow to approximate the viscous effects and simply solved an energy balance across the thermal boundary layer in the continuous phase in order to approximate the quasi-steady heat transfer. References [1–4] neglected the existence of a condensate film and thus assumed that the bubble's surface was at the instantaneous saturation temperature of the vapor based on its partial pressure.

Jacobs et al. [5] noted that the existence of a condensate film within the bubble in a two-component system could have a significant effect on its collapse, particularly if the condensate's thermal conductivity was small. An analysis was conducted for a two-component system using a quasi-steady analytical approach similar to that of Isenberg et al. [4]. The results showed that the condensate film could contribute 20 percent of the resistance to heat transfer. Further, they showed that the interfacial temperature between the condensate and continuous phase is not a function of angular distance from the upper stagnation point, but only a function of the properties of the two fluids.

When the model of Jacobs et al. [5] was modified to account for uniformly distributed noncondensibles, it still appeared to overpredict the collapse rate of initially small bubbles. This led the present authors to assess the possibility of nonuniform distribution of the noncondensibles, and to investigate the hydrodynamics of the condensate film which had been assumed to move in potential flow. This latter assumption was proved to be acceptable for most fluids of interest [6]; however, a truncation error was found in the series solution of [5] which slightly modified the pure fluid bubble collapse rate.

The only attempt known to the present authors to deal with the effect of nonhomogeneous distribution of noncondensibles on bubble collapse was that Moalem and Sideman [7]. They assumed a parabolic concentration profile of the inerts within the bubble. The inert concentration at the center of the bubble was assumed constant. This concentration profile does not satisfy the boundary conditions and represents at best only an approximation to the inert concentration within the bubble. Due to the above perceived shortcomings, the present work was initiated. The basic model utilizes the nontruncated integral binary boundary layer model of Jacobs et al. [5] and then solves the bubble collapse numerically, assuming that the distribution of inerts within the bubble is governed by diffusion.

Analysis of the Physical Model

Heat Transfer. The collapsing bubble is assumed to be spherical and rising freely in a vertical path. Alternatively, it can be envisioned in terms of a moving coordinate system with the continuous medium moving over it as shown in Fig. 1.

The rise velocity of the bubble is assumed to be constant. This assumption has been shown to be reasonable for bubbles of initial radius between 2mm and 4mm [1–4]. For bubbles of this size the translational motion is typically much more rapid

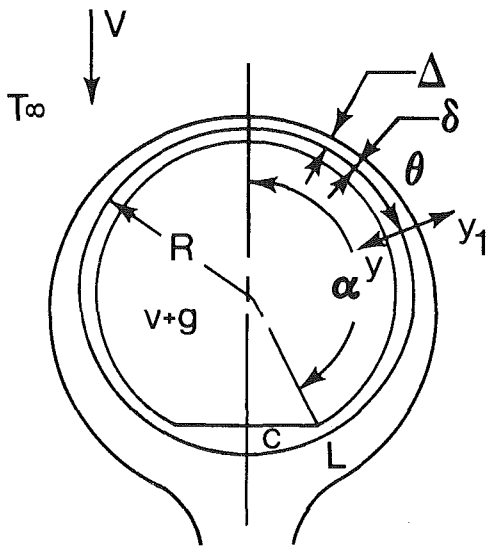

Fig. 1 Schematic model for bubble collapse

Contributed by the Heat Transfer Division and presented at the ASME Winter Annual Meeting, New York, N.Y., December 2–7, 1979. Manuscript received by the Heat Transfer Division December 29, 1980. Paper No. 79-WA/HT-26.

than the rate of decrease in radius (2-4). Thus, a quasi-steady analysis of bubble hydrodynamics and heat transfer is applicable [3-5]. For most fluid combinations, i.e., hydrocarbon bubbles in water, it may be shown that the appropriate interfacial tensions are such that the condensate wets the walls of the bubble and flows down its sides to pool at the bottom of the bubble. This latter characteristic while representative of the condensation of an immiscible vapor is not true for a vapor collapsing in its own liquid. However, even for this system it is reasonable to assume a laminar condensate film which mixes with the continuous phase only in the wake. Thus, for laminar flow, which is assumed here, the model could be applied to a vapor bubble condensing in its own liquid.

Typically the viscosities of both the condensate and the surrounding liquid are much higher than that of the vapor, $\mu_v << \mu_c 0(\mu_L)$. For these conditions it is reasonable to assume that the movement of the condensate is not retarded by the vapor, yet is strongly influenced by the continuous liquid. It will be assumed here that the condensate as well as the liquid attains local velocities consistent with the inviscid flow of a liquid over a sphere [5, 6].

Our primary interest in immiscible vapor bubble collapse had as an impetus condensation with small temperature differences such that

$$C_{pc}(T_{\text{sat}} - T_\infty) << h_{fg} \tag{1}$$

Thus, a simple energy balance across the condensate yields

$$\frac{1}{R}\frac{d}{d\Theta}\int_0^\delta \rho_c V h_{fg} \sin\Theta dy = \lambda_c \frac{\partial T}{\partial y}\bigg|_{y=0} \tag{2}$$

The assumption expressed in equation (1) leads to the use of a linear temperature profile across the condensate [5]

$$T_c = T_{int} + (T_{\text{sat}} - T_{int})\frac{y}{\delta} \tag{3}$$

where T_{int} is the temperature at the interface between the condensate and the continuous phase.

The integral form of the energy equation for the thermal boundary layer in the continuous liquid is

$$\frac{1}{R}\frac{d}{d\Theta}\int_0^\Delta V \sin\Theta (T\infty - T_L) dy_1 = \frac{\lambda_L}{\rho_L C_{p_L}}\frac{\partial T_L}{\partial y_1}\bigg|_{y_1=0} \tag{4}$$

where T_L can be represented by the quadratic

$$T_L = T_{int} + \frac{T_{int} - T\infty}{\Delta^2}(y_1^2 - 2\Delta y_1) \tag{5}$$

There exists in the above equations unknowns, T_{int}, δ, and Δ. To make the problem analytical an additional relationship is needed. This is provided by the equality of heat fluxes at the interface, $y = y_1 = 0$:

$$q_c|_{y=0} = -q_L|_{y_1=0} \tag{6}$$

Application of Fourier's Law and the temperature profiles of equations (3) and (5) yields

$$\frac{\lambda_c(T_{\text{sat}} - T_{int})}{\delta} = \frac{2\lambda_L(T\infty - T_{int})}{\Delta} \tag{7}$$

Simultaneous solution of equations (2), (4), and (7) provide expressions for the three variables δ, Δ, and T_{int} as functions of Θ. It has been shown in reference [5] that T_{int} is not a function of Θ but is dependent only on the physical properties of the fluids.

$$\phi = \frac{T_{int} - T\infty}{T_{\text{sat}} - T\infty} = \sqrt{C_1^2 + 2C_1} - C_1 \tag{8}$$

where

$$C_1 = \frac{0.75\,\lambda_c \rho_c C_{pc}}{\lambda_L \rho_L C_{p_L} Ja_c} \tag{9}$$

Utilizing Fourier's Law of Heat Conduction, the temperature profile across the liquid thermal boundary layer, and the resulting solutions for Δ and T_{int}, the local heat flux can be obtained. This may be integrated over the surface of the bubble to give the instantaneous heat flux [6]:

$$q(t) = \int_0^\alpha 2\pi R^2 \sin\Theta\left(-\lambda_L \frac{\partial T_L}{\partial y_1}\bigg|_{y_1=0}\right) d\Theta \tag{10}$$

Nomenclature

α = angular distance to pool of condensate at bottom of drop
β = R/R_0
β_f = final nondimensional radius, defined in equation (18)
C_c = mass concentration of vapor
C_{c_0} = initial mass concentration of vapor
C_p = specific heat at constant pressure
C_1 = defined in equation (9)
D_c = mass diffusion coefficient
δ = thickness of condensate film
Δ = thickness of thermal boundary layer in continuous liquid
Fo_L = $\lambda_L t/[\rho_L C_{p_L} R_0^2]$
$1/G$ = ρ_v/ρ_c for immiscible fluids, 0 for a bubble collapsing in its own liquid
Γ = initial mole fraction of noncondensibles
θ = angular distance from top of bubble
h_{fg} = heat of vaporization
Ja_c = $C_{p_c}(T_{\text{sat}} - T\infty)/h_{fg}$
Ja^* = $Ja_c(\rho_L C_{p_L})/(\rho_c C_{p_c})$
Ja_0^* = $Ja^*(T^* - T\infty)/(T_{\text{sat}} - T\infty)$
K = $D_c \rho_v h_{fg}/[(\text{Re}_{L_0}\text{Pr}_L)^{1/2} \lambda_L (T^* - T\infty)]$
λ = thermal conductivity
m = mass of substance
μ = viscosity
P = pressure
P^* = system pressure
Pr_L = $C_{pL}\mu_L/\lambda_L$
ϕ = defined in equation (8)
q = heat flux
r = radius
$\bar{r}$ = r/R_0
R = instantaneous bubble radius
R_0 = initial bubble radius
Re_{L0} = $2R_0 V \rho_L/\mu_L$
ρ = density
t = time
T = temperature
T_{sat} = saturation temperature of vapor at partial pressure
T^* = saturation temperature of vapor at system pressure
$T\infty$ = temperature of bulk surrounding liquid
T_{int} = interfacial temperature between condensate and surrounding liquid
τ = $(\text{Re}_{L0}\text{Pr}_L)^{1/2} Ja^* \frac{\rho_c - \rho_v}{\rho_v} \text{Fo}_L$
V = rise velocity of bubble
y = local inward normal as shown in Fig. 1
Y_1 = local outward normal as shown in Fig. 1

Subscripts

c = condensate
L = continuous liquid
v = vapor
$v+g$ = vapor and gas mixture

For practical purposes, α can be assumed equal to π with typical errors of less than 5 percent for 95 percent of the bubble collapse history. The resulting heat transfer is

$$g(t) = 2.28\pi\lambda_L \phi(T_{\text{sat}} - T\infty)\sqrt{\frac{\rho_L C_{pL} V}{\lambda_L}} R^{3/2} \quad (11)^1$$

Bubble Collapse. In the present analysis, we follow the definition of Sideman and co-workers [3, 4, 7] as to what is meant by a bubble. This definition states that the volume of a bubble in an immiscible liquid should include the condensate as well as the vapor gas mixture. That is, for a spherical bubble

$$\frac{4}{3}\pi R^3(t) = \frac{m_{v+g}(t)}{\rho_{v+g}} + \frac{m_c(t)}{\rho_c} \quad (12)$$

For a bubble collapsing in its own liquid the condensate is swept away while for a bubble collapsing in an immiscible liquid the condensate stays with the vapor as shown in Fig. 1. This difference in definition eliminates the second term on the right side of equation (12) for a bubble condensing in its own liquid.

If we differentiate equation (12) with respect to time and recognize that

$$-\frac{dm_{v+g}(t)}{dt} = \frac{dm_c(t)}{dt} = \frac{q(t)}{h_{fg}}$$

we find that for a spherical bubble collapsing in an immiscible liquid

$$\frac{d\beta^3}{dt} = \frac{3}{4\pi}\frac{q(t)}{h_{fg}R_0{}^3}\frac{\rho_v - \rho_c}{\rho_v\rho_c} \quad (13)$$

where β is the nondimensional radius $R(t)/R_0$, and R_0 is the initial bubble radius. For the case where $\rho_c >> \rho_v$, equation (13) is identical to that for a bubble collapsing in its own liquid,

$$\frac{d\beta^3}{dt} = \frac{-3}{4\pi}\frac{q(t)}{h_{fg}\rho_v R_0{}^3} \quad (14)$$

For a bubble, in the absense of noncondensibles, equations (11) and (13) yield

$$\beta = \left[1 - 0.6049(\text{Re}_{L_0}\text{Pr}_L)^{1/2}\phi Ja^*\frac{\rho_c - \rho_v}{\rho_v}\text{Fo}\right]^{2/3} \quad (15)$$

for the time dependent nondimensional radius of a bubble collapsing in an immiscible liquid. For a bubble collapsing in its own liquid we obtain

$$\beta = \left[1 - 0.6049(\text{Re}_L\text{Pr}_{L_0})^{1/2}\phi Ja^*\frac{\rho_c}{\rho_v}\text{Fo}\right]^{2/3} \quad (16)$$

which is essentially the same as that given in equation (15) when $\rho_c >> \rho_v$.

Uniform Distribution of Noncondensibles. Noncondensible gases may well be present in a vapor bubble. They significantly affect the bubble collapse. If the noncondensible gases were always uniformly mixed with the vapor, Florschuetz and Chao [1] and Isenberg et al. [3] have shown that the temperature difference $(T_{\text{sat}} - T\infty)$ is governed by the relationship

$$\frac{T_{\text{sat}} - T\infty}{T^* - T\infty} = \frac{\beta^3 - \beta_f{}^3}{\beta^3 - 1/G} \quad (17)$$

Here, T_{sat} refers to the actual saturation temperature of the vapor corresponding to its instantaneous partial pressure, and T^* refers to the saturation temperature at the system pressure. The term $1/G$ is due to the condensed liquid which accumulates in the bubble when the continuous phase is immiscible. For this case $1/G = \rho_v/\rho_c$. For the case of a bubble collapsing in its own vapor $1/G$ is zero [1].

The final bubble radius, β_f can be obtained utilizing the Gibbs-Dalton Law and the Clausius-Clapeyron equation knowing the initial concentration of noncondensibles. Isenberg et al. [3] give for the case of immiscible fluids

$$\beta_f = \left(\frac{RT^{*2}\Gamma}{h_{fg}(T^* - T\infty)} + \frac{1}{G}\right)^{1/3} \quad (18)$$

where, for a bubble collapsing in its own fluid, the $1/G$ term is again zero [1].

Utilizing equations (11), (14), and (17), the bubble collapse rate for uniform distribution of noncondensibles can be written as

$$\frac{d\beta^3}{d\tau} = -0.9075\frac{\lambda_c}{Ja_0^*\lambda_L}\left[\sqrt{1 + \frac{8}{3}Ja_0^*\frac{\lambda_L}{\lambda_c}\left(\frac{\beta^3 - \beta_f{}^3}{\beta^3 - 1/G}\right)} - 1\right]\beta^{3/2} \quad (19)$$

where

$$\tau = (\text{Re}_{L_0}\text{Pr}_L)^{1/2}Ja_0^*\frac{\rho_c - \rho_v}{\rho_v}\text{Fo}_L$$

The above equation must be solved numerically. The initial condition is $\beta = 1$ at $\tau = 0$.

Nonuniform Distribution of Noncondensibles. The assumption of uniformly mixed noncondensibles which leads to the derivation of equation (19) is not generally valid. If the bubble remains spherical and there is no means, such as periodic deformation, to include circulation of the gas vapor mixture, the only means of dispersing the noncondensibles is by diffusion. This is particularly true when $\mu_{v+g} < \mu_c$. Assuming a diffusion dominated mechanism and spherical symmetry we have

$$\frac{\partial C_c}{\partial\tau} = \frac{K}{\bar{r}^2}\frac{\partial}{\partial\bar{r}}\left(\bar{r}^2\frac{\partial C_c}{\partial\bar{r}}\right) \quad (20)$$

for the distribution of condensible vapor within the bubble. $\bar{r}$ is the nondimensional radius r/R_0, τ is defined above, and $K = D_c\rho_v h_{fg}/(\text{Re}_{L0}\text{Pr}_L)^{1/2}\lambda_L\ (T^* - T\infty)$. At time zero, $\tau = 0$ and the vapor concentration is assumed uniform throughout the bubble and equal to the initial mass concentration,

$$C_c(\tau = 0) = C_{c_0} \quad (21)$$

By symmetry the concentration gradient at the center of the bubble must vanish, that is

$$\frac{\partial C_c}{\partial\bar{r}}(\bar{r} = 0) = 0 \quad (22)$$

At the bubble wall the boundary condition is complicated by the collapse of the boundary. The final result is a combined diffusion and mass convection at the wall. This was shown to be the case in a similar boundary condition by Sparrow, Ramadhyani, and Patankar [9]. To visualize this condition, consider the mass transfer from a boundary fixed coordinate system. Mass crosses the boundary by convection with a velocity equal to the collapse rate, $-dR/dt$. The total mass crossing the boundary due to the combined diffusion and convection is equal to the mass of vapor converted to liquid through latent heat release. This may be written in mathematical form as

$$-\rho_{v+g}C_c\frac{dR}{dt} - \rho_{v+g}D_c\frac{\partial C_c}{\partial r}\bigg|_R = \frac{q(t)/4\pi R^2}{h_{fg}} \quad (23)$$

The bubble collapse is still defined by equation (13). In terms of the nondimensional time, equation (13) reduces to

[1] Complete details of the derivation can be found in Reference 6.

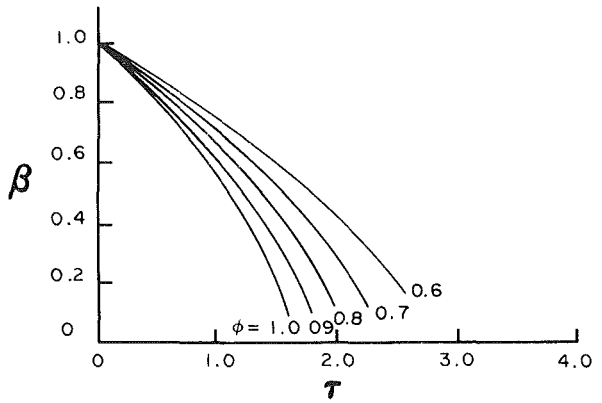

Fig. 2 Bubble collapse of pure vapor for several values of the dimensionless interface temperature

$$\frac{d\beta^3}{d\tau} = 1.71\phi\left(\frac{T_{sat} - T\infty}{T^* - T\infty}\right)\frac{\rho_v - \rho_c}{\rho_c}\beta^{3/2} \tag{24}$$

Using equation (24) and equation (11) and nondimensionalizing, equation (23) becomes

$$\left.\frac{dC_c}{d\bar{r}}\right|_\beta = \frac{\lambda_L(T^* - T\infty)(\mathrm{Re}_{L_0}\mathrm{Pr}_L)^{1/2}}{D_c h_{fg}}\left[\frac{1}{\rho_{v+g}} - \frac{C_c}{\rho_v}\right]\frac{d\beta}{d\tau} \tag{25}$$

The mass diffusion within the bubble is completely defined by equations (20), (21), (22), and (25). These together with equation (24) and the Clausius-Clapeyron equation (to relate the partial pressure of the vapor to the saturation temperature) are sufficient to predict bubble collapse.

Due to the complicated nature of the above equations governing bubble collapse the solution must be determined numerically. Utilizing a finite difference scheme a significant, error might result after many time steps. It is therefore desirable to make a check on the solution after each step. As the noncondensible gas must remain within the bubble, a mass balance on the noncondensibles should yield a constant value. The following relation thus should be satisfied.

$$\int_0^\beta \rho_{v+g}\bar{r}^{\,2}(1 - C_c)d\bar{r} = 1/3(1 - C_{c_0})\rho_{v+g}(\tau = 0) \tag{26}$$

Numerical Solutions

Uniform Mixed Noncondensibles. The complicated nature of equation (19) does not lend itself to direct integration, thus it must be solved numerically. The boundary condition at $\tau = 0$ is $\beta = 1.0$. Using this condition, the solution is advanced using simple forward integration until $\beta = \beta_f$. Care must be taken that as $\beta \to \beta_f$, $d\beta^3/d\tau \to 0$. This is accomplished by choosing $\Delta\tau$ sufficiently small.

Nonuniform Distribution of Noncondensibles. In carrying out the solution for nonuniform distribution of noncondensibles, equation (24) must be solved simultaneously with equations (20), (21), (22), and (25). We have chosen to use a central differencing scheme to solve for the concentration while using a simple forward differencing scheme for the change in bubble radius, equation (24).

The bubble radius at any time is divided into NP-1 intervals, with grid numbering starting at the center with 1 and being equal to NP when $\bar{r} = \beta$. The finite difference equations for the concentration of vapor take the form

$$-C_{\bar{r}-\Delta\bar{r}}^{\tau+\Delta\tau}K\Delta\tau\left(\frac{1}{\Delta\bar{r}^2} - \frac{1}{\bar{r}\Delta\bar{r}} + \frac{1}{4\bar{r}^2}\right) + C_{\bar{r}}^{\tau+\Delta\tau}(1 + \mathrm{K}\Delta\tau) \tag{27}$$

$$\left(\frac{2}{\Delta\bar{r}^2} + \frac{1}{2\bar{r}^2}\right) - C_{\bar{r}+\Delta\bar{r}}^{\tau+\Delta\tau}\mathrm{K}\Delta\tau\left(\frac{1}{\Delta\bar{r}^2} + \frac{1}{\bar{r}\Delta\bar{r}} + \frac{1}{4\bar{r}^2}\right) = C_{\bar{r}}^{\tau}$$

for internal nodes.

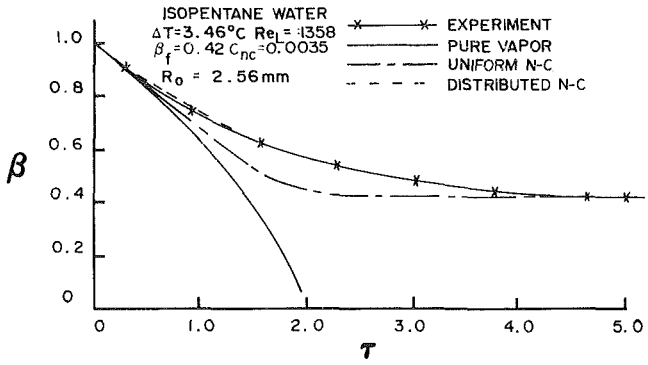

Fig. 3 Comparison of models with experimental data of reference [3] for isopentane bubbles collapsing in water

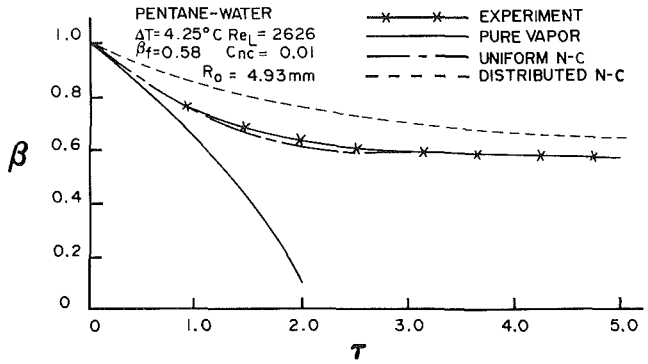

Fig. 4 Comparison of models with experimental data of reference [3] for pentane bubbles collapsing in water

The boundary conditions are

$$C_1^{\tau+\Delta\tau} - C_2^{\tau+\Delta\tau} = 0 \tag{28}$$

and

$$C_\beta^{\tau+\Delta\tau}\left[1 + \frac{\Delta\bar{r}}{\mathrm{K}}\frac{d\beta}{d\tau}\right] - C_{\beta-\Delta\bar{r}}^{\tau+\Delta\tau} = \frac{\Delta r}{\mathrm{K}}\frac{\rho_v}{\rho_{v+g}}\frac{d\beta}{d\tau} \tag{29}$$

The initial conditions are of course

$$C_i = C_{c_0} \tag{30}$$

the assumed initial concentration. The mixture density is calculated at each node assuming

$$\rho_{v+g} = y_c(\rho_v - \rho_g) + \rho_g \tag{31}$$

where y_c is the mole fraction. The partial pressure of the condensing vapor at the bubble radius is found from

$$P_c = P^* y_c(\beta) \tag{32}$$

where P^* is the total system pressure. The relationship between $T_{sat}(\beta)$ corresponding to the partial pressure was found from the Benedict-Webb-Rubin equation of state for actual vapors studied; although it is possible to use an approximate Clausius-Clapeyron equation for sufficiently low concentrations of noncondensibles [6].

Prior to calculating the change in bubble radius from equation (24), equation (26) was used to check the numerical solution for conservation of noncondensibles. Upon convergence of the concentration for a given time, the bubble collapse was advanced one time step. These steps were repeated until T_{sat} reached $T\infty$. At this time $\beta = \beta_f$, since the noncondensibles will diffuse away from the bubble wall and they will at complete collapse reach a uniform distribution.

Discussion and Results

Pure Vapor Systems. Equation (15) presents the bubble collapse of a pure vapor in an immiscible liquid. This

equation differs from the results of reference [5] only in the constant and the quantity $(\rho_c - \rho_v)/\rho_v$ in the second term in the brackets. In our prior work we had attempted to present an exact solution for the heat flux; however, we had truncated the series expansion which led to the constant in equation (15) to be 0.9009 instead of 0.6049, which is obtained numerically. Further in reference [5] we had assumed $\rho_c >> \rho_v$ such that $(\rho_c - \rho_v)/\rho_v \sim \rho_c/\rho_v$. This latter assumption would yield the results shown in equation (16), which is equal to the collapse of a bubble in its own liquid.

Typical results for bubble collapse are shown in Fig. 2 as a function of the parameter ϕ, which is defined in equations (8) and (9). For hydrocarbon bubbles condensing in water $\phi \sim 0.8$. For bubbles collapsing in their own liquid, ϕ is approximately equal to 1.0. Comparison of our results with those of Wittke and Chao [2] for pure vapor bubbles condensing in their own liquid indicate a slightly slower collapse rate being predicted by equation (16) than by Wittke and Chao. In fact, the solutions of Wittke and Chao [2] are well predicted by our prior results when we truncated the series expression for the heat flux [5]

$$\beta = \left[1 = .9009\,(\mathrm{Re}_{L_0}\,\mathrm{Pr}_L)^{1/2} Ja^* \frac{\rho_c}{\rho_v}\,\mathrm{Fo}\right]^{2/3} \tag{33}$$

We would presume that the difference is essentially due to roundoff error in Wittke and Chao [2] numerical solution. It is thus recommended that equation (15) and (16) be used in predicting bubble collapse respectively.

Condensation with Noncondensibles Present. In order to evaluate the diffusion model developed comparison was made with the experimental data of References 3 and 8 for hydrocarbons bubbles collapsing in water. The noncondensible gases present were assumed to be air. The mass diffusion coefficients for the air-hydrocarbon system were obtained from Sherwood, Pigford, and Wilke [10]. Comparison was also made with the uniformly mixed model of equation (19). Analyses were made for the case of each experiment presented in references [3] and [8]. These data covered a range of Reynolds number from 400 to 3000 with initial noncondensible varying from 0.1 to 1.0 percent, and bubble size from 0.426 mm in initial radius to 6.0 mm. The range of $T^* = T\infty$ varied from 3 to 10°C. The complete set of analyses are available in reference [6]. Typical results are shown in Fig. 3 and 4. When the initial bubble radius varied between 1 and 3 mm excellent agreement was found between the diffusion model, and the experimental data for bubble collapse. For bubbles initially of ~ 5 mm in dia the uniformly mixed model accurately described the bubble collapse. At intermediate initial bubble radii the two models bounded the experiments. The reason for these results is explainable if one observes the actual bubble behavior. Below 3 mm in initial radius the bubbles are nearly spherical for their entire history. Above this size the bubbles oscillate significantly in shape and in their trajectory with strong oscillations occurring shortly after their formation. This deformation could cause strong mixing in the vapor which would be slowly damped due to the viscosity of the gas vapor mixture. Thus, larger bubbles subject to more vigorous mixing and oscillations behave as if they were uniformly mixed. In smaller bubbles the vapor's inertia is more easily diminished by viscous effects; thus, diffusion becomes dominant. If the vapor viscosity were high damping would also occur.

Figure 5 shows a comparison of all of the models presented in the present paper together with the collapse of a bubble of pentane vapor in pentane. The initial radius is less than 1 mm. For this condition (1-4) the bubble does not rise at constant velocity, but rather $V \sim R^{1/2}$. It is quite apparent that the use of an average rise velocity for the bubble grossly misrepresents the collapse. An accurate representation of the rise velocity

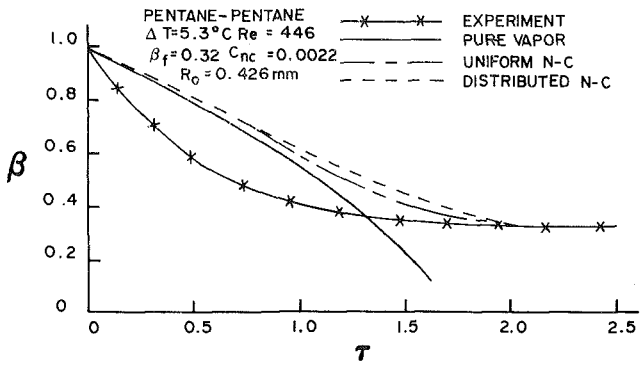

Fig. 5 Comparison of models with experimental data of reference [3] for pentane bubble collapsing in pentane

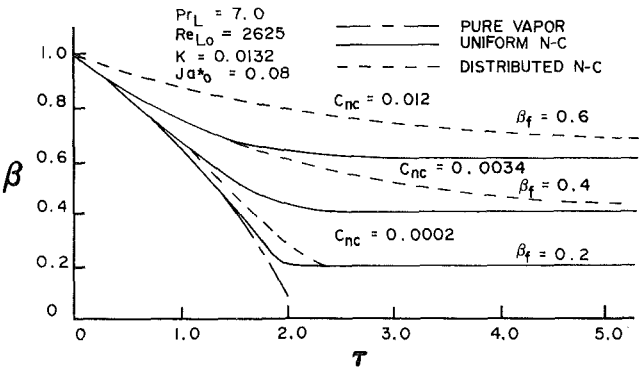

Fig. 6 Comparison of theoretical models showing the effect of mass concentration of noncondensable gas on the bubble collapse rate

could be used in order to evaluate bubble collapse in this size range. As an alternative one might utilize a different model for predicting the heat transfer during collapse. The present model assumes a thin boundary layer. This is incorrect for very small bubbles. The heat transfer could be greater or less. As an example, if one were to use the formula for bubble collapse with the truncated series we developed in reference [5] together with our diffusion model for the noncondensibles, nearly exact agreement is found using the average bubble rise velocity. Thus, it appears that the heat transfer could be higher for small bubbles (< 1 mm) than is predicted by the present analysis. Further investigation is needed.

Figure 6 illustrates the effect of noncondensibles for a typical bubble for fixed fluid-system properties. It is apparent that as little as 0.02 percent noncondensibles on a mass basis can significantly reduce the degree of collapse while noncondensible concentration of 1.2 percent can result in only a thirty percent decrease in bubble radius. These numbers would correspond to $T^* - T\infty$ of approximately 4°C for pentane-water and isobutane-water systems with air as the noncondensible gas.

Conclusions

1 For pure vapor bubbles retaining effectively spherical geometry while collapsing in an immiscible fluid it is shown that the collapse can be described by equation (15) when the bubble translates at constant velocity.

2 For pure vapor bubbles collapsing in their own liquid, equation (16) can be used with $\phi = 1.0$. This result indicates a somewhat slower collapse than was previously found by the

numerical analysis of Wittke and Chao [2]. The latter analysis was in agreement with our previous results where we erroneously truncated an infinite series [5].

3 For pentane bubbles containing noncondensible gases, the collapse is described by a diffusion controlled model for bubbles of initial radius between 1.0 and 3.0 mm. For bubbles larger than 4.0 mm in initial radius, a uniform mixed model applies. For intermediate size bubbles these two analyses form the limits.

4 For extremely small amounts of noncondensibles, $\sim 0.01 - 0.02$ percent by mass, significant final radii, β_f, may result unless the modified Jakob number Ja^* is large. As the amount of noncondensibles increase the difference in bubble collapse time as predicted by the uniform distribution model and the diffusion model increase such that errors of more than 100 percent can result by applying the wrong model for a given bubble size. It is thus important to determine the range of bubble initial radii that are best predicted by a given model. Lacking experimental results, for other hydrocarbon vapors in water, the results for pentane should be used.

Acknowledgment

The authors would like to express their appreciation for the support of this work which was given by the U.S. Department of Energy under contract No. E(10-1) 1523.

References

1 Florschuetz, L. W., and Chao, B. T., "On the Mechanism of Vapor Bubble Collapse," ASME JOURNAL OF HEAT TRANSFER, Series C, Vol. 87, 1965, pp. 209-220.

2 Wittke, D. D., and Chao, B. T., "Collapse of Vapor Bubbles with Translatory Motion," ASME JOURNAL OF HEAT TRANSFER, Series C, Vol. 89, 1967, pp. 17-24.

3 Isenberg, J., and Sideman, S., "Direct Contact Heat Transfer with Change of Phase: Bubble Condensation in Immiscible Liquids," *International Journal of Heat and Mass Transfer*, Vol. 13, 1970, pp. 997-1011.

4 Isenberg, J., Moalem, D., and Sideman, S., "Direct Contact Heat Transfer with Change of Phase: Bubble Collapse with Translatory Motion in Single and Two Phase Systems," *Proceedings of the Fourth International Heat Transfer Conference*, Vol. V, B.2.5, 1970.

5 Jacobs, H. R., Fannar, H., and Beggs, G. C., "Collapse of a Bubble of Vapor in an Immiscible Liquid," *Proceedings of the Sixth International Heat Transfer Conference*, Vol. 2, 1978, pp. 383-388.

6 Major, B. H., "Direct Contact Bubble Condensation," MS thesis, Department of Mechanical and Industrial Engineering, University of Utah, Salt Lake City, Utah, 1978.

7 Moalem, D., Sideman, S., "Bubble Condensation with Non-Homogeneous Distribution of Non-Condensibles," *International Journal of Heat and Mass Transfer*, Vol. 14, 1971, pp. 2152-2156.

8 Fannir, H., "Experimental Data for Pentane Bubbles Collapsing in Water," Unpublished work toward a PhD degree, Strathclyde University, Glasgow, Scotland, United Kingdom.

9 Sparrow, E. M., Ramadhyani, S., and Patankar, S. V., "Effect of Subcooling on Cylindrical Melting," ASME JOURNAL OF HEAT TRANSFER, Series C, Vol. 100, 1971, pp. 395-402.

10 Sherwood, T. K., Pigford, R. L., and Wilke, C. R., *Mass Transfer*, McGraw-Hill, Inc., New York, 1975, p. 23.

W. W. Yousef
Nuclear Studies and Safety Department,
Ontario Hydro,
Toronto, Ontario, Canada,
M5G 1X6

J. D. Tarasuk

W. J. McKeen
Faculty of Engineering Science,
The University of Western Ontario,
London, Ontario, Canada,
N6A 5B9

Free Convection Heat Transfer From Upward-Facing Isothermal Horizontal Surfaces

Heat transfer by free convection in air from isothermal horizontal surfaces heated and facing upward has been experimentally studied by using a Mach-Zehnder interferometer. The local and the average heat-transfer coefficients and the temperature distributions were determined in the range of Gr Pr from 1.9 × 10^6 to 1.7 × 10^8. Measurements were compared with available experimental and theoretical results. Periodical flow instabilities caused random changes, which could reach +45 and −35 percent of mean values in the local Nusselt number and +23 and −15 percent of mean value in the average Nusselt number. The nature of the free convection flow over the heated surface and the separation of the boundary layer were inferred from these random changes in the local and average Nusselt numbers.

Introduction

Free convection from horizontal surfaces has received less attention than free convection from vertical surfaces. The result is that information about horizontal surfaces is sometimes inconsistent, and the physical nature of the boundary layer flow is inadequately understood. Free convection from horizontal surfaces is vital to meteorological and industrial applications [1]. The difficulty arises from the unsteady three-dimensional disturbances [2] over a heated upward-facing horizontal surface, making the momentum and energy equations not amenable to analytical solutions. Thus, it becomes more expedient to determine experimentally the temperature distributions and heat-transfer coefficients. In this study a Mach-Zehnder Interferometer was used to study free convection above a heated horizontal surface.

For a heated horizontal surface the buoyancy force, which is the only driving force in a free convection situation, has no component along the surface. Therefore any tangential flow, which may arise, must be driven indirectly. This indirect drive [1] is produced by a negative pressure gradient which is created originally by the buoyancy force. This type of boundary layer flow was observed early by Schmidt [3] and Weise [4] near the leading edge of the plate.

The early work of Fishenden and Saunders [5] may be considered the first that is directly related to the present study. They found that the heat-transfer data could be correlated by equation of the form

$$\mathrm{Nu} = C(\mathrm{GrPr})^m \tag{1}$$

for the laminar region ($10^5 < \mathrm{GrPr} < 2 \times 10^7$): $C = 0.54$ and $m = 1/4$ and for the turbulent region ($2 \times 10^7 < \mathrm{GrPr} < 3 \times 10^{10}$): $C = 0.14$ and $m = 1/3$. In correlation (1), as well as most of the forthcoming correlations, the physical properties were evaluated at the arithmetic mean temperature of surface and bulk fluid.

Mikheyev [6] derived an equation with constants very similar to those of Fishenden and Saunders [5], except that the value of the heat-transfer coefficient determined by equation (1) should be increased by 30 percent if the heated surface was facing upward and decreased by 30 percent if the heated surface was facing downward. No particulars were given to support such conclusions.

Hassan and Mohamed [7] determined the local heat-transfer coefficients along isothermal surfaces in air at different inclinations and surface temperatures using Boelter-Schmidt heat flux meters. They reported that separation starts well before the onset of turbulence in the boundary layer.

Rotem and Claassen [8, 9] carried out a flow visualization experiment using a semifocusing Schlieren apparatus to show the existence of a laminar boundary layer which starts at the leading edges of the plate and then breaks down into irregular convection pattern some distance from the edges.

Fujii and Imura [10] determined by a heat balance the heat transfer from rectangular plates with a wide range of inclinations. They reported that for a horizontal heated plate facing upwards, the flow in the boundary layer is turbulent and the exponent in equation (1) was determined as 1/3 for GrPr as low as 2.2 × 10^6. This apparently seems to conflict with Rotem and Claassen's work [8, 9] in which they indicated that the boundary layer is laminar. The heat balance method, as applied by Fujii and Imura [10], is particularly error prone [11], especially for free convection situations, because the heat transfer rates from the surface are low and the radiation mode of heat transfer to the surrounding is important. The result is that the net convective heat transfer is difficult to determine accurately. Thus the results of Fujii and Imura [10] are subjected to some uncertainty.

Al-Arabi and El-Riedy [12] obtained local and average heat-transfer data from plates of square, rectangular, and circular shapes by collecting steam condensate from compartments underneath the horizontal plates. Plate corners were found to have a negligible effect on the average heat transfer. They developed two equations which give heat-transfer values 30 and 11 percent higher than the values given by Fishenden and Saunders' equations [5] for the laminar and turbulent regions, respectively.

Pera and Gebhart [2, 20] measured, for the first time, the temperature distribution and the heat-transfer coefficients in air by using a Mach-Zehnder interferometer. They reported a value of $\mathrm{Gr}_x^{1/3} = 80$ for the first occurrence of separation of the boundary layer. Pera and Gebhart concluded by means of a smoke test that severe instability mechanisms disrupt the boundary layer flow some distance from the leading edge [20] and that the boundary layer did not always separate at the same exact location [2].

Recently, Ishiguro et al. [13] studied the periodical changes in temperature and heat transfer by means of temperature probes and interferometry. They reported that the three-dimensional nature of flow, caused by hot fluid lumps, is the reason behind discrepancies between the reported analytical and experimental results.

Free convection above a horizontal heated surface has also

Contributed by the Heat Transfer Division for publication in the JOURNAL OF HEAT TRANSFER. Manuscript received by the Heat Transfer Division July 1, 1981.

Table 1 Data and correlations used in free convection from horizontal surfaces heated and facing upward

Experimental Studies

Reference	Fluid	Surface dimensions W × L in cm	Correlation	Gr Pr	Deviation	Comments
Fishenden and Saunders [5] 1950	Air	maximum size of 60 × 60	laminar $Nu = 0.54 (Gr Pr)^{1/4}$ turbulent $Nu = 0.14 (Gr Pr)^{1/3}$	$10^5 < Gr Pr < 2 \times 10^7$ $2 \times 10^7 < Gr Pr < 3 \times 10^{10}$		laminar region extends up to $Gr Pr = 2 \times 10^7$
Bosworth [23] 1952			laminar $Nu = 0.71 (Gr Pr)^{1/4}$ turbulent $Nu = 0.17 (Gr Pr)^{1/3}$			no details were given for the shape or size of the surface
Hassan and Mohamed [7] 1970	Air	20 × 50.4	$Nu = 0.12 Gr^{1/3}$ heated and facing downward $Nu = 0.06 Gr^{1/3}$	$1.1 \times 10^3 < Gr < 3 \times 10^8$	±15% ±10%	1. Wall temperature (T_w) = cons. 2. Heat transfer from upward facing surfaces is twice as much from downward facing surfaces
Fujii and Imura [10] 1972	Water	10 × 5 and 15 × 30	$Nu = 0.13 (Gr Pr)^{1/3}$ $Nu = 0.16 (Gr Pr)^{1/3}$	$5 \times 10^8 < Gr Pr$ $Gr Pr < 2 \times 10^8$		1. $T_W \neq$ cons surface heat $f(WX\phi)$ = cons. 2. Leading edges increases Nu by 23%.
Al-Arabi and El-Riedy [12] 1976	Air	square: 5 × 5 up to 45 × 45 circular: 10 dia. up to 40 rectangular: 15 × 15 up to 15 × 60	laminar $Nu = 0.70 (Gr Pr)^{1/4}$ turbulent $Nu = 0.155 (Gr Pr)^{1/3}$	$2 \times 10^5 < Gr Pr < 4 \times 10^7$ $4 \times 10^7 < Gr Pr < 10^9$	±14% ±12%	laminar region extends up to $Gr Pr = 4 \times 10^7$
Ishiguro et al [13] 1978	Water	0.8 × 0.76 13 × 2.8 16 × 8 17 × 20	$Nu = 0.20 (Gr Pr)^{1/3}$	$2 \times 10^5 < Gr Pr$		1. T_w = cons. 2. periodical changes in Nu were noticed for $Gr Pr > 3 \times 10^5$

been treated on a different premise, that is of a buoyant fluid accumulating and breaking away either as a thermal, or as a plume which wanders about the heated surface. In these studies the generation of thermals or plumes above a heated horizontal surface were investigated rather than the heat transfer from the surface itself. For more details the reader may refer to references [14, 15].

Though the present study is experimental, it was found relevant to give a brief account of previous theoretical studies.

Stewartson [16] gave a theoretical analysis for the flow induced by buoyancy on a horizontal surface with a single leading edge. A sign mistake in Stewartson's analysis was corrected by Gill, Zeh, and Del Casal [17], who showed that the boundary-layer flow only exists for a heated surface with a leading edge facing upward or a cooled surface facing downward.

Nomenclature

C = constant
C_p = constant pressure specific heat
Gr = Grashof number, $g\beta L^3(t_w - t_a)/\nu^2$
Gr_x = local Grashof number, $g\beta x^3(t_w - t_a)/\nu^2$
g = gravity
h = average heat-transfer coefficient
h_x = time averaged local heat-transfer coefficient
k = thermal conductivity
L = plate length
m,n = exponents
Nu = average Nusselt number, $hL/k = 1/L\int_0^L Nu_x dx$
Nu_x = local Nusselt number (time averaged), $h_x x/k$
ΔN = fringe shift
Pr = Prandtl number, $C_p\mu/k$
t = average air temperature over the plate length at a location x,y
t_a = ambient air temperature
t_w = plate surface temperature
T = absolute temperature, $t + 273.15$
x = distance along plate from leading edge
y = distance normal to plate
W = plate width
β = coefficient of thermal expansion, $1/T_m$
μ = dynamic viscosity
ν = kinematic viscosity
θ = temperature difference, $t_w - t$
ϕ = nondimensional temperature $(t - t_a)/(t_w - t_a)$
η = nondimensional distance, $(y/x)[Gr_x/(1/n)]^n$

Subscripts

a = evaluated at ambient temperature
m = evaluated at mean temperature $(t_a + t_w)/2$
x = based on x
w = evaluated at wall temperature

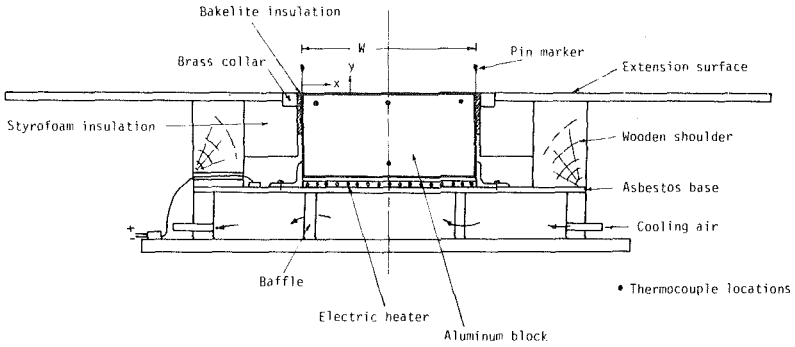

Fig. 1 Schematic of plate assembly

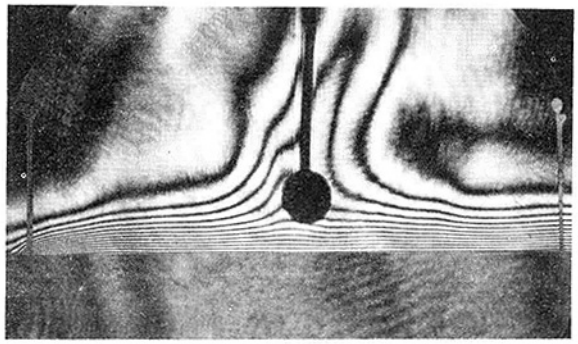

$t_w - t_a = 40°C$
$GrPr = 2.1 \times 10^7$

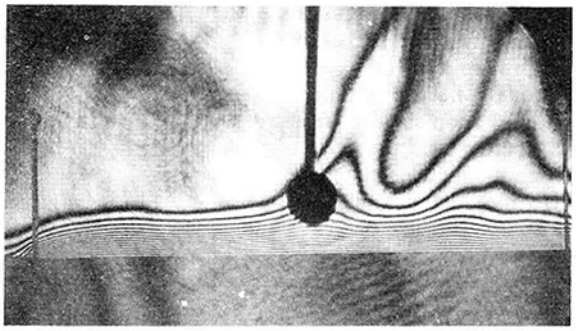

$t_w - t_a = 55°C$
$GrPr = 2.66 \times 10^7$

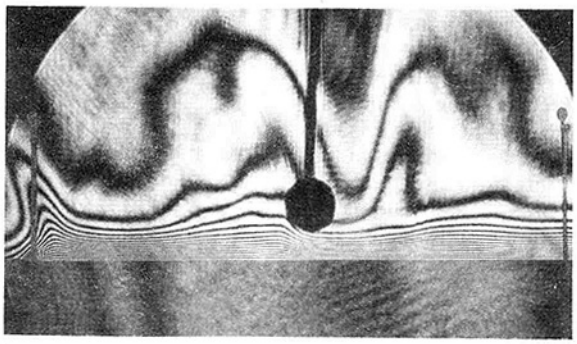

$t_w - t_a = 60°C$
$GrPr = 2.90 \times 10^7$

Fig. 2 Interferograms showing temperature field for half width of the plate, $L = 200$ mm

Rotem and Claassen [8, 18] and Rotem [19] numerically integrated the governing equations of two-dimensional steady flow and gave the velocity and temperature profiles at different Prandtl numbers for an isothermal surface.

Pera and Gebhart [2, 20] obtained numerically the velocity and temperature fields for a wide range of Prandtl numbers (including $Pr = 0.7$), for two-dimensional flows over a horizontal and slightly inclined surfaces with a single leading edge.

Fussey and Warneford [21] used an integral method to obtain a numerical solution with a full range of angles of inclinations from the vertical to the horizontal for upward facing constant heat-flux surfaces.

Fatt [22] determined the local Nusselt number by employing

a suitable expression for the temperature and velocity distributions to solve the integrated momentum and energy equations.

A summary of the available experimental studies and correlations is given in Table 1.

In the present study, the temperature distributions in the convection region above a heated isothermal surface were obtained using a Mach-Zehnder interferometer. The temperature distributions were used to determine the local heat-transfer coefficients which were integrated along the surface to determine average values. The present study considers also the unsteady eddy (or cellular) convection which results from plume formation and its effect on local and average Nusselt numbers. The emphasis in the present work was on determining the amplitude of random variations in both the local and the average Nusselt numbers.

Experimental Apparatus

The experiment was designed to determine the nature of a boundary region flow over horizontal heated surfaces and to obtain the lateral extent of the boundary layer as inferred from the variation in the local heat-transfer coefficients.

The apparatus used in the experiments is shown schematically in Fig. 1. Three square aluminum plates were used with side lengths equal to 100, 200, and 400 mm, respectively, and a thickness of 50 mm. The heat-transfer surface which is facing upward was accurately machined and polished to a surface finish of ± 0.01 mm in order to be compatible with the accuracy of estimating fringe positions. The plates were electrically heated from below by means of 0.25 mm nicrome wire wound around an asbestos sheet at constant pitch. For the larger size plates, eg. 200 × 200 mm and 400 × 400 mm, it was necessary to wrap a heating wire around the plate sides to compensate for the heat loss to the surroundings. A uniform temperature of the top surface was achieved to within a variation of ± 0.25 percent of the surface temperature. Four thermocouples were embedded in the locations shown in Fig. 1 in order to measure the surface temperature and also to check its uniformity.

28-gauge copper constantan wires were used to make the thermocouple junctions which were electrically shielded against stray current produced in the plate. Thermocouple leads were directly connected to a Digitrend 200 data acquisition system where temperatures were recorded with 0.1°C resolution and ± 0.4°C accuracy. An extension surface was used around the heated surface to minimize or to eliminate the leading edge effect [11]. This extension surface was leveled with the upper heated surface and separated from it by a brass collar of square cross section through which air was forced to maintain the extension surface at the room temperature. To minimize the temperature gradient at the leading edge, a lamination of bakelite insulation was introduced between the plate and the brass collar. The model base was maintained at room temperature by blowing air in a closed baffled passage under the heated plate. Great care was taken to avoid the effects of stray air currents in the test room upon the flow pattern. The ventilation ducts were closed and the air used in the experiment was discharged outside the test room.

A 20-cm mirror Mach-Zehnder interferometer was used to obtain the temperature field above the heated surface. A 5-Mw, He-Ne Laser was used as a light source. The interferometer sensitivity near the surface was approximately 2°C/fringe for the 400 mm model.

Visibility studies by Pera and Gebhart [2], Rotem and Claassen [8, 9] and Tarasuk [24] showed clearly the three-dimensional nature of the flow over a heated horizontal surface. Thus with the interferometer set up for the infinite fringe field, the fringes represent lines of average temperature

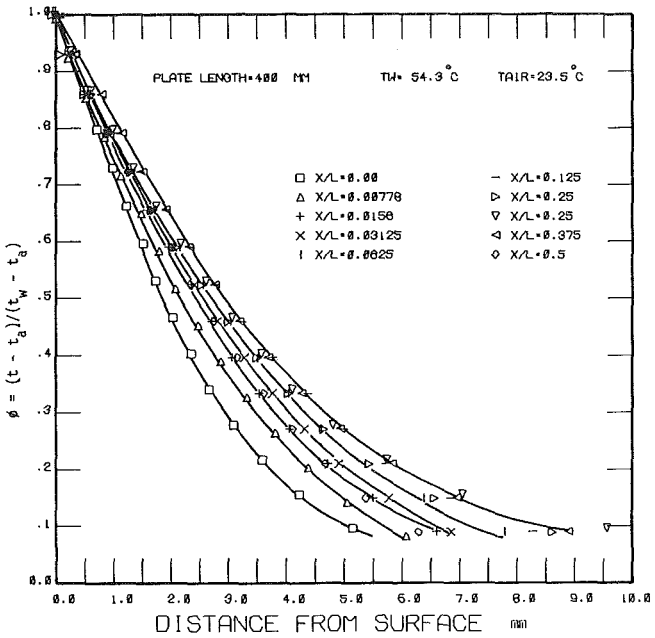

Fig. 3 Temperature profiles in the boundary layer $L = 400$ mm

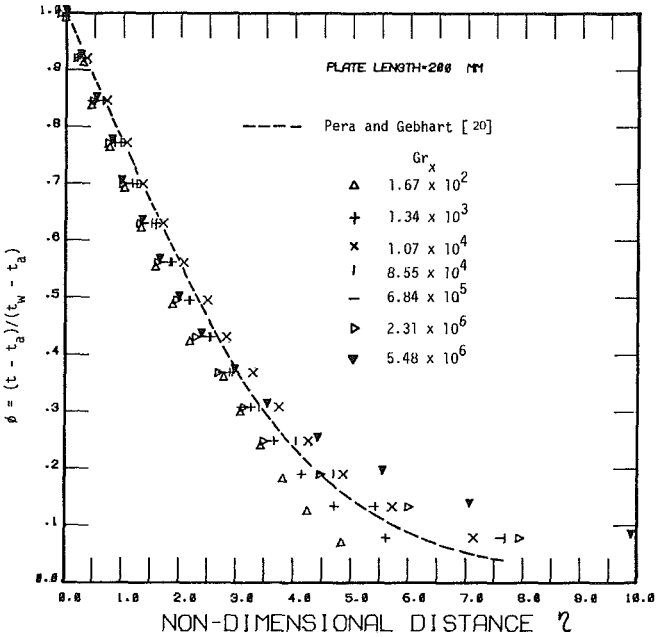

Fig. 4 Nondimensional temperature profile $\eta = \frac{y}{x}\left(\frac{Gr_x}{1/n}\right)^n$

$n = 0.300$

along the light path. The heated surface was leveled horizontal by means of a precision split level and the test beam was made parallel to the surface. After allowing for a long settling period (about 10 min) the interferograms were recorded on a Polaroid 10 × 12.5 cm Land Film, Type 55. The periodic or eddying flow conditions required multiple pictures, first, to establish the upper and lower limits of the local Nusselt number, Nu_x, and second, to obtain a time averaged value for Nu_x. A preliminary set of test runs on the 200 mm plate, at the same surface and air temperatures, was done to determine the necessary number of interferograms needed to define clearly the upper and lower limits in Nu_x. It was found that six interferograms taken at random times, such as to cover all possible fringe patterns over the plates, were sufficient. A similar procedure was applied by Randall, Mitchell, and El-Wakil [25].

The temperature difference $(t_w - t_a)$ ranged from 12 to 140°C. This corresponded to a Gr Pr range of 1.9×10^6 to 1.7×10^8 based on the plate length. The air properties were evaluated at the arithmetic mean of surface and ambient air temperatures.

The local Nusselt number based upon distance from edge, x, and total temperature difference, $\theta_w = t_w - t_a$, is expressed by

$$\mathrm{Nu}_x = \frac{h_x x}{k} = -\frac{x}{\theta_w}\left[\left(\frac{\partial \theta}{\partial y}\right)_w\right]_x \tag{2}$$

It should be pointed out that the temperature gradient $[(\partial\theta/\partial y)_w]_x$ represents a gradient of the average temperatures along the plate length at a location x from the plate edge. Thus for a three-dimensional flow above the plate, h_x would represent the local heat-transfer coefficient at a distance x from the plate edge but averaged along the plate length, L.

The relation between temperature difference, $(T - T_a)$, and fringe shift, ΔN, is given by

$$\Delta N = \frac{(T - T_a)}{T_a}\frac{L}{\lambda_0}\left(\frac{P}{RT}\cdot K\right) \tag{3}$$

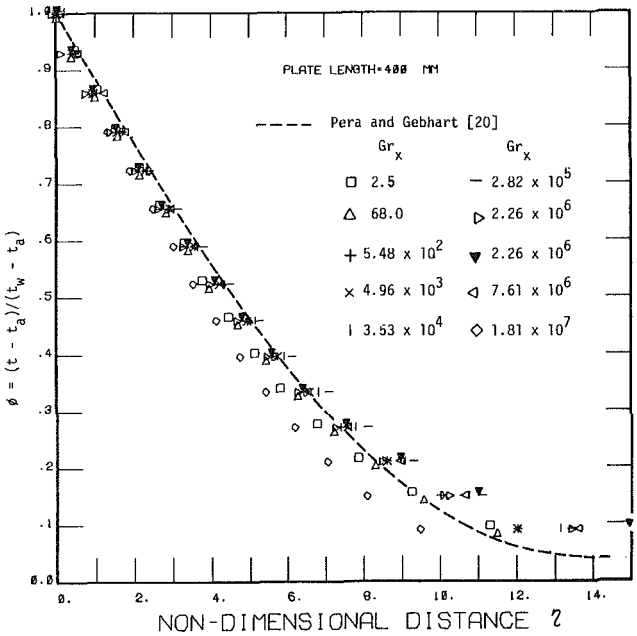

Fig. 5 Nondimensional temperature profile $\eta = \frac{y}{x}\left(\frac{\mathrm{Gr}_x}{1/n}\right)^n$

$n = 0.315$

where K is the Gladstone-Dale constant, P, is the atmospheric pressure, R is the universal gas constant and λ_0 is the wavelength of the light source of the interferometer (6328 °A for He-Ne laser).

The average Nusselt number, Nu, is determined by numerically integrating the local Nusselt numbers over the entire plate width, W [for square plates, $W = L$].

$$\mathrm{Nu} = \frac{1}{L}\int_0^L \mathrm{Nu}_x dx = \sum_{i=1}^{m}\frac{1}{2}[(\mathrm{Nu}_x)_i + (\mathrm{Nu}_x)_{i+1}]\left[\left(\frac{x}{L}\right)_{i+1} - \left(\frac{x}{L}\right)_i\right] \tag{4}$$

where m represents the number of locations at which Nu_x were evaluated. In equation (4), symmetry around the plate centerline was assumed.

The surface temperature as determined by interferograms analysis agreed with thermocouple readings within 1°C. Heat conduction through the bakelite insulation and to the extension surface was inevitable. This resulted in an upstream heating of airstream before it reaches the leading edge, as seen in Fig. 2. However, such temperature disturbance was brought to a minimum by forcing air at room temperature through a collar around the plate. The temperature gradient in the boundary layer and the local Nusselt number were determined with uncertainty of ± 6 percent.

Figure 2 shows three typical interferograms of the temperature fields. The distance between the pin markers was utilized to establish the scaling factor.

The fringe centres, at a given distance from the leading edge, were measured from the plate surface by viewing the film negative on a densitometer. The signal produced by the densitometer was then fed into an electronic device. This device was designed especially [26] to process such a signal. This device gave the mode of the signal, i.e., the location of the brightest spot of the light fringe with a resolution of 0.001 mm. The accuracy of measuring fringe locations was estimated to be better than 0.1 percent [26].

Results and Discussion

Temperature Distribution. The temperature determined from the interferogram analysis represents an average integrated value over the length of the light beam.

A typical set of the temperature profiles in the boundary layer for the large size plate $L = 400$ mm is shown in Fig. 3. The corresponding Grashof number/Prandtl number product for these profiles was $\mathrm{GrPr} = 1.444 \times 10^8$.

The nondimensional temperature profiles expressed as $\phi = (t - t_a)/(t_w - t_a)$ versus $\eta = (y/x)\,[\mathrm{Gr}_x/(1/n)]^n$ for the medium size plate, $L = 200$ mm and large size plate, $L = 400$ mm are shown in Figs. 4 and 5, respectively. It was found that

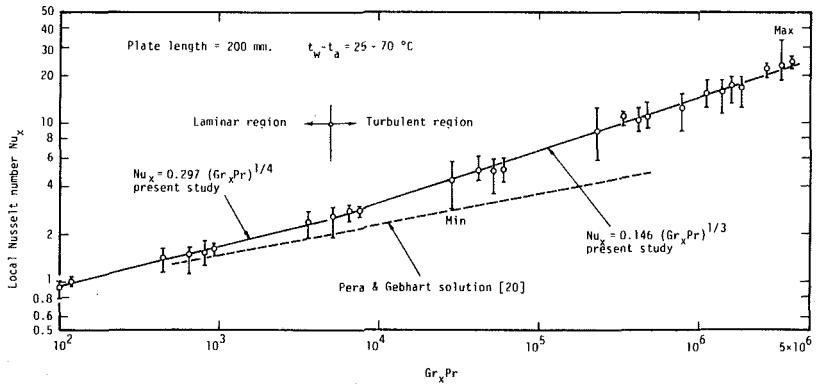

Fig. 6 Random changes in local Nusselt number and correlation of data for $L = 200$ mm

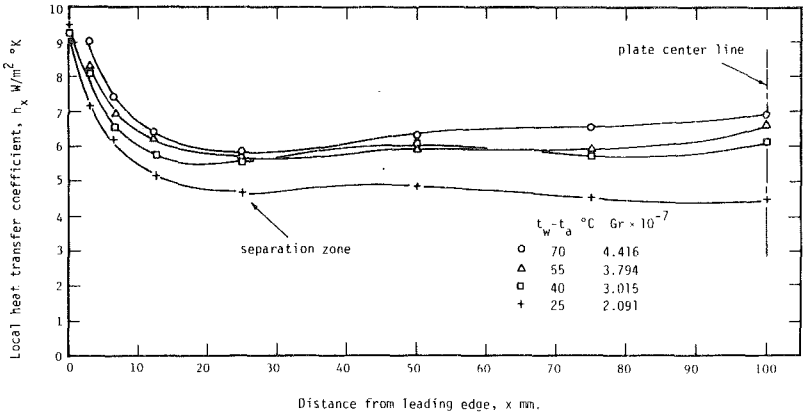

Fig. 7 Local heat transfer coefficient along the surface: $L = 200$ mm

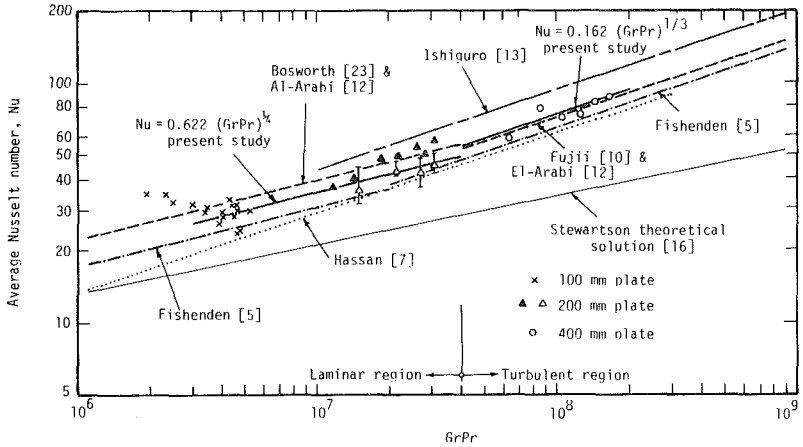

Fig. 8 Average Nusselt number for different square plates as compared with existing correlations

the temperature distribution is quite sensitive to the exponent n. A different value of n varying from 0.2 up to 0.36 was utilized in the nondimensional distance $\eta = (y/x)\,[\mathrm{Gr}_x/(1/n)]^n$ in order to condense the temperature profiles into one curve with a minimum scatter in the data. A value of $n = 0.300$ for the plates $L = 100$ mm and $L = 200$ mm was found to normalize the temperature profiles for $\theta_w = 25 - 140$°C with a minimum scatter. For the larger plate $L = 400$ mm, the value of n was 0.315 for $\theta_w = 10 - 35$°C. A value of $n = 0.2$, as recommended by Rotem and Claassen [8] and Pera and Gebhart [20] in their analytical studies, was found to give an unacceptable scatter in the normalized temperature profile, especially at low temperature differences (i.e., $\theta_w \leq 50$°C for $L = 200$ mm). The analytical solution of Pera and Gebhart [20] which deals with two-dimensional flows, is shown in Figs. 4 and 5. The trend of the data being consistently below the analytical curves as seen in Figs. 4 and 5, has been reported by Pera and Gebhart. Two causes were cited for such disagreement. The first is the upstream heating of air before the leading edge. The upstream heating has been reduced considerably in the present study, as seen in Fig. 2, by the use of the bakelite insulation and the brass collar around the plate. The second cause which seems to create such discrepancy is the three-dimensional disturbance which originates at some downstream location from the leading edge in the form of rising plume. The theoretical solution of Rotem and Claassen [8] for $\mathrm{Pr} = 0.3$ lies fairly close to that profile given by Pera and Gebhart.

Local Heat Transfer. Because of the enormous time and effort to process the interferograms, it was decided to study the random changes in the local Nusselt number for the medium size plate, $L = 200$ mm only. Six interferograms were taken at random intervals such that they cover all the possible temperature profiles as delineated by the fringe patterns. The plate-minus-air temperature differences were taken as 25, 40, 55, and 70°C which resulted in Gr_x Pr ranging from 10^2 to 5×10^6. The arithmetic mean of the local Nusselt number and the random changes from this mean were determined at a given x/L. Figure 6 shows the local Nusselt number with the circle indicating the mean value and the bars representing the limits of the random changes. The random changes in Nu_x from the mean value were found to be considerable and reached $+45$ and -35 percent. Although these random changes increase slightly with increasing $\mathrm{Gr}_x\mathrm{Pr}$, such a trend was inconsistent, i.e., the random changes in Nu_x were of the same order of magnitude at $\mathrm{Gr}_x\mathrm{Pr} < 10^5$ and $\mathrm{Gr}_x\mathrm{Pr} > 10^6$ for some runs as can be seen in Fig. 6. The locations of the maximum and the minimum random changes in Nu_x are also shown in Fig. 6.

The time averaged values of the local Nusselt numbers were correlated in both the laminar and turbulent regions.

In the laminar region an equation of the form

$$\mathrm{Nu}_x = 0.297(\mathrm{Gr}_x\mathrm{Pr})^{1/4} \tag{5}$$

was found to fit closely the data which extended from $\mathrm{Gr}_x\mathrm{Pr} = 10^2$ up to 6×10^3. This, in fact, implied that the laminar region, as expressed by the exponent 1/4, extended up to $\mathrm{Gr}_x\mathrm{Pr} = 6 \times 10^3$. In Al-Arabi and El-Riedy [12], the laminar region was reported to extend up to $\mathrm{Gr}_x\mathrm{Pr}$ of 2×10^5. No justification to such a limit was given in their study.

Equation (5) correlates the present data with deviations of $+4.2$ and -3.2 percent, which are surprisingly low when compared with the magnitude of random changes in Nu_x ($+45$ and -35 percent). This indicates that: (*a*) the averaging of Nu_x by using six interferograms was sufficient, and (*b*) the

local Nusselt number cannot be determined simply from one test run. A further increase in the number of interferograms may slightly reduce the above mentioned deviations [+ 4.2 and −3.2 percent] in equation (5). Considering the uncertainty in determining Nu_x [±6 percent], such an increase in the number of interferograms was not warranted. It should be emphasized that the random changes in Nu_x are an integral part in evaluating Nu_x. These random changes occurred due to changing flow pattern above the heated surface.

No available data for the local heat transfer in the laminar region were found in the literature.

In the turbulent region, i.e., $6 \times 10^3 < Gr_x Pr < 5 \times 10^6$, the time averaged values of Nu_x were fitted by equation of the form

$$Nu_x = 0.146\,(Gr_x Pr)^{1/3} \tag{6}$$

Equation (6) predicts Nu_x with a deviation of +8.6 and −12.7 percent, which also are far below the random changes in Nu_x. Equation (6) agrees very well with the equation suggested by Al-Arabi [12] for the turbulent region.

Pera and Gebhart's theoretical solution [20] is shown in Fig. 6. This solution seems to give consistently lower Nu_x values when compared to the present experimental results. This fact is reported in their paper [20] and was expected by noticing the lower temperature gradients at the wall of their profile in both Figs. 4 and 5.

The extension of the laminar boundary layer and the eventual separation of such a boundary layer was inferred from the local heat transfer distribution along the plate as shown in Fig. 7. The local heat-transfer coefficients are the time averaged values. As can be seen from Fig. 7, a minimum value for h_x occurred consistently in a zone which is approximately 8-mm wide, and its centre is 25 mm from the leading edge. This zone seems to be independent of the plate size. The only plausible explanation for such a dip in the h_x distribution is that the heat-transfer coefficient decreases as the thermal boundary layer develops along the plate. At one point this boundary layer becomes unstable, mainly because of the buoyancy forces [1, 2] which act normal to the plate and the boundary layer forms a thermal plume which breaks away from the surface. This results in a turbulent boundary layer and in a slightly higher local heat transfer. The local heat-transfer coefficient beyond the separation zone is approximately constant. Al-Arabi and El-Riedy's [12] results showed a dip in h_x in the zone 25-45 mm from the edge of the plate. Results of Hassan and Mohamed [7] also showed a dip in h_x, but at a location 50 mm from the leading edge. Both the studies reported in references [7, 12] were not intended originally to locate the separation of the thermal boundary layer.

The edge effect as measured by the difference between the average and the local heat-transfer coefficients in the middle region of the plate (i.e., beyond the separation zone) was found to be no more than 6 percent for the medium size plate, $L = 200$ mm. The ratio $h_{x(\text{leading edge})}/h_{x(\text{middle region})}$ reached a value 2.0. The edge effect is expected to be lower as the plate size increases because the region in which h_x varies is virtually independent of the plate size. By using square plates, the edge effect is assumed to be identical for the four sides.

Average Nusselt Number. The average Nusselt number, Nu, was determined from equation (4) and the results are plotted in Fig. 8 for the three plates covering a range of GrPr from 1.9×10^6 up to 1.7×10^8. The random changes in the average Nusselt number for the plate $L = 200$ mm were determined and reached +23 and −15 percent, which is about half the magnitude of the maximum and minimum random changes in the local Nusselt numbers. The bars in Fig. 8 show these random changes in Nu in four different tests.

The laminar heat transfer (GrPr from 3×10^6 up to 4×10^7) is represented within ±20 percent by the equation

$$Nu = 0.622\,(GrPr)^{1/4} \tag{7}$$

For the data with $GrPr < 3 \times 10^6$, the average Nusselt numbers determined were higher than those given by equation (7). These data points were checked thoroughly and the explanation for such anomaly could be lying in the fact that the flow over the whole plate (in this case it was the 100 mm plate $\theta_w < 50°C$) is controlled by one thermal plume generated from the four sides of the plate. This plume could give rise to a higher heat-transfer coefficient. The authors would like to emphasize that such anomaly is not yet fully understood.

The turbulent heat transfer (for $GrPr > 4 \times 10^7$) is represented, within ±10.5 percent by the equation

$$Nu = 0.162(GrPr)^{1/3} \tag{8}$$

The available correlations [see Table 1] are shown in Fig. 8 for comparison. While equation (7) gives heat-transfer coefficients 13 percent higher than the values given by Fishenden's equation [5], it gives values 12.5 percent lower than the values suggested by Al-Arabi's [12] and Bosworth's [23] equations.

Equation (8) gives heat-transfer coefficients 1.2, 4.3, and 13 percent higher than the values given by Fujii's [10], Al-Arabi's [12] and Fishenden's [6] equations, respectively. Equation (8) gives h values 23.5 percent lower than the values given by Ishiguro's [13] equation.

The heat-transfer values by Hassan's [7] equation are well below the values determined by most of the researchers.

The theoretical solutions (only one is shown in Fig. 8 which is the closest to the experimental data) underpredict considerably the average heat-transfer coefficients. This may be attributed to the three-dimensional disturbances which were ignored in all the theoretical analyses.

Concluding Remarks

The experiments reported here were designed with particular care in order to provide reliable results regarding the local heat-transfer coefficients.

The random changes in Nu_x which reached +45 and −35 percent underscored the unstable nature of the flow over a horizontal heated surface and that a correlation which yields a single value for Nu_x or Nu is unrealistic. The random changes in Nu_x should be incorporated with the value of Nu_x determined from the correlation.

The edge effect increased the heat transfer from the plate by 6 percent. This effect decreases as the plate size increases. The boundary layer separated from the plate at a distance which is independent of the plate size or temperature.

References

1 Gebhart, B., "Buoyancy Induced Fluid Motions Characteristic of Applications in Technology," *ASME Journal of Fluids Engineering*, Vol. 101, 1979, pp. 5-28.

2 Pera, L., and Gebhart, B., "On the Stability of Natural Convection Boundary Layer Flow over Horizontal and Slightly Inclined Surfaces," *International Journal of Heat and Mass Transfer*, Vol. 16, 1973, pp. 1147-1163.

3 Schmidt, E., "Schlierenaufnahmen des Temperaturfeldes in der Nahe Warmeabgebender Korper," *Forsch. Gebiete Ingenieurw*, Vol. 3, 1932, pp. 181-189.

4 Weise, R., "Warmeubergang durch Freie Konvektion an Quadratischen Platten," *Forsch. Gebiete Ingenieurw*, Vol. 6, 1935, pp. 281-292.

5 Fishenden, M., and Saunders, O. A., *An Introduction to Heat Transfer*, Clarendon Press, Oxford, 1957, pp. 89-99.

6 Mikheyev, M., *Fundamentals of Heat Transfer*, 2nd printing, MIR Publishers, Moscow, 1968, pp. 73-81.

7 Hassan, K. E., and Mohamed, S. A., "Natural Convection from Isothermal Flat Surfaces," *International Journal of Heat and Mass Transfer*, Vol. 13, 1970, pp. 1873-1886.

8 Rotem, Z., and Claassen, L., "Natural Convection above Unconfined Horizontal Surfaces," *Journal of Fluid Mechanics*, Vol. 39, part 1, 1969, pp. 173-192.

9 Rotem, Z., and Claassen, L., "Transition to Quasi-Cellular Flow in Natural Convection above Horizontal Plates and Disks," *C.A.S.I. Transactions*, Vol. 3, No. 1, 1970, pp. 31-34.

10 Fujii, T., and Imura, H., "Natural-Convection Heat Transfer from a Plate with Arbitrary Inclination," *International Journal of Heat and Mass Transfer*, Vol. 15, 1972, pp. 755-767.

11 Restrepo, F., and Glicksman, L. R., "The Effect of Edge Conditions on Natural Convection from a Horizontal Plate," *International Journal of Heat and Mass Transfer*, Vol. 17, 1974, pp. 135-142.

12 Al-Arabi, M., and El-Riedy, M. K., "Natural Convection Heat Transfer from Isothermal Horizontal Plates of Different Shapes," *International Journal of Heat and Mass Transfer*, Vol. 19, 1976, pp. 1399-1404.

13 Ishiguro, R. et al, "Heat Transfer and Flow Instability of Natural Convection over Upward-Facing Horizontal Surfaces," *Proceedings of the Sixth International Heat Transfer Conference*, NC-8, Vol. 2, Toronto, 1978, pp. 229-234.

14 Sparrow, E. M., Husar, R. B. and Goldstein, R. J., "Observations and other Characteristics of Thermals," *Journal of Fluid Mechanics*, Vol. 41, part 4, 1970, pp. 793-800.

15 Croft, J. F., "The Convective Regime and Temperature Distribution above a Horizontal Heated Surface," *Quarterly of the Royal Meteorological Society*, Vol. 84, 1958, pp. 418-427.

16 Stewartson, K., "On the Free Convection from a Horizontal Plate," *Z. Angew. Math. Phys.*, Vol. 9a, 1958, pp. 276-281.

17 Gill, W. N., Zeh, D. W. and Del Casal, E., "Free Convection on a Horizontal Plate," *Z. Angew. Math. Phys.*, Vol. 16, 1965, pp. 539-541.

18 Rotem, Z. and Claassen, L., "Free Convection Boundary-layer Flow Over Horizontal Plates and Disks," *The Canadian Journal of Chemical Engineering*, Vol. 47, 1969, pp. 461-468.

19 Rotem, Z., "Contribution to the Theory of Free Convection from Horizontal Plates," *Proceedings of the First Canadian National Congress on Applied Mechanics*, Vol. 2b, 1967, pp. 309-310.

20 Pera, L. and Gebhart, B., "Natural Convection Boundary Layer Flow over Horizontal and Slightly Inclined Surfaces," *International Journal of Heat and Mass Transfer*, Vol. 16, 1973, pp. 1131-1146.

21 Fussey, D. E. and Warneford, I. P., "An Analysis of Laminar Free Convection from an Upward-Facing Inclined Flat Plate," *Letters in Heat and Mass Transfer*, Vol. 3, 1976, pp. 443-448.

22 Fatt, L. F., "Free Convection Heat Transfer above a Heated Horizontal Flat Plate," *Journal of I.E.M.*, Vol. 20, 1976, pp. 24-27.

23 Bosworth, R. L. C., *Heat Transfer Phenomena*, John Wiley, New York, 1952.

24 Tarasuk, J. D., "An Interferometric Study of Natural Convection During the Interaction of Surfaces of a Long Rectangular Block," Ph.D. thesis in Mechanical Engineering, University of Saskatchewan, 1969.

25 Randall, K. R., Mitchell, J. W. and El-Wakil, M. M., "Natural Convection Heat Transfer Characteristic of Flat Plate Enclosures," ASME JOURNAL OF HEAT TRANSFER, Vol. 101, 1979, pp. 120-125.

26 McKeen, W. J. and Tarasuk, J. D., "An Accurate Method for Locating Fringes on an Interferogram," *Review of Scientific Instruments*, Vol. 52, No. 8, 1981, pp. 1223-1226.

Experiments on Free Convection Between Vertical Plates With Symmetric Heating

R. A. Wirtz
Associate Professor,
Department of Mechanical and Industrial Engineering,
Clarkson College of Technology,
Potsdam, N.Y. 13676
Assoc. Mem. ASME

R. J. Stutzman
Associate Engineer,
IBM Corporation,
Endicott, N.Y. 13760

Laboratory experiments on natural convection of air between vertical parallel plates with uniform and symmetric heat fluxes are reported. Data collection was through direct temperature measurement using thermocouples and through analysis of interferograms of the flow. Data were collected over a range of heat fluxes and geometric parameters where the flow was in the developing temperature field regime. A correlation is developed that allows for the calculation of the maximum temperature variation of the plates for a given input heat flux and plate geometry. The equation is expected to be accurate to ±5 percent.

Introduction

In this paper we report on heat transfer measurements of two-dimensional natural convection between vertical plates subjected to uniform heat flux. The geometry is sketched in Fig. 1. The plates are of height, L, and spacing, b. A uniform heat flux, q, induces a vertical flow between the plates, heating the fluid from some inlet temperature, T_0. The plate temperatures vary from T_0 at the entrance to some maximum temperature at the exit of the channel, $T_w(L)$. Side walls prevent inflow along the vertical edges. The depth is sufficiently large so that the presence of the side walls does not significantly retard the flow, so the flow is assumed to be two-dimensional.

Consideration of the two-dimensional mass, momentum, and energy conservation equations for this geometry shows that the temperature variation along the plates, written in dimensionless form as a local Nusselt number, depends on Rayleigh number and Prandtl number

$$\mathrm{Nu}(x) \equiv \frac{qb/k}{T_w(x) - T_0} = f\left(\mathrm{Ra}, \mathrm{Pr}, \frac{x}{L}\right) \tag{1}$$

where

$$\mathrm{Ra} \equiv g\beta q b^5 / L\nu\alpha k \tag{2}$$

In this study the Prandtl number, Pr, is essentially constant; the working fluid was air.

Heat transfer by natural convection from vertical plates with uniform heat flux has been studied by various investigators. Sparrow and Gregg [1] considered a single plate with a constant heat flux surface, developing an analytical model using similarity transforms. Later, the work was generalized to include plates with arbitrary temperature specification, the constant heat flux situation being a special case of the latter [2]. This result forms one possible asymptotic limit for the problem at hand: the case where the plates are very far apart. Aung et al. considered the parallel plate geometry, investigating both the fully developed limit [3] (very closely spaced or very tall plates) and the developing flow situation [4, 5]. For these cases, asymmetric and symmetric heating of the plates were analyzed and compared. The work presented in [4, 5] used a finite difference simulation to solve the conservation equations.

Little experimental data is available in the literature for the uniform heat flux parallel plate situation, although in 1942 Elenbaas [6] reported measurements with isothermal parallel plates having open edges. Bodoia and Osterle [7] reported a finite difference simulation for parallel isothermal plates. Recently Sparrow and Bahrami [8] used the naphthalene sublimation technique for fluids with Pr = 2.5 to obtain mass transport results that are analogous to heat transfer between isothermal plates. They showed that edge effects become significant when $b/L\ \mathrm{Ra} < 10$. Furthermore, their results diverge from reference [6] as $b/L\ \mathrm{Ra} \to 0$.

This study is concerned with obtaining data for the parallel plate geometry where there is symmetric heating and air is the

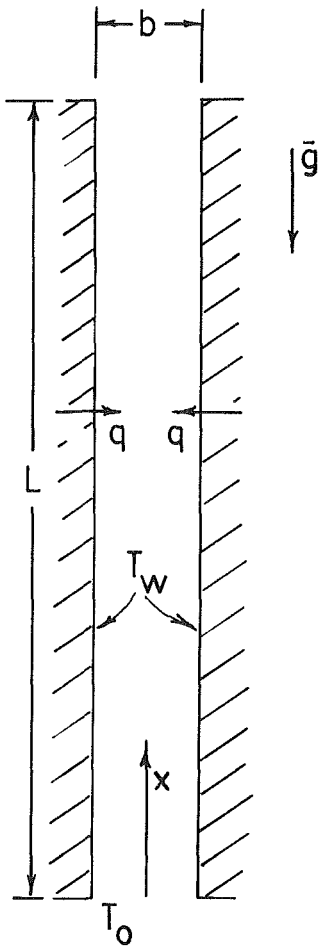

Fig. 1 Geometry and coordinate system of vertical parallel plates with constant heat flux

Contributed by the Heat Transfer Division for publication in the JOURNAL OF HEAT TRANSFER. Manuscript received by the Heat Transfer Division August 10, 1981.

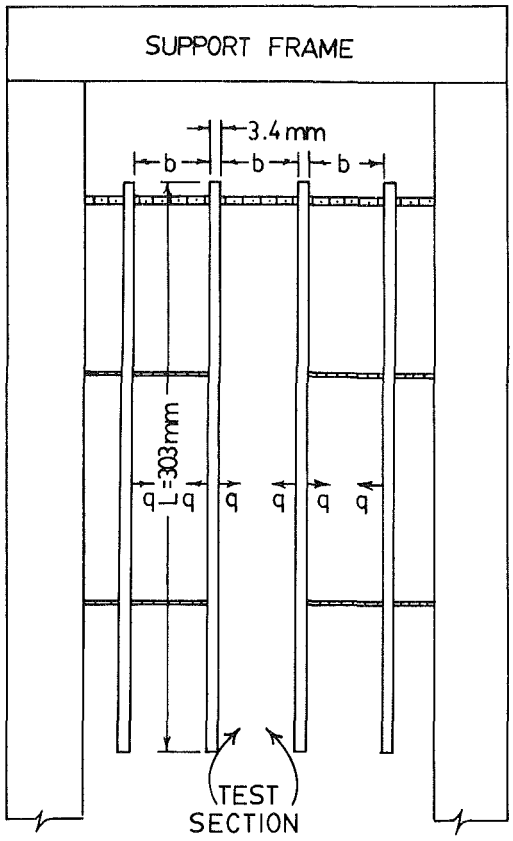

Fig. 2 Edge view of experimental apparatus

fluid. Local temperatures along the walls for various spacing and heating rates of the walls were found using thermocouples embedded in the plates as well as interferometric data. The experimental results are compared to the numerical solutions obtained by Aung et al. [4]. From these results a simple design equation for predicting the maximum wall temperature is developed.

The application of these results lies in the electronics and communication industry where better predictive models of heat transfer requirements are needed. Our uniform heat flux geometry is a first-order model of the situation occurring between convectively cooled, rack-mounted printed circuit boards containing heat dissipating integrated circuitry.

Experimental Apparatus

An edge view of the experimental apparatus is shown in Fig. 2. The two outer plates were added to give symmetry to the heat transfer from the two inner plates which formed the channel. The plates were 303.2-mm high by 303.2-mm deep and 3.4-mm thick, constructed of phenolic fiberboard similar to the material used in the electronics industry (thermal conductivity $\simeq .17$w/°Km).

Stainless steel shim stock of 0.0254-mm (0.001-in.) thickness, cut in a serpentine fashion, formed the heaters that were attached to the phenolic board using 3m mounting adhesive sheets. Heater element runs were 10-mm wide, with a 1-mm gap between each run. Heaters were attached to both sides of the inner plates and to the inner surfaces of the outer plates as shown in Fig. 2. Each heater was connected in series with a Clarostat 25 W variable power resistor and in parallel with each other to a variable transformer. This variable transformer was in series with another variable transformer, allowing a large sensitivity range for the setting of heat flux from the heaters. Voltage and current measurements were made for each heater giving an estimated accuracy of ±5 percent for the heat flux per board.

Wall temperature measurements were made using 0.762-mm (0.003-in.) copper constantan thermocouples spaced at various intervals along the wall of the plates and located in the 1-mm wide gaps between the heater strips. Thermocouple measurements were made using an integrating digital voltmeter with a sensitivity of $\pm 1\mu$v. Calibration of the temperature measuring system using a secondary standard traceable to N.B.S. showed an estimated precision of the thermocouple/readout system of ±0.05°C. Interferometric measurements were made using a 152-mm dia Mach-Zehnder Interferometer. Standard techniques were employed as outlined in references [9, 10]. We estimate that the wall surface temperatures in every case could be determined with a maximum uncertainty of ±0.8°C.

The plates were hung vertically from two #10-24 threaded rods located on each corner of the boards and mounted on an aluminum supporting main frame as shown in Fig. 2. Jacking screws made from #3-48 threaded rods were located along the sides of the plates and secured to the aluminum frame, allowing adjustment of the channel spacing. Machined gauge blocks of sizes 7.937, 9.525, 12.70, and 17.78 mm were used as reference spacing for the channels, giving an accuracy of ±0.25 mm for b.

Side walls were added to model the two-dimensional channel flow. Each wall consisted of a 152-mm dia interferometric quality window mounted inside a wooden frame, with a styrofoam block to complete the wall.

All experiments used air as the fluid medium. Properties for air were based on the bulk temperature of the fluid given as $(T(L)-T_0)/2$, where $T(L)$ is the average temperature of the air at height, L, and midspan between the plates. Radiation effects were assumed negligible.

For this study, data were collected for four plate spacings ($b=7.94$, 9.53, 12.70, 17.78 mm) with $50<q<150$ w/m^2. Aung et al. [4] have characterized the flow between plates of height, L, and spacing b as follows:

(Gr = Ra/Pr):

$0.0<\text{Gr}<0.2$	Fully developed temperature profile
$0.2<\text{Gr}<1000$	Developing temperature profile
$1000<\text{Gr}$	Plates sufficiently far apart so that they act independently (single plate limit)

Nomenclature

b = plate spacing
C = constant
g = gravitational acceleration
Gr = Grashof number
k = fluid conductivity
L = plate height
m = constant
n = constant
Nu = Nusselt number
P = empirical constant
Pr = fluid Prandtl number
q = heat flux
Ra = Rayleigh number
T = temperature
x = vertical coordinate
α = fluid thermal diffusivity
β = fluid thermal expansion coefficient
ν = fluid kinematic viscosity
σ = rms relative difference

Subscripts

0 = initial condition or fully developed condition
w = wall condition
∞ = single plate condition

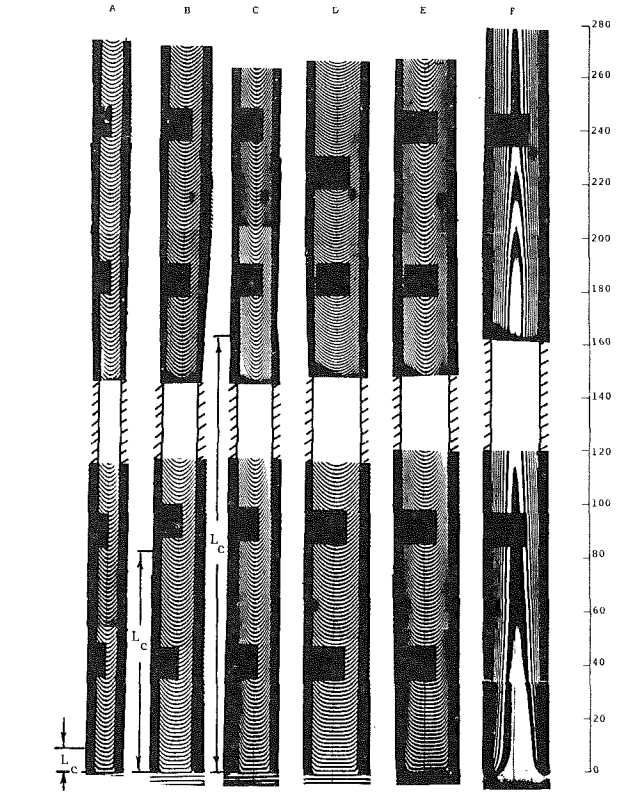

b(mm)	7.9	12.7	12.7	17.8	17.8	17.8
q(w/m^2)	55.7	55.7	114.0	55.7	114.0	114.0
Ra	18.8	191	397	1170	2414	2414
Gr	26.6	270	535	1350	3410	3410
L_c(mm)	8.10	81.9	162	409	1034	1034

Fig. 3 Interferograms of natural convection between parallel plates. Parts 3(*a*)-(*e*) were obtained using the fringe shift configuration of the interferometer. Part 3(*f*) was obtained using the infinite configuration. The table entries below each part of the figure list the operating conditions of the plates for each case shown.

In terms of air flow between plates spaced 6.35 mm apart (1/4 in.) with a heat flux of 50w/m^2 (values representative of printed circuit boards), the fully developed condition would be achieved when $L = 8$ m while the single plate limit would occur when $L = 2$ cm. Therefore, most applications will fall into the developing flow regime. The fifteen data sets reported here span the range $24 < Gr < 3355$ ($17.7 \leq Ra \leq 2414$), so that our data spans the developing flow regime with two sets of plates spaced far enough apart to be in the single plate regime. An error analysis (see reference [10]) gives tolerances of approximately ± 5 percent for Nu and ± 10 percent for Ra. Specific details concerning apparatus construction, methods of data reduction, error analysis, and the characteristics of our Mach-Zehnder system are found in reference [10] which is available from the principal author.

Qualitative Description of the Temperature Field

Figure 3 shows interferograms of the temperature field between the plates for various spacings and heat fluxes. For Figs. 3(*a*)-3(*e*) the interferometer was set in the fringe shift mode with fringes initially horizontal and equispaced. The vertical displacement of the fringes from their original location in the unheated condition is proportional to the temperature increase of the fluid. Therefore, with the fringes originally in the horizontal position, the fringe patterns of Figure 3(*a*)-(*e*) may be thought of as a series of temperature profiles across the air space as one moves upward. For Fig. 3(*f*) the interferometer was set in the infinite fringe mode. The resulting fringes are then isotherms.

Table 1 Tabulation of coefficients for the power-law correlation (equation (3)) for a single plate (large *b*) and for fully developed flow between parallel plates (small *b*). The value C = 0.520 is for Pr = 0.72.

	C	*m*	*n*	Reference
Large *b*	0.520	0.2	0.2	[1]
Small *b*	0.144	1.0	0.5	[3]

Each image actually consists of six or eight separate data records taken at different times; three or four for the lower region ($x \lesssim 120$ mm) and three or four for the upper region ($150 \lesssim x < 280$ mm). No photographic records were taken for the region $120 < x < 150$ mm or $275 < x < 303$. The dark rectangle which appears three or four times in each view was a reference gauge block which was placed in the field of view but external to the channel. The thin vertical line was a plumb line which was located at mid-depth but not necessarily centered between the plates. Our procedure was as follows:

1 The interferometer was initially set and a reference image taken with $q = 0$.
2 The heat flux was set and allowed to equilibrate; an interferogram was recorded.
3 The channel was moved vertically to a new location and a second interferogram recorded.
4 The heat flux was set to zero. Another reference image was recorded for the second interferogram.

Data records were taken in pairs in this way, with as long as several weeks separating adjacent data pairs for a given heat flux and gap width. The images shown in Fig. 3 are composites of that information.

Figure 3(*a*) shows the situation with a small gap width and low heat flux giving a Rayleigh number, Ra = 18.8. Two thermal boundary layers form at the lower leading edges and merge in the first 15-20 mm of height. For $x \gtrsim 25$ mm the shift shapes (temperature profiles) change in a more subtle way as x increases. Figure 3(*b*) shows the effect of a 60 percent increase in gap width (giving an approximate tenfold increase in Rayleigh number). In this case the entry thermal boundary layers merge in the range $60 < x < 80$ mm. Figure 3(*c*) shows the effect of an approximate doubling of the heat flux over the condition of Fig. 3(*b*), resulting in a more pronounced variation of temperature across the slot.

In Figs. 3(*a*) through 3(*c*) the height of an equivalent plate where the plates act independently according to Aung et al.'s criteria (Gr = 1000) has been indicated as L_c. Our analysis of the data to be presented in the following section indicates that the plates never really act independently, even for Grashof numbers which are three times the above limit. Figures 3(*d*) and 3(*e*) show data where Gr > 1000. Figure 3(*e*) represents an approximate doubling in heat flux over Fig. 3(*d*) with Gr = 3410. Our measurements indicate that the heat transfer is asymptotic to a limiting condition which is parallel to, yet approximately 10 percent higher than, the situation where the two plates do not interact. Figure 3(*f*) shows approximately the same conditions as Fig. 3(*e*), however it was made using the infinite fringe configuration of the interferometer. This figure shows that the thermal boundary layers do interact as evidenced by the thermal stratification along the centerline at $x \gtrsim 75$ mm.

Heat-Transfer Results

Figure 4 presents measured wall temperature variation data for two different plate heat fluxes with a spacing $b = 12.7$ mm. Both thermocouple data and interferometeric results are compared; data was extracted from both the left and right plates. In each case the interferometric data was collected at a

Table 2 Tabulation of experimentally determined values of Nu(L) and m. Data numbered 1–10 are from thermocouple measurements while those numbered A–E are from interferograms.

Data #	Ra	Nu(L)	m	Correlation coefficient
E	2414.0	2.80	0.3365	0.987
1	1716.0	2.56	0.3560	0.990
D	1170.0	2.28	0.4025	0.995
2	962.0	2.14	0.3878	0.992
C	397.0	1.72	0.4166	0.985
3	379.0	1.71	0.3988	0.992
4	196.0	1.32	0.4678	0.998
B	191.0	1.24	0.5105	0.992
5	80.5	1.06	0.4713	0.998
6	56.0	0.95	0.4968	0.999
7	43.2	0.83	0.5090	0.999
8	30.9	0.80	0.4994	0.990
9	23.5	0.69	0.5071	0.993
A	18.8	0.52	0.6966	0.995
10	17.7	0.57	0.6078	0.998

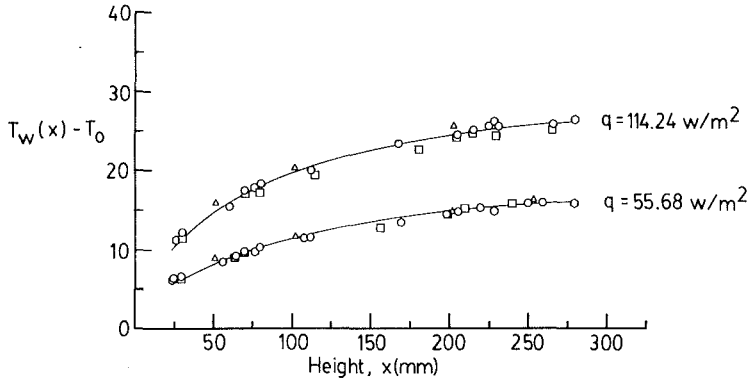

Fig. 4 Temperature variation data for four different data sets where b-12.7mm. The thermocouple data is from the left wall (△) and the right wall (○) for Ra = 379 (upper set) and Ra = 196 (lower set). The interferometry data is from the left wall (○) and the (□) for Ra = 397 (upper set) and Ra = 191 (lower set).

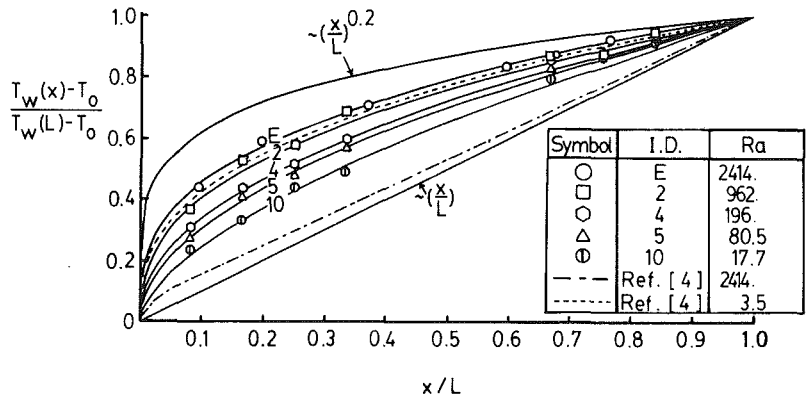

Fig. 5 Dimensionless plate temperature variation data compared with equation (4) and Table 2

time different than the thermocouple data. Differences in ambient conditions resulted in each set having slightly different average property values with consequent differences in the calculated Rayleigh number (379 versus 397 for the upper curve and 196 versus 191 for the lower curve for thermocouple data and interferometric data, respectively). This undoubtly accounts for part of the scatter shown in Fig. 4. For this reason we treated each data set, whether interferometric or from thermocouple readings, as a separate set. The data shown in Fig. 4 is representative of all fifteen data sets investigated.

The variation of the local Nusselt number with respect to the Rayleigh number was first investigated. A correlation for the local Nusselt number in terms of the Rayleigh number and the dimensionless geometric ratio (L/x) was developed by analyzing the asymptotic limits.

The local Nusselt number for large b (a single plate) and for small b (fully developed flow) is given by

$$\mathrm{Nu}(x) = C\left(\frac{L}{x}\right)^{m} \mathrm{Ra}^{n} \tag{3}$$

with C, m, and n for a fluid with $\mathrm{Pr} = 0.72$ tabulated in Table 1. We postulate that $0.2 < m < 1.0$ and $0.2 < n < 0.5$ for flows occurring between these two limiting cases. Since

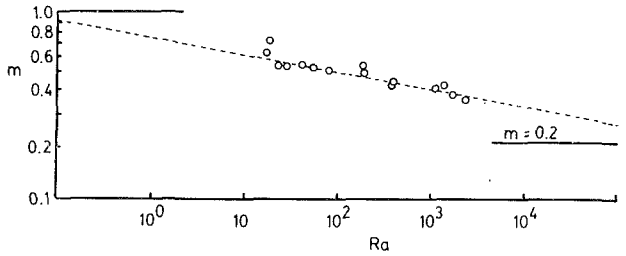

Fig. 6 Experimentally determined values of the exponent m of equation (4) from Table 2

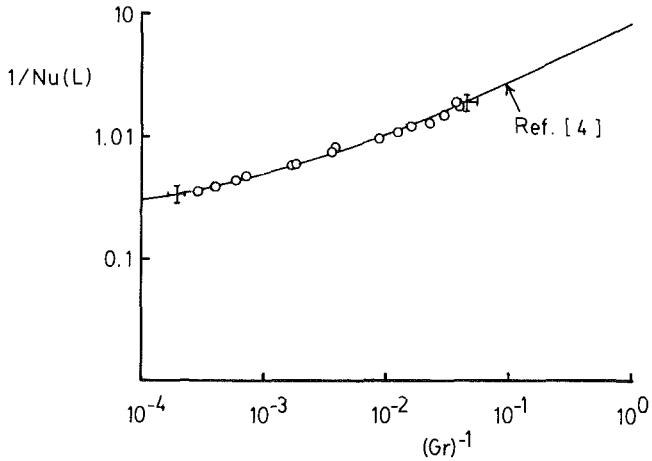

Fig. 7 Experimentally determined dimensionless maximum temperature rise from Table 2 compared with finite difference result of reference [4]. The cross, +, represents an error tolerance of ±5 and ±10 percent placed on Nu and Ra, respectively.

$$\frac{\mathrm{Nu}(L)}{\mathrm{Nu}(x)} = \frac{T_w(x) - T_0}{T_w(L) - T_0} = \left(\frac{x}{L}\right)^m \tag{4}$$

plate temperature variation data may be used to determine m and Nu(L), which is the inverse of the maximum plate temperature in dimensionless form, by plotting the measured values of Nu(x) versus x/L in logarithmic coordinates. Table 2 lists the values of m and Nu(L) as calculated from the data using a least squares fit of equation (4). Column 5 of that table shows the correlation coefficient for the data. As can be seen, excellent correlation of the data is achieved. Data labeled A-E in Table 2 corresponds to the data shown in Fig. 3 while data labeled 1-10 were derived from thermocouple measurements.

A plot of equation (4) is shown in Fig. 5 for five data sets, with m values taken from Table 2. The upper and lower bounds, representing the single-plate and fully developed conditions, respectively, are also included. Also shown are analytical results from reference [4] for Ra = 2414 and 3.50. Our fit for Ra = 2414 falls approximately 5 percent above the corresponding result taken from reference [4].

Figure 6 shows the variation in exponent m with changes in Rayleigh number. It can be seen that the exponent varies continuously between the two limiting conditions, although it is probably not practical to fit an empirical curve through the points.

Figure 7 shows a plot of experimentally determined dimensionless maximum temperature variation of the plates, 1/Nu(L), from Table 2 plotted with 1/Gr. The results are compared with Aung et al.'s [4] numerical results using their coordinates. The crosses near the left edge of the data (single plate limit) and right end of the data (fully developed limit) represent our tolerance bands on Nu and Ra (or Gr) of ±5 percent and ±10 percent, respectively. The data are in good agreement with Aung et al.'s numerical results.

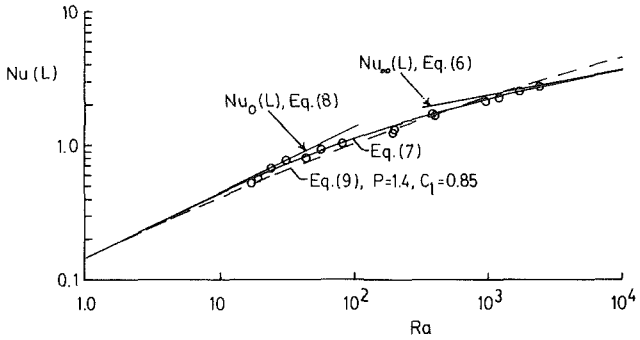

Fig. 8 Plate top Nusselt number, Nu(L) data from Table 2 compared with predictions of equation (7) and equation (9)

Since Nu(L) does not plot as a straight line when plotted against Ra on logarithmic coordinates, the exponent n in equation (3) with $x = L$ is not a constant. A power-law fit is not appropriate. However, two well-defined asymptotic limits for the heat transfer exist so that it is appropriate to use the procedure suggested by Churchill and Usagi [11] for correlating the heat transfer data.

Churchill and Usagi suggest that under these circumstances, the heat-transfer correlation takes the form

$$\left[\frac{1}{\mathrm{Nu}(L)}\right]^P = \left[\frac{1}{\mathrm{Nu}_0(L)}\right]^P + \left[\frac{1}{\mathrm{Nu}_\infty(L)}\right]^P \tag{5}$$

where Nu$_0$ and Nu$_\infty$ are the plate Nusselt numbers at the fully developed and single plate limits, respectively, and P is empirical.

Close inspection of Aung's result shown in Fig. 7 reveals that Nu(L) is asymptotic to the line

$$\mathrm{Nu}_\infty(L) = 0.577\mathrm{Ra}^{0.2} \tag{6}$$

which is about 10 percent higher than equation (3), using $C = 0.52$ given in Table 1. One can argue that if the plates are truly modeling channel flow, the fluid between the plates will exhibit movement due to the pressure gradient term in the x-direction, contrary to the single plate no-flow situation for the fluid far from the plates where the vertical pressure gradient is hydrostatic everywhere. This would account for the slightly higher value of Nu(L) found for large Ra.

A least squares fit of the data in Table 2, using equation (6) for Nu$_\infty$ and C = 0.144 with n = 0.5 from Table 1 for Nu$_0$, gives P = 3 with a rms relative deviation, σ, of approximately 6 percent. (The optimum value is actually P = 2.7, but the improvement over P = 3 is negligible). Equation (5) then becomes

$$\mathrm{Nu}(L) = \frac{0.144\mathrm{Ra}^{0.5}}{[1 + 0.0156\mathrm{Ra}^{0.9}]^{0.33}} \tag{7}$$

This result is shown in Fig. 8, along with the data of Table 2. Equation (7) is asymptotic to the fully developed expression and the Nu(L) calculated is less than 0.01 percent below Aung's fully developed expression [3],

$$\mathrm{Nu}_0(L) = 0.144\mathrm{Ra}^{0.5} \tag{8}$$

at Ra ≤ 0.144 (this corresponds to the limit Gr ≤ 0.2 for fully developed conditions with air cited previously). In fact, equation (7) is within less than 1 percent of equation (8) for Ra ≤ 2.

For large Ra (large b), equation (7) is asymptotic to equation (6). The two equations make predictions that fall within 1 percent of each other for Ra > 2500.

It is tempting to repeat the above procedure for the local Nusselt number. The equation would have the form

$$\mathrm{Nu}(x) = 0.144\frac{L}{x}\mathrm{Ra}^{0.5}\left[1 + \left[\frac{0.144}{C_1}\left(\frac{L}{x}\right)^{0.8}\mathrm{Ra}^{0.3}\right]^P\right]^{-1/P} \tag{9}$$

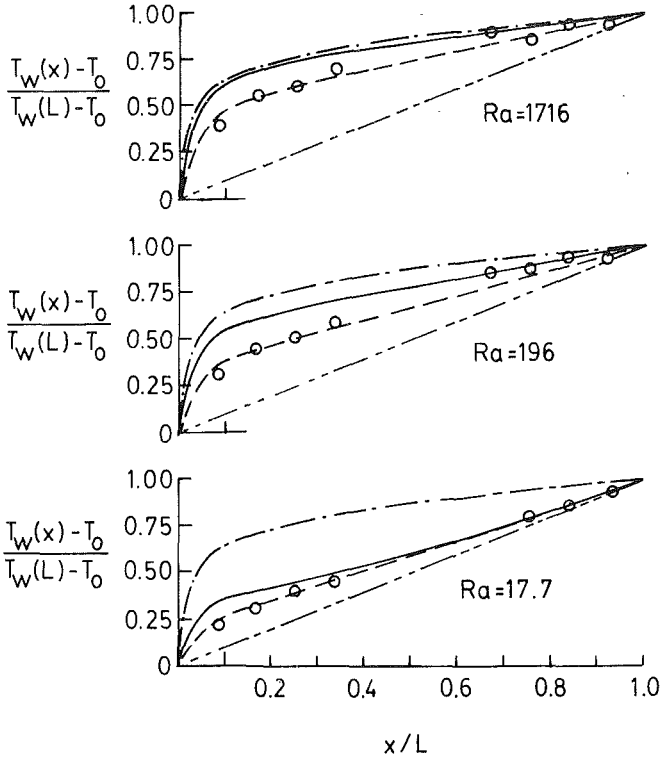

Fig. 9 Dimensionless plate temperature variation data compared with equation (9) and limiting conditions for three different Rayleigh numbers: – $C_1 = 0.577$, $P = 3$; ···$C_1 = 0.847$, $P = 1.4$; –·– single plate limit; – · · –, fully developed limit

where $C_1 = 0.577$ if equation (6) is the appropriate asymptote for large Ra (large b). At $x = L$, equation (9) reduces to equation (7) when $P = 3$. However, equation (9) represents an additional assumption in the $x/L \to 0$ has the same effect as $\mathrm{Ra} \to \infty$. That is, equation (9) indicates that the entry region flow is the same as convection adjacent to a single plate bounded by a quiescent fluid with hydrostatic vertical pressure gradient. This certainly would not be true for closely spaced plates, even very near the entrance, since then the vertical pressure gradient induced by the heating pumps the fluid in the center of the slot upward. As a check on equation (9), we have plotted the dimensionless temperature rise (equation (9) normalized by itself with $x = L$) in Fig. 9 with $P = 3$. The model fails near the leading edge, with σ for all data collected equal to 26 percent. Figure 9 shows that some improvement in the rms relative deviation between the temperature data, and equation (9) may be achieved by adjusting C_1 (and P). This is equivalent to changing the large Ra asymptotic limit. When this is done, $\sigma = 10$ percent for $C_1 = 0.85$, $P = 1.4$. However, then the model fails at the exit. This is shown in Fig. 8 where Nu(L) from equation (9) (with $P = 1.4$, $C_1 = 0.85$) is plotted. The equation clearly does not fit the data well over the range $10 < \mathrm{Ra} < 10^3$. Furthermore, the equation approaches the wrong asymptote as $\mathrm{Ra} \to \infty$.

Also of interest is a comparison of the present result with results obtained for convection from isothermal parallel plates [6]. In order to do this, equation (7) is recast in terms of Rayleigh number based on maximum temperature variation

$$\mathrm{Ra}_T \equiv \frac{g\beta(T_w(L) - T_0)b^4}{\nu\alpha L} \tag{10}$$

The large Rayleigh number limit (equation (6)) becomes

$$\mathrm{Nu}_\infty(L) = 0.577\left[\frac{g\beta[T_w(L) - T_0]b^4}{\nu\alpha L} \cdot \frac{qb}{[T_w(L) - T_0]k}\right]^{1/5}$$
$$= 0.577\mathrm{Ra}_T{}^{0.2}\mathrm{Nu}_\infty(L)^{0.2} \tag{11}$$

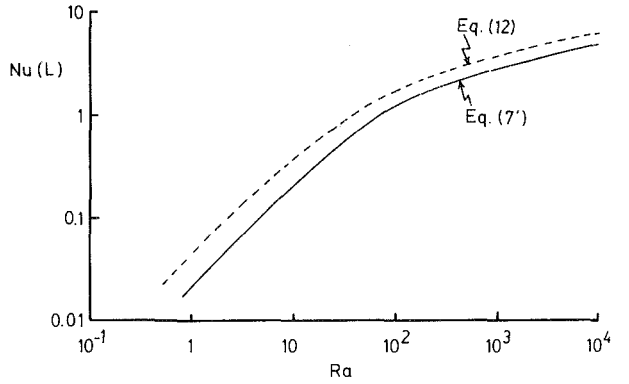

Fig. 10 Plate top Nusselt number, Nu(L) calculated by equation (7′) with Ra based on maximum temperature rise compared with similar correlation equation for isothermal plates (equation (12))

or

$$\mathrm{Nu}_\infty(L) = 0.503\mathrm{Ra}_T^{0.25} \tag{6'}$$

Similarly equation (8) becomes

$$\mathrm{Nu}_0(L) = 0.0207\mathrm{Ra}_T \tag{8'}$$

and finally equation (7) becomes

$$\mathrm{Nu}(L) = \frac{0.021\mathrm{Ra}_T}{[1 + 7\times10^{-5}\mathrm{Ra}_T{}^{2.25}]^{0.333}} \tag{7'}$$

Rohsenow [12] has used Churchill's fitting technique to correlate Elenbaas's [6] data for parallel isothermal plates, arriving at an equation which is very similar to equation (7′). In terms of the present notation it is

$$\mathrm{Nu}(L) = \frac{0.042\mathrm{Ra}_T}{[1 + 5.25\times10^{-3}\mathrm{Ra}_T{}^{1.46}]^{0.513}} \tag{12}$$

Equations (7′) and (12) are compared in Fig. 10. It can be seen that the isothermal calculation results in a higher Nu(L) (and consequent lower plate temperature rise for given quantity of heat removed per plate) than the constant heat flux calculation. The band width between the two results is approximately 50 percent at the fully developed (small Ra) limit and approximately 20 percent at the large Ra limit. The actual band width for small Ra is expected to be larger in the light of Sparrow and Bahrami's [8] findings, since their measured Nu was considerably higher than Elenbaas's as $\mathrm{Ra} \to 0$. A practical situation would have thermal boundary conditions which are neither isothermal nor constant heat flux. It is expected that the heat transfer would lie in the band between the two results shown in Fig. 10.

Conclusions

The experimental results for natural convection from constant heat flux parallel plates obtained in this study are in close agreement with the finite difference calculations of Aung et al. [4]. The data points are well bounded within the expected experimental uncertainty of ±5 percent and ±10 percent placed on Nusselt and Rayleigh numbers, respectively. From the experimental results, a design equation (equation 7) was found which spanned the entire experimental flow regime. Equation (7) predicts the local Nusselt number at the top of the plate when air is the working fluid. From this information the maximum temperature variation of the plates may be calculated for a given plate geometry and plate heat flux.

Inspection of equation (7) showed that the measured heat-transfer performance is within 1 percent of Aung's fully developed flow prediction for $\mathrm{Ra} \le 2$ so that systems with $0 \le \mathrm{Ra} \le 2$ may be treated as having fully developed flow. On the other hand, for $\mathrm{Ra} > 2500$, the data is 10 percent higher

than predictions based on a single plate residing in a quiescent fluid medium. The plates interacted even at these large Rayleigh numbers (large b).

A correlation similar to equation (7) for the local Nusselt number variation over the entire plate height was not successful in that the entry flow may not be treated in the same way as flow where the plates are spaced far apart. In any case, the local Nusselt number (and plate temperature variation) may be easily calculated using equation (7) and equation (4) in conjuction with Fig. 6.

A comparison with experimental results for natural convection between isothermal parallel plates showed the q-constant Nusselt number to be about 20–50 percent lower than the isothermal result if the maximum temperature variation is used as the characteristic temperature of the system. These two results (equation 7 and equation 12) may serve as bounds for situations where the thermal boundary conditions are neither isothermal nor constant heat flux.

References

1 Sparrow, E. M., and Gregg, J. L., "Laminar Free Convection From a Vertical Plate With Uniform Surface Heat Flux," ASME *Transactions*, Vol. 78, 1956, pp. 435–440.

2 Sparrow, E. M., and Gregg, J. L., "Similar Solutions for Free Convection From a Nonisothermal Vertical Plate," ASME *Transactions*, Vol. 80, 1958, pp. 379–386.

3 Aung, W., "Fully Developed Laminar Free Convection Between Vertical Plates Heated Asymmetrically," *International Journal of Heat and Mass Transfer*, Vol. 15, 1972, pp. 1577–1580.

4 Aung, W., Fletcher, L. S., and Sernas, V., "Developing Laminar Free Convection Between Vertical Plates and Asymmetric Heating," *International Journal of Heat and Mass Transfer*, Vol. 16, 1972, pp. 2293–2308.

5 Aung, W., Dessler, T. J., and Beitin, K. I., "Free Convection Cooling of Electronic Systems," *IEEE Transactions on Parts, Hybrids, and Packaging*, Vol. PHP-9, No. 2, 1973, pp. 75–86.

6 Elenbaas, W., "Heat Dissipation of Parallel Plates by Free Convection," *Physica*, Vol. 9, 1942, pp. 1–28.

7 Bodoia, J. R., and Osterle, J. F., "The Development of Free Convection Between Heated Vertical Plates," ASME JOURNAL OF HEAT TRANSFER, Vol. 84, 1962, pp. 40–44.

8 Sparrow, E. M., and Bahrami, P. A., "Experiments on Natural Convection from Vertical Parallel Plates with Either Open or Closed Edges," ASME JOURNAL OF HEAT TRANSFER, Vol. 102, 221–227, 1980.

9 Hauf, W., and Grigull, U., "Optical Methods in Heat Transfer," *Advances in Heat Transfer*, Vol. 6, 1970, pp. 122.

10 Stutzman, R., "Developing Free Convection Flow Between Vertical Plates With Symmetric Heating Using a Mach-Zehnder Interferometer," MIE Report 070, Clarkson College of Technology, Potsdam, N.Y., 1981.

11 Churchill, S. W., and Usagi, R., "A General Expression for the Correlation of Rates of Transfer and Other Phenomena," *AIChE Journal*, Vol. 18, No. 6, 1972, pp. 1121–1138.

12 Rohsenow, W., Lecture notes from the short course "Thermal Control of Electronic and Microelectronic Components," M.I.T., Aug. 17–21, 1979.

A. Mertol[1]
Assoc. Mem. ASME

R. Greif
Mem. ASME

Department of Mechanical Engineering,
University of California,
Berkeley, Calif. 94720

Y. Zvirin
Faculty of Mechanical Engineering,
Technion,
Israel Institute of Technology,
Haifa, Israel

Two-Dimensional Study of Heat Transfer and Fluid Flow in a Natural Convection Loop

A study has been made of the heat transfer and fluid flow in a natural convection loop. Previous studies of these systems have utilized a one-dimensional approach which requires a priori specifications of the friction and the heat-transfer coefficients. The present work carries out a two-dimensional analysis for the first time. The results yield the friction and the heat-transfer coefficients and give their variation along the loop with the Graetz number as a parameter. Comparison is also made with experimental data for the heat flux and good agreement is obtained.

Introduction

A study has been made of the heat transfer and fluid flow in a laminar natural convection loop which is created by heating from below and cooling from above. The driving force for a natural convection loop results from the density difference between the lower and the upper portions of the loop. Previous studies of such loops have utilized a one-dimensional approach by averaging the governing equations over the cross section (see Creveling et al. [1, 2], Damerell and Schoenhals [3], Greif, Zvirin, and Mertol [4], and Bau and Torrance [5]). Studies on a number of natural convection loops have been carried out by Keller [6], Welander [7], Japikse [8], Zvirin et al. [9–11], Torrance et al. [12, 13], Huang [14], Gillette et al. [15], and Mertol et al. [16, 17]. Natural convection loops, in general, have many applications including the production of geothermal energy, solar heating, and the emergency cooling of nuclear reactors. Although most applications involve turbulent flows, many laminar natural convection flows do appear, particularly in solar systems.

The present work differs from the previous studies of natural convection loops in that a two-dimensional analysis is carried out for the first time. It is noted that the previous studies which followed a one-dimensional approach required a priori specifications of the friction and the heat-transfer coefficients, f and h, respectively. One result of the present study is that the Graetz number, Gz, now emerges as a parameter, and it is shown that the quantity fRe varies as a nonmonotonic function of Gz. Another common assumption has been the use of a constant heat-transfer coefficient, h. The present results show the variation of h with respect to distance along the thermosyphon with Gz as a parameter. Results have also been obtained for the detailed temperature and velocity profiles, as well as for averages of these quantities. Lastly, comparison with the experimental data of Creveling et al. [1, 2] shows good agreement.

Analysis

The analysis which follows is for the determination of the velocity and temperature profiles in a toroidal thermosyphon. The loop is heated continuously by a constant heat flux, q, over the bottom half and is cooled continuously over the top half by transferring heat to the surface which is maintained at the constant temperature, T_w. (see Fig 1). Variations in both the radial, r, and axial, θ, directions are considered. Axial symmetry is assumed and axial conduction, viscous dissipation, and the effects of curvature have been neglected. Fluid properties are assumed to be constant except for the evaluation of the density in the buoyancy term of the momentum equation. The flow is assumed to be laminar and to be in the axial, θ, direction; i.e., radial and azimuthal velocities are neglected. With these assumptions, we obtain from the equation of continuity for incompressible flow that the velocity in the θ-direction is only a function of the radius:

$$v = v(r) \tag{1}$$

The momentum equation in the θ-direction is given by

$$0 = -\frac{1}{R}\frac{dp}{d\theta} - \rho g \cos\theta + \frac{\mu}{r}\frac{d}{dr}\left(r\frac{dv}{dr}\right) \tag{2}$$

Integrating equation (2) along the loop and using the relation $\rho = \rho_w[1 - \beta(T - T_w)]$ in the buoyancy term yields

$$0 = \frac{\rho_w g\beta}{2\pi}\int_0^{2\pi}(T - T_w)\cos\theta d\theta + \mu\left(\frac{d^2v}{dr^2} + \frac{1}{r}\frac{dv}{dr}\right) \tag{3}$$

Note that the pressure term has been eliminated by the integration around the loop. Consequently, the use of the momentum equation in the r-direction is not required. The energy equation is given by the following relation:

$$\frac{v}{R}\frac{\partial T}{\partial \theta} = \alpha\left(\frac{\partial^2 T}{\partial r^2} + \frac{1}{r}\frac{\partial T}{\partial r}\right) \tag{4}$$

Note that axial conduction is neglected.

Equations (3) and (4) must be solved simultaneously subject to the following boundary conditions:

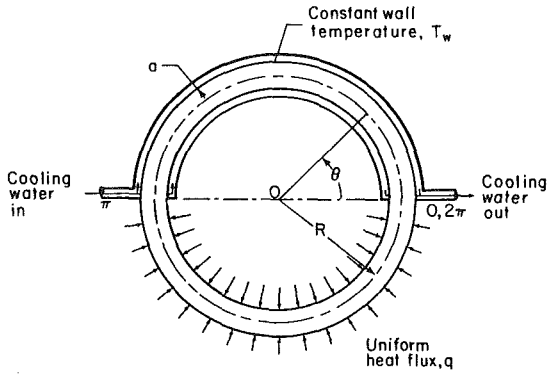

Fig. 1 The circular, toroidal natural circulation loop

[1] Present address: Passive Analysis and Design Group, Lawrence Berkeley Laboratory, University of California, Berkeley, Calif. 94720.

Contributed by the Heat Transfer Division for publication in the JOURNAL OF HEAT TRANSFER. Manuscript received by the Heat Transfer Division July 20, 1981.

$$\left.\frac{dv}{dr}\right|_{r=0} = 0 = \left.\frac{\partial T}{\partial r}\right|_{r=0} \tag{5a}$$

$$v(a) = 0 \tag{5b}$$

$$T(a,\theta) = T_w \quad \text{for} \quad 0 < \theta < \pi \tag{5c}$$

$$k\left.\frac{\partial T}{\partial r}\right|_{r=a} = q \quad \text{for} \quad \pi < \theta < 2\pi \tag{5d}$$

Equations (3-5) are made dimensionless according to the following definitions:

$$\phi = \frac{T - T_w}{qa/k}, \quad w = \frac{v}{V}, \quad \xi = \frac{r}{a} \quad \text{and} \quad \eta = \xi \mathrm{Gz}^{1/2} \tag{6}$$

where V is the characteristic velocity defined by Creveling et al. [1]

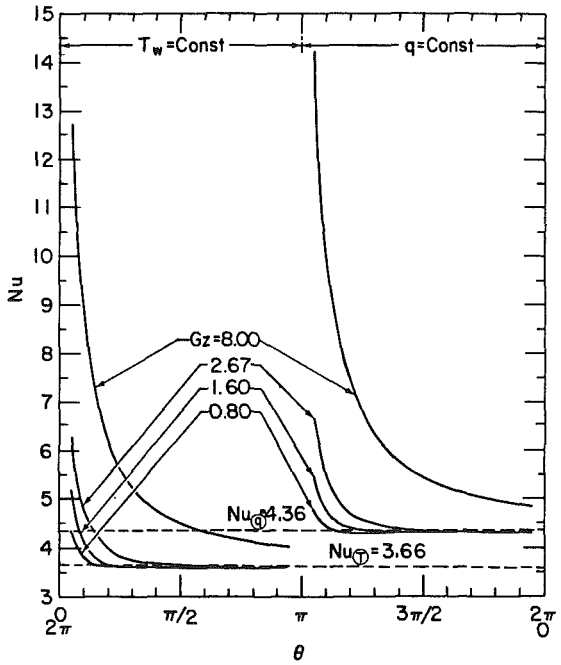

Fig. 2 Nusselt number variation along the loop for different Graetz numbers

$$V = \left(\frac{g\beta Raq}{2\pi c\mu}\right)^{1/2} \tag{7}$$

The Graetz number, Gz, and the characteristic Reynolds number are defined by

$$\mathrm{Gz} = \mathrm{Re}_{ch}\mathrm{Pr}\left(\frac{2a}{2\pi R}\right) = \frac{2\rho_w c a^2 V}{\pi k R}, \quad \mathrm{Re}_{ch} = \frac{\rho_w V 2a}{\mu} \tag{8}$$

The dimensionless form of equations (3-5) then becomes:

$$0 = \int_0^{2\pi} \phi \cos\theta d\theta + \frac{2}{\pi}\left(\frac{d^2 w}{d\eta^2} + \frac{1}{\eta}\frac{dw}{d\eta}\right) \tag{9}$$

$$w\frac{\partial \phi}{\partial \theta} = \frac{2}{\pi}\left(\frac{\partial^2 \phi}{\partial \eta^2} + \frac{1}{\eta}\frac{\partial \phi}{\partial \eta}\right) \tag{10}$$

$$\left.\frac{dw}{d\eta}\right|_{\eta=0} = 0 = \left.\frac{\partial \phi}{\partial \eta}\right|_{\eta=0} \tag{11a}$$

$$w(\mathrm{Gz}^{1/2}) = 0 \tag{11b}$$

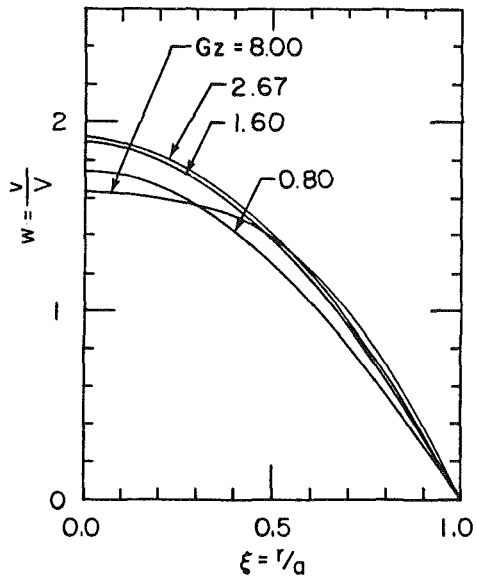

Fig. 3 Velocity distribution

Nomenclature

a = radius of the toroid, Fig. 1
c = specific heat
f = friction coefficient, equations (12) and (13)
G = mass flow rate
Gz = Graetz number, equation (8)
g = acceleration of gravity
h = heat-transfer coefficient, equation (15)
k = thermal conductivity
Nu = Nusselt number, equation (15)
Pr = Prandtl number, $\frac{\mu c}{k}$
p = pressure
q = heat flux
R = radius of the circular loop (see Fig. 1)
Re = Reynolds number, equation (14)
Re_{ch} = characteristic Reynolds number, equation (8)
r = radial space coordinate, $r = 0$ is center of tube
T = temperature
V = characteristic velocity, equation (7)
v = velocity
$\bar{v}$ = cross-sectional average velocity
w = dimensionless velocity, equation (6)
$\bar{w}$ = dimensionless cross-sectional average velocity

Greek Symbols

α = thermal diffusivity, $\frac{k}{\rho_w c}$
β = thermal expansion coefficient
η = dimensionless modified radial space coordinate, equation (6)
θ = axial space coordinate
μ = absolute viscosity
ξ = dimensionless radial space coordinate, equation (6)
ρ = density
ϕ = dimensionless temperature, equation (6)
ϕ_b = dimensionless bulk temperature, equation (16)
ϕ_w = dimensionless wall temperature for the lower loop

Subscripts

0 = location at $\theta = 0$
1 = location at $r = 0$ ($\xi = 0$)
b = bulk
ch = characteristic
i = axial space step in the finite difference equations
j = radial space step in the finite difference equations
M = location at $\theta = 2\pi$
N = location at $r = a$ ($\xi = 1$)
w = wall

$$\phi(\mathrm{Gz}^{1/2},\theta)=0 \quad \text{for} \quad 0<\theta<\pi \tag{11c}$$

$$\left.\frac{\partial\phi}{\partial\eta}\right|_{\eta=\mathrm{Gz}^{1/2}}=\mathrm{Gz}^{-1/2} \quad \text{for} \quad \pi<\theta<2\pi \tag{11d}$$

In terms of presenting results the friction factor and the Nusselt number are also calculated. The friction factor, f, is defined by

$$f=-\frac{\mu\left.\frac{dv}{dr}\right|_{r=a}}{\frac{1}{2}\rho_w\bar{v}^2} \tag{12}$$

where $\bar{v}$ is the average velocity over the cross section given by

$$\bar{v}=\int_0^a v(r)\,2\pi r\,dr/\pi a^2.$$

On a dimensionless basis, f becomes

$$f=-\frac{4}{\mathrm{Re}}\frac{\mathrm{Gz}^{1/2}}{\bar{w}}\left.\frac{dw}{d\eta}\right|_{\eta=\mathrm{Gz}^{1/2}} \tag{13}$$

where $\bar{w}$ is the average dimensionless velocity over the cross section,

$$\bar{w}=\bar{v}/V=\frac{2}{\mathrm{Gz}}\int_0^{\mathrm{Gz}^{1/2}} w\eta d\eta,$$

and Re is the Reynolds number defined by

$$\mathrm{Re}=\frac{\rho_w\bar{v}2a}{\mu}=\frac{\mathrm{Gz}\,\bar{w}}{\mathrm{Pr}}\left(\frac{2\pi R}{2a}\right) \tag{14}$$

The Nusselt number is defined by

$$\mathrm{Nu}(\theta)=\frac{h(\theta)2a}{k}=\begin{cases}-\dfrac{2\mathrm{Gz}^{1/2}}{\phi_b}\left.\dfrac{\partial\phi}{\partial\eta}\right|_{\eta=\mathrm{Gz}^{1/2}} & \text{for } 0<\theta<\pi \quad (15a)\\[2ex] \dfrac{2}{\phi_w-\phi_b} & \text{for } \pi<\theta<2\pi \quad (15b)\end{cases}$$

where the bulk temperature, ϕ_b, is defined by

$$\phi_b=\frac{2}{\bar{w}\mathrm{Gz}}\int_0^{\mathrm{Gz}^{1/2}}\phi(\eta,\theta)\,w(\eta)\eta d\eta \tag{16}$$

Method of Solution

The governing equations, equations (9) and (10), have been solved numerically by using a finite difference method to calculate the temperature and the velocity distributions. The integral in equation (9) was evaluated by using the trapezoidal rule and the derivatives were evaluated by using the backward difference formula. The governing equations are

$$w_j=\Big\{w_{j+1}+w_{j-1}\left(1-\frac{1}{j}\right)+\frac{\pi}{2}\Big[\frac{1}{2}\phi_{0,j}\cos(0)+\sum_{i=1}^{M-1}\phi_{i,j}\cos(i\Delta\theta)+\frac{1}{2}\phi_{M,j}\cos(M\Delta\theta)\Big]\Delta\theta(\Delta\eta)^2\Big\}\Big/\left(2-\frac{1}{j}\right) \tag{17}$$

and

$$\phi_{i,j}=\Big\{w_j\,\phi_{i-1,j}+\frac{2}{\pi}\frac{\Delta\theta}{(\Delta\eta)^2}\Big[\phi_{i,j+1}+\phi_{i,j-1}\left(1-\frac{1}{j}\right)\Big]\Big\}\Big/\Big[w_j+\frac{2}{\pi}\frac{\Delta\theta}{(\Delta\eta)^2}\left(2-\frac{1}{j}\right)\Big] \tag{18}$$

The following boundary conditions have been used:

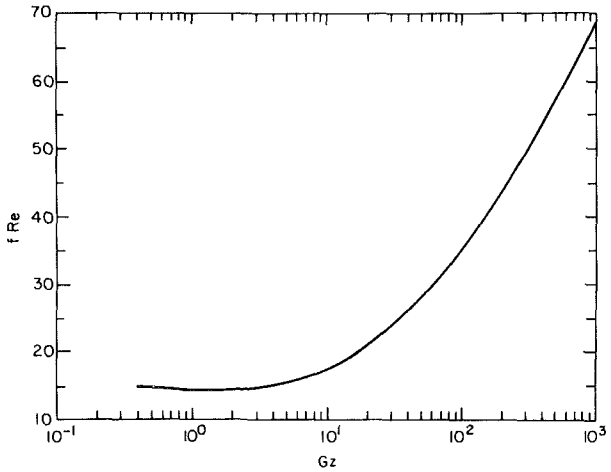

Fig. 5 Friction coefficient as a function of the Graetz number

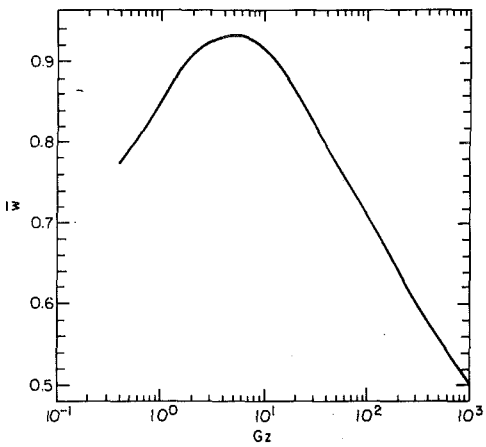

Fig. 4 Average velocity as a function of the Graetz number

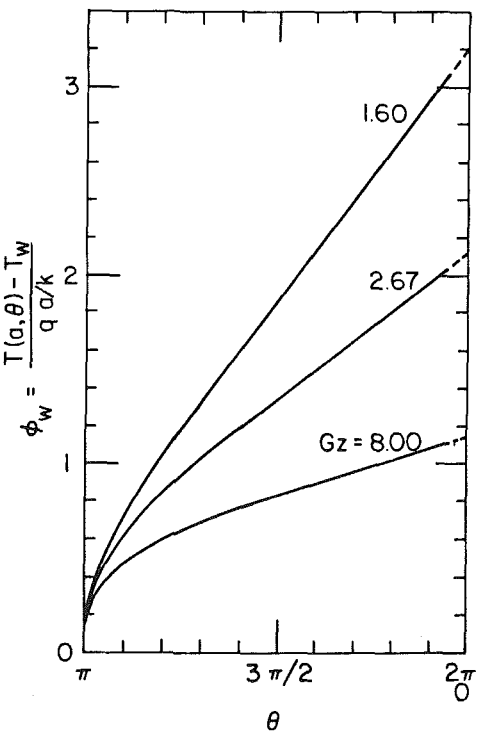

Fig. 6 Wall temperature variation along the heated region of the loop

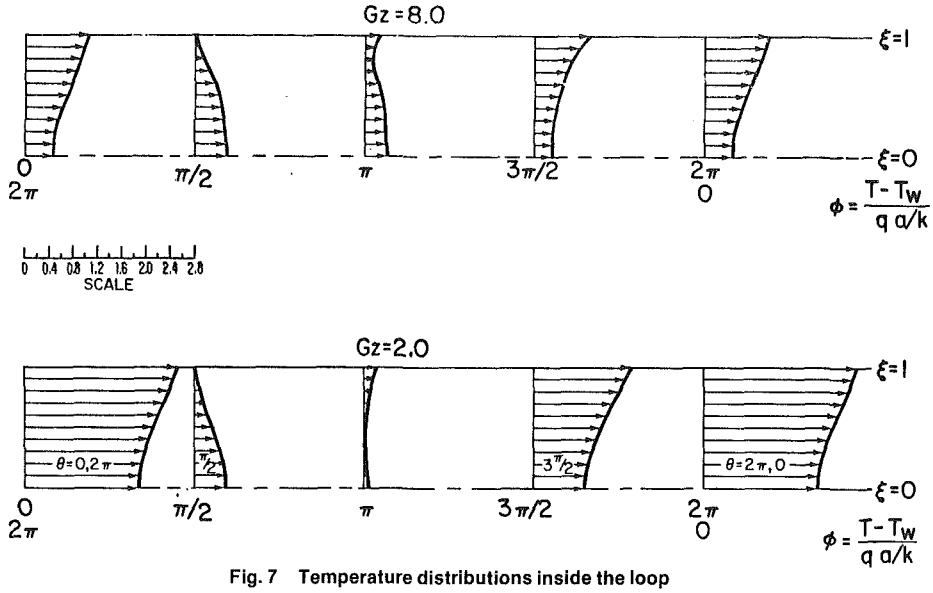

Fig. 7 Temperature distributions inside the loop

(*i*) Symmetry conditions at the centerline, $\eta = 0$ ($\xi = 0$), for the velocity:

$$w_0 = w_1 + \frac{\pi}{8}\left\{\frac{1}{2}\phi_{0,0}\cos(0) + \sum_{i=1}^{M-1}\phi_{i,0}\cos(i\Delta\theta) + \frac{1}{2}\phi_{M,0}\cos(M\Delta\theta)\right\}\Delta\theta(\Delta\eta)^2 \tag{19}$$

and for the temperature:

$$\phi_{i,0} = \left[w_0\,\phi_{i-1,0} + \frac{8}{\pi}\frac{\Delta\theta}{(\Delta\eta)^2}\phi_{i,1}\right]\Big/\left[w_0 + \frac{8}{\pi}\frac{\Delta\theta}{(\Delta\eta)^2}\right] \tag{20}$$

(*ii*) Boundary conditions on the surface, $\eta = \mathrm{Gz}^{1/2}$ ($\xi = 1$) (except at the locations $\theta = 0$, 2π and $\theta = \pi$) for the velocity:

$$w_N = 0 \text{ (no slip condition)} \tag{21}$$

and for the temperature:

$$\phi_{i,N} = 0 \quad \text{for} \quad 0 < \theta < \pi \tag{22a}$$

Using an energy balance for the heated region yields (neglecting axial convection),

$$\phi_{i,N} = \phi_{i,N-1} + \Delta\eta\,\mathrm{Gz}^{-1/2} \quad \text{for} \quad \pi < \theta < 2\pi \tag{22b}$$

Energy balances on the surface ($\xi = 1$) are made at the locations $\theta = 0$, 2π and $\theta = \pi$. The resulting relations are given by (neglecting axial convection because of the vanishing velocity):

$$\phi_{M,N} = \phi_{M,N-1} + \frac{\Delta\eta\mathrm{Gz}^{-1/2}}{(2 - \Delta\eta\mathrm{Gz}^{-1/2}} \quad \text{at} \quad \theta = 0, 2\pi \tag{23a}$$

and

$$\phi_{M/2,N} = \phi_{M/2,N} - 1 + \frac{\Delta\eta\mathrm{Gz}^{-1/2}}{(2 - \Delta\eta\mathrm{Gz}^{-1/2})} \quad \text{at} \quad \theta = \pi \tag{23b}$$

where $\theta = i\Delta\theta$, $\eta = j\Delta\eta$, $2\pi = M\Delta\theta$ and $\mathrm{Gz}^{1/2} = N\Delta\eta$

Equations (17–23) were solved by initially assuming parabolic velocity and temperature distributions and iterating until convergence was obtained. A space increment of $\Delta\theta$ equal to $\pi/40$ was used for all the calculations. Different values of the space increments in the radial direction, $\Delta\xi$, were used. For the larger values of the Graetz number, $\Delta\xi \sim 0.025$ and for the smaller values of the Graetz number, $\Delta\xi \sim 0.05$. Calculations were made to check the sensitivity to the space increments and showed variations for the velocity and temperature distributions of less than 5 percent. With respect to the calculations, it is also noted that for the cylindrical control volume adjacent to the wall, axial convection was neglected. This leads to an energy balance in the heating region that is correct to first order, cf. equations (22*b*), (23*a*), and (23*b*). It is also noted that the backward difference

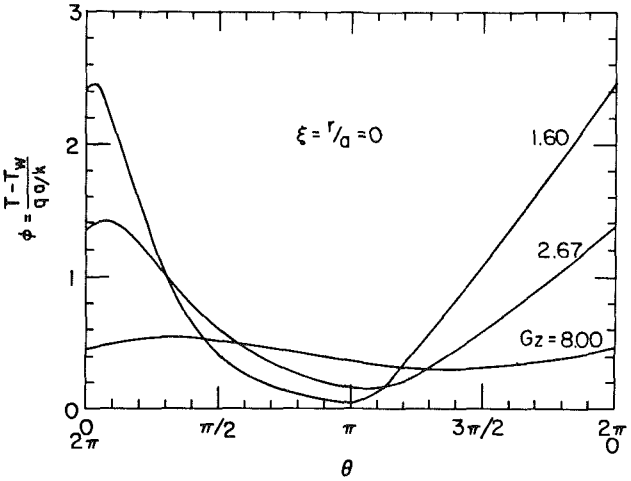

Fig. 8a Centerline ($r = 0$) temperature variation along the loop

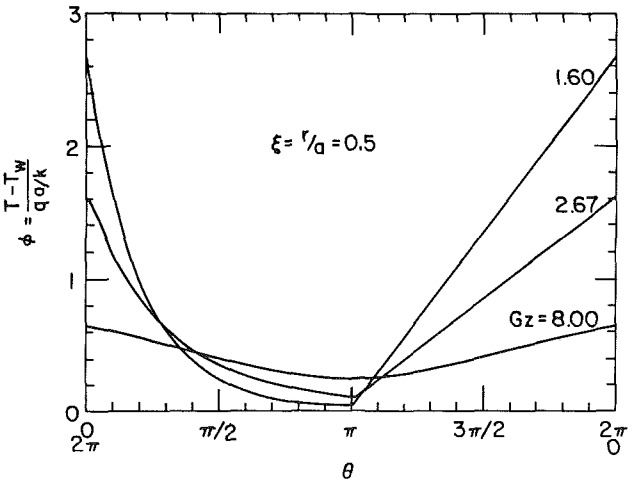

Fig. 8b Temperature variation at $r = a/2$ along the loop

formulation for the axial convection term generates a numerical diffusion. However, a Taylor series expansion shows that this false diffusion is of the order of $(\Delta\theta)^2$ which is smaller than the principal terms (see equation (18)). This is in accord with the sensitivity statement given above concerning the space increments.

Results and Discussion

The steady-state behavior of a natural circulation loop which is heated uniformly over the lower half and cooled by maintaining a constant wall temperature over the upper half has been investigated (see Fig. 1). A two-dimensional, axially symmetric model was used with the independent variables, ξ (or η), for the radial coordinate, and, θ, for the axial coordinate, and the parameter, Gz (defined in equation (8)) which is equal to the Graetz number. The characteristic velocity, V, results from buoyancy so that it is also possible to relate the Graetz number to a Grashof number, Prandtl number, and a diameter to length ratio. However, it is more convenient to use the Graetz number in this study.

Note that axial conduction has been neglected. This is a good approximation for large values of the Peclet number, Pe, where Pe = Gz $(2\pi R/2a)$. For slug flow, the effects of axial conduction should be considered for $0 \leq \text{Pe} \leq 100$ [18]. For the experimental loops of references [1-3], $a = 0.015$ m and $R = 0.38$ m; this would correspond to the range $0 \leq \text{Gz} \leq 1.25$. (This range may be altered for the present velocity profiles which result from buoyancy.) It would therefore appear that the effects of axial conduction are of importance for the lower values of the Graetz number; i.e., Gz = 0.4 and 0.8. It is noted that the range of values of the Graetz number for the experimental data [1, 2] is $44 < \text{Gz} < 172$ (cf. Fig. 10) which should be consistent with the omission of axial conduction.

The increase in the heat transfer for increasing values of the Graetz number is clearly shown in Fig. 2 in both the heating region ($\pi < \theta < 2\pi$, $q_w = \text{const} = q$) and the cooling region ($0 < \theta < \pi$, $T_w = \text{const}$). For small and moderate Graetz numbers, the local Nusselt number approaches the values 4.36 and 3.66 for the heating and cooling regions, respectively. Note that these values are the asymptotic values for fully developed laminar flow inside a circular straight tube for uniform heating and for constant wall temperature, respectively.

The behavior of the velocity profile, $w(\xi)$, and the average cross-sectional velocity, $\bar{w}$, is shown in Figs. 3 and 4 for various values of Gz. As can be seen from the figures, the average velocity (or the flow rate) increases initially with the Graetz number, due to the increase of the buoyancy driving force (as explained above by the relation between the Graetz and Grashof numbers) and the decrease in friction (cf. Fig. 5). As Gz is further increased the resistant friction force increases, as can be seen from the increase in the velocity gradient at the wall in Fig. 3 (cf. Fig. 5). The increase in friction for increasing values of the Graetz number coupled with the accompanying effect of smaller temperature differences, causes the flow rate to increase at a slower rate so that the average velocity, $\bar{w}$, reaches a maximum and then decreases (cf. Fig. 4). For completeness, it is noted that for forced laminar flow, $f\text{Re} = 16$.

At this point we wish to refer to the experiments of Damerell and Schoenhals [3] and their visual observations in the cooled region (close to the connection between the heated and cooled sections, i.e., at $\theta \approx 0^+$). They concluded that at this location the axial velocity, v, near the surface of the tube, was in a direction opposite to that of the main flow. The theoretical velocity profiles shown in Fig. 3 differ from these observations and this is felt to be a consequence of neglecting the radial and azimuthal components of the velocity as specified in obtaining equation (1). It is possible that this effect is most pronounced at the location noted and is of less significance in the rest of the loop. Accordingly, the inversion of the velocity profile has not been treated in this study. Further discussion of the velocity is given later in connection with the comparison of the theoretical results with the experimental data of Creveling et al. [1, 2].

Figure 6 shows the increase of the wall temperature in the heated region with increasing θ, i.e., as the fluid moves through and is heated in this region. The increase becomes smaller as the Graetz number, which characterizes the relative buoyancy effect, increases. As noted above, the heat transfer increases with Gz which results in smaller temperature differences (also see Fig. 7). This figure shows the change in the temperature distribution around the loop.

Table 1 Average velocity, bulk temperature, and friction coefficient for different Graetz numbers

		$\phi_b(\theta)$					
Gz	$\bar{w}$	$\theta=0,2\pi$	$\theta=\pi/2$	$\theta=\pi$	$\theta=3\pi/2$	$\phi_b(0)-\phi_b(\pi)$	$f\text{Re}$
0.4	0.775	12.186	0.001	0.157	6.215	12.029	15.00
0.8	0.831	5.725	0.047	0.074	2.932	5.651	14.64
1.6	0.893	2.688	0.224	0.060	1.390	2.628	14.39
2.0	0.908	2.145	0.280	0.078	1.124	1.021	14.41
2.7	0.922	1.638	0.331	0.111	0.884	1.527	14.54
3.2	0.928	1.399	0.349	0.136	0.775	1.263	14.71
4.0	0.933	1.169	0.358	0.163	0.672	1.006	15.02
8.0	0.923	0.702	0.332	0.226	0.470	0.476	16.75
10.0	0.915	0.607	0.311	0.223	0.420	0.384	17.56
15.0	0.890	0.473	0.273	0.210	0.345	0.263	19.35
20.0	0.867	0.400	0.247	0.197	0.301	0.099	20.85
50.0	0.772	0.246	0.175	0.152	0.200	0.094	26.74
100.0	0.714	0.174	0.135	0.122	0.148	0.052	35.01
150.0	0.672	0.144	0.117	0.107	0.126	0.037	39.79
200.0	0.642	0.126	0.105	0.097	0.112	0.029	43.54
500.0	0.557	0.087	0.077	0.074	0.081	0.013	57.28
1000.0	0.503	0.069	0.064	0.062	0.066	0.007	68.11

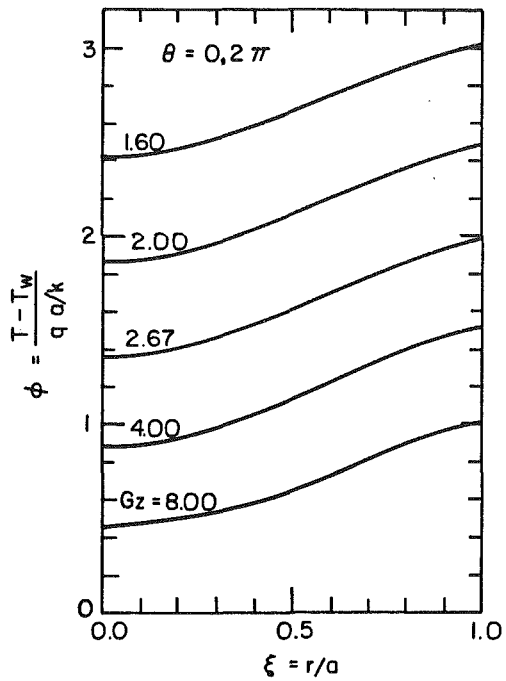

Fig. 9a Temperature variation in the radial direction at $\theta = 0, 2\pi$

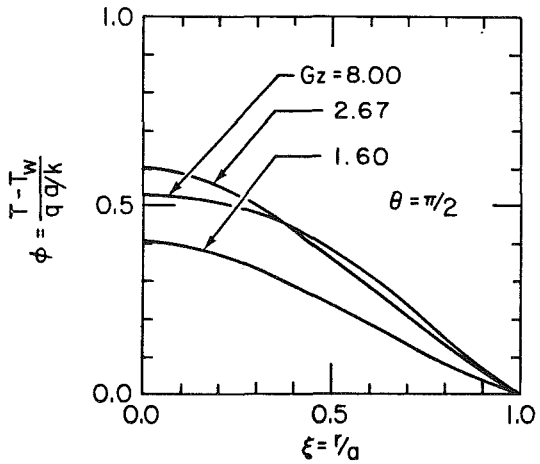

Fig. 9b Temperature variation in the radial direction at $\theta = \pi/2$

The temperature variation with respect to θ on the axis ($r = 0$), at the mid-distance to the wall ($r = a/2$) and the bulk temperature, are shown in Figs. 8(*a*), 8(*b*) and Table 1. As can be seen for short axial distances, the centerline temperature continues to increase in the cooling section, due to radial conduction from the hotter fluid. This effect is reversed as the cooling from the wall penetrates into the fluid and the centerline temperature then decreases. The maximum temperature becomes higher and is reached sooner (for smaller values of θ) as the Graetz number decreases. This is due to the effect of increasing velocities with greater buoyancy effects, as noted above. For completeness, detailed radial temperature variations are presented in Figs. (9*a*–9*d*) for various locations around the loop.

The numerical results of the present work are compared to the experimental results of Creveling et al. [1, 2] in Fig. 10, where the mass flux $G = \rho V \bar{w}$ is plotted versus the heat flux input, q. The comparison is made in the laminar regime only. Average properties of the fluid (water) were taken at the average loop temperature as reported in [2]. The agreement between the numerical results and the data is very good. It is noted that at the higher values of q in Fig. 10, the flows are

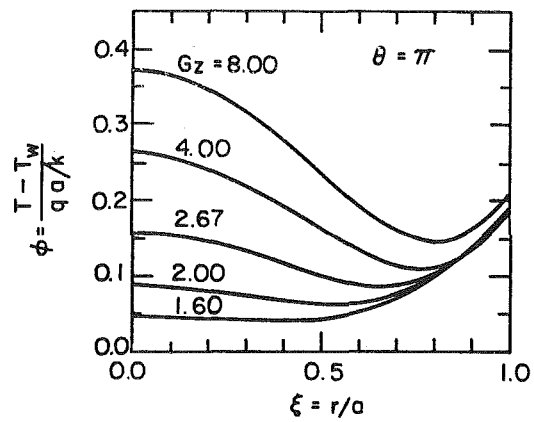

Fig. 9c Temperature variation in the radial direction at $\theta = \pi$

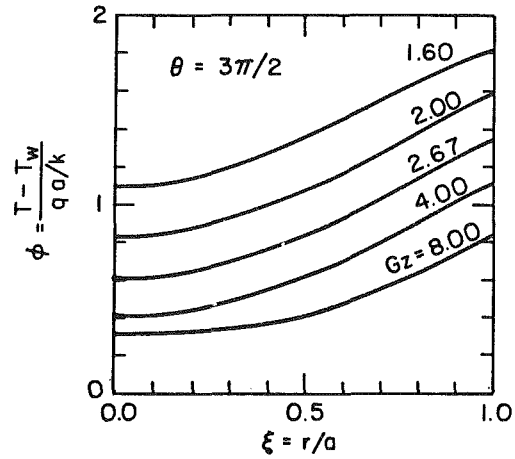

Fig. 9d Temperature variation in the radial direction at $\theta = 3\pi/2$

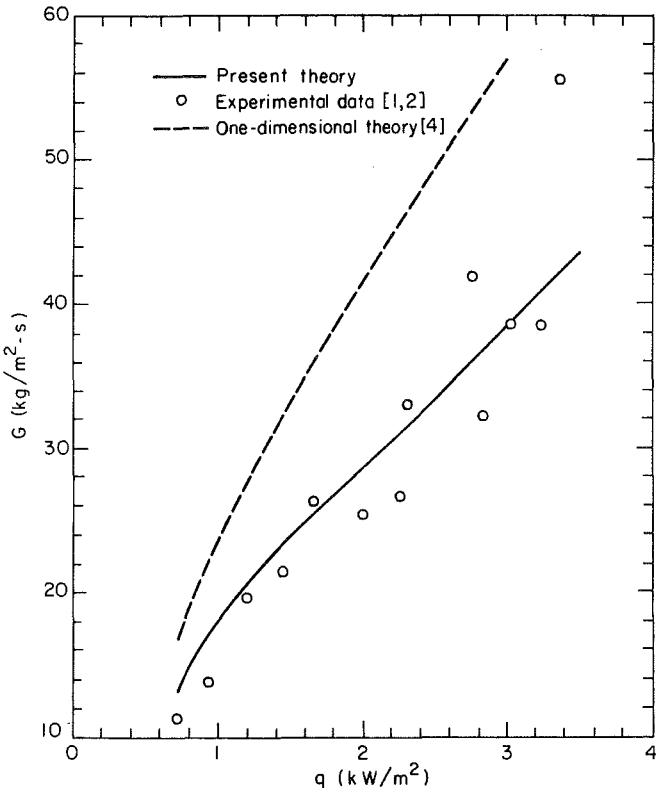

Fig. 10 Comparison between the theoretical and experimental values

unstable, with growing oscillations and reversed flow. It was, therefore, difficult to accurately determine the flow rates and fluid temperatures in this range. For completeness, results based on one dimensional theory are also presented in Fig. 10. The fully developed flow relations, $f = 16/\mathrm{Re}$ and $h = 1.83$ k/a, were used in obtaining this result [4]. Creveling et al. [1, 2] used different relations, but the disagreement between the one-dimensional theory and the data was still large.

In Fig. 10 it is seen that the mass flux $G = \rho V \bar{w}$ increases with respect to the heat input, q. The experimental range of values of the Graetz number [1, 2] is $44 < \mathrm{Gz} < 172$, and it is noted that over this range the calculated values of $\bar{w}$ decrease for increasing Gz (cf. Fig. 4). The calculated increase of the mass flux, $G = \rho V \bar{w}$, with respect to the heat input, q, results from the stronger increase in V with respect to q, i.e., $V \sim q^{1/2}$.

Conclusions

The steady-state velocity and temperature distributions in a natural circulation toroidal loop have been obtained by a numerical solution of the coupled two-dimensional continuity, momentum, and energy equations. A single parameter, the Graetz number, Gz, (related to the Grashof number) governs the motion in the loop. The solutions were used to obtain the friction and the heat transfer. It was found that the friction parameter, $f\mathrm{Re}$, varies significantly as a function of the Graetz number. The local Nusselt numbers in the heated and cooled sections decrease with axial distance, θ. For small and moderate Graetz numbers, Nu approaches the forced convection values 4.36 and 3.66 for constant heat flux and constant wall temperatures, respectively. The heat transfer increases for increasing values of the Graetz number and this is accompanied by smaller temperature differences. The present numerical predictions have been compared with the existing data for the steady state flux and good agreement has been obtained.

Acknowledgment

The authors acknowledge with appreciation the partial support of this research by the National Science Foundation, under Grant No. MEA 81-07202. The authors are indebted to Mr. R. Matavosian-Sanakani of the University of California, Berkeley, and Mr. A. Ronen of the Technion-Israel Institute of Technology for their assistance in carrying out many of the calculations.

References

1 Creveling, H. F., De Paz, J. F., Baladi, J. Y., and Schoenhals, R. J., "Stability Characteristics of a Single-Phase Free Convection Loop," *Journal of Fluid Mechanics*, Vol. 67, 1975, pp. 65–84.

2 Creveling, H. F., "Steady Flow and Stability Characteristics of Free Convection Flow in Circulation Loops," Ph.D. dissertation, Purdue University, 1964.

3 Damerell, P. S., and Schoenhals, R. J., "Flow in a Toroidal Thermosyphon with Angular Displacement of Heated and Cooled Section," ASME JOURNAL OF HEAT TRANSFER, Vol. 101, 1979, pp. 672–676.

4 Greif, R., Zvirin, Y., and Mertol, A., "The Transient and Stability Behavior of a Natural Convection Loop," ASME JOURNAL OF HEAT TRANFER, Vol. 101, 1979, pp. 684–688.

5 Bau, H. H., and Torrance, K. E., "Transient and Steady Behavior of an Open, Symmetrically-Heated, Free Convection Loop," *International Journal of Heat and Mass Transfer*, Vol. 24, 1981, pp. 597–609.

6 Keller, J. B., "Periodic Oscillations in a Model of Thermal Convection," *Journal of Fluid Mechanics*, Vol. 26, 1966, pp. 599–606.

7 Welander, P., "On the Oscillatory Instability of a Differentially Heated Fluid Loop," *Journal of Fluid Mechanics*, Vol. 29, 1967, pp. 17–30.

8 Japikse, D., "Advances in Thermosyphon Technology," in *Advances in Heat Transfer*, edited by T. F. Irvine, Jr. and J. P. Hartnett, Vol. 9, Academic Press, New York, 1973, pp. 1–111.

9 Zvirin, Y., Shitzer, A., and Grossman, G., "The Natural Circulation Solar Heater Models with Linear and Nonlinear Temperature Distributions," *International Journal of Heat and Mass Transfer*, Vol. 20, 1977, pp. 997–999.

10 Zvirin, Y., "A Review of Natural Circulation Loops in Pressurized Water Reactors and Other Systems," EPRI Report NP-1676-SR, Jan. 1981, to appear in *Nuclear Eng. & Design*, Vol. 67, 1981, pp. 203–225.

11 Zvirin, Y., Jeuck, P. R., Sullivan, C. W., and Duffey, R. B., "Experimental and Analytical Investigation of a Natural Circulation System with Parallel Loops," ASME JOURNAL OF HEAT TRANSFER, Vol. 103, 1981, pp. 645–652.

12 Torrance, K. E., "Open-Loop Thermosyphons with Geological Applications," ASME JOURNAL OF HEAT TRANSFER, Vol. 101, 1979, pp. 677–683.

13 Bau, H. H., and Torrance, K. E., "On the Stability and Flow Reversal of an Asymmetrically Heated Open Convection Loop," *Journal of Fluid Mechanics*, Vol. 106, 1981, pp. 417–433.

14 Huang, B. J., "Similarity Theory of Solar Water Heater with Natural Circulation," *Solar Energy*, Vol. 25, 1980, pp. 105–116.

15 Gillette, J. L., Singer, R. M., Tokar, J. V., and Sullivan, J. E., "Experimental Study of the Transition from Forced to Natural Circulation in EBR-II at Low Power and Flow," ASME JOURNAL OF HEAT TRANSFER, Vol. 102, 1980, pp. 525–530.

16 Mertol, A., Greif, R., and Zvirin, Y., "The Transient, Steady State and Stability Behavior of a Thermosyphon with Throughflow," *International Journal of Heat and Mass Transfer*, Vol. 24, 1981, pp. 621–633.

17 Mertol, A., Place, W., Webster, T., and Greif, R., "Detailed Loop Model (DLM) Analysis of Liquid Solar Thermosiphons with Heat Exchangers," *Solar Energy*, Vol. 27, 1981, pp. 367–386.

18 Schneider, P. J., "Effect of Axial Fluid Conduction on Heat Transfer in the Entrance Regions of Parallel Plates and Tubes," ASME JOURNAL OF HEAT TRANSFER, Vol. 79, 1957, pp. 765–773.

Effect of Thermal Boundary Conditions on Natural Convection in Vertical and Inclined Air Layers

S. M. ElSherbiny

K. G. T. Hollands
Mem. ASME

G. D. Raithby
Mem. ASME

Thermal Engineering Group,
Department of Mechanical Engineering,
University of Waterloo,
Waterloo, Ontario, Canada N2L 3G1

Measurements of the heat transfer by natural convection across vertical and inclined air layers are reported. The air layer is bounded by two parallel isothermal flat plates and around the edges by a low thermal conductivity wall of thickness B. A critical wall thickness B_c was determined by solving the two-dimensional conduction equation in the bounding wall region: for $B>B_c$ the convective heat transfer should be insensitive to B. Measurements are reported for air layers with $B>B_c$ and an aspect ratio of 5. They cover a range in Rayleigh number from 10^3 to 10^8, and a range in orientation from horizontal to vertical. The effect of the emissivity of the bounding wall on the heat transfer across the air layer was evaluated from measurements obtained respectively with a low and a high value of the wall emissivity. The paper proposes terminology required to define the thermal conditions, and discusses the impact of these boundary conditions on the total heat transfer.

1 Introduction

As pointed out by Catton [1], the Nu-Ra relation for free convective heat transfer across a rectangular fluid layer, such as sketched in Fig. 1, depends on a long list of parameters – for example, the Prandtl number, the angle of inclination, ϕ, the vertical aspect ratio, A, and the horizontal aspect ratio, A_H. This list must also include parameters that fix the thermal boundary conditions on the fluid along the end walls (see Fig. 1), and the side walls (the walls limiting the horizontal aspect ratio). Theoretical studies of the problem have most often assumed that either a linear temperature profile (LTP) is established at these walls, or that the walls are perfectly adiabatic. In real engineering systems or in an experimental apparatus, however, these ideal conditions can only be approached. If the fluid is air, a close match to the LTP is readily realized[1], but a close match to the adiabatic condition would require that the conductivity of the wall be at least an order of magnitude smaller than the thermal conductivity of air. Since such wall materials do not exist, the adiabatic condition is not attainable for air. Not all engineering problems involving air can be modeled as having an LTP boundary condition, so there is a need to study another, more realistic, class of wall boundary conditions.

When the aspect ratios A and A_H are large the thermal boundary conditions at the walls are unimportant, but for small values of A or A_H there is ample evidence [5–9] that the thermal boundary conditions have a dramatic effect on the free convection. Boundary conditions, neither LTP nor adiabatic, were treated theoretically by Catton [5] who analyzed the stability problem at $\phi=0$ for $A<1$ and $B<<L$. He found a monotonic increase in the critical Rayleigh number from that for $R=k_w/k=0$ to that for $R=\infty$, with the latter exceeding the former by 70 percent. For the same class of problem, Edwards and Sun [10] demonstrated that the radiative transfer at the walls has a very important effect on the free convective heat transfer. Koutsoheras and Charters [6] defined a set of boundary conditions whereby the temperature and the heat flux at the lower face of the bottom wall must match that at the lower face of the upper wall. This boundary condition is appropriate to an array of air cells such as may be used in solar collectors [11, 12, 13].

The present paper suggests two new boundary conditions. It emphasizes the need for reporting all the relevant dimensionless groups when presenting results, and the need to account for heat transfer induced *outside of the air layer* due to convection in the air layer. Finally it reports a set of measurements of the Nu-Ra relation for $A=A_H=5$ and one of the suggested boundary conditions. The primary goal of the paper is to provide a better understanding of the interaction between the boundaries and the fluid flow, and to introduce meaningful terminology, so that designers, experimentalists, and analysts can better understand the needs of each other.

2 Qualitative Discussion of Effect of Thermal Boundary Conditions

Considered here is the situation where the fluid is bounded by a rectangular solid of thermal conductivity, k_w, thickness, L, and width, B, as sketched in Fig. 1. The faces of the solid that are in contact with the hot and cold plate are at temperatures T_h and T_c, respectively. The face opposite the fluid

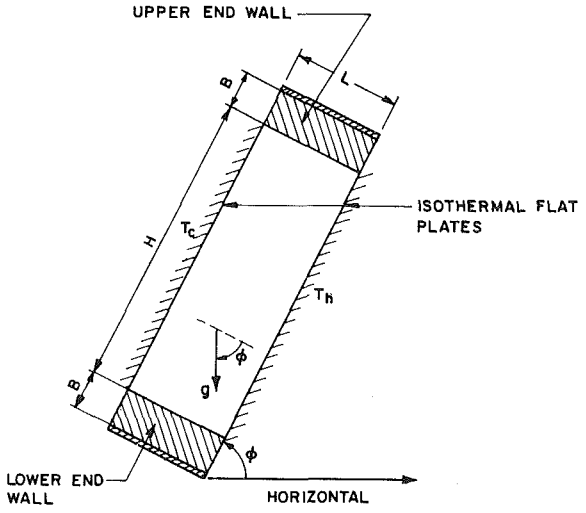

Fig. 1 Schematic of the cavity

[1] For example a relatively thin flat sheet of metal may be thermally bonded to the plates at each end [2, 3]; ElSherbiny [4] has developed a relation giving the necessary thickness of this sheet.

Contributed by the Heat Transfer Division and presented at the 20th ASME/AIChE Heat Transfer Conference, Milwaukee, Wisconsin, August 2–5, 1981. Manuscript received by the Heat Transfer Division May 11, 1981.

has either an LTP from T_c to T_h, forming the "extended LTP" boundary condition, or it is adiabatic, forming the "extended adiabatic" boundary condition.

Natural convection will cause the fluid near the wall to take up a temperature profile usually different from the LTP. Figure 2 sketches some possible temperature and heat flux profiles in the fluid and the associated isotherms and heat flux lines in the solid. Radiation is (for the moment) neglected. At low Ra (Fig. 2(*a*)), natural convection is virtually eliminated; in this case both the fluid and the wall take up the LTP, and there is therefore no heat transfer between wall and fluid. At high Ra and $\phi = 0$, the fluid near the wall takes up the S-shaped profile sketched in Fig. 2(*b*) [14]. Because the solid "tries" to impose a linear profile (dotted line in Fig. 2(*b*)), a local heat flux, q, flows from the wall to the fluid in the bottom half of the layer, and an equal heat flux flows in the reverse direction over the top half. (From the viewpoint of one looking at only the *average* heat flow, the fluid appears to have an adiabatic boundary, but the adiabatic condition is locally violated.) This heat flux forces the wall temperature near the fluid to move away from the LTP and toward the temperature profile of the fluid near the wall. The resulting higher gradients at the hot and cold faces of the wall cause a heat flux into the face of the wall at T_h in excess of that which would flow if the fluid were stationary, i.e., in excess of the flux $k_w \Delta T/L$. This additional heat conduction constitutes a "convectively induced conductive heat transfer," or CICHT. For either of the limits $k_w \to 0$ and $k_w \to \infty$, this induced heat transfer goes to zero.

For the boundary layer regime at $\phi = 90$ deg, the temperature profile of the fluid near the bottom wall is as sketched in Fig. 2(*c*). Because this wall is swept by fluid which has fallen down the cold plate, the fluid temperature near the wall is close to T_c over much of the width L [15], while the wall temperature again "tries" to be linear. This results in a heat flow from the wall into the fluid over the whole width L, as shown in Fig. 2(*c*). For constant property free convection, an equal quantity of heat flows from the fluid to the top wall. The heat exchange with the fluid results in a nonlinear temperature profile in the wall and in turn causes a CICHT, δQ_1 in Fig. 2(*c*), which is into the wall on the hot face of the lower wall, and a CICHT, δQ_2, which is out of the wall (relative to the conduction in Fig. 2(*a*)) on the hot face of the upper wall. The algebraic sum of these two induced heat transfers ($|\delta Q_1|$ is normally larger than $|\delta Q_2|$) is the net CICHT. On the cold faces, the CICHT is negative (δQ_4) on the bottom wall, and positive (δQ_3) on the top wall. For constant property free convection, symmetry demands that $\delta Q_1 = \delta Q_3$ and $\delta Q_2 = \delta Q_4$ so that the net CICHT on the cold face is the same as that on the hot face.

For the extended LTP and adiabatic boundary conditions, the dimensionless groups B/L and $R = k_w/k$ characterize this induced heat transfer and the dependence of the Nu-Ra relation on the thermal boundary conditions at the wall. The various heat-flux lines and isotherms in the wall are sketched in Fig. 2. If B/L is large, there exists a dimension B_c (see Fig. 2(*c*)) representing the size of the region over which the heat-flux lines in the wall are significantly distorted from those in Fig. 2(*a*). Roughly speaking, for $B > B_c$ (or $B/L > B_c/L$) the induced heat transfer and the Nu-Ra relation will be insensitive to B/L. The Appendix describes an analysis aimed at determining an upper bound for B_c, and the results of this analysis are shown in Fig. 3. The analysis treats the $\phi = 90$ deg situation of Fig. 2(*c*), which should have a higher B_c than that at $\phi = 0$. As a worst case, the fluid near the bottom was taken to have a temperature equal to T_c over the whole length of the spacing L. A constant heat-transfer coefficient h_w between the wall and the fluid was assumed to apply over this distance. An LTP was imposed on the solid at the face opposite the fluid-wall interface, and the steady conduction equation over the solid was solved with these boundary conditions, yielding the local heat flux at the fluid-wall interface. B_c was taken as the smallest value of B such that this heat flux at the interface differed from that for $B \to \infty$ by less than 1 percent. The value

Nomenclature

A = aspect ratio, $A = H/L$

A_H = horizontal aspect ratio, $A_H = W/\mathrm{L}$

B = thickness of walls at periphery of air layer (see Fig. 1)

B_c = value of B beyond which Nu is insensitive to B

Bi = Biot number, $\mathrm{Bi} = h_w L/K_w$

g = acceleration of gravity

h = average heat-transfer coefficient, plate to air, except in Appendix where $h = h_w$

h_w = heat-transfer coefficient between wall and fluid

H = height of air layer, see Fig. 1

k = thermal conductivity of fluid

k_w = thermal conductivity of wall material

L = spacing of plates bounding air layer (see Fig. 1)

N = radiation-conduction group, $N = 4\sigma T_m^3 L/k$

Nu = average Nusselt number defined by equation (1)

Pr = Prandtl number of fluid

Q = heat flow over whole length, $H + 2B$, constituting the plate and the wall at each end

Q_s = Q when air is stationary (i.e., at low Ra)

q = local heat flux at the wall into fluid

$\bar{q}$ = average value of q over length L

R = ratio of thermal conductivities, $R = k_w/k$

Ra = Rayleigh number based on L and ΔT, $\mathrm{Ra} = g\beta\Delta T L^3/(\nu\alpha)$

T_h, T_c = temperature of hot and cold plates bounding air layer, respectively

T_m = $(T_h + T_c)/2$

ΔT = $T_h - T_c$

$\delta Q_1, \delta Q_2, \delta Q_3, \delta Q_4$ = convectively induced conduction heat transfer in the walls surrounding air layer (Fig. 2)

W = width of plate in direction normal to drawing of Fig. 1

x, y = spacial coordinate in the wall, see Fig. 6.

Greek Symbols

α = thermal diffusivity of fluid

β = thermal expansion coefficient for fluid

ϕ = angle of tilt (see Fig. 1)

ν = kinematic viscosity of fluid

θ = dimensionless temperature, $\theta = (T - T_c)/(T_h - T_c)$

ϵ_w = emissivity of surface of wall facing the air layer

$\epsilon_{ph}, \epsilon_{pc}$ = emissivities of the hot and cold plates, respectively

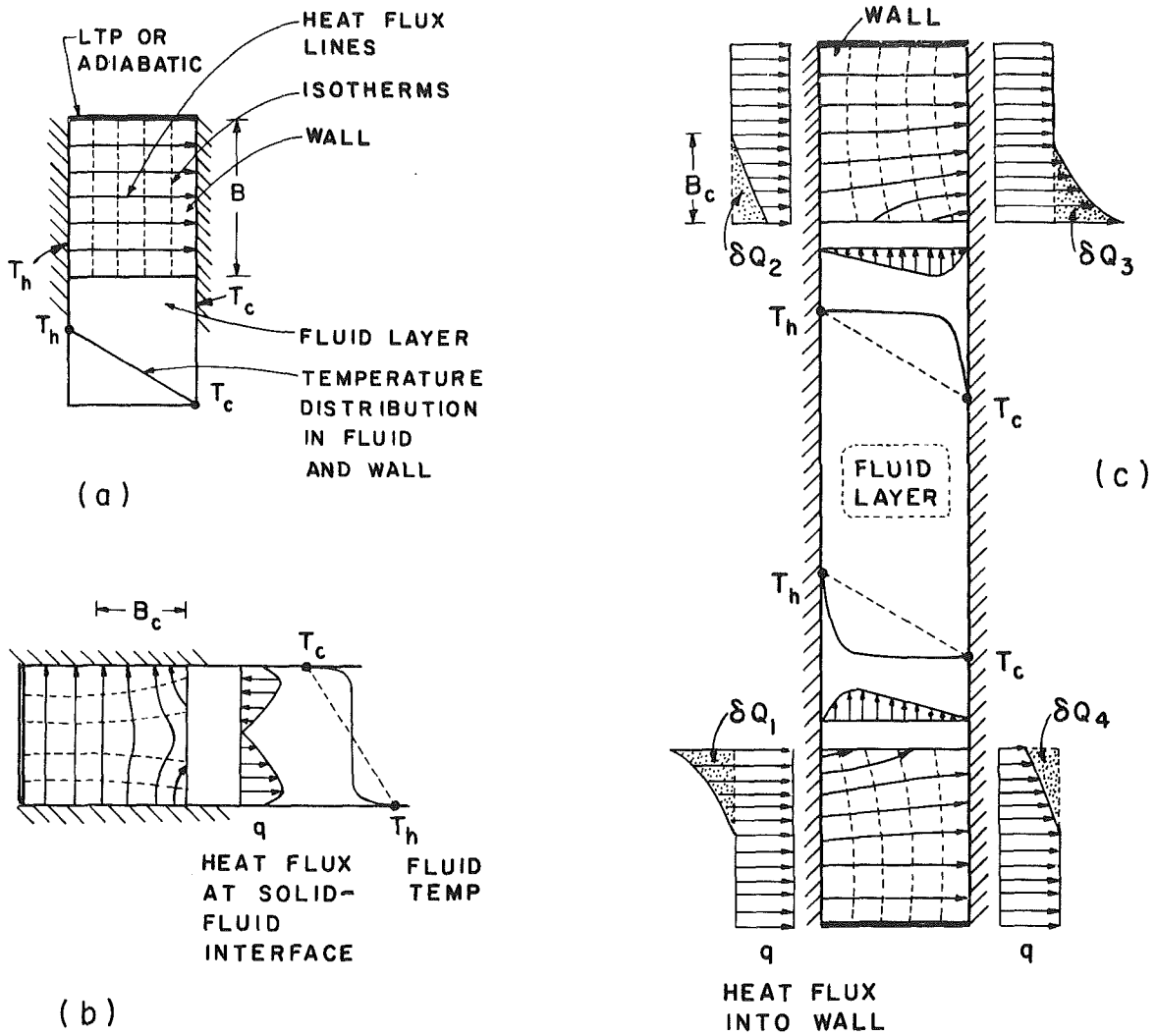

Fig. 2 A schematic showing isotherms and heat-flux lines inside the wall, heat-flux distributions at the wall surfaces, and fluid temperature distributions near the wall

of h_w is not known precisely, but it can be inferred to be roughly the same order as the h between the plate and the fluid, which is that in the definition of Nu. Thus, the $h_w L/k_w$ in Fig. 3 can be approximately taken as equal to $2\text{Nu}/R$. For $h_w L/k_w > \approx 6$, B_c/L is approximately 0.75, independent of h_w. As $k_w \to \infty$, $B_c \to 0$, provided only h_w remains finite. It is concluded that provided $B/L > 0.75$, R is the only group required to represent the wall-fluid interaction.

The preceding arguments apply only if the fluid is opaque. If the fluid is transparent, like air, radiation must be considered, and, in general, a fully coupled convection-conduction-radiation problem results. The relevant additional dimensionless groups characterizing this problem are the radiative-conductive number, N, the emissivities, ϵ_w, ϵ_{ph}, and ϵ_{pc}, and the ratio, T_h/T_c. (The latter group is only important if it departs substantially from unity; since this rarely happens, it will be deleted in future group listings.) For $k_w \to \infty$, a LTP boundary condition on the fluid is established regardless of the values of N, ϵ_w, ϵ_{ph}, and ϵ_{pc}, (provided N is finite), and there is no radiative effect on the free convection and vice versa. However, if $k_w \to 0$, whereas for an opaque fluid the boundary condition on the fluid is adiabatic, for the transparent fluid it is not adiabatic, because heat can be transferred from the fluid into the wall and then radiated to the plates. For simplicity, the following remarks on the radiative-convective coupling will be limited to the situation where

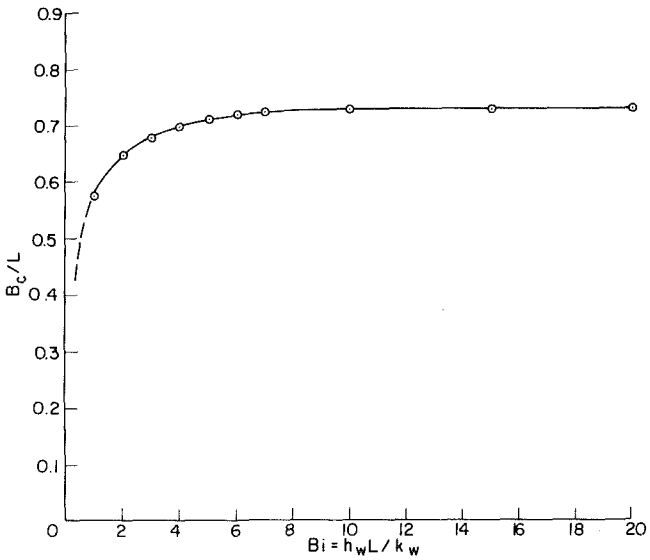

Fig. 3 B_c/L as a function of $h_w L/k_w$ for the extended LTP boundary conditions

$k_w \to 0$, although it will be clear that much of it applies for any finite k_w.

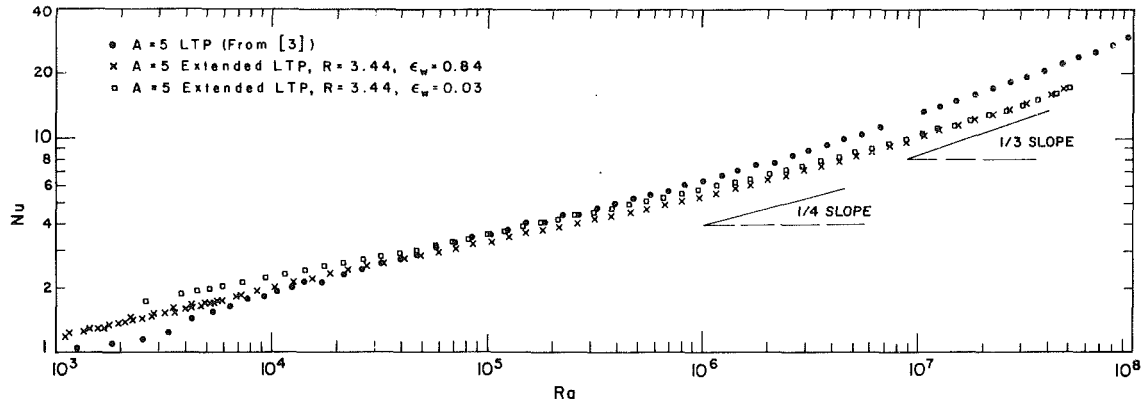

Fig. 4 Measurements for vertical air layers showing effect of boundary thermal conditions

If both A and A_H are large (say > 10), each point on the wall sees virtually the same radiant field; thus, at equilibrium, and in the absence of fluid conduction and convection, the wall would take up very close to a uniform temperature. If, in addition, $\epsilon_{ph} = \epsilon_{pc}$, this wall temperature T_{rw} will simply be given by $T_{rw} = [(T_h^4 + T_c^4)/2]^{1/4}$. For finite fluid conduction but with Ra so small that convection is eliminated, for over the half of the wall nearest the cold plate there will be a local radiative transfer to the wall equal to the local heat loss by conduction to the fluid; over the other, the directions of these heat flows reverse. The resulting wall temperature profile will lie somewhere between the LTP imposed by conduction and the uniform temperature imposed by radiation, depending on the relative importance of the radiative and conductive fields, i.e., depending upon N. This is the base state from which any altered heat transfer caused by the convection must be measured. The net radiant heat transfer at each of the two plates depends upon this temperature profile at the walls. For large Ra and $\phi = 0$, the convection will alter the fluid temperature near the wall from the LTP to one like that sketched in Fig. 2(*b*). This profile is clearly more compatible to that imposed by the radiative field and the heat exchange between the fluid, and the radiative field at the wall will therefore decrease. The temperature profile on the wall will move toward a more uniform temperature, and this will alter the radiant heat transfer at each plate. This change in the radiative heat transfer at the plates from that in the base state constitutes convectively induced radiant heat transfer (CIRHT). CIRHT will also occur at $\phi = 90$ deg, although the details of the direction of the individual heat transfers and the temperature profiles will be different.

From the above discussions a number of conclusions can be drawn which have important implications in the design of experiments aimed at measuring free convective heat transfer across air layers. First, except for the LTP/boundary condition, the experimenter must report the thermal properties and extent of all solids adjacent to and next-to-adjacent to the air layer, until an adiabatic or temperature-specified surface can be identified. Second, the extended LTP and the extended adiabatic boundary conditions appear to be of practical interest, and the extended LTP can be readily achieved in the laboratory; also they have the LTP and the adiabatic boundary conditions as limiting cases. Third, for this class of boundary conditions, the Nusselt number is a function of ten dimensionless groups (not including the Prandtl number and T_h/T_c) – i.e., $\mathrm{Nu} = \mathrm{Nu}\ (\mathrm{Ra}, A, A_H, \phi, B/L, R, N, \epsilon_w, \epsilon_{ph}, \epsilon_{pc})$. Experimentalists should report this full set when presenting results. Fourth, for $B/L > B_c/L$, where the latter is given in Fig. 3, the asymptote for $B/L \to \infty$ will be for practical purposes reached. Fifth, in reporting their results, both experimentalists and theorists should state whether they are including the CICHT and the CIRHT in the Nusselt number. Some measurement techniques, such as the interferometric method, will not measure these induced heat transfers, whereas others – for example, the guarded heater plate or heat flux meter technique – will measure the CIRHT and will also measure the CICHT, depending on the position of the heater plate or flux meter with respect to the solid.

The data reported in the following sections illustrate the practical importance of the above conclusions.

3 Experiment

The apparatus used in the experiments is essentially the same as that used previously for vertical and inclined air layers with conducting boundary conditions [2–4] and hence has been fully described elsewhere. It consists essentially of two parallel isothermal copper plates, each 635 mm by 635 mm by 12.7-mm thick mounted in a pressure (or vacuum) vessel whose pressure can be varied from about 100 Pa to 0.7 MPa. The whole system can be rotated about a horizontal axis so as to produce any required angle of tilt. The lower plate is heated and the upper plate is cooled by two completely separate and thermostatically controlled water streams which pass through tubes soldered to the back of each plate, thereby maintaining a uniform temperature difference of about 20 K across the air layer, and a mean temperature $(T_h + T_c)/2$ of about 323 K. The temperature difference between the plates was determined from six thermocouple junctions embedded in each plate and connected in thermopile. Measurements of the heat flux over the full length of the hot plate were made using three electrically heated "heater plates" imbedded into three recesses machined into the main part of the hot plate. The heater plates were made of copper to ensure a very nearly isothermal surface. A heat flux meter was inserted in each recess below the heater plate in an identical arrangement to that used for the single heater plate used in earlier measurements [2].

The measurements reported in the present study were taken for an air layer with fixed values for aspect ratios A and A_H, namely, $A = A_H = 5$. The experiments were designed to model the extended LTP boundary condition. The end and side walls were made of balsa wood whose thermal conductivity k_w was measured in a separate test on the same apparatus and found to be $k_w = 0.096$ W/mK. This gave a value for R of 3.44. The thickness of balsa-wood, B, was 76.2 mm, and the spacing, L, was 96.5 mm, giving $B/L = 0.79$. From Fig. 3, it was concluded that the measured Nu-Ra relation for this relation will be valid for any $B/L > 0.75$. A thin copper sheet was used on the outer surface of the bounding walls to establish an LTP there, in the same way that a similar copper sheet established an LTP for the air itself in the earlier experiments on the same

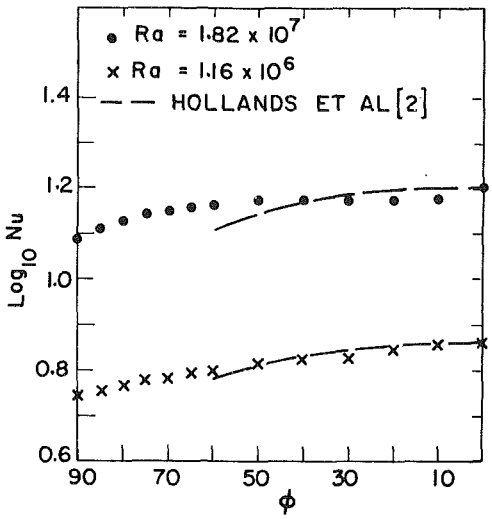

Fig. 5 Angle dependence on Nu for extended LTP: $R = 3.44$, $\epsilon_w = 0.84$, $A = A_w = 5$

apparatus [3]. One of the three heater plates extended over the full width, B, of each of the upper and lower balsa-wood walls. Thus, both the convectively induced conduction heat transfer and the convectively induced radiative heat transfer were measured in the same measurement as the free convection heat transfer; the three heat transfers were in fact not separated out. The base heat transfer was evaluated from measurements taken at a very low pressure. All additional heat transfer at higher pressure was taken to be due to the two convectively induced heat transfers and the convective transfer itself. The data were reduced so that the induced heat transfers appear in the Nusselt number. That is, let Q represent the total heat-transfer rate for all three heater plates (including that through the wood) and let Q_s be the value of Q at low pressure when the air is stationary; then Nu is defined by:

$$\mathrm{Nu} = 1 + \frac{(Q - Q_s)L}{HW\Delta Tk} \tag{1}$$

Experiments were carried out using two values of the wall emissivity, ϵ_w. In the first, the balsa wood was uncoated; the normal emissivity, ϵ_w, of balsa wood was measured at room temperature using a Gier-Dunkle DB100 reflectometer and found to be $\epsilon_w = 0.84 \pm 0.02$. In the second the balsa wood was covered with a very thin sheet of aluminized polyester film giving a normal emissivity measured on the same instrument of $\epsilon_w = 0.034 \pm 0.003$. The thickness of the sheet including its aluminum coating was shown by calculations to be insufficient to cause significant alterations to the conductive field in the balsa wood. The emissivities of the plates were $\epsilon_{ph} = \epsilon_{pc} = 0.06$, and the value of N was 29 for all experiments.

The experimental results are plotted in Fig. 4, along with the previously reported results for the simple (unextended) LTP boundary condition. It is seen that the extended LTP (defined in section 2) results are higher than those for the simple LTP case, provided $\mathrm{Ra} < 4 \times 10^4$. Since the extended LTP case is closer to the simple adiabatic than the LTP, this result confirms the theories (all of which are for laminar flow) predicting higher heat transfer in the adiabatic case. However, for high Ra this behaviour is reversed with the simple LTP giving greater heat transfer than the extended LTP. The data of the extended case follow a line of lower slope than that for the LTP case up to $\mathrm{Ra} = \sim 6 \times 10^6$. For higher Ra, both data follow a line of about 1/3 slope.

The different results for the two values of ϵ_w are interesting. At low Ra, the low ϵ_w results show higher heat transfer. This is consistent with the simple adiabatic case giving greater heat transfer than the simple LTP, since an $\epsilon_w = 0$ is required for the simple adiabatic case to be achieved. At higher Ra the results are the same for the two emissivities. Presumably the free convective coefficient, h_w, is so large that radiative effects are overpowered.

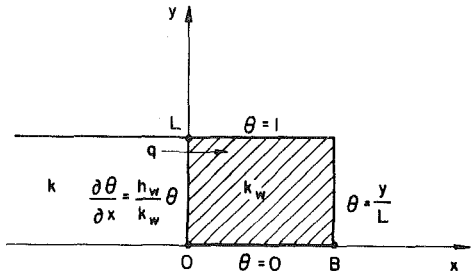

Fig. 6 Boundary value problem solved in appendix

To determine the effect of angle of tilt, ϕ, on Nusselt number for air layers with extended boundary conditions, measurements of heat transfer were made for $A = 5$, and a fixed value of Rayleigh number by incrementing ϕ over the range $0 \leq \phi \leq 90$ deg. This was repeated for two different values of Ra, and the results are plotted in Fig. 5 for the case of plain balsa wood ($\epsilon_w = .84$). As shown in the figure, Nu monotonically decreased when ϕ was increased from 0 to 90 deg. The correlation equation of Hollands et al. [2] for LTP boundary conditions is plotted on the same figure. Although the correlation equation was based on data obtained using simple LTP boundary conditions, there is agreement with the present data to within 10 percent.

4 Conclusions

The heat transfer by natural convection across a fluid layer between two isothermal plates of different temperature depends on the boundary conditions on the side and end walls that confine the extent of the layer. These walls are usually assumed to be perfectly conducting (which generates a linear profile between the plates) or adiabatic. When the fluid is air, or most any other gas, it is argued that the adiabatic condition cannot be achieved in practice, and that experimenters, analysts, and designers must consider a longer list of parameters than is normally used to specify the heat transfer. Not only is a heat transfer induced in the walls due to convection in the layer, but radiation also affects both the convective heat transfer across the layer and the wall heat transfer. The present paper has qualitatively described the wall conduction, radiation, and fluid convection interactions, presented the list of parameters that must be specified, and described how to set up an experiment which will eliminate one of these parameters. Measurements of heat transfer across a vertical air layer, with an aspect ratio of 5, have been reported for three different fluid-wall boundary conditions. The results confirm the importance of the parameters representing both the conductive and radiative interaction. Data for inclined layers have also been reported.

Acknowledgments

This study was partially financed through operating grants from the Natural Sciences and Engineering Research Council, and partially from the Department of Mechanical Engineering, University of Waterloo. This support is gratefully acknowledged.

References

1 Catton, I., "Natural Convection in Enclosures," *Proceedings of 6th International Heat Transfer Conference*, Toronto, 1978, Vol. 6, Hemisphere Press, Washington, D. C., pp. 13-31.

2 Hollands, K. G. T., Unny, T. E., Raithby, G. D., and Konicek, L., "Free Convection Heat Transfer Across Inclined Air Layers," ASME JOURNAL OF HEAT TRANSFER, Vol. 98, 1976, pp. 189–193.

3 ElSherbiny, S. M., Raithby, G. D., and Hollands, K. G. T., "Heat Transfer by Natural Convection Across Vertical and Inclined Air Layers," ASME JOURNAL OF HEAT TRANSFER, Vol. 104, Feb. 1982, pp. 96–102.

4 ElSherbiny, S. M., "Heat Transfer by Natural Convection Across Vertical and Inclined Air Layers," Ph.D. thesis, University of Waterloo, Ontario, Canada, 1980.

5 Catton, I., "Effect of Wall Conduction on the Stability of a Fluid in a Rectangular Region Heated from Below," ASME JOURNAL OF HEAT TRANSFER, Nov. 1972, pp. 446–452.

6 Koutsoheras, W., and Charters, W. W. S., "Natural Convection Phenomena in Inclined Cells with Finite Side Walls—a Numerical Solution," *Solar Energy*, Vol. 19, No. 5, 1977, pp. 433–438.

7 Morrison, G. L., and Tran, V. Q., "Laminar Flow Structure in Vertical Free Convective Cavities," *International Journal of Heat and Mass Transfer*, Vol. 21, 1978, pp. 203–213.

8 Schinkel, W. M. M., and Hoogendoorn, C. J., "An Interferometric Study of the Local Heat Transfer by Natural Convection in Inclined Airfilled Enclosures," *Proceedings of the 6th International Heat Transfer Conference*, Toronto, 1978, Vol. 2, Hemisphere Press, Washington, D.C., pp. 287–292.

9 Catton, I., Ayyaswamy, P. S., and Clever, R. M., "Natural Convection Flow in a Finite Rectangular Slot Arbitrarily Oriented with Respect to the Gravity Vector," *International Journal of Heat and Mass Transfer*, Vol. 17, 1974, pp. 173–184.

10 Edwards, D. K., and Sun, W. M., "Effect of Wall Radiation on Thermal Instability in a Vertical Cylinder," *International Journal of Heat and Mass Transfer*, Vol. 14, 1971, pp. 15–18.

11 Smart, D. R., Hollands, K. G. T., and Raithby, G. D., "Free Convection Heat Transfer Across Rectangular-Celled Diathermous Honeycombs," ASME JOURNAL OF HEAT TRANSFER, Vol. 102, No. 1, 1980, pp. 75–80.

12 Arnold, J. N., Edwards, D. K., and Catton, I., "Effect of Tilt and Horizontal Aspect Ratio on Natural Convection in Rectangular Honeycombs," ASME JOURNAL OF HEAT TRANSFER, Vol. 99, 1977, pp. 120–122.

13 Meyer, B. A., Mitchell, J. W., and El-Wakel, M. M., "Natural Convection Heat Transfer in Moderate Aspect Ratio Enclosures," ASME JOURNAL OF HEAT TRANSFER, Vol. 101, 1979, pp. 655–659.

14 Goldstein, R. J., and Chu, T. Y., "Thermal Convection in a Horizontal Layer of Air," *Prog. Heat and Mass Transfer*, Vol. 2, 1969, pp. 55–75.

15 Eckert, E. R. G., and Carlson, W. O., "Natural Convection in an Air Layer Enclosed Between Two Vertical Plates with Different Temperatures," *International Journal of Heat and Mass Transfer*, Vol. 2, 1961, pp. 106–120.

APPENDIX

Figure 6 shows the wall region with its thermal boundary conditions. As a conservative assumption, the fluid temperature adjacent to the inner wall was assumed constant at the cold plate temperature, T_C. The relevant equations in the wall region are:

$$\nabla^2\theta=0;\ \frac{\partial\theta}{\partial x}=\frac{h_w}{k_w}\theta \text{ at } x=0;\theta=\frac{y}{L} \text{ at } x=B;\theta=0 \text{ at } y=0;$$

and

$$\theta=1 \text{ at } y=L$$

where:

$$\theta=\frac{T-T_C}{T_h-T_C}$$

The solution satisfying the four boundary conditions is:

$$\theta=\sum_{n=1}^{\infty}\left\{C_n\sin\left(\frac{n\pi y}{L}\right)\cdot\sinh\frac{n\pi(x-B)}{L}\right\}+\frac{y}{L}$$

where

$$C_n=\frac{-\frac{2}{n\pi}\cdot\mathrm{Bi}\cdot\cos(n\pi)}{\mathrm{Bi}\cdot\sinh\left(\frac{n\pi B}{L}\right)+n\pi\cosh\left(\frac{n\pi B}{L}\right)}$$

The distribution of the heat flux by conduction through the wall at $x=0$ is given by:

$$q=2h_wL(T_h-T_c)\sum_{n=1,2}^{\infty}\frac{(-1)^n\sin\left(\frac{n\pi y}{L}\right)}{\mathrm{Bi}\tanh\left(\frac{n\pi B}{L}\right)+n\pi}$$

The average value of the heat flux by conduction from the walls is given by:

$$\bar{q}=-4h_wL(T_h-T_c)\sum_{n=1,3,5}^{\infty}\frac{1}{n\pi[\mathrm{Bi}\tanh\left(\frac{n\pi B}{L}\right)+n\pi]}$$

Therefore, the ratio of $\bar{q}$ for a finite wall thickness, B, to that for an infinite thickness ($B\to\infty$) is:

$$\frac{\bar{q}}{\bar{q}_{B\to\infty}}=\frac{\sum_{n=1,3}^{\infty}\frac{1}{n\pi[\mathrm{Bi}\tanh\left(\frac{n\pi B}{L}\right)+n\pi]}}{\sum_{n=1,3}^{\infty}\frac{1}{n\pi[\mathrm{Bi}+n\pi]}}$$

The ratio B/L that makes $\bar{q}/\bar{q}_{B\to\infty}$ equal to 1.01 is given in Fig. 3 for different values of the parameter Bi.

Measurements of Natural Convection Across Tilted Rectangular Enclosures of Aspect Ratio 0.1 and 0.2

R. A. Wirtz
Associate Professor.
Assoc. Mem. ASME

J. Righi
Research Assistant.

F. Zirilli
Instructor.

Clarkson College of Technology,
Potsdam, N. Y. 13676

Laboratory experiments with water are reported for the range $10^8 < Ra_H < 5 \times 10^9$ where the enclosure tilt angle, ϕ, is varied from zero (sideways heating) to 90 deg (heating from below). Shadowgraph observations show that the flow regime studied extends from laminar at $\phi = 0$ and lower Ra_H, to turbulent at $\phi > 0$ and high Ra_H. At $\phi \lesssim 72$ deg the convection consists of a peripheral boundary layer which closely follows the enclosure boundaries. At $\phi \gtrsim 72$ deg the flow axis rotates 90 deg. Convection consists of a single transverse roll with axis oriented upslope of the heated wall. While the average heat transfer is found to be maximum at 50 deg $< \phi < 60$ deg, its variation with ϕ is small. A single correlation equation may be used to predict the average Nusselt number over all angles. The correlation proposed predicts the average Nusselt number with an r.m.s. deviation of ± 10 percent.

Introduction

In this paper we present results of laboratory experiments on natural convection of water across tilted rectangular enclosures where a uniform temperature difference is maintained between two opposite side walls. Figure 1 is a sketch of the test configuration used. The results reported are for enclosures with aspect ratios ($Ar = H/W$) equal to 0.1 and 0.2. The lateral connecting walls were designed to represent adiabatic surfaces. Data is presented for enclosure tilt angles, ϕ, ranging from horizontal orientation ($\phi = 0$) through heating from below ($\phi = 90$ deg).

Buoyancy driven recirculating flows, particularly those in the rectangular enclosure configuration, have received considerable attention in the engineering literature. Catton [1] has discussed this configuration's many applications in his review of the large body of work reported prior to 1978.

Recent studies of natural convection across horizontal ($\phi = 0$), low aspect ratio enclosures include numerical (finite difference) computations by Cormack et al. [2] and Lee and Sernas [3]. Imberger [4] reported on measurements with water ($Ar = 0.01$, 0.02) while Sernas and Lee [5] reported on differential interferometry measurements with air. Cormack et al. [6] developed an asymptotic theory valid for $Ar \to 0$, Ra finite. This is sometimes called the core flow limit. Bejan and Tien [7] developed average Nusselt number equations valid for high Prandtl number fluids for both the core flow limit ($Ar \to 0$) and the boundary layer limit ($Ar < 1$, Ra large).

More limited attention has been given to tilted rectangular enclosures. Catton et al. [8] included some results for $Ar = 0.2$, and 0.5 as part of a numerical calculation. Wirtz and Tseng [9, 10] presented two-dimensional finite difference calculations for $Ar = 0.2$ and 0.5 for tilt angles ranging from $\phi = -90$ deg (heating from above) to $\phi = +90$ deg (heating from below). In reference [10] Bejan and Tien's overall correlation equation for horizontal enclosure orientations was modified to include Prandtl number effects.

To our knowledge, the data presented in this paper is the first experimental result for single tilted enclosures of small aspect ratio. In the following, results are presented for $9 \times 10^7 < Ra_H < 5 \times 10^9$. Our shadowgraph observations indicate that the flow extends from transition to fully turbulent convection. In terms of the three convection regimes identified by Bejan and Tien [7], our results are in the boundary layer regime ($Ar < 1$, Ra large). The range of data is shown in Fig. 2 along with available data for water by Al-Homoud and Bejan [11], and Imberger [4]; data for air by Sernas and Lee [5]; and numerical computations for water by Wirtz and Tseng [9, 10].

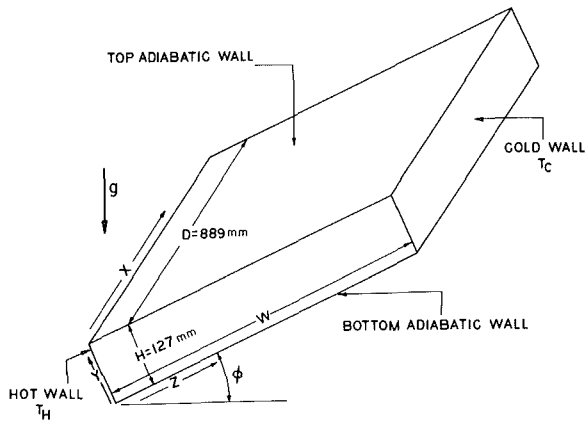

Fig. 1 Schematic representation of tilted enclosure where $W = 1270$ mm and 635 mm, giving $Ar = 0.1$ and 0.2, respectively. The hot and cold surfaces are isothermal while the connecting surfaces are adiabatic.

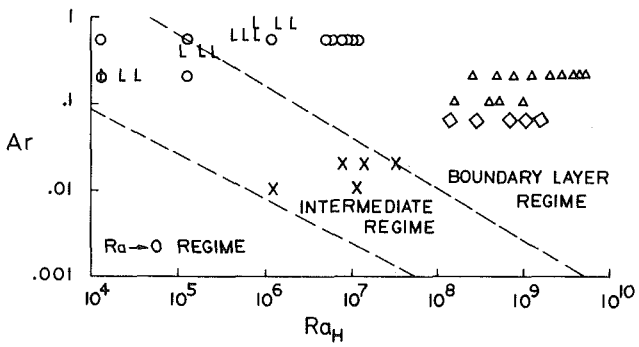

Fig. 2 The data for the present invesitgation (Δ) are in the boundary layer regime (large Ra). Other data shown are: L – [5]; x – [4]; ○ – [9, 10]; and ◇ – [11].

Contributed by the Heat Transfer Division for publication in the JOURNAL OF HEAT TRANSFER. Manuscript received by the Heat Transfer Division September 14, 1981.

Apparatus

A side view of the test enclosure is sketched in Fig. 3. The left end is an electrically heated copper wall 127-mm high × 889-mm deep × 12.7-mm thick. The back of the hot wall is guarded with a second set of heaters which operate across aluminum plates containing two heat flux sensors with a nominal sensitivity of 16 W/m^2 per mV. The guard heaters are adjusted to drive the heat flux through the sensors toward zero, thus minimizing heat losses out the back of the wall. The upper and lower periphery of the hot wall is similarly guarded using thermocouple pairs as sensors.

The right side of the test region consists of another 12.7-mm thick copper wall, backed by a circulating passage containing antifreeze. Heat sinking is obtained by a 10-kW capacity refrigerated circulator with proportional temperature control having a control stability of approximately ±.05°C. Small circulating channels are located above and below the cold wall to help maintain the isothermal condition.

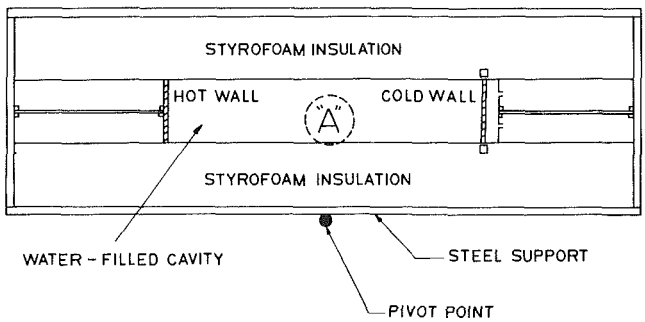

Fig. 3 Schematic of experimental apparatus side view. "A" represents region of shadowgraph views shown in Fig. 5.

The temperature of each side wall is monitored with nine copper-constantan thermocouples; a line of five located along each plate's vertical centerline and five in a horizontal line at each plate's mid-height. Each thermocouple was individually calibrated to within ±0.1°C. During the experiments each plate was found to be isothermal to within less than ± ≈6 percent of the applied temperature difference between the hot and cold walls.

The upper and lower "adiabatic" surfaces represent a considerable surface area for $Ar<1$. The upper adiabatic wall is shown in exploded view in Fig. 4. Each connecting wall consists of 144-mm thick styrofoam backing, a reinforced, rigid 6-mm thick hardboard sheet. (We originally used 3-mm thick plexiglass for the $Ar=0.1$ experiments but found that at elevated temperatures it had poor structural properties). Imbedded 22-mm from each inner surface of each adiabatic wall are a series of flat plate guard heaters which are instrumented with heat flow sensors. Five guards are placed in the upper wall (three for $Ar=0.2$ experiments), while one is placed to the left in the lower wall. Power to the guard heaters is individually adjusted to drive the heat flux through the adiabatic wall toward zero.

The two side walls are 13-mm thick clear plexiglass backed by 50-mm of styrofoam insulation. The entire structure is mounted in a steel chassis which is pedestal mounted so that it may be pivoted to the appropriate tilt angle.

All thermocouple and heat flux readouts were continuously monitored with a 24 point strip chart recorder. Numerical data was recorded at selected time intervals using a digital volt meter connected in parallel with the recorder. The DVM sensitivity was ±1μV. Power to the electrically heated hot wall was measured using an AC DMM having a sensitivity of ±.01 V and an AC current meter with an accuracy of ±.025 amp.

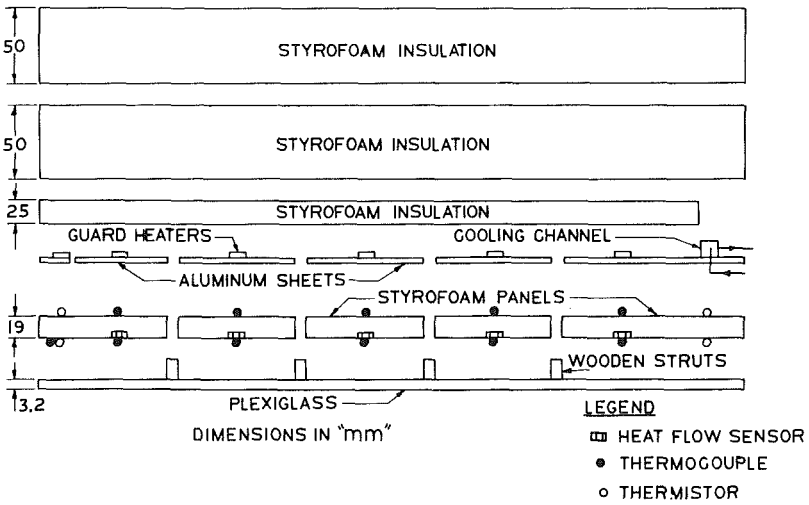

Fig. 4 Exploded view of top adiabatic wall used with $Ar=0.1$ experiments. The $Ar=0.2$ apparatus used three individually controlled guard heaters instead of five.

Nomenclature

A = hot wall surface area
Ar = enclosure aspect ratio
C = empirical constant
D = test enclosure depth
g = acceleration of gravity
H = test enclosure height
k = fluid conductivity
m = empirical constant
n = empirical constant
Nu = Nusselt number
Q = power
Pr = fluid Prandtl number
Ra = enclosure Rayleigh number
T = temperature
W = test enclosure width
x = transverse coordinate
y = transverse coordinate
z = cross enclosure coordinate
ΔT = hot to cold wall temperature difference
ϕ = tilt angle
σ = r.m.s. relative deviation

During the experiments we used a simple shadowgraph system, consisting of an incandescent lamp, lenses, and a 100-mm dia spherical mirror to look across the flow. We also used neutrally buoyant particles (latex paint dust), and injection of vegetable dye from 0.2-mm tubing projecting through the plexiglass side walls to make visual observations of the qualitative nature of the convection.

Our experimental procedure was straightforward. The test region was filled with degassed, distilled water, and the desired tilt angle was set. The cold wall temperature control was set to approximately 10°C and an input power to the hot wall heaters was arbitrarily selected. The system was allowed to approach equilibrium with periodic adjustments of the power inputs to the hot wall and various guard heaters. This process usually took about 12 hrs. When the hot and cold wall temperatures were steady for at least 3 hrs with no adjustment in heater controls necessary, temperature and power input data were recorded. Then selected sections of the insulation covering the transparent side walls were removed and visual observations were made.

A dimensional analysis of this problem or consideration of the governing equations and boundary conditions [10] indicates that

$$\overline{\mathrm{Nu}}_H = f\left(\mathrm{Ra}_H, \mathrm{Pr}, Ar, \frac{H}{D}, \phi\right) \tag{1}$$

where $\overline{\mathrm{Nu}}_H$ is the average Nusselt number based on enclosure height, H, given as

$$\overline{\mathrm{Nu}}_H = \frac{Q_{\mathrm{NET}} H}{A \Delta T k} \tag{2}$$

with $\mathrm{A} = 0.127 \times 0.889\mathrm{m}^2$, and k the fluid conductivity evaluated at the mean fluid temperature. The net heat transfer rate, Q_{NET}, is the total power to the hot wall corrected by the indicated losses from the back of the hot wall and from the adiabatic connecting walls. These corrections were never more than 8 percent and 1 percent, respectively, of the total power input. We also estimated the radiant exchange between the hot and cold copper walls (emissivity of oxidized copper estimated to be 0.95), assuming that the connecting walls were reradiating isothermal surfaces, and that the water in the test enclosure was transparent. Under these assumptions the radiant exchange is estimated to be less than 2 percent of Q_{NET}.

In the experiments reported here $H/D = 0.1428$, a constant. The Prandtl number is also essentially constant; its value is determined at the mean fluid temperature.

We performed experiments for two values of W, 1270 mm and 635 mm leading to $Ar = 0.1$ and 0.2. For $Ar = 0.1$, $9.4 \times 10^7 < \mathrm{Ra}_H < 2.4 \times 10^9$ with $0 < \phi < 40$ deg, the upper angle was limited by structural considerations of our apparatus. For $Ar = 0.2$, the Rayleigh number range was $2 \times 10^8 < \mathrm{Ra}_H < 5 \times 10^9$ with the tilt angle $0 \le \phi \le 90$ deg.

If we include the previously mentioned accuracy estimates of our instrumentation in an error analysis we find that the most probable error on $\overline{\mathrm{Nu}}_H$ is ±8.2 percent, and that on Ra_H is ±10.9 percent. We estimate that our tilt angle measurements are accurate to ±0.5 deg. Details of apparatus construction, data collection, and analysis, and a detailed tabulation of results are found in [12] and [13], both available from the senior author.

Qualitative Observations

Ozoe, et al. [14] studied convection in a three-dimensional enclosure with $Ar = 2.0$ where heating was from below ($\phi \simeq 90$ deg). They found that the flow consisted of transverse rolls where the roll axis aligned itself with the short dimension of the box. As the tilt angle was reduced to about 83 deg, the roll axis rotated slightly but remained oriented upslope, consistent with earlier predictions by Hart [15]. At $\phi < 83$ deg, they observed the flow structure to undergo a sudden transition to a peripheral flow configuration with convection up the slope of the heated wall, across to the cooled wall, and down. We observed the same transition phenomena in our $Ar = 0.2$ experiments, except that the transition angle is in this case at ≈72 deg. At tilt angles less than 72 deg we observe a strong boundary layer flow which follows the periphery of the enclosure; that is, fluid rises near the hot wall, flows across the upper connecting wall to the cooled wall, where it descends and then returns to the bottom of the hot wall. About 2/3 of the volume of fluid in the container resides in a quiescent core region disturbed occasionally by turbulent billows which break from the turbulent boundary layer flow. Except for a very weak secondary flow due to the presence of the plexiglass side walls, the flow is two dimensional and confined to the y-z plane of Fig. 1.

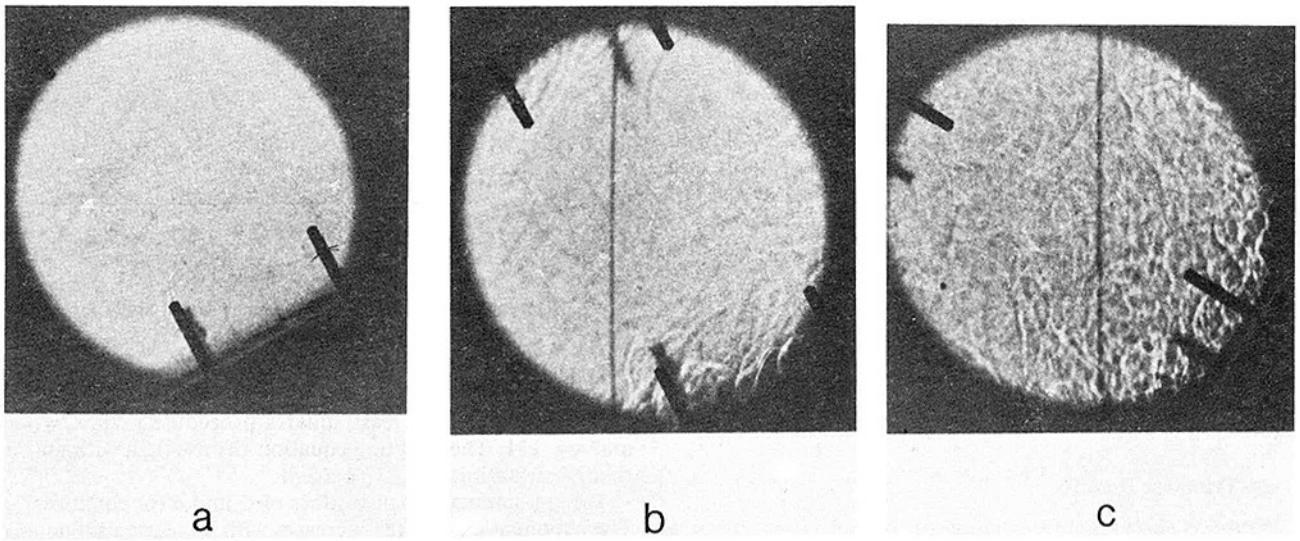

Fig. 5 Shadowgraph view of region "A" of Fig. 3: (a) $\mathrm{Ra}_H = 7 \times 10^8$, $\phi = 30$ deg, (b) $\mathrm{Ra}_H = 2.2 \times 10^9$, $\phi = 30$ deg, (c) $\mathrm{Ra}_H = 2.2 \times 10^9$, $\phi = 60$ deg

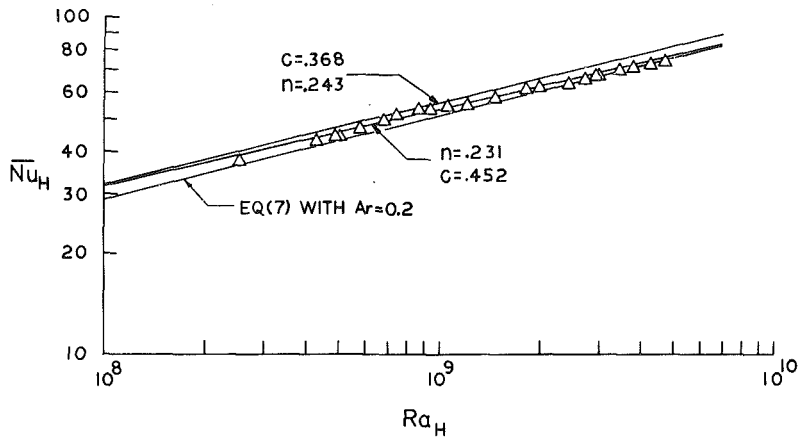

Fig. 6 Measured average Nusselt number for $\phi = 0$, $Ar = 0.2$.

Table 1 Least squares fit of equation (3) for $Ar = 0.1$ and 0.2

	$Ar = 0.1$			$Ar = 0.2$		
ϕ(deg)	C	n	σ(%)	C	n	σ(%)
0	0.85	0.192	7.46	0.452	0.231	2.14
15	1.03	0.182	7.40	0.615	0.216	0.92
30	3.91	0.116	2.68	0.400	0.240	4.65
40	0.67	0.202	1.39	–	–	–
45				0.283	0.257	3.09
60				0.356	0.247	6.23
75				0.197	0.273	1.15
90				0.182	0.275	1.68
All angles	0.97	0.185	6.53	0.368	0.243	11.10

Figure 5 shows shadowgraph views at a point approximately midway between hot and cold wall with $Ar = 0.2$. The photographs give a qualitative indication of the scale of the turbulence in the flow moving between these two side walls. It should be noted that the image is the integral effect obtained by the parallel beam of light as it transverses the 889-mm depth of the enclosure.

Figure 5(*a*) shows the boundary layer flow along the lower connecting wall at $Ra_H = 7 \times 10^8$, $\phi = 30$ deg. There is little evidence of mixing in the flow. We observed this for the entire range of Rayleigh numbers with $\phi = 0$, and for $Ra_H \lesssim 7 \times 10^8$ with $\phi < 30$ deg. The peripheral boundary layer is apparently laminar under these conditions. Figure 5(*b*) shows the same section of the enclosure, with $Ra_H = 2.2 \times 10^9$, $\phi = 30$ deg. The boundary layer is turbulent. The intensity increases with increasing Ra_H. We observed the intensity of mixing to increase with ϕ as well. This is shown in Fig. 5(*c*) with $Ra_H = 2.2 \times 10^9$ and $\phi = 60$ deg.

At tilt angles greater than 72 deg we observe an entirely different situation. The flow now consists of a single roll with axis parallel to the y-axis of Fig. 1. Motion is essentially two dimensional and in the x-z plane. Our observations of neutrally buoyant particles in the flow show that the roll motion is nearly solid body rotation (the core rotates) and turbulent, especially near the corners of the enclosure where secondary oblique rolls are sometimes observed.

We found that the roll had no preferred direction of rotation; sometimes it rotated clockwise, sometimes counterclockwise. We tested this on several occasions by shutting down our apparatus, waiting until the fluid was quiescent, and restarting without changing tilt angle or power settings.

Heat-Transfer Results

Figure 6 shows a typical plot of Nusselt number as a function of Rayleigh number at fixed tilt angle. The data span a range $2 \times 10^8 < Ra_H < 5 \times 10^9$, and are well correlated by a power law equation of the form

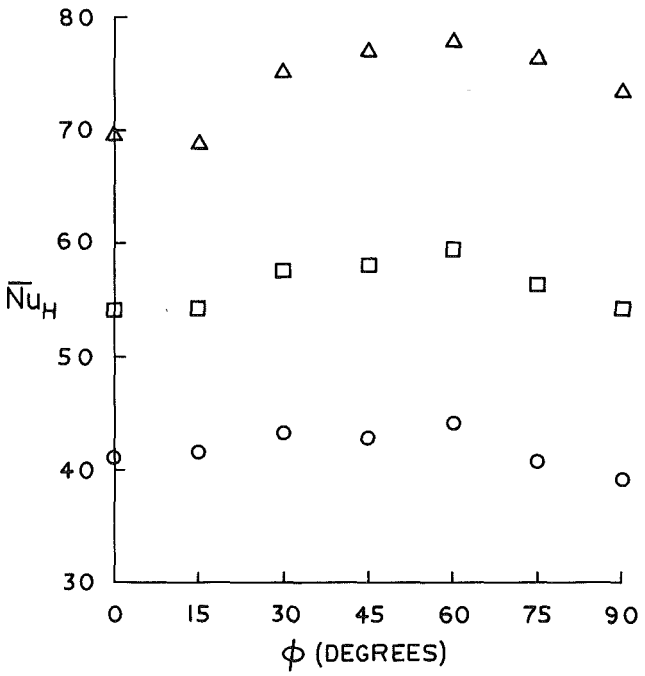

Fig. 7 Average Nusselt number dependence on tilt angle for $Ar = 0.2$: $\Delta - Ra_H = 3 \times 10^9$, $\square - Ra_H = 10^9$, $\circ - Ra_H = 3 \times 10^8$

$$\overline{Nu}_H = C\, Ra_H^n \tag{3}$$

In the case shown, a least squares procedure gives $C = .452$ and $n = .231$. The resulting equation fits the data with an rms relative deviation, $\sigma = 2.14$ percent.

Table 1 summarizes our values of C and n for equation (3). The exponent n generally increases with increasing tilt angle ϕ and with Ar. This is consistent with our qualitative observation that the relative intensity of turbulence increases with Ra_H and ϕ.

In our experiments we controlled the heat-transfer rate and measured the resulting temperature difference between hot and cold walls. Therefore, it would be very difficult to run an experiment where Ra_H was fixed and ϕ varied. However, we can gain an understanding of the effect of tilt angle variations on $\overline{Nu}_H$ by cross plotting the results of Table 1 and equation (3) with Ra_H held constant. This is done in Fig. 7 for three values of Rayleigh number. The figure shows the Nusselt number to be maximum at 50 deg $< \phi <$ 60 deg. This is in general agreement with numerical calculations [10] for $1.25 \times 10^4 < Ra_H < 1.25 \times 10^5$, $Ar = 0.2$, which showed the maximum to be between 45 and 60 deg. However, the numerical calculations showed the maximum shifting toward lower tilt angles as Ra_H increases. The present experiments show an opposite trend with the maximum increasing slightly from about 50 deg at $Ra_H = 3.10^8$ to about 60 deg at $Ra_H = 3 \times 10^9$.

No significant local minimum in heat transfer is evident near the flow transition angle, 72 deg. This was a surprising result. Studies [16, 17] of heat transfer across high aspect ratio tilted enclosures show a distinct local minimum which is presumed to coincide with the transition from the peripheral boundary layer to the transverse roll mode of flow. Figure 7 does show an inflection which grows into a local minimum with Ra_H increasing for small tilt angles, $\phi \approx 15$ deg. This may coincide with the transition from laminar to turbulent peripheral flow shown in Fig. 5; or it may simply be due to scatter of the data.

In any case, the variation in $\overline{Nu}_H$ over the range $0 \leq \phi \leq 90$ deg is relatively small; less than ± 8 percent for the data of the present study. This is the same order of magnitude as the tolerance placed on individual data points. Therefore, it is feasible to neglect the tilt angle effect and propose a correlation which fits all data. The values of C and exponent n so obtained are shown in Table 1 along with the corresponding σ. Equation (3) using $C = 0.368$ and $n = 0.243$ is shown in Fig. 6.

If we supplement our own data for $\phi = 0$ with that of Al-Homoud and Bejan [11] ($Ar = 0.0625$) and the boundary layer regime numerical calculations of [9] ($Ar = 0.5$), it should be possible to assess the effect on the heat transfer of variations in enclosure aspect ratio.

Bejan and Tien's analysis of convection across horizontal enclosures in the boundary layer regime [7] gives

$$\overline{Nu}_H = .623 Ra^{.2} \tag{4}$$

Their model gives $\overline{Nu}_H$ independent of Ar. On the other hand, Imberger [6] considered horizontal enclosures with $Ar < 0.02$. He used Gill's limit, appropriate for large Ra_H, to show that

$$\overline{Nu}_H \sim Ra_H^{.25} Ar^{3/8} \tag{5}$$

Figure 8 shows $\overline{Nu}_H / Ra_H^n$ plotted against Ar using the present data and that of references [9] and [11]. The data have been plotted twice. The upper set is for $n = 0.2$ and the lower set is for $n = 0.25$. For each aspect ratio the data exhibit considerable scatter. This is because neither $n = 0.2$ nor $n = 0.25$ adequately represents the proper Rayleigh number dependence of $\overline{Nu}_H$. As indicated in Fig. 6 and Table 1, our own data at $\phi = 0$ is best fit when $n = 0.19$ and 0.23 for $Ar = 0.1$ and 0.2, respectively, while Al-Homoud and Bejan [11] obtained $n = 0.38$ for $Ar = 0.062$.

As shown in Fig. 8, equation (4) tends to predict low as Ar increases. A least squares fit of the form

$$\overline{Nu}_H = C \ Ra^{.2} Ar^m \tag{6}$$

gives $C = 0.902$ and $m = 0.111$ with $\sigma = 12$ percent. The lower set shows the data plotted with $n = 0.25$ along with a line of slope 3/8. In this case the model gives an aspect ratio dependence which is too strong, even if the $Ar = 0.5$ data is omitted. A least squares fit of the form

$$\overline{Nu}_H = C \ Ra^{.25} Ar^m \tag{7}$$

gives $C = 0.394$, $m = 0.194$ with $\sigma = 7.5$ percent. Neither model accurately predicts the actual aspect ratio dependence of $\overline{Nu}_H$. In fact, if both exponents (m and n) are empirically determined we get $m = 0.24$, $n = 0.27$ with $\sigma = 7.3$ percent. However, equation (7) does reproduce the $\phi = 0$ deg data with an accuracy which is comparable to the estimated precision of the experiments. Furthermore, equation (7) reproduces all available data ($0 \leq \phi \leq 90$ deg) with $\sigma = 9.9$ percent which makes it our recommended correlation equation. Equation (7) is shown plotted with our $\phi = 0$ deg data in Fig. 6.

Conclusions

Our experiments with natural convection of water across tilted rectangular enclosures of small aspect ratio show that two different flow regimes exist. The regimes are separated by a transition at a tilt angle of ≈ 72 deg when $Ar = 0.2$. At $\phi \lesssim 72$ deg, we observe a boundary layer type flow which follows the periphery of the enclosure. At 72 deg $\lesssim \phi < 90$ deg, a transverse roll mode of flow exists where the core of the fluid rotates.

For the Rayleigh number and tilt angle range reported here the convection extends from laminar to turbulent flow. No local minimum in $\overline{Nu}_H$ is observed at the flow transition angle $\phi = 72$ deg. The heat transfer is maximum at a tilt angle of between 50 and 60 deg. However, the variation of $\overline{Nu}_H$ with ϕ is relatively small so that the angular dependence may be

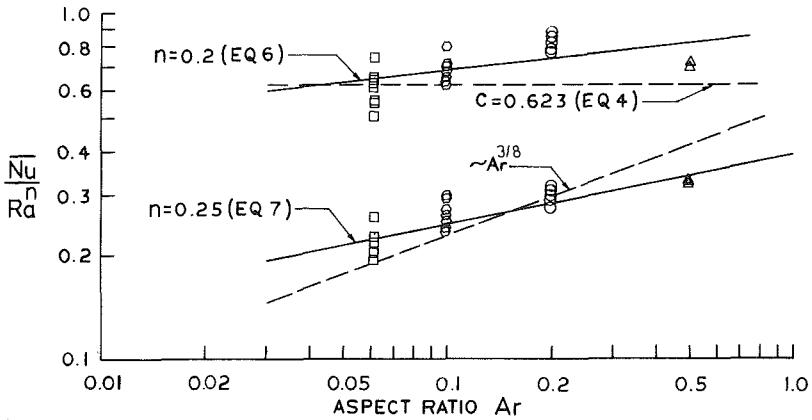

Fig. 8 Average Nusselt number dependence on aspect ratio with $\phi = 0$. The data shown is from: □ – [11], $Ar = 0.0625$; Δ – [9], $Ar = 0.5$; and ○ – present

neglected with an accuracy in $\overline{Nu}_H$ of about ± 8.5 percent. Neither Bejan and Tien's nor Imberger's model adequately predicts the aspect ratio dependence of $\overline{Nu}_H$. However, when these models are suitably empiricized as in equations (6) and (7), the heat transfer may be predicted with rms relative errors which are comparable to the estimated precision of the experiments.

References

1 Catton, I., "Natural Convection in Enclosures," *Proceedings Sixth International Heat Transfer Conference*, Vol. 6, 1978, pp. 13-31.

2 Cormack, D. E., Leal, L. G., and Seinfield, J. H., "Natural Convection in a Shallow Cavity with Differentially Heated End Walls: Part 2—Numerical Solutions," *Journal of Fluid Mechanics*, Vol. 65, 1974, pp. 231-246.

3 Lee, E. I., and Sernas, V., "Numerical Study of Heat Transfer in Rectangular Air Enclosures of Aspect Ratio Less Than One," ASME Paper No. 80-WA/HT-43, 1980.

4 Imberger, J., "Natural Convection in a Shallow Cavity With Differentially Heated End Walls: Part 3—Experimental Result," *Journal of Fluid Mechanics*, Vol. 65, 1974, pp. 247-260.

5 Sernas, V., and Lee, E. I., "Heat Transfer in Air Enclosures of Aspect Ratio Less Than One," ASME Paper No. 78-WA/HT-7, 1978.

6 Cormack, D. E., Leal, L. G., and Imberger, J., "Natural Convection in a Shallow Cavity With Differentially Heated End Walls: Part 1—Asymptotic Theory," *Journal of Fluid Mechanics*, Vol. 65, 1974, pp. 209-229.

7 Bejan, A., and Tien, C. L., "Laminar Natural Convection Heat Transfer in a Horizontal Cavity With Different End Temperatures," ASME JOURNAL OF HEAT TRANSFER, Vol. 100, 1978, pp. 641-647.

8 Catton, I., Ayyaswamy, P. S., and Clever, R. M., "Natural Convection Flow in a Finite Rectangular Slot Arbitrarily Oriented With Respect to the Gravity Vector," *International Journal of Heat and Mass Transfer*, Vol. 17, 1974, pp. 173-184.

9 Wirtz, R. A., and Tseng, W. F., "A Finite Difference Simulation of Free Convection in Tilted Enclosures of Low Aspect Ratio," *Numerical Methods in Thermal Problems*, edited by R. W. Lewis and K. Morgan, Pineridge Press, Swansea, U.K., 1979, pp. 381-390.

10 Wirtz, R. A., and Tseng, W. F., "Natural Convection Across Tilted Rectangular Enclosures of Small Aspect Ratios," *Natural Convection in Enclosures*, edited by K. E. Torrance and I. Catton, ASME HTD-Vol. 8, 1980, pp. 47-54.

11 Al-Homoud, A. A., and Bejan, A., "Experimental Study of High Rayleigh Number Convection in Horizontal Cavity with Different End Temperatures," University of Colorado, CUMER-79-1, May 1979.

12 Zirilli, F., "Physical Experiments on Free Convection in a Tilted Rectangular Enclosure of Aspect Ratio 0.1," MIE Report 053, Clarkson College of Technology, Potsdam, N.Y., 1979.

13 Righi, J., "Physical Experiments on Free Convection in a Tilted Rectangular Enclosure of Aspect Ratio 0.2," MIE Report 062, Clarkson College of Technology, Potsdam, N.Y., 1980.

14 Ozoe, H., Sayama, H., and Churchill, S. W., "Natural Convection in a Long Inclined Rectangular Box Heated Below: Part 1—Three-Dimensional Photography," *International Journal of Heat and Mass Transfer*, Vol. 20, 1977, pp. 123-129.

15 Hart, J. E., "A Note on the Structure of Thermal Convection in a Slightly Slanted Slot," *International Journal of Heat and Mass Transfer*, Vol. 16, 1973, pp. 747-753.

16 Ozoe, H., Sayama, H., and Churchill, S. W., "Natural Convection in an Inclined Rectangular Channel at Various Aspect Ratios and Angles-Experimental Measurements," *International Journal of Heat and Mass Transfer*, Vol. 18, 1975, pp. 1425-1431.

17 Arnold, J. N., Catton, I., and Edwards, D. K., "Experimental Investigation of Natural Convection in Inclined Rectangular Regions of Differing Aspect Ratios," ASME Paper 75-HT-62, 1975.

Experimental Investigation of Natural Convection in Partitioned Enclosures

S. M. Bajorek[1]

J. R. Lloyd
Mem. ASME
Department of Aerospace and Mechanical Engineering,
University of Notre Dame,
Notre Dame, Ind. 46556

Natural convection heat transfer within a two-dimensional, partitioned enclosure of aspect ratio 1 was investigated experimentally using a Mach-Zehnder interferometer. The vertical walls were maintained isothermal at different temperatures, while the horizontal walls and the partitions were insulated. Local and average heat-transfer coefficients were determined for the air and carbon dioxide filled enclosures both with and without partitions for Grashof numbers between 1.7×10^5 and 3.0×10^6. Good agreement was found between the results in the present study for the nonpartitioned enclosure and those previously published. The partitions were found to significantly influence the convective heat transfer. Observations of the interferometric fringes indicated that the core region is unsteady, with the unsteadiness occasionally affecting the flow along the vertical isothermal walls, beginning at Grashof numbers as low as 5×10^5.

Introduction

Natural convection in enclosures is a topic of considerable current interest. Simple enclosures, defined as single chambers with no partitions or obstructions in them, have been studied in the past, but current interest has now shifted to complex enclosures which contain the partitions and obstructions. The resurgance of interest has been the result, in large part, of energy conscious design. In the present study, heat transfer in a simple square enclosure geometry is first studied to establish a reference for the second part of the study which focuses on a complex partitioned enclosure of the same external dimensions. The effect of the partitioning is clearly demonstrated through examination of the local and average heat-transfer coefficient measurements.

Since there are several comprehensive review articles on natural convection heat transfer in simple enclosures (eg., [1-3])[2], studies of complex geometries will be the primary topic of discussion herein. Emery [4] has experimentally investigated the effects of a vertical baffle mounted through the core of an enclosure for aspect ratios ranging from 10 to 40. He found only minor effects on the convective heat-transfer distribution which were apparently due to the location of the baffle. Duxbury [5], Bauman et al. [6], and recently Nansteel and Greif [7] have studied the effects of a single partition which is suspended from the enclosure ceiling, but does not reach the floor. Duxbury [5] experimentally investigated air-filled enclosures for aspect ratios between 5/8 and 5 for Rayleigh numbers less than 10^6. The experimental and numerical study by Bauman et al. [6] was done for a water-filled rectangular enclosure with aspect ratio of 1/2. Experimental data was reported in the turbulent Rayleigh number range from 1.6×10^8 to 5.4×10^{10}, and numerical predictions were made for the local and average heat transfer in a square nonpartitioned cavity for Rayleigh numbers as high as 10^8. The investigation carried out by Nansteel and Greif [7] used an experimental setup similar to that used by Bauman et al. [6]. Temperature profiles were obtained with thermocouple probes, and dye was injected into the enclosure in order to visualize the flow. Correlations were obtained giving the average Nusselt number as a function of Rayleigh number, partition conductance, and a parameter describing the partition height. Janikowski et al. [8] used a Mach-Zehnder interferometer to investigate natural convection in an air-filled, two-dimensional enclosure with solid and porous partitions protruding from both the floor and ceiling of the enclosure into the cavity. Local and average heat-transfer coefficients were obtained for an enclosure with aspect ratio of 5 at a Grashof number of 1.1×10^6.

Chang [9] has recently completed a detailed numerical study investigating natural convection-thermal radiation interactions in a square enclosure with isothermal sidewalls and adiabatic partitions extending from the floor and ceiling. The effects of both surface radiation and gaseous radiation were considered in the enclosure for $10^4<\mathrm{Ra}_w<10^8$. Heretofore, there has been no experimental data to evaluate the accuracy of this numerical study.

The intent of the present investigation is to experimentally investigate natural convection in an enclosure with an aspect ratio of 1 having partitions protruding into the cavity from both the floor and ceiling of the enclosure. Air and carbon dioxide were used as the working fluids between isothermal side walls and adiabatic horizontal walls so that the results may be directly compared to the numerical calculation by Chang [9]. Results presented for the simple enclosure are also comparable to several previously published works. Local and average heat-transfer coefficients were determined for both enclosure geometries for Grashof numbers over the range $10^5\le\mathrm{Gr}_w<3\times10^6$

Experimental Apparatus and Procedure

Details of the experimental apparatus and procedure are found in reference [10] and therefore only a brief description is provided herein. The experimental apparatus shown schematically in Fig. 1 consisted of a long rectangular enclosure with height, $H=6.35$ cm, width, $W=6.35$ cm, and length $L=50.8$ cm so that the aspect ratio $A=H/W=1$ and end effects will be negligible. The horizontal floors, ceilings, and the partitions were made from plexiglas which has a thermal conductivity of about $0.5-1$ W/mK. In order to reduce conduction from the hot wall to the cold wall through the horizontal pieces, the sides of the floors and ceilings were milled at an angle so that the edge of the plexiglas pieces in contact with the vertical plates were less than 1.6-mm wide. The horizontal pieces were supported and adjusted by steel elevator bolts epoxied to the backside of each piece as shown in Fig. 2. A pressure chamber machined from stainless steel enclosed the entire test section and contained port hole

[1] Current address: Westinghouse Electric Corporation, Pittsburgh, Pa.

Contributed by the Heat Transfer Division for publication in the JOURNAL OF HEAT TRANSFER. Manuscript received by the Heat Transfer Division September 24, 1981.

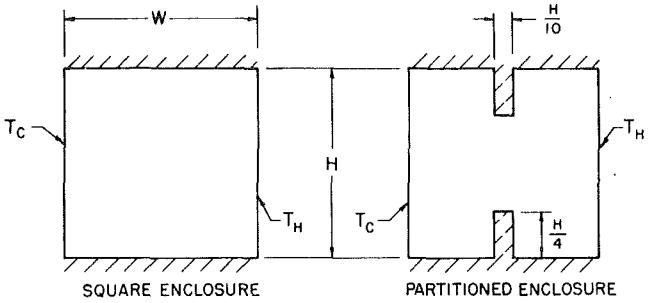

Fig. 1 Schematic diagram of enclosure geometries

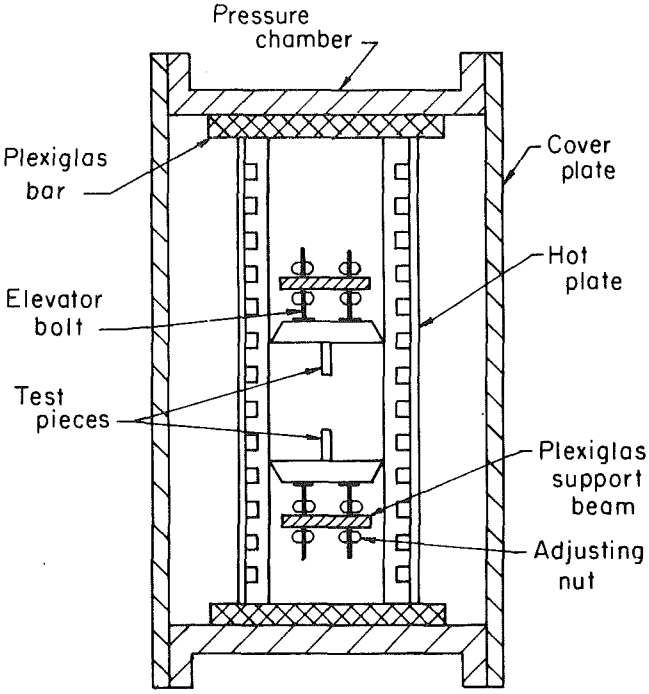

Fig. 2 Side view schematic of test section in pressure chamber

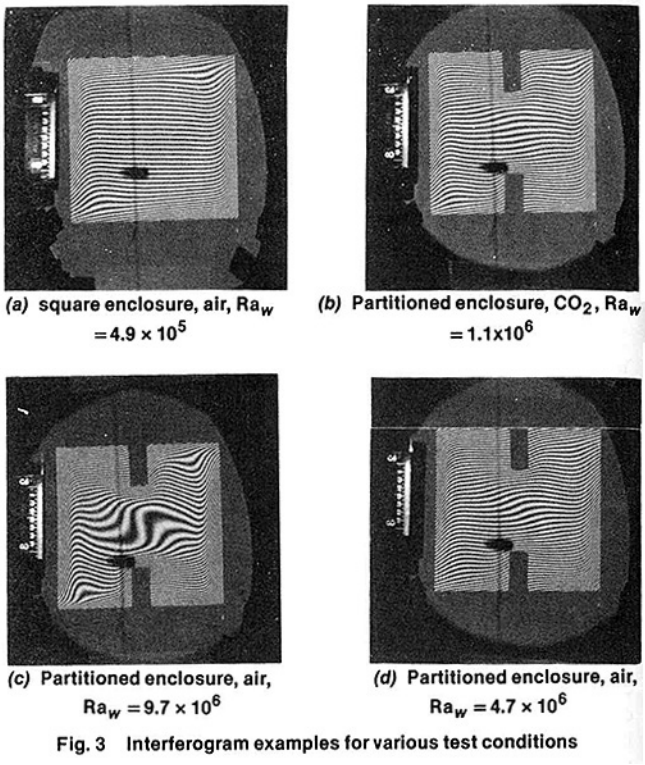

(a) square enclosure, air, $Ra_w = 4.9 \times 10^5$

(b) Partitioned enclosure, CO_2, $Ra_w = 1.1 \times 10^6$

(c) Partitioned enclosure, air, $Ra_w = 9.7 \times 10^6$

(d) Partitioned enclosure, air, $Ra_w = 4.7 \times 10^6$

Fig. 3 Interferogram examples for various test conditions

mountings for optical flats so that the beam of the interferometer could pass through the enclosure.

A Mach-Zehnder interferometer was used to evaluate the temperature distribution within the enclosure. The interferometer is ideally suited for the investigation of two-dimensional temperature fields since it does not introduce disturbances into the gas layer, and the entire temperature field can be recorded instantaneously. Alignment of the test section was facilitated by a plumb line hung in the interferometer reference beam. The walls were precisely positioned so that each interior angle was 90.0 deg, and each side of the square was 6.35 cm. Once the alignment procedure was complete, the pressure chamber was sealed and tested for leaks. In order to remove trace quantities of water vapor, the entire volume of air or carbon dioxide in the pressure chambers was filtered through a hydrous calcium sulfate desicant a minimum of ten times in order to guarantee a working fluid purity of at least 99.95 percent. In this investigation, the interferometer was adjusted to produce fringe widths such that the fringe locations could be precisely measured close to the hot and cold walls. Figure 3 presents several of the interferograms analyzed in this study.

In all experimental runs, the temperature of the cold wall was maintained at room temperature by use of a special constant temperature bath. Thus, a ray of light just grazing the cold wall passes through the test chamber unrefracted and does not undergo any fringe shift. The hot wall was adjusted to its desired temperature, and the apparatus was left undisturbed for typically 4 hrs so that the temperatures of the hot and cold walls were no longer changing. The pressure in the chamber was then adjusted to approximately 1 bar, and the apparatus was again left undisturbed while the readings were monitored. Steady-state conditions were assumed if there was little or no change in the readings over the course of an hour. As extra insurance, after these assumed steady-state conditions were reached, the apparatus was left undisturbed for an additional 4 hrs before a photograph was taken.

Nomenclature

A = test section aspect ratio, H/W

G = Gladstone – Dale constant, $\frac{n-1}{\rho}$

Gr_w = Grashof number, $\frac{g\beta(T_H - T_c)w^3}{\nu^2}$

g = gravitational acceleration

H = test-section height

k = thermal conductivity

L = test-section length

n = refractive index

Nu_w = Nusselt number

P = gas pressure

R = gas constant

Ra_w = Rayleigh number

T = temperature

W = test-section width

β = thermal-expansion coefficient

ϵ = fringe shift

ξ = dimensionless wall height

τ = dimensionless distance from wall

ρ = gas density

ν = kinematic viscosity

θ = dimensionless temperature, $\frac{T - T_c}{T_H - T_c}$

λ_0 = light beam wavelength

Subscripts

f = based on film temperature

H = based on hot wall temperature

All of the photographs were analyzed using a toolmaking microscope which could be read directly to 2.54×10^{-4} cm. For each photograph, local heat-transfer coefficients were determined at nineteen vertical locations on the hot wall by measuring the fringe shifts at least ten locations directly adjacent to the wall. A linear correction was applied to resultant plots of fringe shift versus distance from the wall in order to account for the additional fringe shift due to end effects. This correction is identical of that used successfully by Bratis and Novotny [11] and Schimmel et al. [12]. Relating the fringe shift to temperature by the relation:

$$\epsilon = \frac{GLP}{R\lambda_0}\left[\frac{1}{T} - \frac{1}{T_c}\right] \tag{1}$$

the temperature profile near the wall was found. The local Nusselt number, Nu(ξ) was equal to the slope of the tangent to the measured dimensionless temperature profile at the hot wall surface $\Delta\theta/\Delta\tau|_{\tau=0}$, and the average Nusselt number based on the film temperature was

$$\overline{\mathrm{Nu}}_w = \frac{k_h}{k_f}\int \mathrm{Nu}(\xi)d\xi \tag{2}$$

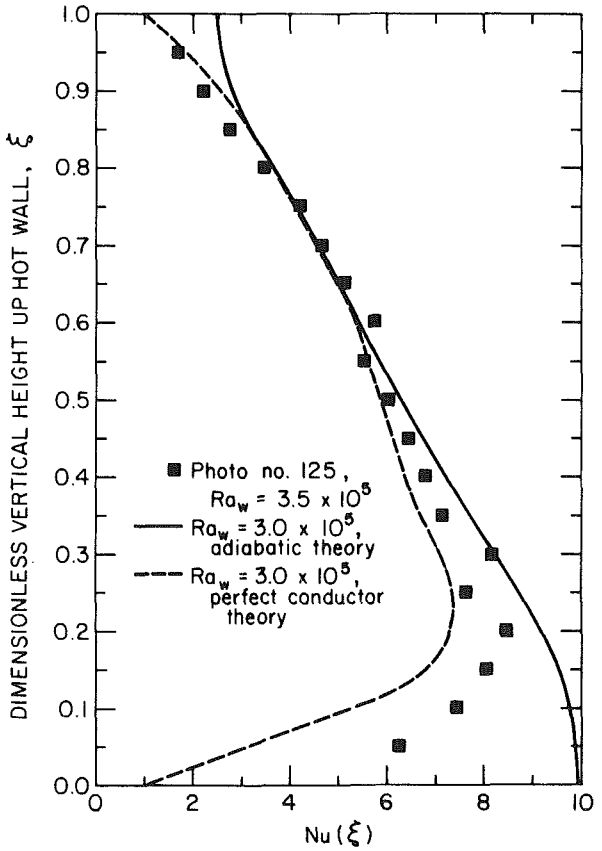

Fig. 4 Comparison of experimentally determined local heat-transfer coefficients and the theoretical predictions of Catton, Ayyaswamy, and Clever [2]

Results and Discussion

A typical local heat-transfer distribution for the hot wall of the air-filled, nonpartitioned reference enclosure is presented in Fig. 4. The local Nusselt number Nu(ξ) is plotted as a function of the nondimensional wall height, ξ. As can be seen in the figure, Nu(ξ) attains its highest value near $\xi = 0.20$. This is caused by the cold fluid, which descended from the cold wall, moved along the lower surface, and impinged on the hot wall near its base. Figure 4 also presents a comparison of the experimental local heat-transfer coefficients along the hot wall of the square enclosure to the prediction by Catton et al. [2]. Both of the theoretical curves are for $\mathrm{Ra}_w = 3.0 \times 10^5$, while the data is for 3.5×10^5. The two theoretical curves represent different boundary conditions on the unheated walls. The solid line is for the case where the unheated wall is adiabatic while the dashed line is for the case where the unheated wall is conducting perfectly between the hot and cold walls.

In a low aspect ratio enclosure, the boundary conditions on the horizontal connecting walls take on much greater importance than do the connecting surfaces in high aspect ratio enclosures. Thus, a more complete description of the horizontal boundary conditions is appropriate at this point. One difference between this investigation and other similar studies lies in the fact that all interior surfaces were carefully sprayed with at least six coats of 3M Nextel Black Velvet to give the surface an emissivity greater than 0.995. Unlike investigations with highly polished hot and cold walls, surface radiation has a significant effect on the unheated walls. For an adiabatic surface with no radiation present, the convective flux at the surface is identically zero. The black insulated surface in this investigation absorbs a radiative flux from the surrounding enclosure, but since it is insulated, it returns a radiative and convective flux back into the fluid. Thus, it is not surprising to note that on Fig. 4 the experimental data lie between the theoretical curves for adiabatic and perfectly conducting boundary conditions. The perfectly conducting boundary condition is also a case in which the horizontal surfaces have a non-zero convective flux. Given the experimental curve, the agreement with the results of Catton et al. [2] is considered excellent.

The average heat-transfer results for this air-filled, nonpartitioned enclosure are presented and compared to other previous studies in Fig. 5, as the average Nusselt number, $\overline{\mathrm{Nu}}_w$, presented as a function of the Grashof number. The data for this air-filled, nonpartitioned enclosure can be

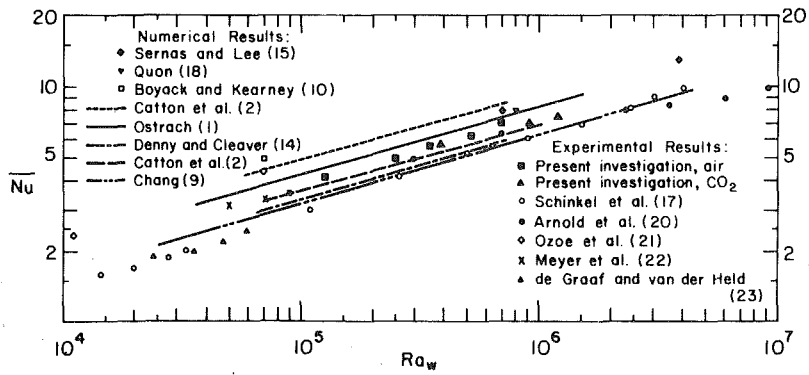

Fig. 5 Average heat-transfer results in nonpartitioned enclosures

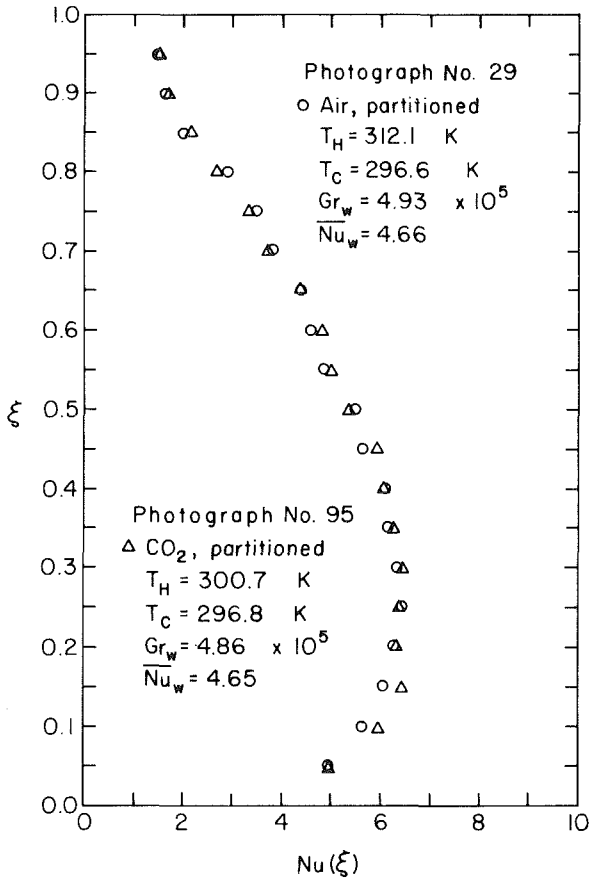

Fig. 6 Local heat-transfer results for a partitioned enclosure at $GR_w = 4.93 \times 10^5$

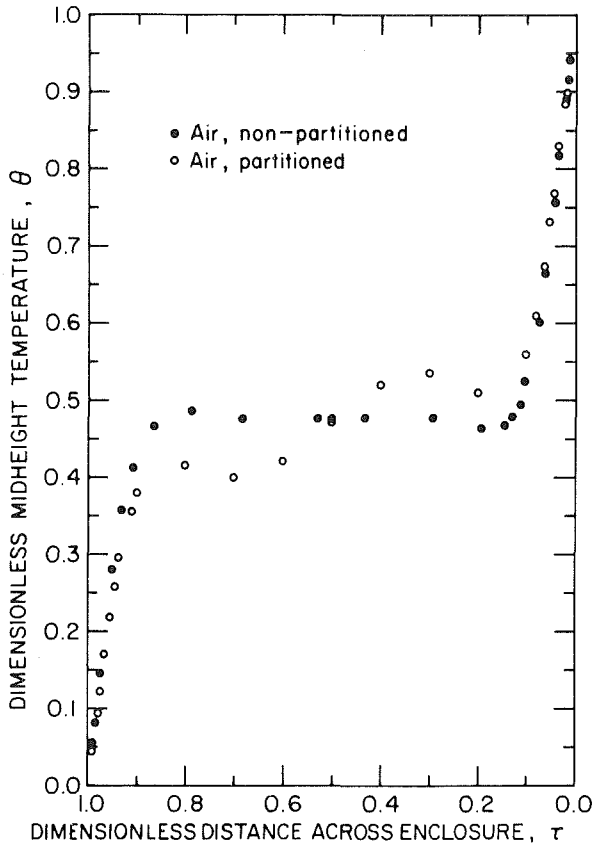

Fig. 7 Midheight temperature profiles ($\xi = 0.50$) at $Gr_w = 4.93 \times 10^5$

adequately represented by the correlation obtained by the least squares fit:

$$\overline{Nu}_w = 0.111\ Gr_w^{0.30} \tag{3}$$

Typical local heat-transfer data for the air-filled, partitioned enclosure and for the CO_2 at about the same Grashof number of 4.9×10^5 are presented in Fig. 6. The local Nusselt number Nu(ξ) is plotted versus the nondimensional wall height ξ. The maximum value of Nu(ξ) again occurs near $\xi = 0.20$, however the peak is not as well defined in the nonpartitioned enclosure as it is in the partitioned enclosure. One of the effects of the partitions is to reduce the local Nusselt numbers along the entire length of the hot wall, with the greatest reduction occurring at the base of the hot wall. It should be noted that the carbon dioxide data can be reported along with the air data without regard to gaseous radiation effects since the temperatures involved in the investigation were not high enough to be significant.

The effects of the partitions can also be seen by examination of the temperature profiles across the middle of the enclosure. Figure 7 presents the mid-height dimensionless temperature profiles ($\xi = 0.50$) of a partitioned and of a nonpartitioned enclosure at $Gr_w = 4.93 \times 10^5$. The figure shows that the temperature for the partitioned enclosure is significantly higher for $0.10 \le \tau \le 0.45$ and lower for $0.65 \le \tau \le 0.90$ than the temperature in the nonpartitioned enclosure. This is due to the deflection of the relatively warm fluid downward and the cold fluid upward by the top and bottom partitions, respectively. These deflections are clearly evident in Fig. 8, which shows the experimentally determined isotherms in the partitioned enclosure at $Gr = 4.8 \times 10^5$.

The average heat-transfer results for the partitioned and nonpartitioned enclosures are summarized in Fig. 9. As can be

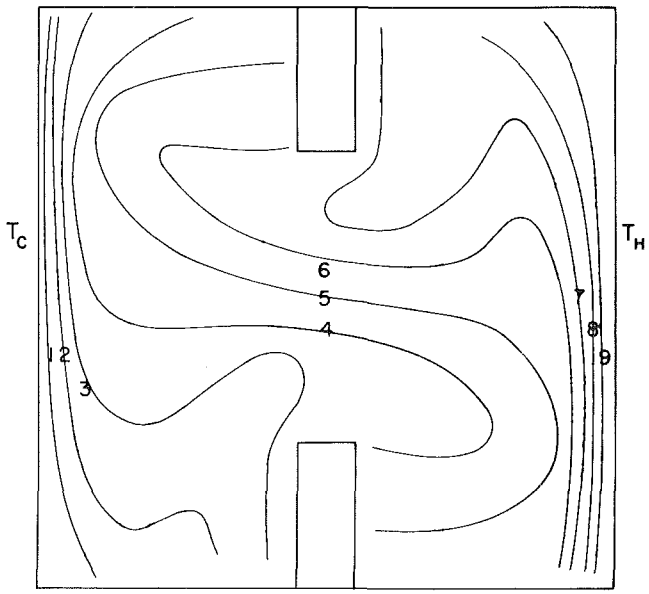

Fig. 8 Experimentally determined isotherms in the partitioned enclosure: $Gr_w = 4.74 \times 10^5$

seen in the figure, the overall effect of the partitions is to reduce the average heat transfer by approximately 15 percent. It is also significant to note that the slope of the partitioned data is slightly higher than that of the nonpartitioned enclosure. The expression obtained by the least squares fit of the data,

$$\overline{Nu}_w = 0.063 Gr^{0.33} \tag{4}$$

can be used to correlate all of the results within the partitioned enclosure to within 3.5 percent.

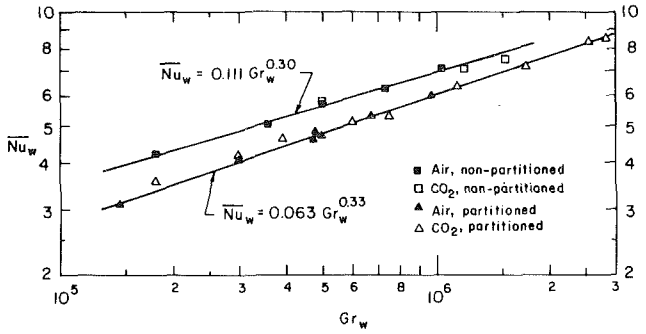

Fig. 9 Average heat-transfer results in partitioned and nonpartitioned enclosures

In the numerical studies by Chang [9], it was found that the effect of partitioning on the convective heat transfer was to reduce the Nusselt number in this Grashof number range by about 10 percent at the high Grashof numbers to 20 percent at the low Grashof numbers. The corresponding reductions in this study are, correspondingly, 12 and 21 percent.

It is appropriate at this point to mention the initiation of unsteady flow conditions. Before a photograph was taken, the image of the enclosure and the fringe shift pattern was carefully monitored on the ground glass screen of the camera in order to dectect motions in the fringe field which would indicate instabilities in the fluid. The core of the partitioned enclosure could be seen to be in motion at Grashof numbers as low as 5×10^5. Figure 10 presents a sequence of photographs showing the unsteady character of the fringe structure at a Grashof number of $Gr_w = 3.1\times10^6$. This necessitated a time averaging of the data by analyzing several interferograms. Fluctuations in the core increased and reached up into the upper corner of the hot wall and in the lower corner of the cold wall above $Gr_w = 10^6$. At a Grashof number of approximately 3.0×10^6 the motion became intense enough to bend some of the fringes such that they would break away from the main part of the fringe and form an independent circular fringe. The circular fringes would often rejoin the main fringes within 0.1 s. It is interesting that Chang [9] predicts that at about 10^6 the flow changes from a single vortex in the enclosure to a double vortex. This clearly indicates a transition process beginning. At $Gr_w = 4.0\times10^6$ it became apparent that fringes were continually moving at the hot wall for $\xi = \leq 0.20$. This turbulence is not necessarily two dimensional although the initiation of transition for free standing vertical surfaces in an infinite medium is characterized by the approximately 2-dimensional waves [24].

(a) Observe the independent circular fringes, one in the lower left hand corner, and another slightly and left of the lower partition.

(b) Faint, but distinct dots form in the relatively large white areas of the upper right hand corner and slightly below and right of the top partition.

(c) The white area becomes black in the upper right hand corner, while the dot just below the top partition is being surrounded by an adjacent fringe.

(d) The adjacent fringe has now pinched in on itself and completely enveloped the dot, while nearly breaking away from the main part of the fringe.

(e) Later, the fringe reopens from around the dot, which in this case becomes larger and darker. Notice that another circular fringe has nearly formed just left of the already independent circular fringe slightly above the lower partition.

Fig. 10 Unsteady fringe structure in the partitioned enclosure at $Gr_w = 3.1\times10^6$

Concluding Remarks

These studies show a very significant affect due to the presence of partitions in the convective heat transfer in an enclosure of aspect ratio 1. The effect is less pronounced as the Grashof number is increased. The partitions appear to have an unsettling effect on the flow field an dinduce unsteady effects at lower Grashof numbers for the nonpartitioned enclosure. The CO_2 data presented herein form the basis for follow up studies on the effects of gas radiation on enclosure heat transfer. Significant studies remain to be completed such as the determination of the velocity field within the enclosure. It would also be very significant to study conditions where gas radiation would result in enhancement of the total heat transfer.

Acknowledgments

The authors gratefully acknowledge support of this work under NSF Grant CME 7918682. The authors also wish to thank Dr. K. T. Yang for his valuable input in this study.

References

1 Ostrach, S., *Advances in Heat Transfer*, Vol. 8, Academic Press, 1972, pp. 161-227.

2 Catton, I., Ayyaswamy, P. S., and Clever, R. M., "Natural Convection Flow in a Finite, Rectangular Slot Arbitrarily Oriented with Respect to the Gravity Vector," *International Journal of Heat and Mass Transfer*, Vol. 17, 1974, pp. 173-184.

3 Catton, I., "Natural Convection in Enclosures," *Proceedings of the 6th International Heat Transfer Conference*, Vol. 6, 1978, pp. 13-31.

4 Emery, A. F., "Exploratory Studies of Free Convection Heat Transfer Through an Enclosed Vertical Liquid Layer with a Vertical Baffle," ASME JOURNAL OF HEAT TRANSFER, Vol. 91, pp. 163-164.

5 Mynett, J. A., and Duxbury, D., "Temperature Distributions Within Enclosed Plane Air Cells Associated with Heat Transfer by Natural Convection," *Proceedings of the 5th International Heat Transfer Conference*, Vol. 3, 1974, pp. 13-31.

6 Bauman, F., Gadgil, A., Kammerud, R., and Greif, R., "Buoyancy-Driven Convection in Rectangular Enclosures: Experimental Results and Numerical Calculations," ASME Paper 80-HT-66, 1980.

7 Nansteel, M. W., and Greif, R., "Natural Convection Heat Transfer in Undivided and Partially Divided Rectangular Enclosures," Personal Communications.

8 Janikowski, H. E., Ward, J., and Probert, S. D., "Free Convection in Vertical, Air-Filled Rectangular Enclosures Fitted With Baffles," *Proceedings of the 6th International Heat Transfer Conference*, Vol. 6, 1978, pp. 257–263.

9 Chang, L. C., "Finite Difference Analysis of Radiation Convection Interactions in Two-Dimensional Enclosures," Ph.D. thesis, Department of Aerospace and Mechanical Engineering, University of Notre Dame, May 1981, 302 pages.

10 Bajorek, S. M., "An Experimental Investigation of Radiation-Convection Interactions in Complex Enclosures," M.S. thesis, Department of Aerospace and Mechanical Engineering, University of Notre Dame, May 1981, 183 pages.

11 Bratis, J. C., and Novotny, J. I., "Radiation-Convection Interaction in the Boundary Layer Regime of an Enclosure," *International Journal of Heat and Mass Transfer*, 17, 1974, pp. 23–36.

12 Schimmel, W. P., Novotny, J. I., and Olsofka, F. A., "Interferometer Study of Radiation-Conduction Interaction," *Proceedings of the 4th International Heat Transfer Conference*, Vol. 2, Paper No. R2.1, 1970.

13 Eckert, E. R. G., and Carlson, W. C., "Natural Convection in an Air Layer Enclosed Between Two Vertical Plates at Different Temperatures," *International Journal of Heat and Mass Transfer*, Vol. 2, 1961, pp. 110–116.

14 Portier, J. J., and Arnas, O. A., "Accuracy of the Finite Difference Computation of Free Convection," *Heat Transfer and Turbulent Buoyant Convection*, Vol. 2, Hemisphere Publishing Co., 1977, pp. 979–806.

15 Denny, V. E., and Clever, R. M., "Comparisons of Galerkin and Finite Difference Methods for Solving Highly Nonlinear Thermally Driven Flow," *Computational Physics*, Vol. 16, 1974, pp. 271–284.

16 Sernas, V., and Lee, E. I., "Numerical Study of Heat Transfer in Rectangular Air Enclosures of Aspect Ratio Less than One," ASME Paper 80-WA/HT-43, 1980.

17 Schinkel, W. M. M., and Hoogendoorn, C. J., "An Interferometric Study of the Local Heat Transfer by Natural Convection in Inclined Airfilled Enclosures," *Proceedings of the Sixth International Heat Transfer Conference*, Vol. 6, 1978, pp. 287–292.

18 Quon, C., "High Rayleigh Number Convection in an Enclosure—A Numerical Study," *Physics of Fluids*, Vol. 15, 1972, pp. 12–19.

19 Boyack, B. E., and Kearney, D. W., "Heat Transfer by Laminar Natural Convection in Low Aspect Ratio Cavities," ASME Paper 72-HT-52, 1972.

20 Arnold, J. N., Catton, I., and Edwards, D. K., "Experimental Investigation of Natural Convection in Inclined Rectangular Region of Differing Aspect Ratios," ASME JOURNAL OF HEAT TRANSFER, Vol. 98, 1976, pp. 67–71.

21 Ozoe, H., Sayama, H., and Churchill, S. W., "Natural Convection in an Inclined Rectangular Channel at Various Aspect Ratios and Angles—Experimental Measurements," *International Journal of Heat and Mass Transfer*, Vol. 18, 1975, pp. 1425–1431.

22 Meyer, B. A., Mitchell, J. W., and El-Wakil, M. M., "Natural Convection Heat Transfer in Moderate Aspect Ratio Enclosures," ASME JOURNAL OF HEAT TRANSFER, Vol. 101, 1979, pp. 655–659.

23 DeGraaf, J. G. A., and Van Der Held, E. M.F., "The Relation Between the Heat Transfer and Convection Phenomenon in Enclosed Plane Air Layers," *Appl. Sci. Res.*, Vol. 3, 1953, pp. 393.

24 Lloyd, J. R., and Sparrow, E. M., "On the Instability of Natural Convection Flow on Inclined Plates," *Journal of Fluid Mechanics*, Vol. 42, 1970, pp. 465–470.

R. Yewell

D. Poulikakos

A. Bejan
Assoc. Mem. ASME

Department of Mechanical Engineering,
University of Colorado,
Boulder, Colo. 80309

Transient Natural Convection Experiments in Shallow Enclosures

This paper reports experimental observations on transient natural convection in enclosures at high Rayleigh numbers (1.28×10^9, 1.49×10^9) and low aspect ratios (0.0625, 0.112). The phenomenon consists of the establishment of thin intrusion layers along the horizontal adiabatic surfaces; in time, the intrusion layers exchange heat with the isothermal core of the cavity, leading to the thermal stratification of the core. The approach to steady state is gradual, contrary to the theoretical prediction of Brunt-Vaisala wave motion (Patterson and Imberger [6]). The measured durations of the observed transients agree very well with theoretical estimates.

Introduction

The objective of this paper is to report a series of experimental observations on transient natural convection in a shallow enclosure with heated vertical ends and adiabatic horizontal walls. The most recent review article on natural convection in enclosures [1] shows that the research effort on this topic is focused almost exclusively on the steady-state regime of the phenomenon. With few exceptions [2, 3], the transient regime has been overlooked, despite its fundamental role in the establishment of any steady state. Furthermore, many engineering applications of the enclosure problem operate not in the steady state but in the transient regime (e.g., solar collectors, attics and other closed spaces in buildings, the discharge of thermal pollution into shallow bodies of water).

In this paper we report experimental results documenting the transient regime in the parametric domain of high Rayleigh numbers ($10^9 - 10^{10}$) and low geometric aspect ratios (H/L = 0.0625, 0.112). As pointed out in the preceding paragraph, the present transient experiments bridge a gap in the research on convection in enclosures. The present experiments add also to the relatively scarce information available on the steady state in the (high Ra, low H/L) domain: the only steady-state experiments in this domain have just been reported [4, 5].

An important stimulus for present experimental study has been the recent theoretical paper by Patterson and Imberger [6], to which the authors of this report have had early access. Patterson and Imberger relied on pure scaling arguments to piece together complete "scenarios" for the evolution of the bouyancy-driven phenomenon in the transient regime. Patterson and Imberger were able to test some of their predictions by simulating the transient flow numerically in the parametric domain $10^{-1} < \mathrm{Ra} < 1.4\times10^5$, $H/L = 1$ and Pr = 2, 7. Inasmuch as the scaling scenarios constructed by Patterson and Imberger [6] are essential to understanding the theoretical foundation of the transient regime, it is important to verify them experimentally in the parametric domain in which they have not been tested.

The First Transient Experiment

We carried out two transient experiments in two separate enclosures, using water (Pr = 6) as the working fluid. The positions of the two experiments are labeled A, B on the (aspect ratio – Rayleigh number) chart of Fig. 1. On the same chart we show the regions occupied by four of the transient scenarios (regimes II–V) described in reference [6]. We also show some of the characteristics of each scenario. In addition to the present experiments (A,B), Fig. 1 shows the location of the numerical experiments (runs 2–5) reported in reference [6] for a square cavity filled with water. The present experiments (A,B) lie in a parametric domain which has not been investigated previously.

We performed the first experiment (A) in a shallow enclosure 2.44-m long, 15.2-cm tall and 76-cm wide (Fig. 2). The main construction details of this apparatus are reported in reference [5]. For the present experiment we increased the number of access ports through the upper wall, from 8 to 30; through these ports we lowered thermocouples and velocity probes into the cavity. In addition, we used a special temperature probe consisting of eleven bead-in-glass (1-mm dia) thermistors aligned in the vertical direction. Details of this special probe are presented in Fig. 2. The probe was mounted close to the geometric center of the cavity, with the thermistor stems oriented perpendicularly to the two-dimensional flow (i.e., normal to the enclosure cross-section shown in the top half of Fig. 2). Through this thermistor array we were able to monitor the history of the vertical temperature profile across the enclosure.

The experiment consisted of instantaneously changing the end-temperatures of the apparatus, at a time when the water space was isothermal ($T_0 = 24.0°\mathrm{C}$) and in equilibrium with the ambient. The cold-end temperature was lowered to $T_L = 15°\mathrm{C}$, by suddenly circulating precooled fluid (from a constant-temperature-bath refrigerator) through the cooling jacket of the apparatus. The warm-end temperature was raised to $T_H = 35°\mathrm{C}$, by suddenly turning the power on and dissipating 300 W in the heaters embedded in the warm end.

The selection of the proper temperature levels, T_L and T_H, formed the subject of a series of preliminary experiments in which the power dissipated in the electric heaters and the refrigerated bath temperature were adjusted until the resulting average temperature $(T_H + T_L)/2$ matched, as closely as feasable, the initial temperature of the fluid. Thus, we were able to reproduce in the laboratory the experiment theorized in [6], where both ends of the enclosure experience step temperature changes of equal magnitude. In the experiment, the end temperatures reached T_H, T_L not suddenly, but over a period of order 15 min. However, considering the time scale of the transient flow observed in the cavity (hrs, Fig. 3) we regard the temperature boundary conditions imposed on the apparatus as adequate to simulate the experiment of [6].

We monitored the experiment by recording the temperature at points under the access ports and at the eleven points defined by the thermistor array (Fig. 2). In all cases, the approach to the steady-state temperature occurred gradually. Within the accuracy of our instruments (±0.1°C), we did not detect any temperature oscillation, regardless of the position

Contributed by the Heat Transfer Division for publication in the JOURNAL OF HEAT TRANSFER. Manuscript received by the Heat Transfer Division March 1, 1982.

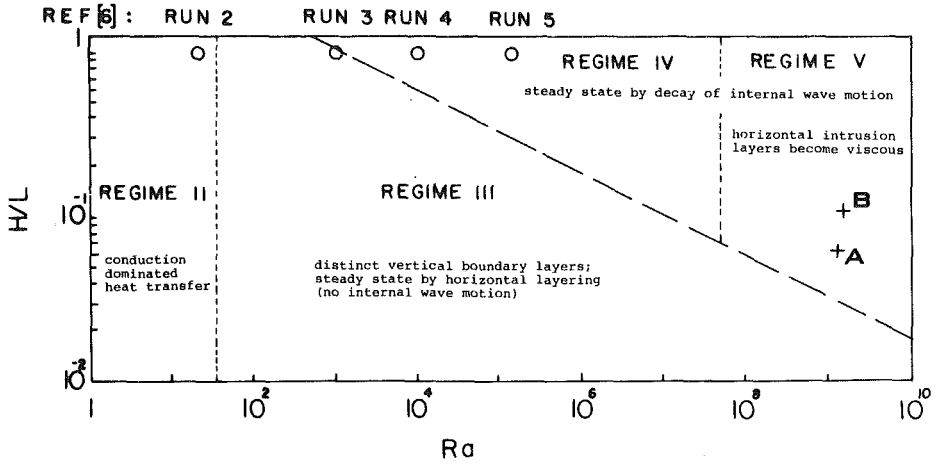

Fig. 1 Aspect ratio (H/L) – Rayleigh number chart, showing the position of the present transient experiments. The circles represent the numerical runs reported in [6].

of the temperature probe and the stage in the approach to the steady-state. In Fig. 3(*a*) and 3(*b*), we report the most representative part of this record, supplied by the thermistor array. Figure 3(*a*) shows the temperature history of each point tested in the center region of the enclosure; Fig. 3(*b*) displays the same information in a manner which emphasizes the evolution of the vertical temperature profile. The gradual approach to the steady state occurs in two distinct phases. In the first phase, which lasts approximately 4 hrs, the fluid achieves a thermally layered structure. The second phase lasts approximately 18 hrs, as is due to the slight discrepancy between the average temperature $(T_H + T_L)/2$ and the ambient T_0. In the second phase, the enclosure "as a whole" reaches a new thermal equilibrium with the ambient: the duration of this process is governed by the conductance of the thermal insulation surrounding the apparatus. In principle, this second phase could be avoided by slightly increasing the Joule heating rate or by slightly increasing the temperature of the refrigerated bath; the experiment documented in Fig. 3(*a*) and 3(*b*) represents the best we were able to do to achieve this ideal condition.

Comparison With Theory

Comparing the experimental results with scenario V envisioned by Patterson and Imberger [6], we find agreement as well as one important discrepancy. The main feature of transient regime V is the approach to steady-state via thermal layering by diffusion between the two intrusion layers (wall jets) lining the horizontal walls of the cavity. This prediction is confirmed strongly by experiment. For example, Fig. 3(*b*) shows the formation of thin thermal wall layers in the early stages of the transient (0–1hr). These thin layers surround a region of fluid which is essentially isothermal. In time, the two wall layers are cooled and, respectively, heated by the inner region. In the steady state the fluid sandwiched between the two intrusion layers is linearly stratified.

The final thermal layering and the intrusion layers are shown with great clarity in Figs. 4 and 5. Figure 4 was drawn by first measuring the vertical temperature profile under each of the 30 access ports and, on this basis, by constructing the temperature surface $T(x,y)$ prevailing over the cavity cross section. Figure 5 shows a sequence of velocity profiles measured under twelve of the thirty access ports. The velocity measurements were based on the thymol blue pH indicator method which has been used in a number of free convection experiments [7, 8]; the actual velocity probes and the velocity calculation procedure on which Fig. 5 is based are described in [8]. The velocity profiles of Fig. 5 and the isotherms of Fig. 4 show that at the end of the transient the cavity is filled by thermally stratified stationary fluid bounded above and below by wall intrusion layers. These results agree with scenario V described in [6], which predicts the presence of distinct horizontal intrusion layers in the steady state.

The duration of the thermal layering of the transient experiment, Fig. 3, is also predicted correctly by the scaling arguments presented in [6]. According to the theory, the horizontal layering should be complete when

$$t^* \sim \left(\frac{H}{L}\right)^{-1} \mathrm{Ra}^{-1/4} \tag{1}$$

where t^* is the dimensionless time

$$t^* = \frac{t}{H^2/\alpha} \tag{2}$$

and the sign "$\sim$" stands for "is of the same order of magnitude as." The time estimate t^* is based on the argument that vertical end boundary layers are well established and of order $\delta \sim H\mathrm{Ra}^{-1/4}$; the duration of the transient, t, is obtained

Nomenclature

D = vertical dimension of the second experimental apparatus, shown in the upper half of Fig. 6
g = gravitational acceleration
H = vertical dimension
k = thermal conductivity
L = horizontal dimension
N = Brunt – Vaisala frequency, equation (7)
Pr = Prandtl number
Ra = Rayleigh number, equation (3)
t = overall duration of the transient phase, equation (2)
t^* = dimensionless time of transient, equation (1)
T_H = warm end temperature
T_L = cold end temperature
T_0 = initial temperature
ΔT = temperature difference, $T_H - T_0$
x,y = horizontal and vertical coordinates
α = thermal diffusivity
β = coefficient of thermal expansion
δ = thickness of the vertical boundary layers
ν = kinematic viscosity
ω = frequency of internal wave motion, equation (6)

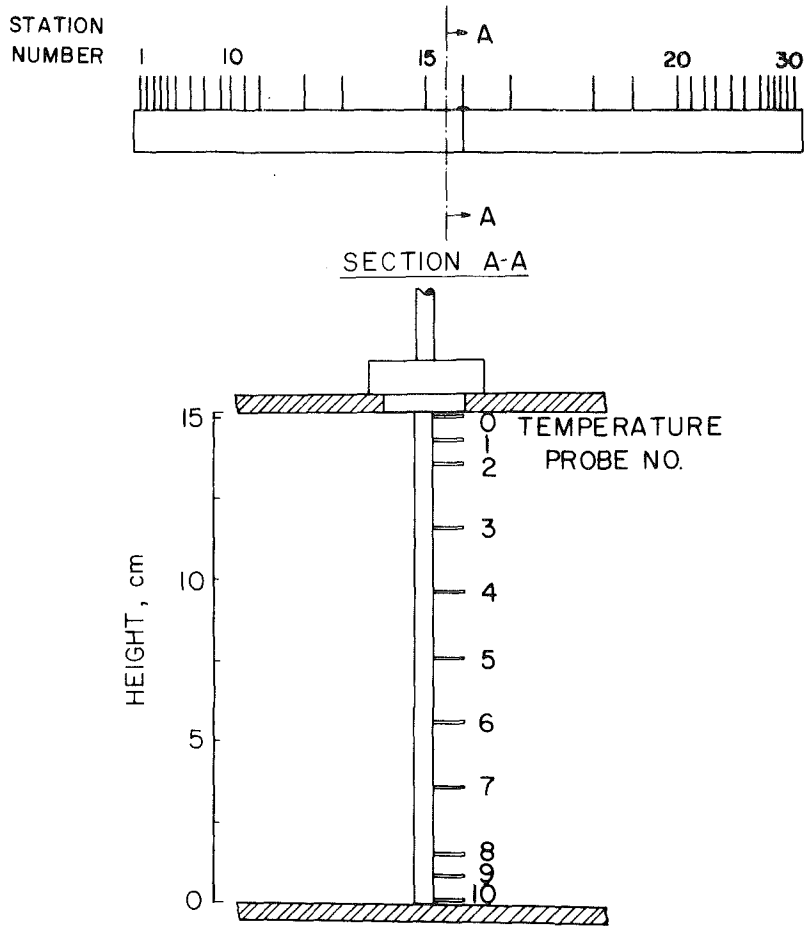

Fig. 2 Top: longitudinal vertical cross section through the first experimental apparatus: bottom: details of the aggregate temperature probe

by dividing the thermal inertia of the entire cavity, $(k/\alpha)\ HL\Delta T$, by the end heat-transfer rate, $kH\Delta T/\delta$. For the transient experiment of Fig. 3, we have

$$\mathrm{Ra} = \frac{g\beta H^3 (T_H - T_L)}{\alpha\nu} = 1.28 \times 10^9 \tag{3}$$

which, combined with $H/L = 0.0625$ and expressions (1, 2) yields

$$t \sim 3.7 \text{ hr} \tag{4}$$

This estimate agrees very well with the duration of the approach to thermal stratification shown in Fig. 3(*a*); for example, the highest probe (no. 0, bottom of Fig. 2) records the peak temperature in the upper intrusion layer at t = 4 hr. The same time constant governs the evolution of the temperature measured by the remaining thermistors in the array.

The important discrepancy between experimental results and theory [6] concerns the absence of oscillations in the approach to steady state. Patterson and Imberger argued that for Rayleigh numbers in excess of

$$\mathrm{Ra} \sim \left(\frac{\mathrm{Pr}}{H/L}\right)^4 \tag{5}$$

one should observe an internal wave motion with a frequency of order

$$\omega \sim \frac{N}{[1 + (H/L)^2]^{1/2}} \tag{6}$$

where N is the Brunt-Vaisala frequency [9]

$$N \sim \frac{(\alpha\nu \mathrm{Ra})^{1/2}}{H^2} \tag{7}$$

According to criterion (5), the internal wave motion is to be expected in domains IV and V on Fig. 1. For the first transient experiment (A), expressions (6, 7) yield

$$N \sim \omega \sim 0.55 \mathrm{s}^{-1} \tag{8}$$

The corresponding period of the oscillation is of order 11.5s. Although a fluctuation of this type is well within our measuring capability, we were unable to detect it. As mentioned in the preceding section, the temperature of all the points sampled in the cavity evolved smoothly.

The discrepancy between the "wave" prediction and the "no-wave" observation could be attributed to the fact that experiment (A) lies relatively close to the wave/no-wave boundary (5) (frontier between scenarios III and IV on Fig. 1). To check the validity of this explanation, we conducted a second transient experiment which, parametically, is situated further from the wave/no-wave boundary (5).

The Second Transient Experiment

We performed the second experiment (B) in a water-filled horizontal cylindrical enclosure with different end-temperatures. Details regarding the construction of this apparatus were given in an earlier paper on steady-state natural convection in a horizontal pipe [8]. The enclosure has a 14-cm dia and a length of 1.25 m, hence, the geometric aspect ratio ($D/L = 0.112$) is almost double compared with that of the first experiment. We consider this enclosure adequate for testing the two-dimensional theoretical arguments [4] because, as shown in [8], in the high Ra regime the end (vertical) boundary layers as well as the horizontal

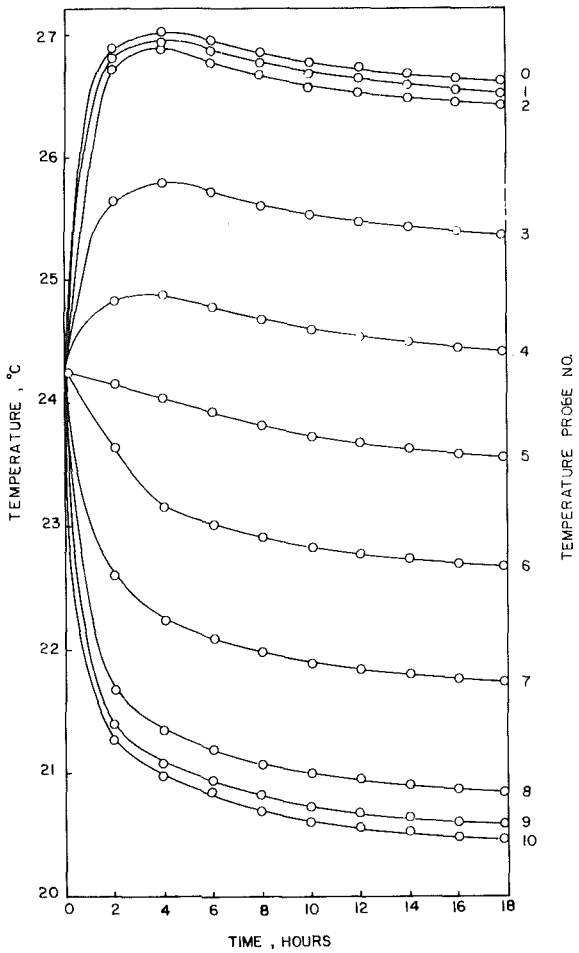

Fig. 3 (*a*) Temperature history at points 0–10 situated along the aggregate temperature probe (Fig. 2)

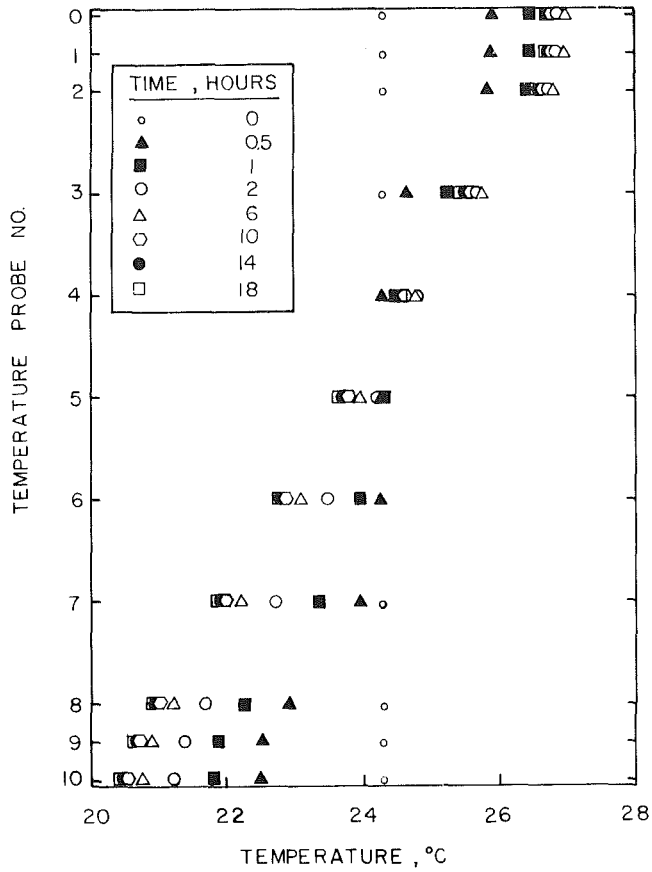

Fig. 3 (*b*) The evolution of the vertical temperature profile in the center of the enclosure

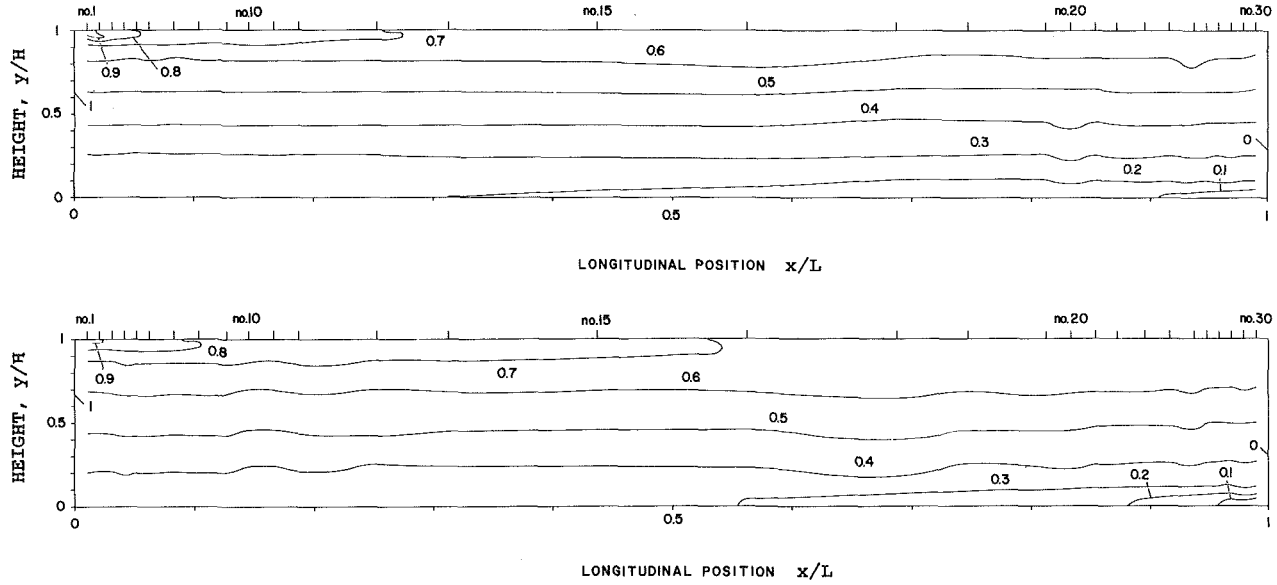

Fig. 4 Pattern of isotherms at the end of the transient experiment: top, Ra = 7.67 × 10^8; bottom, Ra = 1.82 × 10^9. The numbers on the isotherms represent $(T-T_L)/(T_H-T_L)$.

intrusion layers are *thin* relative to the third dimension of the enclosure (D, perpendicular to the sketch shown in the upper half of Fig. 6). At a high enough Ra, the horizontal cylinder behaves very much like a horizontal two-dimensional cavity. This opinion is the result of the earlier experiment [8] which sought and was unable to document the effect of wall curvature. It was found that at a Rayleigh number of order 10^9 the vertical end layers have a thickness of order $D\mathrm{Ra}^{-1/4} \sim 1$

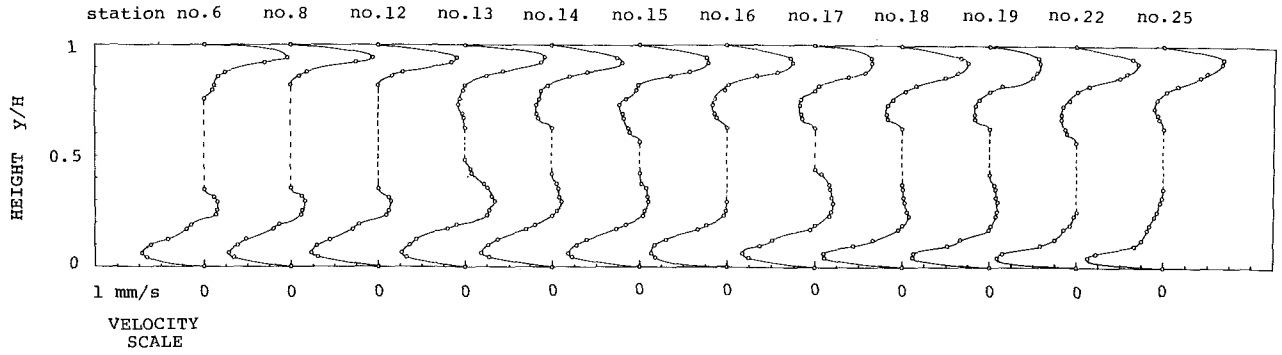

Fig. 5 Horizontal velocity profiles at twelve longitudinal positions *along the cavity* (Ra = 7.67 × 10^8); *see Fig. 2 for the numbering* sequence of the access ports (stations)

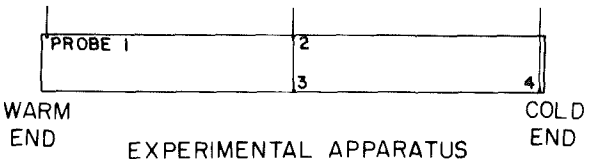

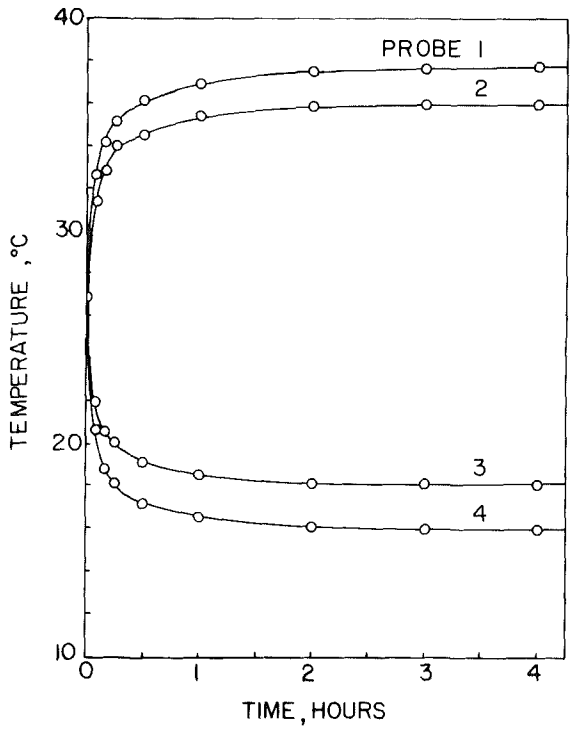

Fig. 6 Top: longitudinal vertical cross section through the second experimental apparatus; bottom: Temperature history at four representative locations in the cavity

mm, whereas the horizontal layers have a maximum thickness of order 1 cm. These scales are the same as the ones measured in a two-dimensional cavity at the same Ra [5]. The experiment of [8] also showed that the core of the horizontal cylinder is nearly identical to the two-dimensional core observed in [5]. Thus, the high Ra circulation established in experiment B is fundamentally the same as the flow observed in experiment A. Indeed, in a circular cross section through the cylinder, the top and bottom horizontal layers have flat cross sections (as in experiment A) which indicate that the wall curvature effect on the horizontal jets is minimal.

The experimental procedure was essentially the same as in the first experiment. The pertinent data describing this second transient are

$$T_0 = 27.5°C$$
$$T_H = 42°C,\ T_L = 12°C \tag{9}$$
$$\mathrm{Ra} = 1.49 \times 10^9,\ D/L = 0.112$$

The end temperatures were established within 7 min by dissipating 115 W in the warm-end electric heaters, and by connecting the cooling jacket of the cold-end to a constant-temperature-bath refrigerator. The water temperature was monitored using chromel-alumel (type K) thermocouples, which were lowered into the cavity through the access ports. Since we were primarily interested in temperature fluctuations, the output from the thermocouples was recorded on tape or, if desired, displayed on the screen of an oscilloscope.

The observed transient behavior of the cavity is similar to the behavior documented in experiment A (Figs. 3–5). Once again, we *did not* detect any temperature fluctuations. Figure 6 shows the temperature history at four places in the cavity, labeled 1–4 on the apparatus cross section. The steady state is achieved in approximately 2 hrs: this time interval is in very good agreement with the theoretical calculation

$$t^* \sim \left(\frac{D}{L}\right)^{-1} \mathrm{Ra}^{-1/4} = 0.0454 \tag{10}$$
$$t = \frac{D^2}{\alpha} t^* \sim 1.68 \text{ hrs}$$

The approach to the steady state is gradual, suggesting once again that at least in the area covered by experiments A and B, the thermal waves are not a feature of scenario V envisioned by Patterson and Imberger [6].

In both experiments, A and B we searched for temperature oscillations using thermocouple probes (not thermistors). We used chromel-alumel thermocouples with a bead diameter of 0.4 mm. The response time of the thermocouples is 2 s, which makes them compatible with the task of detecting an oscillation of period 11.5 s. Thermistors were used only in the array (Fig. 2) to track the evolution of the entire temperature profile. The thermistor response time is 20 s, which is adequate for recording a transient phenomenon with a 2 hr time constant (Fig. 3(*a*)).

Conclusions

This paper reported experimental observations on transient natural convection in shallow enclosures, at high Rayleigh numbers, and low aspect ratios. When the end-temperatures of the enclosure are changed suddenly, the approach to the steady state exhibits the following general characteristics:

1 The horizontal adiabatic walls of the cavity are lined by thin intrusion layers surrounding an isothermal (motionless) core region.

2 The thermal diffusion between the core region and the intrusion layers leads, in time, to the thermal stratification of the core region.

3 The steady state is achieved within a time of order

$$t \sim \frac{H^2}{\alpha}\left(\frac{H}{L}\right)^{-1} \mathrm{Ra}^{-1/4}$$

4 The approach to steady state is gradual, i.e., free of the wave activity predicted by [6].

Overall, the experimental observations support the theoretical scenario V constructed by Patterson and Imberger [6] for the high Ra - low H/L limit considered in this study. The only discrepancy between theory and experiment is in the absence of Brunt-Vaisala waves (conclusion 4, above). Therefore, the boundary between scenarios III and V (Fig. 1) is not realistic as frontier between "gradual" and "fluctuating" transients.

Acknowledgment

This research was supported by the National Science Foundation through grant No. ENG. 78-20957. The authors acknowledge the discussion held on this subject with Professors John Patterson and Jorg Imberger, during the summer of 1980.

References

1 Catton, I., "Natural Convection in Enclosures," *Proceedings of the 6th International Heat Transfer Conference*, Toronto, 1979, Vol. 6, pp. 13-43.

2 Wilkes, J. O., and Churchill, S. W., "The Finite-Difference Computation of Natural Convection in a Rectangular Enclosure," *AIChE Journal*, Vol. 12, 1966, pp. 161-166.

3 Cormack, D. E., Leal, L. G., and Seinfeld, J. H., "Natural Convection in a Shallow Cavity With Differentially Heated End Walls: Part 2—Numerical Solutions," *Journal of Fluid Mechanics*, Vol. 65, 1974, pp. 231-246.

4 Ostrach, S., Loka, R. R., and Kumar, A., "Natural Convection in Low-Aspect Ratio Rectangular Enclosures," paper presented at the 19th National Heat Transfer Conference, Orlando, Fla., July 27-29, 1980, ASME publication HTD, Vol. 8, pp. 1-10.

5 Bejan, A., Al-Homoud, A. A., and Imberger, J., "Experimental study of high Rayleigh Number Convection in Horizontal Cavity With Different End Temperatures," *Journal of Fluid Mechanics*, Vol. 109, Aug. 1981, pp. 283-299.

6 Patterson, J., and Imberger, J., "Unsteady Natural Convection in a Rectangular Cavity," *Journal of Fluid Mechanics*, Vol. 100, 1980, pp. 65-86.

7 Imberger, J., "Natural Convection in a Shallow Cavity With Differentially Heated End Walls: Part 3—Experimental Results," *Journal of Fluid Mechanics*, Vol. 65, 1974, pp. 247-260.

8 Kimura, S., and Bejan, A., "Experimental Study of Natural Convection in a Horizontal Cylinder With Different End Temperatures," *International Journal of Heat and Mass Transfer*, Vol. 23, 1980, pp. 1117-1126.

9 Turner, J. S., *Bouyancy Effects in Fluids*, Cambridge University Press, Cambridge, 1979, p. 11.

S. A. Korpela
Associate Professor,
Department of Mechanical Engineering,
The Ohio State University,
Columbus, Ohio 43210
Mem. ASME

Yee Lee
Advanced Engineer,
Technical Center,
Owens-Corning Fiberglas,
Granville, Ohio 43023
Assoc. Mem. ASME

J. E. Drummond
Assistant Professor,
Department of Mechanical Engineering,
University of Akron,
Akron, Ohio 44325
Assoc. Mem. ASME

Heat Transfer Through a Double Pane Window

By finite difference calculations the convective flow in a vertical enclosure heated from a side is investigated. The emphasis in the study is for the flow of air in a window cavity. Detailed plots of the stream patterns and isotherms in a multicellular flow are shown and vertically averaged Nusselt numbers as well as typical local values are given. The calculations compare favorably with the experiments of ElSherbiny, Raithby, and Hollands. A working formula for window spacings is suggested.

1 Introduction

Heat transfer across an air cavity such as exists in a double pane window is an old problem in natural convection. Although in practice the temperature of neither of the two windowpanes may be uniform, to estimate the heat transfer across the air gap the best one can do today is to use correlations obtained from experiments on cavities in which the vertical sidewalls were kept isothermal. Whether the top and bottom of the cavity are made of highly conducting material or of material of low conductivity introduces further uncertainty to the estimate.

The circulating flow in a window cavity is sufficiently complex that a closed form solution has not been found. Consequently, our present understanding of the flow is the result of a slow progress through what might be called a rocky road of experiments and approximate analyses. On the one hand the well quoted experiments of De Graaf and van der Held [1] are inconsistent with the analysis by Jacob [2] of some of the other early experiments. And neither Jacob's nor de Graaf and van der Held's correlation lends itself to a good theoretical explanation. On the other hand, lack of detailed experimental information about the flow and temperature field inside the cavity led Batchelor [3] to advance a theory which later needed to be reworked.

It was only after the interferometric studies by Soehngen [4] and Eckert and Carlson [5], that the thermal structure of the flow became known. Important also was the study of Elder [6] of the velocity field, and it was these two studies which allowed Gill [7] shortly thereafter to work out a boundary layer theory for the flow. Some improvements into Gill's theory have been made by Bejan [8] and Graebel [9], but the dependence of the Nusselt number on the aspect ratio is still not completely settled.

To obtain the best insulation from the double pane window, the flow in the cavity turns out to be different than that which the boundary layer theory explains. For the range of parameters appropriate for double pane windows numerical methods have best promise to predict the flow patterns. In the early numerical solutions the emphasis was, however, on low aspect ratio cavities, for the reason that the number of grid points could thus be kept tolerably low. The notable exceptions are the studies of Newell and Schmidt [10], Thomas and de Vahl Davis [17] and Jones [12], who have considered cavities with aspect ratios as high as 20. We have taken another look at this problem, and by numerical experiments hope to give a clearer picture of the behavior of the convective flow in a window cavity and the heat transfer resulting thereof.

We assume that an independent calculation is made of the contribution of thermal radiation and that the model of isothermal sidewalls is adequate to describe a double pane window. We are then concerned with the relative contribution of conduction and convection to the transfer of energy across the enclosed air space. For a small spacing convection is absent and from Fourier's law one sees that the heat transfer is inversely proportional to the gap width; thus increasing the spacing of the panes decreases the heat transfer. On the other hand, when convection dominates it is not obvious at first sight how the heat transfer should vary with the pane spacing. One can get at a partial answer by a couple of straight forward steps from a heat-transfer correlation, which is of the form

$$\mathrm{Nu} = C\mathrm{Ra}^{\alpha}A^{-\beta}$$

In the Nusselt and Rayleigh numbers the length scale, L, is the gap width. Also in this expression the letter A is meant to stand for the aspect ratio. Under the conditions when this correlation is valid, the heat transfer increases as the gap is made wider if $3\alpha + \beta - 1 > 0$.

Emery and Chu [13] report the values of $\alpha = 0.250$ and $\beta = 0.250$. These show that the heat transfer is independent of L. The same conclusion was drawn by Mynett and Duxbury [14] who based on their experiments, concluded that $\alpha = 0.263$ and $\beta = 0.210$. Other correlations give different values for α and β. If these two particular sets of values are nearly correct, one is lead to ask whether the heat transfer decreases monotonically, or is there an overshoot. In the latter case there would be an optimum spacing for the panes. Calculations by de Vahl Davis [15] and Thomas and de Vahl Davis [11] indicate that an optimum exists. Rather than trying to fit their data into a single correlation, they organized it according to the classification of the flow by Eckert and Carlson [5], and provided three correlations, one for the conduction, another for the transition, and a third for the boundary layer regime. It was in the boundary layer regime in which they found the heat transfer to be quite independent of the aspect ratio. This case corresponds to a wide gap between the panes. As the gap is made narrower the flow enters the

Contributed by the Heat Transfer Division for publication in the JOURNAL OF HEAT TRANSFER. Manuscript received by the Heat Transfer Division July 23, 1981.

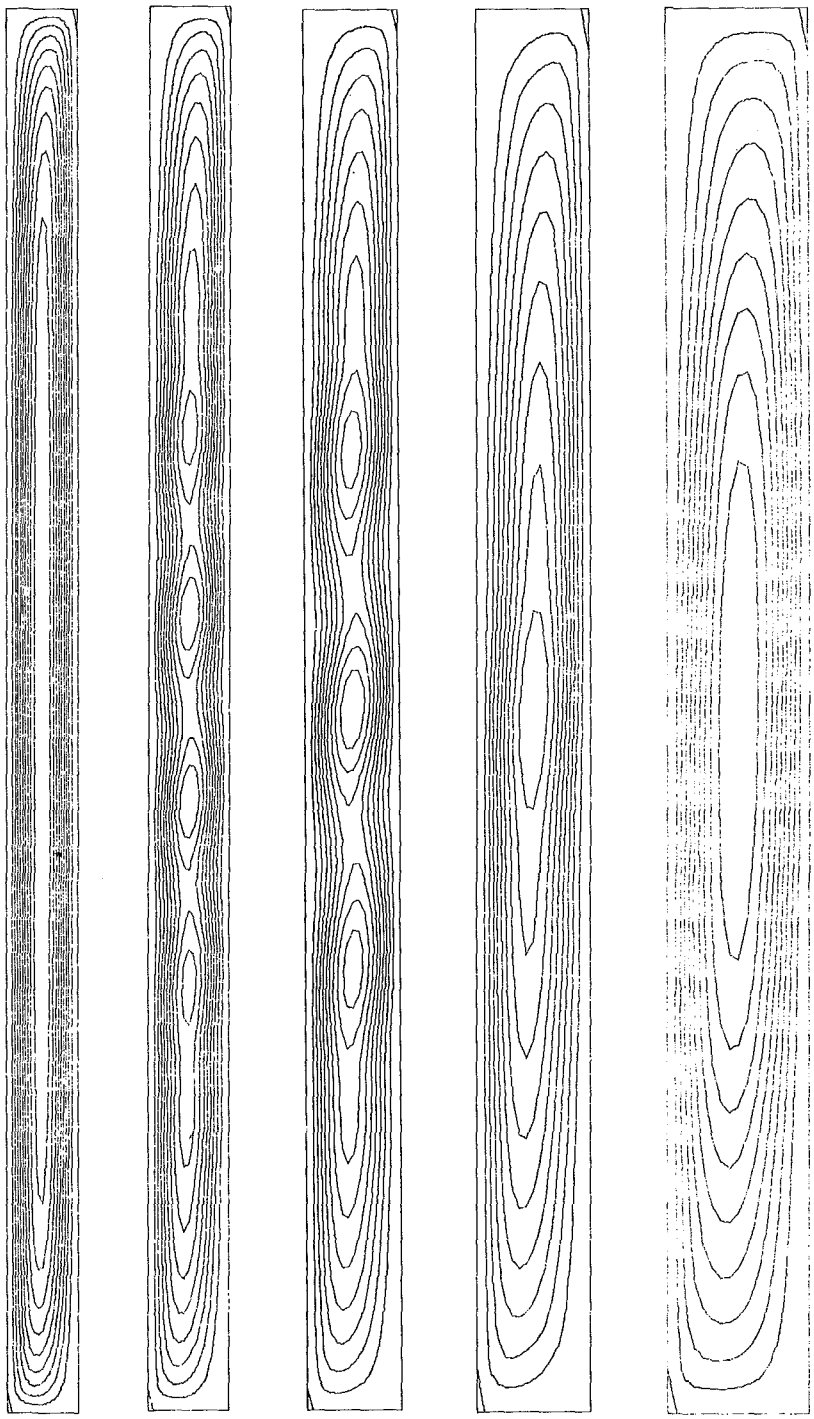

Fig. 1 Natural convection of air in a cavity of $Gr_H = 6.4 \times 10^7$ as a functions of aspect ratio A

Nomenclature

A = aspect ratio, H/L
C = constant
g = gravitational acceleration
Gr = Grashof number, $g\beta\Delta TL^3/\nu^2$
Gr_H = Grashof number, $g\beta\Delta TH^3/\nu^2$
h = heat-transfer coefficient
H = height of the enclosure
k = thermal conductivity
L = width of the enclosure
Nu = Nusselt number, $\bar{h}L/k$
Nu_H = Nusselt number, $\bar{h}H/k$
Nu_y = local Nusselt number, h_yH/k
Pr = Prandtl number, ν/α
Ra = Rayleigh number, $g\beta\Delta TL^3/\alpha\nu$
ΔT = temperature difference
α = thermal diffusivity
β = coefficient of volumetric expansion
ν = kinematic viscosity

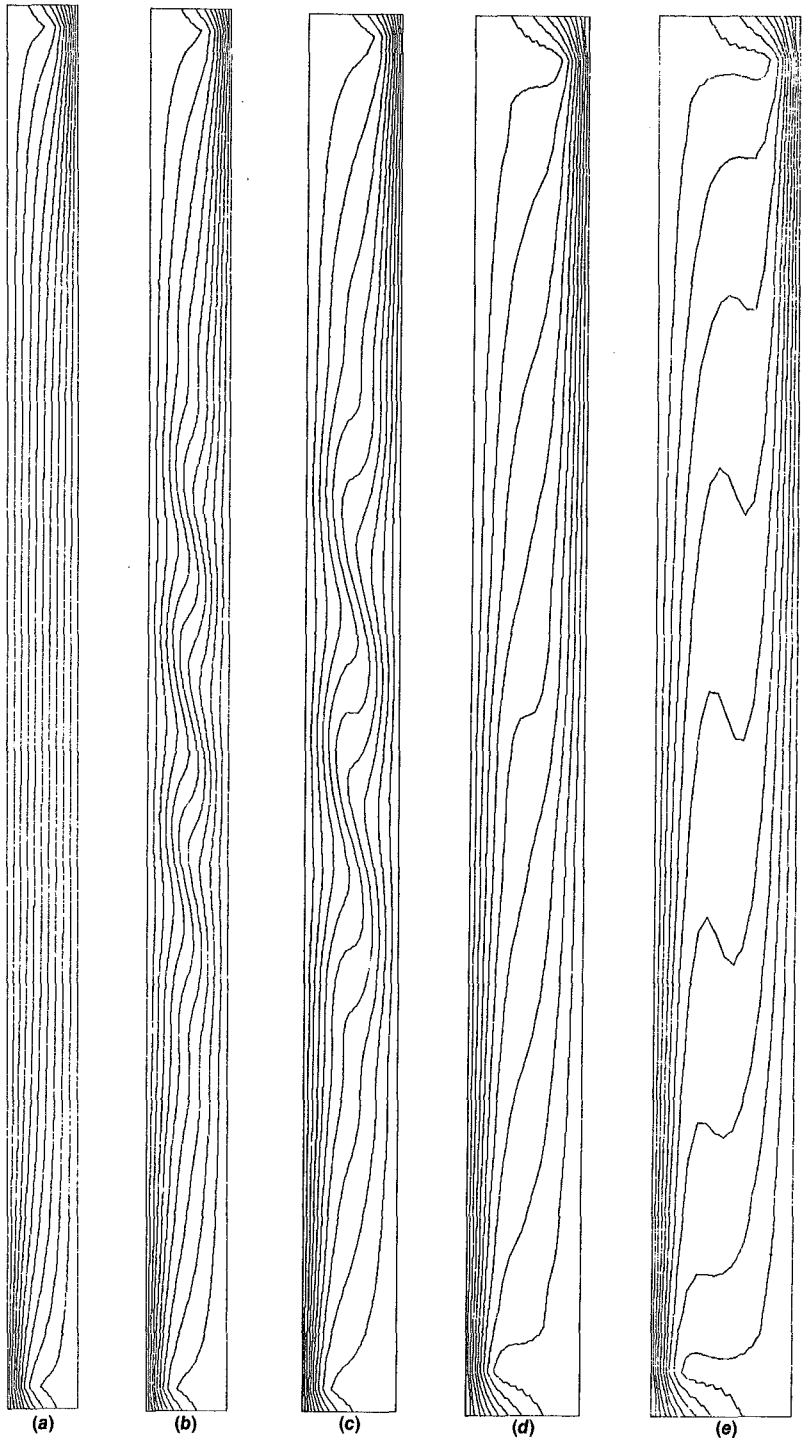

Fig. 2 Isotherms corresponding to conditions cited in Fig. 1

transition regime and the heat transfer drops until conduction becomes the dominant mode. Further reduction in the gap width increases the heat transfer as predicted by Fourier's law. The optimum gap width appears to be near the changeover from the conduction to the transition regime. It may be that in many of the correlations which can be found in the literature, data to construct a correlation have been included from both the transition and boundary layer regimes, with the result that α, and particulary β, have values which vary greatly from one correlation to the next.

So far so good, but there is another aspect to be thought about; namely, window cavities often have very large aspect ratios and in such cases the structure of the convective flow in the cavity is known to be quite different than it is in enclosures of low aspect ratio. Experiments by Vest and Arpaci [16] show that above $Gr = 8000$ or so the flow undergoes a transition to a multicellular pattern. Stability calculations by Rudakov [17], Korpela, Gözüm, and Baxi [18] and by Bergholz [10] affirm this as well. This changes the picture, because if the Nusselt number for a multicellular flow is correlated as above the factor involving the aspect ratio drops out for a very tall cavity. The reason for this is that increasing the aspect ratio only changes the number of cells and not the heat transfer across them. The correlation would now become similar in form to the one in the boundary layer regime, but for a different reason. Actually, for cavities of only

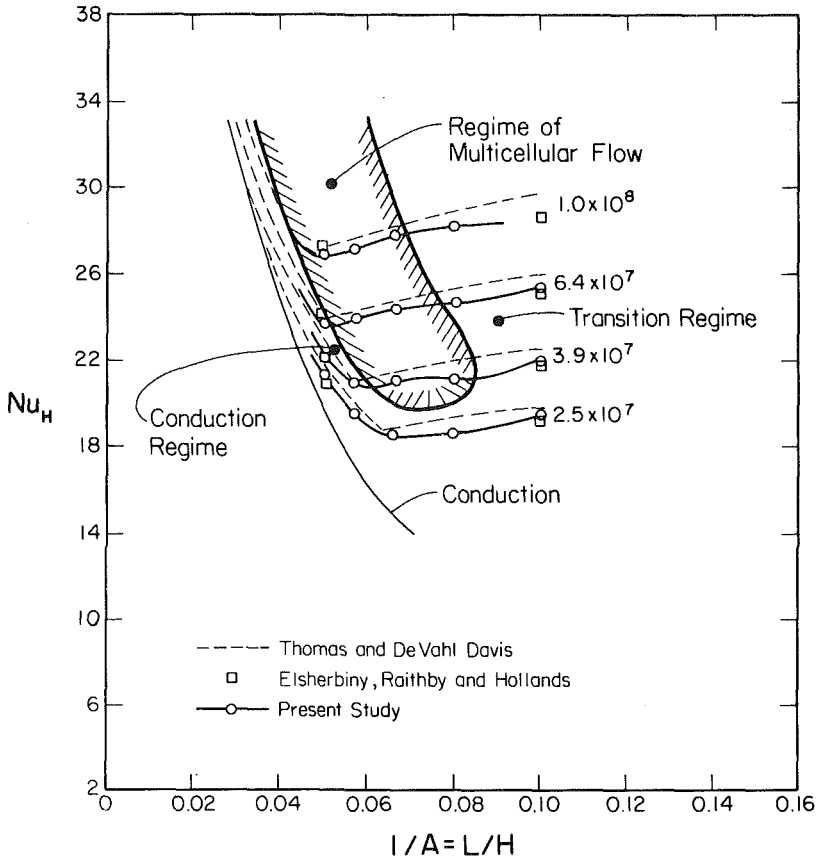

Fig. 3 Average Nusselt numbers Nu_H as a function of inverse of the aspect ratio for convection of air, Pr = 0.71, in a vertical cavity. The four curves correspond to different values of Grashof number, Gr_H.

moderately large aspect ratio a substantial part of the energy is still convected across the top end of the slot so that the Nusselt number for this reason does depend on the aspect ratio. In any case the question of heat transfer in multicellular flow of air is still open and the aim of this note is to provide a small contribution to this area of knowledge.

2 Analysis

Our approach has been to integrate the Boussinesq equations numerically, using finite difference techniques. In particular we cast the equations in the vorticity-stream function form and used centered time differences, the Arakawa differencing for the convective terms, and the DuFort-Frankel method for the diffusive terms. The Poisson equation we solved by the Buneman's odd-even reduction scheme with a program given to us by Horne [20]. The Arakawa's method we chose with the expectation that it would work well in a problem which undergoes a transition to a multicellular flow as a result of hydrodynamic instability. The reason why it ought to work, as pointed out by Roache [21], is that the method conserves vorticity, square of vorticity and kinetic energy, and similar quantities in the energy equation. The technique has been used in natural convection by Quon [22], Wirtz and Liu [23] and Horne [20]. The DuFort-Frankel method of differencing the diffusion term removes the diffusive stability criterion and only the Courant condition must be observed.

Most of our calculations were made on a 17 × 65 grid. The Nusselt number we calculated with a three point finite difference formula at the wall, and obtained the average value by integrating over the height of the cavity using Simpson's rule. We checked our calculations against the results of Chu and Churchill [24] and Roux et al. [25] for a square cavity. We found that our Nusselt number, calculated on 17 × 17 grid, was 5.7 percent higher at Gr = 70420 than that obtained by averaging their results. For a 33 × 33 grid the difference reduced to 1.7 percent. Their results differed by 3.9 percent from one another. This is the order of magnitude of the error we were forced to tolerate to keep the computation time within reason. For tall cavities we checked the steady-state energy transport across each vertical plane and found that for 17 × 65 grid it varied no more than ± 1.9 percent from the mean.

3 Results

The result of computing the stream pattern and isotherms is shown in Fig. 1 and 2. In these figures the hot wall is at the left and the fluid in the cavity is air with Pr = 0.71. The Grashof number, $Gr_H = g\beta\Delta TH^3/\nu^2$, is based on the vertical height, H, and has the constant value 6.4 × 10^7 for these plots. The aspect ratio varies from 20 to 10. On the leftmost figure the flow is unicellular and dominated by conduction. In the next two the flow has undergone a transition to a multicellular flow. From the isotherms in Fig. 2, one sees there is little background thermal stratification in the flow in the region where the cells are. This is in contrast to flows at large value of Prandtl number in which de Vahl Davis and Mallinson [26] and Seki et al. [27] have shown that a strong stable vertical temperature gradient exists in the flow and distortion of the isotherms by the cellular structure perturbs this only mildly. At the value of A = 12.5 and 10, the flow is in the transition regime according to the classification by Eckert and Carlson [5]. The flow is unicellular and free from effects of hydrodynamic instability. In both of these figures a

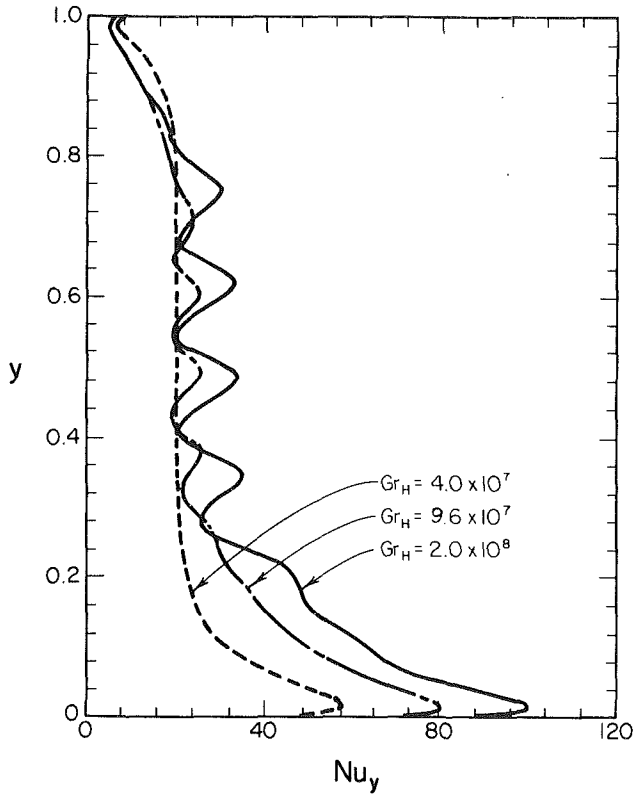

Fig. 4 Local values of Nusselt number for convection of air in Cavity with an aspect ratio $A = 20$

vertical stable temperature gradient is evident. Actually the flow in cavities with aspect ratios from 12.5 to 15 change from a conduction dominated flow to a multicellular flow and then to a unicellular flow in a transition regime, as the Grashof number based on the height is increased. Thus, at $A = 12.5$ the flow shown in the figure would actually look more like that for $A = 15$ were the Grashof number lower. For $A = 10$ this does not happen.

We have made a map of the multicellular flow conditions and show this in Fig. 3. That figure also shows the average Nusselt number, based again on height, as a function of the inverse of the aspect ratio. The Grashof number based on height is a parameter for the curves. This way of presenting the data is useful for a designer because he or she can immediately see how the gap width changes the heat transfer, for now the ordinate is directly proportional to the heat transfer and the abscissa to the gap width. The Grashof number, for a cavity of given constant height and for a given fluid, is then directly proportional to the temperature difference between the walls of the cavity. Also shown in the figure are curves obtained from the correlations of Thomas and de Vahl Davis [11]. Throughout the entire range of the calculations our results differ from theirs by only a couple of percent. We have plotted only their correlations from the conduction and transition regimes. The boundary layer regime occurs further to the right in the figure and we have no results there. Other correlations for the boundary layer and transition regimes such as that of Newell and Schmidt [10] is about 10 percent higher than our values, and that of Berkovsky and Polevikov [28] about 10 percent lower.

So far we have not mentioned the study of ElSherbiny, Raithby and Hollands [29]. This is an important experimental investigation for they report data in it for cavities with aspect ratios as high as 110. It complements the study of Hollands and Konicek [30] nicely, and the data they present in this article is probably the most accurate obtained so far. When we plot the data from their correlation on Fig. 3, we see that our calculations fall very close to their experimental values. We think this close agreement to be actually somewhat fortuitous. There are two reasons why the two sets of data should differ. First, we were not able extrapolate our results to zero grid size for the reason that the Nusselt numbers did not vary monotonically at first as the grid spacing was made smaller, and we could not afford to calculate at sufficiently small grid spacings to obtain monotonicity. From the trends, however, we estimate that our results are approximately 4–5 percent too high. The second reason why our results should differ from theirs is that their experimental cavity was constructed to have a highly conducting top and bottom. For a square cavity, Roux et al. [25] show that a conducting top and bottom boundaries give lower values for the Nusselt number than those obtained for insulated lateral walls. How large this influence is for cavities with aspect ratios greater than 10 is not clear at this time but correcting for it would shift that data of ElSherbiny, Raithby and Hollands above our calculated values.

As near as we can tell from our calculations, the cavity insulates best just before the flow undergoes a transition to a multicellular flow. But the curves are rather flat after the minimum, so it is better to make the gap too wide than too narrow. As the flow enters the multicellular regime the local Nusselt numbers undergo a change. In Fig. 4, these are shown at the hot wall for three values of Grashof number. The aspect ratio in this case is 20. The maximum value occurs at the bottom corner where the cold fluid which has been swept across the bottom end comes to contact with the hot wall creating a steep temperature gradient. Once heated the fluid ascends and for a flow without cells does not change in temperature. The Nusselt number is equal to the aspect ratio, which means that energy under these conditions gets transferred across the slot entirely by conduction. At the top the fluid turns toward the cold wall creating a mild temperature gradient at the hot wall and thus a lower value for the local Nusselt number. In the cellular flow, energy is transferred by convective motion across the cells. The local peaks are at the locations where the returning colder flow again comes to the closest contact with the hot wall.

From Fig. 3 one sees that the multicellular flow structure actually does not change the heat transfer by much. The reason is that most of the energy is transferred across the ends. Only for cavities with aspect ratios of the order of 40 or more would the multicellular convection be truly significant. We don't have calculations for such high aspect ratios, but they would be worthwhile to carry out because, particularly in commercial buildings, windows are often very tall. In the meantime near optimum insulating capacity can be obtained by spacing the panes wide enough apart so that the flow is on a verge of undergoing a transition to a multicellular flow. From the results of Bergholz [19] one can derive a working formula for the spacing. In terms of the aspect ratio it becomes,

$$A^3 + 5A^2 = 1.25 \times 10^{-4} \mathrm{Gr}_H$$

For $\mathrm{Gr}_H = 1 \times 10^8$ this equation gives $1/A = 0.046$ and for $\mathrm{Gr}_H = 6.4 \times 10^7$ it gives $1/A = 0.054$. Both of these values are near the minimum of our calculated curves. For aspect ratios sufficiently large so that the second term can be neglected the equation reduces to $\mathrm{Gr} = 8000$, the value corresponding to a transition to a multicellular flow from the conduction regime.

4 Acknowledgment

The results we have put forth in this paper were intended as a guide to spacing of panes in windows. We have written two additional articles [31, 32] in which we discuss more fully such

things as the effect of Prandtl number on the flow in a vertical cavity and the structure of natural convection in a vertical annulus. Our research has been supported by the Heat Transfer Program of the National Science Foundation and in part by the Instructional and Research Computer Center of The Ohio State University in the form of computing funds to the Department of Mechanical Engineering. We are grateful to both of these sources for their support.

We are also grateful to the reviewers for their constructive criticisms of the earlier version of this manuscript.

References

1 De Graaf, J. G. A., and van der Held, E. F. M., "The Relation Between the Heat Transfer and the Convection Phenomena in Enclosed Plane Air Layers," *Journal of Applied Science Research*, Vol. 3, 1953, p. 393.

2 Jacob M., "Free Convection Through Enclosed Plane Gas Layers," *Trans. ASME*, Vol. 68, 1946, p. 189.

3 Batchelor, G. K., "Heat Transfer by Free Convection Across a Closed Cavity Between Vertical Boundaries at Different Temperatures," *Quarterly of Applied Mathematics*, Vol. 12, 1954, p. 209.

4 Soehngen, E. E., "Interferometric Studies on Heat Transfer," *Proceedings of the 9th International Congress of Applied Mechanics*, Brussels, 1956, p. 475.

5 Eckert, E. R. G., and Carlson, W. O., "Natural Convection in an Air Layer Enclosed Between Two Vertical Plates of Different Temperatures," *International Journal of Heat and Mass Transfer*, Vol. 2, 1961, p. 106.

6 Elder, J. W., "Laminar Free Convection in a Vertical Slot," *Journal of Fluid Mechanics*, Vol. 23, 1965, p. 77.

7 Gill, A. E., "Boundary Layer Regime for Convection in Rectangular Cavity," *Journal of Fluid Mechanics*, Vol. 26, 1966, p. 515.

8 Bejan, A., "Note on Gill's Solution for Free Convection in Vertical Enclosure," *Journal of Fluid Mechanics*, Vol. 90, 1979, p. 561.

9 Graebel, W. P., "The Influence of Prandtl Number on Free Convection in a Rectangular Cavity," *International Journal of Heat and Mass Transfer*, Vol. 24, 1981, p. 125.

10 Newell, M. E., and Schmidt, F. W., "Heat Transfer by Laminar Natural Convection within Rectangular Enclosures," *Journal of Heat Transfer*, Vol. 92, 1970, p. 159.

11 Thomas, R. W., and deVahl Davis, G., "Natural Convection in Annular and Rectangular Cavities: A Numerical Study," *Proceedings of the 4th International Heat Transfer Conference*, Paris, NC 2.4, 1970.

12 Jones, I. P., "A Numerical Study of Natural Convection in an Air-Filled Cavity: Comparison with Experiment," *Numerical Heat Transfer*, Vol. 2, 1979, p. 193.

13 Emery, A. F., and Chu, N. C., "Heat Transfer across Vertical Layers," ASME *Journal of Heat Transfer*, Vol. 87, 1965, p. 110.

14 Mynett, L. A., and Duxbury, D., "Temperature Distributions within Enclosed Plane Air Cells Associated with Heat Transfer by Natural Convection," *Proceedings of the 5th International Heat Transfer Conference*, Tokyo, NC 3.8, 1974, p. 110.

15 deVahl Davis, G., "Laminar Natural Convection in an Enclosed Rectangular Cavity," *International Journal of Heat and Mass Transfer*, Vol. 11, 1968, p. 1675.

16 Vest, C. M., and Arpaci, V. S., "Stability of Natural Convection in a Vertical Slot," *Journal of Fluid Mechanics*, Vol. 36, 1969, p. 1.

17 Rudakov, R. N., "Spectrum of Perturbations and Stability of Convection Motion between Vertical Planes," *Prikl. Mat. Mekh.*, Vol. 31, 1967, p. 376.

18 Korpela, S. A., Gozum, D., and Baxi, C. B., "On the Stability of Conduction Regime of Natural Convection in a Vertical Slot," *International Journal of Heat and Mass Transfer*, Vol. 16, 1973, p. 1683.

19 Bergholz, R. F., "Instability of Steady Natural Convection in a Vertical Fluid Layer," *Journal of Fluid Mech.*, Vol. 84, 1978, p. 743.

20 Horne, R. N., "Convection in a Porous Medium Heated from Below: The Effect of Temperature Dependent Viscosity and Thermal Expansion Coefficient," ASME Paper No. 77-HT-56, 1977.

21 Roache, P. J., *Computational Fluid Dynamics*, Hermosa Publisher, Albuquerque, New Mexico, 1972.

22 Quon, C., "High Rayleigh Number Convection in an Enclosure: A Numerical Study," *Physics of Fluids*, Vol. 15, 1972, p. 12.

23 Wirtz, R. A., and Liu, L. H., "Convection of a Narrow Slot Containing a Stably Stratified Fluid," *International Journal of Heat and Mass Transfer*, Vol. 18, 1975, p. 1299.

24 Chu, H. N. S., and Churchill, S. W., "The Development of Testing of a Numerical Method for Computation of Laminar Natural Convection in Enclosures," *Computers and Chemical Engineering*," Vol. 1, 1977, p. 103.

25 Roux, B., Grondin, J. C., Bontoux, P., and Gilly, B., "On a High-order Accurate Method for the Numerical Study of Natural Convection in a Vertical Square Cavity, *Numerical Heat Transfer*, Vol. 1, 1978, p. 331.

26 deVahl Davis, G., and Mallinson, G. D., "A Note on Natural Convection in a Vertical Slot," *Journal of Fluid Mech.*, Vol. 72, 1975, p. 87.

27 Seki, N., Fukusako, S., and Inaba, H., "Visual Observations of Natural Convection Flow in a Narrow Vertical Cavity," *Journal of Fluid Mech.*, Vol. 84, 1978, p. 695.

28 Berkovsky, B. M., and Polevikov, V. K., *Heat Transfer and Turbulent Buoyant Convection*, Hemisphere Publishing, edited by D. B. Spalding and H. Afgan, Vol. II, 1977, p. 443.

29 ElSherbiny, S. M., Raithby, G. D., and Hollands, K. G. T., "Heat Transfer by Natural Convection Across Vertical and Inclined Air Layers," ASME Paper No. 80-HT-67.

30 Hollands, K. G. T., and Konicek, L., "Experimental Study of the Stability of Differentially Heated Inclined Air Layers," *International Journal of Heat and Mass Transfer* Vol. 16, 1973, p. 1467.

31 Lee, Yee, and Korpela, S. A., "Natural Convection in a Vertical Slot," submitted for publication.

32 Lee, Yee, Korpela, S. A., and Horne, R. N., "Structure of Multicelluar Convection in a Tall Vertical Annulus," *Proceedings of the 7th International Heat Transfer Conference*, Munich NC-17, Germany, 1982.

High Rayleigh Number Solutions to Problems of Latent Heat Thermal Energy Storage in a Horizontal Cylinder Capsule

T. Saitoh
Associate Professor.

K. Hirose
Research Associate.

Department of Mechanical Engineering,
Tohoku University,
Sendai, Japan 980

An analysis was made of the melting and solidification heat transfer inside a horizontal circular cylinder capsule in which n-octadecane or water was used as a phase change material. Special efforts were made to obtain solutions with high Rayleigh numbers (i.e., for large diameters). To this end, the following three tools had been adopted: (i) To save computation time, a high-accuracy, multipoint, explicit finite difference scheme was adopted; (ii) To eliminate complex moving boundaries, two-dimensional Landau transformation was adopted; (iii) To suppress the strong numerical instability, a smoothing technique using the least square method of the sixth order was devised. Transient aspects for natural convection flow, temperature profiles, and melting interfaces were clarified in detail. It is especially noted that entirely different results from those of Pannu et al. were obtained.

Introduction

Since the first study by Neumann more than 120 years ago, scientists have investigated freezing and melting problems extensively because of their broad applications to many fields of engineering and science, including meteorology. The development of these problems have been reviewed by several investigators [1-6].

These fundamental problems have recently attracted a great deal of interest because, among other things, of their role in thermal energy storage (TES) of solar energy. Two pioneering works on this subject have been elaborated by Sparrow, Schmidt and Ramsey [7], and Bathelt, Viskanta, and Leindenfrost [8, 9]. These authors have performed experiments dealing with the melting of phase change material around a horizontal heated cylinder. In determining heat-transfer characteristics, their papers especially emphasized that natural convection plays a dominant role; this approach contrasts to the findings of Neumann who considered conduction to be the only mode of heat transfer in Stefan problems. The analysis for the melt region created by a heated vertical tube embedded in a solid at its fusion temperature was performed by Sparrow et al. [10]. The importance of natural convection was also indicated for the freezing of a phase change material (PCM) around a cooled vertical cylinder [11]. The effect of subcooling on one-dimensional melting around a heated cylinder was analyzed by Sparrow et al. [12], using a coordinate transformation method. The results were compared with those for plane melting at the same degree of subcooling. An experiment was also conducted to examine the subcooling effect for melting around a horizontal cylinder [13].

In spite of the fact that there exist some experimental works on melting and freezing around or inside a horizontal cylinder controlled by natural convection, it seems that theoretical analyses are relatively scarce. Of these theoretical analyses, an analysis of the two-dimensional freezing of water controlled by natural convection around a cooled horizontal circular cylinder has been performed by Saitoh [6], and by Saitoh and Hirose [14], employing an extended Landau transformation method. The transient freezing front contours, isotherms in the solid and liquid region, streamlines in the liquid region, and Nusselt number distribution around the solid-liquid interface were obtained.

A regular perturbation solution was obtained by Yao and Chen [15] in the melt region surrounding a heated horizontal cylinder. In their paper, they focused their attention on the short time solution where conduction was the dominant mode, and natural convection was treated as a perturbed quantity. However, it is noted that the expansion procedure is restricted to small Rayleigh numbers and Stefan numbers, which, in nature, restrict the scope of application to practical cases. Concurrently, the natural convection melting of ice in a horizontal circular cylinder was numerically analyzed by the present authors [6], making use of the method used in [14]. The density inversion effect on melting heat transfer was clarified.

A numerical solution to natural convection heat transfer in a cylinder filled with PCM (a paraffin) has been obtained by Pannu et al. [16]. Their study seems to have been conducted concurrently with our study. The basic equations were transformed by virtue of two-dimensional Landau variables, though the details were not described in their paper. Various forms of multidimensional Landau transformations have already been proposed by a few researchers [10, 17, 18, 19]. Transient isotherms, streamlines, and the unmelted core area were calculated and shown in their graphs.

This paper proposes a numerical method for problems of melting (also of solidification in part) controlled by natural convection inside a horizontal circular cylinder capsule packed with either a paraffin (n-octadecane), or water in the case of relatively high-Rayleigh numbers. The present problem involves: (*i*) a two-dimensional moving boundary, (*ii*) a strong numerical instability induced by natural convection flow in the liquid region, especially for high-Rayleigh number cases, and (*iii*) a formidable computing time (i.e., computer running cost) in order to raise the resolving power of computation for high Rayeigh numbers. To overcome these difficulties, we have developed three improved tools: (*i*) a high-accuracy, multipoint, explicit difference method was developed to decrease the computing time, (*ii*) a two-dimensional Landau transformation method was adopted to treat liquid-solid interfaces of various shapes, and (*iii*) the least square method of the sixth order was devised to suppress the strong numerical instability. The temperature, stream function, vorticity, and moving boundaries were smoothed

Contributed by the Heat Transfer Division for publication in the JOURNAL OF HEAT TRANSFER. Manuscript received by the Heat Transfer Division July 9, 1981.

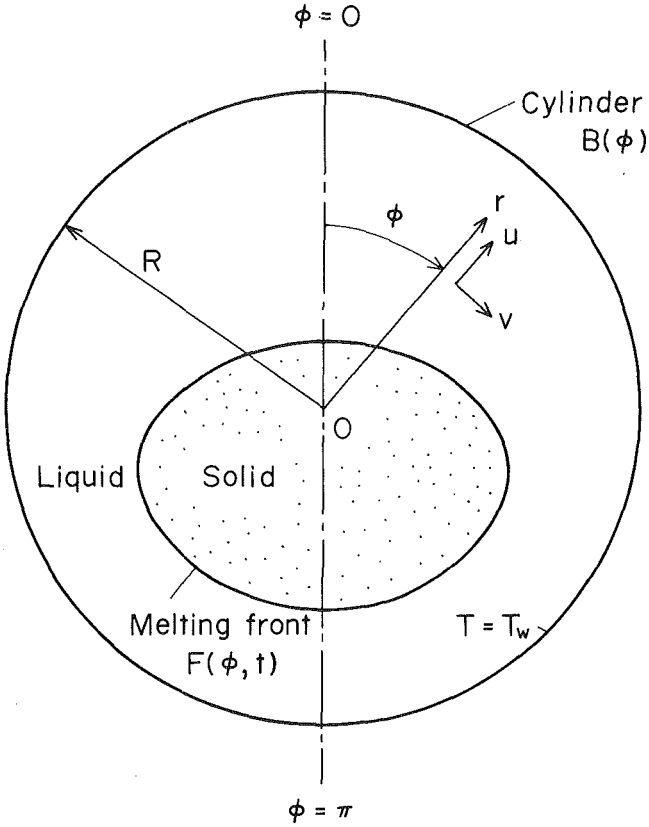

Fig. 1 Schematic diagram and coordinate system of natural convection melting in a horizontal cylinder capsule

out by the above approximations, thereby enabling the high Raleigh number computations. The illustrative computations were made, in the main, for n-octadecane as a PCM. The reason for selecting n-octadecane is that its thermophysical properties are relatively well established, and that its liquid phase is transparent, which makes it convenient for experimentation.

The transient liquid-solid interface, streamlines, isotherms, and heat-stored fraction were obtained. Similar calculations were performed for water. Calculations using the same parameters as those used in the paper of Pannu et al. were also carried out, and the results of the two papers were compared.

Analysis

A schematic diagram and coordinate system of natural convection melting in a horizontal cylinder capsule are presented in Fig. 1. The origin, O, of the cylindrical polar coordinate is usually positioned at the center of a circular capsule, although it may be placed rather arbitrarily. At first, the solid PCM, initially at temperature θ_i, which is equal to or lower than the fusion temperature, T_f, occupies the capsule. Then, from the moment the wall temperature is set at $T_w (> T_f)$, melting proceeds inwardly. At time, t, it is assumed that the contour of the melting front is represented by the shape function $r = F(\phi, t)$.

The problem then becomes one of obtaining the transient solid-liquid interface, temperature in the solid and liquid, and streamlines and vorticity in the liquid. The following principal assumptions and restrictions for the analysis are made: (*i*) flow is laminar, (*ii*) Boussinesq approximation is valid, (*iii*) the unmelted solid core remains stationary, and (*iv*) volume change due to phase transformation is minor.

Governing Equations

The heat-transfer process in the liquid and solid regions is governed by the following equations in cylindrical coordinates.

Liquid region:

$$\frac{\partial \Omega^+}{\partial t^+} + \frac{1}{\pi r^+}\frac{\partial(\psi^+, \Omega^+)}{\partial(r^+, \phi^+)} = \mathrm{Pr}\cdot\nabla^2\Omega^+ + \mathrm{Pr}\cdot\mathrm{Ra}\left[\sin\pi\phi^+ \frac{\partial}{\partial r^+}\left(f(T^+)\right) + \frac{\cos\pi\phi^+}{\pi r^+}\frac{\partial}{\partial\phi^+}\left(f(T^+)\right)\right] \quad (1)$$

$$\frac{\partial T^+}{\partial t^+} + \frac{1}{\pi r^+}\frac{\partial(\psi^+, T^+)}{\partial(r^+, \phi^+)} = \nabla^2 T^+ \quad (2)$$

$$\Omega^+ = \nabla^2\psi^+ \quad (3)$$

Solid region:

$$\frac{\partial\theta^+}{\partial t^+} = \frac{a_s}{a}\nabla^2\theta^+ \quad (4)$$

where an operator, ∇^2, means

$$\nabla^2 \equiv \frac{\partial^2}{\partial(r^+)^2} + \frac{1}{r^+}\frac{\partial}{\partial(r^+)} + \frac{1}{\pi^2(r^+)^2}\frac{\partial^2}{\partial(\phi^+)^2} \quad (5)$$

and the function $f(T^+)$ represents the dependence of density change on temperature and is expressed by

$$f(T^+) = T^+(1 + aT^+ + b(T^+)^2 + c(T^+)^3) \quad (6)$$

The coefficient a, b, and c are taken to be zero except for water, and for water they can be decided by the same manner as in reference [20]. Furthermore, Pr, Gr, and Ra stand for Prandtl number, Grashof number, and Rayleigh number,

Nomenclature

a = thermal diffusivity
$B(\phi)$ = boundary shape function
c_p = specific heat at constant pressure
d = diameter of cylinder
$F(\phi,t)$ = position of melting front
Fr = stored heat fraction, $Fr = Q/Q_m$
g = acceleration of gravity
Gr = Grashof number; $\mathrm{Gr} = g(-\beta)(T_w - T_f)R^3/\nu^2$
h = heat-transfer coefficient
k = thermal conductivity
L = latent heat
Nu = Nusselt number, $\mathrm{Nu} = 2hR/k$
Pr = Prandtl number, $\mathrm{Pr} = \nu/a$
Q = stored heat, $Q = L\cdot V$
Q_m = maximum stored heat, $Q_m = L\cdot V_0$
R = radius of cylinder
Ra = Rayleigh number, $\mathrm{Ra} = \mathrm{Pr}\cdot\mathrm{Gr}$
Ste = Stefan number, $\mathrm{Ste} = c_p(T_w - T_f)/L$
t = time
T = temperature of liquid phase
T_f = fusion temperature
ΔT = $T_w - T_f$
u,v = velocities in r and ϕ directions, respectively
V = melt volume
V_0 = volume of the test cylinder

Greek symbols

β = thermal expansion coefficient
θ = temperature of solid phase
θ_i = initial temperature
$\Delta\theta$ = $T_f - \theta_i$
ρ = density of liquid
ν = kinematic viscosity
ϕ = circumferential angle
ϕ_0 = reference angle
ψ = stream function
Ω = vorticity

Subscripts and superscript

$+$ = dimensionless quantity
w = cylinder surface
s = solid phase

respectively, the definitions of which are shown in the list of symbols. The stream function ψ^+, and the vorticity, Ω^+, have been defined as

$$u^+ = -\frac{1}{\pi r^+}\frac{\partial \psi^+}{\partial \phi^+}, v^+ = \frac{\partial \psi^+}{\partial r^+}. \tag{7}$$

The basic equations (1–3) were already made dimensionless by the following variables (letters with superscript "+" mean the dimensionless quantities).

$$t^+ = \frac{at}{R^2}, \psi^+ = \frac{\psi}{a}, r^+ = \frac{r}{R}, \phi^+ = \frac{\phi}{\pi}, u^+ = \frac{uR}{a}, v^+ = \frac{vR}{a}$$

$$T^+ = \frac{T-T_f}{T_w-T_f}, \Omega^+ = \frac{\Omega R^2}{a}, \theta^+ = \frac{\theta - T_f}{T_f-\theta_i},$$

$$F^+(\phi^+, t^+) = \frac{F(\phi,t)}{R} B^+(\phi^+) = \frac{B(\phi)}{R} \tag{8}$$

The boundary conditions including a joint condition for the above equations, are described below.

Liquid:

$$r^+ = B^+(\phi^+); T^+ = 1, \psi^+ = \frac{\partial \psi^+}{\partial n^+} = 0, \Omega_w^+ = \Omega^+ \mid_{r^+ = B^+(\phi^+)}$$

$$r^+ = F^+(\phi^+, t^+); \psi^+ = \frac{\partial \psi^+}{\partial n^+} = 0, \Omega_w^+ = \Omega^+ \mid_{r^+ = F^+(\phi^+, t^+)}$$

$$\phi^+ = 0,1; \frac{\partial T^+}{\partial \phi^+} = 0, \psi^+ = \Omega^+ = 0 \tag{9}$$

Joint condition:

$$r^+ = F^+(\phi^+, t^+); T^+ = 0,$$

$$\frac{\partial F^+}{\partial t^+} = \frac{k_s}{a\rho_s L}\left[(T_f - \theta_i)\left(\frac{\partial \theta^+}{\partial r^+} - \frac{F_\phi^+}{(F^+\phi_0)^2}\frac{\partial \theta^+}{\partial \phi^+}\right)\right. \tag{10}$$

$$\left. - \frac{k}{k_s}(T_w - T_f)\left(\frac{\partial T^+}{\partial r^+} - \frac{F_\phi^+}{(F^+\phi_0)^2}\frac{\partial T^+}{\partial \phi^+}\right)\right]$$

Solid:

$$r^+ = F^+(\phi^+, t^+); \theta^+ = 0$$

$$r^+ = 0; \frac{\partial \theta^+}{\partial r^+}\Big|_- = \frac{\partial \theta^+}{\partial r^+}\Big|_+ \tag{11}$$

$$\phi^+ = 0,1; \frac{\partial \theta^+}{\partial \phi^+} = 0$$

Inasmuch as it is quite difficult to handle the moving and fixed boundaries if the above equations are employed, the boundary fixing method that is a two-dimensional extension of the Landau transformation was adopted [19, 21].

More specifically, the following independent variables were utilized.

In the liquid phase:

$$\eta = \frac{r^+ - F^+(\phi^+, t^+)}{B^+(\phi^+) - F^+(\phi^+, t^+)} \tag{12}$$

In the solid phase:

$$\zeta = \frac{r^+}{F^+(\phi^+, t^+)} \tag{13}$$

The transformed governing equations can be rewritten as follows (Hereafter, plus signs are omitted for simplification):

Liquid:

$$\frac{\partial \Omega}{\partial t} + \frac{1}{\pi r}\frac{\partial \eta}{\partial r}\frac{\partial(\psi,\Omega)}{\partial(\eta,\phi)} = \mathrm{Pr}\nabla^2\Omega - \frac{\partial \Omega}{\partial \eta}\frac{\partial \eta}{\partial t} + \mathrm{Pr}\cdot\mathrm{Ra}\left[\sin\pi\phi\frac{\partial f}{\partial T}\frac{\partial T}{\partial \eta}\frac{\partial \eta}{\partial r} + \frac{\cos\pi\phi}{\pi r}\frac{\partial f}{\partial T}\left(\frac{\partial T}{\partial \eta}\frac{\partial \eta}{\partial \phi} + \frac{\partial T}{\partial \phi}\right)\right] \tag{14}$$

$$\frac{\partial T}{\partial t} + \frac{1}{\pi r}\frac{\partial \eta}{\partial r}\frac{\partial(\psi,T)}{\partial(\eta,\phi)} = \nabla^2 T - \frac{\partial T}{\partial \eta}\frac{\partial \eta}{\partial t} \tag{15}$$

$$\Omega = \nabla^2\psi \tag{16}$$

where

$$\nabla^2 \equiv \left[\left(\frac{\partial \eta}{\partial r}\right)^2 + \frac{1}{\pi^2 r^2}\left(\frac{\partial \eta}{\partial \phi}\right)^2\right]\frac{\partial^2}{\partial \eta^2} + \left(\frac{1}{r}\frac{\partial \eta}{\partial r} + \frac{1}{\pi^2 r^2}\frac{\partial^2 \eta}{\partial \phi^2}\right)\frac{\partial}{\partial \eta} + \frac{2}{\pi^2 r^2}\frac{\partial \eta}{\partial \phi}\frac{\partial^2}{\partial \eta \partial \phi} + \frac{1}{\pi^2 r^2}\frac{\partial^2}{\partial \phi^2} \tag{17}$$

$$\frac{\partial \eta}{\partial r} = \frac{1}{B-F}, \frac{\partial \eta}{\partial \phi} = \frac{-1}{B-F}\{F_\phi + \eta(B_\phi - F_\phi)\}, r = \eta(B-F) + F$$

$$\frac{\partial^2 \eta}{\partial \phi^2} = \frac{-1}{B-F}\left\{F_{\phi\phi} + 2\frac{\partial \eta}{\partial \phi}(B_\phi - F_\phi) + \eta(B_{\phi\phi} - F_{\phi\phi})\right\} \tag{18}$$

Solid:

$$\frac{\partial \theta}{\partial t} = \frac{a_s}{a}\nabla^2\theta - \frac{\partial \theta}{\partial \zeta}\frac{\partial \zeta}{\partial t} \tag{19}$$

where

$$\nabla^2 \equiv \left[\left(\frac{\partial \zeta}{\partial r}\right)^2 + \frac{1}{\pi^2 r^2}\left(\frac{\partial \zeta}{\partial \phi}\right)^2\right]\frac{\partial^2}{\partial \zeta^2} + \left(\frac{1}{r}\frac{\partial \zeta}{\partial r} + \frac{1}{\pi^2 r^2}\frac{\partial^2 \zeta}{\partial \phi^2}\right)\frac{\partial}{\partial \zeta} + \frac{2}{\pi^2 r^2}\frac{\partial \zeta}{\partial \phi}\frac{\partial^2}{\partial \zeta \partial \phi} + \frac{1}{\pi^2 r^2}\frac{\partial^2}{\partial \phi^2} \tag{20}$$

$$\frac{\partial \zeta}{\partial r} = \frac{1}{F}, \frac{\partial \zeta}{\partial \phi} = -\frac{\zeta}{F}F_\phi, r = F\cdot\zeta,$$

$$\frac{\partial^2 \zeta}{\partial \phi^2} = \frac{-1}{F}\left\{2\frac{\partial \zeta}{\partial \phi}F_\phi + \zeta F_{\phi\phi}\right\} \tag{21}$$

Solution Methodology

As stated earlier, solutions will be obtained by numerical techniques. The parabolic type equations, i.e., heat conduction equations, energy equations, and vorticity equations, were solved by the multipoint explicit finite difference method [22], which was employed to contrive a one-order of magnitude reduction of the computing time for multidimensional problems. The first and second spatial derivatives are represented by the next finite difference equations.

$$\frac{\partial Y}{\partial x}\Big|_{i,j,k} = \sum_{l=i-2}^{i+2} A_l Y_{l,j,k}$$
$$\frac{\partial^2 Y}{\partial x^2}\Big|_{i,j,k} = \sum_{l=i-2}^{i+2} B_l Y_{l,j,k} \tag{22}$$

where

$$A_{i-2} = -A_{i+2} = \frac{1}{12\Delta x}, A_{i-1} = -A_{i+1} = \frac{-8}{12\Delta x}, A_i = 0$$

$$B_{i-2} = B_{i+2} = \frac{-1}{12\Delta x^2}, B_{i-1} = B_{i+1} = \frac{4}{3\Delta x^2}, B_i = \frac{-5}{2\Delta x^2} \tag{23}$$

The time derivative is simply approximated by the forward difference.

$$\frac{\partial Y}{\partial t} = \frac{Y_{i,j,k+1} - Y_{i,j,k}}{\Delta t} \tag{24}$$

In the present multipoint scheme, central differences of the type of equation (22) can also be utilized in Jacobian terms,

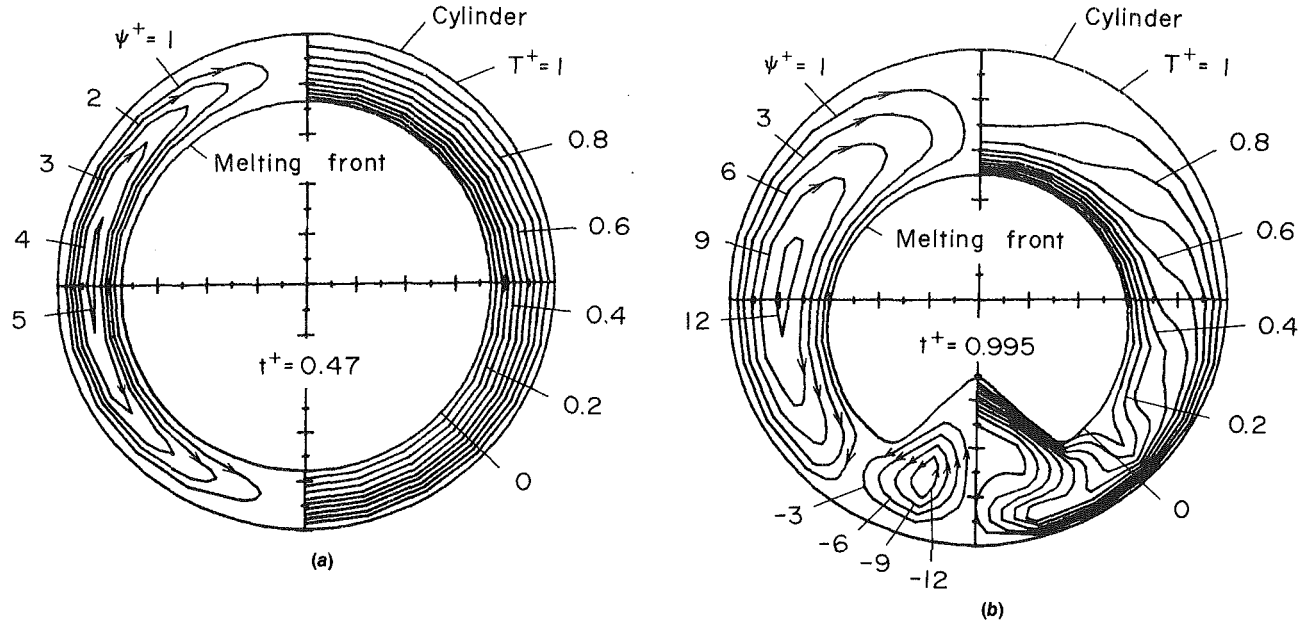

Fig. 2 Typical time sequences of streamlines and isotherms in the liquid, and melting front contours for $Pr = 54.6$, $Ra = 126{,}300$, $d = 0.02$ m, and $\Delta T = 7K$

which enables the discretization error of the present scheme to be the order of $0(\Delta x^3)$, compared to $0(\Delta x^2)$ for the existing schemes, while Poisson's equation (16) was solved by the multipoint successive over relaxation method.

To cope with the strong numerical instability arising when the Rayleigh number becomes large, the following smoothing techniques based on least square approximation were devised. The function $f(x_k)$, which may be one of temperature, stream function, and vorticity, is approximated by a polynomial of the sixth order as below:

$$f(x_k) = \sum_{n=0}^{6} a_n x_k^n \tag{25}$$

where x_k and a_n are the spatial coordinate and the coefficient, respectively.

The coefficient, a_n, can be determined so that the deviations from the given data become minimum in the sense of a least square approximation. If the function $G(a_n, a_{n-1}, \ldots, a_0)$ is defined as

$$G(a_n, a_{n-1}, \ldots, a_0) = \sum_{k=1}^{m} \left(f(x_k) - \sum_{n=0}^{6} a_n x_k^{(n)} \right)^2 \tag{26}$$

the coefficients, a_n, are decided so as to satisfy the following equation:

$$\frac{\partial G}{\partial a_n} = 2 \sum_{k=1}^{m} \left(f(x_k) - \sum_{i=0}^{6} a_i x_k^i \right) (-x_k^n) = 0 \tag{27}$$

In the above equation, m means the number of sampling data.

When small differences in calculated values appear at a certain time stage prior to the overflow of computation, the smoothing techniques become effective and eliminate these disturbances. All distributions including temperature, vorticity, and stream function are smoothed out at this time stage. For the above reason, the adaptation of these techniques made it possible to considerably extend the usual stability limits. The accuracy for obtaining the melting front contours is not greatly affected by using the smoothing techniques. First of all, we preferred obtaining a high Rayleigh number solution. By doing this accuracy of the solution was sacrificed. The Rayleigh numbers for which the present computation was possible were about 10 to 20 times as large as those for the past standard method. Another advantage of the above techniques is that grid spacing can be changed freely at arbitrary time stages of computation because the values at arbitrary positions are readily compatible by equation (25). Therefore, the grid spacing was altered at least twice in the course of transient computations.

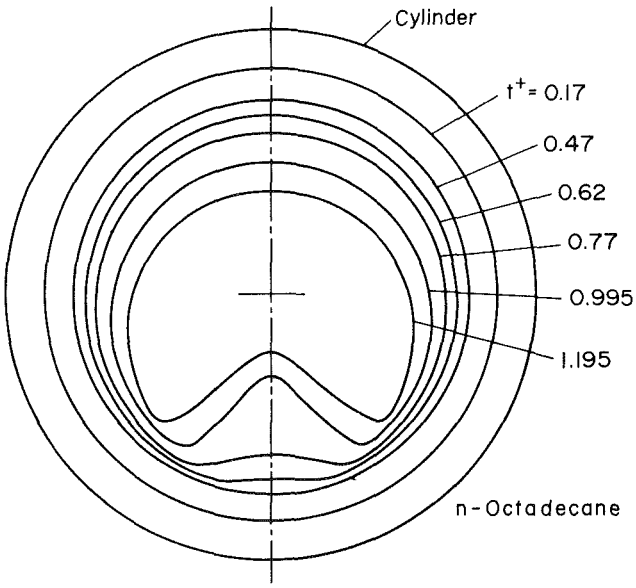

Fig. 3 Superposed transient melting front contours. Conditions are the same as in Fig. 2.

Since the Stefan number is much smaller than unity, the time needed for stabilization of the flow field is much shorter than that needed for growth of the melt layer. For the above reason, quasi-steady approximation can be rigorously utilized for this problem. The convergent fields of flow and temperature for the liquid region with interface being fixed was

obtained. In a typical case, the number of iteration needed for calculating the liquid flow field at one time level was some 600 ($\Delta t^+ = 10^{-6}$). To save computing time, the values of the temperature, stream function, and vorticity were maintained at convergent values during a certain period of melting, e.g., $\Delta t^+ = 0.1$, which was varied according to numbers and the melting front position, etc. The number of iteration for calculating the melting front was about 1000 ($\Delta t^+ = 10^{-4}$). The above process was performed iteratively, until melting proceeded to the desired extent.

For the calculation in the liquid phase, the initial thickness of the melt layer was usually assumed to be 15 percent of the radius of the cylinder, which was varied according to the Rayleigh number. The effect of natural convection in the early time stage is relatively small because the Prantl number is large. It is dominated mainly by heat conduction for a certain period from the start of melting. Therefore, it seems that the assumed thickness of the melt layer is reasonable.

For a typical computation, the initial spacing network was 10×14, and, later, it was altered to 14×14 and 18×14. The computer running time (CPU) for a particular set of data was typically 1200 s on NEAC 2200/ACOS 900 at the Tohoku University. The computing speed of ACOS 900 is about 3.5 MIPS.

The computing time was decreased, in its entirety, to one-tenth of that of the existing standard method.

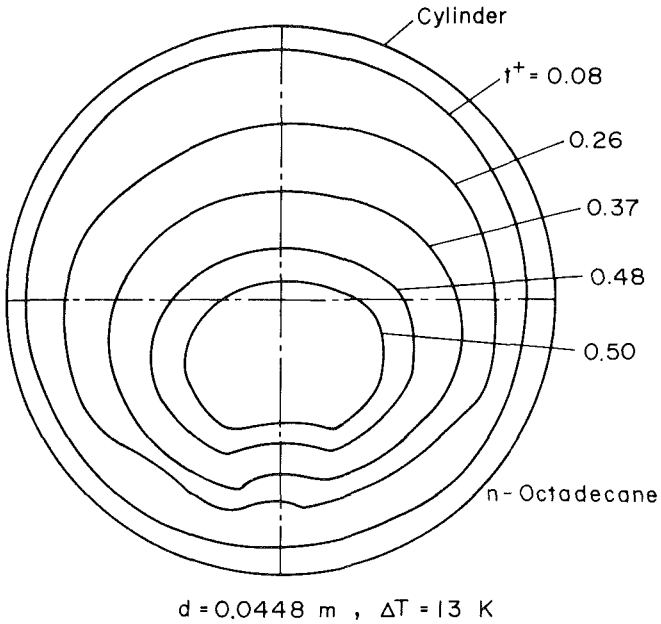

Fig. 4 Transient melting front contours in the case of $Pr = 50.6$, $Ra = 2{,}914{,}000$, $d = 0.0448$ m, and $\Delta T = 13$ K with center axis being supported

Results and Discussion

Numerical computations were performed for three types of PCM: n-octadecane, water, and paraffin. The third PCM was taken up only for comparison with the work of Pannu et al. [16].

All computations were performed for the case in which the solid core is fixed. However, in practical situations, the solid core moves up or down according to the gravitational effect. Nicholas and Bayazitoglu [23] have analyzed the problem including the gravitational effects by solving the heat-conduction equation in the liquid phase. However, according to the recent study of Katayama et al. [24], other factors such as contact surface pressure that were not considered in the analysis play an important role in contact heat transfer. The heat-transfer mechanism is not well understood at the present time. Therefore, this effect was not taken into account in the present theory.

Typical time sequences of streamlines and isotherms in the liquid region, and melting front contours for n-octadecane are shown in Fig. 2. The cylinder surface temperature is kept constant in this and all other cases treated in the present paper. During the early stages of the process when heat conduction is dominant, the melting front shape and isotherms are almost concentric. However, as melting advances further, a characteristic feature appears. A small vortex is found forming at the bottom portion of the melt layer because of thermal instability in this region. Though the test cylinder is placed horizontally, a convexo-concave melting front in the axial direction is formed at the bottom portion of the unmelted core. It seems that a three-dimensional flow instability is induced in this region. Such a phenomenon is rigorously explained by three-dimensional

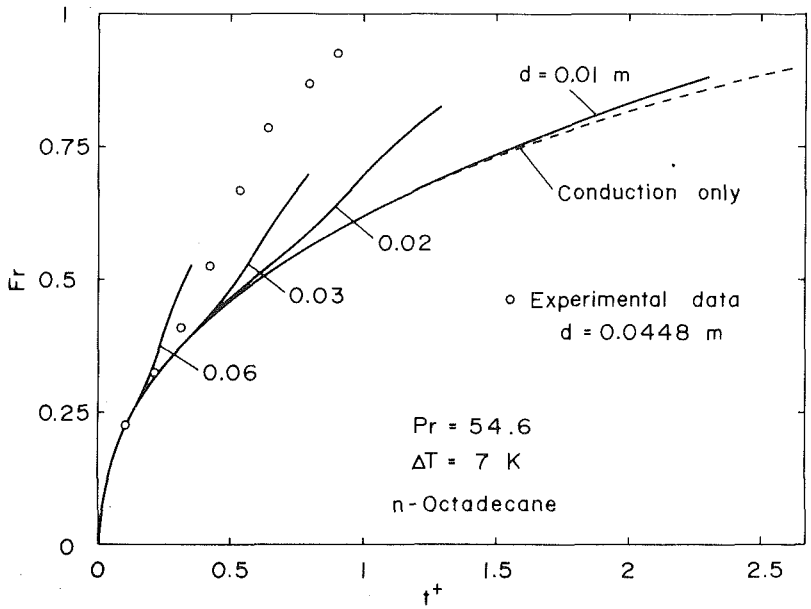

Fig. 5 Variation of stored heat fraction versus time with cylinder diameter

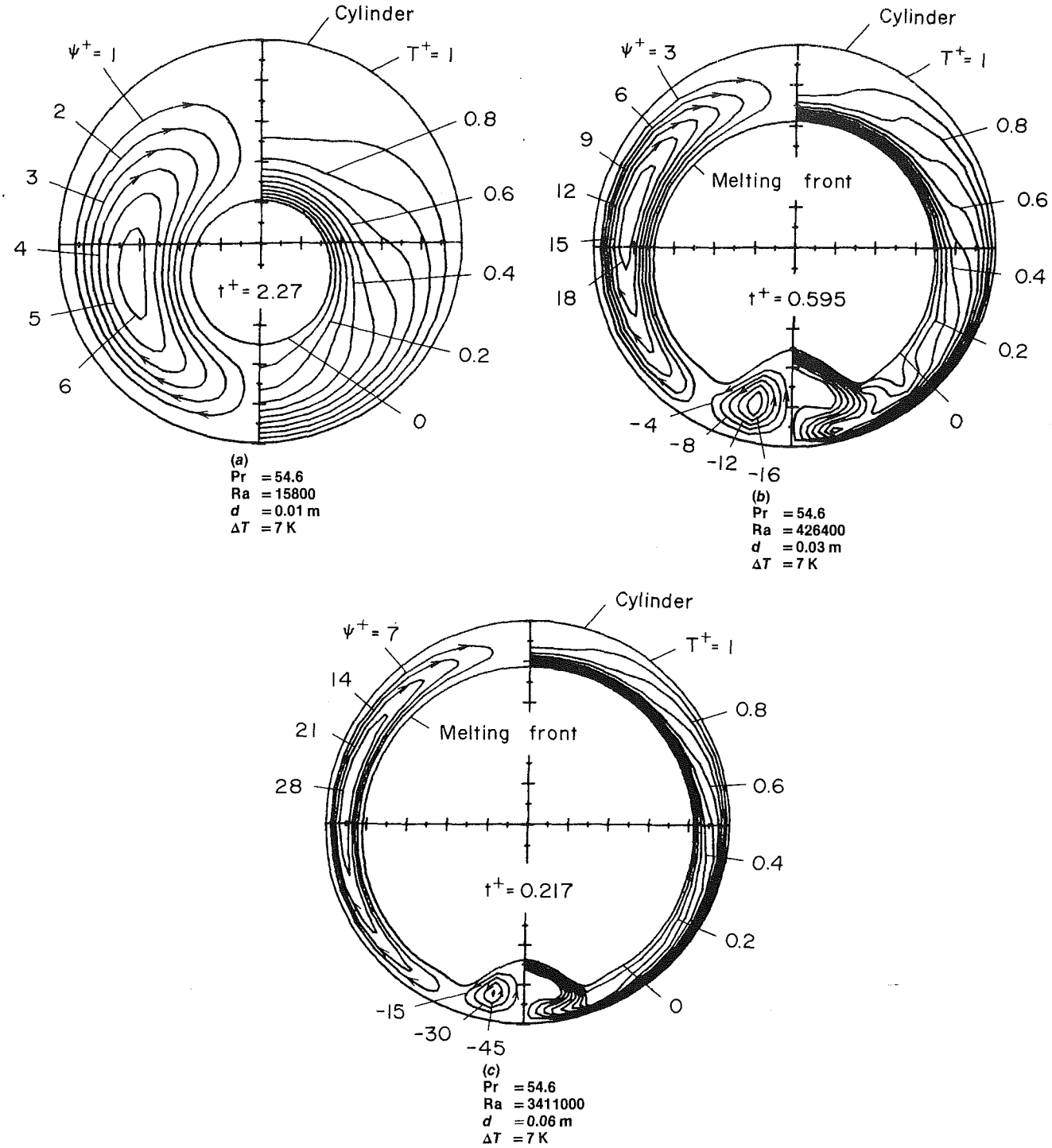

Fig. 6 Streamlines and isotherms at typical time stages with $\Delta T = 7K$, $d = 0.01$ m, 0.03 m, and 0.06 m

thermal instability of natural and forced convection flows that have been studied separately [25, 26]. The onset of such a vortex and its growth have a very important role in heat-transfer characteristics of this problem.

Because of the formation of the eddy, the heat-transfer rate at the vicinity of the lower stagnation point is raised. As a consequence, melting at that portion is promoted. The next figure in Fig. 2, in which a concavity is clearly shown, indicate the aforementioned features.

Transient melting front contours corresponding to those in Fig. 2 are collectively shown in Fig. 3. The computations to reach complete melting were impossible because the origin of coordinate transformation was placed at the center of the cylinder. When the solid-liquid interface exceeded the origin for coordinate transformation, melting front shape function $F(\phi, t)$ became a double-valued function, thereby making it impossible to evaluate the position of melting front, etc. However, such a computation would be possible if the origin were positioned in advance at a part lower than the center.

Figure 4 shows experimental transient melting front contours which were obtained by the authors [27] in order to compare with our numerical results of Fig. 3 when $Pr = 50.6$, $Ra = 2{,}914{,}000$, $d = 0.0448$ m, and $\Delta T = 13$ K. In this experiment, n-octadecane (99.86 percent pure, Wako Pure

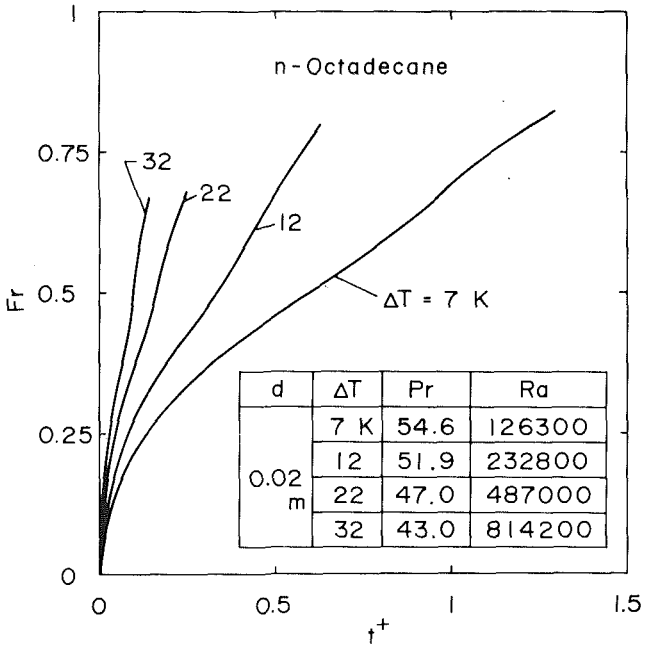

Fig. 7 Variation of the stored heat fraction curve with cylinder surface temperature

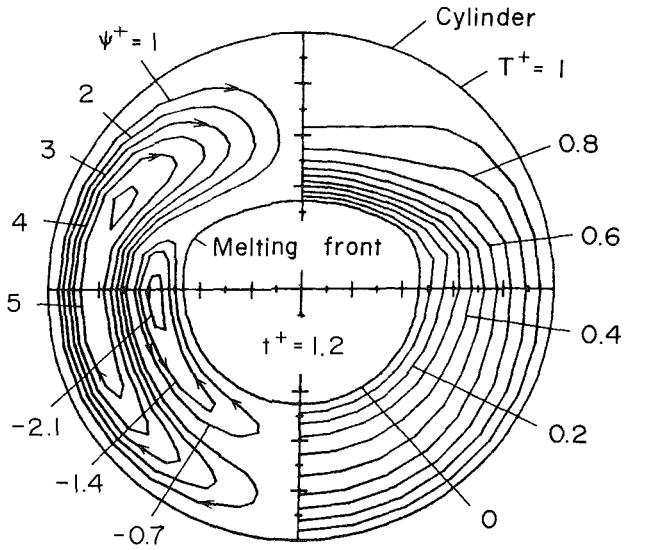

Fig. 8 Melting characteristics of ice. Pr = 11.85, Ra = 202000, $d = 0.04$ m, and $\Delta T = 8$ K

Chemical Industries, Ltd.) was used as a PCM. Though strict comparison is not possible because the diameters of the cylinder in the two cases are different, the concavity of the melting front contour at the bottom portion has a similar shape. The melting front concavity in the experiment is smaller than that in the numerical prediction. Thus, owing to the occurrence of three-dimensional vortex flow in the axial direction, the heat-transfer rate at the bottom portion becomes less than that obtained by the present two-dimensional theory.

Figure 5 represents stored heat fraction versus time with cylinder diameter as a parameter. In the figure, the result of pure heat conduction is also shown by a broken line, from which it is found that the stored heat fraction increases rapidly as the increase in the diameter of the cylinder, d. Circles indicate the experimental result when $\Delta T = 7$ K and $d = 0.0448$ m. There exists a moderate agreement between the numerical and experimental results at least qualitatively. The strength of natural convection in the melt layer increases with the diameter of the cylinder, d, and thus, the role of natural convection becomes dominant.

The variations of streamlines and isotherms with the cylinder diameter are shown in Fig. 6. The comparison of three figures reveals that the gap width between the solid and the cylinder (i.e., Rayleigh number) plays an important role in melting characteristics. In particular, no eddies appear when the cylinder diameter is small (Fig. 6(a)).

The effect of variation of the cylinder surface temperature on the stored heat fraction is shown in Fig. 7. The stored heat fraction increases rapidly as the increase of the surface temperature of the cylinder. It is found that these curves have similar inflection points as seen from the figure.

A typical result employing water as a PCM is shown in Fig. 8. The cylinder surface temperature was chosen so that the density inversion effect would appear prominently. Water is an anomalous substance among PCMs, which exhibits peculiar heat-transfer characteristics. Both an outer vortex along the cylinder surface and an inner vortex along the ice surface exist. The melting front contour becomes flat gradually in proportion to the growth of the outer vortex.

In order to compare the present results with existing ones, computations were performed for the same data as those used by Pannu et al. [16]. The values of Prandtl number, Stefan number, and Rayleigh number used are $\mathrm{Pr} = 145$, $\mathrm{Ste} = 0.115$, and $\mathrm{Ra} = 2 \times 10^5$.

Shown in Fig. 9(a) are the transient streamlines, isotherms, and melting front contours that were obtained by the present solution procedure. The numerical result shown in Fig. 9(b) is cited from the paper of Pannu et al. [6]. The paraffin was used as a PCM in Fig. 9(a) and (b). Some thermophysical properties are listed in the paper of Pannu et al. From these, an outstanding difference from results by Pannu et al. can be seen. The two sets of results differ from each other both quantitatively and qualitatively. First of all, the positions of concavity which are produced by eddy formation are in contrast, i.e., it is at the upper stagnation point in Pannu et al.'s figure; on the other hand, it is at the lower stagnation point in our figure. It should be emphasized that it is at the lower position and not at the upper portion that thermal instability occurs. There is no indication of the appearance of thermal instability in the results of Pannu et al. Further, it seems unnatural that a vortex appears in the stratified region above the solid.

Concluding Remarks

Numerical solutions have been obtained for melting and solidification heat transfer inside a horizontal cylinder capsule in which n-octadecane or water is used as a PCM. Particular efforts were made to find solutions with high Rayleigh numbers, and to improve the resolution of solutions.

The following conclusions can be derived from this study:

1 As was noted in the pioneering works of Sparrow et al. and Bathelt et al., natural convection also plays a dominant role in melting heat transfer inside a horizontal cylinder capsule.

2 Thermal instability appears at the bottom portion of the cylinder. The onset of vortices drastically influences melting near the bottom. The appearance of such vortices may be the most important characteristic of melting heat transfer inside a capsule.

3 A comparison with the results by Pannu et al. reveals that the present results are quite different from theirs both quantitatively and qualitatively. We conclude that their study may be in error.

4 The numerical scheme developed in this paper is applicable to other general melting systems, including

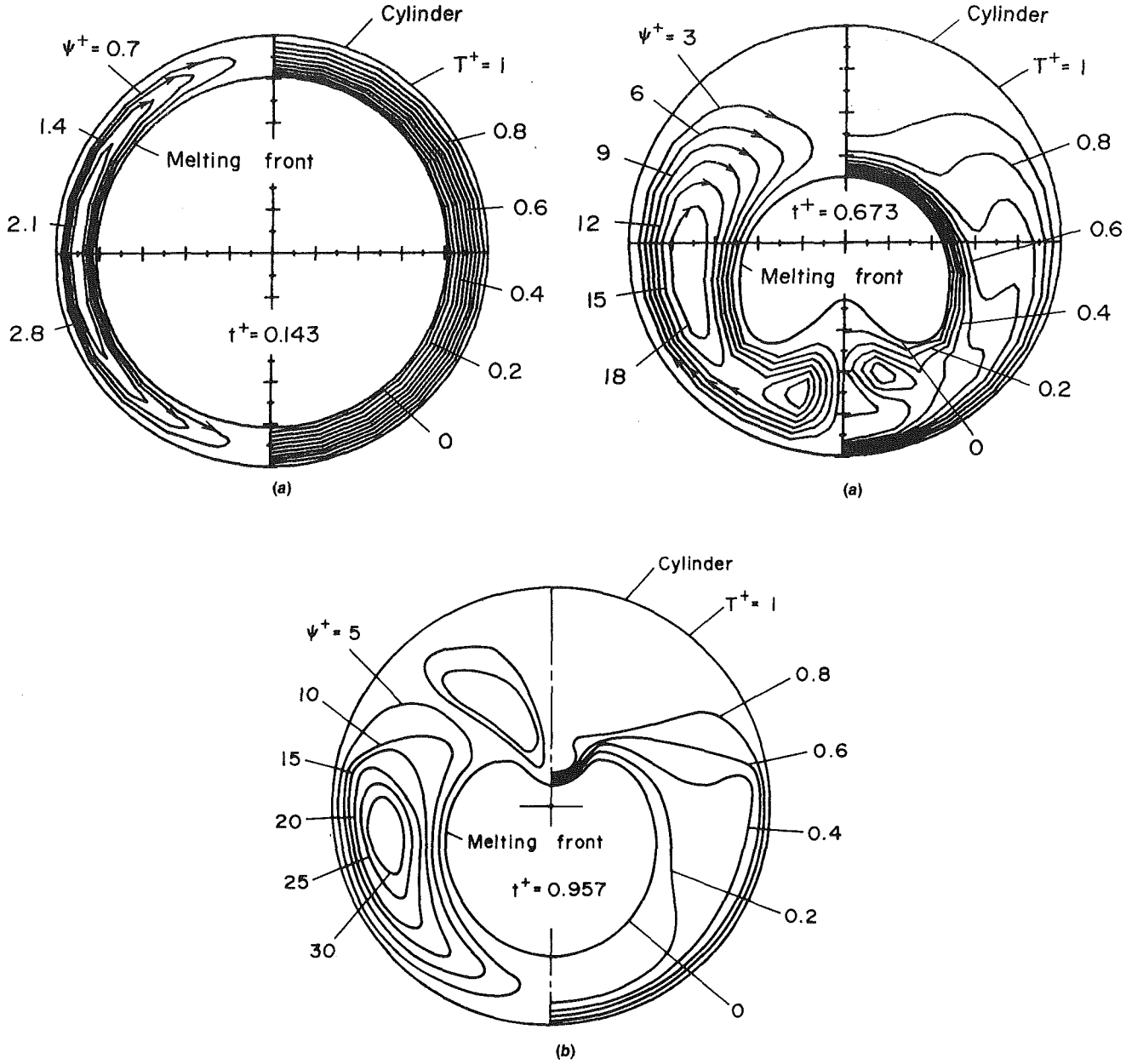

Fig. 9 Comparison of the present results with those of Pannu et al. The same data as those used by them were employed. Pr = 145, Ra = 200000, and Ste = 0.115. ((a) Present numerical results, (b) Pannu et al.'s numerical result cited from the reference [16].)

simultaneous natural convection outside and inside cylinders of various cross sections, including a circle.

In closing, experiments corresponding to the present work have been performed in part, and will be published in the near future [27]. A similar analysis for melting around a heated cylinder has also been done, but the results have been ommitted here.

Acknowledgment

The authors extend their sincere thanks to the referees for valuable suggestions received in the course of reviewing. Also thanks are due to the Computer Center at the Tohoku University for the use of NEAC 2200/ACOS 900 Time Sharing System.

References

1 Bankoff, S. G., "Heat Conduction or Diffusion with Change of Phase," *Advances in Chemical Engineering*, Vol. 5, Academic Press, N.Y., 1964, pp. 75–150.

2 Muehlbauer, J. C., and Sunderland, J. E., "Heat Conduction with Freezing or Melting," *Appl. Mech. Rev.*, Vol. 18, No. 12, 1965, p. 951.

3 Ockendon, J. R., and Hodgkins, W. R., ed., *Moving Boundary Problems in Heat Flow and Diffusion*, Clarendon Press, Oxford, 1975.

4 Wilson, D. G. et al., ed., *Moving Boundary Problems*, Academic Press, N.Y., 1978.

5 Saitoh, T., "Recent Developments of Solution Methods for the Freezing Problem: Part I," *Refrigeration*, Vol. 55, No. 636, 1980, pp. 875–883.

6 Saitoh, T., "ibid: Part II," *Refrigeration*, Vol. 55, No. 637, 1980, pp. 1005–1015.

7 Sparrow, E. M., Schmidt, R. R., and Ramsey, J. W., "Experiments on the Role of Natural Convection in the Melting of Solids," ASME JOURNAL OF HEAT TRANSFER, Vol. 100, 1978, pp. 11–16.

8 Bathelt, A. G., Viskanta, R., and Leidenfrost, W., "Experiments on the Role of Natural Convection and Heat Source Arrangement in the Melting of a Solid," ASME Paper, No. 78-HT-47, 1978.

9 Bathelt, A. G., Viskanta, R., and Leidenfrost, W., "Latent Heat-of-Fusion Energy Storage: Experiments on Heat Transfer from Cylinders During Melting," ASME JOURNAL OF HEAT TRANSFER, Vol. 101, 1979, pp. 453-458.

10 Sparrow, E. M., Patankar, S. V., and Ramadhyani, S., "Analysis of Melting in the Presence of Natural Convection in the Melt Region," ASME JOURNAL OF HEAT TRANSFER, Vol. 99, 1977, pp. 520-526.

11 Sparrow, E. M., Ramsey, J. W., and Kemink, R. G., "Freezing Controlled by Natural Convection," ASME JOURNAL OF HEAT TRANSFER, Vol. 101, 1979, pp. 578-584.

12 Sparrow, E. M., Ramadhyani, S. and Patankar, S. V., "Effect of Subcooling on Cylindrical Melting," ASME JOURNAL OF HEAT TRANSFER, Vol. 100, 1978, pp. 395-402.

13 Abdel-Wahed, R. M., Ramsey, J. W., and Sparrow, E. M., "Photographic study of Melting about an Embedded Horizontal Heating Cylinder," *International Journal of Heat and Mass Transfer*, Vol. 22, 1979, pp. 171-173.

14 Saitoh, T., and Hirose, K., "Numerical Method For the Two-dimensional Freezing Problem Around a Horizontal Cylinder Encompassing a Density Inversion Point," Trans. JSME, Vol. 46, No. 405, 1980-5, pp. 971-979.

15 Yao, L. S., and Chen, F. F., "Effect of Natural Convection in the Melted Region Around a Heated Horizontal Cylinder," ASME JOURNAL OF HEAT TRANSFER, Vol. 102, 1980, pp. 667-672.

16 Pannu, J., Joglekar, G., and Rice, P. A., "Natural Convection to Cylinders of Phase Change Material used for Thermal Storage," AIChE Symposium Series, 1980, pp. 47-55.

17 Duda, J. L., Michael, F. M., Notter, R. H., and Vrentas, J. S., "Analysis of Two-dimensional Diffusion-controlled Moving Boundary Problems," *International Journal of Heat and Mass Transfer*, Vol. 18, 1975, pp. 901-910.

18 Saitoh, T., "Numerical Method for Moving Boundary Problems (3rd Report)," *Proceedings of the 11th National Heat Transfer Symposium*, Japan, 1974, pp. 333-336.

19 Saitoh, T., "Numerical Method for Multi-dimensional Freezing Problems in Arbitrary Domains," ASME JOURNAL OF HEAT TRANSFER, Vol. 100, 1978, pp. 294-299.

20 Saitoh, T., "Natural Convection Heat Transfer from a Horizontal Ice Cylinder," *Appl. Sci. Res.*, Vol. 32, 1976, pp. 429-451.

21 Landau, H. G., "Heat Conduction in Melting Solid," *Quarterly of Applied Mathematics*, Vol. 8, 1950, pp. 81-94.

22 Saitoh, T., "A Numerical Method for Two-dimensional Navier-Stokes Equation by Multipoint Finite Differences," *International Journal for Numerical Method in Engineering*, Vol. 9, 1977, pp. 1439-1454.

23 Nicholas, D., and Bayazitoglu, Y., "Heat Transfer and Melting Front Within a Horizontal Cylinder," ASME *Journal of Solar Engineering*, Vol. 102, 1980, pp. 229-232.

24 Katayama, K. et al., "A Study on Contact Heat Transfer with Melting," *Proceedings of the 18th National Heat Transfer Symposium*, Japan, 1981, pp. 70-72.

25 Saitoh, T., and Hirose, K., "Thermal Instability of Natural Convection Flow Over a Horizontal Ice Cylinder Encompassing a Maxmum Density Point," ASME JOURNAL OF HEAT TRANSFER, Vol. 102, 1980, pp. 261-267.

26 Sparrow, E. M., Lee, L., and Shamsunder, N., "Convective Instability in a Melt Layer Heated From Below," ASME JOURNAL OF HEAT TRANSFER, Vol. 98, 1976, pp. 88-94.

27 Saitoh, T., and Hirose, K., "Latent Heat Thermal Energy Storage of Solar Energy," *Proceedings of the 18th National Heat Transfer Symposium*, Japan, 1981, pp. 67-69.

Journal of Heat Transfer

Technical Notes

This section contains shorter technical papers. These shorter papers will be subjected to the same review process as that for full papers.

Laminar Mixed Convection From a Vertical Heated Surface in a Crossflow

G. H. Evans[1] and O. A. Plumb[2]

Nomenclature

f = dimensionless vertical vector potential
g = dimensionless horizontal vector potential, acceleration of gravity
Gr_x = Grashof number, $g\beta(T_w - T_\infty)x^3/\nu^2$
h = local convective heat-transfer coefficient
$\bar{h}$ = overall convective heat-transfer coefficient
k = fluid thermal conductivity
K = vertical dimension of surface
K^* = arbitrary length of scale
L = horizontal dimension of surface
n = power in combining law
Nu_z = local Nusselt number based on z, hz/k
Nu_L = overall Nusselt number for mixed convection, $\bar{h}L/k$
Nu_{zFC} = local Nusselt number for pure forced convection, hz/k
Nu_{FC} = overall Nusselt number for pure forced convection, $\bar{h}L/k$
Nu_{NC} = overall Nusselt number for pure natural convection, $\bar{h}K/k$
Pr = Prandtl number
Re = Reynolds number
T = temperature
u = vertical component of velocity
u_∞ = horizontal velocity in free stream
v = velocity component normal to surface
w = horizontal velocity component
x = vertical coordinate
x_1 = dimensionless vertical coordinate
y = coordinate normal to surface
Y = dependent variable in combining law
z = horizontal coordinate
z_1 = dimensionless horizontal coordinate
Z = dependent variable in combining law
α = mixed convection parameter, $g\beta\Delta TK/u_\infty^2$
β = coefficient of thermal expansion
η = dimensionless coordinate normal to surface
ψ = vertical vector potential
ξ = horizontal vector potential
ϕ = dimensionless temperature
ν = kinematic viscosity

Subscripts

∞ = evaluated at free stream condition
FC, = pure forced convection
NC, = pure natural convection
K, = based on the vertical dimension
L, = based on the horizontal dimension
w, = evaluated at wall temperature
x, = based on the local value of the vertical coordinate
z, = based on the local value of the horizontal coordinate

Introduction

Several studies of three-dimensional mixed convection boundary layers have appeared during the past few years. Such flows result when inertial and buoyancy forces are not aligned. For example, Yao and Chen [1] considered natural convection from a vertical heated cylinder perturbed by a horizontal forced flow. The perturbation parameter in this case was the ratio $\mathrm{Re}_D/\sqrt{\mathrm{Gr}_D}$, both based on the cylinder diameter. Their results indicate that forced convection becomes dominant at higher vertical positions on the cylinder. A disadvantage to perturbation solutions to boundary layers of this type is that two parameters appear in the dimensionless equations – the ratio $\mathrm{Gr}/\mathrm{Re}^2$ or $\mathrm{Re}/\sqrt{\mathrm{Gr}}$ and an aspect ratio consisting of the horizontal coordinate divided by the vertical coordinate or visa versa. Both parameters, or at least the product of the two, must be small if the results of a perturbation analysis are to be relied upon severely restricting the range of validity of the solution. Oosthuizen [2] solved numerically the boundary layer equations for a horizontal forced flow around a vertical heated cylinder with an unheated starting length. The results indicate that buoyancy has its greatest influence near the horizontal leading edge of the heated region. Plumb [3] and Eichhorn and Hasan [4]

[1]Thermal Sciences Division, Sandia National Laboratories, Livermore, Calif. 94550
[2]Department of Mechanical Engineering, Washington State University, Pullman, Wash. 99164. Assoc. Mem. ASME
Contributed by the Heat Transfer Division for publication in the JOURNAL OF HEAT TRANSFER. Manuscript received by the Heat Transfer Division September 18, 1981.

have obtained similarity solutions for Falkner-Skan type three-dimensional mixed convection. However, similarity results only for certain power law surface temperature distributions which depend upon the horizontal pressure gradient or wedge angle.

Experimental data for three-dimensional mixed convection boundary layers is currently not available in the literature, however, experiments are underway [5-7]. The impetus behind these experimental studies as well as the analytical and numerical studies cited is to provide a basis for predicting convective losses from solar central power receivers. However, results might also be applicable to the prediction of heat losses from solar collectors, buildings, and petroleum storage tanks.

The present study is concerned with mixed convection from a vertical heated surface in a horizontal crossflow. The governing boundary layer equations were solved numerically using an extension of the technique developed by Cebeci and Keller [8]. The combining law of Churchill and Usagi [9] was utilized to develop a correlation for the average Nusselt number.

Analysis

A vertical isothermal flat plate maintained at a temperature greater then the ambient fluid and exposed to a horizontal crossflow parallel to the plate surface is considered.

Upon introduction of the three-dimensional velocity potential

$$u(x,y,z) = \frac{\partial \psi}{\partial y}(x,y,z)$$

$$v(x,y,z) = -\left[\frac{\partial \psi}{\partial x}(x,y,z) + \frac{\partial \xi}{\partial z}(x,y,z)\right] \tag{1}$$

$$w(x,y,z) = \frac{\partial \xi}{\partial y}(x,y,z)$$

the continuity equation is eliminated. The following transformation can then be applied to the horizontal momentum, vertical momentum, and energy equations in the boundary layer and Boussinesq approximations:

$$\psi(x,y,z) = \frac{\nu}{K^*}\left(\frac{x}{K^*}\right)^{1/2} z\sqrt{\mathrm{Re}_z} f(x_1, \eta, z_1)$$

$$\xi(x,y,z) = \nu\left(\frac{x}{K^*}\right)^{1/2}\sqrt{\mathrm{Re}_z} g(x_1, \eta, z_1) \tag{2}$$

$$T(x,y,z) - T_\infty = (T_w - T_\infty)\phi(x_i, \eta, z_1)$$

where

$$\eta = \frac{y}{\sqrt{xz}}\left(\frac{K^* u_\infty}{\nu}\right)^{1/2}$$

and

$$x_1 = x/K, \; z_1 = z/L$$

where K and L are the vertical and horizontal dimensions of the plate, respectively. The arbitrary length scale K^* is utilized to control the transformed boundary layer thickness. Solving the boundary layer equations in this transformed coordinate system offers several advantages over a solution in physical coordinates. First the dependent variables change more slowly in the streamwise directions, thus, allowing larger steps to be taken in the x and z directions. This saves computer storage space as well as CPU time. The transformation also stretches the y coordinate and reduces the variation in boundary layer thickness, thus, eliminating the need to expand the solution domain as the boundary layer grows. This particular transformation was selected because it eliminates singularities at both $x=0$ and $z=0$ and results in ordinary differential equations which can be solved at the leading edges of the plate, thus, eliminating the need to prescribe profiles of dependent variables to start the numerical solutions. The resulting transformed equations can be written

$$f''' + \frac{1}{2}\left(\frac{L}{K^*}\right)^2 z_1^2 ff'' + \frac{1}{2}\left(\frac{K}{K^*}\right)x_1[gf'' - 2g'f'] + \left(\frac{g\beta\Delta TK}{u_\infty{}^2}\right)x_1\phi = \left(\frac{L}{K^*}\right)^2 z_1^2 x_1\left[f'\frac{\partial f'}{\partial x_1} - f''\frac{\partial f}{\partial x_1}\right] + \left(\frac{K}{K^*}\right)x_1 z_1\left[g'\frac{\partial f'}{\partial z_1} - f''\frac{\partial g}{\partial z_1}\right] \tag{3}$$

$$g''' + \frac{1}{2}\left(\frac{K}{K^*}\right)x_1 gg'' + \frac{1}{2}\left(\frac{L}{K^*}\right)^2 z_1^2 fg'' = \left(\frac{L}{K^*}\right)^2 z_1^2 x_1\left[f'\frac{\partial g'}{\partial x_1} - g''\frac{\partial f}{\partial x_1}\right] + \left(\frac{K}{K^*}\right)x_1 z_1\left[g'\frac{\partial g'}{\partial z_1} - g''\frac{\partial g}{\partial z_1}\right] \tag{4}$$

$$\frac{\phi''}{\mathrm{Pr}} + \frac{1}{2}\left(\frac{L}{K^*}\right)^2 z_1^2 f\phi' + \frac{1}{2}\left(\frac{K}{K^*}\right)x_1 g\phi' = \left(\frac{L}{K^*}\right)^2 z_1^2 x_1\left[f'\frac{\partial \phi}{\partial x_1} - \phi'\frac{\partial f}{\partial x_1}\right] + \left(\frac{K}{K^*}\right)x_1 z_1\left[g'\frac{\partial \phi}{\partial z_1} - \phi'\frac{\partial g}{\partial z_1}\right] \tag{5}$$

$$\text{at } \eta = 0: f = f' = g' = g = 1 - \phi = 0 \tag{6}$$

$$\text{at } \eta \to \infty: g' - 1, f', \phi \to 0$$

The primes in equations (3-6) imply differentiation with respect to η. In the above system of equations the mixed convection parameter

$$\alpha = \frac{g\beta\Delta TK}{u_\infty{}^2} \tag{7}$$

appears as the coefficient of the buoyancy term in the vertical momentum equation. Thus, the equations are reduced to those for the Blasius flow when $\alpha = 0$. The length scale ratio, K/K^*, was set at 20 to provide an initial transformed boundary layer thickness of $\eta \sim 5$. A square plate was considered, thus $K = L$ for a fluid with a Prandtl number of 0.7.

Numerical Solution. An extended version of the box scheme as detailed in Cebeci and Bradshaw [8] was used to obtain a numerical solution to the system of equations (3-6). After solving the ordinary differential equations which result for $x_1 = 0$ and $z_1 = 0$, x_1 was incremented and the solution marched in the z_1 direction. This process was continued until the entire region of interest was covered. Details of the numerical solution can be found in [10]. A number of test cases were run to verify the accuracy of the numerical results and establish the necessary number of cross stream grids and size of the streamwise steps.

The first two test cases were used to establish the necessary number of cross stream grids. These cases were run with $x_1 = z_1 = .1$ and $\alpha = 5.0$, which should be the worst case because of large cross stream buoyancy. The first case utilized fifty uniformly spaced grids of $\eta = .1$ while the second utilized the following nonuniform grid:

$$\Delta\eta_j = .05\ ,\quad 1 \le j \le 40$$
$$\Delta\eta_j = .10\ ,\quad 41 \le j \le 50$$
$$\Delta\eta_j = .20\ ,\quad 51 \le j \le 61$$

The wall shear stress and heat flux calculated using these two cross stream grid distributions agreed to within .5 percent for all positions on the plate. The nonuniform grid was used for the calculations presented since it did not increase the required storage or CPU time significantly. In the transformed coordinate the boundary layer thickness decreases slowly in the vertical direction. The nonuniform grid results in approximately fifty grids within the boundary layer at the top of the plate whereas the uniform grid results in approximately thirty.

The following tests involving the streamwise step size were run for $\alpha = .50$:

Case 1:	$\Delta x_1 = .1,$	$\Delta z_1 = .1$
Case 2:	$\Delta x_1 = .1,$	$\Delta z_1 = .05$
Case 3:	$\Delta x_1 = .05,$	$\Delta z_1 = .1$

The resulting shear stress and heat flux at the wall agreed to within .5 percent for all locations on the plate for cases 1 and 2. Cases 1 and 3 agreed to within .5 percent, except near the vertical leading edge ($x_1 \le .2$) where the difference was as large as 1.8 percent. Streamwise steps of $\Delta x_1 = \Delta z_1 = .1$ were used for the results presented.

The three-dimensional code was compared to the similarity solution for pure forced flow by setting the mixed convection parameter, α, to zero. The results for both the local shear stress and the local heat flux were in excellent agreement with the similarity solution. Of primary importance is the overall heat-transfer coefficient or Nusselt number since this is the parameter which is of practical interest. Overall heat-transfer coefficients were calculated by performing the following integrations across the boundary layer at the exit edges of the plate:

$$q = \rho c_p \int_0^\infty u(T - T_\infty)\, dy \quad (\text{at } x_1 = 1.0) \tag{8}$$

$$q = \rho c_p \int_0^\infty w(T - T_\infty)\, dy \quad (\text{at } z_1 = 1.0) \tag{9}$$

The integrations indicated in (8) and (9) were performed at each boundary node and summed to obtain the overall heat-transfer coefficient. For pure forced convection

$$\frac{\overline{\mathrm{Nu}_L}}{\mathrm{Re}_L^{1/2}} = \mathrm{Pr}\left(\frac{K}{K^*}\right)^{1/2} \Sigma\,(x_1 z_1)^{1/2} \int_0^{\eta_{\mathrm{EDGE}}} g'\phi d\eta = .5834 \tag{10}$$

as compared to .584 from the similarity solution—a difference of .10 percent. The code was then tested against the three-dimensional mixed convection similarity solution [3]. The case examined was a vertical flat plate in stagnation flow with a uniform surface temperature in the horizontal direction and a linearly increasing surface temperature in the vertical direction. Agreement with the similarity solution was within .8 percent, except near the stagnation line ($z_1 = 0$) where the discrepancy was as high as 3 percent. This error is due to the fact that the transformation utilized resulted in a singularity at $z_1 = 0$ for the stagnation flow. Thus, for this case, and only this case, initial profiles had to be given at $z_1 = 0$ to start the numerical solution.

Results. The effect of the local heat transfer as well as the three-dimensional nature of the flow is demonstrated in Fig. 1. In this figure the local Nusselt number divided by that for pure forced convection as given by the Blasius solution is plotted as a function of the horizontal coordinate, z_1, with α and x_1 as parameters. The local heat-transfer coefficient

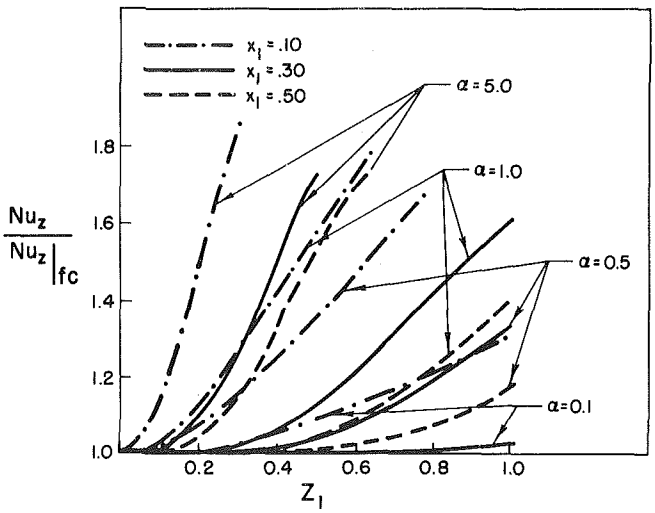

Fig. 1 Local Nusselt number for mixed convection normalized with that for pure forced convection

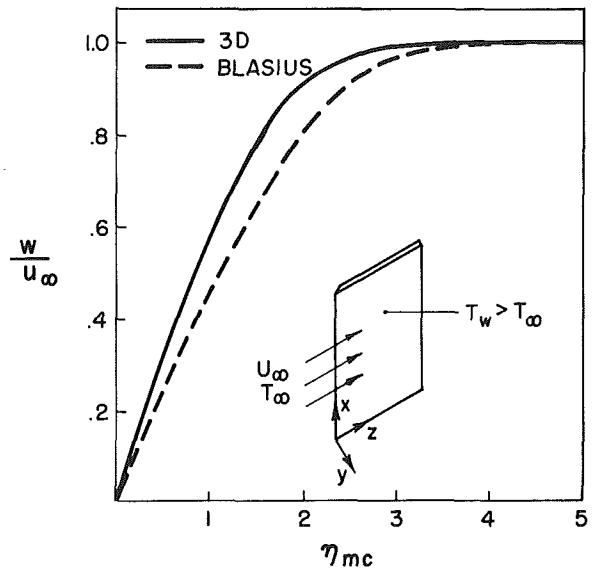

Fig. 2 Comparison of horizontal velocity distribution at $x_1 = 0.1$, $z_1 = 1.0$, and $\alpha = 0.1$ with the Blasius profile

deviates more from the pure forced convection value near the lower edge of the plate. The deviation is greater for larger values of the mixed convection parameter as would be expected. At a fixed vertical position on the surface, buoyancy effects are more pronounced for large horizontal positions. The results can be interpreted by considering two boundary layers separately instead of a single mixed flow boundary layer. When the buoyancy induced boundary layer is thin in comparison to the forced boundary layer, it has a more pronounced effect on the results and visa versa. Thus, the results are closer to those for pure forced convection at small values of z_1, the horizontal coordinate and large values of x_1, the vertical coordinate. Similar conclusions can be drawn with regard to the wall shear stress.

The effect of buoyancy is to thin the forced convection boundary layer. This is demonstrated in Fig. 2 where the Blasius profile is compared to the mixed convection profile in the horizontal direction for $x_1 = .1$, $z_1 = 1.0$, and $\alpha = 1$. Even though α is quite small, the effect of buoyancy is large at this (x_1, z_1) location. The effect of the crossflow on the vertical buoyancy induced velocity profile is shown in Fig. 3. At a horizontal location, $z_1 = .5$, the magnitude of vertical

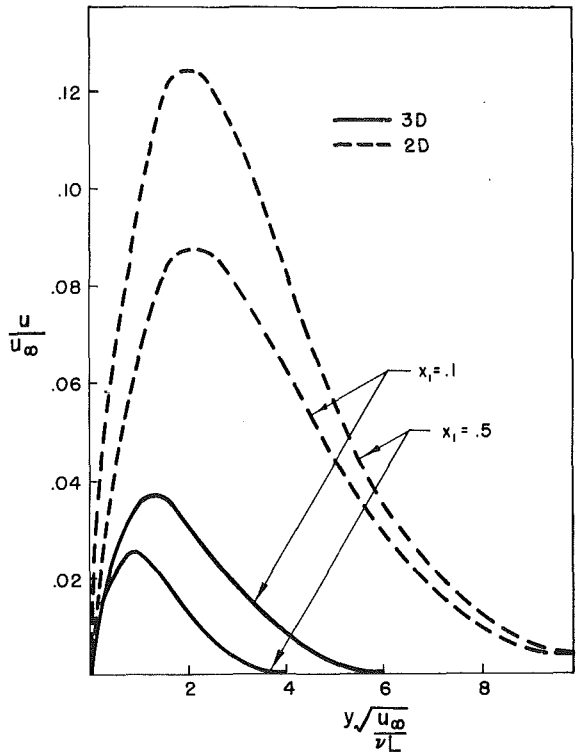

Fig. 3 Comparison of vertical velocity distribution for $\alpha = 0.1$ and $z_1 = 0.5$ with the pure natural convection profile

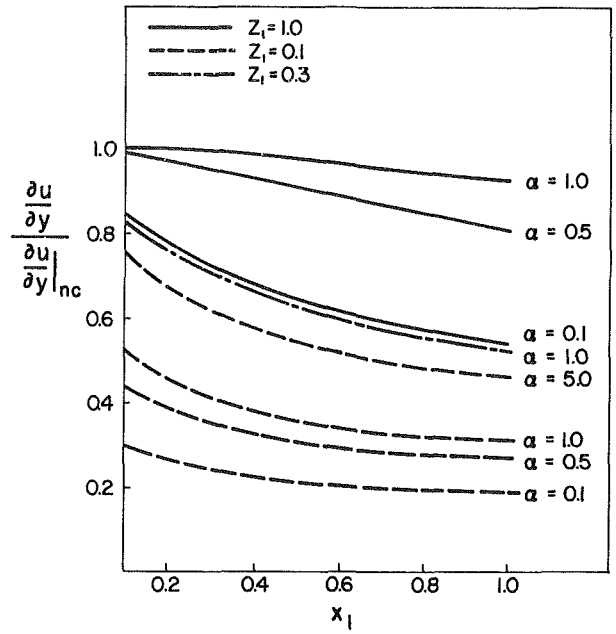

Fig. 4 Vertical component of wall shear stress normalized with that for pure natural convection

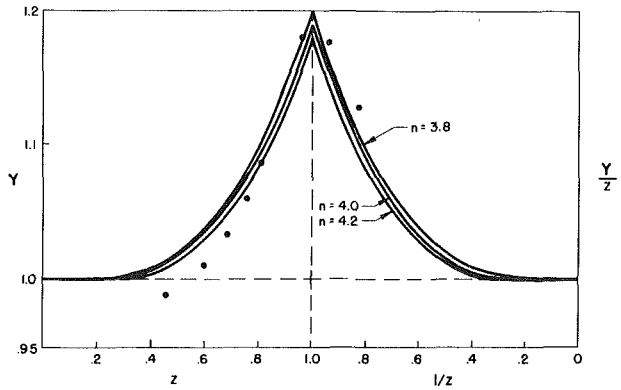

Fig. 5 Combining law for the average Nusselt number compared with computed values

velocity is greater and the profile fuller than it is at $z_1 = .1$ for a fixed vertical position.

Results for the vertical component of the shear stress are shown in Fig. 4. In this case the shear stress is referenced to the pure natural convection value and plotted as a function of the vertical coordinate, x_1. The deviation from that for pure natural convection is greatest at large values of x_1 and increases with the mixed convection parameter. Consistent with the discussion thus far, forced convection is seen to be dominant near the vertical leading edge. This figure demonstrates that the numerical solution does approach the pure natural convection limit when α and z_1 are large and x_1 is small.

The most useful result in terms of the practical applications which were cited earlier is an estimate of the average convective heat-transfer coefficient or average Nusselt number. Average heat-transfer coefficients were determined by numerically integrating equation (8) and (9) as indicated earlier. This procedure was carried out for several values of α and the results compared to the combining law of Churchill and Usagi [9].

In general form the combining law can be written

$$Y = (1 + Z^n)^{1/n} \tag{11}$$

For this problem the average Nusselt number divided by its value when the mixed convection parameter, α, is zero is represented by the dependent variable Y. Z represents the dependent variable when the parameter, α, goes to infinity divided by its value when $\alpha = 0$. Thus, for the case of mixed convection,

$$Y = \frac{\mathrm{Nu}_L}{\mathrm{Nu}_{FC}}, \quad Z = \frac{\mathrm{Nu}_{NC}}{\mathrm{Nu}_{FC}} \tag{12}$$

The exponent n is chosen to provide the best fit to the data. Figure 5 shows the combining law for $n = 3.8$, 4.0, and 4.2, along with the numerical data for the average Nusselt number. The combining law does not result in a precise representation of the numerical results, however, it does yield a correlation for the overall Nusselt number which is adequate for engineering calculations. The combining law with $n = 4.0$ agrees with the numerical data to within 2 percent except at $\alpha = 5.0$ where the discrepancy is 2.5 percent. From the combining law the correlation for the average Nusselt number can be written with $n = 4$ as

$$\overline{\mathrm{Nu}}_L = 0.584\,\mathrm{Re}_L^{1/2}\left[1.0 + 0.433\,\frac{\mathrm{Gr}_K}{\mathrm{Re}_L^2}\right]^{1/4} \tag{13}$$

for a square plate ($K = L$) and a Prandtl number of .7. This correlation is based on the assumption that the pure forced convection and pure natural limits are given by

$$\overline{\mathrm{Nu}}_{FC} = 0.584\,\mathrm{Re}_L^{1/2} \tag{14}$$

$$\overline{\mathrm{Nu}}_{NC} = 0.473\,\mathrm{Gr}_K^{1/4} \tag{15}$$

For a plate with $L > K$, n should be less than 4 since natural convection should be more dominant. For a tall, narrow plate ($K > L$), n should be greater than 4 since forced convection would be expected to be more dominant.

References

1 Yao, L. S., and Chen, F. M., "Analysis of Convective Heat Loss from the Receiver of Solar Power Plants," presented at ASME Winter Annual Meeting, New York, Dec. 1979, Paper No. 79-WA/HT-36.

2 Oosthuizen, P. H., "Numerical Study of Combined Convective Heat Transfer from a Vertical Cylinder in a Horizontal Flow," 6th International Heat Transfer Conference, Toronto, Paper No. MC-4, Vol. 1, 1978, pp. 19-24.
3 Plumb, O. A., "The Effect of Crossflow on Natural Convection from Vertical Heated Surfaces," presented at 19th National Heat Transfer Conference, Orlando, 1980, ASME Paper No. 80-HT-71.
4 Eichhorn, R., and Hasan, M. M., "Mixed Convection about a Vertical Surface in a Crossflow—a Similarity Solution," ASME JOURNAL OF HEAT TRANSFER, Vol. 102, 1980, pp. 775-777.
5 Schwind, R. G., Reed, R., and Seibers, D. L., "Three Meter Plate Mixed Convection Boundary Layer Test Program," presented at DOE/SERI/SNLL Workshop on Convective Losses from Solar Central Receivers, Sandia National Laboratories, Livermore, Calif., Mar. 25-27, 1981.
6 Kraabel, J. S., personal communication, Apr. 1981.
7 Clausing, A. C., Presentation at DOE/SERI/SNLL Workshop on Convective Losses from Solar Central Receivers, Sandia National Laboratories, Livermore, Calif., Mar. 25-27, 1981.
8 Cebeci, T., and Bradshaw, P., *Momentum Transport in Boundary Layers*, Hemisphere Pub. Co./McGraw-Hill 1977.
9 Churchill, S. W., and Usagi, R., "A General Expression for the Correlation of Rates of Transfer and Other Phenomena," *AIChE Journal*, Vol. 18, No. 6, pp. 1121-1128.
10 Evans, G. L., "A Numerical Study of Three-Dimensional Laminar Mixed Convection," Ph.D. dissertation, Department of Mechanical Engineering, Washington State University, Aug. 1981.

Mixed Convection Flow Over a Semi-Infinite Horizontal Plate With Vectored Mass Transfer

J. Dey[1]

Introduction

This note is concerned with the mixed convection flow over a semiinfinite horizontal flat plate with vectored mass transfer at the wall. Earlier investigations [1-3] with vectored mass transfer were confined to forced convection flows. As such, the present results should be of general interest in understanding the role of buoyancy force in boundary-layer problems of practical importance, such as transpiration cooling of turbine blades and rocket engines, control of boundary-layer on bodies, etc. The normal mass-transfer component (v_w) is assumed as $v_w \propto x^{-1/2}$ (x denotes the distance from the leading edge) to include dual solutions, as observed by Inger and Swean [1]. Such dual solutions are not possible for uniform v_w. Also, uniform v_w does not permit similarity solution, which is possible for $v_w \propto x^{-1/2}$.

Analysis, Results, and Discussion

For incompressible, laminar, steady flow over a horizontal plate, which is maintained at a temperature that is inversely proportional to the square root of the distance from the leading edge, the governing boundary-layer similarity equations are [4]

$$2f''' + ff'' + K\eta\theta = 0 \tag{1}$$

$$2\theta'' + \mathrm{Pr}[f\theta' + f'\theta] = 0 \tag{2}$$

Here $f(\eta)$ denotes the nondimensional stream function such that the two velocity components in x and y directions are $u = f'(\eta)$ and $v = (\eta f' - f)x^{-1/2}/2$, respectively. The free-stream conditions are assumed to be uniform. The similarity variable is given by $\eta = yx^{-1/2}$. $\theta(\eta)$ denotes the nondimensional temperature function; Pr denotes the Prandtl number; K denotes the buoyancy parameter, defined as the ratio of Archimedes number to the square root of the Reynolds number, based on the free-stream velocity and characteristic length (for details see reference [4]). $K > 0$ (plate temperature larger than the free-stream temperature) buoyancy supports the flow. For $K < 0$ (plate temperature lower than the free-stream temperature), the opposite is true. The boundary conditions for (1) and (2) are

$$v(\text{wall}) = -2v_w x^{1/2} = f(0); u(\text{wall}) = u_w = f'(0)$$

$$\theta(0) = 1 \tag{3a}$$

$$f'(\infty) \to 1;\ \theta(\infty) \to 0 \tag{3b}$$

For the wall temperature distribution, mentioned above, the solutions of the boundary-layer equations (1, 2) are exact, which is not possible for the uniform wall temperature. Here, it is assumed that $v_w \propto x^{-1/2}$ to obtain similarity solutions. Hence the boundary conditions 3(a) become

$$f(0) = f_w = \text{constant (given)};\ f'(0) = f_w' = \text{constant (given)}$$

$$\theta(0) = 1 \tag{3c}$$

Equations (1-2), along with the boundary conditions 3(b) and 3(c) were solved using Hemmings's predictor corrector method on DEC-10 computer for $\mathrm{Pr} = 0.7$ and $f_w = \pm 0.1$; ± 0.2; $f_w' = \pm 0.1$; $^{\circ} \pm 0.2$ (in order to keep the mass-transfer value low) and for $0.05 \le K \ge 0.5$. The results are shown in Figs. 1-3. Solution could not be obtained for $K = -0.05$ with upstream vectored injection ($f_w = f_w' = -0.1$; -0.2 and combinations). It is interesting to note that the wall heat-transfer mode ($\theta'(0) = -\mathrm{Pr}\ f_w/2$) depends on f_w, which causes the boundary-layer fluid either to receive heat from the wall ($f_w > 0$) or transfer heat to the wall ($f_w < 0$). Also, the numerical values of $\theta'(0)$ can be verified with the exact values and were found to be in excellent agreement.

Figure 1 shows that the buoyancy force enhances the wall shear values ($f''(0)$) as in the case of mixed convection without mass transfer ($f_w' = f_w = 0$). It has been shown [1] that the wall shear values are higher with downstream vectored suction (DVS) than those with upstream vectored injection (UVI). Figure 1 shows that this is true up to $K \simeq 0.15$ for $f_w' = f_w = 0.1$ or 0.2 (i.e., DVS). For $K > 0.15$, the wall shear values with UVI ($f_w' = f_w = -0.1$ or -0.2) are higher than those with DVS ($f_w' = f_w = 0.1$ or 0.2). Injection or suction angle being proportional to f_w and f_w', we find that for the same injection or suction angle ($f_w/f_w' = -0.1/-0.1$; $0.1/0.1$ or $-0.2/-0.2$; $0.2/0.2$) and $K \simeq 0.15$, the boundary-layer fluid with either UVI or DVS undergoes the same wall shear stress. Comparison with $f_w' = f_w = 0$ shows that wall shear values with DVS ($f_w' = f_w = 0.1$ or 0.2) are higher for $K < 0.1$. For $K > 0.1$, the reverse is true. Similarly, the wall shear values with UVI ($f_w' = f_w = -0.1$ or -0.2) are higher than those without mass transfer for $K > 0.2$. For $K < 0.2$ the reverse is true. Also, upstream vectored suction ($f_w' = -0.2$; $f_w = 0.2$) enhances the wall shear stress while downstream vectored injection ($f_w' = 0.2$; $f_w = -0.2$) reduces the wall shear stress. Such change in shear values are due to vectored mass transfer acting as favourable pressure gradient or adverse pressure gradient. For example, comparing upstream vectored suction ($f_w' = -0.2$; $f_w = 0.2$) with $f_w' = f_w' = f_w = 0$ we find that $\theta'(0)$ is negative with upstream vectored suction. This means that the fluid receives heat from the wall, and it should be expected that the fluid near the wall is hotter than the fluid far away from the wall (in the transverse direction). Now, this particular suction causes the colder fluid to appear near the wall where it experiences a buoyancy force due to density difference. This appears as pressure gradient (since the axial pressure gradient is associated with the density variation) in addition to that without mass transfer causing higher wall shear values than those without mass transfer. Similarly, suitable explanations can be given to other situations which are more complicated.

Dual solutions were possible only with upstream vectored

[1]Department of Mechanical Engineering, Indian Institute of Science, Bangalore, 560012, India

Contributed by the Heat Transfer Division for publication in the JOURNAL OF HEAT TRANSFER. Manuscript received by the Heat Transfer Division July 6, 1981.

2 Oosthuizen, P. H., "Numerical Study of Combined Convective Heat Transfer from a Vertical Cylinder in a Horizontal Flow," 6th International Heat Transfer Conference, Toronto, Paper No. MC-4, Vol. 1, 1978, pp. 19-24.
3 Plumb, O. A., "The Effect of Crossflow on Natural Convection from Vertical Heated Surfaces," presented at 19th National Heat Transfer Conference, Orlando, 1980, ASME Paper No. 80-HT-71.
4 Eichhorn, R., and Hasan, M. M., "Mixed Convection about a Vertical Surface in a Crossflow—a Similarity Solution," ASME JOURNAL OF HEAT TRANSFER, Vol. 102, 1980, pp. 775-777.
5 Schwind, R. G., Reed, R., and Seibers, D. L., "Three Meter Plate Mixed Convection Boundary Layer Test Program," presented at DOE/SERI/SNLL Workshop on Convective Losses from Solar Central Receivers, Sandia National Laboratories, Livermore, Calif., Mar. 25-27, 1981.
6 Kraabel, J. S., personal communication, Apr. 1981.
7 Clausing, A. C., Presentation at DOE/SERI/SNLL Workshop on Convective Losses from Solar Central Receivers, Sandia National Laboratories, Livermore, Calif., Mar. 25-27, 1981.
8 Cebeci, T., and Bradshaw, P., *Momentum Transport in Boundary Layers*, Hemisphere Pub. Co./McGraw-Hill 1977.
9 Churchill, S. W., and Usagi, R., "A General Expression for the Correlation of Rates of Transfer and Other Phenomena," *AIChE Journal*, Vol. 18, No. 6, pp. 1121-1128.
10 Evans, G. L., "A Numerical Study of Three-Dimensional Laminar Mixed Convection," Ph.D. dissertation, Department of Mechanical Engineering, Washington State University, Aug. 1981.

Mixed Convection Flow Over a Semi-Infinite Horizontal Plate With Vectored Mass Transfer

J. Dey[1]

Introduction

This note is concerned with the mixed convection flow over a semiinfinite horizontal flat plate with vectored mass transfer at the wall. Earlier investigations [1-3] with vectored mass transfer were confined to forced convection flows. As such, the present results should be of general interest in understanding the role of buoyancy force in boundary-layer problems of practical importance, such as transpiration cooling of turbine blades and rocket engines, control of boundary-layer on bodies, etc. The normal mass-transfer component (v_w) is assumed as $v_w \propto x^{-1/2}$ (x denotes the distance from the leading edge) to include dual solutions, as observed by Inger and Swean [1]. Such dual solutions are not possible for uniform v_w. Also, uniform v_w does not permit similarity solution, which is possible for $v_w \propto x^{-1/2}$.

Analysis, Results, and Discussion

For incompressible, laminar, steady flow over a horizontal plate, which is maintained at a temperature that is inversely proportional to the square root of the distance from the leading edge, the governing boundary-layer similarity equations are [4]

$$2f''' + ff'' + K\eta\theta = 0 \tag{1}$$

$$2\theta'' + \Pr[f\theta' + f'\theta] = 0 \tag{2}$$

Here $f(\eta)$ denotes the nondimensional stream function such that the two velocity components in x and y directions are $u = f'(\eta)$ and $v = (\eta f' - f)x^{-1/2}/2$, respectively. The free-stream conditions are assumed to be uniform. The similarity variable is given by $\eta = yx^{-1/2}$. $\theta(\eta)$ denotes the nondimensional temperature function; Pr denotes the Prandtl number; K denotes the buoyancy parameter, defined as the ratio of Archimedes number to the square root of the Reynolds number, based on the free-stream velocity and characteristic length (for details see reference [4]). $K>0$ (plate temperature larger than the free-stream temperature) buoyancy supports the flow. For $K<0$ (plate temperature lower than the free-stream temperature), the opposite is true. The boundary conditions for (1) and (2) are

$$v(\text{wall}) = -2v_w x^{1/2} = f(0); u(\text{wall}) = u_w = f'(0)$$

$$\theta(0) = 1 \tag{3a}$$

$$f'(\infty) \to 1;\ \theta(\infty) \to 0 \tag{3b}$$

For the wall temperature distribution, mentioned above, the solutions of the boundary-layer equations (1, 2) are exact, which is not possible for the uniform wall temperature. Here, it is assumed that $v_w \propto x^{-1/2}$ to obtain similarity solutions. Hence the boundary conditions 3(a) become

$$f(0) = f_w = \text{constant (given)};\ f'(0) = f_w' = \text{constant (given)}$$

$$\theta(0) = 1 \tag{3c}$$

Equations (1-2), along with the boundary conditions 3(b) and 3(c) were solved using Hemmings's predictor corrector method on DEC-10 computer for $\Pr = 0.7$ and $f_w = \pm 0.1$; ± 0.2; $f_w' = \pm 0.1$; $^{\circ} \pm 0.2$ (in order to keep the mass-transfer value low) and for $0.05 \le K \ge 0.5$. The results are shown in Figs. 1-3. Solution could not be obtained for $K = -0.05$ with upstream vectored injection ($f_w = f_w' = -0.1$; -0.2 and combinations). It is interesting to note that the wall heat-transfer mode ($\theta'(0) = -\Pr\ f_w/2$) depends on f_w, which causes the boundary-layer fluid either to receive heat from the wall ($f_w > 0$) or transfer heat to the wall ($f_w < 0$). Also, the numerical values of $\theta'(0)$ can be verified with the exact values and were found to be in excellent agreement.

Figure 1 shows that the buoyancy force enhances the wall shear values ($f''(0)$) as in the case of mixed convection without mass transfer ($f_w' = f_w = 0$). It has been shown [1] that the wall shear values are higher with downstream vectored suction (DVS) than those with upstream vectored injection (UVI). Figure 1 shows that this is true up to $K \simeq 0.15$ for $f_w' = f_w = 0.1$ or 0.2 (i.e., DVS). For $K > 0.15$, the wall shear values with UVI ($f_w' = f_w = -0.1$ or -0.2) are higher than those with DVS ($f_w' = f_w = 0.1$ or 0.2). Injection or suction angle being proportional to f_w and f_w', we find that for the same injection or suction angle ($f_w/f_w' = -0.1/-0.1$; $0.1/0.1$ or $-0.2/-0.2$; $0.2/0.2$) and $K \simeq 0.15$, the boundary-layer fluid with either UVI or DVS undergoes the same wall shear stress. Comparison with $f_w' = f_w = 0$ shows that wall shear values with DVS ($f_w' = f_w = 0.1$ or 0.2) are higher for $K < 0.1$. For $K > 0.1$, the reverse is true. Similarly, the wall shear values with UVI ($f_w' = f_w = -0.1$ or -0.2) are higher than those without mass transfer for $K > 0.2$. For $K < 0.2$ the reverse is true. Also, upstream vectored suction ($f_w' = -0.2$; $f_w = 0.2$) enhances the wall shear stress while downstream vectored injection ($f_w' = 0.2$; $f_w = -0.2$) reduces the wall shear stress. Such change in shear values are due to vectored mass transfer acting as favourable pressure gradient or adverse pressure gradient. For example, comparing upstream vectored suction ($f_w' = -0.2$; $f_w = 0.2$) with $f_w' = f_w' = f_w = 0$ we find that $\theta'(0)$ is negative with upstream vectored suction. This means that the fluid receives heat from the wall, and it should be expected that the fluid near the wall is hotter than the fluid far away from the wall (in the transverse direction). Now, this particular suction causes the colder fluid to appear near the wall where it experiences a buoyancy force due to density difference. This appears as pressure gradient (since the axial pressure gradient is associated with the density variation) in addition to that without mass transfer causing higher wall shear values than those without mass transfer. Similarly, suitable explanations can be given to other situations which are more complicated.

Dual solutions were possible only with upstream vectored

[1]Department of Mechanical Engineering, Indian Institute of Science, Bangalore, 560012, India

Contributed by the Heat Transfer Division for publication in the JOURNAL OF HEAT TRANSFER. Manuscript received by the Heat Transfer Division July 6, 1981.

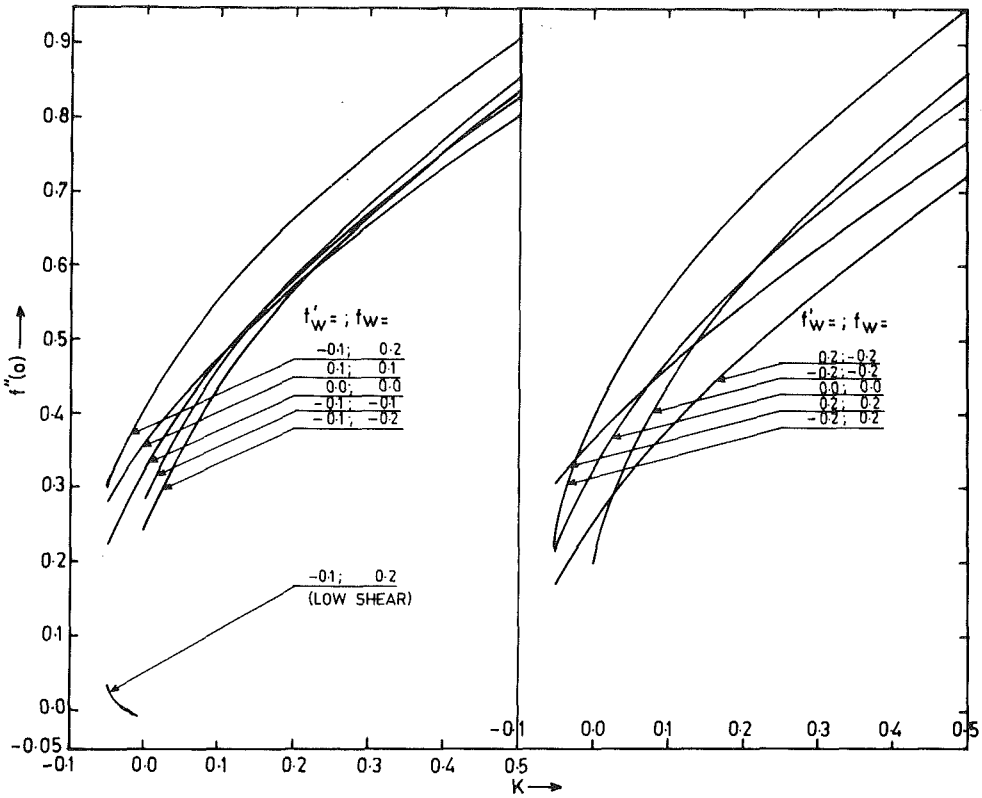

Fig. 1 Dimensionless wall shear values as a function of the buoyancy parameter (K) for various vectored mass transfer values

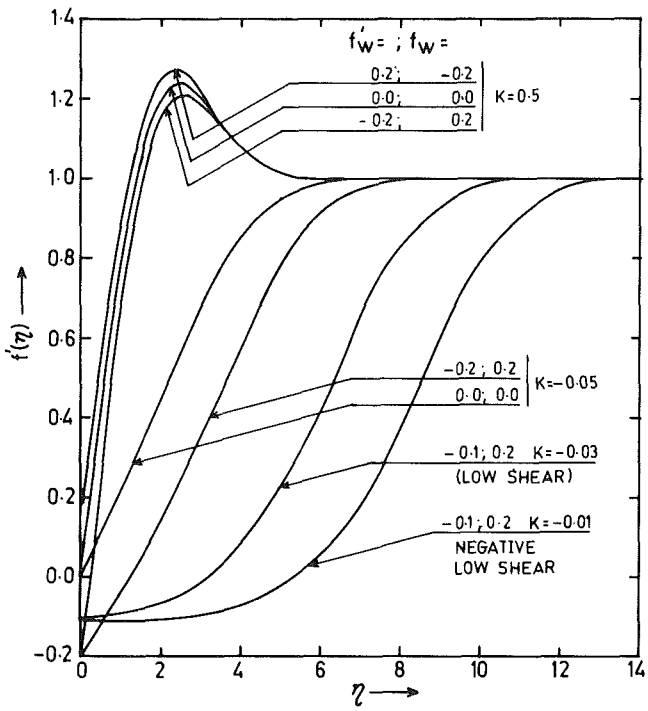

Fig. 2 Velocity profiles with vectored mass transfer for various values of the buoyancy parameter (K)

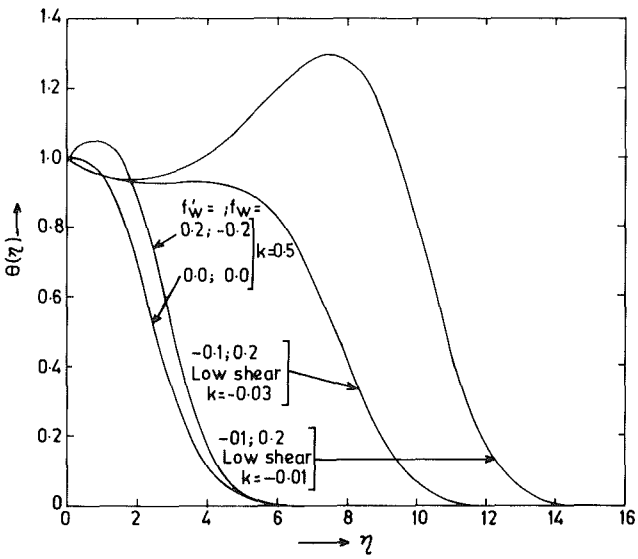

Fig. 3 Temperature profiles with vectored mass transfer for various values of the buoyancy parameter (K)

suction ($f_w' = -0.1$; $f_w = 0.2$) and $K<0$. The low shear values, Fig. 1, decrease with increasing buoyancy parameter. This trend is opposite to that for high shear solutions. It appears that low shear and high shear solutions (for $f_w' = -0.1$; $f_w = 0.2$) are two branches of one and the same curve. The vertical tangent at this curve defines a critical value below which no similarity solution exists. High and low shear solutions are the solutions of the same equations for given values of f_w' and f_w.

Typical velocity and temperature profiles are shown in Figs. 2 and 3. For $K = -0.01$ the low shear velocity profile, Fig. 2, exhibits undershoot, i.e., negative wall shear stress. Such a result was not reported earlier. However, after completion of this work it was pointed out [5] that a double-valued solution for $K<0$ and $\Pr = 1$ was also observed for the same flow geometry without mass transfer. When the curve passes through $f''(0) = 0$ the shear stress become negative exhibiting velocity undershoot. That situation has been explained [5] as the separated flow region with flow reversal. It appears from the present results that even with upstream vectored suction

($f_w' = -0.1$; $f_w = 0.2$) a similar situation exists. This can be attributed to the retarding buoyancy force. The corresponding temperature profile, Fig. 3, shows a large overshoot. Low shear thermal boundary-layer thickness appears to increase with buoyancy parameter.

Conclusions

From the above discussion we can conclude that the buoyancy force plays an important role in defining the flow field. For the flow geometry studied, it can be concluded that (*i*) for equal suction or injection angle and $K \simeq 0.15$, the boundary-layer fluid experiences the same wall shear stress, (*ii*) the buoyancy force plays opposite role for high- and low-shear solutions, (*iii*) the wall shear values with downstream vectored suction can be higher or lower than those with upstream vectored suction depending on the buoyancy parameter.

Acknowledgment

The author wishes to thank Prof. B. C. Dutta and ARDB (India) for the financial help and the referees for valuable suggestions.

References

1 Inger, G. R., and Swean, T. F., "Vectored Injection into Laminar Boundary Layers with Heat Transfer," *AIAA Journal*, Vol. 13, 1975, pp. 616-622.

2 Chen, T. S., and Sparrow, E. M., "Flow and Heat Transfer Over a Flat Plate with Uniformly Distributed, Vectored Surface Mass Transfer," ASME JOURNAL OF HEAT TRANSFER, Vol. 98, 1976, pp. 674-676.

3 Venkatachala, B. J., and Nath, G., "Nonsimilar Laminar Incompressible Boundary Layers with Vectored Mass Transfer," *Proceedings Indian Academy of Sciences: Engineering Sciences*, Vol. 3, 1979, pp. 129-142.

4 Schneider, W., "A Similarity Solution for Combined Forced and Free Convection Flow Over a Horizontal Plate," *International Journal of Heat and Mass Transfer*, Vol. 22, 1979, pp. 1401-1406.

5 One of the referees.

Buoyancy Effects on the Temperature Field in Downward Spreading Flames

R.A. Altenkirch[1], D. C. Winchester[2], and R. Eichhorn[3]

Nomenclature

- B = preexponential factor ($1 \times 10^6 \text{m}^3/\text{mol}\cdot\text{s}$)
- $\bar{B}$ = Damköhler number
- C_p = constant pressure, gas-phase specific heat (1.063 kJ/kg•K)
- E = activation energy (167.35 kJ/mol)
- g = acceleration of gravity
- g_e = earth's normal acceleration of gravity (9.807 m/s^2)
- i = mass of oxygen needed to burn a unit mass of fuel (1.185)
- k = gas-phase thermal conductivity (0.0459 J/m•s•K)
- L = effective heat of vaporization for solid fuel at T_∞ and gas-phase fuel at T_v (753 kJ/kg)
- l_b = buoyant length
- M = molecular weight of the oxidizer
- M_{ox} = molecular weight of oxygen (32 kg/kmol)
- $m_{ox,\infty}$ = mass fraction of oxygen in the oxidizer (0.233)
- P = pressure
- R = universal gas constant (8.314 J/mol•K)
- T = temperature
- $\bar{T}$ = dimensionless temperature, $T/(\Delta H_c m_{ox,\infty}/iC_p)$
- $\bar{T}_a$ = dimensionless activation temperature, $(E/R)/(\Delta H_c m_{ox,\infty}/iC_p)$
- T_f = flame temperature (2822 K)
- $\bar{T}_f$ = dimensionless flame temperature, $T_f(\Delta H_c m_{ox,\infty}/iC_p)$
- T_v = vaporization temperature (618 K)
- T_∞ = ambient temperature (298 K)
- U_b = buoyant velocity
- V_f = flame spread rate
- x = streamwise distance
- $\bar{x}$ = dimensionless streamwise distance (x/l_b)
- y = normal distance
- $\bar{y}$ = dimensionless normal distance (y/l_b)
- ΔH_c = heat of combustion (1.674×10^4 kJ/kg)
- μ = viscosity (3.047×10^{-5} kg/m•s)
- ν = kinematic viscosity

Introduction

Experiments show that buoyancy influences the rate at which a flame spreads down a thermally thin, solid fuel bed [1]. Buoyancy should also affect the general characteristics of the flame, e.g., size, shape, temperature, etc., because these characteristics in turn contribute to determining the spread rate.

Theoretical determination of the spread rate and flame characteristics is difficult owing to the fact that the differential equations that must be solved to obtain them are nonlinear and elliptic in character. As a result, it has been suggested recently that spread rate predictions be based on dimensionless correlations [1, 2] in which a dimensionless spread rate that is a measure of the heat transferred forward of the flame to the virgin fuel is correlated against a Damköhler number, the ratio of a gas-phase reactant residence time to a chemical reaction time. Such correlations have been developed for thermally thin fuels spreading vertically downward in free convection [1] and against an opposing forced flow [2] and for thermally thick fuels in the same flow configurations [2, 3].

In downward flame spread in free convection, buoyancy generates a flow that opposes the spreading flame. The speed of the flow is proportional to the characteristic buoyant velocity, U_b, where

$$U_b = \left[\frac{\mu R T_v g \Delta H_c m_{ox,\infty}}{T_\infty P M i C_p} \right]^{1/3} \quad (1)$$

[1]Department of Mechanical Engineering, University of Kentucky, Lexington, Ky. 40506, Mem. ASME

[2]Department of Mechanical Engineering, University of Kentucky

[3]Department of Mechanical Engineering, University of Kentucky, Fellow ASME

Contributed by the Heat Transfer Division for publication in the JOURNAL OF HEAT TRANSFER. Manuscript received by the Heat Transfer Division November 9, 1982.

($f_w' = -0.1$; $f_w = 0.2$) a similar situation exists. This can be attributed to the retarding buoyancy force. The corresponding temperature profile, Fig. 3, shows a large overshoot. Low shear thermal boundary-layer thickness appears to increase with buoyancy parameter.

Conclusions

From the above discussion we can conclude that the buoyancy force plays an important role in defining the flow field. For the flow geometry studied, it can be concluded that (*i*) for equal suction or injection angle and $K \simeq 0.15$, the boundary-layer fluid experiences the same wall shear stress, (*ii*) the buoyancy force plays opposite role for high- and low-shear solutions, (*iii*) the wall shear values with downstream vectored suction can be higher or lower than those with upstream vectored suction depending on the buoyancy parameter.

Acknowledgment

The author wishes to thank Prof. B. C. Dutta and ARDB (India) for the financial help and the referees for valuable suggestions.

References

1 Inger, G. R., and Swean, T. F., "Vectored Injection into Laminar Boundary Layers with Heat Transfer," *AIAA Journal*, Vol. 13, 1975, pp. 616-622.

2 Chen, T. S., and Sparrow, E. M., "Flow and Heat Transfer Over a Flat Plate with Uniformly Distributed, Vectored Surface Mass Transfer," ASME JOURNAL OF HEAT TRANSFER, Vol. 98, 1976, pp. 674-676.

3 Venkatachala, B. J., and Nath, G., "Nonsimilar Laminar Incompressible Boundary Layers with Vectored Mass Transfer," *Proceedings Indian Academy of Sciences: Engineering Sciences*, Vol. 3, 1979, pp. 129-142.

4 Schneider, W., "A Similarity Solution for Combined Forced and Free Convection Flow Over a Horizontal Plate," *International Journal of Heat and Mass Transfer*, Vol. 22, 1979, pp. 1401-1406.

5 One of the referees.

Buoyancy Effects on the Temperature Field in Downward Spreading Flames

R.A. Altenkirch[1], D. C. Winchester[2], and R. Eichhorn[3]

Nomenclature

- B = preexponential factor ($1 \times 10^6 \text{m}^3/\text{mol}\cdot\text{s}$)
- $\bar{B}$ = Damköhler number
- C_p = constant pressure, gas-phase specific heat (1.063 kJ/kg•K)
- E = activation energy (167.35 kJ/mol)
- g = acceleration of gravity
- g_e = earth's normal acceleration of gravity (9.807 m/s^2)
- i = mass of oxygen needed to burn a unit mass of fuel (1.185)
- k = gas-phase thermal conductivity (0.0459 J/m•s•K)
- L = effective heat of vaporization for solid fuel at T_∞ and gas-phase fuel at T_v (753 kJ/kg)
- l_b = buoyant length
- M = molecular weight of the oxidizer
- M_{ox} = molecular weight of oxygen (32 kg/kmol)
- $m_{ox,\infty}$ = mass fraction of oxygen in the oxidizer (0.233)
- P = pressure
- R = universal gas constant (8.314 J/mol•K)
- T = temperature
- $\bar{T}$ = dimensionless temperature, $T/(\Delta H_c m_{ox,\infty}/iC_p)$
- $\bar{T}_a$ = dimensionless activation temperature, $(E/R)/(\Delta H_c m_{ox,\infty}/iC_p)$
- T_f = flame temperature (2822 K)
- $\bar{T}_f$ = dimensionless flame temperature, $T_f(\Delta H_c m_{ox,\infty}/iC_p)$
- T_v = vaporization temperature (618 K)
- T_∞ = ambient temperature (298 K)
- U_b = buoyant velocity
- V_f = flame spread rate
- x = streamwise distance
- $\bar{x}$ = dimensionless streamwise distance (x/l_b)
- y = normal distance
- $\bar{y}$ = dimensionless normal distance (y/l_b)
- ΔH_c = heat of combustion (1.674×10^4 kJ/kg)
- μ = viscosity (3.047×10^{-5} kg/m•s)
- ν = kinematic viscosity

Introduction

Experiments show that buoyancy influences the rate at which a flame spreads down a thermally thin, solid fuel bed [1]. Buoyancy should also affect the general characteristics of the flame, e.g., size, shape, temperature, etc., because these characteristics in turn contribute to determining the spread rate.

Theoretical determination of the spread rate and flame characteristics is difficult owing to the fact that the differential equations that must be solved to obtain them are nonlinear and elliptic in character. As a result, it has been suggested recently that spread rate predictions be based on dimensionless correlations [1, 2] in which a dimensionless spread rate that is a measure of the heat transferred forward of the flame to the virgin fuel is correlated against a Damköhler number, the ratio of a gas-phase reactant residence time to a chemical reaction time. Such correlations have been developed for thermally thin fuels spreading vertically downward in free convection [1] and against an opposing forced flow [2] and for thermally thick fuels in the same flow configurations [2, 3].

In downward flame spread in free convection, buoyancy generates a flow that opposes the spreading flame. The speed of the flow is proportional to the characteristic buoyant velocity, U_b, where

$$U_b = \left[\frac{\mu R T_v g \Delta H_c m_{ox,\infty}}{T_\infty P M i C_p} \right]^{1/3} \quad (1)$$

[1]Department of Mechanical Engineering, University of Kentucky, Lexington, Ky. 40506, Mem. ASME

[2]Department of Mechanical Engineering, University of Kentucky

[3]Department of Mechanical Engineering, University of Kentucky, Fellow ASME

Contributed by the Heat Transfer Division for publication in the JOURNAL OF HEAT TRANSFER. Manuscript received by the Heat Transfer Division November 9, 1982.

Table 1
Experimental conditions

g/g_e	P kPa	V_f^* mm/s	l_b mm	$\bar{B}\times 10^3$
1.0	101.3	1.62	0.30	16.91
2.5	101.3	1.49	0.22	9.18
1.0	40.5	1.42	0.56	9.18

*Averaged over all experiments at a particular condition.

For thermally thin fuels, the upstream heat transfer occurs by gas-phase conduction [4] so that the flow near the leading edge of the flame is not of the boundary layer type. This fact leads to equation (1) [1] and dictates that heat is conducted normal and parallel to the fuel bed over comparable distances that are proportional to the characteristic buoyant length, l_b, where

$$l_b = \left[\frac{(\mu R T_v)^2 T_\infty i C_p}{g(PM)^2 \Delta H_c m_{ox,\infty}}\right]^{1/3} \quad (2)$$

As a result, the actual upstream conduction rate is proportional to the difference between the actual flame and vaporization temperature, but it is independent of the pressure and gravity level.

When the Damköhler number, which is proportional to U_b^{-2}, is large, the flame temperature is at its maximum, and the dimensionless spread rate, which does not contain U_b, is unity. At small Damköhler numbers, both the dimensionless spread rate and the actual flame temperature depend on the Damköhler number. Flames that spread in a particular oxidizer at the same Damköhler number (fixed flame temperature) should have the same dimensionless temperature field when temperature is measured in the units of (ΔH_c $m_{ox,\infty}/iC_p$) and distances in the units of l_b. The temperature scale is a measure of T_f when $m_{ox,\infty}/i$, $L/\Delta H_c$ and T_∞/T_f are small [1], a condition that is met in our experiments. Thus we expect dimensionless temperatures to be of order unity or less.

The effect of pressure on the gas-phase temperature field for downward spread on thermally thin fuels has been qualitatively demonstrated before [5]. For paper samples burnt in an oxygen-nitrogen oxidizer with an oxygen mole fraction of 0.3, a decrease in pressure from 68.9 kPa to 20.7 kPa caused an increase in flame size. Temperature gradients both parallel and normal to the fuel near the onset of pyrolysis were found to be comparable; downstream of the onset of pyrolysis, gradients in the normal direction were large compared to those in the parallel direction.

Here we present measurements of the temperature fields for flames spreading vertically down index cards in air as not only pressure but also the acceleration of gravity were varied. We find that flames spreading at the same Damköhler number have the same dimensionless temperature field, demonstrating quantitatively that l_b is the proper scale in which to measure the distances in the flame spread problem.

Experiment

Experimental data consist of spread rate and gas- and solid-phase temperatures for flames spreading down index card samples (0.0098 cm half-thickness) burnt in air. The samples were mounted in an environmental chamber attached to one arm of a 15 m dia centrifuge. This arrangement, which is described in detail in [6], allowed the oxidizer pressure and the acceleration of gravity to be varied. Samples were mounted vertically and ignited at the top by an electrically heated coil. Because the chamber was gimballed, the flames always spread downward in the direction of the effective gravitational acceleration.

Gas-phase temperatures were measured with 0.0076 cm dia coated Pt/Pt-10 percent Rh thermocouples [7] placed in an array so that each thermocouple was located at a different $x-y$ position. Thus adjustment of the array provided temperature information at three distinct $x-y$ locations for each experiment. Solid-phase temperatures were measured at the same x locations as the gas-phase temperatures using thermocouples made of the same materials as the gas-phase ones. Details of the experimental apparatus and procedures may be found in [8].

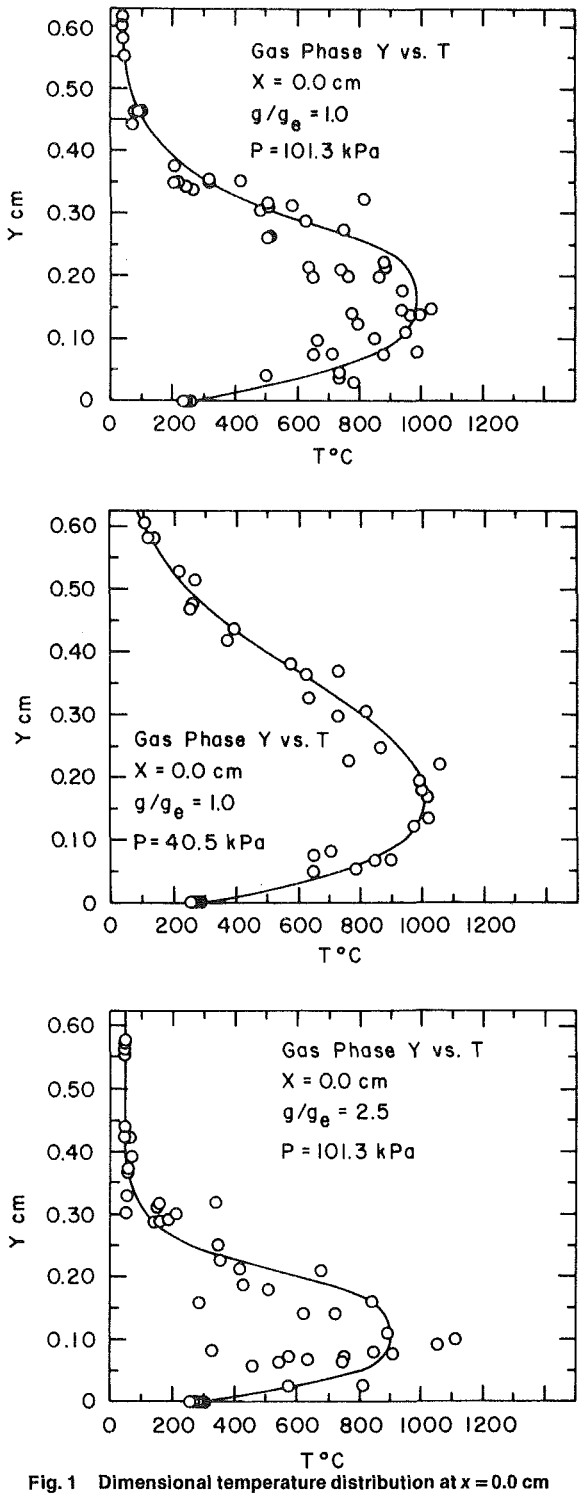

Fig. 1 Dimensional temperature distribution at $x = 0.0$ cm

Results and Discussion

Gas- and solid-phase temperatures were measured for the conditions indicated in Table 1, where $\bar{B}$, from [1], is

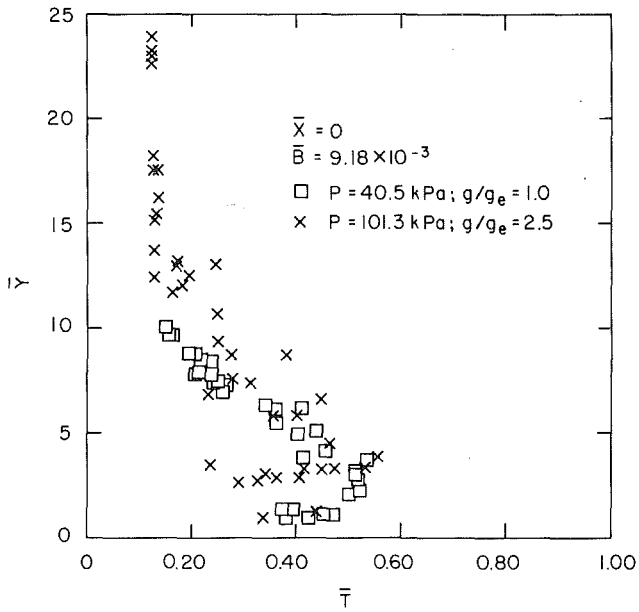

Fig. 2 Dimensionless temperature distribution at $\bar{x} = 0$, $\bar{B} = 9.18 \times 10^{-3}$

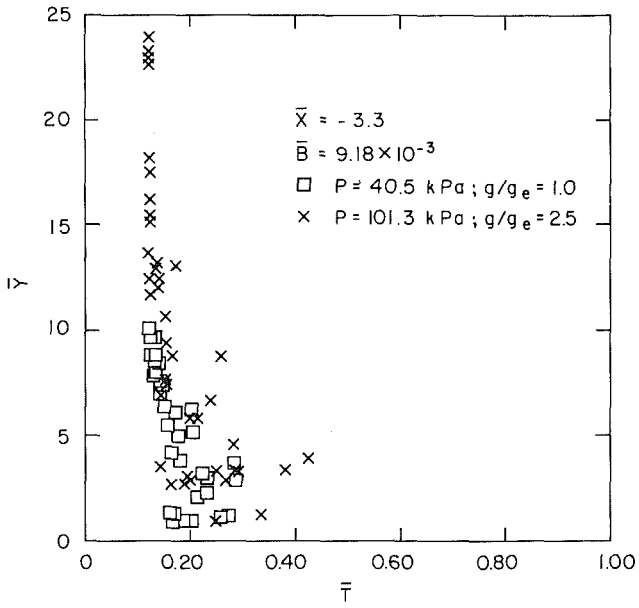

Fig. 3 Dimensionless temperature distribution at $\bar{x} = -3.3$, $\bar{B} = 9.18 \times 10^{-3}$

$$\bar{B} = \frac{Bkm_{ox,\infty}}{M_{ox}C_p\left(\nu g\frac{\Delta H_c m_{ox,\infty}}{T_\infty i C_p}\right)^{2/3}}\left(\frac{\bar{T}_f^{\,2}}{\bar{T}_a}\right)^3 e^{-(\bar{T}_a/\bar{T}_f)} \tag{3}$$

Property values used to calculate $\bar{B}$ and l_b are the same as in [1] and are given in the nomenclature.

For each condition, several experiments were conducted with the gas-phase thermocouple array adjusted to provide temperature data at many y locations. Each point on the plots that follow represents a single thermocouple measurement at a particular position; no corrections were made for radiation or conduction errors. The most probable uncertainty for the gas-phase temperature is 3.1 percent while for the solid-phase temperature it is 4.5 percent [8].

The temperature-time history of each thermocouple pair was converted into a $y-T$ profile at a particular x location by using the measured spread rate. A datum in time and space was chosen to be the point in the solid phase where fuel pyrolysis first became apparent [8]. Positive x is downstream and negative x upstream from this datum.

Solid-phase temperatures are not presented here, but can be found in [8]. However, one interesting point worth mentioning about them is that the pyrolysis temperature for the paper samples does not appear to be sensitive to the environmental conditions, for the range of conditions studied here. This finding supports assumptions made in current flame spread correlations [1, 2].

Figure 1 shows the temperature distribution in the gas, in dimensional terms, at $x=0$ for the three conditions of Table 1. The figure is consistent with other results in the literature [5], and shows that a decrease in pressure causes an increase in flame size as the extent over which heat can be transferred, l_b, increases. An increase in gravity causes flame size to decrease as l_b decreases. Because the decreased pressure and elevated gravity conditions have the same Damköhler number, $\bar{B}$, we expect them to have the same spread rate as discussed above. The spread rates listed in Table 1 for the two conditions differ by less than 5 percent.

The data presented in Fig. 1 at the reduced pressure and elevated gravity condition are replotted in Fig. 2 in dimensionless form. Because the data were taken at the same value of $\bar{B}$ they should have the same dimensionless temperature field. This is confirmed in Fig. 2. From the figure it is clear that the flame extends, at $\bar{x}=0$, about 10 buoyant lengths away from the fuel surface and, as we expected, the dimensionless temperatures are somewhat less than unity.

The temperature distribution 3.3 buoyant lengths upstream of the onset of pyrolysis is shown in Fig. 3. Again, the two conditions have about the same distribution. We also plotted the distribution at $\bar{x}=-6.7$ and found little evidence of flame influence there.

The above behavior is understandable in view of the facts that the thermal diffusivity is inversely proportional to P and for upstream heat conduction to be influential at all, the local Peclet number near $x=0$ based on the buoyant velocity and length must be of order unity. So as U_b increases as P is decreased, the length over which upstream conduction can be felt must increase to maintain a Peclet number of unity. On the other hand, an increase in U_b owing to an increase in g causes the upstream distance influenced by conduction to decrease so that the Peclet number can remain of order unity.

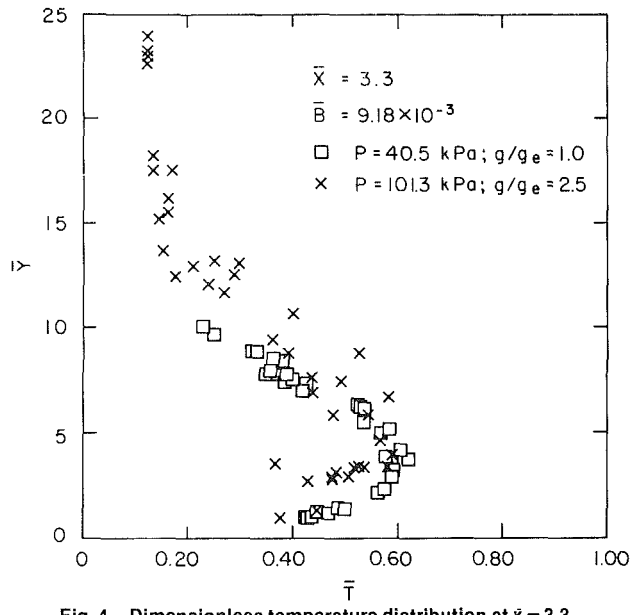

Fig. 4 Dimensionless temperature distribution at $\bar{x} = 3.3$, $\bar{B} = 9.18 \times 10^{-3}$

Figure 4 shows the temperature distribution at about 3.3 buoyant lengths downstream of $\bar{x}=0$. It again shows that the dimensionless profiles are essentially the same. In addition, the temperature level has increased somewhat over the maximum value found at $\bar{x}=0$, and the flame has grown.

Conclusion

Flames that spread vertically down thermally thin fuels at the same Damköhler number have the same dimensionless spread rate [1]. Here we have shown that such flames also have the same dimensionless temperature fields although their physical size and hence temperature fields might be quite different. The effects of pressure on flame size that have been reported here and elsewhere [5] are due to the effects of pressure on the character of the induced buoyant flow.

Acknowledgment

We wish to thank the National Aeronautics and Space Administration for providing the funds for this work under grant NSG-3114 with T. H. Cochran as technical monitor.

References

1 Altenkirch, R. A., Eichhorn, R., and Shang, P. C., "Buoyancy Effects on Flames Spreading Down Thermally Thin Fuels," *Combustion and Flame*, Vol. 37, 1980, pp. 71-83.

2 Fernandez-Pello, A. C., Ray, S. R., and Glassman, I., "Flame Spread in an Opposed Forced Flow: The Effect of Ambient Oxygen Concentration," *18th International Symposium on Combustion*, The Combustion Institute, 1981, pp. 579-589.

3 Altenkirch, R. A., Eichhorn, R., and Rizvi, A. R., "Surface Regression Effects on Flame Spread Correlations," Eastern Section of the Combustion Institute Fall Technical Meeting, 1981.

4 Parker, W. J., "Flame Spread Model for Cellulosic Materials," *Journal of Fire and Flammability*, Vol. 3, 1972, pp. 254-269.

5 Frey, A. E., Jr. and T'ien, J. S., "Near-Limit Flame Spread over Paper Samples," *Combustion and Flame*, Vol. 26, 1976, pp. 257-267.

6 Shang, P. C., "Experimental Studies of the Effects of Buoyancy on Flame Spread Rate over Thin Paper Samples," MSME thesis, University of Kentucky, Lexington, Kentucky, 1978.

7 Kent, J. H., "A Noncatalytic Coating for Platinum-Rhodium Thermocouples," *Combustion and Flame*, Vol. 14, 1970, p. 279.

8 Winchester, D. C., "An Experimental Determination of the Effect of an Opposed Buoyant Flow on Flame Spread Rate over Solid Combustibles," MSME thesis, University of Kentucky, Lexington, Kentucky, 1980.

Heat Transfer Between a Horizontal Cylinder and a Mixed Particle Size Fluidized Bed

D. R. Pitts[1], R. S. Figliola[1], and K. M. Hamlyn[1]

Introduction

There exists a real need for design information concerning the operation of fluidized bed heat-transfer devices utilizing (*i*) a wide spectrum of mixed particle sizes in a particular bed and (*ii*) a broad range of mean mixed particle size beds. A search of the literature revealed a lack of investigations of mixed particle size effects upon heat transfer. The present paper reports an initial experimental study of heat transfer between a horizontal cylinder and mixed particle size bed of glass beads.

The Experiments

Fluidization of a 0.3-m high (packed height) bed of spherical glass beads was accomplished in a rectangular column having a 0.31-m by 0.66-m cross-sectional area and a height of 1.0 m. Air was supplied with a low pressure air blower system. The distribution plate was made of porous acoustic tile supported with 6-mm mesh hardware cloth, and this provided very uniform flow over the cross section. The heated surface was a 15.9-mm dia, 0.55-m long, hard copper tube mounted horizontally 152 mm above the distributor plate and 152 mm from each side wall of the bed. The tube outer surface was nickel plated, polished and then hard chrome plated with a resulting emissivity of approximately 0.08. A cartridge-type electrical heater was close-fitted inside this tube, and the heater extended over the entire tube heated length. Insulated end mountings resulted in conduction losses which were typically less than 4 percent of the total heat transfer. The low surface emissivity of the cylinder resulted in radiation losses which were typically 0.3 percent of the total heat flux from the tube. Power to the cartridge heater was supplied with an a-c variable transformer and measured with a digital power analyzer.

Table 1 Distribution of particle size by weight

Size (μm)	Fraction by weight, χ_i	Mean diameter for size spread (μm), $\bar{d}_{pi}$
<53	0.134	50[a]
53–74	0.026	67
74–105	0.159	90
105–149	0.526	127
149–210	0.162	180
>210	0.005	210[a]

[a]Arbitrarily set

Heater surface and fluidized bed temperatures were measured with calibrated iron-constantan thermocouples. During tests it was found that the eight thermocouples, which were located throughout the bed, agreed to within 0.1°C with each other for all flow rates above the onset of bubbling. When tested in a natural convection mode with a heater-to-bed temperature difference of 60°C, heater surface temperatures, as measured by thermocouples around the tube, agreed within 1.5°C of each other.

The air flow rate to the fluidized bed was measured with a laminar flow element together with an inclined manometer and a thermocouple. Additional manometers were used to measure the pressure drop through the fluidized bed and across a protective filter upstream of the laminar flow element. A calibrated laboratory barometer provided atmospheric pressure data.

The bed was a mixture of two batches of glass beads, one in the nominal 105–149 μm size range and the other being fines less than 53-μm dia. The glass beads were spherical with a density of 150 lbm/ft^3; the sphericity was confirmed by microscopic observation. The packed bed void fraction measured by water displacement was 0.31 and the measured particle size distribution was as given in Table 1.
The weight-averaged particle size as given by

$$\bar{d}_p = \frac{1}{\sum_i (\chi/d_p)_i} \tag{1}$$

was 101 μm. No stratification of particles was visually observed during tests and no elutriation of fine particles occurred as confirmed by sieve analyses after tests. Also, sieve analysis of samples taken from different bed depths confirmed that no significant particle size segregation existed.

All tests were run at steady-state conditions within the bubble flow regime. Before taking data, the bed was operated with no heating for 2 hrs. Following this a run of 1 hr with the tube heated was employed to assure steady conditions prior to data acquisiton.

[1] Department of Mechanical Engineering, Clemson University, Clemson, S.C. 29631

Contributed by the Heat Transfer Division for publication in the JOURNAL OF HEAT TRANSFER. Manuscript received by the Heat Transfer Division October 5, 1981.

Figure 4 shows the temperature distribution at about 3.3 buoyant lengths downstream of $\bar{x}=0$. It again shows that the dimensionless profiles are essentially the same. In addition, the temperature level has increased somewhat over the maximum value found at $\bar{x}=0$, and the flame has grown.

Conclusion

Flames that spread vertically down thermally thin fuels at the same Damköhler number have the same dimensionless spread rate [1]. Here we have shown that such flames also have the same dimensionless temperature fields although their physical size and hence temperature fields might be quite different. The effects of pressure on flame size that have been reported here and elsewhere [5] are due to the effects of pressure on the character of the induced buoyant flow.

Acknowledgment

We wish to thank the National Aeronautics and Space Administration for providing the funds for this work under grant NSG-3114 with T. H. Cochran as technical monitor.

References

1 Altenkirch, R. A., Eichhorn, R., and Shang, P. C., "Buoyancy Effects on Flames Spreading Down Thermally Thin Fuels," *Combustion and Flame*, Vol. 37, 1980, pp. 71-83.

2 Fernandez-Pello, A. C., Ray, S. R., and Glassman, I., "Flame Spread in an Opposed Forced Flow: The Effect of Ambient Oxygen Concentration," *18th International Symposium on Combustion*, The Combustion Institute, 1981, pp. 579-589.

3 Altenkirch, R. A., Eichhorn, R., and Rizvi, A. R., "Surface Regression Effects on Flame Spread Correlations," Eastern Section of the Combustion Institute Fall Technical Meeting, 1981.

4 Parker, W. J., "Flame Spread Model for Cellulosic Materials," *Journal of Fire and Flammability*, Vol. 3, 1972, pp. 254-269.

5 Frey, A. E., Jr. and T'ien, J. S., "Near-Limit Flame Spread over Paper Samples," *Combustion and Flame*, Vol. 26, 1976, pp. 257-267.

6 Shang, P. C., "Experimental Studies of the Effects of Buoyancy on Flame Spread Rate over Thin Paper Samples," MSME thesis, University of Kentucky, Lexington, Kentucky, 1978.

7 Kent, J. H., "A Noncatalytic Coating for Platinum-Rhodium Thermocouples," *Combustion and Flame*, Vol. 14, 1970, p. 279.

8 Winchester, D. C., "An Experimental Determination of the Effect of an Opposed Buoyant Flow on Flame Spread Rate over Solid Combustibles," MSME thesis, University of Kentucky, Lexington, Kentucky, 1980.

Heat Transfer Between a Horizontal Cylinder and a Mixed Particle Size Fluidized Bed

D. R. Pitts[1], R. S. Figliola[1], and K. M. Hamlyn[1]

Introduction

There exists a real need for design information concerning the operation of fluidized bed heat-transfer devices utilizing (*i*) a wide spectrum of mixed particle sizes in a particular bed and (*ii*) a broad range of mean mixed particle size beds. A search of the literature revealed a lack of investigations of mixed particle size effects upon heat transfer. The present paper reports an initial experimental study of heat transfer between a horizontal cylinder and mixed particle size bed of glass beads.

The Experiments

Fluidization of a 0.3-m high (packed height) bed of spherical glass beads was accomplished in a rectangular column having a 0.31-m by 0.66-m cross-sectional area and a height of 1.0 m. Air was supplied with a low pressure air blower system. The distribution plate was made of porous acoustic tile supported with 6-mm mesh hardware cloth, and this provided very uniform flow over the cross section. The heated surface was a 15.9-mm dia, 0.55-m long, hard copper tube mounted horizontally 152 mm above the distributor plate and 152 mm from each side wall of the bed. The tube outer surface was nickel plated, polished and then hard chrome plated with a resulting emissivity of approximately 0.08. A cartridge-type electrical heater was close-fitted inside this tube, and the heater extended over the entire tube heated length. Insulated end mountings resulted in conduction losses which were typically less than 4 percent of the total heat transfer. The low surface emissivity of the cylinder resulted in radiation losses which were typically 0.3 percent of the total heat flux from the tube. Power to the cartridge heater was supplied with an a-c variable transformer and measured with a digital power analyzer.

Table 1 Distribution of particle size by weight

Size (μm)	Fraction by weight, χ_i	Mean diameter for size spread (μm), $\bar{d}_{pi}$
<53	0.134	50[a]
53–74	0.026	67
74–105	0.159	90
105–149	0.526	127
149–210	0.162	180
>210	0.005	210[a]

[a]Arbitrarily set

Heater surface and fluidized bed temperatures were measured with calibrated iron-constantan thermocouples. During tests it was found that the eight thermocouples, which were located throughout the bed, agreed to within 0.1°C with each other for all flow rates above the onset of bubbling. When tested in a natural convection mode with a heater-to-bed temperature difference of 60°C, heater surface temperatures, as measured by thermocouples around the tube, agreed within 1.5°C of each other.

The air flow rate to the fluidized bed was measured with a laminar flow element together with an inclined manometer and a thermocouple. Additional manometers were used to measure the pressure drop through the fluidized bed and across a protective filter upstream of the laminar flow element. A calibrated laboratory barometer provided atmospheric pressure data.

The bed was a mixture of two batches of glass beads, one in the nominal 105–149 μm size range and the other being fines less than 53-μm dia. The glass beads were spherical with a density of 150 lbm/ft^3; the sphericity was confirmed by microscopic observation. The packed bed void fraction measured by water displacement was 0.31 and the measured particle size distribution was as given in Table 1.

The weight-averaged particle size as given by

$$\bar{d}_p = \frac{1}{\sum_i (\chi/d_p)_i} \tag{1}$$

was 101 μm. No stratification of particles was visually observed during tests and no elutriation of fine particles occurred as confirmed by sieve analyses after tests. Also, sieve analysis of samples taken from different bed depths confirmed that no significant particle size segregation existed.

All tests were run at steady-state conditions within the bubble flow regime. Before taking data, the bed was operated with no heating for 2 hrs. Following this a run of 1 hr with the tube heated was employed to assure steady conditions prior to data acquisiton.

[1] Department of Mechanical Engineering, Clemson University, Clemson, S.C. 29631

Contributed by the Heat Transfer Division for publication in the JOURNAL OF HEAT TRANSFER. Manuscript received by the Heat Transfer Division October 5, 1981.

Results and Discussion

The measured electrical power to the heated surface together with the calculated end conduction and radiation losses (q_{heater}), the tube surface area, and the mean temperature difference between the tube wall and the fluidized bed were used to obtain the average convective heat-transfer coefficient from

$$\bar{h} = \frac{\dot{q}_{\text{heater}}}{A_{\text{tube}}(T_w - T_b)} \tag{2}$$

The values of the heat-transfer coefficient obtained have an uncertainty of less than 7.5 percent. The precision of these values as evaluated from data reproducibility is about 4 percent.

Approaches to correlation of heat transfer between a horizontal cylinder and a fluidized bed have been recently reviewed by Saxena et al. [1]. Dimensionless correlations include those of Vreedenberg [2], Wender and Cooper [3], Ainshtein [4], Andeen and Glicksman [5], and Grewal and Saxena [6]. The experimental results of the present study are compared with the correlations of Vreedenberg, Andeen and Glicksman, and Grewal and Saxena in Figs. 1, 2, and 3, respectively. The value of the bulk bed porosity in our work was not measured directly. For use in the Andeen-Glicksman correlation, the void fraction was found from the linearized form of the Leva condition [7], which for spherical particles is given by:

$$\epsilon = \frac{1}{2.1}\left\{0.4\left[\frac{200\, V_g\, \mu}{\bar{d}_p^{\,2}(\rho_p - \rho_g)g}\right]^{1/3}\right\} \tag{3}$$

In this and the following expressions, V_g is the gas superficial velocity; μ is the gas viscosity; ρ_p and ρ_g are the particle and gas densities, respectively; g is the local acceleration due to gravity; and $\bar{d}_p$ is the mean particle diameter. For the Grewal-Saxena heat-transfer correlation, the bulk bed void fraction was estimated using the form given by Grewal and Saxena, (*op. cit*)

$$\epsilon = \frac{1}{2.1}\left\{0.4 + \left[4\left(\frac{\mu V_g}{\bar{d}_p^{\,2}(\rho_p - \rho_g)g}\right)^{0.43}\right]^{1/3}\right\} \tag{4}$$

It is generally assumed that if the condition,

$$(V_g\, d_p\, \rho_p/\mu) < 2050 \tag{5}$$

is met, that the Vreedenberg correlation for fines is to be used. Even though satisfying this condition, however, our results showed a markedly poorer agreement to that correlation than for the coarse particle correlation. The latter correlation is that shown in Fig. 1.

As expected, the mixed-bed results are underpredicted by all three correlations. This is considered to be a result of the addition of approximately 13 percent by weight of fines, even though this material was included in the computation of the mean particle size. With our results, the correlations proposed by Vreedenberg are inferior to those proposed by Andeen and Glicksman and by Grewal and Saxena; there appears to be little difference, however, between the agreement obtained with either of these latter two correlations. Specifically, the Vreedenberg correlation underpredicted the experimental data with a 22.7 percent mean rms deviation, whereas the Andeen and Glicksman and Grewal and Saxena correlations underpredicted the data by 10.3 and 17.2 mean rms deviation, respectively. Even though the mean rms deviation was least using the Andeen-Glicksman correlation, the actual deviations from this correlation became increasing larger with increasing superficial velocity. This condition was not as clearly evident with the other correlations used. While these rms deviations are not excessive for design purposes, the consistent underprediction of our mixed particle size, bubble flow, shallow bed, heat-transfer data indicates that there may

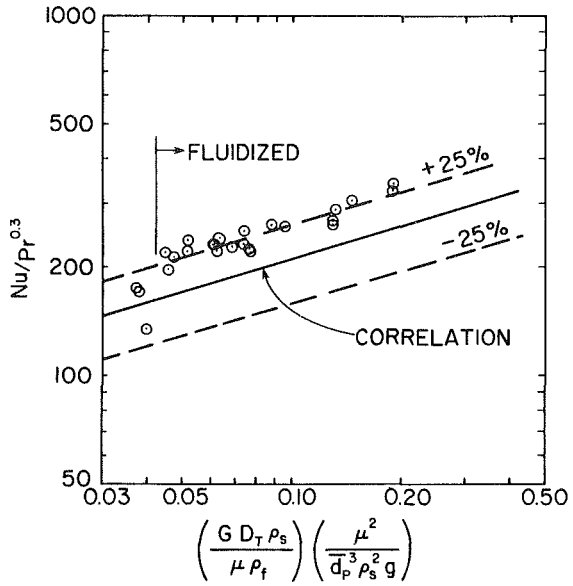

Fig. 1 Comparison of mixed particle size, bubble flow regime heat-transfer results with the Vreedenberg coarse particle correlation

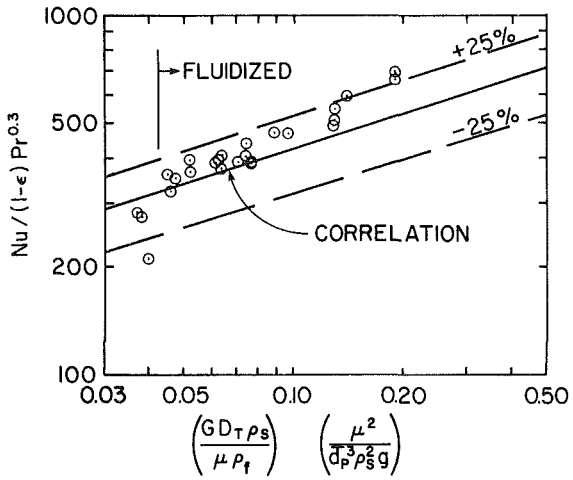

Fig. 2 Comparison of mixed particle size, bubble flow regime heat-transfer results with the Andeen-Glicksman correlation

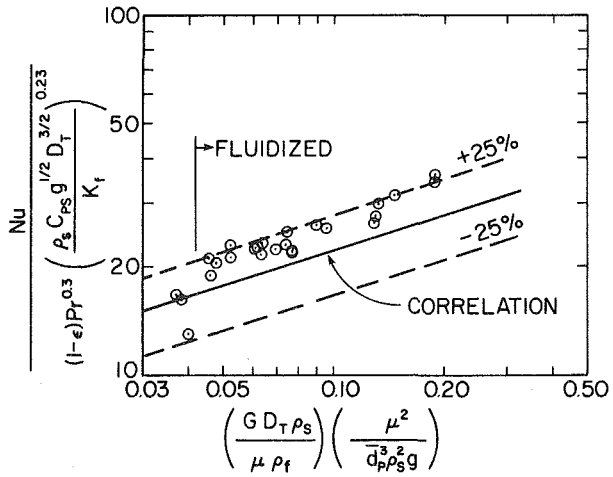

Fig. 3 Comparison of mixed particle size, bubble flow regime heat-transfer results with the Grewal-Saxena correlation

be a mechanistic effect not accounted for in the correlations. However, there is little reason to attempt to propose a modified correlation for mixed beds at this point based on our limited set of data. Such an attempt awaits the establishment of a broader data base of mixed-sized particle experimental results.

References

1 Saxena, S. C., Grewal, N. S., Gabor, J. D., Zabrodsky, S. S., and Galershtein, D. M., "Heat Transfer Between a Gas Fluidized Bed and Immersed Tubes," in *Advances in Heat Transfer*, Vol. 14, edited by T. F. Irvine, Jr. and J. P. Hartnett, Academic Press, New York, 1978, pp. 149–247.

2 Vreedenberg, H. A., "Heat Transfer between a Fluidized Bed and a Horizontal Tube." *Chem. Engr. Sci.*, Vol. 9, 1958, pp. 52–60.

3 Wender, L., and Cooper, G. T., "Heat Transfer Between Fluidized Solids Beds and Boundary Surfaces—Correlation of Data," *AIChE J.*, Vol. 4, 1958, pp. 15–23.

4 Ainshtein, V. G., "An Investigation of Heat Transfer Process Between Fluidized Beds and Single Tubes Submerged in the Bed," in *Hydrodynamics and Heat Transfer in Fluidized Beds*, edited by S. S. Zabrodsky, MIT Press, Cambridge, Mass., 1966, pp. 270–272.

5 Andeen, B. R., and Glicksman, L. R., "Heat Transfer to Horizontal Tubes in Shallow Beds," ASME-AIChE Heat Transfer Conference, Paper No. 76-HT-67, St. Louis, Mo., 1976.

6 Grewal, N. S. and Saxena, S. C., "Heat Transfer Between a Horizontal Tube and A Gas-Solid Fluidized Bed", *International Journal of Heat and Mass Transfer*, Vol. 23, 1980, pp. 1505–1518.

7 Leva, M., "Correlations of the Dense Phase Fluidized State and Their Applications," *Canadian Journal of Chemical Engineering*, Vol. 35, 1958, pp. 71–76.

An Approximate Model of Bubble Phase Convective Heat Transfer to a Horizontal Tube in a Large Particle Fluid Bed

R. L. Adams[1]

Introduction

The convective heat transfer within a gas bubble contacting a heat-transfer surface in a large particle or high pressure fluidized bed can be a significant fraction of the total heat transfer. Instantaneous local heat-transfer data for a horizontal tube immersed in a two-dimensional bed obtained by Catipovic [1] suggest that this convective contribution can account for as much as 30 percent of the total time-averaged heat transfer for a bed of 6.6-mm dia dolomite particles.

The purpose of this note is to present an approximate model of bubble phase convective heat transfer to a horizontal tube immersed in a two-dimensional fluidized bed. The model makes use of the exact solution for the inviscid flow field within a single two-dimensional slow bubble of Adams [2] and the one parameter integral method of Smith and Spalding [3]. The effect of interstitial turbulence present in the bubble flow field is included as an ad hoc correction to the results. This makes the model much less cumbersome for heat-transfer estimates than the numerical model of instantaneous heat transfer developed previously (see Adams and Welty [4, 5]) and allows calculation of the time-averaged bubble convective heat transfer contribution. Calculations based upon the model are compared with local time-averaged, heat-transfer data for a horizontal tube immersed in a low temperature two-dimensional bed obtained by Catipovic [1].

Analysis

Consider a single, two-dimensional slow bubble contacting a horizontal tube as shown in the inset of Fig. 1. Assuming that the region within the contacting bubble is free of particles, the flow field within the bubble will be determined by boundary conditions at the tube wall and bubble boundary and will be characterized by a Reynolds number based upon minimum fluidizing velocity and tube diameter. This Reynolds number is sufficiently large for cases in which bubble convective heat transfer is important so that viscous effects are confined to a thin boundary layer adjacent to the tube surface. Furthermore, the gas velocity at the edge of this boundary layer is determined from the inviscid flow field within the contacting bubble in accordance with classical boundary layer theory.

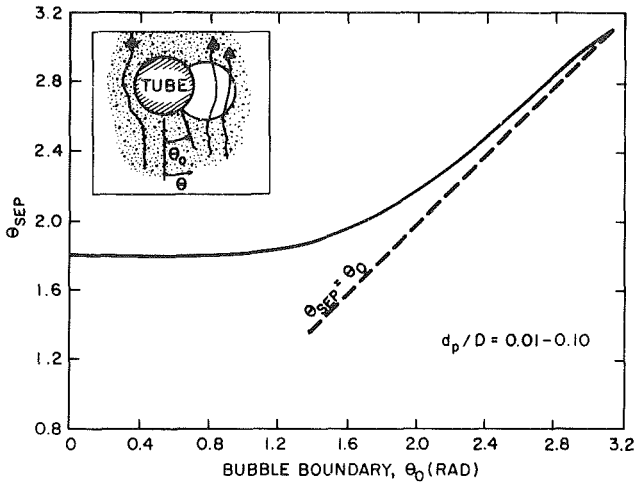

Fig. 1 Location of boundary layer separation within a two-dimensional bubble contacting a horizontal tube

To obtain the heat transfer to the tube surface, the one-parameter method of Smith and Spalding [3] is used in place of the more complex two-equation model of boundary layer flow with free stream turbulence developed by Adams and Welty [4]. Since Smith and Spalding's method does not account for free stream turbulence, a correction to the results is made by assuming that the amplification in heating is the same as that for a stagnation point flow.

According to the method of Smith and Spalding [3] the local Nusselt number (here based upon D, tube diameter) is obtained from the following

$$\mathrm{Nu}_D = \left(\frac{a}{\mathrm{Re}_D} \frac{\int_{x_0}^{x} U^{b-1} dx}{U^b} + \frac{U_0^b}{U^b \mathrm{Nu}_{D_0}^{\ 2}} \right)^{-1/2} \tag{1}$$

where $a \simeq 9.07\ \mathrm{Pr}^{-0.7}$, $b \simeq 2.95\ \mathrm{Pr}^{0.07}$, Pr is the gas Prandtl number, x is the dimensionless streamwise coordinate (here relative to D), U is the dimensionless edge velocity (here relative to U_{mf}, minimum fluidizing velocity), Re_D is the Reynolds number based upon U_{mf} and D, and U_0 and Nu_{D_0} are evaluated at x_0.

Considering a single, two-dimensional slow bubble contacting a tube (valid for large particle beds operating near U_{mf}), Adams [2] has shown that the boundary layer edge velocity for the flow at the tube surface is independent of bubble size and given by

$$U = 4 \sin\theta \tag{2}$$

with θ measured from the lower stagnation point of the tube. Note that this velocity distribution is identical to that for the case of flow past a cylinder with a free stream velocity of 2 U_{mf}, an empirical assumption also made by Catipovic et al. [6] in their estimate of total heat transfer to a horizontal tube.

[1] Assistant Professor, Department of Mechanical Engineering, Oregon State University, Corvallis, Ore. 97331. Mem. ASME

Contributed by the Heat Transfer Division for publication in the JOURNAL OF HEAT TRANSFER. Manuscript received by the Heat Transfer Division October 2, 1981.

be a mechanistic effect not accounted for in the correlations. However, there is little reason to attempt to propose a modified correlation for mixed beds at this point based on our limited set of data. Such an attempt awaits the establishment of a broader data base of mixed-sized particle experimental results.

References

1 Saxena, S. C., Grewal, N. S., Gabor, J. D., Zabrodsky, S. S., and Galershtein, D. M., "Heat Transfer Between a Gas Fluidized Bed and Immersed Tubes," in *Advances in Heat Transfer*, Vol. 14, edited by T. F. Irvine, Jr. and J. P. Hartnett, Academic Press, New York, 1978, pp. 149–247.

2 Vreedenberg, H. A., "Heat Transfer between a Fluidized Bed and a Horizontal Tube." *Chem. Engr. Sci.*, Vol. 9, 1958, pp. 52–60.

3 Wender, L., and Cooper, G. T., "Heat Transfer Between Fluidized Solids Beds and Boundary Surfaces—Correlation of Data," *AIChE J.*, Vol. 4, 1958, pp. 15–23.

4 Ainshtein, V. G., "An Investigation of Heat Transfer Process Between Fluidized Beds and Single Tubes Submerged in the Bed," in *Hydrodynamics and Heat Transfer in Fluidized Beds*, edited by S. S. Zabrodsky, MIT Press, Cambridge, Mass., 1966, pp. 270–272.

5 Andeen, B. R., and Glicksman, L. R., "Heat Transfer to Horizontal Tubes in Shallow Beds," ASME-AIChE Heat Transfer Conference, Paper No. 76-HT-67, St. Louis, Mo., 1976.

6 Grewal, N. S. and Saxena, S. C., "Heat Transfer Between a Horizontal Tube and A Gas-Solid Fluidized Bed", *International Journal of Heat and Mass Transfer*, Vol. 23, 1980, pp. 1505–1518.

7 Leva, M., "Correlations of the Dense Phase Fluidized State and Their Applications," *Canadian Journal of Chemical Engineering*, Vol. 35, 1958, pp. 71–76.

An Approximate Model of Bubble Phase Convective Heat Transfer to a Horizontal Tube in a Large Particle Fluid Bed

R. L. Adams[1]

Introduction

The convective heat transfer within a gas bubble contacting a heat-transfer surface in a large particle or high pressure fluidized bed can be a significant fraction of the total heat transfer. Instantaneous local heat-transfer data for a horizontal tube immersed in a two-dimensional bed obtained by Catipovic [1] suggest that this convective contribution can account for as much as 30 percent of the total time-averaged heat transfer for a bed of 6.6-mm dia dolomite particles.

The purpose of this note is to present an approximate model of bubble phase convective heat transfer to a horizontal tube immersed in a two-dimensional fluidized bed. The model makes use of the exact solution for the inviscid flow field within a single two-dimensional slow bubble of Adams [2] and the one parameter integral method of Smith and Spalding [3]. The effect of interstitial turbulence present in the bubble flow field is included as an ad hoc correction to the results. This makes the model much less cumbersome for heat-transfer estimates than the numerical model of instantaneous heat transfer developed previously (see Adams and Welty [4, 5]) and allows calculation of the time-averaged bubble convective heat transfer contribution. Calculations based upon the model are compared with local time-averaged, heat-transfer data for a horizontal tube immersed in a low temperature two-dimensional bed obtained by Catipovic [1].

Analysis

Consider a single, two-dimensional slow bubble contacting a horizontal tube as shown in the inset of Fig. 1. Assuming that the region within the contacting bubble is free of particles, the flow field within the bubble will be determined by boundary conditions at the tube wall and bubble boundary and will be characterized by a Reynolds number based upon minimum fluidizing velocity and tube diameter. This Reynolds number is sufficiently large for cases in which bubble convective heat transfer is important so that viscous effects are confined to a thin boundary layer adjacent to the tube surface. Furthermore, the gas velocity at the edge of this boundary layer is determined from the inviscid flow field within the contacting bubble in accordance with classical boundary layer theory.

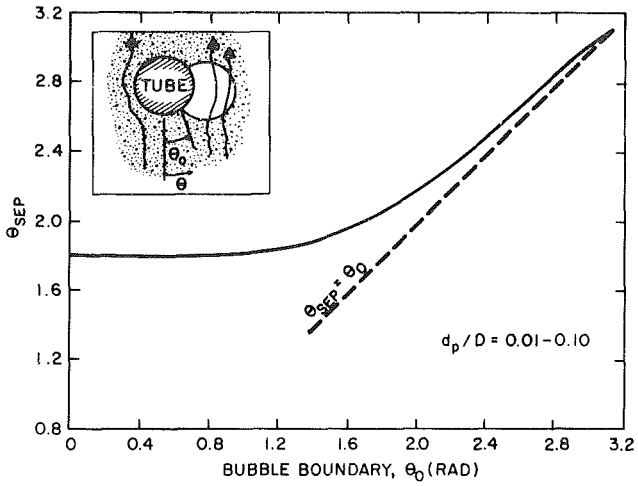

Fig. 1 Location of boundary layer separation within a two-dimensional bubble contacting a horizontal tube

To obtain the heat transfer to the tube surface, the one-parameter method of Smith and Spalding [3] is used in place of the more complex two-equation model of boundary layer flow with free stream turbulence developed by Adams and Welty [4]. Since Smith and Spalding's method does not account for free stream turbulence, a correction to the results is made by assuming that the amplification in heating is the same as that for a stagnation point flow.

According to the method of Smith and Spalding [3] the local Nusselt number (here based upon D, tube diameter) is obtained from the following

$$\mathrm{Nu}_D = \left(\frac{a}{\mathrm{Re}_D} \frac{\int_{x_0}^{x} U^{b-1} dx}{U^b} + \frac{U_0^b}{U^b \mathrm{Nu}_{D_0}^{\ 2}} \right)^{-1/2} \tag{1}$$

where $a \simeq 9.07\ \mathrm{Pr}^{-0.7}$, $b \simeq 2.95\ \mathrm{Pr}^{0.07}$, Pr is the gas Prandtl number, x is the dimensionless streamwise coordinate (here relative to D), U is the dimensionless edge velocity (here relative to U_{mf}, minimum fluidizing velocity), Re_D is the Reynolds number based upon U_{mf} and D, and U_0 and Nu_{D_0} are evaluated at x_0.

Considering a single, two-dimensional slow bubble contacting a tube (valid for large particle beds operating near U_{mf}), Adams [2] has shown that the boundary layer edge velocity for the flow at the tube surface is independent of bubble size and given by

$$U = 4 \sin\theta \tag{2}$$

with θ measured from the lower stagnation point of the tube. Note that this velocity distribution is identical to that for the case of flow past a cylinder with a free stream velocity of 2 U_{mf}, an empirical assumption also made by Catipovic et al. [6] in their estimate of total heat transfer to a horizontal tube.

[1] Assistant Professor, Department of Mechanical Engineering, Oregon State University, Corvallis, Ore. 97331. Mem. ASME

Contributed by the Heat Transfer Division for publication in the JOURNAL OF HEAT TRANSFER. Manuscript received by the Heat Transfer Division October 2, 1981.

For the contacting bubble, x_0 is the trailing edge location of the bubble so that Nu_{D_0} is taken as the two-dimensional Nusselt number for the interstitial flow at this point. Thus, when the approximations for Nu_{D_0} of Adams [7] are used, the local instantaneous Nusselt number within the contacting bubble becomes

$$\mathrm{Nu}_D(\theta,\theta_0) \simeq \left(\frac{\mathrm{Pr}^{0.7}\mathrm{Re}_D \sin^b\theta}{1.13\int_{\theta_0}^{\theta} \sin^{b-1}\theta_1 d\theta_1 + \sqrt{\dfrac{0.297\epsilon_\infty}{1-\epsilon_\infty}} \dfrac{d_p}{D} \sin^{b-1}\theta_0} \right)^{1/2} \quad (3)$$

where θ_0 locates the bubble trailing edge, d_p is the particle diameter and ϵ_∞ is the bed voidage. Now, the time-averaged local bubble Nusselt number is obtained by assuming that the bubble trailing edge position, θ_0, is uniformly distributed between the lower stagnation point ($\theta_0 = 0$) and the position of interest ($\theta_0 = \theta$). Thus the time-averaged local bubble Nusselt number is

$$\bar{\mathrm{Nu}}_D(\theta) = \frac{1}{\theta}\int_0^{\theta} \mathrm{Nu}_D(\theta,\theta_0) d\theta_0 \quad (4)$$

The effect of free stream turbulence arising from the interstitial flow is included by assuming that the relative change is given by that for stagnation point flow. Adams [7] has shown on the basis of a two-parameter integral method that for stagnation point flow

$$\frac{(\mathrm{Nu}_D)_{u'}}{(\mathrm{Nu}_D)_{u'=0}} = \left(\frac{\Omega_{v_0}}{\Omega_v}\right)^{1/2} \simeq \left(0.2 + 0.8e^{-0.0849u'}\sqrt{\frac{\mathrm{Re}_D d_p}{\epsilon_\infty D}}\right)^{-1/2} \quad (5)$$

where Ω_v is the velocity profile shape parameter and u' is the interstitial turbulence intensity.

When equations (3) and (4) are combined, and equation (5) is used to account for the free stream turbulence effect, the following expression is obtained for the time-averaged local bubble Nusselt number

$$\frac{\bar{\mathrm{Nu}}_d(\theta)}{\sqrt{\mathrm{Re}_D\mathrm{Pr}^{0.7}\Omega_{v_0}/\Omega_v}} = \frac{\sin^{b/2}\theta}{\theta}\int_0^{\theta} \frac{d\theta_0}{\sqrt{1.13\int_{\theta_0}^{\theta} \sin^{b-1}\theta_1 d\theta_1 + \dfrac{0.297\epsilon_\infty}{1-\epsilon_\infty}\dfrac{d_p}{D}\sin^{b-1}\theta_0}} \quad (6)$$

Note that the r.h.s. of equation (6) serves as an influence coefficient which depends primarily upon θ, since b is a weak function of Prandtl number and the second term under the radical is small.

In conjuction with equation (6), it is also necessary to know the location of boundary layer separation within the contacting bubble so that the results can be properly applied. The separation location will depend upon the trailing edge location of the bubble (θ_0); however, estimates made using Thwaites method (see, e.g., White [3]) give boundary layer separation at $\theta = 1.8$ radians (103 deg) for θ_0 up to 1 radian (57.3 deg). For $\theta_0 > 1$ radian, the location of separation asymptotically approaches θ_0. These results are shown in Fig. 1. From these results it would seem that contacting slow bubbles which do not surround the tube should not exist on the upper part of the tube, because the reverse flow produced would cause the bubble leading edge to collapse at the tube surface. This observation seems to be consistent with the results of experimental studies of bubble/tube interaction performed by Hagar and Thomson [8].

Comparison With Experiment

The time-averaged local bubble Nusselt number parameter given by equation (6) is shown for particle sizes of 1.3 to 6.6-mm dia and for a 50.8-mm dia horizontal tube in Fig. 2. For these calculations, the bed voidage was assumed to be 0.5, and the gas Prandtl number was taken as 0.72. The theoretical values of the heat-transfer parameter are seen to be relatively insensitive to position (except near the lower stagnation point, $\theta = 0$) and particle size. Shown with the calculated values are experimental results based upon Catipovic's [1] minimum local heat-transfer coefficients obtained in a cold, two-dimensional bed and with an assumed turbulence intensity, u', of 0.2 based upon measurements by Galloway and Sage [9]. The theoretical values based upon single bubble contact compare at least qualitatively with the experimental results with reasonable agreement at $\theta = 0$ and $\pi/2$ (except for 1.3-mm dia particles at $\theta = 0$). However, there are uncertainties in the comparison; the experimental results represent the effects of multiple bubble interaction, the bubbles are not circular, and minimum heat-transfer levels may not always represent bubble levels. Since bubble convective heat transfer accounts for about 30 percent or less of the total heat transfer for most cases of interest, the model would seem to provide a reasonable estimate of the effect in two-dimensional beds and, due to its fundamental nature, can be extended beyond the cases covered by Catipovic's experiments. The extension

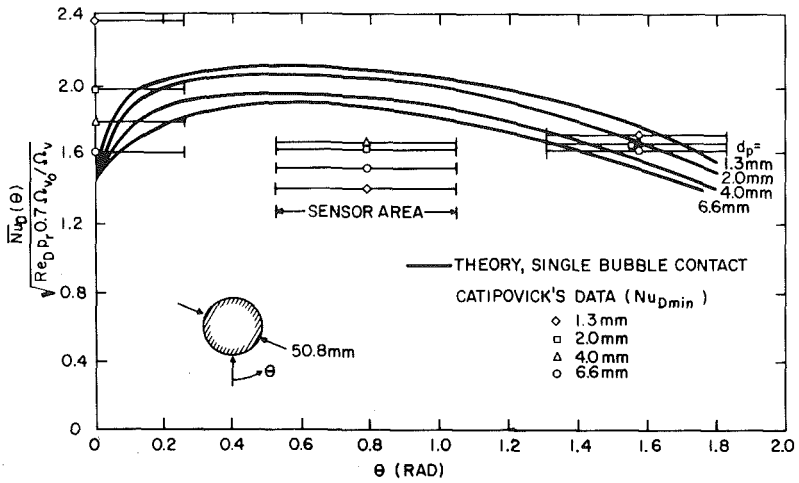

Fig. 2 Time-averaged local Nusselt number parameter for a contacting bubble with $u' = 0.2$, $\mathrm{Pr} = 0.72$, and $\epsilon_\infty = 0.5$

of the model to the three-dimensional case could be accomplished by increasing the bubble through flow velocity by a factor of 1.5 as suggested by Catipovic et al. [6] and according to the isolated bubble fluid mechanical theory of Davidson [10]. This would result in 22 percent increase in heat transfer relative to the two-dimensional case. However, rigorous treatment of three-dimensional bubble convective heat transfer awaits solution of the inviscid flow field problem for three-dimensional bubble contact.

Acknowledgement

Funding for this work was provided by the Battelle Memorial Institute Distributions to Universities Program.

References

1 Catipovic, N. M., "Heat Transfer to Horizontal Tubes in Fluidized Beds: Experiment and Theory," Ph.D. thesis, Oregon State University, Corvallis, Ore., 1979.

2 Adams, R. L., "An Exact Solution for the Inviscid Flow Field Within a Two-Dimensional Bubble Contacting a Horizontal Tube in a Gas Fluidized Bed," to appear in *Chem. Engrg. Sci.*, 1982.

3 White, F. M., *Viscous Fluid Flow*, McGraw-Hill, New York, 1974.

4 Adams, R. L., and Welty, J. R., "A Gas Convection Model of Heat Transfer in Large Particle Fluidized Beds," *AIChE J.*, Vol. 25, No. 3, 1979, pp. 395-405.

5 Adams, R. L., and Welty, J. R., "An Analytical Study of Bubble and Adjacent Tube Influence on Heat Transfer to a Horizontal Tube in a Gas Fluidized Bed," ASME JOURNAL OF HEAT TRANSFER, Vol. 104, 1982, pp. 206-209.

6 Catipovic, N. M., Jovanovic, G. N., Fitzgerald, T. J., and Levenspiel, O., "A Model for Heat Transfer to Horizontal Tubes Immersed in a Fluidized Bed of Large Particles," in *Fluidization—Proceedings of the 1980 International Fluidization Conf.*, edited by J. R. Grace and J. M. Matsen, Plenum Press, New York, 1980.

7 Adams, R. L., "An Approximate Formula for Gas Convection Dominant Heat Transfer in Large-Particle Fluidized Beds," ASME JOURNAL OF HEAT TRANSFER, Vol. 103, 1981, pp. 395-397.

8 Hager, W. R., and Thomson, W. J., "Bubble Behavior Around Immersed Tubes in a Fluidized Bed," *AIChE Symp. Ser.*, Vol. 69, No. 128, 1973, pp. 68-77.

9 Galloway, T. R., and Sage, B. H., "A Model of the Mechanism of Transport in Packed, Distended, and Fluidized Beds," *Chem. Engrg. Sci.*, Vol. 25, 1970, pp. 495-516.

10 Davidson, J. F., and Harrison, D., *Fluidised Particles*, Cambridge University Press, 1963.

Incipient Vapor Nucleation of Methanol From an Artificial Site - Uniform Superheat

T. R. Jemison[1], R. J. Rivers[2], and R. Cole[3]

Introduction

The onset of boiling in most engineering systems is thought to be a result of nucleation from a pre-existing gas or vapor phase entrapped in surface imperfections [1]. For vapor filled cavities, under constant temperature conditions, the superheat required for the vapor to emerge from, and "cap" the cavity is given by

$$T - T_s = \frac{2\sigma T_s}{\rho_v \Delta H_v R_c f} \tag{1}$$

where T is the system temperature, T_s is the saturation temperature corresponding to the system pressure, σ is the surface tension, ρ_v is the vapor density, ΔH_v is the latent heat of vaporization, and R_c is the cavity mouth radius. The function f equals unity when $r/R_c \geq 1$ and is dependent upon cavity geometry and contact angle for $r/R_c < 1$, as discussed in [1]. Here r is the radius of curvature of the vapor-liquid interface. For cylindrical cavities such as used in this study, geometrical considerations show that r/R_c is always greater than or equal to unity. Thus the appropriate equation is

$$T - T_s = \frac{2\sigma T_s}{\rho_v \Delta H_v R_c} \tag{2}$$

Because of the excellent wetting properties of most organic liquids, experimental measurements of incipient nucleation from artificial cavities in uniformly superheated systems have previously been limited to water. In effect, the organic liquids fill the cavities prior to nucleation, rendering them inactive. Thus experimental verification of equation (2) has, to this point, been limited to a single fluid.

This note describes a modification of the Griffith-Wallis experimental technique [2] which circumvents the filling problem and allows the procedure to be extended to include organic liquids. Additionally, some preliminary experimental data using methanol are presented and compared with equation (2) and with previous water data [3].

Experimental System and Procedure

The test surface used in this study is the same as that reported as test surface 1 in [3], and from which superheat data on water had been obtained and reported. It consisted of a 50 mm × 50 mm by 0.5 mm thick copper sheet which was metallurgically polished prior to precision drilling of the nucleation site. The site was originally cylindrical (except at the bottom where it was conical) with a mean cavity mouth radius of 24.1 μm and a depth of 240 μm. Following a number of years of only intermittent use, all of the nucleation sites were remeasured for this study. All of the radii were the same within the uncertainty limits of the optical micrometer. Thus the cavity mouth radius for the site on test surface 1 is here reported as 23.4 μm. Interestingly, the depressions surrounding the original cavities (and reported in [3]) were not observed this time. It seems reasonable to assume that the surfaces had been repolished in the interval.

The experimental system is shown schematically in Fig. 1. The boiling tank was a large test tube, specially tapered to cause the test surface to drop to approximately the same position for each run. The temperature was measured at the level of the nucleation cavity by a calibrated copper-constantan thermocouple referenced to the ice point. To prevent large quantities of condensate from dripping back

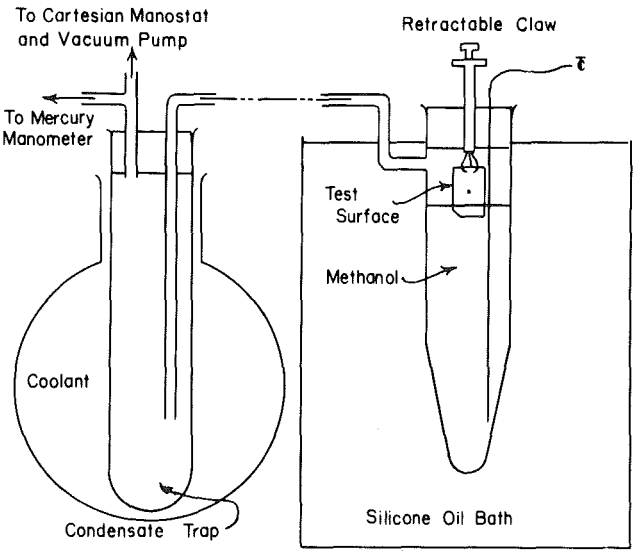

Fig. 1 Experimental system

[1] E. I. DuPont, South Carleston, W.V. 25302

[2] Proctor and Gamble, Cincinnati, Ohio 45206

[3] Department of Chemical Engineering, Clarkson College of Technology, Potsdam, N.Y. 13676. Mem. ASME

Contributed by the Heat Transfer Division for publication in the JOURNAL OF HEAT TRANSFER. Manuscript received by the Heat Transfer Division August 31, 1981.

of the model to the three-dimensional case could be accomplished by increasing the bubble through flow velocity by a factor of 1.5 as suggested by Catipovic et al. [6] and according to the isolated bubble fluid mechanical theory of Davidson [10]. This would result in 22 percent increase in heat transfer relative to the two-dimensional case. However, rigorous treatment of three-dimensional bubble convective heat transfer awaits solution of the inviscid flow field problem for three-dimensional bubble contact.

Acknowledgement

Funding for this work was provided by the Battelle Memorial Institute Distributions to Universities Program.

References

1 Catipovic, N. M., "Heat Transfer to Horizontal Tubes in Fluidized Beds: Experiment and Theory," Ph.D. thesis, Oregon State University, Corvallis, Ore., 1979.

2 Adams, R. L., "An Exact Solution for the Inviscid Flow Field Within a Two-Dimensional Bubble Contacting a Horizontal Tube in a Gas Fluidized Bed," to appear in *Chem. Engrg. Sci.*, 1982.

3 White, F. M., *Viscous Fluid Flow*, McGraw-Hill, New York, 1974.

4 Adams, R. L., and Welty, J. R., "A Gas Convection Model of Heat Transfer in Large Particle Fluidized Beds," *AIChE J.*, Vol. 25, No. 3, 1979, pp. 395-405.

5 Adams, R. L., and Welty, J. R., "An Analytical Study of Bubble and Adjacent Tube Influence on Heat Transfer to a Horizontal Tube in a Gas Fluidized Bed," ASME JOURNAL OF HEAT TRANSFER, Vol. 104, 1982, pp. 206-209.

6 Catipovic, N. M., Jovanovic, G. N., Fitzgerald, T. J., and Levenspiel, O., "A Model for Heat Transfer to Horizontal Tubes Immersed in a Fluidized Bed of Large Particles," in *Fluidization—Proceedings of the 1980 International Fluidization Conf.*, edited by J. R. Grace and J. M. Matsen, Plenum Press, New York, 1980.

7 Adams, R. L., "An Approximate Formula for Gas Convection Dominant Heat Transfer in Large-Particle Fluidized Beds," ASME JOURNAL OF HEAT TRANSFER, Vol. 103, 1981, pp. 395-397.

8 Hager, W. R., and Thomson, W. J., "Bubble Behavior Around Immersed Tubes in a Fluidized Bed," *AIChE Symp. Ser.*, Vol. 69, No. 128, 1973, pp. 68-77.

9 Galloway, T. R., and Sage, B. H., "A Model of the Mechanism of Transport in Packed, Distended, and Fluidized Beds," *Chem. Engrg. Sci.*, Vol. 25, 1970, pp. 495-516.

10 Davidson, J. F., and Harrison, D., *Fluidised Particles*, Cambridge University Press, 1963.

Incipient Vapor Nucleation of Methanol From an Artificial Site - Uniform Superheat

T. R. Jemison[1], R. J. Rivers[2], and R. Cole[3]

Introduction

The onset of boiling in most engineering systems is thought to be a result of nucleation from a pre-existing gas or vapor phase entrapped in surface imperfections [1]. For vapor filled cavities, under constant temperature conditions, the superheat required for the vapor to emerge from, and "cap" the cavity is given by

$$T - T_s = \frac{2\sigma T_s}{\rho_v \Delta H_v R_c f} \tag{1}$$

where T is the system temperature, T_s is the saturation temperature corresponding to the system pressure, σ is the surface tension, ρ_v is the vapor density, ΔH_v is the latent heat of vaporization, and R_c is the cavity mouth radius. The function f equals unity when $r/R_c \geq 1$ and is dependent upon cavity geometry and contact angle for $r/R_c < 1$, as discussed in [1]. Here r is the radius of curvature of the vapor-liquid interface. For cylindrical cavities such as used in this study, geometrical considerations show that r/R_c is always greater than or equal to unity. Thus the appropriate equation is

$$T - T_s = \frac{2\sigma T_s}{\rho_v \Delta H_v R_c} \tag{2}$$

Because of the excellent wetting properties of most organic liquids, experimental measurements of incipient nucleation from artificial cavities in uniformly superheated systems have previously been limited to water. In effect, the organic liquids fill the cavities prior to nucleation, rendering them inactive. Thus experimental verification of equation (2) has, to this point, been limited to a single fluid.

This note describes a modification of the Griffith-Wallis experimental technique [2] which circumvents the filling problem and allows the procedure to be extended to include organic liquids. Additionally, some preliminary experimental data using methanol are presented and compared with equation (2) and with previous water data [3].

Experimental System and Procedure

The test surface used in this study is the same as that reported as test surface 1 in [3], and from which superheat data on water had been obtained and reported. It consisted of a 50 mm × 50 mm by 0.5 mm thick copper sheet which was metallurgically polished prior to precision drilling of the nucleation site. The site was originally cylindrical (except at the bottom where it was conical) with a mean cavity mouth radius of 24.1 μm and a depth of 240 μm. Following a number of years of only intermittent use, all of the nucleation sites were remeasured for this study. All of the radii were the same within the uncertainty limits of the optical micrometer. Thus the cavity mouth radius for the site on test surface 1 is here reported as 23.4 μm. Interestingly, the depressions surrounding the original cavities (and reported in [3]) were not observed this time. It seems reasonable to assume that the surfaces had been repolished in the interval.

The experimental system is shown schematically in Fig. 1. The boiling tank was a large test tube, specially tapered to cause the test surface to drop to approximately the same position for each run. The temperature was measured at the level of the nucleation cavity by a calibrated copper-constantan thermocouple referenced to the ice point. To prevent large quantities of condensate from dripping back

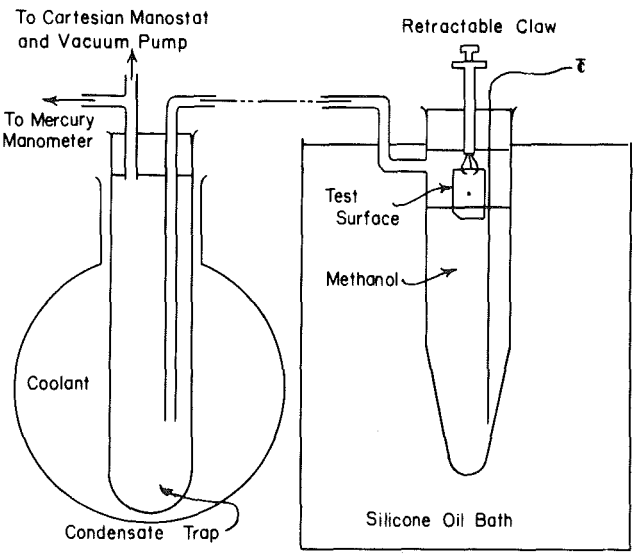

Fig. 1 Experimental system

[1] E. I. DuPont, South Carleston, W.V. 25302

[2] Proctor and Gamble, Cincinnati, Ohio 45206

[3] Department of Chemical Engineering, Clarkson College of Technology, Potsdam, N.Y. 13676. Mem. ASME

Contributed by the Heat Transfer Division for publication in the JOURNAL OF HEAT TRANSFER. Manuscript received by the Heat Transfer Division August 31, 1981.

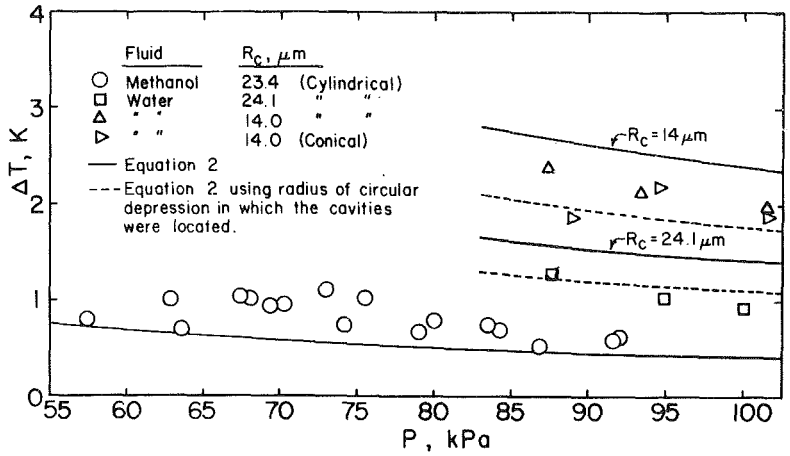

Fig. 2 Deactivation superheat versus system pressure

into the boiling tube and subcooling the liquid, the vapor was passed to a water cooled trap. The trap was, in turn, connected to a mercury *U*-tube manometer. A vacuum was drawn on the system by means of a vacuum pump and controlled by a Cartesian manostat. In order to heat the methanol in the test tube as uniformly as possible, it was placed in a large heated oil bath.

Procedure

The previous operating procedure [2, 3] had been to place the test surface in the liquid filled test tube, raise the system temperature to the desired value, and draw a vacuum on the system causing it to become uniformly superheated and simultaneously causing the nucleation site to activate. Unfortunately this procedure does not work with liquids which wet the surface well. By the time that the system reaches the desired temperature, the cavity has filled with liquid and is unable to activate, when the pressure is reduced. (Nucleation could occur by a molecular mechanism if a sufficient superheat could be achieved). One means by which the problem may be overcome is by introducing the test surface into the liquid after it has been superheated to the desired level. This was accomplished in these experiments by holding the test surface in a retractable claw such that, although a portion of the surface was in the superheated methanol, the nucleation cavity itself was in the vapor phase. Once the system temperature had been brought to the desired value (333–338 K), the system pressure had been reduced to yield the desired initial level of superheat (~5K), and an apparent equilibrium had been achieved, the claws were extended and the test surface allowed to drop into the superheated methanol. The resulting "explosion" generally caused a loss of perhaps 25 percent of the system methanol out through the vacuum line. In some instances the explosion was so violent that too much of the methanol was lost and the run had to be terminated. In all instances the superheat dropped by several degrees as a result of the vaporization, so that it was necessary to wait for the superheat to be re-established. Now, however, the site was active and continually producing bubbles. The system temperature was then allowed to decrease very slowly (1 K per 10 min, maximum) by decreasing the heat input to the surrounding oil bath. Near cessation, the rate of temperature change was about 10 times less than the maximum, or 0.1 K per 10 min. The temperature was recorded within 5 s of cessation and the manometer reading within one min (the latter was not critical because the pressure remained constant). The remaining data – barometric pressure and liquid head above the nucleation site – were recorded shortly after.

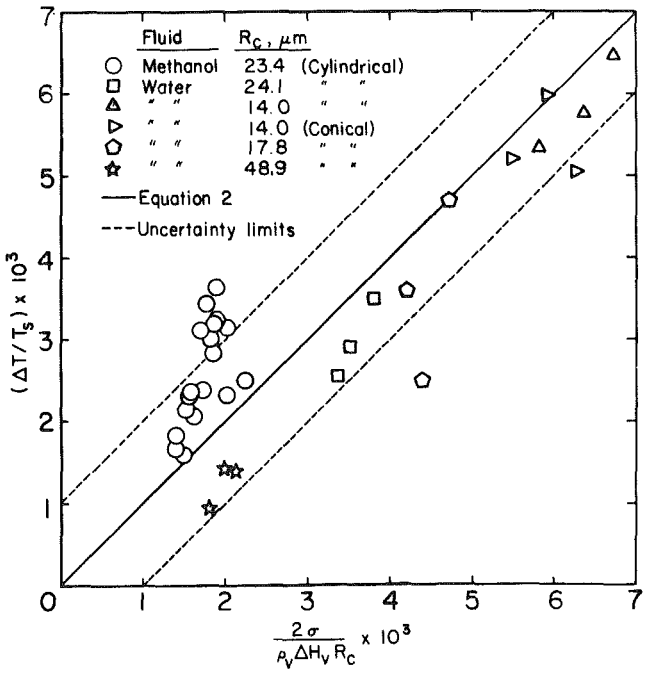

Fig. 3 Dimensionless representation of experimental data

Results and Discussion

Experimental superheats in this study were measured only at cessation. As the condition of cessation of boiling activity is a matter of judgment, a waiting period of one min was strictly adhered to. If a bubble did not appear by the end of that time, the superheat was recorded and the liquid reheated in an attempt to determine the emergent superheat. In the water studies reported in [3], this was sometimes possible and only the inability to reheat rapidly enough and the use (in that study) of a slow response thermocouple, prevented obtaining reliable data. In this study, the excellent wetting properties of the methanol caused the cavity to die (i.e., fill with liquid) almost instantly upon deactivation. Thus, in no instance was it possible to reactivate a nucleation cavity in this study, after bubbling had ceased. In fact, it is felt that quite often, premature deactivation occurred, resulting in the measured deactivation superheat being on the high side. Such deactivation was usually characterized by the sudden appearance of an abnormally large vapor bubble.

The experimental results are presented in Figs. 2 and 3. In

Fig. 2, the data are plotted as deactivation superheat versus system pressure (the experimental parameter) and compared with the predictions of equation (2). Also shown, for purposes of comparison, are some of the water data from [3]. The square symbols represent the water data from the same cavity as used in this study. The triangles represent water data from two cavities (test surfaces 2 and 4 of [3]) which had approximately the same cavity mouth radius. One was cylindrical and the other was conical. The deviation of the data from the predictions of equation (2) seem to be similar for all of the surfaces, except that the methanol data has a positive deviation and the water a negative deviation. It is felt that the positive deviation of the methanol data is due to premature deactivation as earlier discussed (excellent wetting properties of methanol); the negative deviation of the water data is however a result of only one theoretical line being drawn for each test surface. In the original study, the cavities were found to be located in a circular depression. When the radius of the depression is substituted into equation (2) and plotted versus pressure, the deviation is positive, and the two curves nearly bracket the experimental data. These curves are represented by the dashed lines in Fig. 2 (water data only).

The data are replotted in Fig. 3 in dimensionless form. All of the water data reported in [3] are represented here. The solid 45 deg line represents the predictions of equation (2); i.e., the ordinate and abscissa are equal. The dashed lines represent the experimental uncertainty band about the theoretical curve as determined by the procedure in [4] using an uncertainty of 20 percent in the superheat (ΔT) and 10 percent in the cavity mouth radius. Data falling within the band are assumed to be in agreement with the prediction. Of the fifteen data points for water, only two fall outside of the band. Of those for methanol, seven of eighteen fall outside of the band.

Cole [5] has shown that for cylindrical cavities, a contact angle less than $\pi/4$ rads yields a very unstable nucleation cavity. It appears that as long as the system superheat is greater than that required by the cavity mouth radius (equation (2)), and that the vapor volume is sufficiently high so the required superheat as given by the curvature $1/r$ does not exceed the system superheat, the cavity will continue to bubble. If, however, the system superheat drops below that given by equation (2), or due to dynamic effects, the liquid penetrates too deeply into the cavity, the vapor will condense and the cavity will fill with liquid and die. The latter effect is believed to be the reason for seven of eighteen methanol data points having deactivation superheats outside of the uncertainty band. A deeper cavity should yield more consistent results.

Conclusions

A modification of the experimental procedure for obtaining deactivation superheats has resulted in the first such information on fluids other than water. In general, the data are in agreement with the entrapped vapor model of boiling nucleation. The data also exhibit the instabilities predicted by the model for well wetting liquids in not-too-deep cavities. These instabilities, resulting in premature deactivation by liquid penetration into the cavity, and subsequent condensation of the vapor, are believed to have caused seven to eighteen data points to lie outside of the band of experimental uncertainty. Increasing the ratio of depth to mouth radius is expected to minimize this effect.

References

1 Van Stralen, S. J. D., and Cole, R., *Boiling Phenomena*, Vol. 1, Hemisphere Publishing Corporation/McGraw-Hill, 1979, pp. 119–129.

2 Griffith, P., and Wallis, J. D., "The Role of Surface Conditions in Nucleate Boiling," *AIChE Symposium*, Series 30, Vol. 56, 1960, pp. 49–63.

3 Schultz, R. R., Kasturirangan, S., and Cole, R., "Experimental Studies of Incipient Vapor Nucleation," *The Canadian Journal of Chemical Engineering*, Vol. 53, 1975, pp. 408–413.

4 Schultz, R. R., and Cole, R., "Uncertainty Analysis in Boiling Nucleation," *AIChE Symposium*, Series 180, Vol. 75, 1979, pp. 32–39.

5 Cole, R., "Boiling Nucleation," *Advances in Heat Transfer*, Vol. 10, Academic Press, 1974, p. 123.

Film Breakdown and Bundle-Depth Effects in Horizontal-Tube, Falling-Film Evaporators

J. J. Lorenz[1] and D. Yung[1]

Introduction

In a horizontal-tube, falling-film evaporator, a working fluid is fed to the top of a bundle of heated horizontal tubes, and the fluid evaporates as it flows filmwise over the tube surfaces. The unevaporated liquid from any given tube falls (drips) onto the next lower tube in the bundle. This type of evaporator with ammonia as the working fluid is a leading candidate for use in Ocean Thermal Energy Conversion (OTEC) power systems. In support of the development of OTEC heat exchangers, a number of experimental studies were conducted with single tubes [1–3]. But questions have arisen concerning the applicability of the single-tube data to the design of large-scale evaporators. Recently, the authors participated in a test of a large-scale, falling film evaporator for OTEC [4]. Some remarkable differences – and similarities – were discovered between these large-bundle test results and the single-tube test results of references [1–3]. The purpose of this paper is to compare the single-tube data with the present large-bundle data in an effort to shed some light on two important questions: (*i*) heat-transfer performance degradation resulting from film breakdown, and (*ii*) heat-transfer coefficient variations with bundle depth.

Large-Bundle Tests

A horizontal-tube, falling-film evaporator was tested as part of a program to evaluate the performance of large-scale OTEC heat exchangers under actual conditions in an ocean environment. Details of this test program, known as the OTEC-1 Power System Test Program, are reported in [4].

The evaporator was a single-pass, shell-and-tube heat exchanger, 16.5-m long and having a 4-m dia shell. The unit was unique in that it consisted of two separate bundles (a plain-tube upper bundle and an enhanced-tube lower bundle) enclosed within a single cylindrical shell. Each bundle could be tested separately. Only results for the plain-tube bundle are presented herein.

The plain-tube portion of the heat exchanger consisted of 3000 titanium tubes, having a 2.54 cm o.d. and arranged in a 30 deg triangular tube-field layout with a pitch-to-diameter ratio of 1.25. This produced a vertical spacing of 0.64 cm between the tubes. The overall envelope of the plain bundle was rectangular, consisting of one hundred columns of tubes with thirty tubes in each column.

Ammonia liquid was directed onto the tubes from a set of spray nozzles located at the top of the bundle. Nominally, the shell-side saturation temperature was set at 22.2°C. The heat source was warm seawater, which flowed inside the tubes, entering at 26.6°C and exiting at about 24.4°C. (In contrast,

[1] Argonne National Laboratory, Argonne, Ill. 60439

Contributed by the Heat Transfer Division for publication in the JOURNAL OF HEAT TRANSFER. Manuscript received by the Heat Transfer Division November 12, 1981.

Fig. 2, the data are plotted as deactivation superheat versus system pressure (the experimental parameter) and compared with the predictions of equation (2). Also shown, for purposes of comparison, are some of the water data from [3]. The square symbols represent the water data from the same cavity as used in this study. The triangles represent water data from two cavities (test surfaces 2 and 4 of [3]) which had approximately the same cavity mouth radius. One was cylindrical and the other was conical. The deviation of the data from the predictions of equation (2) seem to be similar for all of the surfaces, except that the methanol data has a positive deviation and the water a negative deviation. It is felt that the positive deviation of the methanol data is due to premature deactivation as earlier discussed (excellent wetting properties of methanol); the negative deviation of the water data is however a result of only one theoretical line being drawn for each test surface. In the original study, the cavities were found to be located in a circular depression. When the radius of the depression is substituted into equation (2) and plotted versus pressure, the deviation is positive, and the two curves nearly bracket the experimental data. These curves are represented by the dashed lines in Fig. 2 (water data only).

The data are replotted in Fig. 3 in dimensionless form. All of the water data reported in [3] are represented here. The solid 45 deg line represents the predictions of equation (2); i.e., the ordinate and abscissa are equal. The dashed lines represent the experimental uncertainty band about the theoretical curve as determined by the procedure in [4] using an uncertainty of 20 percent in the superheat (ΔT) and 10 percent in the cavity mouth radius. Data falling within the band are assumed to be in agreement with the prediction. Of the fifteen data points for water, only two fall outside of the band. Of those for methanol, seven of eighteen fall outside of the band.

Cole [5] has shown that for cylindrical cavities, a contact angle less than $\pi/4$ rads yields a very unstable nucleation cavity. It appears that as long as the system superheat is greater than that required by the cavity mouth radius (equation (2)), and that the vapor volume is sufficiently high so the required superheat as given by the curvature $1/r$ does not exceed the system superheat, the cavity will continue to bubble. If, however, the system superheat drops below that given by equation (2), or due to dynamic effects, the liquid penetrates too deeply into the cavity, the vapor will condense and the cavity will fill with liquid and die. The latter effect is believed to be the reason for seven of eighteen methanol data points having deactivation superheats outside of the uncertainty band. A deeper cavity should yield more consistent results.

Conclusions

A modification of the experimental procedure for obtaining deactivation superheats has resulted in the first such information on fluids other than water. In general, the data are in agreement with the entrapped vapor model of boiling nucleation. The data also exhibit the instabilities predicted by the model for well wetting liquids in not-too-deep cavities. These instabilities, resulting in premature deactivation by liquid penetration into the cavity, and subsequent condensation of the vapor, are believed to have caused seven to eighteen data points to lie outside of the band of experimental uncertainty. Increasing the ratio of depth to mouth radius is expected to minimize this effect.

References

1 Van Stralen, S. J. D., and Cole, R., *Boiling Phenomena*, Vol. 1, Hemisphere Publishing Corporation/McGraw-Hill, 1979, pp. 119–129.

2 Griffith, P., and Wallis, J. D., "The Role of Surface Conditions in Nucleate Boiling," *AIChE Symposium*, Series 30, Vol. 56, 1960, pp. 49–63.

3 Schultz, R. R., Kasturirangan, S., and Cole, R., "Experimental Studies of Incipient Vapor Nucleation," *The Canadian Journal of Chemical Engineering*, Vol. 53, 1975, pp. 408–413.

4 Schultz, R. R., and Cole, R., "Uncertainty Analysis in Boiling Nucleation," *AIChE Symposium*, Series 180, Vol. 75, 1979, pp. 32–39.

5 Cole, R., "Boiling Nucleation," *Advances in Heat Transfer*, Vol. 10, Academic Press, 1974, p. 123.

Film Breakdown and Bundle-Depth Effects in Horizontal-Tube, Falling-Film Evaporators

J. J. Lorenz[1] and D. Yung[1]

Introduction

In a horizontal-tube, falling-film evaporator, a working fluid is fed to the top of a bundle of heated horizontal tubes, and the fluid evaporates as it flows filmwise over the tube surfaces. The unevaporated liquid from any given tube falls (drips) onto the next lower tube in the bundle. This type of evaporator with ammonia as the working fluid is a leading candidate for use in Ocean Thermal Energy Conversion (OTEC) power systems. In support of the development of OTEC heat exchangers, a number of experimental studies were conducted with single tubes [1–3]. But questions have arisen concerning the applicability of the single-tube data to the design of large-scale evaporators. Recently, the authors participated in a test of a large-scale, falling film evaporator for OTEC [4]. Some remarkable differences – and similarities – were discovered between these large-bundle test results and the single-tube test results of references [1–3]. The purpose of this paper is to compare the single-tube data with the present large-bundle data in an effort to shed some light on two important questions: (*i*) heat-transfer performance degradation resulting from film breakdown, and (*ii*) heat-transfer coefficient variations with bundle depth.

Large-Bundle Tests

A horizontal-tube, falling-film evaporator was tested as part of a program to evaluate the performance of large-scale OTEC heat exchangers under actual conditions in an ocean environment. Details of this test program, known as the OTEC-1 Power System Test Program, are reported in [4].

The evaporator was a single-pass, shell-and-tube heat exchanger, 16.5-m long and having a 4-m dia shell. The unit was unique in that it consisted of two separate bundles (a plain-tube upper bundle and an enhanced-tube lower bundle) enclosed within a single cylindrical shell. Each bundle could be tested separately. Only results for the plain-tube bundle are presented herein.

The plain-tube portion of the heat exchanger consisted of 3000 titanium tubes, having a 2.54 cm o.d. and arranged in a 30 deg triangular tube-field layout with a pitch-to-diameter ratio of 1.25. This produced a vertical spacing of 0.64 cm between the tubes. The overall envelope of the plain bundle was rectangular, consisting of one hundred columns of tubes with thirty tubes in each column.

Ammonia liquid was directed onto the tubes from a set of spray nozzles located at the top of the bundle. Nominally, the shell-side saturation temperature was set at 22.2°C. The heat source was warm seawater, which flowed inside the tubes, entering at 26.6°C and exiting at about 24.4°C. (In contrast,

[1] Argonne National Laboratory, Argonne, Ill. 60439

Contributed by the Heat Transfer Division for publication in the JOURNAL OF HEAT TRANSFER. Manuscript received by the Heat Transfer Division November 12, 1981.

electrical heating was used in the single-tube experiments of references [1-3].) The inlet and outlet waterboxes of the heat exchanger were instrumented with sets of Resistance Temperature Detectors (RTDs), such that both bundle-average and local tube-to-tube variations could be measured. Overall heat-transfer coefficients (i.e., combined ammonia-side, water-side, and tube wall)[2] were calculated in the usual manner from measured temperatures and flows. Then the separate ammonia-side heat-transfer coefficient was determined from the overall heat-transfer coefficient by subtracting the tube-wall thermal conductance and the forced-convective heat-transfer coefficient on the seawater side – where the latter coefficient was calculated from the Petukhov-Popov correlation [5]. With this data reduction procedure, the uncertainty in the ammonia-side heat-transfer coefficient was estimated to be ± 10 percent.

Results

Figure 1 shows a comparison between the large-bundle data of the present study and the single-tube data of references [1-3]. Results are plotted in terms of dimensionless ammonia-side heat-transfer coefficient versus film Reynolds number, $Re = 4\Gamma/\mu$, where 2Γ is the liquid flowrate per unit length of tube. To facilitate comparison with the single tube results, the Reynolds number for the bundle is based on the calculated amount of liquid reaching the *bottom* row of tubes (i.e., row number 30). The ammonia-side heat-transfer coefficient of the bundle is the bundle-average value.

Film Breakdown. Figure 1 shows that, as Re is reduced, the bundle data follow the single tube data until a critical (minimum) Reynolds number of $Re \simeq 300$ is reached. Below this critical value, the heat-transfer coefficient of the bundle decreases, while the heat-transfer coefficient of the single tubes increases. The drop-off in the heat-transfer coefficient of the bundle reflects the onset of film breakdown (dry-patch formation) on the lowermost rows of tubes. Film breakdown occurs when the liquid flowrate is too low (or the heat flux too high) to sustain a continuous liquid film on the tube surface. (See [6-8] for a discussion of the fundamental mechanism of film breakdown.) The critical Reynolds number is an important design parameter because it dictates the minimum flowrate of liquid that must reach the lowermost tubes to ensure complete wetting and, hence, maximum performance of the evaporator.

The single-tube data are quite different from the bundle data. For single tubes, no drop-off in the heat-transfer coefficient is observed at some critical Reynolds number, implying that film breakdown did not occur. In fact, the single-tube heat-transfer coefficient increases slightly as the film gets progressively thinner at the lower Reynolds numbers. This apparent absence of film breakdown might be attributable to the very careful and controlled manner in which the liquid was fed to the single tubes. In a large bundle, on the other hand, the feed to the lower rows of tubes cannot be directly controlled but depends on the history of the fluid as it drips from tube to tube in the bundle. The cumulative effect of slight tube misalignments, coupled with perturbations due to vapor crossflow[3] and ship motion, can produce flow nonuniformities and instabilities which accelerate the onset of film breakdown.

Another possible explanation for the variance between the single-tube results and the bundle results is that film breakdown did occur in the single-tube tests, but because the measurements were localized (generally instrumentation was placed only in a few planes along the length of the tube), the dry patches were missed. Indeed, at very low Re, nonwetting behavior was observed in the single-tube experiments of references [1-3]. Moreover, it appears that the reported heat-transfer coefficients were for the wetted portions of the tubes and, hence, did not reflect the influence of dry patches.

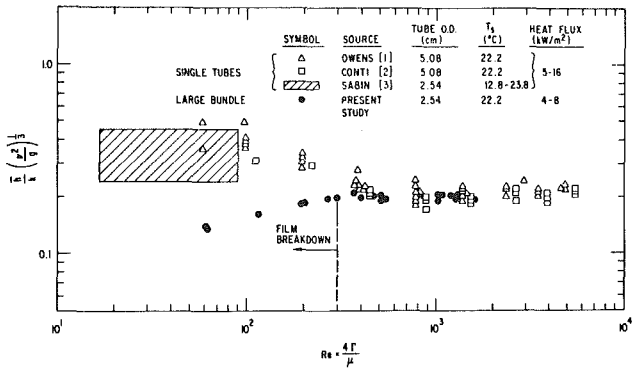

Fig. 1 Comparison between large-bundle data and single-tube data for ammonia evaporating on smooth horizontal tubes

The critical Reynolds number of Re = 300, obtained in this study, is not universal. Heat exchangers having different working fluids and operating conditions will generally require a different critical flowrate. Heat flux, surface tension, and even tube spacing can influence film breakdown [7, 8]. In the absence of experimental data on film breakdown for a particular evaporator design, [7, 8] might provide insight on how to extrapolate the results of the present study.

Bundle-Depth Effects. For Re > 300, where most of the tube surfaces are fully wetted, Fig. 1 shows that the average heat-transfer coefficient of the bundle is equal to the heat-transfer coefficient of a single tube. A limited number of measurements taken inside the bundle (not plotted) revealed that the local (i.e., not at a point, but an entire tube) heat-transfer coefficients were fairly uniform over the bundle cross section. The local coefficients generally fell within ±10 percent of the bundle-averaged value, and there was no systematic variation in the heat-transfer coefficient with bundle depth.

Conclusions

Large-bundle test results were compared with single-tube test results in an effort to shed some light on the questions of film breakdown and bundle-depth effects in horizontal-tube, falling-film evaporators.

It was found that single tube results do not properly reflect the film breakdown behavior of large bundles. Below a critical Reynolds number of $Re \simeq 300$, where film breakdown occurred in the bundle test, the heat-transfer coefficients were lower than those that were reported for single tubes.

For Re > 300, where the majority of tubes are fully wetted, the average heat-transfer coefficient of the bundle was found to be equal to the heat-transfer coefficient of a single tube. No bundle-depth variations in the heat-transfer coefficient were observed.

In a strict sense, these results apply only to falling-film evaporators having thirty rows of tubes wetted by a single feed system at the top and operating with ammonia at low heat fluxes, typical of OTEC. Nevertheless these results provide valuable insight into the general applicability of single-tube data to the design of large-scale evaporators.

[2] It should be pointed out that the biofouling thermal resistance was measured by special biofouling monitoring devices and was found to be negligibly small.

[3] The vapor crossflow velocities were relatively small and not sufficient to cause gross entrainment and deflection of the liquid.

References

1 Owens, W. L., "Correlation of Thin Film Evaporation Heat Transfer

Coefficients for Horizontal Tubes," *Proceedings of the Fifth Ocean Thermal Energy Conversion Conference*, Miami Beach, Fla., 1978.

2 Conti, R. J., "Experimental Investigation of Horizontal-Tube Ammonia Film Evaporators With Small Temperature Differentials," *Proceedings of the Fifth Ocean Thermal Energy Conversion Conference*, Miami Beach, Fla., 1978.

3 Sabin, C. M., and Poppendiek, H. F., "Film Evaporation of Ammonia over Horizontal Round Tubes," *Proceedings of the Fifth Ocean Thermal Energy Conversion Conference*, Miami Beach, Fla., 1978.

4 Lorenz, J. J., et al., "OTEC-1 Heat Exchanger Test Results," *Proceedings of the Eighth Ocean Thermal Energy Conversion Conference*, Washington, D.C., 1981.

5 Petukhov, B. S., "Heat Transfer and Friction in Turbulent Pipe Flow with Variable Physical Properties," *Advances in Heat Transfer*, Vol. 6, 1970, p. 503.

6 Hartley, D. E., and Murgatroyd, W., "Criteria for the Breakup of Thin Liquid Layers Flowing Isothermally Over Solid Surfaces," *International Journal of Heat and Mass Transfer*, Vol. 7, 1964, pp. 1003–1015.

7 Ganic, E. N., and Roppo, M. N., "An Experimental Study of Falling Liquid Film Breakdown on a Horizontal Cylinder During Heat Transfer," ASME JOURNAL OF HEAT TRANSFER, Vol. 102, 1980, pp. 342–346.

8 Getachew, D., "Falling Film Breakdown Heat Flux and Heat Transfer Coefficients on Vertical and Horizontal Cylinders," M. S. thesis, University of Illinois at Chicago Circle, 1981.